Haiyan Xu
Ning Gu *Editors*

Nanotechnology in Regenerative Medicine and Drug Delivery Therapy

Springer

Nanotechnology in Regenerative Medicine and Drug Delivery Therapy

Haiyan Xu • Ning Gu
Editors

Nanotechnology in Regenerative Medicine and Drug Delivery Therapy

Springer

Editors
Haiyan Xu
Department of Biomedical Engineering
Institute of Basic Medical Sciences,
Chinese Academy of Medical Sciences &
Peking Union Medical College
Beijing, China

Ning Gu
School of Biological Science and Medical
Engineering
Southeast University
Nanjing, China

ISBN 978-981-15-5385-1 ISBN 978-981-15-5386-8 (eBook)
https://doi.org/10.1007/978-981-15-5386-8

This Springer imprint is published by the registered company Springer Nature Singapore Pte Ltd.
The registered company address is: 152 Beach Road, #21-01/04 Gateway East, Singapore 189721, Singapore

Acknowledgments

The authors would like to thank for supports from the National Key Research and Development Program of China (2017YFA0205500, 2017YFA0205001), the National Natural Science Foundation of China (31571013, 21673055, 21773042, 31971295, 21790394, 31901007, 81471793, 81801771), the CAMS Innovation Fund for Medical Sciences (CIFMS 2016-I2M-3-004, CIFMS 2018-I2M-3-006, CIFMS 2019-I2M-1-004), the State Key Laboratory Special Fund (2060204), the Fundamental Research Funds for the Central Universities (3332019064, 2018PT31028), the Key Research Program of Frontier Sciences, Chinese Academy of Science (QYZDJ-SSW-SLH048), the Youth Innovation Promotion Association of Chinese Academy of Science (2018048), the Open Project Fund provided by Key Laboratory for Biomedical Effects of Nanomaterials and Nanosafety, CAS (NSKF201812), the Zhongyuan Thousand Talents Project (204200510016), the Program for Innovative Research Team (in Science and Technology) in the University of Henan Province (19IRTSTHN026), the Guangdong Natural Science Foundation of Research Team (2016A030312006), and the Shenzhen Science and Technology Program (JCYJ20160429191503002).

Contents

Abbreviation 1

124 polymer	Poly(octamethylene maleate (anhydride) 1,2,4-butanetricarboxylate)
AFM	Atomic force microscopy
AML	Acute myeloid leukemia
APDCs	Amphiphilic peptide-drug conjugates
APL	Acute promyelocytic leukemia
ATRA	All-trans retinoic acid
BP	Bispyrene
BSA	Bovine serum albumin
CA	Cellulose acetate
CD	Circular dichroism
CEC	*N*-carboxyethyl chitosan
CMC	Carboxymethyl cellulose
CNCs	Cellulose nanocrystals
Col	Collagen
CR	Complete remission
cryo-EM	Cryo-electron microscope
CS	Chitosan
CTCs	Circulating tumor cells
DM1	Maytansinoid
DTT	Dithiothreitol
EGCG	(−)-epigallocatechin-3-gallate
EPR	Enhanced permeability and retention
ESEM	Environmental scanning electron microscopy
FDA	Food and drug administration
Gel	Gelatin
GelMA	Methyl acrylic anhydride-gelatin
GGMA	Methacrylated gellan gum
GS	Gelatin sponge
HA	Hyaluronic acid
HA-SH	Thiol-modified hyaluronic acid

HCD	Hydrophobic central domain
HDAC	Histone deacetylase
hIAPP	Human islet amyloid polypeptide
HLB	Hydrophilic-lipophilic balance
HME	Hot melt extrusion
HPLC	High-performance liquid chromatography
IC_{50}	50% inhibiting concentration
IHC	Immunohistochemical
LbL	Layer-by-layer
MAAG	Methacrylated aminated gelatin
MDS	Myelodysplastic syndrome
MEL	Melamine
MeTro	Methacryloyl-substituted recombinant human tropoelastin
MIDAS	Metal ion-dependent adhesion site
MNPs	Magnetic nanoparticles
NFs	Nanofibers
NMR	Nuclear magnetic resonance
Nrp-1	Neuropilin-1
OHA	Oxidized hyaluronic acid
OPF	Oligo(poly(ethylene glycol) fumarate)
P(VDF-TrFE)	Poly(vinylidene fluoride-co-trifluoroethylene)
PAA	Poly(acrylic acid)
PAAm	Polyacrylamide
PAH	Poly(allylamine hydrochloride)
PANi	Polyaniline
PCL	Poly-ε-caprolactone or polycaprolactone
PDA	Polydopamine
PDCs	Peptide-drug conjugates
PDLLA	Poly(D, L-lactic acid)
PEDOT	Poly(3,4-ethylenedioxythiophene)
PEG	Poly(ethylene glycol)
PEGDA	Polyethyleneglycol diacrylate
PEGS	Poly(ethylene glycol)-co-poly(glycerol sebacate)
PG	Polyglycolide
PGS	Poly(glycerol sebacate)
PHEMA	Poly(2-hydroxyethyl methacrylate)
pI	Isoelectric point
PLA	Poly-DL-lactide or poly(lactic acid)
PLGA	Poly(lactic-co-glycolic acid)
PLL	Poly-L-lysine
PLLA	Poly(L-lactide)
PNIPAAm	Poly(*N*-isopropylacrylamide)
PPY	Polypyrrole
PSS	Poly(4-styrene sulfonate)
PTAA	Poly(thiophene-3-acetic acid)

PU	Polyurethane
PVA	Polyvinyl alcohol
PVDF	Polyvinylidene fluoride
PVP	Polyvinylpyrrolidone
QCSG	Glycidyl methacrylate functionalized quaternized chitosan gel
RIF	Realgar-indigo naturalis formula
ROS	Reactive oxygen species
RTG	Reverse thermal gel
SD	Standard deviation
SDS	Sodium dodecyl sulfate
SF	Silk fibroin
SPR	Surface plasma resonance
SSM	Sterically stabilized micelle
STM	Scanning tunneling microscopy
TCP	Tissue-culture-treated polystyrene
TEAR	Transformation-enhanced accumulation and retention
ThT	Thioflavin T
TKIs	Tyrosine kinase inhibitors
TNBC	Triple-negative breast cancer
TPU	Thermal plastic polyurethane
TTR	Transthyretin
VEGFR2	Vascular endothelial growth factor receptor 2
VNTR	Variable number of tandem repeats
κC	κ-carrageenan

Abbreviation 2

Cell types	Cell name	Abbreviation
Muscle cells	Rat smooth muscle cells	SMCs
	Cardiomyocyte/cardiac myocytes	CMs
	Neonatal rat ventricular myocytes	NRVM
	Neonatal rat cardiomyocytes	/
	hiPSC-derived cardiomyocytes	hiPSC-CMs
	Embryonic-stem-cell-derived cardiomyocytes	/
	Mouse embryonic stem cell derived cardiomyocytes	mES-CM
	Primary cardiomyocytes	/
	Murine neonatal cardiomyocytes	/
Myoblast cell	H9c2 rat cardiac myoblast cells	H9c2
	C2C12 myoblast cells	C2C12
Stem cell	Human pluripotent stem cells	hPS
	Human pluripotent stem cells-derived cardiomyocytes	hPSC
	Brown adipose-derived stem cells	/
	Human induced pluripotent stem cells	hiPSCs
	Mouse embryoid bodies	Ebs
	Mesenchymal stem cells	MSCs
	Human embryonic stem cells	hESC
	Umbilical cord blood (UCB)-derived multipotent mesenchymal stem cells	CB-hMSCs
	Stem cells	/
	Human mesenchymal stem cells	hMSCs
	Bone marrow derived stem cells	BMSCs
	Rat bone-marrow-derived mesenchymal stem cells	MSCs
Osteoblasts	Osteoblasts	/
	Osteosarcoma	MG-63
	Mouse osteoblast cells	/

Cell types	Cell name	Abbreviation
Nerve-related cells	Nerve stem cells	/
	Rat pheochromocytoma 12	PC12
	Neural stem cells	/
	Schwann cells	SCs
	Rat Schwann cell	RSC
	Dorsal root ganglion neurons	DRG neurons
	Neuron	/
	Human neural stem/progenitor cells (hNSPCs)	/
	Central nervous system neurons	CNS neurons
Stromal cell	Adipose tissue-derived stromal cells	ADSCs
	Fibroblasts	/
	Human cardiac fibroblast	/
	Mouse osteoblast cells	/
Epithelial cell	Epithelial cells derived from breast adenocarcinoma	MCF-7
Blood-related cells	Neutrophil	/
	Macrophage	/
	RAW 264.7 cells	/
	Platelet	/
	Endothelial cell	/

Chapter 1
Magnetically Actuated Scaffolds to Enhance Tissue Regeneration

Haiyan Xu, Suisui Hao, and Jiawei Zhou

Abstract Tissue defects beyond critical sizes and organ failure are great challenges in human health care. Biomaterial scaffold-guided tissue regeneration is one important and promising way to develop more effective therapeutic strategies to meet the clinical demands by creating microenvironments mimicking natural physiological conditions from the aspects of biochemistry and biophysics. The combination of nanotechnology in the biomaterial scaffolds have opened a new field in regenerative medicine and provided more powerful tools for developing strategies to modulate biochemical and mechanical microenvironments for tissue regeneration. In this chapter, we focused on the evolution and research progress of magnetic nanoparticles-based tissue engineering scaffolds. This chapter emphasized the synergistic effects of magnetic scaffolds in combination with external magnetic fields on cells differentiation and tissue regeneration through comprehensively reviewing the applications in multiple cells and tissues including bone, cartilage, cardiac, endothelial, nerve, Schwann cells, fibroblasts and macrophages, following the introduction of biological effects exerted by magnetic fields and magnetic scaffolds separately. The combination strategy allows for providing mechanical stimulations directly and remotely controls cells behaviors and fates in vivo without invasion, and provides promising platforms for drug screening in vitro and ex vivo.

Keywords Regenerative medicine · Tissue engineering · Magnetic scaffold · Mechanical stimulation · Remotely control

H. Xu (✉)
Department of Biomedical Engineering, Institute of Basic Medical Sciences, Chinese Academy of Medical Sciences and Peking Union Medical College, Beijing, P. R. China
e-mail: xuhy@pumc.edu.cn

S. Hao
Department of Pharmacology and Chemical Biology, University of Pittsburgh School of Medicine, Pittsburgh, PA, USA

J. Zhou
Peking Union Medical College, Beijing, P. R. China

H. Xu, N. Gu (eds.), *Nanotechnology in Regenerative Medicine and Drug Delivery Therapy*, https://doi.org/10.1007/978-981-15-5386-8_1

1.1 Introduction

Magnetism is a long historical and intriguing physical cue that can alter the behaviors of a broad range of cells; therefore, the implementation of magnetic features in biomaterial scaffolds may offer innovative opportunities to control cell populations within engineered 3D microenvironments, with the potential to enhance their use in tissue regeneration or in cell-based therapies. For decades, magnetic nanoparticles, especially iron oxide nanoparticles, have attracted intense research interests in biomedical fields because the manufacture technologies are maturing, and they have shown promising perspectives in various applications, such as bio-separation, detection and diagnosis, medical imaging, thermal treatment against tumor, and targeting drug delivery [1–3]. In the past decade, a new application potential of magnetic nanoparticles in tissue engineering and regenerative medicine has been explored with increasing interests from the aspects of magnetically actuated mechanical stimulation and remote control, by integrating magnetic nanoparticles into substrates or implantable scaffolds to provide mechanical forces directly to cells grown on and inside. The application modality included magnetic scaffolds alone or in combination with external applied magnetic fields.

Motivations of integrating magnetic nanoparticles into various matrices for uses in tissue engineering can be summarized into following aspects: First, magnetic nanoparticles would form magnetic phases in microscale that distribute in matrices. These aggregated nanoparticles would provide local magnetic moments or magnetic fields, which is assumed to be beneficial to the tissue regeneration according to the literatures of biological effects of magnetic fields. Second, the induction of magnetic nanoparticles brings magnetic property to scaffolds, which endows the scaffolds capacity of reloading with bioagents in situ after implantation. For example, magnetic scaffolds are expected to attract and take up growth factors, stem cells or other bioagents bound to magnetic nanoparticles in vivo by the guidance of an external magnetic field. The magnetic property of scaffolds can also be used to control microstructures of scaffolds (for example, to form aligned morphology) or to improve implant fixation and stability in vivo, by the remote control of external magnetic fields. And third, implantable scaffolds containing superparamagnetic nanoparticles can be magnetized by responding to external applied magnetic fields, which allow for generating local strain-induced deformation to apply mechanical stimulations directly to cells grown on the scaffolds.

This chapter will emphasize the synergistic effects of magnetic scaffolds in combination with external magnetic fields on cells differentiation and tissue regeneration, through comprehensive reviewing the applications in multiple cells and tissues including bone, cartilage, cardiac, endothelial, nerve, Schwann cells, fibroblasts, and macrophages, following the introduction of biological effects exerted by magnetic fields and magnetic scaffolds separately. The combination strategy allows for providing mechanical stimulations directly and remotely controls cells behaviors and fates in vivo without invasion and provides promising platforms for drug screening in vitro and ex vivo.

1.2 Biological Effects of Magnetic Fields on Tissue Regeneration

Magnetic fields include static (SMF) and electromagnetic fields (EMF). The therapeutic functions of magnetic fields have attracted clinical and research attentions for many years [4]. The SMF is usually generated by permanent magnetic materials, and there are various methods for obtaining the electromagnetic field generated by an arbitrarily moving point charge in free space. The EMF can be subdivided into pulse electromagnetic fields (PEMFs), alternating magnetic field (AMFs), or rotating magnetic fields (RMFs). Among them, SMFs and PEMFs are used most widely. According to the field intensity, SMF can be classified into weak field (less than 1 mT), moderate field (1 mT–1 T), strong field (1–5 T), and ultra-strong field (>5 T). It has been reported that the magnetic field with moderate intensity could enhance pre-osteoblasts proliferation and ECM production, and templated mineral deposition more rapidly than the control culture [5]. As an example, exposure to SMF of 160–340 mT enhanced the bone formation of rat calvaria cells [6] through the activation of p38 phosphorylation at the cellular level to stimulate osteoblastic differentiation [7]. There are also literature reports about the effects of magnetic fields on nerve system. For example, low-frequency magnetic fields could activate *N*-methyl-D-aspartate receptors in glutamatergic Ca^{2+} channels to promote neuronal differentiation [8] and might improve depressant behavior and cognitive dysfunction mainly by modulating synaptic function [9].

Impacts of the magnetic stimulation on human mesenchymal stem cells (hMSCs) have also been explored, as hMSCs are widely accepted as seeding cells, and the control of mesenchymal stem cells (MSC) by physical cues is of great interest in regenerative medicine. A group reported that equine adipose-derived mesenchymal stem cells (ASCs) exhibited higher mRNA levels of bone morphogenetic protein-2/4 (BMP-2/4), Sox9, and type I collagen when cultured under the magnetic field of 0.2 T. In addition, the cells cultured in the magnetic field reached the population doubling time earlier, because the colony-forming potential of equine ASCs was higher when cells were cultured under magnetic field conditions. Interestingly, exposure to the magnetic field increased the number of secreted microvesicles in comparison to the control culture as well as increased the production of growth factors [10]. Another study reported the effect of low-frequency EMF on hMSCs during chondrogenic differentiation, the cultures were exposed to the low-frequency magnetic fields (5 mT) [11]. It was observed that the effect of EMF on collagen type II expression was cell passage-dependent and exclusively detected at higher cell passages. Under the EMF and the addition of human fibroblast growth factor 2 (FGF-2) and human transforming growth factor-β3 (TGF-β3), hMSCs showed a significant increase in collagen type II expression at passage 6, indicating that the very low-frequency EMF was able to improve the growth factor-induced chondrogenic differentiation of hMSCs, however, when growth factors were absent, there was no staining detected for safranin-O and collagen type II, indicating that the EMF could not induce chondrogenic differentiation alone. SMF exposure could

also affect the cell viability and capacity of osteogenic differentiation in rat dental pulp cells (DPCs) [12]. It is interesting to note that exposure to SMF alone did not affect the dental pulp cell proliferation, only when exposed to SMF with the supplementary Dex/b-GP, the cell differentiation was significantly enhanced at the seventh and ninth day of culture when compared with the control culture, which was speculated that the magnetic field played a cooperative role via the ECM-mediated activation of ERK1/2-Cbfa1 signaling, while the new ECM deposition was time consuming. Another study showed that the magnetic field could stimulate biological functions of MSC; however, the responses of cells depended strongly on the substrate to which they adhere and on the crosstalk between integrin-mediated signals and soluble factors [13]. The results again implied that the magnetic stimulation alone on cells is not enough for the bone repair and regeneration, the microenvironment where the bone cells live is likely to play crucial synergy roles in the regeneration process. Another group had MSCs seeded in a composite scaffold composed of hydroxyapatite and collagen I, the construct was placed in a dynamic perfusion bioreactor and exposed to EMF of 15 Hz/1 mT. The applied EMF could promote osteogenic differentiation with the inducing medium. When implanted in a defect hole of 4 mm in width and 8 mm in depth that was created in each lateral femur condyle of rabbits, micro-CT results revealed that EMF could promote integration at bone–implant interface and bone regeneration after 12 weeks [14]. These results implied that scaffolds might be necessary as media for magnetic fields to elicit promoting effects on MSCs differentiation.

1.3 Biological Effects of Magnetic Materials on Tissue Regeneration

Inspired by the biological effects elicited by the low or moderate intensity of magnetic fields, it has been considered that magnetic materials may have positive effects on scaffold-guided tissue regeneration as well, because magnetic materials usually consist of iron (Fe), cobalt (Co), or nickel (Ni), and these materials can produce magnetic fields directly or indirectly, as it is well known that permanent magnets produce static magnetic fields (SMFs). As examples of the efforts, the roles of magnetic scaffolds in the guidance of bone tissue regeneration have been investigated largely. In case of degenerative disease or lesion, bone tissue replacement and regeneration are an important clinical goal. In long period the repair for critical size defects rely on implantable grafts that are not biodegradable. The emerging of tissue engineering and regenerative medicine provide the concept of developing biodegradable scaffolds that are 3D structural supports, allowing cellular infiltration and subsequent integration with the native tissue. Several ceramic hydroxyapatite (HA) scaffolds with high porosity and good osteointegration have been developed in the past few decades but they have not solved completely the problems related to bone defects, a major challenge is the speed of scaffold-induced new bone formation is

too low to meet the clinical demand [15, 16]. Researchers have been making great efforts to overcome the problem; the utilization of magnetic nanoparticles is one of the directions.

Early investigations mainly addressed the biocompatibility of magnetic nanoparticles incorporated in matrices. For example, researchers developed a simple and inexpensive technique able to transform standard commercial scaffolds made of hydroxyapatite and collagen into magnetic scaffolds by dip-coating the scaffolds in aqueous ferrofluids containing iron oxide nanoparticles coated with various biopolymers. By this way, the nanoparticles were integrated into the structure of the scaffolds, providing the latter with magnetization values as high as 15 emu/g at 10 kOe [17]. These values were considered suitable for generating magnetic gradients, enabling magnetic guidance in the vicinity and inside the scaffold. It was reported that the magnetic scaffolds did not suffer from any structural damage during the process, maintaining their specific porosity and shape. Moreover, they do not release magnetic particles under a constant flow of simulated body fluids over a period of 8 days, indicating the good stability of the scaffold. Computer simulations revealed that the magnetic field generated by magnetic scaffolds was ready within the useful range for in vivo applications. Cellular experimental results showed that the composite scaffold supported the proliferation of human bone marrow-derived stem cells (HBMSCs), the cells covered the whole surface and filled most of the macropores of scaffolds, and no statistically significant differences in cellular viability and osteoblastic differentiation among all types of scaffolds at each time point were observed. Furthermore, the composite of hydroxyapatite (HA) dipping magnetic fluids was tested in a magnetic field of 320 mT, no negative effects arising from the presence of magnetite [18]. A comprehensive comparison study for the bone tissue formation was conducted by the same group in a preclinical rabbit model of critical femoral defect treated either with a HA/magnetite (90/10 wt%) or pure HA porous scaffolds at 4 and 12 weeks after implantation, indicating that both scaffolds were able to allow bone regeneration, and that the HA scaffold dipping magnetic fluids did not have short-term adverse effects on biocompatibility and bone formation ability [19]. Another pioneer work is to fabricate magnetic composites that were composed of CaP ceramic and magnetic nanoparticles (CaP-MNP). In the fabrication, superparamagnetic nanoparticles were integrated to two kinds of CaP ceramics, one was hydroxyapatite (HA), the other one was a composite of HA and tricalcium phosphate in a ratio of 65:35, named HT. When bone-related cell line Ros17/2.8 and MG63 cells were seeded in the composites and incubated for 4 or 7 days, the cell proliferation was significantly promoted compared with that of non-magnetic scaffolds. The possible influence of magnetic materials on bone morphological protein (BMP) was concerned in this investigation. BMP-2 was loaded on the magnetic scaffolds that were implanted subcutaneously in the fasciae of rat back muscles for 30 days. The in vivo test showed that the expression of BMP-2 was accelerated by HT containing superparamagnetic nanoparticles, and new bone-like tissue formation was observed, indicating the function of loaded BMP-2 was not affected by the incorporation of superparamagnetic nanoparticles. Importantly, it was observed that ALP secretion of Ros17/2.8 cells was increased on the magnetic

composites more than those on nonmagnetic composites after 14 days incubation, but the magnetic composites did not affect the ALP secretion of MG63 cells. Those results showed an important cue that the CaP-MNP composites could promote osteogenetic differentiation as well as the proliferation [20].

In addition to inorganic scaffolds, iron oxide nanoparticles are widely employed in polymer-based scaffolds, aiming to improve the biocompatibility and mechanical strength. One typical example is that a nanofibrous scaffold made by electrospinning technique from a mixture of poly-ε-caprolactone (PCL) and γ-Fe_2O_3 nanoparticles of 23 nm in diameter. The scaffolds obtained the magnetic responsive property, which contributed to the enhancement of adhesion and proliferation of porcine mesenchymal stem cells. Importantly, the PCL-based scaffold-induced osteogenic differentiation of mesenchymal stem cells, which was evidenced by the increased ALP activity [21]. Similarly, magnetic nanofibrous scaffolds of PCL incorporating citrated magnetic nanoparticles (MNP) of 12 nm in diameter were fabricated by using electrospinning technique, the content of MNPs was up to 20% in the solution. The incorporation of MNPs greatly improved the hydrophilicity of the nanofibers as well as enhanced the tensile mechanical properties of the nanofibers. In particular, the tensile strength increase was as high as 25 MPa at 15% MNPs, much higher than 10 MPa for pure PCL. The PCL-MNP nanofibers exhibited magnetic behaviors, with a high saturation point and hysteresis loop area, which increased gradually with MNP content. The incorporation of MNPs substantially increased the degradation rate of the PCL nanofibers in a content dependent manner. When subcutaneously implanted in rats, the composited nanofibers significantly improved initial cell adhesion and subsequent penetration through the nanofibers for rat bone marrow MSCs, compared to the pure PCL control, and increased the alkaline phosphatase activity and the gene expression of collagen I, osteopontin, and bone sialoprotein. Noted that they induced substantial neoblood vessel formation which greatly limited in the pure PCL, while exhibited minimal adverse tissue reactions [22]. The same formulation of PCL and MNPs was processed into porous scaffolds by using salt-leaching approach, which also showed the superparamagnetic behavior. When applied on bone repair, similar results were obtained, confirming the effects observed in the nanofibrous scaffolds. As shown that the incorporation of MNPs greatly improved the hydrophilicity and water swelling of scaffolds. More mineral nanocrystallites covered on the surfaces of the composite scaffolds than on the PCL scaffolds in the in vitro acellular mineralization experiment. The mechanical stiffness increased significantly with the addition of MNPs when tested under both static and dynamic compressed wet conditions. The subcutaneous implantation in rats for 2 weeks revealed favorable tissue compatibility, with substantial fibroblastic cell invasion and neoblood vessel formation while exerting minimal inflammatory reactions in the testing groups [23]. From these investigations we can notice the important roles of iron oxide nanoparticles in the scaffolds for enhancing bone tissue regeneration. When make further comparison with data from above references, it seemed the smaller the nanoparticles (23 nm vs. 12 nm), the stronger the enhancing effects. Another example is magnetic PLGA/PCL scaffolds that were fabricated using a combination of the electrospinning technique and layer-by-layer

assembly of superparamagnetic iron oxide nanoparticles (IONPs) greatly enhanced the hydrophilicity and increased the elastic modulus of the scaffolds. At the early stage of cell culture, the adhesion and spreading of ADSCs of IONPs group were more stretched and spindle-like compared to those on the control groups, which indicated that IONPs-containing scaffolds affected cellular behavior at an early stage. It could be noticed that IONPs group induced ADSCs osteogenic differentiation, evidenced by the highest ALP activity. Higher mineralization rate also confirmed the importance of magnetic nanomaterials as a bioactive interface between cells and scaffolds [24].

Chitosan and collagen are two kinds of biological materials widely investigated for scaffolds fabrication. A group prepared composite scaffolds containing hydroxyapatite nanoparticles (nHAP) and Fe_3O_4 nanoparticles (Fe_3O_4 NPs), and the substrate of the scaffolds was the mixture of chitosan and collagen (CS/Col). It is interesting that during the cell culture, a mass of hydroxyapatite microparticles could be observed forming on the surfaces of scaffolds containing Fe_3O_4, whereas did not on the surface of CS/Col/nHAP, suggesting that Fe_3O_4 NPs enhanced mineralization. The composite scaffolds (CS/Col/Fe_3O_4/nHAP) not only showed superior structural and mechanical performance for pre-osteoblasts cell line MC3T3-E1 cells adhesion and proliferation, but also had a higher bone regeneration ability when implanted into the SD rats' skull defects comparing to control group [25]. In another kind magnetic scaffold composed of HA, collagen, and magnetic nanoparticles, the magnetic phase could act as a sort of cross-linking agent for the collagen, inducing a chemical-physical-mechanical stabilization of the material and allowing for the control of the porosity network of the scaffold, while the hydroxyapatite (HA) was directly nucleated onto collagen fibers during their self-assembly, representing the biomineral calcium phosphate phase [26]. Gelatin is also one widely applied biological material in tissue engineering. When integrated with superparamagnetic nanoparticles (SPIONs), the magnetic gelatin sponge (GS) was implanted in the incisor sockets of Sprague-Dawley rats sacrificed at 2 and 4 weeks. In addition to the enhancement of the bone regeneration, the scaffold degradation and interaction with host tissues could be visually monitored over time by MRI, and a significant decrease in the signal intensity of T2-weighted magnetic resonance imaging (MRI) was also observed. This is another advantage of superparamagnetic iron oxide nanoparticles, the residual SPIONs, together with newly formed bone [27]. Magnetic composites also showed application potentials in the treatment of tumor related-bone defects. For example, magnetic $SrFe_{12}O_{19}$ nanoparticles modified-mesoporous bio-glass (BG)/chitosan (CS) porous scaffold (MBCS) not only triggered tumor apoptosis and ablation by elevating the temperatures of tumors under the irradiation of near-infrared (NIR) laser, because the $SrFe_{12}O_{19}$ nanoparticles in MBCS improved the photothermal conversion property, but also promoted the expression levels of osteogenic-related genes (OCN, COL1, Runx2, and ALP) and the new bone regeneration by activated BMP-2/Smad/Runx2 pathway, indicating the osteogenic differentiation was effectively induced by the magnetic composite nanoparticles. In this process, the residual SPIONs and newly formed bone could be monitored in the treatment of tumor related-bone defects [28]. Another example

is the fabrication of 3D porous Mg_2SiO_4-$CoFe_2O_4$ nanocomposite scaffolds with interconnected porosity and desirable mechanical properties close to cancellous bone, loading chemotherapeutics for bone cancer treatment. When exposed with electromagnetic fields of 100, 125, 150, and 200 Oe under 200 kHz, the scaffolds could produce heat for hyperthermia-based chemotherapies and displayed good biocompatibility with MG63 cells [29]. Nevertheless, it should be noted that there were literatures reporting no osteogenestic differentiation was induced by polymeric magnetic scaffolds. For instances, the induction of osteogenestic differentiation was not detected upon the electrospun membrane of integrating magnetic nanoparticles of Fe_3O_4 into biodegradable chitosan (CS) and poly vinyl alcohol (PVA), though human osteoblast-like cells MG63 grew well on the composite scaffold [30]. The electrospun membrane composed of poly(lactic-co-glycolic acid) (PLGA) and hydrophobic superparamagnetic nanoparticles (MNPs) showed good biocompatibility and significantly promoted cell proliferation compared with PLGA nanofibrous scaffold. Again, the composite scaffolds had no effects on the differentiation of MC3T3-E1 cells [31].

As for the dental tissue regeneration, magnetic scaffolds are being investigated in recent years, which is still an unmet clinical need. So far, no therapies have been completely successful in regenerating dental tissue complexes such as periodontium. One of the major challenges is the lack of scaffolds that can guide and direct cell fate toward the reconstruction of different mineralized and nonmineralized dental tissues. The osteogentic effect was reported by using magnetic scaffolds in some investigations. For example, composite foam-like scaffolds of PCL and Fe_3O_4 nanoparticles were fabricated by a salting out procedure, there were pores ranging from 250 to 500 μm inside of the scaffold, the size distribution was considered suitable for cellular population and odontogenic differentiation. When human dental pulp cells (HDPCs) were cultured on the magnetic composite scaffolds containing Fe_3O_4 nanoparticles up to 10 wt%, they exhibit good viability. It is interesting that the migration rate of the cells was enhanced after incubated with the composite scaffolds, determined by the in vitro scratch assay. At the same time, the adhesion of HDPCs was significantly promoted. Furthermore, the magnetic scaffolds significantly influenced the odontogenic differentiation of HDPCs, supported by the increased ALP activity, mRNA expression of odontogenic markers, and mineralized nodule formation. Mechanisms may include the upregulation of integrin subunits of α1, α2, β1 and β3, and the activation of downstream pathways including FAK, paxillin, p38, ERK MAPK, and NF-κB [32]. The magnetic scaffolds with nanofibrous structures were also showed similar positive effects on the human dental pulp cell (HDPCs) behaviors. The growth of HDPCs was significantly enhanced on the magnetic scaffolds compared with that on the nonmagnetic counterpart. The odontogenic differentiation of cells was significantly upregulated by the culture with magnetic scaffolds. Furthermore, the magnetic scaffolds promoted the HDPCs-induced angiogenesis of endothelial cells. Mechanistic studies indicated that the expression of signaling molecules, Wnt3a, phosphorylated GSK-3β and nuclear β-catenin, was substantially stimulated by the magnetic scaffolds; in parallel, the MAPK and NF-κB were highly activated when cultured on the magnetic nanofiber scaffolds [33]. Considering that tooth is a complex organ made of highly

mineralized tissues where the nonmineralized periodontal ligament (PDL) connects the alveolar bone to the cementum and ensures tooth functionality and stability, a very compact scaffold was made by integrating three layers, one was the bone-like layer, consisting iron-doped hydroxyapatite (FeHA), acting as mineral phase nucleated on collagen fibers; the second one was a ligament-like layer consisting of collagen, the third one was the cementum-like layer consisting of FeHA and cellulose acetate (CA), preserving its dense morphology. The scaffold was endowed with a superparamagnetic ability and showed that the chemical composition and morphology of the scaffolds favor substantial cell viability and proliferation [34].

Magnetic nanoparticles are also utilized as carriers of loading growth factors in the treatment of spinal cord injuries and might act together as imaging contrast to monitor the healing process by MRI. For example, free bFGF has short half-life of about 3–10 min due to rapid enzymatic degradation, this disadvantage leads to loss of biological activity and functions. A magnetic fibrin hydrogel scaffolds were prepared by blending thrombin-conjugated γ-Fe_2O_3 nanoparticles with fibrinogen to form magnetic fibrin hydrogel, with the addition of magnetic nanoparticles conjugated with basal fibroblast growth factor (bFGF). The composite hydrogel was applied to human nasal olfactory mucosa (NOM) cells that are primary cells of interest for implantation into spinal cord injuries. The conjugated bFGF enhanced the growth and differentiation of the NOM cells in the fibrin scaffolds significantly, compared to the same or even five times higher concentration of the free bFGF. In the presence of the bFGF-conjugated magnetic nanoparticles, the cultured NOM cells proliferated and formed a three-dimensional interconnected network composed mainly of tapered bipolar cells [35].

Data collected from some of above investigations were summarized in Table 1.1. It is seen that all the magnetic scaffolds showed biocompatibility, in some cases magnetic scaffolds alone did not induce osteogenesis though some did. It seems whether magnetic scaffolds could induce osteogenic differentiation or maturation is largely involved with the cell type and the chemistry and microstructures of scaffolds. And should be noted that even the osteogenesis was induced by magnetic scaffolds, there was still a large space for the degree to increase.

1.4 Combination of Magnetic Scaffolds and Magnetic Fields to Accelerate Tissue Regeneration

The combination of magnetic scaffolds and magnetic fields has emerged since 2010. This strategy's aim is to provide stronger and remotely controllable stimulations to bone-related cells to enhance osteogenesis and new bone formation. In recent years, this combination strategy has gained increasing research interests and has been demonstrated effective to multiple cell type including bone, cartilage, endothelial, nerve, fibroblasts, macrophages, and Schwan cells. Data from some investigations are summarized in Table 1.2, the magnetic component, magnetic field strength, scaffolds composition, and biological effects were emphasized.

Table 1.1 Magnetic scaffolds and biological effects on cells

Magnetic component	Other components	Preparation methods	Structure	Cell and animal model	Biological effects	Refs.
Fe_3O_4 NPs (5 nm)	Hydroxyapatite and/or $Ca_3(PO_4)_2$	Foamed and sintered, followed by immersed into Fe_3O_4 NPs colloid	Porous	Ros17/2.8; MG63; implanted in the skin incision at the midline of the SD rat back	Enhanced proliferation and ALP activity increased; new bone-like tissue formation observed	[1]
Fe_3O_4 NPs	Hydroxyapatite nanoparticles, Chitosan and Collagen	in situ crystallization and freeze-drying	Porous	MC3T3-E1; Full-thickness defects with diameter of 5 mm on the middle ridge of skull in SD rats	Enhanced adhesion, proliferation, and differentiation; better tissue compatibility and higher bone regeneration ability	[17]
Fe_3O_4 NPs (10.7 nm)	PCL	Salt-leaching	Porous	MC3T3-E1; subcutaneous implantation of SD rats	Enhanced proliferation, differentiation, and mineralization Favorable tissue compatibility, neoblood vessel formation, minimal inflammatory reactions	[8]
Iron-doped hydroxyapatite (FeHA)	PCL/FeHA	Rapid Prototyping	3D porous	Bone marrow mesenchymal stem cells (hBMSCs) Implantation in critical bone defect in lateral femoral condyle of male rabbits	Promote adhesion, proliferation, and differentiation; new bone formation after 4 weeks	[10]
Magnetic nanoparticle (Mgn)	Hydroxyapatite	Casting	Porous	Saos-2; critical bone defect in lateral femoral condyle of male rabbits	Enhanced proliferation Good compatibility and bone regeneration in vivo	[5]
Fe_3O_4 NPs (12 nm)	PCL	Electrospinning	Nanofibrous	Rat bone marrow mesenchymal stem cells (MSCs) Small subcutaneous pouches in the back area laterally from the spine of SD rats	Promote adhesion, penetration and differentiation Induce neoblood vessel formation and bone regeneration	[7]

Iron oxide nanoparticles (<50 nm)	Hydroxyapatite	Foamed and sintered	Porous	Critical femoral defect of rabbit	No short-term adverse effects on biocompatibility and bone formation ability	[19]
SPOINs (9 nm)	Gelatin sponge	Sponge immersed into SPIOs colloid	Sponge	A rat model of mandible incisor sockets	Enhanced bone repair and preserved the alveolar ridge after tooth extraction	[18]
Fe_3O_4 NPs (12–15 nm)	Chitosan and PVA	Electrospinning	Nanofibrous	MG63	Enhanced adhesion and proliferation	[2]
Fe_3O_4 (8.47 nm)	PLGA	Electrospinning	Nanofibrous	Ros17/2.8; MC3T3-E1	Enhance proliferation and induce differentiation	[4]
Commercial magnetic NPs (50–100 nm)	PCL	Electrospinning	Nanofibrous	Porcine mesenchymal stem cells (MSCs)	Enhanced adhesion, proliferation, and ALP activity increased	[12]
Fe_3O_4 NPs (20–40 nm)	Hydroxyapatite and collagen	Assembly and drop-wise	Porous	Human bone marrow mesenchymal stem cells (hBMSCs)	Support adhesion, proliferation, and differentiation	[3]
$SrFe_{12}O_{19}$ (30 nm in thicknesses, 50–150 nm in widths	Bio-glass and Chitosan	Sol-gel	Mesoporous	Human bone marrow mesenchymal stem cells (hBMSCs)	Promote proliferation and induce differentiation	[20]
Mg_2SiO_4-$CoFe_2O_4$		Sol-gel	3D porous	MG63	Good biocombability	[29]
γ-Fe_2O_3 (10 nm)	PLGA/PCL	Electrospinning and layer-by-layer assembly	3D macroporous	Adipose-derived stem cell (ADSCs)	Enhanced adhesion and differentiation	[23]
Fe_3O_4 NPs	Chitosan	Covalent conjugation and co-precipitation	3D sphere	mesenchymal stem cells (MSCs)	Promoted viability and mineralization	[21]
FeCaP (<2 μm)	Calcium phosphate	One-pot hydrothermal and post-reduction annealing	Microsphere	Adipose-derived stem cell (ADSCs)	Good biocompatibility	[16]

(continued)

Table 1.1 (continued)

Magnetic component	Other components	Preparation methods	Structure	Cell and animal model	Biological effects	Refs.
Fe_3O_4 NPs	Hydroxyapatite	Dissolution–precipitation reaction, coating	Orientated nanorods	Human bone marrow mesenchymal stem cells (hBMSCs)	Better adhesion, spreading and proliferation	[9]
Fe_3O_4 NPs (5–10 nm)	PCL	Salt-leaching	Porous	Human dental pulp cells (hDPCs)	Enhance adhesion, migration, and induce differentiation	[13]
Fe_3O_4 and Fe_2O_3 NPs	Hydroxyapatite/collagen	Hybrid assembly	Tri-layer porous	Mesenchymal stem cells (MSCs)	Favor viability and proliferation	[22]
Fe_3O_4 NPs (10.8 nm)	PCL	Electrospinning	Nanofibrous	Human dental pulp cells (hDPCs) and human umbilical vein endothelial cells (HUVECs)	Enhance proliferation and induce differentiation, pro-angiogenesis	[15]
γ-Fe_2O_3 (19.8 nm)	Thrombin/bFGF	Physical/covalent conjugation	3D porous	Nasal olfactory mucosa (NOM) cells	Show migration, growth, and differentiation	[6]
Fe_3O_4 NPs (9 nm)	Collagen	Electrospinning	Aligned fibers	Neurons PC12	Leading neurons to be elongated and directed	[11]

Table 1.2 Effects of magnetic scaffolds in combination with magnetic fields on tissue regeneration

Magnetic component	Other components	Preparation	Structure	Magnetic field	Cell and animal model	Biological effects	Refs
γ-Fe_2O_3 NPs (14 nm)	PLA/hydroxyapatite nanoparticles	Electrospinning	Nanofibrous	1 mT to cells, 25 mT to rabbit	MC3T3-E1 Rabbit model of lumbar transverse defects	Enhanced proliferation and differentiation in cell Accelerated repair for bone defect	[1, 5]
Fe_2O_3 NPs (10 nm)	PCL	Salt-leaching	Porous	15–25 mT	Mouse calvarial osteoblasts and Human umbilical vein endothelial cells (HUVECs) 5-mm-diameter calvarial critical-sized defect of mice	Differentiation, endothelial cells angiogenesis In vivo results showed improved bone formation	[9]
Commercial magnetic NPs (50 nm)	Composite of hydroxyapatite and collagen	Concurrent nucleation and immersed in MNPs colloid	Porous	1.2 T	Cylindrical defects in the lateral condyle of the distal femoral epiphysis on rabbits	Well-ordered regenerated tissue and higher level of bone maturation	[6, 10]
Fe_2O_3 NPs (8 nm)	Hydroxyapatite	Microwave-assisted foaming and immersing	Porous	10 Oe, 50 Hz	ROS 17/2.8 MC3T3-E1	Enhanced proliferation and differentiation	[4]
FeHA	Collagen	pH-driven self-assembly	Porous	320 mT	MG63	Promote proliferation and differentiation	[7]
Fe_2O_3 NPs	nHA/PLLA	Low-temperature rapid prototyping	3D porous	100 mT	Bone marrow mesenchymal stem cells (bMSCs)	Induce differentiation	[12]
Fe_3O_4 NPs	PLLA	Electrospinning	Nanofibrous	100 mT	MC3T3-E1	Promote adhesion, proliferation, and differentiation	[8]

(continued)

Table 1.2 (continued)

Magnetic component	Other components	Preparation	Structure	Magnetic field	Cell and animal model	Biological effects	Refs
Fe_3O_4 NPs (10 nm)	PLA/hydroxyapatite nanoparticles	Electrospinning	Nanofibrous	10 mT	Bone marrow mesenchymal stem cells (BMSCs)	Induce differentiation	[9]
γ-Fe_2O_3 NPs (10 nm)	PLA/nHA	Electrospinning	Nanofibrous	10 mT	MC3T3-E1, Bone marrow mesenchymal stem cells (bMSCs)	Promote differentiation, angiogenesis and osteogenesis	[36]
$CoFe_2O_4$ nanoparticles	PVDF and methacrylated gellan gum (GGMA) gel	Casting	Film	220 mT	MC3T3-E1	Good viability	[52]
$CoFe_2O_4$ nanoparticles	$CoFe_2O_4$/PVDF nanoparticles	Using a nylon template	3D porous	230 Oe at a frequency of 0.3 Hz	MC3T3-E1	Higher proliferation rate and elongated morphology	[53]
Terfenol-D particles	P(VDF-TrFE) polymer	Casting	Film	Varying magnetic field	MC3T3-E1	Enhanced the proliferation of pre-osteoblast	[54]
Fe_3O_4 NPs	Collagen gel	Plastic compression	3D collagen	72–144 mT	MG63	Promote proliferation, mineralization, and differentiation	[16]
Iron oxide nanoparticles (4–20 nm)	Collagen/ hydroxyapatite	Direct laser writing	3D multilayered	100–250 mT	MG63	Enhance proliferation and induce differentiation	[17]
Fe_2O_3 NPs	Silk fibroin/chitosan	Freeze-casting	Hydrogel with lamellar structure	3 mT	MG63	Good biocompatibility	[42]
Fe_3O_4 (250 nm)	κ-Carrageenan hydrogels	Casting	Membrane	350 mT, 2 Hz	Human adipose-derived stem cells (hADSCs)	Promote chondrogenic differentiation	[18]

Commercial magnetic NPs	RADA16 peptide		Hydrogel	1 mT with a pulse frequency of 15 Hz	Human adipose-derived mesenchymal stem cells (hASCs)	Enhanced osteogenic differentiation	[44]
FeHA nanoparticles	PCL	Pellets assembly	Cylindrical scaffolds	30 mT under the frequency 70 Hz for 6 h with 20 intervals of 18 min	Human mesenchymal stem cells	Better cell adhesion and spreading	[50]
Commercial magnetic NPs (100 nm)	Agarose gel	Partial thermal setting	Trilayered	0.4, 0.5 or 0.75 T	Bovine chondrocytes	Good viability	[19]
Fe_3O_4 MNPs	Poly(lactic-co-glycolic acid) (PLGA)		3D porous	45 mT	D1 mouse MSCs	Increase adhesion and migration and chondrogenic differentiation	[61]
Fe_3O_4	Agarose hydrogels	Covalently bound	Porous	0.8 T	Human mesenchymal stem cells (MSCs)	Induce chondrogenesis	[20]
Superparamagnetic iron oxide NPs (11–12 nm)	PLLA/collagen	Electrospinning	Fibrous	0.03–0.62 T	Primary neurons	Promote neurite outgrowth and directional guidance	[35]
Magnetic NPs (100 nm)	Alginate gels	Magnetic manipulation	3D hydrogel	255 G	Primary neurons PC12	Enhanced growth and elongation	[68]
Fe_3O_4 NPs (30 nm)	Chitosan/ glycerophosphate	Freeze-dry	Porous	2 mT, 50 Hz	Schwann cells; left sciatic nerve of SD rats	Enhance proliferation and higher regeneration-related gene expression In vivo, viability increased, nerve regeneration and functional recovery promoted	[28, 80]

(continued)

Table 1.2 (continued)

Magnetic component	Other components	Preparation	Structure	Magnetic field	Cell and animal model	Biological effects	Refs
γ-Fe_2O_3 (10 nm)	PLA/Hydroxyapatite nanoparticles	Electrospinning	Nanofibrous	5 mT, 10 mT	Macrophage cell line RAW264.7 Subcutaneous implantation of C57 mice	Enhanced proliferation, promote M2 phenotype polarization Conditioned medium-enhanced angiogenesis and osteogenesis Enhanced angiogenesis around the implant	[32]
Fe_3O_4 NPs	Alginate	Freeze-dry	Macroporous	10–15 Oe, 5 Hz	Cardiac cells, fibroblasts	Promote adhesion, spreading, and integration of cardiac patch	[26]
γ-Fe_2O_3 (10 nm)	PLA/nHA	Electrospinning	Nanofibrous	5 mT, 10 mT	NIH3T3	Promote pro-regeneration phenotype polarization, induce angiogenesis, and osteogenesis	[33]
Fe_3O_4 nanoparticles	Mixture of fibrin and agarose	Casting	Hydrogel	0–48 kA/m in intensity	Oral mucosa fibroblasts	The mechanical properties of the substitutes could be reversibly tuned by the magnetic fields	[78]
Fe_3O_4 NPs	Alginate	Freeze-dry	Macroporous	10–15 Oe, 40 Hz	Bovine aortic endothelial cells	Promote proliferation and vasculogenesis	[24, 25]

1.4.1 Bone

To verify whether magnetic scaffolds can be actuated by external applied magnetic field and play roles together in the scaffold-guided bone tissue regeneration, a nanofibrous composite film was fabricated with poly lactide (PLA), hydroxyapatite nanoparticles (nHA), and γ-Fe_2O_3 nanoparticles of 14 nm in diameter by using electrospinning technique, while nanofibrous films composed of PLA and nHA was fabricated as control. The magnetic composite film displayed superparamagnetic property, showing an almost immeasurable coercive force and remanence. For the cell culture, the films were placed on the bottom of cell culture wells, and the static magnetic field (MF) was set up by fixing permanent magnets to the culture system. There was a high intensity area along the plate sides, which decreased sharply and form a homogeneous and low intensity area in some culture wells with the intensity of 1 mT, where pre-osteoblasts (MC3T3-E1) were seeded. It was not surprise that the superparamagnetic nanoparticles of γ-Fe_2O_3 embedded in the fibers and the applied static magnetic field acted in a synergistic way to boost the cells proliferation, but striking and more importantly, the combination strategy enhanced the osteogenic differentiation of cells, evidenced by the significantly increased ALP amount after 17 days of culture than that on the same composite films but without the applied magnetic field. This result for the first time clearly showed a sign that γ-Fe_2O_3 nanoparticles incorporated in the PLA and the magnetic field enhanced the osteogenesis in a synergistic way [36]. Further animal experiments validated this concept in vivo. The magnetic composite film was folded into scaffolds with proper shape and size and implanted in white rabbit model of lumbar transverse defects. The rabbits after surgery were housed in cages, permanent magnets were fixed to the two sides of the cages to provide static magnetic field of 25 mT in the middle area or housed in normal cages as control. The rabbits implanted with magnetic scaffolds and stayed in the magnetic cages showed faster new bone formation and scaffold degradation than those stayed in normal cages (Fig. 1.1). Besides, the former exhibited the higher level of OC and collagen in the tissue of implanted scaffold, indicating more new bone formation. More evidence came from the monitoring by CT scan. The CT images showed incomplete fracture in the right transverse process in group of magnetic scaffold (group S) and the combination of magnetic scaffold and magnetic field (group S+M) on day 10 after implantation, when the filled defect exhibited not homogeneous with blurred bright spots in the two groups. On the day 50, the cortical bone had become connected and homogeneous, and the bone marrow cavity was mostly clear for group S+M, instead, there was still nonhomogeneous bone density hyperplasia for group S (Fig. 1.2). These indicated that the applied static magnetic field promoted the density increase of the defects area. On the day 90, bony connection was further improved in both groups. The newly formed bone in group S+M became more homogenous, and the shape was close to that of natural bone, suggesting the repair process had completed, while the process in group S not yet [37]. These results indicated that the combination of superparamagnetic scaffold with external applied magnetic field provided a novel strategy for

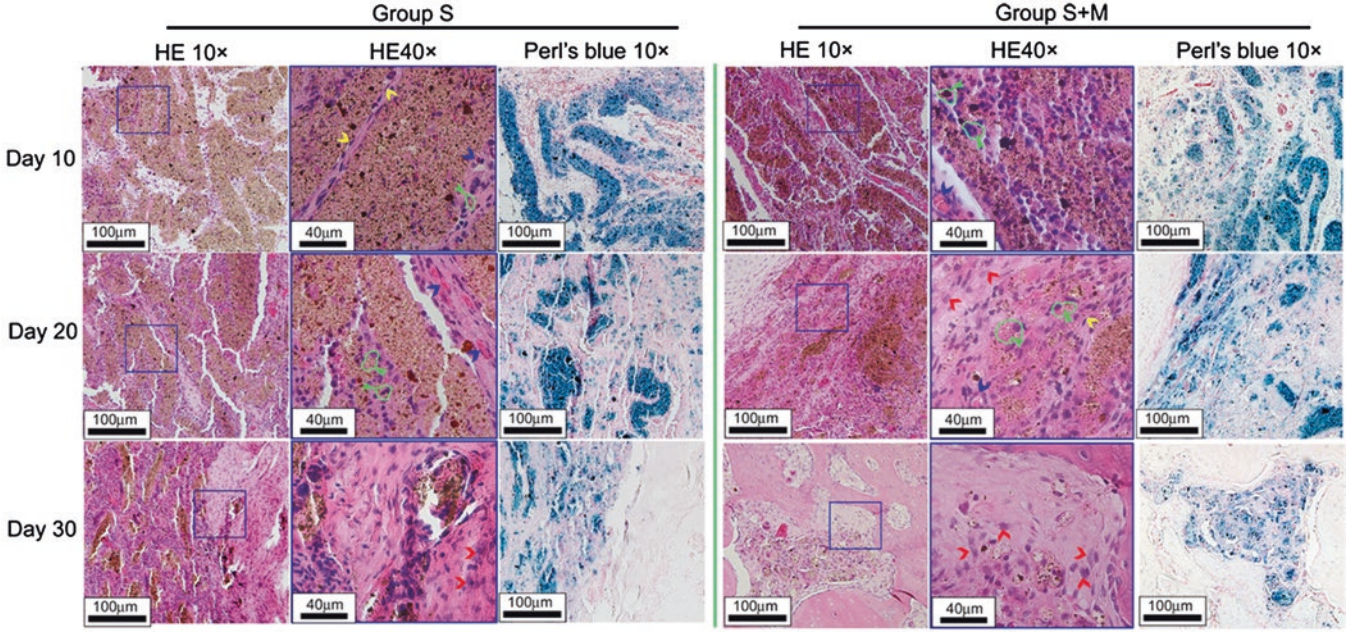

Fig. 1.1 Representative histological images of the scaffolds implanted in the bone defect on day 10, 20, 30 post implantation. Left column: Groups S; Right column: Group S1M. Macrophages were circled by green line and pointed by green arrow; Fibroblasts were pointed by yellow arrow; Vessels were pointed by blue arrow; Osteoblast cells were pointed by red arrow [37]

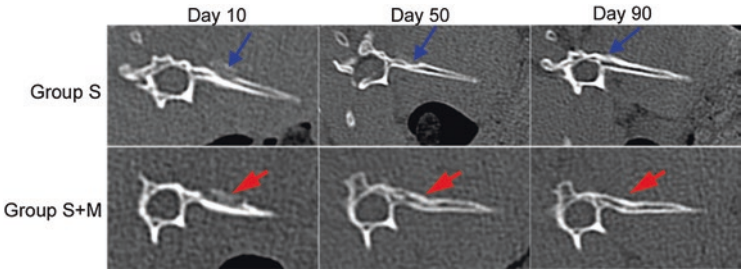

Fig. 1.2 CT images of the bone defects for group S and Group S 1 M post 10, 50-, and 90-days implantation. The arrows pointed to the defects [37]

scaffold-guided bone repair in situ, and this can be easily integrated to various kinds of commercially available scaffolds. At the same time, it has been validated that a "dynamic scaffold" can be realized by superparamagnetic scaffolds that are magnetically actuated.

Accumulating experimental evidence have increased for this strategy, following are more examples. Magnetic scaffolds with iron oxide nanoparticles (MNPs) of 0.2–2% were fabricated by immersing hydroxyapatite scaffolds into MNPs colloid, and cell line of ROS 17/2.8 and MC3T3-E1 cells were seeded on the scaffolds under the condition of with and without the external applied magnetic field. Results clearly showed that the magnetic scaffolds with exterior magnetic fields enhanced the production of ALP and bone gla protein (BGP) on the two cell lines, indicating the occurrence of osteogenic differentiation of the cells, and noted that the synergistic effect was intensified with the increase of MNPs content [38]. Scaffolds constructed by (Fe^{2+}/Fe^{3+})-doped hydroxyapatite nanocrystals nucleated on self-assembling collagen fibers also showed similar effects on human osteosarcoma cell line MG63. Within the 7-day incubation, the optimal formulation (FeHA/Coll25) showed the highest ability of enhancing cell proliferation under the external static magnetic field. It could be noticed that the magnetic scaffold alone increased the gene expression of COL1A1, RUNX2 and ALP compared with the nonmagnetic scaffold control, while the combination with the external static magnetic field made the expression of COL1A1 even higher [39]. A nanofibrous composite scaffold composed of poly(L-lactide) (PLLA) and ferromagnetic nanoparticles and processed by using electrospinning technique also showed positive effects on osteogenesis when incubated with MC3T3-E1 cells under applied magnetic fields. In comparison with PLLA nanofibrous sheet, the scaffolds containing Fe_3O_4 nanoparticles increased the cell adhesion percentage remarkably within the initial several hours, while the application of static magnetic field further increased the cell adhesion and increased the ALP activity and calcium deposition of the cells [40, 41]. Silk fibroin/chitosan-based magnetic scaffolds with lamellar structure were prepared using different amounts of Fe_2O_3 nanoparticles of 0, 0.5, 1 and 2% by freeze-casting method, which showed good physicochemical and biological properties. Under magnetic field of 3 mT, MG63 cells viability test verified the compatibility of the scaffolds [42].

Besides, the bone-related cell lines, effects of the combination strategy have been employed on stem cells. Some examples are given below: Magnetic nanofibrous scaffold composed of PLA, nHA, and Fe_3O_4 nanoparticles (mag-PLA/NF) combining with a static magnetic field of 10 mT could significantly enhance the expression of Runx2 and BMP2 of bone marrow-derived mouse mesenchymal stem cells (bMSCs), compared with mag-PLA/NF in the absence of magnetic field. Furthermore, by western blot assay, it was demonstrated that mag-PLA/NF combining with the magnetic field promoted the expression of OPN and OCN significantly in a time-dependent manner [41]. Another group combined PLA with thermal plastic polyurethane (TPU) to prepare a solution in which Fe_2O_3 nanoparticles were dispersed at 1–5%. The mixture solution was used to prepare magnetic composite sponges that were seeded with adipose-derived mesenchymal stem cells (ASCs) and subjected to a magnetic field of 200–600 mT. The magnetic field stimulation enhanced the expression of osteopontin and collagen type I while decreased expression of bone morphogenetic protein 2 in tested magnetic materials including TPU + PLA/1% Fe_2O_3 and TPU + PLA/5% Fe_2O_3. These results indicated that the magnetic composite sponges with magnetic field enhanced osteogenic differentiation of ASC, in particular, the stimulation of magnetic field accelerated late osteogenic protein markers including collagen I and OPN and increased the phosphorus level, as well as promoted the cells proliferation [43]. A group developed a three-dimensional (3D) hydrogel scaffold based on self-assembled RADA16 peptides containing superparamagnetic iron oxide nanoparticles (NPs). Human adipose-derived mesenchymal stem cells (hASCs) were seeded in the magnetic hydrogel subjected to an extremely low-frequency pulsed electromagnetic field (1 mT with a pulse frequency of 15 Hz), showing better viability at day 14 and day 21. At day 7, the increased ALP activity suggested an early osteogenic differentiation. After 21 days, there was a significant increase ($P < 0.05$) in calcium deposition. The elongated cells also represented signs of differentiation [44]. The enhancement of the combination strategy on the osteogenesis was also validated in the repair of mouse calvarium defects, showing a systematic therapeutic effect on the bone defect repair. When the magnetic scaffolds were implanted in mouse calvarium defects, the application of static magnetic field significantly enhanced the new bone formation at 6 weeks. In addition, the magnetic scaffolds upregulated the gene expression of Runx2 and Osterix of mouse calvarial osteoblasts with the static magnetic field applying at 15 mT, as well as the ALP activity, which were associated with integrin pathway, BMP, MAPK, and NF-kB signaling pathway [45].

A research group found out that the magnetic scaffold architecture could be influenced by a closely attached magnet, when they investigated the possibility of preventing efficient fixation from the micromotion at the interface between the implant and body tissue by using the magnet. In the study, cylindrical NdFeB magnets were implanted by minimally invasive surgery near the magnetic scaffolds composed of collagen and iron oxide nanoparticles within the lateral condyles of the distal femoral epiphyses on 12 rabbits. The magnetic scaffolds were firmly attracted to the magnets, confirming a “magnetic fixation” effect, and at the same time, in the scaffold, collagen fibers became aligned following the magnetic field,

and furthermore, a well-ordered regenerated tissue was obtained [46]. In the follow-up study, the research group presented the pattern of bone regeneration after 12 weeks in an experimental bone defect model in rabbit femoral condyle received the same implantation. It was clearly shown that the synergic combination of magnetic field and magnetized biomaterials was able to generate a characteristic bone pattern with dense and highly interconnected bone trabeculae orthogonally oriented nearly with respect to the magnetized collagen fibrils and parallel to the isomagnetic lines of the permanent magnet. In contrast, only partial defect healing was achieved within the control groups. The comparison of mechanical gap data indicated that the combination strategy provided new bone tissue with a higher level of maturation than the other groups [47]. Besides, static magnetic fields, pulse electromagnetic fields were demonstrated effective in the combination strategy. For examples, a pulsed electromagnetic field of 100 mT was applied to the magnetic porous composite scaffold composed of Fe_2O_3 nanoparticles, nHA and PLLA, on which bone marrow mesenchymal stem cells (BMSCs) were seeded. The combination of pulsed electromagnetic field and magnetic scaffolds significantly enhanced the ALP activity and gene expression of type I collagen, however, the expression of osteocalcin was not significantly changed in comparison with other incubation conditions [48].

The effect of magnetic field duration on the osteogenesis was investigated as well. Fox example, exterior static magnetic fields (SMFs) of 72–144 mT (at the center of the field, with a diameter of 1 cm) were applied to a 3D collagen scaffold that was processed using plastic compression. Significant differences were able to observe gradually between different groups after MG-63 cells seeding. Employing SMFs or iron oxide nanoparticles (IONPs) alone could only stimulate cell proliferation up to 7 days, while the combination of both factors could extend the stimulatory effect until 14 days. Moreover, in the group employing SMFs alone, increased cell activity was observed from 3 days but fell slightly after 14 days. The significant absorbance difference between the combination group and the other groups was observed at 21 days, which proved the combining effect of IONPs and SMFs for long time use. The cell mineralization also showed a significant difference after 21 days. In addition, the applied SMFs might induce an earlier osteogenic induction in MG-63 cell lines, evidenced by the upregulation of Runx2 that is an early osteoblastic gene, and the expression of BMP-2 and BMP-4 that are two differentiation-related gene could only be enhanced by the combination of SMFs and IONPs over 14 days of culture [49]. In another study, nanocomposite pellets composed of PCL and FeHA nanoparticles were prepared and used as building blocks to fabricate 3D cylindrical scaffolds. The scaffolds were featured with a fiber diameter of 500 mm, a layer thickness of 390–400 μm and a strand distance of approximately 1800 μm. The nanocomposite magnetic surface was roughness, due to the presence of FeHA nanoparticles. Exposed every day with the magnetic field of intensity 30 mT under the frequency 70 Hz for 6 h with 20 intervals of 18 min, better cell adhesion and spreading were observed, however, under the continuous exposure of the same magnetic field, cells showed lower viability [50]. There is another investigation reporting the effect of scaffold architecture and magnetic field intensity on the osteogenesis of MG-63 osteoblast-like cells up to 30 days incubation. In this study, 3D

biomimetic magnetic structures of ellipsoidal or hexagonal units were fabricated in a multilayered architecture, which were coated with a thin layer of magnetic composite consisting collagen, chitosan, hydroxyapatite, and magnetic nanoparticles. The static magnetic field ranging of 100–250 mT was applied to study the potential effect on cell osteogenic differentiation. Over the whole investigation period of 30 days, ALP (Alkaline Phosphatase) and osteocalcin were both increased when the magnetic field intensity was ranging from 110 to 250 mT while the cell viability was slightly decreased at day 20 of incubation. Moreover, it is interesting that the investigation figured out an optimum pore size between 20 and 40 μm and the optimum 3D structure of ellipsoidal [51].

An interesting design came from porous spheres composed of PVDF and $CoFe_2O_4$ nanoparticles, aiming to utilize the magnetoelectric (ME) effect of the composite. The ME $CoFe_2O_4$/PVDF composite spheres were integrated with methacrylated gellan gum (GGMA) gel to generate a composite hydrogel that was expected to be capable of providing magnetic, electric, and mechanical stimuli to specific cells. The gel-based scaffolds with 20 kPa Young's modulus exhibited a magnetoelectric response at a magnetic field of 220 mT, meanwhile, biocompatible to MC3T3-E1 cells with the viability superior to 80% [52]. With magnetic stimulation of 230 Oe at a frequency of 0.3 Hz, MC3T3-E1 cells grown on a 3D porous ME scaffold fabricated with the ME spheres by using a nylon template exhibited significantly higher proliferation rate and elongated morphology covering the pores [53]. Similarly, a kind of ME polymeric composite was fabricated by dispersing Terfenol-D particles of 1 μm in diameter in P(VDF-TrFE) polymer followed by casting into films. It was observed that the composite film enhanced the proliferation of pre-osteoblast cells MC3T3-E1 under magnetically stimulation or electrically stimulation [54].

1.4.2 Cartilage

Articular cartilage forms a thin tissue layer lining the articulating bony ends of synovial joints to absorb the stresses generated during joint loading and to contribute to the lubrication of the joint over a lifetime. It is known that adult articular cartilage has a limited capacity to regenerate, which is the primary reason that osteoarthritis is a leading cause of chronic disability and is a significant global health problem. Articular cartilage has electromechanical properties due to its electrically charged nature and its depth-dependent mechanical properties; thus, provides a unique environment in which chondrocytes are exposed to multiple biophysical cues. The extracellular matrix (ECM) of cartilage can be considered a mechanical signal transducer receiving input in the form of joint loading and yielding an output of multiple biophysical signals. Therefore, articular cartilage is closely associated with physical stimulations.

Effects of biophysical stimulation on cartilage regeneration have been extensively explored in past decades in the field of tissue engineering, stimulation

modalities mainly include mechanical, magnetic, and electrical stimulation. These physical stimulations are usually applied to the cell culture system. As for the magnetic stimulation, the static field or pulse electrical magnetic field (PEMF) is applied to the cells cultured in petri dishes. Most of these studies have been in either monolayer chondrocyte cultures or tissue explant models. Some groups reported positive effects of the magnetic stimulation on the proliferation of human articular chondrocytes and proteoglycan (PG) synthesis within tens of hours incubation, however, conflicting results have been reported [55, 56] as well. We consider the reason is that in the monolayer cell culture system there are lack of scaffolds that can mimic the ECM to generate enough mechanical forces to the cells and to last longer culture period. Hence, the strategy of magnetic responsive scaffolds combining with external magnetic fields may provide a novel solution.

One group had iron oxide nanoparticles (MNPs) integrated in κ-carrageenan (κC) hydrogels at different concentrations of 2.5%, 5%, 10% (v/v). The MNPs have a Zeta potential of 11.6 mV, stable in aqueous buffers with pH > 4, and present a magnetization value of 46 emu/g iron (H = 1000 Oe), a saturation magnetization >71 emu/g iron (H > 10,000 Oe) and a coercive field Hc of 0.481 kA/m. MNPs-free-κChydrogels were prepared and considered as reference materials. In this study, a magnetic stimulation of 350 mT applied to human adipose-derived stem cells (hASCs) grown on the magnetic kC hydrogels through an oscillation frequency of 2 Hz. It was shown that the concentration of MNPs in the hydrogels influenced cellular behavior, tuning a positive effect on cell viability and metabolic activity of hASCs, and the most promising outcomes were observed in 5% MNP-κC matrices. Although hASCs laden in MNPs-free- and MNPs-κC hydrogels showed similar metabolic and proliferation levels, the mRNA transcripts of Collagen I, Collagen II, and Sox9 was upregulated more, pronounced by Day 14 in hASCs laden in MNPs-κC hydrogels under the magnetic field, suggesting that the magnetic stimulation induced an earlier and stronger upregulation of chondrogenic-specific transcripts. In particular, the enhanced expression of Sox9 suggests that the combination of MNP-κC hydrogel and magnetic stimulation plays a role in the regulation of the chondrogenic commitment of hASCs, especially in chondrogenic cultures [57]. In order to develop scaffolds mimicking the depth-dependent material properties of native articular cartilage, a research group fabricated a tri-layered magnetic composite agarose gel (ferrogel) with a gradient in compressive modulus from the top to the bottom layers of the construct. The three layers have different weight percentages of dextran-coated iron oxide nanoparticles 20%, 7%, and 10%. Rare earth NdFeB magnets were used to generate an external magnetic field (0.4, 0.5, or 0.75 T). The ferrogel was able to respond to the external magnetic stimulation, exhibiting an elastic, depth-dependent strain gradient. When bovine chondrocytes (BCs) were seeded in the ferrogel scaffolds and cultured for up to 14 days, it was shown that sulfated glycosaminoglycan increased with the depth from the surface and was more significant at the 12 days of culture, indicating a biochemical gradient was formed, and meanwhile good cell viability was detected [58]. In another study, agarose hydrogels containing Fe_3O_4 nanoparticles were seeded with human mesenchymal stem cells and placed under external magnetic fields. By this way the

hydrogels provided a pressureless, soft mechanical stimulation. The study presented that the magnetic hydrogels under magnetic fields could induce significant chondrogenesis of mesenchymal stem cells without any additional chondrogenesis transcription factors, with the upregulation of aggrecan, SOX9, and collagen II in protein level, and the effect could be remarkably enhanced by the supplementary of TGF-β1 or dexamethasone. In addition, the movement frequency of the magnetic hydrogels was investigated as well to figure out the optimal parameters [59]. In another example, to closely mimic the hierarchical architecture and biomechanical behavior of native tendons, continuous and aligned electrospun fiber threads were fabricated using PCL matrix filled with hybrid rod-shaped cellulose nanocrystals (CNCs) decorated with iron oxide MNPs (MNP@CNC). Human adipose stem cells (hASCs) were grown on the magnetic scaffolds under magnetic stimulating conditions (oscillation frequency of 2 Hz and 0.2 mm of horizontal displacement) for 21 days, which displayed higher degrees of cell cytoskeleton anisotropic organization and steered the mechanosensitive YAP/TAZ signaling pathway. As consequent results, the stimulated cells showed increased expression of tendon-related markers and pro-healing cytokines and lowered inflammatory cytokines in gene level [60]. An interesting and a little complex design is 3D porous magnetic microbead. The main body was microspheres of poly(lactic-co-glycolic acid) (PLGA) with gelatin beads distributing inside. When the gelatin beads were removed, the microsphere became porous while magnetic nanoparticles were conjugated to the surface of the walls via amino bond formation. This composite microscaffold was used to the culture of D1 mouse MSCs to increase adhesion, migration and chondrogenic differentiation under magnetic fields, and could be magnetically guided to the target area by the magnetic field guidance, for example, to the medial condyle of the femur in the knee joint model created by a 3D printer [61].

1.4.3 Endothelial, Cardiac, and Neuron Cells

Vascularization is one of the major challenges in engineering tissues, especially thick and complex tissue such as cardiac muscle, which would enable the engineering tissue efficiently integrated with host tissue upon implantation. For example, the vascularization is one of the greatest hurdles hindering the successful implementation of tissue-engineered cardiac patch as a therapeutic strategy for myocardial repair. A group investigated the effect of magnetite-impregnated alginate scaffolds on aortic endothelial cells. The magnetic field was applied during the first 7 days to stimulate the cells out of a total 14-day experimental course, which was set up by passing an electrical current through serially connected coils at frequency of 40 Hz. The scaffold was generated by a freeze-dry technique from a mixture of alginate stabilized ferro-fluid and alginate to obtain 1.2 (w/v)% of final concentration of magnetite post-crosslinking while the control was fabricated by the same method without magnetite. The investigation showed that the employed strategy significantly elevated the metabolic activity of the endothelial cells during the stimulation

period and suggested that the elevated metabolic activity was related to the cell migration and re-organization. Although the magnetic stimulation alone has the positive effect on the activity of cells grown on the nonmagnetic scaffold, the magnetic hydrogel significantly further enhanced this effect. The study also observed that cellular vessel-like (loop) structures were formed on day 14 in the magnetically stimulated scaffolds without supplementation of any growth factors, while little was observed in the non-stimulated (control) scaffolds. The loop structure is known as indicators of vasculogenesis and angiogenesis, therefore this study provided strong evidence that the magnetically actuated scaffolds could enhance the vascularization of engineered tissues, which indicated possibility of fabricating pre-vascularized tissue construct with potential applicability for transplantation [62, 63].

Magnetically actuated scaffolds were also used to generate strain stimulus on rat aortic smooth muscle cells. Interestingly the strategy of inducing magnetic scaffolds to generate deformation under the magnetic field was utilized to improve cell viability in the scaffold interior by pumping nutrients throughout the structure. The magnetic scaffolds were fabricated in a tube shape by winding electrospun sheets of a biodegradable polymer 50/50 blend of polyglycolide (PG) and polycaprolactone (PCL), in which were dispersed magnetic γ-Fe_2O_3 nanoparticles. The tubular scaffolds were seeded with smooth muscle cells and actuated by a static magnetic field to induce a cyclic crimping deformation, permanent magnets mounted on actuators were used to apply a cyclically varying magnetic field to each culture and magnetic actuation was cycled for 60 s on and 60 s off to ensure adequate time for deflection and recovery for a time period of 1–15 days, which applied strain stimulus to the cells and pumped nutrient fluid through the porous tube walls. Results were that the magnetically actuated scaffolds significantly increased the secretion of Type I collagen that is one of the most abundant ECM proteins and synthesized by vascular SMC. On the contrary, collagen production of non-actuated scaffolds was minimal at the same time point compared with the actuated scaffolds [64]. A group built a functional cardiac patch by combining the use of a macroporous alginate scaffold impregnated with magnetically responsive nanoparticles (MNPs) and the external magnetic stimulation. Researchers seeded neonatal rat cardiac cells on the magnetically responsive scaffolds that were stimulated by an alternating magnetic field of 5 Hz. It was shown that a short-term stimulation of 20 min external magnetic field increased the phosphorylation of AKT in the cardiac cell constructs, meanwhile there was a greater extent of striated fibers in the stimulated group than in the non-stimulated group, and the level of contractile protein Troponin-T and adhesive conjunction protein Connexin-43 was higher in the stimulated group than that in the control group on day 15. These results indicated that a synergistic effect of magnetic field stimulation together with the magnetic responsive scaffolds provided a favor regenerating environment for cardiac cells, driving their organization into functionally mature tissue [65].

Nerve regeneration and recovery of nerve function have been a major issue in neuroscience. For the regeneration of peripheral nerves, functional recovery is totally dependent on the growth and extension of axons from the proximal end across the injured site until they reach their distal target. Because rate of axonal

regeneration in humans occurs about 2–5 mm/day, it can take many months to get recovery of the functions for significant complete injuries, such as neurotmesis. Great efforts have been made to develop more effective approaches for accelerating the recovery time. One approach is the "guidance therapy" based on the use of scaffolds working as nerve guidance conduit for the diffusion of growth factors secreted by the injured nerve ends and to limit the injury site infiltration by scar tissue. Recently the importance of physical stimuli for neuronal growth and development has been widely recognized and appealing in literatures. Specifically, results from published experimental studies indicate that carefully controlled forces can modulate neuronal regeneration. Based on above knowledge, roles of magnetic scaffolds have been explored in remotely controlling nanofibers orientation in scaffolds is important for neuronal cells growth.

A research group proposed a noninvasive approach for physical guidance of nerve regeneration based on the synergic use of magnetic nanoparticles and magnetic fields. In the study, researchers synthesized MNPs functionalized with nerve growth factor beta (NGF-β), which were applied to neuron-like cell line PC12 cells in combination with a magnetic field to validate the concept that the application of a tensile force to a neuronal cell can stimulate neurite initiation or axon elongation in the desired direction. The magnetic nanoparticles were used to generate this tensile force under the effect of a static external magnetic field providing the required directional orientation. They have confirmed that MNPs direct the neurite outgrowth preferentially along the direction imposed by an external magnetic field, by inducing a net angle displacement (about 30°) of neurite direction, as well as demonstrated that this approach could trigger PC12 differentiation in a neuronal phenotype [66]. A group reported another interesting design. Magnetic electrospun nanofibrous membranes were generated with the solution of PLLA and magnetic nanoparticles, which were cut into small pieces and rolled into conduits of 10 mm in length. The shortened conduits were next injected with collagen hydrogel in situ. Here the magnetic responsive property of scaffolds was utilized to reposition the small conduits dispersing in the hydrogel. A magnetic field was applied to guide the conduits aligned in situ. This injectable guidance system provided consistent topographical guidance to cells, increased both neurite alignment and neurite length within the hydrogel scaffold, neurites that contacted the fiber conduits followed the orientation of the fibers [67]. By integrating magnetic nanoparticles into collagen hydrogels, the gel orientation could be controlled dynamically and remotely in situ under an external magnetic field. In this design, magnetic particles aggregated into magnetic particle strings during the gelation period, leading to the alignment of the collagen fibers. Results showed that neurons within the 3D gels exhibited normal electrical activity and viability. Importantly, neurons formed elongated and co-oriented morphology under the guidance of the particle strings and fibers as supportive cues for growth [68]. A similar design was given below. To overcome the lack of the required structural complexity to regenerate aligned tissues, an injectable rod-shaped, magnetoceptive microgel was prepared by subjecting the prepolymer solution within a magnetic field before molding and curing and interlocking the oriented microgels. The obtained hybrid hydrogel with global unidirectional anisotropy was applied to primary dorsal root ganglions (DRGs), showing a strong guidance effect [69].

1.4.4 Immune Cells and Supportive Cells

Macrophages play crucial roles in various immune-related responses, such as host defense, wound healing, and tissue regeneration, they perform distinct and dynamic functions in vivo, depending on their polarization states, pro-inflammatory M1 phenotype and pro-healing M2 phenotype are the two extremes of the phenotypes. In the process of natural wound healing, macrophages are involved in all phases with dynamically changing phenotypes, orchestrating the transition from an inflammatory to regenerative phenotype to guide all other cell types to complete the wound-healing process [70, 71]. When macrophages encounter implanted scaffolds, their phenotype would be affected and even regulated by the scaffolds that are necessary when a tissue defect is large beyond the critical size. Therefore, harnessing macrophages by scaffolds is important for facilitating tissue regeneration in situ.

To explore the effects of mechanical forces generated by the combination of superparamagnetic scaffolds and magnetic fields on macrophages, macrophage cell line RAW264.7 cells were seeded on nanofibrous scaffolds composed of γ-Fe_2O_3 nanoparticles (MNP), hydroxyapatite nanoparticles (nHA) and poly lactide (PLA) and subjected to magnetic fields (MF) that was applied alternatively in an interval of 12 h. The magnetically actuated scaffolds did not affect the proliferation of RAW.7, but showed regulatory effects on the phenotype of the macrophages. As shown that the level of Arg1 was upregulated significantly in magnetically actuated scaffolds (mag-S+MF) and that of iNOS was decreased in comparison with that in the other groups. These variations suggested that mag-S+MF guided the macrophages to M2 phenotype and had their M1 phenotype weakened, which was verified by the cytokines profiles, as shown that pro-inflammatory cytokines (IL-1β, TNF-a, and MCP-1) were significantly decreased, and wound healing associated cytokines (IL-4 and IL-10) were significantly increased in mag-S+MF group compared with those in control group (Fig. 1.3). Interestingly, the conditioned medium prepared from macrophages grown in mag-S+MF promoted human umbilical vein endothelial cells (HUVECs) to form more vessel-like tubes, which could be attributed to the enhanced production of VEGF and PDGF of macrophages. The conditioned medium also played positive roles in the osteogenesis of pre-osteoblast cell MC3T3-E1, the medium showed capacity of recruiting and inducing osteogenesis of MC3T3-E1. At the same time, mag-S+MF could inhibit the secretion of MMP-9 and TRAP, the two molecules are characteristic osteoclast marker proteins. In addition, the level of TLR2 and TLR4 for macrophages in mag-S+MF was down-regulated in western blot analysis, and the nuclear NF-κB expression was reduced as well, while the autocrine loop of VEGF/VEGFR2/HIF-1α for macrophages in mag-S+MF group was obviously activated (Fig. 1.4) [72]. These results explained how the magnetically actuated scaffolds enhanced bone tissue regeneration through regulating the phenotype of macrophages, as well as demonstrated that macrophages are mechanosensitive, their phenotype can be regulated by mechanical stimulations generated by the combination of magnetic scaffolds and magnetic fields.

A group investigated the effect of frequency of magnetic fields on the phenotype of macrophages. They prepared RGD ligand-bearing superparamagnetic iron oxide

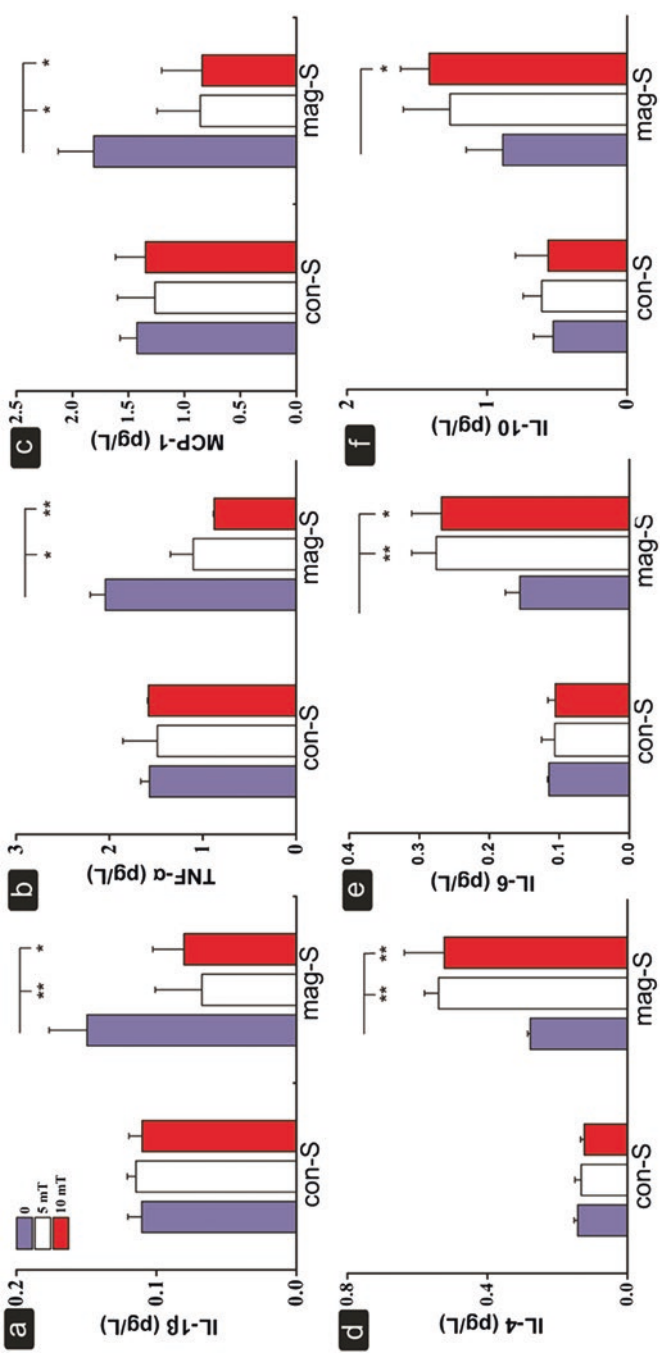

Fig. 1.3 Cytokine profiles of macrophages grown in mag-S or con-S under different MFs for 72 h. Data are means ± SEM. $**p < 0.01$, $*p < 0.05$ vs. MF = 0 group ($n = 3$) [72]

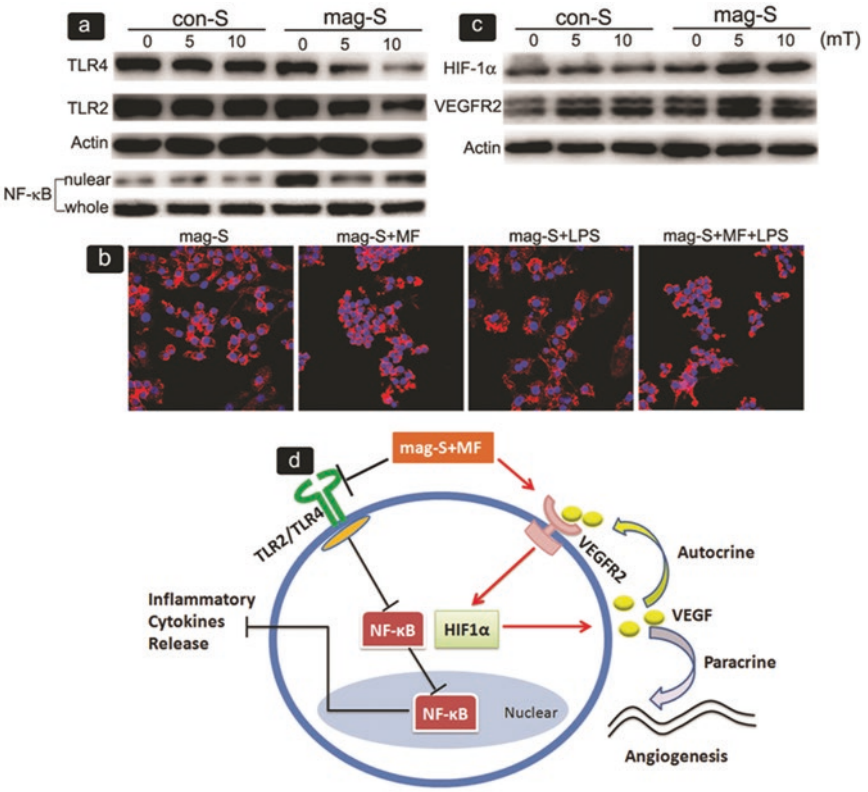

Fig. 1.4 Activation of membrane receptors and the response to LPS in macrophages grown in different scaffolds under different MFs. (**a**) Representative Western blots of TLR2, TLR4 and NF-κB. (**b**) Responses of macrophages to LPS; red, actin; blue, DAPI. (**c**) Representative Western blots of VEGFR2 and HIF-1α. (**d**) Schematic graph of the mechanism [72]

nanoparticles (SPIONs) and have the particles grafted to a planar matrix via a long flexible PEG linker. To set up the magnetic field, the magnet was placed at approximately 1 cm distance from the in vitro cultures and in vivo mouse cage bottom, different oscillation frequencies of the magnetic field including 0.1, 0.5, and 2 Hz, and "zero frequency" was set as "no magnetic field" group. It is interesting that low frequency significantly upregulated M2 markers (arginase-1 and Ym2) while the high frequency group exhibited significantly upregulated expression of M1 markers (iNOS and CD80), which proved the effect of frequency of magnetic field on macrophage polarization. When it comes to in vivo study, the planar matrix coated with the RGD-bearing SPIONs was subcutaneously implanted to BALB/c mice, and the adhesion and phenotypes of macrophages from host were examined in the absence or presence of M2 induction cytokines injection, and similar results to that of in vitro were obtained [73]. This study demonstrated that a low oscillation frequency of the magnetic field stimulated the adhesion and M2 polarization of macrophages,

whereas a high oscillation frequency suppressed the adhesion of macrophages but promoted their M1 polarization, which verified the possibility of remotely manipulating the adhesion and polarization phenotype of macrophages, both in vitro and in vivo. Furthermore, the result that the low frequency benefited to M2 polarization is consistent with that the low or meddle intensity of magnetic fields are beneficial to tissue regeneration. Results from this study also provided cues to explain that weak magnetic fields were applied in many experimental studies aforementioned, in which significant effects of enhancing tissue regeneration were achieved.

Fibroblasts are one of the matrix cells supporting tissue regeneration as well as a kind of immune cell [74, 75], playing important roles during wound healing, as they synthesize extracellular matrix (ECM) components to support new tissue formation. It has been well established that fibroblasts are mechanical sensitive [76]. When fibroblasts were seeded on electrospun nanofibrous scaffolds composed of γ-Fe_2O_3 nanoparticles (MNP), hydroxyapatite nanoparticles (nHA), and poly lactide (PLA) that were placed in applied static magnetic fields (mag-S+ MF), results from enzyme-linked immunosorbent and transwell assays showed that fibroblasts cultivated in this condition secreted significantly higher type I collagen (collagen I), vascular endothelial growth factor A (VEGFA), and transforming growth factor-β1 (TGF-β1) in a time-dependent manner, while produced fewer pro-inflammatory cytokines, including interleukin-1β (IL-1β) and monocyte chemoattractant protein-1 (MCP-1). Meanwhile, fibroblasts grown on the magnetic scaffolds or nonmagnetic scaffolds proliferated normally within the tested period of 120 h when the MF intensity did not exceed 60 mT. Cells growing on mag-S+ MF for 5 days exhibited much better spreading morphology and cell–cell connection under the magnetic field of 10 mT. Mechanistic studies revealed that the cultivation system activated components of integrin, focal adhesion kinase, and extracellular signal-regulated kinase signaling pathways while inhibited Toll-like receptor-4 and nuclear factor κB, thus modulating the phenotypic polarization of fibroblasts [77]. It should be noted that all above effects accelerated the osteogenesis of pre-osteoblasts MC3T3-E1 cells, evidenced by the promotion of osteogenesis of pre-osteoblasts cultivated in the conditioned medium prepared from fibroblasts grown on the magnetically actuated scaffolds, there were more growth factors and balanced extracellular matrix components. Results from this study provided the evidence that the magnetically actuated scaffolds were able to promote the wound-healing phenotype of fibroblasts, benefiting to the scaffold-guided tissue regeneration, and it also implied that remotely control the phenotype of fibroblasts is of significance in scaffold-guided tissue regeneration as well as control tissue specific cells. In order to further verify the phenotypic advantages of macrophages and fibroblasts modulated by the combination of magnetic scaffolds and magnetic fields, a conditioned medium was prepared by mixing the culture supernatants from the incubation of macrophages and fibroblasts grown on PLA based-nanofibrous magnetic scaffolds under magnetic fields with inductive medium at 1:1 (volume ratio), and then used in the bottom chamber of transwell device. It was striking that the conditioned medium not only recruited more bMSCs from the top well, but also induced faster osteogenic differentiation than the other control conditioned media [41]. These results

clearly verified that the combination strategy could facilitate the cross talk of bMSCs with macrophages and fibroblasts, which well explained how magnetic scaffolds play roles of enhancing tissue regeneration in combination with external applied magnetic fields. Oral mucosa fibroblasts were also reported to be able to sense the interaction generated by magnetic biological hydrogels. It was shown that the hydrogel composed of Fe_3O_4 nanoparticles and a mixture of fibrin and agarose was biocompatible to oral mucosa fibroblasts. Moreover, the cells could be encapsulated by the magnetic hydrogel to form magnetic tissue substitutes, and interestingly, the mechanical properties of the substitutes could be reversibly tuned by the magnetic fields [78].

Schwann cells (SCs) are supportive cells and the main gliocyte type in peripheral nervous system and undergo dedifferentiation and proliferation in the distal injured segment after injury, forming Büngner bands at injury sites, which create favorable environment for axon regeneration and ensuing remyelination. Therefore, integration of SCs with scaffolds for nerve regeneration has been becoming an important and promising strategy to repair nerve injuries. To meet the clinic demand, a considerable number of SCs with enhanced cell viability and biological properties would be required. However, there are still challenges remained in SC culture, which resulted in low viability and biological activities of SC, significantly limiting the application of SCs in nerve-injury repair. A research group applied a magnetic nanocomposite made of magnetic nanoparticles (MNPs) and a biodegradable chitosan-glycerophosphate polymer to Schwann cells. The magnetic nanocomposites contained 10% of MNPs with a magnetization of 5.691 emu/g at 8 kOe. It should be noted that SCs were more sensitive than other kinds of cells mentioned before. Noticed that the intensity of magnetic field was higher than 2 mT induced obvious apoptosis, while the combination of nanocomposite and magnetic field of 2 mT could promote the proliferation of SC cells. It was further found out that the magnetic scaffold significantly increased the expression of BDNF, GDNF, NT-3, and VEGF, both in gene and in protein levels. This work showed availability of regulating the viability and biological activities of SCs in tissue engineering grafts by remotely modulation of magnetically actuated scaffolds [79]. This strategy was further employed in peripheral nerve repair challenging for surgeons. Although autologous nerve transplantation is well known therapy; however, the application is limited by the scarcity of available donor nerves, donor area morbidity, and neuroma formation. The magnetic field was generated with a frequency of 50 Hz and an intensity of 0–20 mT. A 15 mm long gap was made in the sciatic nerve in male adult Sprague-Dawley rats weighing 220–250 g, and the exposure of magnetic field was applied to the rats at 2 mT for 2 h each day after surgery. From the analysis of data collected from many animals, it was shown that the magnetic scaffolds could synergize with the applied magnetic field to increase the viability of SCs after transplantation. Furthermore, nerve regeneration and functional recovery were promoted by the synergistic effect of SCs-loaded magnetic scaffold and magnetic field [80].

Taken above together, we could indicate that the mechanical stimulations generated by the combination of magnetic scaffolds and magnetic fields not only

modulated the fate of stem cells and tissue specific cells, but also control the phenotype of immune cells and supportive cells, which collectively led to the accelerated tissue regeneration.

1.4.5 Mechanisms and Modulation of Mechanical Stimulations by Magnetic Materials and Magnetic Fields

It is crucial for designing scaffolds of providing proper stimulatory conditions in vitro and in vivo to promote tissue development for regenerative medicine, therefore, deep understanding mechanisms of the generation of mechanical forces by magnetically actuated scaffolds is very necessary. A research group proposed that magnetically responsive alginate scaffolds can undergo reversible shape deformation due to alignment of scaffold's walls in a uniform magnetic field, and investigated the hypothesis in magnetic alginate hydrogels using custom made Helmholtz coil setup adapted to an atomic force microscope by monitoring changes in matrix dimensions in situ as a function of applied magnetic field, concentration of magnetic particles within the scaffold wall structure and rigidity of the matrix [81]. It has been well documented that colloidal suspensions of superparamagnetic nanoparticles dispersing in a carrier medium can move freely due to their super small size. When the superparamagnetic nanoparticles are exposed to a magnetic field, the dipole moment induced in the particles causes them to form chains or aggregates. However, when these magnetic nanoparticles are integrated with scaffolds made of polymeric materials or hydrogels or inorganic substrates, they are assumed to be locked in the solid phase, having little mechanical freedom. Theoretically, polymeric materials are in their condensed state that can be taken as "extreme concentrated solution," and hydrogels can be taken as semisolid. Therefore, it is reasonable to assume that the movement of superparamagnetic nanoparticles driven magnetically in scaffolds would be local in microscale and mainly associated with the movement of the scaffold wall or fibers of the scaffolds. In this case, the scaffolds are expected to respond to external applied magnetic fields as an entire structure, changing their fibrous alignment, porosity, and dimensions. This study provided experimental evidence for a reversible 3D deformation of magnetically responsive scaffolds exposed to an externally applied time-varying uniform magnetic field, indicating that bending/stretching forces might be generated by the responses of magnetic hydrogels to external applied magnetic fields, which would exert a mechanical effect on cells due to alternating patterns of scaffold wall alignment and relaxation. The investigation also demonstrated that the matrix deformation was reversible, and the estimated mechanical force that could play on cells in the order of 1 pN that was considered in agreement with reported threshold to induce mechanotransduction effects on cellular level. This mechanistic study demonstrated that uniform magnetic fields coupled with magnetizable nanoparticles embedded within three-dimensional (3D) scaffold structures could remotely create transient physical forces that can be transferrable to cells present in close proximity to the

nanoparticles, which is valuable to understand how to accurately create proper stimulatory microenvironment for promotion of cellular organization to form mature tissue-engineered constructs. In an investigation on the magnetization of magnetic bacteria cellulose, the curve of magnetization versus magnetic field strength showed no hysteresis loops formed, indicating that at room temperature and under the alternative magnetic field, the magnetic bacteria cellulose showed superparamagnetic behavior, that could predict the magnetization was directly proportional to the concentration of magnetic nanoparticles, even those nanoparticles were rigidly fixed to the materials. Moreover, the magnetic field gradient formed along the magnetic bacteria cellulose when exposed to the magnetic field generated by two magnets placed oppositely could by visualized by magnetic force microscopy [82].

The fate of stem cells, such as cell migration, differentiation, proliferation, and apoptosis, are also controlled by mechanical forces generated by extracellular matrix, which can largely determine the process of tissue regeneration. Mesenchymal stem cells have the potential to differentiate into many cell phenotypes such as tissue- or organ-specific cells to perform special functions. A group used a three-dimensional (3D) computational model to study how the stem cells interpret and transduce the mechanical signals in force-free substrates and force-induced substrates to differentiate and/or proliferate during the mechanosensing process. By using magnetic scaffolds in the magnetic field, researchers stimulated the substrate with an internal force to induce mesenchymal stem cells differentiation and proliferation. They found out that cells require a longer time to grow and maturate within force-free substrates than within force-induced substrates. They also reported that the magnitude of the net traction force should be increased within chondrogenic and osteogenic substrates while reduced within neurogenic substrates for inducing mesenchymal stem cells differentiate into a compatible phenotype [83]. This model explained the capacity of magnetically actuated scaffolds inducing mesenchymal stem cells differentiation as well as provided understandings for the role of force-induced substrates in remotely controlling the cell fate during cell–matrix interaction.

Up to date, various kinds of superparamagnetic scaffolds with different microstructures have been investigated in the modulation of tissue regeneration, especially the composition and microstructure of existing reported scaffolds for bone tissue regeneration are largely different. From the view of microstructure, there have been at least nanofibrous, porous, hydrogels, and even casting films involved; from the view of chemical composition, also many kinds of materials have been employed, such as PLA, PLGA, PCL, chitosan, collagen, gelatin, hydroxyapatite, and bio-glass. Whether the magnetization property is different for various magnetic scaffolds, and what if associated with the function of enhancing osteogenesis under the magnetic fields, are necessary to demonstrate and of implications to design magnetic scaffolds for uses in the guidance of targeting tissues regeneration.

We had fabricated nine kinds of superparamagnetic scaffolds, and measured their magnetization property and the function of osteogenesis induction in pre-osteoblasts, to verify the hypothesis that the magnetization property of scaffolds is dependent on their compositions and microstructures, because the chemical molecules and microstructures of the scaffolds provide different microenvironments to the

embedded iron oxide nanoparticles, which would be associated with their function of osteogenic induction. The nine kinds of superparamagnetic scaffolds were made of PLA, polyurethane, and gelatin with incorporated Fe_3O_4 nanoparticles (MNPs), followed by processing with the technique of electrospinning, salt-leaching, and solution casting, resulting in the nanofibrous, porous, and smooth microstructures, respectively. In addition, hydroxyapatite nanoparticles (nHA) were composited in all the scaffolds with the same percentage, acting as the bone conductive component. PLA is one plastic material with relative higher mechanical strength than PU, while PU is highly elastic, and Gel is one typical soft hydrogel.

As shown by SEM images that in the nanofibrous scaffolds there were numerous homogenous nanofibers entangling with each other, porous scaffolds showed good and similar porosity, and the casting films exhibited smooth plane-like structure. Noticed that scaffolds prepared from different polymeric components (PLA, PU, and gelatin) showed different mechanical properties. Importantly, all scaffolds possessed superparamagnetic performance, and the saturated magnetization of mag-PLA was much more dependent on the physical structure of scaffolds than mag-PU and mag-Gel; noted that porous structure weakened the magnetization for the scaffolds compared with the nanofibrous and smooth structure; the saturated magnetization of mag-Gel was lower than that of mag-PU and mag-PLA regardless of the microstructure. Besides, all the scaffolds supported the pre-osteoblasts growth under the magnetic field.

Three protein markers that referring to osteogenic differentiation displayed interesting profiles when the magnetic scaffolds were subjected to the same magnetic field of 10 mT. Under the magnetic field of 10 mT, mag-PLA exhibited obvious advantage to enhance the expression of Runx2 than mag-PU and mag-Gel, no matter what microstructures. When it came to BMP2 expression, nanofibrous structure showed the strongest enhancement if the polymer was PLA or Gel, while the effect of the microstructures was not significant if the polymer was PU. But mag-PLA with nanofibrous structure induced the highest level of Runx2 and BMP2 among the nine scaffolds, as well as the ALP activity. In the presence of magnetic field, the effects of scaffolds on the gene expression of Runx2 and BMP2 were stronger, while the difference of ALP activity was only observed in the nanofibrous structure scaffolds.

The results verified the hypothesis that the magnetization for scaffolds was associated with both chemical compositions and physical microstructures. The difference might be partly resulted from the mechanical properties of the polymers. In addition, the chemical composition had influence on the dispersion of MNPs in the scaffolds, which would also affect the mechanical properties of composite scaffolds. It was shown that MNPs incorporated in the plastic PLA generated much stronger superparamagnetic response, while those in the hydrogel of gelatin generated weak response to the magnetic field. Correspondingly, cells grown on mag-PLA exhibited higher degree of differentiation than those on mag-PU and mag-Gel. The higher the saturated magnetization was, the stronger the promotion to the osteogenesis. Therefore, among the three kinds of polymers, mag-PLA was more potent in the enhancement of osteogenesis. These results could provide important cues in the design of superparamagnetic scaffolds for guiding tissue regeneration in different demands.

1.5 Summary and Perspective

Accumulating experimental evidence has confirmed the distinguished capacity of magnetic scaffolds and their combination with external applied magnetic fields to modulate or/and remotely control multiple cells differentiation and immune cells phenotypic responses to promote tissue regeneration, which exhibits promising and attractive perspectives of magnetic actuated scaffolds in tissue engineering and regenerative medicine for different therapeutic purposes. In addition, the combination system also provides powerful tools and open possibilities of building organoids for gaining insights and understanding of human body as well as screening drugs in vitro. Besides, it is worth considering the combination of electrically conductive materials with magnetic scaffolds to create electric-magnetic scaffolds and explore their potentials for uses of modulating cell behaviors and fate in the future.

References

1. M. Duan et al., Recent progress in magnetic nanoparticles: synthesis, properties, and applications. Nanotechnology **29**(45), 452001 (2018)
2. V.F. Cardoso et al., Advances in magnetic nanoparticles for biomedical applications. Adv. Healthc. Mater. **7**(5), 1700845 (2018)
3. A. Sobczak-Kupiec et al., Magnetic nanomaterials and sensors for biological detection. Nanomedicine **12**(8), 2459–2473 (2016)
4. Hai-Yan et al., Magnetic responsive scaffolds and magnetic fields in bone repair and regeneration. Front. Mater. Sci. **8**(1), 20–31 (2014)
5. X. Ba et al., The role of moderate static magnetic fields on biomineralization of osteoblasts on sulfonated polystyrene films. Biomaterials **32**(31), 7831–7838 (2011)
6. Y. Yamamoto et al., Effects of static magnetic fields on bone formation in rat osteoblast cultures. J. Dent. Res. **82**(12), 962–966 (2003)
7. L. Yuge et al., Physical stress by magnetic force accelerates differentiation of human osteoblasts. Biochem. Biophys. Res. Commun. **311**(1), 32–38 (2003)
8. A. Ozgun et al., Extremely low frequency magnetic field induces human neuronal differentiation through NMDA receptor activation. J. Neural Transm. (Vienna) **126**(10), 1281–1290 (2019)
9. J. Yang et al., Low-frequency pulsed magnetic field improves depression-like behaviors and cognitive impairments in depressive rats mainly via modulating synaptic function. Front. Neurosci. **13**, 820 (2019)
10. M. Maredziak et al., Static magnetic field enhances synthesis and secretion of membrane-derived microvesicles (MVs) rich in VEGF and BMP-2 in equine adipose-derived stromal cells (EqASCs)-a new approach in veterinary regenerative medicine. In Vitro Cell. Dev. Biol. Anim. **51**(3), 230–240 (2015)
11. S. Mayer-Wagner et al., Effects of low frequency electromagnetic fields on the chondrogenic differentiation of human mesenchymal stem cells. Bioelectromagnetics **32**(4), 283–290 (2011)
12. S.H. Hsu, J.C. Chang, The static magnetic field accelerates the osteogenic differentiation and mineralization of dental pulp cells. Cytotechnology **62**(2), 143–155 (2010)
13. A. Kasten et al., Mechanical integrin stress and magnetic forces induce biological responses in mesenchymal stem cells which depend on environmental factors. J. Cell. Biochem. **111**(6), 1586–1597 (2010)

14. H. Wang et al., Enhanced osteogenesis of bone marrow stem cells cultured on hydroxyapatite/collagen I scaffold in the presence of low-frequency magnetic field. J. Mater. Sci. Mater. Med. **30**(8), 89 (2019)
15. A. Ho-Shui-Ling et al., Bone regeneration strategies: engineered scaffolds, bioactive molecules and stem cells current stage and future perspectives. Biomaterials **180**, 143–162 (2018)
16. G. Turnbull et al., 3D bioactive composite scaffolds for bone tissue engineering. Bioact. Mater. **3**(3), 278–314 (2017)
17. N. Bock et al., A novel route in bone tissue engineering: magnetic biomimetic scaffolds. Acta Biomater. **6**(3), 786–796 (2010)
18. S. Panseri et al., Magnetic hydroxyapatite bone substitutes to enhance tissue regeneration: evaluation in vitro using osteoblast-like cells and in vivo in a bone defect. PLoS One **7**(6), e38710 (2012)
19. A. Russo et al., Bone regeneration in a rabbit critical femoral defect by means of magnetic hydroxyapatite macroporous scaffolds. J. Biomed. Mater. Res. B Appl. Biomater. **106**(2), 546–554 (2018)
20. Y. Wu et al., A novel calcium phosphate ceramic-magnetic nanoparticle composite as a potential bone substitute. Biomed. Mater. **5**(1), 15001 (2010)
21. J. Dankova et al., Highly efficient mesenchymal stem cell proliferation on poly-epsilon-caprolactone nanofibers with embedded magnetic nanoparticles. Int. J. Nanomedicine **10**, 7307–7317 (2015)
22. R.K. Singh et al., Potential of magnetic nanofiber scaffolds with mechanical and biological properties applicable for bone regeneration. PLoS One **9**(4), e91584 (2014)
23. J.J. Kim et al., Magnetic scaffolds of polycaprolactone with functionalized magnetite nanoparticles: physicochemical, mechanical, and biological properties effective for bone regeneration. RSC Adv. **4**(33), 17325 (2014)
24. H. Chen et al., Magnetic cell-scaffold interface constructed by superparamagnetic IONP enhanced osteogenesis of adipose-derived stem cells. ACS Appl. Mater. Interfaces **10**(51), 44279–44289 (2018)
25. Y. Zhao et al., Magnetic bioinspired micro/nanostructured composite scaffold for bone regeneration. Colloids Surf. B Biointerfaces **174**, 70–79 (2019)
26. A. Tampieri et al., A conceptually new type of bio-hybrid scaffold for bone regeneration. Nanotechnology **22**(1), 015104 (2011)
27. S. Hu et al., Enhanced bone regeneration and visual monitoring via superparamagnetic iron oxide nanoparticle scaffold in rats. J. Tissue Eng. Regen. Med. **12**(4), e2085–e2098 (2018)
28. J.W. Lu et al., Magnetic nanoparticles modified-porous scaffolds for bone regeneration and photothermal therapy against tumors. Nanomedicine **14**(3), 811–822 (2018)
29. A. Bigham et al., Nanostructured magnetic Mg2SiO4-CoFe2O4 composite scaffold with multiple capabilities for bone tissue regeneration. Korean J. Couns. Psychother. **99**, 83–95 (2019)
30. Y. Wei et al., Magnetic biodegradable Fe3O4/CS/PVA nanofibrous membranes for bone regeneration. Biomed. Mater. **6**(5), 055008 (2011)
31. K. Lai et al., Superparamagnetic nano-composite scaffolds for promoting bone cell proliferation and defect reparation without a magnetic field. RSC Adv. **2**(33), 13007–13017 (2012)
32. H.M. Yun et al., Magnetic nanocomposite scaffold-induced stimulation of migration and odontogenesis of human dental pulp cells through integrin signaling pathways. PLoS One **10**(9), e0138614 (2015)
33. H.M. Yun et al., Magnetic nanofiber scaffold-induced stimulation of odontogenesis and proangiogenesis of human dental pulp cells through Wnt/MAPK/NF-kappaB pathways. Dent. Mater. **32**(11), 1301–1311 (2016)
34. S. Sprio et al., A graded multifunctional hybrid scaffold with superparamagnetic ability for periodontal regeneration. Int. J. Mol. Sci. **19**(11) (2018). pii: E3604
35. O. Ziv-Polat et al., Novel magnetic fibrin hydrogel scaffolds containing thrombin and growth factors conjugated iron oxide nanoparticles for tissue engineering. Int. J. Nanomedicine **7**, 1259–1274 (2012)
36. J. Meng et al., Paramagnetic nanofibrous composite films enhance the osteogenic responses of pre-osteoblast cells. Nanoscale **2**(12), 2565–2569 (2010)

37. J. Meng et al., Super-paramagnetic responsive nanofibrous scaffolds under static magnetic field enhance osteogenesis for bone repair in vivo. Sci. Rep. **3**, 2655 (2013)
38. X.B. Zeng et al., Magnetic responsive hydroxyapatite composite scaffolds construction for bone defect reparation. Int. J. Nanomedicine **7**, 3365–3378 (2012)
39. A. Tampieri et al., Magnetic bioinspired hybrid nanostructured collagen-hydroxyapatite scaffolds supporting cell proliferation and tuning regenerative process. ACS Appl. Mater. Interfaces **6**(18), 15697–15707 (2014)
40. Q. Cai et al., Osteogenic differentiation of MC3T3-E1 cells on poly(L-lactide)/Fe3O4 nanofibers with static magnetic field exposure. Korean J. Couns. Psychother. **55**, 166–173 (2015)
41. S. Hao et al., Modulatory effects of the composition and structure on the osteogenic enhancement for superparamagnetic scaffolds. Eng. Sci. **4**, 100–110 (2018)
42. S. Aliramaji, A. Zamanian, M. Mozafari, Super-paramagnetic responsive silk fibroin/chitosan/magnetite scaffolds with tunable pore structures for bone tissue engineering applications. Korean J. Couns. Psychother. **70**(Pt 1), 736–744 (2017)
43. K. Marycz et al., Promotion through external magnetic field of osteogenic differentiation potential in adipose-derived mesenchymal stem cells: design of polyurethane/poly(lactic) acid sponges doped with iron oxide nanoparticles. J. Biomed. Mater. Res. B Appl. Biomater. **108**, 1398–1411 (2020)
44. A.I. Aldebs et al., Effect of pulsed electromagnetic fields on human mesenchymal stem cells using 3D magnetic scaffolds. Bioelectromagnetics **41**, 175–187 (2020)
45. H.M. Yun et al., Magnetic nanocomposite scaffolds combined with static magnetic field in the stimulation of osteoblastic differentiation and bone formation. Biomaterials **85**, 88–98 (2016)
46. S. Panseri et al., Modifying bone scaffold architecture in vivo with permanent magnets to facilitate fixation of magnetic scaffolds. Bone **56**(2), 432–439 (2013)
47. A. Russo et al., Magnetic forces and magnetized biomaterials provide dynamic flux information during bone regeneration. J. Mater. Sci. Mater. Med. **27**(3), 51 (2016)
48. J. Huang et al., Osteogenic differentiation of bone marrow mesenchymal stem cells by magnetic nanoparticle composite scaffolds under a pulsed electromagnetic field. Saudi Pharm. J. **25**(4), 575–579 (2017)
49. Z. Yuan et al., Development of a 3D collagen model for the in vitro evaluation of magnetic-assisted osteogenesis. Sci. Rep. **8**(1), 16270 (2018)
50. U. D'Amora et al., 3D additive-manufactured nanocomposite magnetic scaffolds: effect of the application mode of a time-dependent magnetic field on hMSCs behavior. Bioact. Mater. **2**(3), 138–145 (2017)
51. I.A. Paun et al., 3D biomimetic magnetic structures for static magnetic field stimulation of osteogenesis. Int. J. Mol. Sci. **19**(2) (2018). pii: E495
52. B. Hermenegildo et al., Hydrogel-based magnetoelectric microenvironments for tissue stimulation. Colloids Surf. B Biointerfaces **181**, 1041–1047 (2019)
53. M.M. Fernandes et al., Bioinspired three-dimensional magnetoactive scaffolds for bone tissue engineering. ACS Appl. Mater. Interfaces **11**(48), 45265–45275 (2019)
54. C. Ribeiro et al., Proving the suitability of magnetoelectric stimuli for tissue engineering applications. Colloids Surf. B Biointerfaces **140**, 430–436 (2016)
55. M.A. Brady, S.D. Waldman, C.R. Ethier, The application of multiple biophysical cues to engineer functional neocartilage for treatment of osteoarthritis. Part I: cellular response. Tissue Eng. Part B Rev. **21**(1), 1–19 (2015)
56. M.A. Brady, S.D. Waldman, C.R. Ethier, The application of multiple biophysical cues to engineer functional neocartilage for treatment of osteoarthritis. Part II: signal transduction. Tissue Eng. Part B Rev. **21**(1), 20–33 (2015)
57. E.G. Popa et al., Magnetically-responsive hydrogels for modulation of chondrogenic commitment of human adipose-derived stem cells. Polymers (Basel) **8**(2) (2016). pii: E28
58. M. Brady et al., Bio-inspired design of a magnetically active trilayered scaffold for cartilage tissue engineering. J. Tissue Eng. Regen. Med. **11**, 1298–1302 (2015)
59. R. Fuhrer et al., Pressureless mechanical induction of stem cell differentiation is dose and frequency dependent. PLoS One **8**(11), e81362 (2013)

60. A.R. Tomas et al., Magneto-mechanical actuation of magnetic responsive fibrous scaffolds boosts tenogenesis of human adipose stem cells. Nanoscale **11**(39), 18255–18271 (2019)
61. G. Go et al., A magnetically actuated microscaffold containing mesenchymal stem cells for articular cartilage repair. Adv Healthc Mater Jul;**6**(13) (2017) https://doi.org/10.1002/adhm.201601378
62. Y. Sapir et al., The promotion of in vitro vessel-like organization of endothelial cells in magnetically responsive alginate scaffolds. Biomaterials **33**(16), 4100–4109 (2012)
63. Y. Sapir et al., Magnetically actuated alginate scaffold: a novel platform for promoting tissue organization and vascularization. Methods Mol. Biol. **1181**, 83–95 (2014)
64. J.J. Mack et al., Enhanced cell viability via strain stimulus and fluid flow in magnetically actuated scaffolds. Biotechnol. Bioeng. **110**(3), 936–946 (2013)
65. Y. Sapir, B. Polyak, S. Cohen, Cardiac tissue engineering in magnetically actuated scaffolds. Nanotechnology **25**(1), 014009 (2014)
66. C. Riggio et al., The orientation of the neuronal growth process can be directed via magnetic nanoparticles under an applied magnetic field. Nanomedicine **10**(7), 1549–1558 (2014)
67. C.D.L. Johnson et al., Injectable, magnetically orienting electrospun fiber conduits for neuron guidance. ACS Appl. Mater. Interfaces **11**(1), 356–372 (2019)
68. M. Antman-Passig, O. Shefi, Remote magnetic orientation of 3D collagen hydrogels for directed neuronal regeneration. Nano Lett. **16**(4), 2567–2573 (2016)
69. J.C. Rose et al., Nerve cells decide to orient inside an injectable hydrogel with minimal structural guidance. Nano Lett. **17**(6), 3782–3791 (2017)
70. M.L. Novak, T.J. Koh, Phenotypic transitions of macrophages orchestrate tissue repair. Am. J. Pathol. **183**(5), 1352–1363 (2013)
71. T.A. Wynn, K.M. Vannella, Macrophages in tissue repair, regeneration, and fibrosis. Immunity **44**(3), 450–462 (2016)
72. S. Hao et al., Macrophage phenotypic mechanomodulation of enhancing bone regeneration by superparamagnetic scaffold upon magnetization. Biomaterials **140**, 16–25 (2017)
73. H. Kang et al., Remote manipulation of ligand nano-oscillations regulates adhesion and polarization of macrophages in vivo. Nano Lett. **17**(10), 6415–6427 (2017)
74. M.B. Buechler, S.J. Turley, A short field guide to fibroblast function in immunity. Semin. Immunol. **35**, 48–58 (2018)
75. M.B. Furtado, M. Hasham, Properties and immune function of cardiac fibroblasts. Adv. Exp. Med. Biol. **1003**, 35–70 (2017)
76. R. Kuang et al., Influence of mechanical stimulation on human dermal fibroblasts derived from different body sites. Int. J. Clin. Exp. Med. **8**(5), 7641–7647 (2015)
77. S. Hao et al., Integration of a superparamagnetic scaffold and magnetic field to enhance the wound-healing phenotype of fibroblasts. ACS Appl. Mater. Interfaces **10**(27), 22913–22923 (2018)
78. M.T. Lopez-Lopez et al., Generation and characterization of novel magnetic field-responsive biomaterials. PLoS One **10**(7), e0133878 (2015)
79. Z. Liu et al., Activation of Schwann cells in vitro by magnetic nanocomposites via applied magnetic field. Int. J. Nanomedicine **10**, 43–61 (2015)
80. Z. Liu et al., A magnetically responsive nanocomposite scaffold combined with Schwann cells promotes sciatic nerve regeneration upon exposure to magnetic field. Int. J. Nanomedicine **12**, 7815–7832 (2017)
81. Y. Sapir-Lekhovitser et al., Magnetically actuated tissue engineered scaffold: insights into mechanism of physical stimulation. Nanoscale **8**(6), 3386–3399 (2016)
82. S.L. Arias et al., Magnetic targeting of smooth muscle cells in vitro using a magnetic bacterial cellulose to improve cell retention in tissue-engineering vascular grafts. Acta Biomater. **77**, 172–181 (2018)
83. S.J. Mousavi, M.H. Doweidar, Numerical modeling of cell differentiation and proliferation in force-induced substrates via encapsulated magnetic nanoparticles. Comput. Methods Programs Biomed. **130**, 106–117 (2016)

Chapter 2
Conductive Nanostructured Scaffolds for Guiding Tissue Regeneration

Haiyan Xu, Jie Meng, and Tao Wen

Abstract Biological electricity is ubiquitous in life to maintain many functions of organs. Therefore, conductivity is one crucial factor to biomaterial scaffolds guiding electrically excitable tissue regeneration. Accumulating evidence has indicated the importance of providing electrical active microenvironments mimicking natural physiological conditions. In this chapter, various kinds of conductive scaffolds and processing technologies are introduced, and application potentials of the conductive scaffolds are revealed by typical examples of guiding different tissue regeneration include cardiac, skeletal, nerve, and skin. In addition, synergistic effects of conductivity and mechanical property of tissue engineering scaffolds are addressed as well, and underling mechanisms have been explored and discussed.

Keywords Conductive · Scaffolds · Tissue regeneration · Nanoparticles · Nanostructures

2.1 Introduction

Biological electricity is ubiquitous in life; for example, excitable tissues such as heart and nerve have closer relationship with electricity, and bone and skin are reported having electromagnetic activity as well [1]. These tissues can rapidly change electrochemical impulses at the cell membranes to transmit signals along the muscle membranes or nerves, maintaining the functions of the organs. For example, heart is composed of three major types of cardiac muscle including atrial muscle, ventricular muscle, and specialized excitatory and conductive muscle fibers that play vital roles in the electrical signal transduction. The cardiac muscle generates action potentials passing over the cardiac muscle membrane and spreading to the interior of the cardiac

H. Xu (✉) · J. Meng · T. Wen
Department of Biomedical Engineering, Institute of Basic Medical Sciences, Chinese Academy of Medical Sciences and Peking Union Medical College, Beijing, P. R. China
e-mail: xuhy@pumc.edu.cn

H. Xu, N. Gu (eds.), *Nanotechnology in Regenerative Medicine and Drug Delivery Therapy*, https://doi.org/10.1007/978-981-15-5386-8_2

muscle fiber along the membranes of the transverse tubules and then the membranes of the longitudinal sarcoplasmic tubules to cause release of calcium ions into the muscle sarcoplasm from the sarcoplasmic reticulum. These calcium ions diffuse into the myofibrils and catalyze the chemical reactions that promote sliding of the actin and myosin filaments along one another, which produces muscle contraction. Therefore, the normal functions of excitable tissues rely on the electrical signal transduction between the cells. This nature can explain why conductive scaffolds have attracted intense research interests on tissue regeneration. Experimental evidence is increasing that conductive scaffolds can promote adhesion, proliferation, migration, and differentiation of cells, including cardiac, nerve, bone, muscle, fibroblasts, keratinocytes, and mesenchymal stem cells. In this chapter, conductive scaffolds are introduced from design and fabrication, electrical and mechanical properties, and the interactions between the scaffolds and tissue specific cells as well as stem cells, mainly including cardiomyocytes, neuron cells, skeletal cells, bone related cells, and fibroblasts, and their therapeutic effects on the tissue regeneration.

2.2 Classification and Fabrication of Conductive Scaffolds

Conductive scaffolds can be in general summarized to two main categories according the conductive substances included in scaffolds (Fig. 2.1), one kind of additives is conductive polymers such as polypyrrole (PPY) and polyaniline (PANi), and the other one is conductive nanoparticles such as carbon nanotubes, graphene, gold nanoparticles, and silica wire. From the view of structures, nanostructures are highly involved in the fabrication of conductive scaffolds; hence, the two categories can be further divided into subclasses, including nanocomposite hydrogels and scaffolds with nanofibrous, nano-roughness, micro–nano-patterned structures, and casting or molding scaffolds with embedded nanomaterials, all of which are intended to mimic the structural features of natural extracellular matrix where cells live in.

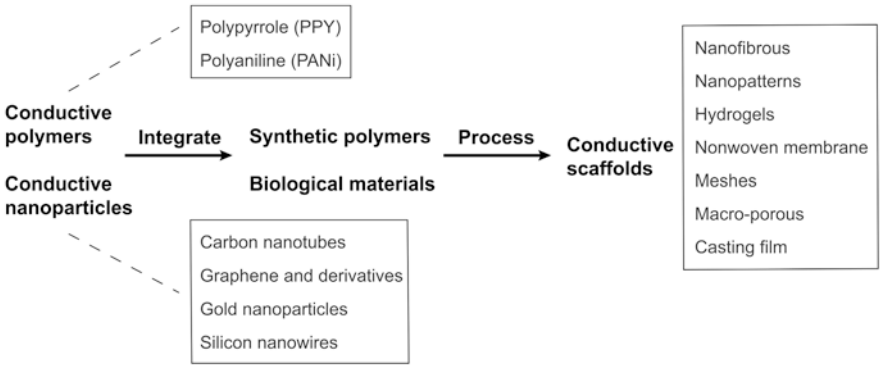

Fig. 2.1 Summary of conductive materials and scaffolds for tissue engineering and regenerative medicine

2.2.1 Conductive Polymers

Conductive polymers are organic electronically conjugated polymers with electro-optic properties like those of metals, which is one important class of the candidates as conductive components to give scaffolds conductivity. The polymers can form electrical pathways of charge carriers because π-electrons move freely within the molecular chain [2, 3]. Polymers with intrinsic conductive properties have been largely studied in relation to their incorporation into various scaffolds for uses in tissue engineering and regeneration. The reason for this interest is that such scaffolds could electrically stimulate cells and thus regulate specific cellular activities and by this means influence the process of regeneration of those tissues that respond to electrical impulses.

There are several kinds of conductive polymers that have been reported in literatures, mostly investigated in tissue engineering and regenerative medicine are polypyrrole (PPY) and polyaniline (PANi). The two macromolecules possess the good conductivity of 10^2~5×10^3 and 10–10^7 S/m, respectively [3]. For comparison, the range of conductivity of ventricular muscle, blood, and skeletal muscle is 0.03–0.6 S/m [4]. However, disadvantages of mechanical properties and biocompatibility for these polymers are obvious as well. For examples, PPY is insoluble in water, susceptible to irreversible oxidation, and fragile; and PANi has low solubility in aqueous solution, lack of plasticity, and poor cell adhesion and growth. Therefore, it is no surprise that the two conductive polymers are usually used in combination with other materials to develop conducting composite scaffolds for tissue engineering and regenerative medicine.

2.2.2 Conductive Inorganic Nanoparticles

Some kinds of nanoparticles are electrically conductive, mainly including graphene, carbon nanotubes, gold nanoparticles, silver nanoparticles, and silica nanowire, which have been investigated in the tissue engineering and regenerative medicine. Below is a brief introduction about the conductive nanoparticles.

Graphene is strictly a two-dimensional (2D) material that exhibits exceptionally high crystal and electronic quality, rapidly rising on the horizon of materials science and physics, and has already revealed a cornucopia of new physics and potential applications [5]. The 2D carbon nanomaterials commonly include three kinds of graphene: graphene oxide (GO), a highly oxidative form of graphene, reduced graphene oxide (rGO), and graphene sheets [6]. There are several methods to synthesize graphene, commonly classified to four different methods including chemical vapor deposition and epitaxial growth, micromechanical exfoliation, epitaxial growth on electrically insulating surfaces, and the creation from colloidal suspensions [7]. Graphene is a giant aromatic macromolecule that conducts both electricity and heat well in two dimensions. It has a large theoretical specific surface area

(2630 m^2/g), high intrinsic mobility (200,000 cm^2/v s), high Young's modulus (~1.0 TPa) and thermal conductivity (~5000 W/m K), good optical transmittance (~97.7%), and good electrical conductivity [8]. These fascinating properties of GOs are mainly derived from its unique chemical structures composed of small sp^2 carbon domains surrounded by sp^3 carbon domains and oxygen containing hydrophilic functional groups [6]. The graphene is honeycomb lattice, which is composed of two equivalent sub-lattices of carbon atoms bonded together with σ-bonds. Each carbon atom in the lattice has a π orbital that contributes to a delocalized network of electrons. This atomic structure, combined with the electron distribution of graphene, results in high electrical conductivity. Electrons in graphene, obeying a linear dispersion relation, behave like massless relativistic particles [9]. Chemically functionalized graphene can be readily mixed with other polymers in solution, producing a new class of electrically conductive nanocomposites [10].

Carbon nanotubes are unique tubular structures of nanometer diameter and large length/diameter ratio. There are two main types of carbon nanotubes: single-walled carbon nanotubes (SWNTs) and multi-walled carbon nanotubes (MWNTs). SWNTs consist of a single graphite sheet seamlessly wrapped into a cylindrical tube. MWNTs are composed of coaxial nanotube cylinders, of different helicities, with a typical spacing of ~0.34 nm, which corresponds closely to the inter-layer distance in graphite of 0.335 nm [11]. There are different types of CNTs depending on the orientation of the tube axis relative to the carbon network, which are described by the indices of the chiral vector, n and m. Armchair CNTs ($n = m$) usually show metallic conductivity while zigzag ($m = 0$) or chiral ($n \neq m$) CNTs are semiconducting [12, 13]. SWNTs and MWNTs are usually made by carbon-arc discharge, laser ablation of carbon, or chemical vapor deposition (typically on catalytic particles) [14]. The excellent mechanical and electronic properties of carbon nanotubes result from their quasi-one-dimensional (1D) structure and the graphite-like arrangement of the carbon atoms in the shells. Thus, the nanotubes have high Young's modulus and tensile strength, which makes them preferable for composite materials with improved mechanical properties. The electronic band structure of the nanotube can be described by considering the bonding of the carbon atoms arranged in a hexagonal lattice. Each carbon atom ($Z = 6$) is covalently bonded to three neighbor carbons via sp^2 molecular orbitals. The fourth valence electron, in the p_z orbital, hybridizes with all the other p_z orbitals to form a delocalized π-band [15]. SWNTs can be either metals or semiconductors depending on the chirality (the chiral angle between hexagons and the tube axis), which have relatively large band gaps (~0.5 eV for typical diameter of 1.5 nm) or small (~10 meV) [16]. The electronic properties of perfect MWNTs are rather similar to those of perfect SWNTs, because the coupling between the cylinders is weak in MWNTs. Because of the nearly one-dimensional electronic structure, electronic transport in metallic SWNTs and MWNTs occurs ballistically (i.e., without scattering) over long nanotube lengths, enabling them to carry high currents with essentially no heating [17].

Nanowires are an important class of 1D materials that have been attracting a great deal of interest in recent years. Nanowires are regarded as an alternative to

CNTs because it is easier to control their electrical properties. As long as the surface is properly passivated (something that occurs naturally during or right after growth), they are invariably semiconducting. The 1D semiconductors usually exhibit excellent electronic, optical, mechanical, thermal, and chemical properties, which lead to various applications ranging from chemical, biological, and environmental sensors and field-effect transistors to logic circuits [18]. Silicon nanowires (SiNWs) are one of the most important 1D semiconductors. With doped p type and n type, SiNWs can be assembled to form p-n junctions, bipolar transistors, and complementary inverters. Thus, SiNWs may be the crucial components for nanoscale electronics [19]. SiNWs may be fabricated through both "top-down" (i.e. through lithographic patterning) and "bottom-up" (chemical synthesis of SiNWs) approaches. The methods include chemical vapor deposition, laser ablation, vapor transport and condensation, molecular beam epitaxy, annealing on silicon, solution growth, and catalytic etching [20]. Among them, chemical vapor deposition, vapor transport condensation, and annealing of catalytic nanoclusters on silicon have been commonly used for their simplicity, minimal equipment needs, and large-scale production capability [21]. The properties of nanowires are determined by the surface area to volume ratio and defects. NWs can possess good electronic and optical properties, such as enhanced ohmic contact resistance, carrier depletion, which can severely influence electrical conduction and surface passivation abound [22]. On the other hand, silicon nanowires are rodlike systems constructed around a single-crystalline core. When there are sufficiently small diameters and a strong anisotropy, most of their properties emerge: the band gap, the Young's modulus, the electrical conductance, or the specific heat [23]. A fundamental modification of electronic properties from the bulk can be evidenced in SiNWs. For example, the indirect bandgap (e.g., ~1.1 eV) between the conduction band minimum and the valence band (VB) maximum of bulk Si could be modified to a direct bandgap due to quantum confinement effects of SiNWs. The diameter dependence of the dopant ionization efficiency, the influence of surface traps on the charge carrier density and the charge carrier mobility in silicon nanowires are the three effects essential for the conductivity of a silicon nanowire [24].

Among the different metal nanoparticles, gold nanoparticles (AuNPs) have a rich history in chemistry. Dating back to ancient Roman times, they were used to stain glasses for decorative purposes. The modern era of AuNP synthesis began over 150 years ago, Michael Faraday was possibly the first to observe that colloidal gold solutions have properties that differ from bulk gold [25]. Due to the distinct optical and electronic properties, AuNPs attract particular interest and are widely used [26, 27]. A wide array of solution-based approaches has been developed in the past few decades to control the size, shape, and surface functionality of AuNPs. The top-down method of AuNPs produces nanoparticles by shattering from bulk gold, while the top-up method involves building up of nanomaterials starting from the atomic level. Typically, the top-up preparation of AuNPs by chemical reduction of gold ions from a solution involves two major parts: (1) reduction of a gold precursor to produce the Au (0) and (2) stabilization of the obtained AuNPs by suitable

stabilizing or capping agents which prevent aggregation of nanoparticles from forming metallic precipitate [28]. Bulk gold is known as a shiny, yellow noble metal that does not tarnish, has a face-centered cubic structure, is non-magnetic, melts at 1336 K, and has density a 19,320 g/cm. However, a nanostructure containing the same gold is quite different: 10-nm particles absorb green light and thus appear red. The melting temperature decreases dramatically as the sample size goes down [29]. Moreover, it was revealed that AuNPs show efficient catalytic activity, particularly those below 10 nm in size. As the particle size of gold is smaller than 2 nm, the valence and conduction bands become narrower, and a gap appears between them causing the metallic character to disappear [30]. Nevertheless, the key characteristic that distinguishes AuNPs from many other nanomaterials is their unique optical properties resulting from a physical phenomenon known as localized surface plasmon resonance (LSPR), which is present typically in nanostructures of plasmonic materials, such as gold, silver, copper, and aluminum. LSPR involves coherent oscillation and excitation of conduction band electrons on the surface of plasmonic nanostructures. For AuNPs, the irradiation of light can range in the ultraviolet-visible-near infrared (UV-VIS-NIR) spectral region. The conditions for the occurrence of LSPR are known to be highly sensitive to their geometric parameters (e.g., size, shape, and symmetry), the material composition and distribution, as well as the overall arrangement of NPs [31, 32]. Electrical conductivity of AuNPs decreases with a reduced dimension due to increased surface scattering, and the surrounding conditions are also important [33]. The gold nanoparticles are generally dispersed in or combined with other materials, that the dispersing process and preparation methods are important in nanofabricaton. A number of studies have shown that the electrical and mechanical properties of the conducting polymers can be improved by the incorporation of gold nanoparticles [34].

Silver nanoparticles (AgNPs) are nanoparticles of silver which are in the range of 1 and 100 nm in size. AgNPs are known to exhibit antimicrobial/antiviral properties, superior catalytic activity and improved enhancement factors for surface-enhanced Raman spectroscopy (SERS) [35, 36]. Silver also has the highest electrical and thermal conductivity among all metals, making it an ideal component for electrical interconnection, though AgNPs toxicity has been demonstrated and raised concerns for the safety when intended to use in biomedical products in vivo [37–39]. In AgNPs, the electrons move freely in the conduction band and valence band which lie very close to each other [36]. Because of surface scattering, the effective resistivity of a nanoscale metal film or wire is higher than the bulk value. However, the scatter of the silver nanoparticle is random variations in the resistance of the contacts, thus AgNPs largely retain the electrical conductivity of the bulk material [40]. For example, the silver nanoparticle-filled polymer composites can be used as conductive adhesives, which meet the demand of preparing conductive polymer composites achieving the highest electrical and/or thermal conductivity [41].

2.2.3 *Summarization of Physical Properties for Conductive Scaffolds*

In the following Table 2.1, scaffolds that reported electrical properties and/or mechanical properties in literatures cited in this chapter are collected and summarized for comparisons that may help to gain insights of roles of the conductivity. It is noted from the tables that the conductivity is determined by various kinds of measurement from different laboratories, and the range of the conductivity value for those scaffolds is quite wide, from semiconductive to conductive to some extents, and those scaffolds not reported the conductivity and mechanical properties are not included in Table 2.1.

2.3 Conductive Scaffolds in Myocardial Tissue Regeneration

Cardiovascular diseases are the leading cause of morbidity and mortality in the world, also resulting in huge economic burdens on national economies. Among those, myocardial infarction (MI) is the most frequently identified specific cause of dilated cardiomyopathy, leading to symptomatic congestive heart failure over time. The main reasons are that nonconductive scar tissue formed in the infarct region after myocardial infarction, which interrupts the electrical communication between adjacent cardiomyocytes, resulting in the propagation of electrical impulse and the delay of regional contraction, contributes to ventricular dysfunction that are common in heart after myocardial infarction (MI); at the same time, the regional structural changes, especially in left ventricular (LV) remodeling after MI can lead to global LV geometric change, which contributes to an increase in LV wall stress and mitral regurgitation [42].

A cardiac patch strategy is a promising option to regenerating an infarcted heart. Besides applying biocompatible scaffolds with or without cells acting as the patch, it has been recognized gradually that conductive scaffolds can contribute more to restore impulse propagation to synchronize contraction and restore ventricular function by electrically connecting isolated cardiomyocytes to intact tissue, allowing them to contribute to global heart function. Meanwhile, it should be emphasized that when designing scaffolds for heart tissue regeneration, mechanical stiffness of the scaffolds should be particularly taken considerations as well as the electrical conductivity, because the scaffolds have to withstand the continuous stretching/relaxing motion of the myocardium that occurs during each heartbeat as well as to provide mechanical support to prevents cardiac remodeling and to improve LV function after MI [43]. Therefore, appropriate stiffness and conductivity are both important factors for scaffolds to enhance cardiomyocyte maturation and to support the contractile and physiological loads of heart tissue. In the past years, a considerable amount of effort has been devoted toward the development of biomimetic scaffolds for cardiac tissue engineering. The major challenges include that most of the

Table 2.1 Summary of conductive scaffolds for tissue engineering and regeneration

Electrical active component	Scaffold	Conductivity	Young's modulus (unless noted)	References
Cardiac tissue				
Conductive polymers	PPY grafted to chitosan sidechain, hydrogel	0.005–0.03 S/m	2–6 kPa	[46, 47]
	PPY grafted to chitosan sidechain was integrated to gelfoam GelMA to form 3D patches	~0.012 S/m	Tensile strength: ~20 kPa; ultimate strain: ~120%	[48]
	PPY-GelMA nanoparticles blended in electrospun film of GelMA/PCL by crosslinking	0.025–0.3 S/m		[51]
	PPY deposited on the acid-modified silk fibroin patterned with nanoscale ridges and grooves	Resistivity: 200–500 Ω/sq (corresponding to ~1 S/cm)	Tensile strength: ~7 MPa Elastic modulus: ~200 MPa	[52]
	PANi/poly(glycerol sebacate), casting film	0.129–1.77 S/m	2.4–6.3 MPa	[114]
	PANi-contained gelatin, electrospun fibers	1–2.1 S/m	499–1384 MPa	[54]
	Electrospun PANi blended with PLGA, followed by HCL doping	0.31 S/m	91.7 MPa	[55]
	PANi blended with PLA, electrospun fibers	2.1×10^{-5} S/m		[56]
	PANi coating on chitosan films micropatterned with a re-entrant honeycomb (bow-tie) pattern	1-direction: 9.3 S/m 2-direction: 2.4 S/m	6.73 MPa	[57]
	Poly (thiophene-3-acetic acid) and methacrylated aminated gelatin (MAAG)	0.01 S/m	22.7–493.1 kPa	[60]
	PLA mixed with PANi as core, PLA and PEG composed the out layer, electrospun fibers	$0.23–0.99 \times 10^{-4}$ S/m	39 MPa	[58]
	PANi on tissue-culture-treated polystyrene, drop-drying	2 kΩ/sq		[53]

Carbon nanomaterials	Graphene	4170 $cm^2/V\ s$		[72]
	Graphene patterned with ridges	7.0 kΩ		[73]
	rGO blended with GelMA	1.5–4 kΩ	22.6 kPa	[79]
	Graphene/collagen biohybrid, casting	0.65 S/m	0.77–1.29 MPa	[74]
	Collagen scaffolds coated covalently with GO reduced in 2% sodium hydrosulfite	3.8–29 × 10^{-4} S/m	160–750 kPa	[75]
	rGO/methacryloyl-substituted tropoelastin	~1 kΩ under 10 Hz	19.3 kPa	[77]
	Graphene blended with PCL, electrospun fibers	1.5 × 10^{-11} to 1.5 × 10^{-8} S/m		[78]
	rGO blended with silk fibroin, electrospun fibers	4.3 kΩ	~12.5 MPa	[76]
	GO with oligo(poly(ethylene glycol) fumarate, injectable hydrogel	0.42 S/m		[80]
	GO incorporated in PEGDA700-Melamine crosslinked with thiol-modified hyaluronic acid	0.03 S/m	25 Pa	[81]
	Gold nanoparticle-modified GO blended with chitosan	0.012 S/m		[93]
	MWCNTs blended with GelMA	~2.2 kΩ under 1 Hz	20–54 kPa	[70]
	SWCNTs blended with poly (*N*-isopropylacrylamide), hydrogel	1.08 × 10^{-4} Ω^{-1}		[71]
	SWCNTs blended with collagen, hydrogel	1.72 × 10^{-6} S/m		[96]
	SWNTs/gelatin, hydrogel	5 × 10^{-5} S/m		[61]
	CNT dispersed in aligned poly(glycerol sebacate): gelatin, electrospun nanofibers	~5 kΩ under 100 Hz	Tensile strength: ~1.4 MPa	[65]
	Injectable reverse thermal gel functionalized with MWCNTs	6.93 × 10^{-4} S/m	Shear modulus: 221 Pa	[63]
	CNTs blended with 124 polymer	60.9–76.2 kΩ	1.6–2.2 MPa	[64]
	CNTs blended with polycaprolactone and silk fibroin, aligned nanofiber yarns	6.5–8.1 × 10^{-5} S/m	In sutures warp direction: 110 MPa; in weft direction: 20 MPa	[68]
	MWCNT sprayed on polyurethane electrospun film	0.005–2.13 S/m	2.32–5.83 MPa	[66]
	Carbon fibers blended with PVA, hydrogel	0.3 S/m	2.3 MPa	[99]

(continued)

Table 2.1 (continued)

Electrical active component	Scaffold	Conductivity	Young's modulus (unless noted)	References
Gold nanoparticles (GNPs)	GNPs blended with chitosan, hydrogel	0.13 S/m	6.8 kPa	[86]
	GNR blended with GelMA, bioprinting	12.0 kΩ under 20 Hz 5.0 kΩ under 100 Hz	4.7 kPa	[90]
	GNRs/GelMA, hydrogel	810 Ω under 20 Hz 700 Ω under 100 Hz	1.3 kPa	[89]
	GNPs blended with HEMA	15.3 S/m	0.6–1.6 MPa	[85]
	GNPs blended with reverse thermal gel	140.1 kΩ	0.26 kPa	[88]
	GNPs deposited on fibrous decellularized matrix	~285 Ω		[92]
	Gold nanorods (GNRs)/GelMA Silica nanoparticles (SNP) blended with GelMA	GNRs/GelMA: 2.5 kΩ under 20 Hz SNP/GelMA: 30.77 kΩ under 20 Hz	GNR/GelMA: 1.37 kPa SNP/GelMA: 0.55 kPa	[98]
Nerve				
Conductive polymers	PPY blended with PDLLA	5.65–15.56 mS/cm		[124]
	PPY blended with polyphenol/tannic acid, hydrogel	0.05–0.18 S/cm	0.3–2.2 kPa	[126]
	PPY/hyaluronic acid with CNTs	12.59 kΩ under 1 Hz 1.67 kΩ under 10 Hz	3.17 kPa	[136]
	PANi in poly (epsilon-caprolactone)/gelatin, electrospun nanofibers	2.4×10^{-8} Ω^{-1}	Tensile strength: 8.19–8.75 MPa	[122]
	PANi blended with polyethylene glycol diacrylate	1.1×10^{-3} mS/cm		[123]
	poly(glycerol sebacate) mixed with aniline pentamer conjugated with polyurethane	1.4×10^{-6} to 8.5×10^{-5} S/cm	5.6–75.5 MPa	[127]

Carbon nanomaterials	Graphene on tissue culture plate	350 Ω (50 μm × 50 μm)		[128]
	rGO blended with poly(3,4-ethylenedioxythiophene)	0.017–0.025 S/m	84 MPa	[132]
	Single layered graphene (SG) or multilayered graphene (MG) coated with PDA/RGD and polycaprolactone (PCL), 3D printing and layer by layer casting	SG/PCL: 0.89 S/m MG/PCL: 0.64 S/m	SG/PCL: 68.74 MPa MG/PCL: 58.63 MPa	[130]
	highly-conductive few-walled-CNT (fwCNT) blended with gum Arabic	3000 S/cm		[137]
	agarose modified carbon nanofibers, wet spinning	145 S/cm	LN+: 867 MPa	[133]
	CNT/chitin, plasma-treated	2.89 S/m	420 MPa	[135]
	SWCNTs modified by PPY and blended with hyaluronic acid	12.59 kΩ under 1 Hz 1.67 kΩ under 10 Hz	3.17 kPa	[136]
Skeletal				
Conductive polymers	PANi blended with PCL, electrospun fibers,	63.6 mS/cm	55.2 MPa	[117]
	Grafting aniline pentamer to poly(ethylene glycol)-co-poly(glycerol sebacate)	1.84×10^{-4} S/cm	24.6 MPa	[115]
	Self-healable conductive injectable hydrogels synthesized by tetramer-graft-4-formylbenzoic acid /*N*-carboxyethyl chitosan	$2.7–3.4 \times 10^{-2}$ mS/cm	The storage modulus: 300–600 Pa	[116]
Carbon nanomaterials	r(GO/PAAm), Casting film	$1.3–1.4 \times 10^{-4}$ S/cm	r(GO/PAAm): 49–57 kPa	[113]
	GO/PCL, electrospun fibers	10^{-7} S/m	Tensile strength: 4.0 MPa	[108]
	GO and hydroxyapatite nanoparticles, hydrogel	0.12–0.2 S/m	200–320 kPa	[110]
	MWCNT/PLA, electrospun fibers	Random: 1×10^4 Ω/sq Aligned: 1×10^3 Ω/sq	Random: 20–80 MPa Aligned: 40–90 MPa	[107]
	MWCNTs membrane functionalized by the [4 + 2] Diels–Alder cycloaddition reaction of 1,3 butadiene	3×10^3 S/m		[105]

(continued)

Table 2.1 (continued)

Electrical active component	Scaffold	Conductivity	Young's modulus (unless noted)	References
Wound				
Conductive polymers	Quaternized chitosan grafted with polyaniline blended with benzaldehyde group functionalized poly(ethylene glycol)-co-poly(glycerol sebacate), hydrogel	2.25–3.5 mS/cm	58–368 Pa	[138]
	Oxidized hyaluronic acid-graft-aniline tetramer/*N*-carboxyethyl chitosan, hydrogel	0.1–0.45 mS/cm	Shear modulus: 0.13–1.40 kPa	[139]
Carbon nanomaterials	rGO/hyaluronic acid graft dopamine	$(1.2–2.5) \times 10^{-4}$ S/m	Shear modulus: 0.32–0.42 kPa	[147]
	Polydopamine-reduced GO dispersed in mixture of chitosan and silk fibroin, freeze-drying	0.05–0.25 S/cm	Compressive strength: 60–90 kPa	[146]
	CNTs blended with glycidyl methacrylate functionalized quaternized chitosan	0.04–0.12 S/m		[148]

polymers to be used as scaffolds are electrically insulating, and scaffolds lack the structural and mechanical robustness to engineer cardiac tissue constructs with suitable electrophysiological functions. Strategies to overcome the problems are incorporating conductive polymers or/and conductive nanomaterials into polymeric materials to bring the electrical conductivity to the scaffolds, and the incorporated conductive materials can increase the stiffness of the scaffolds at the same time. In addition, the conductive engineered cardiac tissue-like constructs are also expected to provide a powerful platform for drug screening and assessment of cardiac toxicity in vitro, because they are simple, fast, relatively cheap, and require fewer animals, therefore would be a significant advancement for developing new drugs and have led to a growing interest in recent years.

2.3.1 Composite Scaffolds Containing Conductive Polymers

2.3.1.1 Polypyrrole

Polypyrrole (PPY) is a well-known conductive polymer in tissue engineering. However, as introduced before, PPY is a non-thermal plastic, mechanically rigid, and brittle. Hence, it is usually conjugated to or just blended with insulating polymers for fabricating conductive scaffolds. By this way, its biocompatibility is improved due to compositing with other polymers and the resulting scaffolds obtained improved conductivity [44, 45].

Hydrogels containing PPY have been widely investigated. Chitosan is biodegradable, produces minimal immune reaction in humans, and has been used extensively as a biomaterial for decades. For example, when PPY was grafted to chitosan side chain by a chemical oxidative polymerization, a PPY-chitosan hydrogel could be generated, which did not reduce the attachment, metabolism, or proliferation of rat smooth muscle cells (SMCs) in vitro. Importantly, the PPY-chitosan hydrogels formed hysteresis loops when subjected to a cyclic voltammetry, suggesting they are semiconductive, whereas ungrafted chitosan was not. When neonatal rat cardiomyocytes were seeded on the semiconductive hydrogel, they showed enhanced Ca^{2+} signal conduction in comparison with those on the chitosan alone. In addition to the semiconductivity, the PPY-chitosan had good mechanical properties and was injectable, these features collectively in turn significantly improved border zone conduction velocity with improved cardiac function around the scar of rat hearts after MI [46]. Furthermore, the PPY-chitosan injected was reported to form a hydrogel in situ and restore tissue conductivity of the scar and re-establish synchronous ventricular contraction, which were evidenced by the improvement of electrical impulse propagation across the scarred tissue and the decreased QRS interval, whereas saline control or chitosan alone continued to have delayed propagation patterns and significantly reduced conduction velocity compared to healthy controls [47]. When the PPY-chitosan was integrated with a conventional gelfoam GelMA (methyl acrylic anhydride-gelatin), the two components formed a three-dimensional conductive

patch (PPY-chitosan+GelMA) used to support cardiomyocyte (CM) viability and function in vitro. The PPY-chitosan+GelMA patch not only showed a higher mean breaking stress but also showed higher conductivity than GelMA or GelMA soaked with chitosan (chitosan+GelMA) in the ex vivo conductivity testing. As a result, the Ca^{2+} transient velocity of cardiomyocytes cultured on the conductive patch was 2.5-fold higher than that of cardiomyocytes cultured on GelMA or chitosan+GelMA. When the patches were implanted in a full-thickness right ventricular outflow tract defect of rats, the patch-implanted hearts had faster conduction velocities, as measured on the epicardial surface by optical mapping at 4 weeks post-implantation. Furthermore, the composite looked biocompatible, since continuous electrocardiographic telemetry did not reveal any pathologic arrhythmias after patch implantation and noted that there was higher inflammatory cell infiltration in the two control groups compared with the conductive GelMA patch [48].

Besides combined with hydrogels, PPY can be integrated into nanofibrous scaffolds by utilizing electrospinning technique. It is well documented that nanofibrous structures are to some extent like that of natural extracellular matrix, and electroactive scaffolds that provide topographical cues as well as electrical and mechanical properties are attractive and have been largely investigated in the past decades. One of the simple approaches of generating conductive nanofibers was to have poly(lactic-co-glycolic acid) (PLGA) fibers coated with PPY, the resulting product was named as electromechanically active fiber scaffold. Interestingly, the scaffold was reported to be capable of generating mechanical actuation through the volume change of the individual fibers as well as delivering direct electrical stimulation to induced human pluripotent stem cells (iPS). By this way, the scaffold increased the expression of cardiomyocyte-specific genes (*Actinin*, *NKX2.5*, *GATA4*, *Myh6*, *c-kit*) and downregulated the expression of stemness genes (*Oct4*, *Nanog*) for both electrical stimulated and unstimulated protocols, and the scaffold while exhibiting no cytotoxic effects on the iPS [49]. Nevertheless, the biocompatibility of high concentrations of PPY remains controversial, higher than 9.7 μg/mL PPY polymerized by oxidative doping has been considered harmful for cell viability/proliferation [50]. To overcome this challenge, a research group proposed an approach to reduce the amount of PPY but to retain the necessary conductivity: to integrate conductive nanoparticles composed of GelMA and PPY with electrospun nanofibrous membrane composed of polycaprolactone (PCL) and GelMA (ES-GelMA/PCL) following the separate preparations. First step was to prepare the conductive nanoparticles (GelMA-PPY); next, the GelMA-PPY nanoparticles were uniformly crosslinked on the ES-GelMA/PCL membrane, the more deposition of conductive nanoparticles, the higher conductivity the scaffold had. In addition, GelMA-PPY nanoparticles brought rough topography to the nanofibrous membrane, which was considered beneficial to the vascularization in vitro. The conductive scaffolds enhanced the function of cardiomyocytes and yielded their synchronous contraction. After implanted on the infarcted heart for 4 weeks, the conductive membrane had the infarct area decreased by about 50%, the left ventricular shortening fraction percent was increased by about 20%, and the neovascular density in the infarct area was significantly increased by about nine times compared with that in the MI group [51].

PPY was also used in nanostructural patterns that are extracellular cues to guide cell proliferation and differentiation. For example, through polymerization on surface, PPY was deposited directly on the acid-modified silk fibroin-patterned nanoscale ridges and grooves mimicking of native myocardial extracellular matrix (ECM) topography, which made a remarkable reduction of resistance for the silk fibroin film, from 10^6 Ω/sq for the unmodified sheet to the range of 200–500 Ω/sq [52]. Consequently, the patterned conductive substrates maintained high cell viability over 21 days incubation, meanwhile, the structural and functional properties of cultured human pluripotent stem cells (hPSC)-derived cardiomyocytes were enhanced due to the electroconductive and the anisotropic topographical cues, evidenced by the increase of cellular organization and sarcomere development and significantly upregulated the expression and polarization of connexin 43 (Cx43) and the expression of genes that encode key proteins involved in regulating the contractile and electrophysiological function of mature human cardiac tissue.

2.3.1.2 Polyaniline and Derivatives

Another frequently investigated conductive polymer is polyaniline (PANi) that is a substance polymerized chemically or electrochemically with monomeric aniline. In an earlier literature, a group investigated the adhesion and proliferation properties of rat cardiac myoblast H9c2 cells on the polyaniline substrate. It was reported that the conductive polyaniline allowed for cell attachment and proliferation. In comparison with tissue-culture-treated polystyrene (TCP), the initial adhesion of H9c2 cells to the conductive PANi was slightly reduced by 7%, but the overall rate of cell proliferation on the conductive surfaces was like that on the control TCP surfaces. After 6 days in culture, the cells formed confluent monolayers which were morphologically indistinguishable. However, the stability of conductivity remained a challenge. Although the conductive PANi retained a significant level of electrical conductivity for at least 100 h in an aqueous physiologic environment, the conductivity gradually decreased by about three orders of magnitude over time [53]. It is easy to fabricate conductive scaffolds by blending PANi with various kinds of polymers. For example, PANi was able to be blended with gelatin and co-electrospun into nanofibers. The blend fibers containing less than 3% PANi in total weight showed uniform morphology without phase segregation, and interestingly, the average diameter of fibers was reduced from 803 nm to less than 100 nm, and the tensile modulus increased from 499 to 1384 MPa, due to the addition of PANi. The resulting fibrous scaffolds could support rat cardiac myoblast H9c2 cell attachment and proliferation, and the cells grown on the fibers of smaller diameter showed more stressful morphology [54]. A mesh made of aligned nanofibers of PANi and poly(lactic-co-glycolic acid) (PLGA) was reported to be able to attract negatively charged fibronectin and laminin that are beneficial to enhance cell adhesion. The adhered cardiomyocytes became connected to each other and formed isolated cell clusters; the cells within each cluster elongated and aligned their morphology along the major axis of the fibrous mesh, and the cardiomyocytes within each cluster beat

synchronously. At the same time, the gap-junction protein connexin 43 was observed upregulated, implying that the cells have developed coupling between each other. Furthermore, the beating rates among these isolated cell clusters were capable of being synchronized under an electrical stimulation imitating that generated in a native heart, which is an important feature, because the impaired heart function depends on electrical coupling between the engrafted cells and the host myocardium to ensure their synchronized beating [55]. Similar conductive nanofibrous sheets composed of poly(L-lactic acid) (PLA) blending with PANi were reported for cardiac tissue engineering and cardiomyocyte-based 3D bioactuators. By incorporating PANi up to 3 wt% into the PLA polymer, the electrospun nanofibrous sheets gained enhanced conductivity. These conductive nanofibrous sheets not only enhanced the cell–cell interaction, maturation, and spontaneous beating of primary cardiomyocytes but were also a kind of suitable fundamental material to fabricate cardiomyocyte-based 3D bioacutuators. The folding bioactuator formed by cardiomyocyte-laden PLA/PANi displayed stronger spontaneous contraction at 1.6 Hz and displacement without any trigger, which was driven by synchronous beating of the cardiomyocytes than that formed by cardiomyocyte-laden PLA nanofibrous sheets [56]. The blend of chitosan and PANi was employed to process a re-entrant honeycomb pattern that can provide negative Poisson's ratio, aiming to obtain the auxetic behavior for scaffolds of cardiomyocytes. It is known that the Young's modulus of native human heart varies from 0.02 to 0.50 MPa depending on whether the heart is in systole or diastole, with infarct tissue being even stiffer. In order to meet the demand of cardiomyocytes contracting on scaffolds, auxetic behavior can be imparted into a material. The scaffold design addressed the match of dynamic mechanical properties between heart tissue and cardiac patch. The micropattern of the re-entrant honeycomb structure was developed by using excimer laser microablation, which produced patches that could be tuned to match native heart tissue. The resulting scaffolds with the ultimate tensile strength and strain at failure of 0.06–1.53 MPa and 27–96%, respectively, are comparable to the reported values for native human heart tissue. The patches were determined to have Poisson's ratios in the range of −1.45 to −0.15. It is noticeable that the conductivity of the patterned patches was also anisotropic and maintained a similar level of conductivity compared to the unpatterned patches composed of the same composite. As an encouraging result, the auxetic patches were cytocompatible with murine neonatal cardiomyocytes in vitro and had no detrimental effect on the electrophysiology of both healthy and MI rat hearts and conformed better to native heart movements than unpatterned patches of the same material in ex vivo. Besides, the implantation in a rat MI model for 2 weeks had not shown detrimental effects on cardiac function, and negligible fibrotic responses were detected [57].

Like PPY, the biocompatibility of PANi is still a concerned issue. To avoid the potential toxicity of PANi to cardiomyocytes grown on the nanofibrous scaffold, a group fabricated a kind of core–shell fiber using coaxial electrospinning technique. The mixture of poly(lactic acid) (PLA) and PANi doped with dodecylbenzenesulfonic acid (DBSA) was used as the component of the core, and the mixture of PLA and poly(ethylene glycol) (PEG) was taken as the out layer of the fiber. Interestingly,

the incorporation of PEG could enhance the packing of PLA and PANi chains. The PANi and PEG affected the thermal and electrical properties of the fibers, both decreasing the glass transition temperature and increasing the electrical conductivity, and at the same time, the biocompatibility of the core-shell fibers increased [58]. Another strategy of avoiding the potential cytotoxicity of PANi was to have PANi grafted to the backbone of chitosan molecules. For example, PANi was grafted to the backbone of quaternized chitosan. The resulting hydrogel gained the conductivity similar to that of native cardiac tissue (~10^{-3} S/cm) and showed good biocompatibility with adipose-derived mesenchymal stem cells (ADMSCs) as well as the H9C2 cardiac cells and myoblasts C2C12 cells [59]. Besides PPY and PANi, some new conductive polymers have been explored for uses in the fabrication of conductive scaffolds. For example, a homogeneous electronically conductive double network hydrogel (HEDN) was fabricated by a rigid, hydrophobic and conductive network of chemical crosslinked poly(thiophene-3-acetic acid) and a flexible hydrophilic biocompatible network of photo-crosslinking methacrylated aminated gelatin. By adjusting the component ratio, the swelling, mechanical, and conductive properties of HEDN hydrogel could be modulated. The Young's moduli for the resulting double network hydrogel varied from 22.7 to 493.1 kPa, and its conductivity was about 0.01 S/m, falling in the range of the conductivity for native myocardium tissue. The hydrogel is biocompatible, could well support brown adipose-derived stem cells survival and proliferation, as well as improve the cardiac differentiation of the stem cells and electrical stimulation can further improve this effect [60].

2.3.2 Conductive Scaffolds Containing Inorganic and Metal Nanoparticles

It has been widely recognized that conductive nanoparticles are ideal contents to bring conductivity and nano-scale topography to scaffolds, as well as to reinforce mechanical properties of the scaffolds. Carbon nanotubes, grapheme, gold nanoparticles, silicon wire, and silver nanoparticles are mostly investigated ones.

2.3.2.1 Carbon Nanotubes

Carbon nanotubes (CNTs) can be easily incorporated with various kinds of hydrogels. For example, SWNTs were incorporated into gelatin hydrogels to construct three-dimensional engineered cardiac tissues. The SWNTs in the hydrogel could provide cellular microenvironment in vitro favorable for cardiac contraction and increased the expression of electrochemical associated proteins Cx43 and TnT. Upon implantation into the infarct hearts in rats, the engineered cardiac tissues structurally integrated with the host myocardium, with different types of cells observed to

mutually invade into implants and host tissues, showing essential roles of SWNTs to improve the performance of ECTs in inhibiting pathological deterioration of myocardium [61]. In another research, by blending single-walled carbon nanotubes at subtoxic concentrations with a gelatin-chitosan hydrogel, a composite hydrogel was developed, in which the SWCNTs were designed to act as electrical nanobridges between cardiomyocytes, resulting in the enhancement of electrical coupling, synchronous beating, and cardiomyocyte function. The conduction velocity of NRVM cultured in hydrogels containing SWNTs was ~23 cm/s, which was significantly faster than NRVM cultured in hydrogels without SWNTs, and close to ~27 cm/s in 10-day-old neonatal rat heart [62]. When conjugated with an injectable reverse thermal gel (RTG), multiwalled carbon nanotubes (MWCNTs) brought conductivity to RTG, which transited from a solution at room temperature to a three-dimensional (3D) gel-based matrix shortly after reaching body temperature (RTG-CNT). The resistance of MWCNTs functionalized with –COOH was 24.3 kΩ, and RTG-CNT had a resistance of 144.3 kΩ at 37 °C. The 3D RTG-CNT system supported long-term CM survival, promoted CM alignment and proliferation, and improved CM function when compared with traditional two-dimensional gelatin controls and 3D RTG system without CNTs [63].

Casting is a facile approach to introduce carbon nanotubes (CNTs) into synthetic polymers. An elastomeric film was produced by blending multiwalled carbon nanotubes (MWCNTs) into poly(octamethylene maleate (anhydride) 1,2,4-butanetricarboxylate) (124 polymer) for cardiac tissue engineering, in which the MWCNTs provided electrical conductivity and structural integrity to 124 polymer. The 124 polymer with 0.5% and 0.1 wt% MWCNTs exhibited improved conductivity and swelling against pristine 124 polymer. The bulk modulus of composite film was increased proportionally to the MWCNT content while the bulk modulus was decreased. Consequently, the excitation threshold of engineered cardiac tissue on the film with 0.5% MWCNTs was 3.6 V/cm, significantly shorter than 5.1 V/cm of the control and 5.0 V/cm of 0.1% CNTs, suggesting greater tissue maturity due to the electrical and mechanical advantages of the scaffolds [64]. Besides integrating in casting films, multiwalled carbon nanotubes can also be dispersed in aligned poly(glycerol sebacate):gelatin (PG) electrospun nanofibers (CNT-PG) to enhance the fibers' alignment and improved the electrical conductivity and toughness of the scaffolds. The CNT-PG was observed to maintain the viability, retention, alignment, and contractile activities of cardiomyocytes, leading to a stronger spontaneous and synchronous beating behavior, the cells showing 3.5-fold lower excitation threshold and 2.8-fold higher maximum capture rate compared to those cultured on the nonconductive PG scaffold after 7-day culture, no matter with or without electrical stimulations [65]. Multiwalled carbon nanotubes (MWCNTs) could be combined with polyurethane nanofibers by electrospray technique to generate electroconductive nanofibrous patches. The MWCNTs were reported to well adhere on the polyurethane nanofibers that created an interconnected web-like structures, and the MWCNT content could reach to 0.2 wt%, 0.3 wt%, and 0.6 wt% when deposited in the nanofibrous patches. The addition of MWCNTs decreased the diameter of the nanofibers and significantly enhanced the electrical conductivity, tensile strength,

Young's modulus, and hydrophilicity of the nanocomposites. Importantly, the scaffolds showed better cytocompatibility and improved interactions between the scaffold and cardiomyoblasts. Noted that the composite nanofibrous patches also friendly enhanced the interactions between scaffolds and endothelial cells, and this would be beneficial to the angiogenesis in the engineered constructs of heart [66]. Similarly, the positive interactions of MWCNT-containing nanofibrous polyurethane to human umbilical vein vascular endothelial cells were reported by our previous work. The aligned nanofibrous structure and incorporated MWCNT acted in a coordinated way to promote the endothelial cells to produce type IV collagen, meanwhile the cells seeded on the aligned nanofibrous composite films released significantly lower amounts of tissue factor and PAI-1 than those growing on the control. These results again showed that MWCNTs component embedded in the nanofibrous polyurethane films benefited to the endothelial cells to preserve their anticoagulant functions [67].

An interesting design of scaffold fabricated with aligned conductive nanofiber yarn network was proposed and fabricated with polycaprolactone, silk fibroin, and carbon nanotubes (NFYs-NET). The nanofiber yarn network was intended to mimic the native cardiac tissue structure to control cellular orientation and enhance cardiomyocyte (CM) maturation. When encapsulated within a hydrogel shell, the NFYs-NET layers formed 3D hybrid scaffolds, and these 3D scaffolds promoted aligned and elongated CM maturation on each layer and individually control cellular orientation on different layers in a 3D environment. When CMs were cultured on the NFYs-NET layer, and endothelial cells were within the hydrogel shell, endothelialized myocardium was constructed, as the NFYs-NET layer induced cellular orientation, maturation, and anisotropy, and the hydrogel shell provided a suitable 3D environment for endothelialization [68]. Besides employed as fillers in composites, carbon nanotubes can be used as scaffolds directly to cardiac cells in the form of nonwoven film or mesh. For example, superaligned carbon nanotube sheets (SA-CNTs) were employed to culture cardiomyocytes, mimicking the aligned structure and electrical impulse transmission behavior of the natural myocardium. The SA-CNTs not only induced an elongated and aligned cell morphology of cultured cardiomyocytes but also provided efficient extracellular signal transmission pathways required for regular and synchronous cell contractions. Furthermore, the SA-CNTs reduced the beat-to-beat and cell-to-cell dispersion in repolarization of cultured cells, which is essential for a normal beating rhythm, and potentially reduced the occurrence of arrhythmias. The SA-CNT-based flexible one-piece electrodes also demonstrated a multipoint pacing function. These features make SA-CNTs promising in applications in cardiac resynchronization therapy by enhancing cells to communicate electronic signals [69].

In addition to the conductivity, the function of ROS clearance for carbon nanotubes may contribute to the scaffold-induced tissue regeneration, since ROS would severely impair the adhesion of engrafted stem cells. In one study, carbon nanotubes (CNTs) were incorporated in the gelfoam (GelMA). By seeding neonatal rat cardiomyocytes on the hydrogels, cardiac constructs were developed. Researchers noticed that the addition of CNTs brought an important function to the cardiac patches, that

is, to resist the damage induced by a model cardiac inhibitor heptanol as well as a cytotoxic compound doxorubicin. In this investigation, heptanol or doxorubicin was applied to the cardiac patches for 5-day culture. Heptanol is a widely used reversible inhibitor of cell-to-cell coupling, which prevents gap-junctional permeability of Ca^{2+} and interrupts beating propagation. A rapid disappearance of synchronous beating was observed on the pristine GelMA surface within 20 min, while beating persisted on CNT-GelMA. More CNT addition led to more gradual disturbance to beating rhythm. It means that cardiomyocytes on CNT-GelMA continued to beat synchronously even after the gap junctional beating propagation was inhibited, indicating that the conductive CNT network played a role in propagating calcium transient and action potential between cells. The generation of free oxygen radicals is believed to be the main mechanism for the cardiotoxicity of doxorubicin. When 300 μM of doxorubicin was perfumed into the growth chamber, tissues on pristine GelMAs showed an immediate decrease (>50%) in the beating amplitude, as well as the beating rates, while the amplitude and beat-to-beat variation of cardiac tissues on CNT-GelMA were not significantly affected, which suggests a protective role of CNT against oxidative stress by acting as free radical scavengers, and might be an important feature of carbon nanomaterial-containing scaffolds [70]. Similarly, another research group reported that single-walled carbon nanotubes (SWCNTs) were able to clear ROS after MI. In this study, poly (*N*-isopropylacrylamide) (PNIPAAm) hydrogel was used for encapsulating brown adipose-derived stem cells, and a small amount of SWCNTs were introduced into the hydrogel. Although the conductivity of the resulting hydrogels was only 10^{-4} Ω^{-1}, it could be noticed that in the presence of H_2O_2, the stem cells in the SWCNT-containing hydrogel showed significantly higher bioactivities including promoted cell adhesion and proliferation compared with those in the control hydrogel. Furthermore, the SWCNT-containing hydrogel encapsulating the stem cells could be injected in situ in rats with myocardial infarction and significantly enhanced the engraftment of seeding cells in infarct myocardium and augmented their therapeutic efficacies [71].

2.3.2.2 Graphene and Derivatives

Graphene and graphene derivatives including graphene oxide (GO) and partly reduced GO (rGO) have been extensively employed as novel components to fabricate electrically conductive composites that can effectively deliver electrical signals to biological systems. Graphene is a superconductive material that can be used directly for the growth and differentiation of stem cells and human induced pluripotent stem cells (hiPSCs). The ability of iPS to differentiate into cardiomyocytes provides abundant sources for disease modeling, drug screening, and regenerative medicine; however, hiPSC-derived cardiomyocytes (hiPSC-CMs) display a low degree of maturation and fetal-like properties. To overcome this problem, one example is to seed hiPSCs on graphene sheets. It was assumed that the graphene substrate could facilitate the intrinsic electrical propagation, mimicking the microenvironment of the native heart to promote the global maturation of hiPSC-CMs.

It was reported that the graphene substrate markedly increased the myofibril ultrastructural organization, elevated the conduction velocity, and enhanced both Ca^{2+} handling and electrophysiological properties of the stem cells even without electrical stimulation. On the graphene substrate, the level of connexin 43 increased as well along with the conduction velocity, and the bone morphogenetic protein signaling was significantly activated during the early period of cardiogenesis in RNA level [72]. In some studies, micro- and nano-scale topographies were brought into graphene membranes by specifically processing technology, which have been demonstrated mimicking the extracellular matrix structures to some extent. One group selected polyethylene glycol (PEG) as substrates on which there were ridges and grooves of 800 nm in widths fabricated by using capillary force lithographic techniques. The graphene membrane was placed on the patterned PEG following the oxygen-plasma treatment, which allows them to have more profound effect on cellular phenotype than the pristine graphene membrane. As shown that the tissue constructs displayed the enhancement of myofibrils and sarcomeres and exhibited the expression of cell–cell coupling, meanwhile, calcium-handling proteins were all significantly increased, suggesting that directional electrical conductivity could impact the functional phenotype of cultured cardiac cells [73].

Like carbon nanotubes, graphene can be easily incorporated with various kinds of polymeric materials that are further processed into scaffolds with different nanostructures or blended in hydrogels. By this way, one can design and fabricate conductive scaffolds with controllable mechanical properties and versatile microstructures. For example, collagen and pristine graphene were mixed to prepare a kind of biological composite to harness both the biofunctionality of the protein component and the increased stiffness and enhanced electrical conductivity to matching that of native cardiac tissue. The biological composite containing 32 wt% graphene significantly increased metabolic activity and cross-striated sarcomeric structures of embryonic stem-cell-derived cardiomyocytes, and electrical stimulation further enhanced the alignment and maturation of the embryonic stem-cell-derived cardiomyocytes. In addition, the biological composite also enhanced human cardiac fibroblast growth and simultaneously inhibited the attachment of bacterial such as *Staphylococcus aureus* [74]. Partly reduced graphene oxide (rGO) is also a candidate in the fabrication of conductive composites. Although the oxidation treatment decreases the conductivity of pristine graphene, following partly reduction can restore part of the conductivity of graphene oxide; hence, rGO usually has a higher conductivity than GO while holding better hydrophilic property than pristine graphene. For example, a composite of collagen and graphene oxide (Col-GO) with a reduction treatment was fabricated for uses as a cardiac patch. In the fabrication process, collagen scaffolds were generated using a freeze-drying method, followed by conjugated covalently with GO. At the final step, the scaffold Col-GO was subjected to a reduction treatment by an immersion in 2% sodium hydrosulfite for 3 min. By this way, the electrical conductivity of the final scaffolds fell in the range of semiconductive materials about 10^{-4} S/m. At the same time, the highest tensile strength of the scaffolds could reach to 162 kPa and the Young's modulus to 750 kPa. As for the morphology of the scaffolds, there were randomly oriented

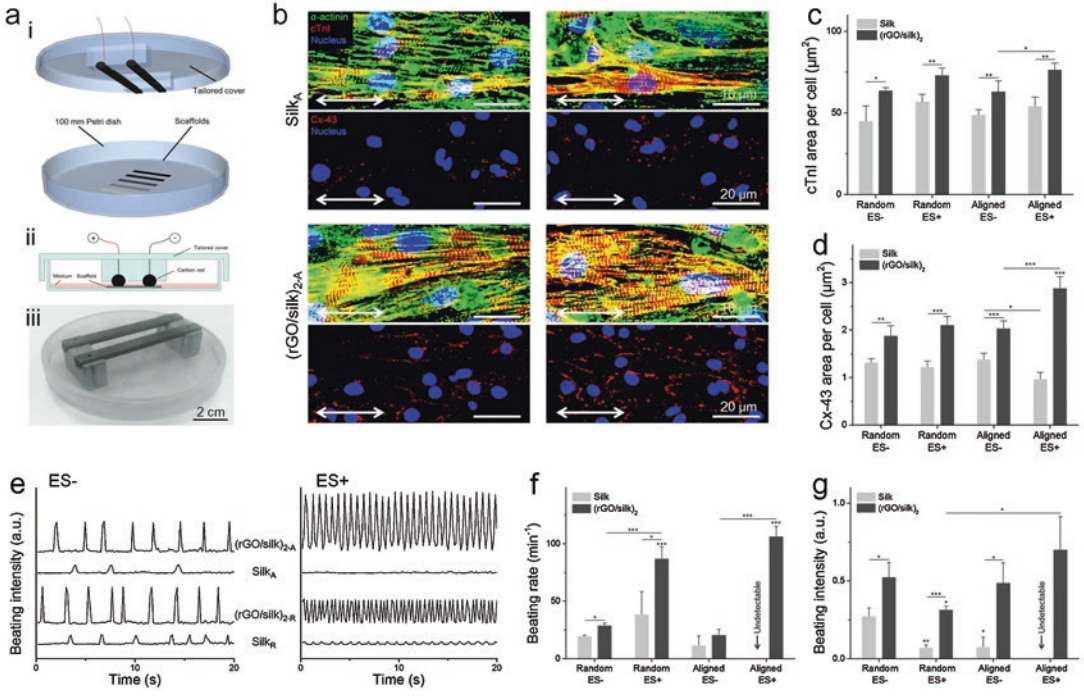

Fig. 2.2 The synergy of electrical stimulation and rGO/silk scaffolds on the functionalities of cardiac tissues. (**a**) (*i*) 3D, (*ii*) 2D schematics, and (*iii*) photograph of a custom-made Petri dish cover (100 mm) that provides parallel electric fields to cells when connected to an electrostimulator. (**b**) Immunofluorescence images showing the expression of α-actinin, cTnI, and Cx-43 for cardiomyocytes cultured on silk and $(rGO/silk)_{2\text{-}A}$ without and with electrical stimulation. The double arrows indicate the orientation of the nanofibers in the aligned groups. (**c**, **d**) Quantitative analysis of (**c**) cTnI and (**d**) Cx-43 expression showing the significantly enhanced formation of calcium ion-sensing sarcomeres and gap junctions in the aligned rGO/silk group with electrical stimulation. (**e**) Beating profiles of cardiomyocytes cultured on silk and $(rGO/silk)_2$ scaffolds without and with electrical stimulation. (**f**, **g**) Statistical analysis of (**f**) the beating rate and (**g**) beating intensity of cardiomyocytes cultured on silk and $(rGO/silk)_2$ scaffolds without and with electrical stimulation [76]

interconnected pores of 120–138 μm in diameter in the Col-GO scaffolds where GO flakes being well distributed in the pore walls. It is interesting and should be noted that the scaffolds showed the function of enhancing angiogenesis as higher VEGF expression observed in the scaffolds collected at 4 weeks after subcutaneous implantation as well as supported neonatal cardiomyocyte adhesion and upregulated the expression of the cardiac genes, including Cx43, Actin4, and Trpt-2 than their non-conductive counterparts [75]. Reduced graphene oxide was also used to modify silk nanofibrous biomaterials with controllable surface deposition on the nanoscale. A reduced graphene oxide (rGO) nanolayer could be attained, and the thickness was well controlled on the silk nanofibrous scaffolds by using a vacuum filtration system. The electrical resistance of the composites was 4.3 kΩ, and the Young's modulus was not affected by the rGO deposition. The composite nanofibrous scaffolds promoted the expression of cardiac-specific proteins including α-actinin, cTnT, and Cx43 and increased the tissue contraction under the external electrical stimulation (Fig. 2.2) [76]. There are many investigations using GO as fillers in composites though the conductivity of GO is not so high. For example, a highly elastic hybrid hydrogel composed of methacryloyl-substituted recombinant human tropoelastin (MeTro) and graphene oxide (GO). In this investigation, the features of flexibility, biocompatibility, and ease of dispersion in aqueous solutions for GO were addressed, instead of the conductivity that is compromised due to the oxidation process. The synergistic effect of MeTro and GO significantly enhanced ultimate strain (250%), reversible rotation (9700°), and the fracture energy (38.8 ± 0.8 J/m^2) in the hybrid network. At the same time, the hybrid hydrogels improved electrical signal propagation and subsequent contraction of the muscles connected to some extents in the ex vivo tests [77].

Besides compositing with biological materials, a large number of investigations have reported the integration of graphene with synthetic polymeric materials for cardiac tissue engineering. One example is that the combination of graphene and poly(caprolactone) (PCL) led to the formation of three-dimensional (3D) nanofibrous composite scaffolds for cardiac tissue engineering. It was assumed that the addition of graphene provided local conductive sites within the PCL matrix, which enabled the application of external electrical stimulation throughout the scaffolds. It was observed that mouse embryonic stem cell-derived cardiomyocytes (mES-CM) well adhered on the composite scaffolds and contracted spontaneously and exhibited cardiomyocyte phenotype. Noted that mES-CM cultured on the composite scaffolds exhibited significantly higher fractional release compared to 2D control, and also exhibited a significantly shorter caffeine-induced transient T50 compared to 2D control, all of which indicated that the added graphene especially affected Ca^{2+} handling properties of mES-CM [78]. Another example is a reduced graphene oxide (rGO)-incorporated gelatin methacryloyl (GelMA) hybrid hydrogel. The incorporation of rGO into GelMA hydrogel significantly enhanced the electrical conductivity and mechanical properties of the material. Moreover, cells cultured on the composite hydrogel rGO-GelMA exhibited better biological activities including cell viability, proliferation, and maturation, compared to those cultured on GelMA hydrogels.

Moreover, cardiomyocytes showed stronger contractility and faster spontaneous beating rate on rGO-GelMA sheets compared to those on GelMA sheets [79].

Injection of a conductive hydrogel was designed to provide mechanical support to the infarcted region and synchronize contraction and restore ventricular function by electrically connecting isolated cardiomyocytes to intact tissue. By combining graphene oxide (GO) nanoparticles with oligo(poly(ethylene glycol) fumarate) (OPF), an injectable semiconductive hydrogel was prepared and injected in rats 4 weeks after myocardial infarction. The composite hydrogel OPF/GO provided mechanical support and improved the electric connection between healthy myocardium and the cardiomyocytes in the scar by activating the canonical Wnt signal pathway associating with the generation of Cx43 and gap junction-associated proteins. The Ca^{2+} signal conduction of cardiomyocytes was also enhanced in the infarcted region in comparison with PBS or OPF alone and promoted the generation of cytoskeletal structure and intercalated disc assembly. After 4 weeks of injection, the heart function of load-dependent ejection fraction/fractional shortening was improved [80]. Another example of soft injectable hydrogel with conductive property was produced by incorporating graphene oxide (GO) with a multi-armed crosslinker PEGDA700-Melamine (PEG-MEL), which could crosslink with thiol-modified hyaluronic acid (HA-SH) to form an injectable hydrogel, which exhibited a soft and anti-fatigue mechanical property and conductive property reached to 0.03 S/m. The hydrogel encapsulating adipose tissue-derived stromal cells (ADSCs) was injected into MI area of rats, which significantly increased the expression of α-smooth muscle actin (α-SMA) and connexin 43 (Cx43). Meanwhile a distinct increase of ejection fraction (EF), smaller infarction size, less fibrosis area, and higher vessel density were achieved [81]. By integrating multiple techniques, a group established an approach to fabricate 3D multilayered constructs using layer-by-layer assembly of cardiomyocytes and fibroblasts. In the design, films of GO-containing GelMA gel served as cell adhesive sheets to facilitate the formation of multilayer cell constructs with interlayer connectivity. PLL-modified GO particles were deposited in the first monolayer of the cells grown on the film, followed by the cell adhesion of the second layer. The process was repeated to fabricate the final 3D engineered tissue. This approach might be used to create dense and tightly connected cardiac tissues through the co-culture of cardiomyocytes and other cell types [82].

In addition to the use of fabricating conductive scaffolds, graphene may have potentials in the application of stem cell therapy. An investigation showed that graphene of 0.2 mg/mL embedded into the structure of mouse embryoid bodies (EBs) using hanging drop technique could enhance the mechanical properties and electrical conductivity of the EBs and accelerated the cardiac differentiation of the EB-graphene in the 5-day cultivation, confirmed by high-throughput gene analysis. In addition, electrical stimulation of 4 V and 1 Hz for 10 ms within 2 continuous days further enhanced the cardiac differentiation of the EBs, evidenced by analysis of the cardiac protein and gene expression and the beating activity of the EBs [83]. Like carbon nanotubes, graphene and derivatives are also reported to have the function of ROS scavenging. For example, graphene oxide (GO) flakes could protect the

implanted MSCs from ROS-mediated death and thereby improve the therapeutic efficacy of mesenchymal stem cell (MSC). It is known that MSC implantation is a potential therapy for myocardial infarction (MI). However, the poor survival of the implanted MSCs in the injury sites significantly limited the therapeutic efficacy of this approach, one of the reasons is that reactive oxygen species (ROS) are generated in the ischemic myocardium after the restoration of blood flow, forming a harmful microenvironment to the injected stem cells. This investigation reported that GO significantly prolonged the survival of MSCs due to its clearance ability to ROS and enhanced the paracrine secretion from the MSCs following MSC implantation, which in turn promoted cardiac tissue repair and cardiac function restoration [84].

2.3.2.3 Gold Nanoparticles

Incorporation of electroconductive gold nanoparticles (GNPs) into hydrogels have reported enhancements of myocardial constructs' properties. The advantages are contributed by GNPs not only their metal conductivity and biocompatibility but also the very small size distribution and mechanical reinforcement to the composites in nanoscale. It is not surprising that GNPs can bring conductivity and stiffness to polymeric material poly(2-hydroxyethyl methacrylate) (PHEMA), the resulting Young's moduli of the composites were closer to that of myocardium. Neonatal rat cardiomyocytes exhibited increased expression of connexin 43 on the hybrid scaffolds composed of GNPs and PHEMA, no matter with or without electrical stimulation [85]. A similar example is that hydrogels composed of chitosan (CS) and GNPs were produced with a highly porous network of interconnected pores (CS-GNP). The GNPs of 7 nm in diameter were evenly dispersed throughout the CS matrix to provide electrical and thermal cues. The gelation response and electrical conductivity of the hydrogel were controlled by different concentrations of GNPs, and the conductivity of the CS-GNP hydrogels at the optimal ratio reached 0.13 S/m that was like that of natural heart tissue. The CS-GNP hydrogels supported viability, metabolism, migration, and proliferation of mesenchymal stem cells (MSCs) along with the development of uniform cellular constructs within the 14 days of incubation. Immunohistochemistry for early and mature cardiac markers such as α-MHC and Nkx-2.5 showed enhanced cardiomyogenic differentiation of MSCs within the CS-GNP compared to the CS matrix alone [86]. GNPs were also blended with collagen to form a composite hydrogel. Not addressing the conductivity of the composite hydrogel, researchers focused on the effect of GNPs on topography and the nanoscale local elasticity of scaffolds. They demonstrated that the GNPs increased the hydrogel stiffness locally in nanoscale, which increased the interaction between cardiac myocytes and the substrates, evidenced by the activation of β1-integrin signaling and mediation of the activation of integrin-linked kinase (ILK) and its downstream signal kinase by stimulating the expression of the transcription factors GATA4 and MEF-2c [87]. GNPs could combine with injectable reverse thermal gel (RTG) system that is expected to provide a particularly attractive approach of

being delivered in a minimally invasive manner, thus avoiding mechanical stress on the cells during injection and providing structural support at the injury area. In addition, the injectable hydrogels provide cells encapsulated in three-dimensional (3D) environments; therefore, the hydrogels better mimic the in vivo microenvironment than two-dimensional (2D) cultures. A RTG consisting of poly(serinol hexamethylene urea)-copoly(*N*-isopropylacrylamide) functionalized with lysine was synthesized (RTG-lysine), which conjugated with gold nanoparticles (AuNPs) by free amine groups. The generated RTG-AuNP hydrogel was conductive and could support the survival of neonatal rat ventricular myocytes (NRVMs) for up to 21 days when cocultured with cardiac fibroblasts, the level of connexin 43 (Cx43) for the NRVMs was significantly upregulated in relative to control cultures without AuNPs [88].

Gold nanorods (GNRs) with aspect ratio of 3.15 were reported to be capable of combing with gelatin methacrylate (GelMA) and inducing crosslink among the hydrogel molecules under the irradiation of UV light. The embedded GNRs in hydrogels promoted electrical conductivity and mechanical stiffness of the hydrogel matrix, which properly accommodated cardiac cells and consequently led to excellent cell adhesion, spreading, metabolic activity, homogeneous distribution of cardiac specific markers including sarcomeric α-actinin and connexin 43, cell–cell coupling, as well as robust synchronized beating behavior in the tissue level. In particular, the increased cell adhesion resulted in abundance of locally organized F-actin fibers, leading to the formation of an integrated tissue layer on the GNR-embedded hydrogels. The GelMA-GNR hybrids supported synchronous tissue-level beating of cardiomyocytes in the absence of electrical stimulation and showed good ability for the accommodation of external electrical stimuli, as a significantly lower excitation threshold was gained by the hybrid hydrogels with 1.5 mg/mL of GNRs [89]. It is noticeable that GNRs have been introduced in bioprinting that is one microfabrication method able to create biomimetic three-dimensional (3D) tissue constructs. For example, the composite of gold nanorods (GNRs) and gelatin methacryloyl (GelMA) could be a conductive bioink for printing 3D functional cardiac tissue constructs. An optimal bioink could be prepared by adjusting the concentration of GNRs, which had a low viscosity like pristine inks and allowed rapid deposition of cell-laden fibers at a high resolution, while reducing shear stress on the encapsulated cells. In the printed constructs, cardiac cells showed better adhesion and organization compared to the constructs control without GNRs. The incorporated GNRs bridged the electrically resistant pore walls formed by the polymeric materials (bioink), improving cell-to-cell coupling and promoting synchronized contraction of the bioprinted constructs [90].

Besides blending with macromolecular materials, GNPs can be deposited directly on substrates to play the role of conductivity. It is known that coiled perimysial fibers within the heart muscle can contract and relaxing efficiently. Inspired by the structure of natural coiled perimysial fibers, researchers synthetically fabricated similar coiled electrospun fibers of PCL. The coiled fibers had diameters ranging from a few hundreds of nanometers to several micrometers, and the scaffolds composed with the coiled fibers exhibited an average pore area >4000 μm^2. On the

surface of the fibers, GNPs were evaporated with a nominal thickness of 10 nm to give the fibers conductivity. As a consequence, the composite scaffolds promoted cardiac cell organization into elongated and aligned tissues generating a strong contraction force, high contraction rate and low excitation threshold [91]. This deposition strategy is especially suitable be applied to biological materials that are not able to endure complicated and harsh chemical reactions. For example, GNPs were deposited on fibrous decellularized omental matrices to make the decellularized matrices conductive, which is an attractive design for fabricating engineering functional cardiac patches for treating myocardial infarction. Consequently, the cardiac cells growing within the composite scaffolds exhibited elongated and aligned morphology, massive striation, and organized connexin 43 electrical coupling proteins. The hybrid patches displayed superior function, including a stronger contraction force, lower excitation threshold, and faster calcium transients, as compared to pristine patches [92]. In some cases, GNPs are used with graphene together. A conductive biodegradable scaffold was generated by incorporating graphene oxide gold nanosheets (GO-Au) into a clinically approved natural polymer chitosan (CS). The composite scaffold composed of CS and GO-Au nanosheets displayed two folds increase in electrical conductivity in reference to the chitosan alone scaffold, reaching 0.012 S/m that is 1/10 of that for natural heart tissue. At the same time, the scaffold exhibited excellent porous architecture with desired swelling. In particular, the inclusion of GO-Au reduced the degradation rate of the scaffold because GO-Au sheets hinder the penetration of hydrolytic enzymes inside the polymer matrix that slows down the degradation. In a rat model of MI, the conductive scaffold after 5 weeks of implantation showed a significant improvement in QRS interval, which was associated with enhanced conduction velocity and contractility in the infarct zone by increasing connexin 43 levels [93].

2.3.2.4 Silicon Nanowires

Although silicon nanowires are not well known, they have attractive features of high conductivity and mechanical stiffness, but also biodegradable, and their degradation products are found mainly in the form of $Si(OH)_4$ and are metabolically tolerant in vivo. In one study, n-type SiNWs of 100 nm in diameter and 10 μm in length, and with a ratio of 500 (silane to phosphane) were prepared, the conductivity was as high as150−500 μS/μm, which is much higher than that of cell culture medium (∼1.75 μS/μm) and myocardium (∼0.1 μS/μm). The resulting nanowires were used to improve the differentiation and maturation of human embryonic stem cells (hESC) and human-induced pluripotent stem cells (hiPSC), because current cardiomyocytes derived from hESCs and hiPSCs retain an immature phenotype, including poorly organized sarcomere structures due to the lack of ability for assembling in a controlled manner and led to compromised, unsynchronized contractions. In this study, a trace amount of electrically conductive silicon nanowires (e-SiNWs) was added in scaffold-free cardiac spheroids to create highly electrically conductive microenvironments within spheroids, leading to synchronized and significantly

enhanced contraction, as well as significantly more advanced cellular structural and contractile maturation [94]. In a follow-up study, researchers investigated important factors that could affect functions of hiPSC cardiac spheroids cultured with silicon nanowires, including cell number per spheroid and the electrical conductivity of the silicon nanowires. They explained with a semi-quantitative theory that the two factors were competitive in the improvement of 3D cell–cell adhesion and the reduction of oxygen supply to the center of spheroids with the increase of cell number, and the critical role of electrical conductivity of silicon nanowires was confirmed in improving tissue function of hiPSC cardiac spheroids [95].

2.3.2.5 Mechanistic Exploration of Conductive Scaffolds Enhance Cardiac Tissue Regeneration

Several studies have explored and discussed underlying mechanisms of how conductive scaffolds promote the mechanical integrity and electrophysiological function of cardiac myocytes. For example, single-walled carbon nanotubes were incorporated into collagen or GelMA that was used as growth supports for neonatal cardiomyocytes. Researchers demonstrated that the composite hydrogel enhanced cardiomyocyte adhesion and maturation through β1-integrin-mediated signaling pathway. As is known, a variety of intracellular signaling pathways can be initiated by β1-integrin signaling, including FAK, Src, and ILK, and it was found out that CNTs remarkably accelerated gap junction formation via activation of the β1-integrin-mediated FAK/ERK/GATA4 pathway. In the investigation, a notably higher level of p-FAK was observed in a composite of carbon nanotubes and collagen (CNT-Col) compared to those on collagen alone at all the measured time points, whereas no remarkable changes of p-Src and ILK were noted between two groups, suggesting that FAK was activated and acted as a downstream signaling molecule from β1-integrin. Once FAK is phosphorylated, several downstream signaling kinases can be further activated, including AKT and ERK. Western blotting analysis revealed significant increases in the expression of p-ERK in NRVMs grown on CNT-Col substrates at various developmental phases while no apparent change of p-AKT expression was observed between the two groups, suggesting that ERK was activated by FAK and might be the downstream effector of FAK [96]. It was further demonstrated that the downstream signaling protein RhoA and FAK was responsible for CNT-induced upregulation mechanical junction proteins of NRVMs grown on CNT-GelMA substrates [97].

A recent work compared the effect of mechanical stiffness and nanoscale topography of scaffolds on cell–cell coupling, maturation, and electrical excitability of engineered cardiac tissues. The conductive performance was adjusted by the incorporation of conductive gold nanoparticles or nonconductive silicon nanoparticles. Scaffolds contained silicon nanoparticles. Four different hydrogels were prepared including soft GelMA gel, stiff GelMA gel, GelMA gel containing silicon nanoparticles (nonconductive with nano-topographies and soft), and GelMA gel containing gold nanoparticles (conductive with nano-topographies and stiff). Results highlighted that the influence of nanoscale topography provided by the integrated

nanomaterials was stronger than the elastic modulus and conductivity on cellular adhesion and retention, as well as on the promotion of cardiac cells maturation, suggesting the prominent role of the nanoscale surface topography of nanocomposite scaffolds in the cardiac cell–cell coupling, maturation, and functionalities of the engineered tissue [98]. These results worth of further consideration though they are not consistent with experimental results from nanofibrous scaffolds containing conductive polymers. To gain insights from different views, we fabricated a conductive hydrogel (PVA/CFs) by blending carbon fibers of 7 μm in diameter and PVA that has a simple molecular structure and forms very soft hydrogels [99]. In this composite hydrogel, there were not obvious nanostructures while the carbon fibers are highly conductive with high tensile strength as well as modulus. In addition, the conductive element was carbon, instead of gold. The carbon fibers brought distinguished conductivity of 0.3 S/m and stiffness of 2.3 MPa to the PVA. It was observed that α5 and β1 integrin were both significantly upregulated in neonatal rat cardiomyocytes grown on PVA/CFs compared with those on PVA control, meanwhile the levels of ILK and p-AKT were elevated correspondingly. In addition, hypoxia-inducible factor-1α (HIF-1α) was increased, which was assumed that the cells on PVA/CFs were subjected to a stronger material-support pulling, therefore might experience hypoxia, implying that CFs might provide a microenvironment of promoting angiogenesis in the cells (Fig. 2.3). Noted that these signals are highly

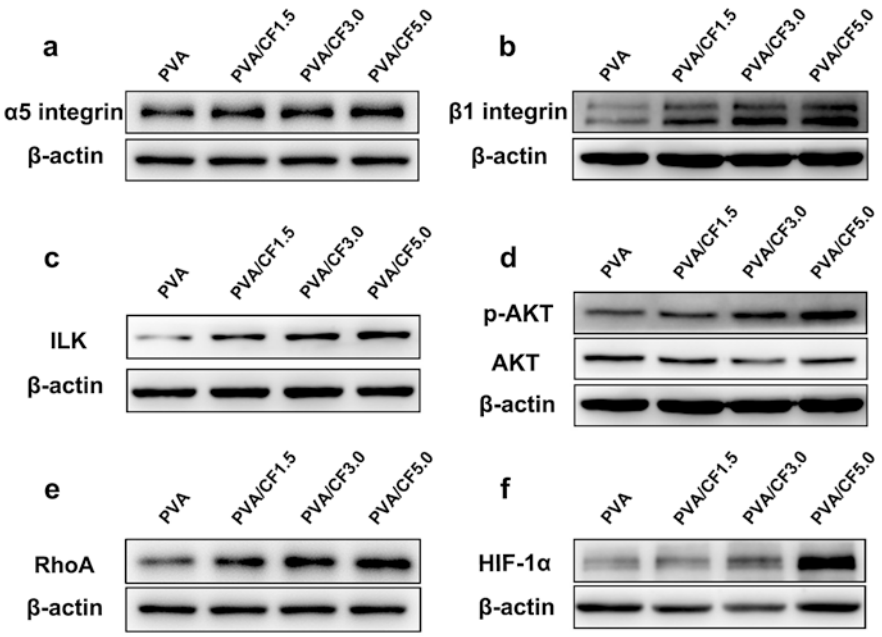

Fig. 2.3 Mechanotransduction signaling is involved in the modulation of CFs with NRCMs. Western blot analysis of the expression of (**a**) α5 integrin, (**b**) β1 integrin, (**c**) ILK, (**d**) p-AKT, (**e**) RhoA, and (**f**) hypoxia-inducible factor 1-α in NRCMs grown on PVA/CFs or PVA alone for 5 days. Data are represented as mean ± standard deviation (SD); $*p < 0.05$, $**p < 0.01$, $***p < 0.001$ by one-way ANOVA analysis [99]

related: AKT can regulate the expression of the gap junction protein Cx43 [100], ILK is a proximal receptor kinase that can regulate integrin-mediated signal transduction and is a key component of sarcomeric contractile apparatus in vertebrate hearts [101], and the integrin-dependent ILK/AKT pathway is involved in the activation of HIF-1α [102]. Besides, RhoA, one of the Rho family members, is also regulated by integrin and plays an important role in regulating the formation and stability of adherent junctions [103], its expression level was also up regulated by PVA/CFs. Therefore, CFs embedded in PVA could enhance cell maturation and tissue regeneration by activating the integrin-mediated mechanotransduction pathway and by accelerating the electrical charges moving. The conductivity and stiffness both are of importance for cardiac tissue engineering scaffolds.

2.4 Conductive Scaffolds for Skeletal and Bone Regeneration

Musculoskeletal system includes skeletal muscle, bone, cartilage, and tendon/ligament, which is one of the main targets for tissue engineering, because there is an increasing need for regeneration and/or repair. Skeletal muscles comprise about 40–45% of an adult human body mass, they are mainly responsible for generating forces which facilitate voluntary movement, postural support, breathing, and locomotion. Skeletal muscle injuries may occur from a variety of events, including direct trauma, such as muscle lacerations, contusions or strains, and indirect causes, such as ischemia, infection, or neurological dysfunction. Even though skeletal muscle cells can naturally regenerate as a response to insignificant tissue damages due to their remarkable robust innate capacity for regeneration, more severe injuries that result in muscle mass loss of more than 20% can cause irreversible loss of muscle cell mass and lead to irreversible fibrosis and scaring. In addition, aging and severe congenital disorders also result in the loss of muscle mass and function. However, so far, cell therapies have not become a good approach to treat those injuries. It has been recognized that electrical stimulation is a very important biophysical cue for skeletal muscle maintenance and myotube formation, for example, the absence of electrical signals from motor neurons can cause denervated muscles to atrophy. Therefore, conductive scaffolds are naturally expected and developed for musculoskeletal system regeneration, since they can mediate electrical stimulation as well as provide cell microenvironments to grow. Moreover, conductive materials usually have capacity of scavenging reactive oxygen species (ROS), which is another advantage that would be beneficial to the protection of cells and tissues.

2.4.1 Carbon-Based Materials Used in Conductive Scaffolds

Carbon nanotubes (CNTs) have been used in skeletal muscle engineering to modulate the conductivity or the mechanical strength of scaffolds toward myotube formation due to their unique mechanical and electrical properties. For example, one

study showed that CNTs can be used directly as substrates for inducing skeletal myogenic differentiation of human mesenchymal stem cells (hMSCs). Because pristine MWCNTs were extremely hydrophobic and rapidly precipitate in aqueous solutions, polyethylene glycol (PEG) was used to modify MWCNTs to increase their hydrophilicity to facilitate scaffold preparation, cell adherence, and growth. The film of PEG-modified MWCNT (PEG-CNT) had nanoscale surface roughness, orderly arrangement, high hydrophilicity, and high mechanical strength [104]. It is noticeable that the films alone could induce the skeletal myogenic differentiation of hMSCs, without any myogenic induction factors. The hMSCs seeded on PEG-CNT films presented significant upregulation of general myogenic markers, including early commitment markers of myoblast differentiation protein-1 (MyoD) and desmin, as well as a late phase marker of myosin heavy chain-2 (MHC), either in the gene level or in the protein level, compared with those on nonconductive control. The gene expression of skeletal muscle-specific marker troponin-C (TnC) and ryanodine receptor-1 (Ryr) was also significantly upregulated in hMSCs on PEG-CNT films. Meanwhile, those cells did not show enhanced adipogenic, chondrogenic, and osteogenic markers. These results suggested the important roles of MWCNTs in the skeletal muscle injury repair. To reduce potential toxicity, multiwalled carbon nanotube (MWCNT) membranes were functionalized by the [4 + 2] Diels–Alder cycloaddition reaction of 1,3-butadiene. In this process, the cycloadducts would disrupt the sp^2 C–C structure into sp^3 geometry at the two neighboring C atoms, weakening but not breaking the C lattice. When subcutaneously implanted in a rat model, the functionalized membranes (p,f-CNTs) induced a slighter intense inflammatory response compared to non-functionalized CNT membranes (p-CNTs), showing a reduced cytotoxicity profile. More important features are that the p,f-CNTs showed in vivo biodegradable property, likely mediated by the oxidation-induced myeloperoxidase (MPO) in neutrophil and macrophage inflammatory milieus. This could potentially avoid long-term tissue accumulation and notable toxicological threats [105].

In many cases, CNTs were taken as fillers in polymeric materials for the fabrication of composite scaffolds. For example, researchers fabricated composite fibers by utilizing carbon nanotubes (CNTs) to enhance the formation of aligned myotubes with improved contractibility of skeletal tissues. The fibers were composed of gelatin and multiwalled carbon nanotubes (MWCNTs) and produced by using electrospinning technique. The aligned fibers were used as scaffolds for the growth of myoblasts (C2C12). It was reported that the incorporated MWCNTs increased the Young's modulus of gelatin but did not improve the bulk fiber conductivity because the concentration of embedded MWCNTs were too low to link to each other, breaking the charge displacement path. Even though, the MWCNTs were considered to possibly generate local conductivity. Experimental results showed that the composite hydrogels enhanced myotube formation by upregulating the expression of mechanotransduction-related genes, and the maturation of the myotubes and the amplitude of the myotube contractions could be further promoted under electrical stimulation [106]. Bone healing can be significantly expedited by applying electrical stimuli in the injured region. An example is to produce randomly oriented and aligned electrically conductive nanofibers of biodegradable poly-DL-lactide (PLA)

by using electrospinning technique, in which MWCNTs were embedded to give conductivity to the fibers. The meshes formed by the conductive fibers offered both topographic cues and electrical stimulation on osteoblasts. In the absence of electrical stimulation, the aligned nanofibers enhanced the extension and directed the outgrowth of osteoblasts better than the random fibers. The cellular elongation and proliferation were mainly dependent on the electrical stimulation. Interestingly, the osteoblasts on all samples grew along the electrical current direction in the presence of direct current (DC) of 100 μA. In this situation, the topographical features played a minor role in them. Therefore, conductive substrate with electrical stimulation was suggested an attractive potential in the application of bone tissue engineering [107].

Graphene and graphene-based composites are emerging rapidly and investigated intensively as conductive materials to fabricate scaffolds for uses in tissue engineering and regenerative medicine. Addition of graphene oxide (GO) nanoplatelets in bioactive polymers was found to enhance the conductivity and dielectric permittivity along with biocompatibility and mechanical properties. A research group prepared thin GO sheets and nanofibrous meshes composed of GO and PCL (GO-PCL) for the cultures of umbilical cord blood (UCB)-derived multipotent mesenchymal stem cells (CB-hMSCs). The GO sheets were dielectric and semiconductive, and the GO-PCL fibrous meshes acquired enhanced conductivity and dielectric permittivity when compared to PCL alone. When CB-hMSCs were seeded, GO-PCL composite was reported to provide more favorable cues to the cells for the formation of superior multinucleated myotubes than the thin GO sheets, enhancing CB-hMSCs differentiate to skeletal muscle cells (hSkMCs) [108]. In another example, nanocomposite materials composed of graphene oxide nanoribbons and hydroxyapatite nanoparticles (nHA) were designed for uses in bone tissue engineering, in which nHA is a bone conductive material and graphene oxide nanoribbons are an electrically conductive material. The composites were detected as nontoxic and enhanced the osteogenesis process compared to controls in a dose-dependent manner, upregulating the expression of ALP, OPN, OCN, COL1, and RUNX2 genes and the secretion of alkaline phosphatase of human osteoblast cell line MG-63. Furthermore, the composites showed higher bone neoformation after 15 days of implantation in a rat tibia defect model and better lamellar bone formation compared to control after 21 days implantation [109]. Similar investigations include following two examples: one is the fabrication of 3D scaffolds composed of graphene and citrate-stabilized hydroxyapatite nanoparticles (nHA) by a facile and universal method that can be used to synthesize such structures based on colloidal chemistry. The resulting gels were reported highly porous, strong, electrically conductive, and biocompatible [110]. The other one is composite scaffolds composed of three kinds of biological materials including alginate, chitosan and collagen, and graphene oxide (GO). The resulting scaffolds had enriched porous structures that were generated by freeze-drying technique, interconnected pores ranging 10–250 μm in diameter. The incorporation of GO increased both crosslinking density and polyelectrolyte ion complex of the polymeric composite, as well as increased mechanical properties. In addition, the GO played a role of stabilizing the porous structures, scaffolds containing GO without chemical crosslinking and was more stable in the aqueous solution compared with the control

scaffolds without GO incorporation. When mouse osteoblast cells were seeded and grown on the scaffolds, cell adhesion was significantly increased [111].

Enthesis is a special complex tissue interface that connects mechanically dissimilar tissues and transfers stress between tendon/ligament and bone. Some sports injuries, such as rotator cuff tendon tear and cruciate ligament rupture, require the reconnection of tendon or ligament to bone. However, these normal critical entheses are not reestablished after repair by surgical techniques; instead, the new connections of tendon or ligament to bone are filled with fibrovascular scar tissue, which would affect the long-term clinical outcome. Therefore, promoting the healing of the bone and tendon/ligament at the implant site is particularly important, and it is surely of significance to develop integrative biomaterials that can facilitate functional tendon to bone integration. It was reported that GO-containing electrospun nanofibrous membranes could provide an effective approach for the regeneration of tendon to bone enthesis. A kind of highly interconnective GO-doped poly(lactide-co-glycolide acid) (GO-PLGA) nanofibrous membrane was fabricated by using electrospinning technique, in which GO was expected to play osteoconductive roles for enhancing tendon/ligament to bone integration. In vitro evaluations demonstrated that GO-PLGA accelerated the proliferation of rabbit bone marrow mesenchymal stem cells (BMSCs) and induced osteogenic differentiation. In a rabbit transosseous supraspinatus tendon repair model, GO-PLGA increased the new bone and cartilage generation in the gap between the tendon and the bone and improved collagen arrangement and biomechanical properties, in comparison with PLGA control, all of which collectively augmented the rotator cuff repairs [112]. For myoblast cells, higher conductivity may be more suitable. The conductivity of graphene oxide (GO) usually lower than pristine graphene because defects are formed during the oxidation process though GO has better dispersibility in aqueous solutions and is more biocompatible than graphene. Reduced GO (rGO) gains increased conductivity compared to that of GO, because the sp^2 carbon bond is partly resorted due to reduction. One study addressed this concern and conducted a mild chemical reduction to graphene oxide/polyacrylamide (GO/PAAm) composite hydrogels to prepare conductive hydrogels r(GO/PAAm), which had electrochemical impedance decreased more than ten times compared to that of GO/PAAm, meanwhile had a Young's modulus of 50 kPa that is similar to the muscle tissue-like stiffness. The r(GO/PAAm) significantly enhanced proliferation and myogenic differentiation compared with GO/PAAm. Moreover, with electrical stimulation, the myogenic gene expression of myoblasts grown on r(GO/PAAm) for 7 days was significantly enhanced compared to unstimulated controls [113].

2.4.2 Conductive Polymers

Conductive polymers are used in the development of scaffolds for skeleton-related tissue regeneration, especially used for skeletal muscle cells of cardiac tissue, possibly due to the requirement of higher conductivity from this specific type of cells.

For example, polyaniline (PANi) was doped with camphorsulfonic acid and blended with poly(glycerol-sebacate) at 10, 20, or 30%, followed by solvent casting to fabricate electrically conductive composite cardiac patches. The electrical conductivity of the composites increased to 0.018 S/cm when PANi content reached 30%. Moreover, the conductivity was preserved for at least 100 h post fabrication, indicating the stability of the composite. At the same time, the elastic modulus, tensile strength, and elasticity were increased as well with the going up of PANi content, and the resulting composites were biocompatible to C2C12 cells [114]. An elastic conductive copolymer (PEGS-AP) was synthesized by grafting aniline pentamer (AP) to poly(ethylene glycol)-co-poly(glycerol sebacate) (PEGS) with an optimal ratio to promote the proliferation and myogenic differentiation of C2C12 cells. The copolymer film showed a proper surface hydrophilicity for cell attachment, conductivity, and mechanical properties. The maximum conductivity of the films reached 0.0184 S/m, and the Young's modulus of these films could range from 14.58 to 24.62 MPa [115].

As it has been mentioned, injectable conductive hydrogels have attracted development interests because they can act as tissue engineering scaffolds and delivery vehicles for electrical signal sensitive cell therapy, especially for myoblast cell therapy and skeletal muscle regeneration. Importantly, the self-healing property can prolong the lifespan of these hydrogels. A kind of self-healable conductive injectable hydrogels was synthesized by using dextran-graft-aniline tetramer-graft-4-formylbenzoic acid and *N*-carboxyethyl chitosan at physiological conditions. The dynamic Schiff base bonds between the formylbenzoic acid and amine group from *N*-carboxyethyl chitosan brought rapid self-healing ability to the hydrogels and biocompatibility as well as the injectability and a linear-like degradation behavior. When mouse myoblasts (C2C12) were encapsulated in the hydrogels by utilizing the self-healing effect, the cells were able to escape from the conductive hydrogels with a linear-like profile, which implied that the hydrogels were potential candidates as cell delivery vehicles and scaffolds for skeletal muscle repair. In the volumetric muscle loss injury model, within the 4 weeks post the implantation, more new muscle tissue formation could be observed at each testing time point in the group of the conductive self-healing than the other control groups [116]. Besides self-healing hydrogels, highly aligned and electrically conductive nanofibers that can simultaneously provide topographical and electrical cues for cells have been reported, which served as functional scaffolds for skeletal muscle tissue engineering. For example, well-ordered nanofibers composed of PANi and poly(ε-caprolactone) (PCL) were produced by using electrospinning technique. The incorporated PANi significantly increased the electrical conductivity of PCL fibers, from a non-detectable level for the pure PCL fibers to 63.6 mS/cm for the fibers containing 3 wt% of PANi. The electrically conductive aligned PCL/PANi nanofibers enhanced myotube maturation compared with nonconductive aligned PCL fibers or random PCL/PANi fibers as well as guided mouse C2C12 myoblasts orientation [117]. Additionally, conductive polymers are considered to have antioxidative effects. For example, a multifunctional material was designed for uses as a coating in porous Ti scaffolds, which was expected to be electroactive, cell affinitive,

persistent ROS-scavenging, and osteoinductive. A composite film composed of polypyrrole, polydopamine, and hydroxyapatite (PPY-PDA-HA) was fabricated in situ synthesized and uniformly coated on a porous scaffold from inside to outside by utilizing a layer-by-layer pulse electrodeposition (LBL-PED) method. In this design, there were PPY-PDA nanoparticles (NPs) and HA NPs in the coating, aiming for bring conductivity and osteoconductivity, respectively. The content of PDA was expected to enhance the ROS scavenging rate of the scaffold within a long period, the content of HA and electrical stimulation synergistically promote osteogenic cell differentiation films [118]. Piezoelectric materials are also important candidates in the application of skeletal tissue regeneration. For example, piezoelectric polymer poly(vinylidene fluoride) (PVDF) can present physical cues to muscle cells that mimic the natural regeneration environment to improve muscle regeneration, because it is able to induce transient surface charge boosting cell growth and differentiation compared with non-piezoelectric controls. One group investigated how the surface properties of the material, in terms of both the charge state and the morphology, influenced myoblast differentiation. They observed enhanced myogenic differentiation of C2C12 cells grown on PVDF by quantitative examination of myotube fusion, maturation index, length, diameter, and number. It is interesting to see that charged surfaces improved the fusion of muscle cells into differentiated myotubes, while the fiber orientation generated influence upon the cell morphology; contrary to the randomly oriented fibers, oriented PVDF electrospun fibers promoted the alignment of the cells [119]. Besides being used in scaffolds for skeletal muscle cells of cardiac tissue, there are investigations of utilizing conductive polymers in bone tissue engineering. As one example, therefore, a three-dimensional (3D) ceramic conductive tissue engineering scaffold for large bone defects was prepared by employing a biocompatible conductive polymer, poly(3,4-ethylenedioxythiophene) poly(4-styrene sulfonate) (PEDOT:PSS), in the optimized nanocomposite of gelatin and bioactive glass. The resulting composite scaffold enhanced the viability of adult human mesenchymal stem cells; meanwhile, the incorporation of PEDOT:PSS increased the physiochemical stability of the composite, resulting in improved mechanical properties and biodegradation resistance. These results suggested that conductive bioactive glass could be produced, which would be structurally more favorable for bone tissue engineering, and may by combined with tissue engineering techniques to enhance bone healing by electrical stimuli [120].

2.5 Conductive Materials for Nerve Regeneration and Treatment

The peripheral nervous system (PNS) is capable of regeneration in adult mammals. Immediately after injury, the tip of the proximal stump swells to two or three times its original diameter and the severed axons retract. Several days later, the proximal

axons begin to sprout vigorously, and growth cones emerge to elicit numerous extensions that extend outward in all directions until the first sprout reaches an appropriate target. In successful regeneration, axons sprouting from the proximal nerve stump traverse the injury site, enter the distal nerve stump, and make new connections with target organs. The most severe injury is a complete transaction of the nerve, interrupting communication between the nerve cell body and its target, disrupts the interrelations between neurons and their support cells, destroys the local blood–nerve barrier, and triggers a variety of cellular and humoral events. Although current surgical techniques allow surgeons to realign nerve ends precisely when the lesion does not require excision of a large nerve segment. However, damages in large scale depend on nerve guidance channels to help the regeneration process, because the rate of axon elongation is as low as 1 mm per day in average in humans. When a nerve guidance channel is used, the mobilized ends of a severed nerve are introduced in the lumen of a tube and anchored in place with sutures. The channel can provide a path between nerve stumps, directional guidance for elongation neurites and migrating cells, proximal-distal stump communication, and minimal number of epineurial stay sutures, prevent scar tissue invasion into the regenerating environment, and preserve endogenous trophic or growth factors released by the traumatized nerve ends within the channel lumen. In addition, guidance channels are useful to experimental studies, for example, control the gap distance between the nerve stumps, examine the fluid and tissue entering the channel, modulate the physicochemical properties of the channel, and apply various drugs, gels, and Shawn cells in channels to investigate the regulatory effects [121]. Technologies in the fabrication of tissue engineering scaffolds provide more choices for conventional nerve conduits, especially that to introduce conductive materials and nanostructures into scaffolds. Advances in the past decade have showed that conductive scaffolds by utilizing nanotechnology and conductive materials promoted neuronal proliferation and differentiation by providing an environment around nerve tissue of electrical signal exchange and conduction properties.

2.5.1 Conductive Polymers

In an early study, an electrospun scaffold (PANI/PG) was prepared by blending doped polyaniline (PANi) in the mixed solution of poly (epsilon-caprolactone) and gelatin in a ratio of 70:30 solution, followed by processed with electrospinning technique. The nanofibrous scaffolds containing 15% PANi showed the most balanced properties to meet the required specifications for electrical stimulation and were suitable for the attachment and proliferation of nerve stem cells. When an electrical stimulation was directly applied, both cell proliferation and neurite outgrowth were enhanced compared to the PANI/PG scaffolds that were not subjected to electrical stimulation [122]. When blended with polyethyleneglycol diacrylate (PEGDA), PANi brought conductivity to the macroporous hydrogels crosslinked

via UV irradiation, 1.1×10^{-3} mS/cm with 3 wt% of PANi and improved the biological response of rat pheochromocytoma 12 (PC12) and hMSC cells. The hydrophilic nature of PANi also enhanced water retention and proton conductivity by more than one order of magnitude [123]. Polypyrrole (PPY) is also a good candidate for being used as a conductive component in scaffolds of nerve engineering. In one study, a conducting nerve conduit composed of PPY and poly(D, L-lactic acid) (PDLLA) was fabricated, and the PPY content of PPY 5%, 10%, and 15% resulted in the conductivity 5.65, 10.40, and 15.56 mS/cm, respectively. When PC12 cells were seeded on these conduits and stimulated with 100 mV for 2 h, there was a marked increase in both the percentage of neurite-bearing cells and the median neurite length in a PPY concentration-dependent manner. More encouragingly, when the PPY/PDLLA nerve conduit was used to repair a rat sciatic nerve defect, it performed similarly to the gold standard autologous graft in the 6-month investigation. In particular, the PPY/PDLLA conduit started degradation at the 3-month post implantation when the 10 mm gap was bridged by regenerative tissue [124]. Another form of three-dimensional PPY conductive fibrous scaffold was fabricated by using electrospinning technique to produce PLLA fibers and have PPY coated on the fiber surface with a thickness of 45 nm. The average diameter of the PPY-coated PLLA fibers was 2.1 μm. The size of interconnected pores in the scaffolds ranged from 50 to 100 μm. This conductive 3D scaffold was superior to the conductive fibrous mesh, which ensured cells entry into inside of the scaffolds to achieve three-dimensional cell culture. It was reported that more PC12 cells were detected in the 3D scaffolds than that on the fibrous meshes in the 3 days culture and developed cell–fiber constructs in the central of conductive 3D scaffolds [125]. In some situations, mechanical properties of scaffolds are addressed, that the mechanical performance would be better close to that of the corresponding natural tissue. For example, it is considered that it is crucial to mimic mechanical properties and high conductivities of soft tissues in the design for nerve tissue regeneration scaffolds, as that are required for electrical transmission in the native spinal cord. For example, a soft, highly conductive hydrogel was prepared by using a plant-derived polyphenol, tannic acid (TA), and conducting polypyrrole (PPY) for guiding tissue regeneration after a spinal cord injury. The hydrogel obtained electrical conductivity of 0.05–0.18 S/cm and mechanical property of 0.3–2.2 kPa, which was controlled by TA concentration. The increased conductivity of the scaffolds accelerated the differentiation of neural stem cells into neurons while suppressing the development of astrocytes and, more importantly, activated the neurogenesis of endogenous neural stem cells in the lesion area to recover the locomotor function [126]. As mentioned before, Schwann cells play important roles in the nerve regeneration as they are the supportive cells to the neuronal cells. The myelination of Schwann cells is crucial for the success of peripheral nerve regeneration, and scaffolds promoting Schwann cells to secret neurotrophin would be beneficial for nerve repair. An investigation reported a highly tunable conductive biodegradable flexible polyurethane by polycondensation of poly(glycerol sebacate) and aniline pentamer, which significantly enhanced Schwann cells' myelin gene expression and neurotrophin secretion. The mechanism of Schwann cells' neurotrophin secretion on conductive films is

attributed to the increase of intracellular Ca^{2+} level. The enhanced Schwann cells' myelin gene expressions and sustained neurotrophin secretion would be of potential for nerve regeneration [127].

2.5.2 Inorganic Nanoparticles

The utilization of conductive nanomaterials as fillers in various polymeric materials is one important and effective solution to develop neural tissue engineering scaffolds. As one of the conductive nanomaterials, graphene has huge potentials in nerve function restoration by promoting electrical signal transduction and metabolic activities with unique topological properties. The underlying mechanisms are involved with the interface interaction between graphene and neural cell membrane. A mechanistic study indicated that graphene did not affect the basic membrane electrical parameters of neural stem cells, the electric field produced by the electronegative cell membrane was much higher on graphene substrates than that on control, which indicated that graphene was able to accelerate neural stem cell maturation during development, especially with regard to bioelectric evolvement [128]. It was reported that reduced GO (rGO) nanosheets could be integrated with porcine acellular dermal matrix (PADM) mainly composed of type I collagen to prepare a porous 3D, biodegradable, conductive, and biocompatible PADM-rGO hybrid. The rGO in the scaffold did not induce a significant change in the microstructure but endowed the PADM-rGO composite with good conductivity. Rat bone-marrow-derived mesenchymal stem cells (MSCs) cultured on PADM-rGO composite showed a higher level of neural markers including Nestin, Tuj1, GFAP, and MAP2, both in protein and gene level, after 7 days under neural differentiation conditions than those on PADM alone, suggesting that the PADM-rGO promoted the differentiation of MSCs into neuronal cells as well as support the growth of MSCs at a high proliferation rate [129]. It is well known that polydopamine (PDA) and arginylglycylaspartic acid (RGD) can improve cell adhesion in tissue engineering. A study combined the technology of 3D printing and layer-by-layer casting (LBLC) to fabricate a multilayered porous scaffold composed of multilayered graphene (MG) coated with PDA/RGD and polycaprolactone (PCL). The conductive 3D graphene scaffold significantly improved neural expression both in vitro and in vivo, promoting successful axonal regrowth and remyelination after peripheral nerve injury [130]. The rGO-based composite can also act as a medium for step-driven TENG pulse electrical simulation signals in the nerve regeneration. Currently almost all electrical stimulation for clinical or experimental nerve regeneration is supplied by traditional electrical stimulators using a 220 V power supply, which are considered expensive, not portable, and need an external power supply however may with safety risk. Battery-like power suppliers may have problems such as low-voltage, short duration, and difficult to adhere to the animal models of patients. To meet the needs, a group established a long-lasting and portable self-powered electrical stimulation system by combining reduced graphene oxide (rGO) and a conductive

polymer poly(3,4-ethylenedioxythiophene) (PEDOT). The highly electrically conductive composite (rGO-PEDOT) microfiber with a diameter of 80 μm was prepared as neural scaffolds. A step-driven self-powered neural differentiation system was integrated by combining the composite microfiber and a TENG system [131] with outputs of 250 V and 30 μA. The rGO-PEDOT composite microfiber could not only enhance the proliferation of MSCs but also act as a medium for step-driven TENG pulse electrical simulation signals, inducing MSCs to differentiate into neural cells. This approach showed the application potentials of a self-powered wearable TENG electrical stimulation system to assist nerve regeneration for a walking person [132].

Carbon nanotubes are another typical conductive nanomaterial easily to be combined with various polymeric materials to generate conductive composites. One example is the integration of carbon nanotube fibers (CNFs) with polysaccharide agarose to prepare conductive hydrogels for neural tissue engineering and biointerfacing with the nervous system. The CNFs can be chemically functionalized by agarose to gain biological moieties. The agarose-modified CNF was reported conductive and nontoxic and could facilitate cell attachment and response both in vitro and in vivo [133]. As another example, multiwalled carbon nanotubes (MWCNTs) were combined with poly(lactic-co-glycolic acid) (PLGA) to generate electrically conductive and aligned nanofibrous scaffolds for nerve regeneration. The surface was modified with poly-L-lysine to provide a better environment for cell attachment. The aligned conductive fibers were reported to guide PC12 cells and dorsal root ganglion (DRG) neurons growing along the fiber direction and be beneficial for neurite outgrowth. Moreover, PC12 cells and DRG neurons stimulated with electrical shock of 40 mV showed longer neurite length. In this study, the cell attachment, proliferation, and MBP expression of Schwann cells were also enhanced with the synergistic effect of aligned nanofibers and electrical stimulation [134]. Carbon nanotubes could be combined with plasma-treated chitin to generate composite scaffolds for neuron repair/regeneration. The addition of carbon nanotubes to the chitin biopolymer improved the electrical conductivity and the assisted oxygen plasma treatment introduced more oxygen species onto the scaffold surface, which in turn increased neuron adhesion as well as maintained synaptic function of neurons [135]. To promote the differentiation of human neural stem/progenitor cells (hNSPCs), single-walled carbon nanotubes (SWCNTs) were introduced with polypyrrole (PPY) together into hyaluronic acid (HA) hydrogel by the oxidative catechol chemistry used for hydrogel cross-linking. The prepared electroconductive HA hydrogels were reported to be dynamic, electrically conductive, and biocompatible, significantly promoted neuronal differentiation of human fetal neural stem cells (hfNSCs) and human-induced pluripotent stem cell-derived neural progenitor cells (hiPSC-NPCs) with improved electrophysiological functionality when compared to the control HA hydrogel, as shown that calcium channel expression was upregulated, depolarization was activated, and intracellular calcium influx was increased in hNSPCs that were differentiated in 3D electroconductive HA-CA hydrogels [136]. In neural injury, potassium chloride cotransporter 2 (KCC2) was repressed, which plays a co-contributory role by corrupting inhibitory neurotransmission. It was

detected that highly conductive few-walled-CNT (fwCNT) had influence on primary CNS neurons originating from the cerebral cortex, inducing Cl− downregulation and KCC2 upregulation, which made the chloride shift robustly and strikingly accelerated. This effect was demonstrated specific for fwCNT since SiOx nanowires (a nanomaterial with similar nanostructure yet not conductive) did not affect the chloride shift. The result is of implications to the development of novel devices that interface with nervous tissues [137].

2.6 Wound Healing

Serious injuries resulted from trauma, burns, and clinical surgery would severely affect one's life and health. Wound repair and tissue regeneration are complex processes that bring challenges in the development of wound dressings with potent biological activity and physiological signal response ability to accelerate the process of wound healing. There is a large need of wound dressing for seriously injured skin wound in clinical practices, because skin is the largest organ in human body protecting the body from damage and bacterial infection and maintaining body fluid, electrolytes, and nutritional component.

It is known that skin is an electrical signal-sensitive tissue; the conductivity values can be from 1×10^{-4} mS/cm to 2.6 mS/cm, depending on skin components [138]; therefore, induction of conductive materials in skin wound dressing would be beneficial to the skin regeneration. In addition, when a wound dressing gains a certain degree of conductivity, it would hold an ability of free radical scavenging, which is likely to benefit to tissue regeneration possibly by reducing proinflammatory substances.

For example, a conductive self-healing and injectable hydrogel fabricated by using two polymeric materials formed a crosslinking network: one is quaternized chitosan grafted with polyaniline and the other is benzaldehyde group functionalized poly(ethylene glycol)-co-poly(glycerol sebacate) (PEGS-FA). The conductivity of the resulting hydrogel was 0.23–0.35 S/m. Noted that the hydrogel showed free radical scavenging ability, biocompatibility, and intrinsic antibacterial activity that was attributable to chitosan. Interestingly, the hydrogel with an optimal formulation showed excellent in vivo blood clotting capacity, and it significantly enhanced in vivo wound healing process in a full-thickness skin defect model than the control of nonconductive hydrogel and commercial dressing control. At the same time, the hydrogel increased the gene expression level of growth factors including VEGF, EGF, and TGF-β in the regenerated skin tissue, and the granulation tissue thickness and collagen deposition were promoted. These results indicated the important contribution of the conductivity of the hydrogel among the multifunctional properties [138]. Similar multifunctional hydrogels were designed by mixing the biocompatible *N*-carboxyethyl chitosan (CEC) and oxidized hyaluronic acid-graft-aniline tetramer (OHA-AT) under physiological conditions. The hydrogels exhibited stable rheological property, high swelling ratio, suitable gelation time, good in vitro

biodegradation property, electroactive property, and free radical scavenging capacity. The antibacterial activity of this hydrogel was contributed by the addition of antibiotic amoxicillin, effectively preventing the wound infection. In vivo experiments indicated that hydrogel with aniline tetramer addition significantly accelerated wound healing rate with higher granulation tissue thickness, collagen disposition, and more angiogenesis in a full-thickness skin defect model, suggesting the conductive component made main contribution to the tissue regeneration instead of the antibacterial property [139].

Besides polymeric conductive components, potentials of inorganic nanomaterials have also been investigated in conductive wound dressing. Carbon nanomaterials have become attractive to wound dressing mainly due to the excellent biocompatibility of carbon materials, for example, carbon materials have been used as coatings in various kinds of blood-contacting medical devices [140], as well as their conductivity. Carbon nanotubes are one typical carbon-based nanomaterials and have been demonstrated excellent blood compatibility when in the form of non-woven membrane [141] or to improve biocompatibility of polyurethane when embedded in the polymeric matrix [142, 143]. We have reported that electrospun nanofibrous membranes composed of multiwalled carbon nanotubes (MWCNTs) and polyurethane (PU) showed friend interactions to fibroblast cells that are major supportive cells in skin. The MWCNTs increased the content of pure carbon to improve the biocompatibility and conductivity of the nanofibrous membrane. Interestingly, the composite nanofibrous membrane displayed stronger function of supporting cell adhesion and proliferation than the control membrane without MWCNTs. In particular, the composite membrane enhanced cell–cell connection compared with the control membrane, and fibroblasts grown on the composite nanofibrous membrane formed cell sheets (Fig. 2.4), suggesting the membrane provided a favorite environment for the fibroblasts to migrate and communicate. Furthermore, the cells growing on the nanofibrous composite membrane released the biological signals to the population growing on the smooth film of PU to encourage the population's proliferation [144]. In addition, single-walled carbon nanotube non-woven films could be used directly as scaffolds to support fibroblast cell growth for long-term proliferation [145].

Reduced graphene is another kind of conductive carbon nanomaterial explored in wound healing dressings; it also has strong adsorption capacity to various biological molecules as well as high conductivity. Researchers developed a polydopamine (PDA)-reduced graphene oxide (pGO) that was then dispersed into a mixture of chitosan (CS) and silk fibroin (SF) (CS/SF), aiming to acquire adhesive property and conductivity at the same time. In the resulting hydrogel, pGO was considered as nanoreinforcement to enhance the mechanical properties of the scaffold and comprised a well-connected electric pathway to provide a channel for the transmission of electrical signals in the scaffold. Moreover, pGO could scavenge reactive oxygen species (ROS) to inhibit excessive ROS oxidation. Due to these collective properties, the electroactive pGO-CS/SF scaffolds could respond to electrical signals and enhance the wound healing in full-thickness skin defect model [146]. A similar design of adhesive hemostatic antioxidant conductive photothermal antibacterial

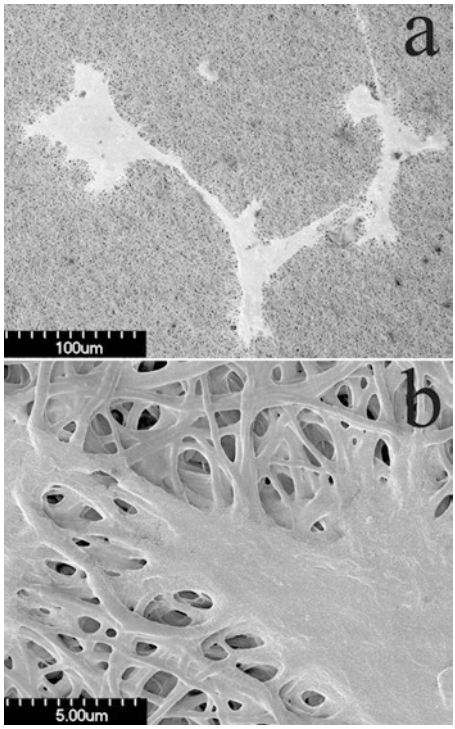

Fig. 2.4 Morphological observation of cells growing on nanofibrous scaffold of MWNT/PU under SEM, in which (**a**) exhibited the cell sheets and cell "chains" formed on nanofibrous scaffold of MWNT/PU; (**b**) SEM image with higher magnification showed the cells spread and integrated well with the nanofibrous scaffold of MWNT/PU [144]

hydrogels was reported, and the hydrogel was composed of hyaluronic acid-graft-dopamine and reduced graphene oxide, having high swelling, degradability, tunable rheological property, and similar mechanical properties to human skin. It had been noted that the hydrogel dressings significantly enhanced vascularization by upregulating growth factor expression of CD31 and improved the granulation tissue thickness and collagen deposition to promote wound closure in a mouse full-thickness wounds model [147].

Hemorrhage control is an important issue of wound healing, not only in military and civilian trauma centers, but also in clinics. Uncontrolled hemorrhage leads to over 30% of trauma deaths in the world, and more than 50% of those occur before the emergency care can reach. Hence, hemostatic agents that can quickly control massive hemorrhage from vessels and visceral organs are highly needed, however have remain challenged. A research group designed an injectable antibacterial conductive cryogels by integrating carbon nanotubes (CNTs) and glycidyl methacrylate functionalized quaternized chitosan for uses in lethal noncompressible hemostasis and wound healing (Fig. 2.5). It is noticeable that the CNT content varying from 2 to 4 and 6 mg/mL resulted in the increase of conductivity for the cryogels, increasing from 0.04 to 0.095 and 0.12 S/m, respectively, showing the obvious contribution of CNT to the cryogels' conductivity. These cryogels were reported to have better blood-clotting ability and higher blood cell and platelet adhesion and activation than gelatin sponge and gauze in mouse liver injury model and mouse tail amputation

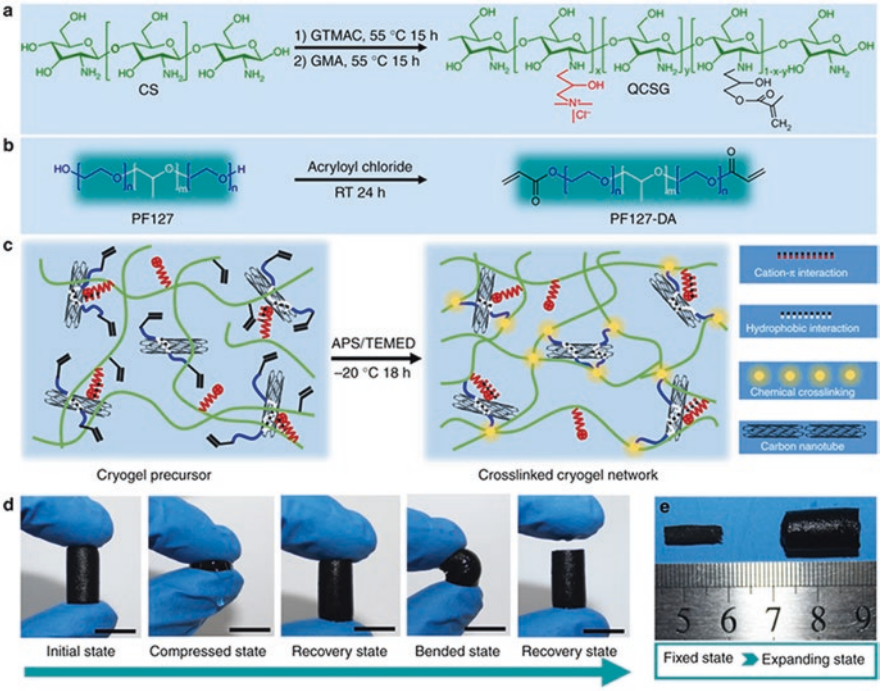

Fig. 2.5 Injectable antibacterial conductive nanocomposite cryogels with rapid shape recovery for noncompressible hemorrhage and wound healing. Schematic representation of QCSG/CNT cryogel synthesis. (**a**) Synthesis of QCSG copolymer. GTMAC and GMA with a fixed 0.5:1 molar ratio of GMA to amino groups and varying the GTMAC:amino groups from 1:1 (coded as QCSG1) to 2:1 (coded as QCSG2) and 3:1 (coded as QCSG3). (**b**) Synthesis of PF127-DA copolymer. (**c**) Preparation of QCSG/CNT cryogel. (**d**) Photographs of the compression and bending resistance capability of QCSG/CNT4 cryogels: initial state, compressed state by squeezing out of the free water, recovery state by absorbing water, bending, and squeezing out of part free water, and recovery state after absorbing water. (**e**) Shape-fixed state after removing the free water (left) and expanding state after absorbing water (right). Scale bar: 1 cm [148]

model (Fig. 2.6), and excellent hemostatic performance in rabbit liver defect lethal noncompressible hemorrhage model [148]. Here one issue could be discussed that in this investigation, the rapid clotting was mainly attributed to the chitosan component, and the CNT was considered to trigger the platelet activation as well. We would like to address that whether CNTs play anticoagulant roles (hemocompatibility) or play hemostatic performance is highly dependent on the application way of CNTs, that is, the way of contacting blood. It has been demonstrated that the carbon nanotubes integrated with polyurethane improved the blood compatibility of the composite [143] or showed excellent performance of inhibiting the activation of platelets when in the form of nonwoven membrane [141]. However, when carbon nanotubes were dispersed in buffer saline, they exhibited the effect of inducing blood coagulation [149]. It could be noted that the CNTs in the hydrogel for

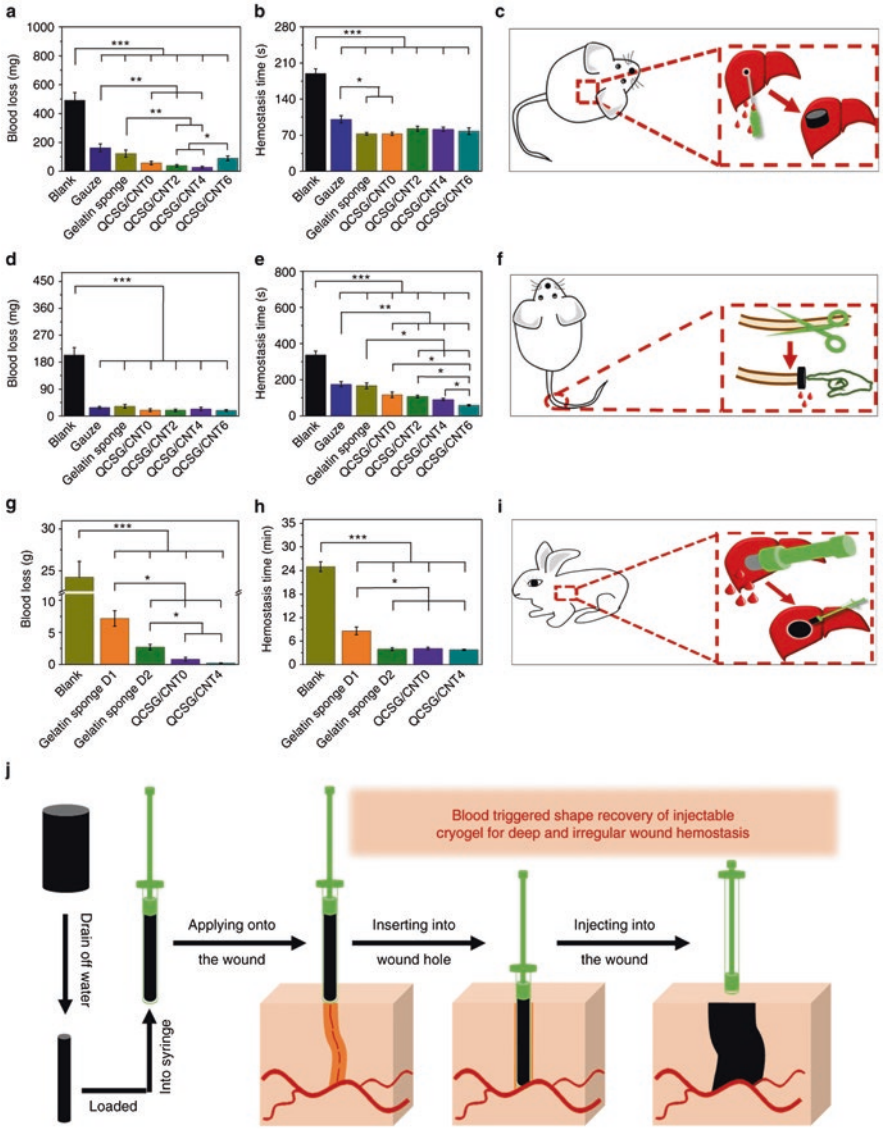

Fig. 2.6 Injectable antibacterial conductive nanocomposite cryogels with rapid shape recovery for noncompressible hemorrhage and wound healing. In vivo hemostatic capacity evaluation of the cryogels. Blood loss (**a**) and hemostatic time (**b**) in the mouse liver injury model. The blank group showed the highest blood loss of 492 mg than the other groups ($P < 0.001$). Gauze and gelatin sponge, as two control groups, presented much decreased blood loss of about 163 and 123 mg, respectively, when compared to blank group ($P < 0.001$). However, all the four cryogels except for QCSG/CNT6 showed significantly decreased blood loss of 57, 38, and 27 mg than those of gauze, and the cryogel QCSG/CNT2 and cryogel QCSG/CNT4 also showed significantly decreased blood loss than that of gelatin sponge ($P < 0.05$). (**c**) Scheme representation of the mouse liver injury model during hemostasis. Blood loss (**d**) and hemostatic time (**e**) in the mouse tail amputation

hemostasis might contact platelets in a status of dispersing nanoparticles when the hydrogel was injected in liver, because there is a large amount of water in the hydrogel. In this case, the CNTs could trigger platelet activation to a certain extent. Differently, when carbon nanotubes were integrated with polymeric materials, they combined with polymer chains tightly, therefore exhibiting the performance of macroscale carbon materials.

2.7 Perspectives

Large numbers of investigations have showed that conductive materials are of great significance to tissue engineering and regenerative medicine, they have remarkable impacts on important events of cell growth, differentiation, and formation of new tissues with physiological functions by creating electrically active microenvironments mimicking natural physiological conditions. The conductive scaffolds with or without electrical stimulations have been applied to excitable tissues such as cardiac and skeletal and nerve and also bone and skin, therefore exhibiting promising potentials in the repair of tissue defects and injury as well as in creating tissue in vitro. Nevertheless, challenges are existing, including improvements of conductive polymers' stability and biocompatibility and long-term safety of conductive nanomaterials. Moreover, it is necessary to have the measurements for conductivity of different scaffolds standardized and data comparable in the future, which would be helpful to design novel conductive scaffolds that are available to be controlled precisely.

References

1. F.A. Duck, *Physical Properties of Tissues: A Comprehensive Reference Book* (Academic, San Diego, 2013)
2. R. Balint, N.J. Cassidy, S.H. Cartmell, Conductive polymers: towards a smart biomaterial for tissue engineering. Acta Biomater. **10**(6), 2341–2353 (2014)
3. J.H. Min, M. Patel, W.G. Koh, Incorporation of conductive materials into hydrogels for tissue engineering applications. Polymers (Basel) **10**(10) (2018). pii: E1078

Fig. 2.6 (continued) model. The blank group (337 s) showed the longest hemostatic time than other groups ($P < 0.001$). All the four cryogels showed shorter hemostatic times than gauze group (176 s) ($P < 0.01$), while all the four cryogels except for QCSG/CNT0 showed shorter hemostatic times than gelatin sponge group (167 s) ($P < 0.05$). (**f**) Schematic representation of the mouse tail amputation model during hemostasis; Blood loss (**g**) and hemostatic time (**h**) in the rabbit liver defect lethal noncompressible hemorrhage model. (**i**) Scheme representation of the rabbit liver defect lethal noncompressible hemorrhage model during hemostasis. (**j**) Schematic representation of the hemostatic application of injectable shape memory cryogel hemostatic in a deep and irregularly shaped wound model. $*P < 0.05$, $**P < 0.01$, $***P < 0.001$ using Student's *t*-test (two-sided). The error bars stand for SEM ($n = 10$ for **a**, **b**, **d**, **e**; $n = 5$ for **g**, **h**) [148]

4. M. Potse, B. Dube, A. Vinet, Cardiac anisotropy in boundary-element models for the electrocardiogram. Med. Biol. Eng. Comput. **47**(7), 719–729 (2009)
5. A.K. Geim, K.S. Novoselov, The rise of graphene. Nat. Mater. **6**(3), 183–191 (2007)
6. C. Chung et al., Biomedical applications of graphene and graphene oxide. Acc. Chem. Res. **46**(10), 2211–2224 (2013)
7. S. Park, R.S. Ruoff, Chemical methods for the production of graphenes. Nat. Nanotechnol. **4**(4), 217–224 (2009)
8. Y. Zhu et al., Graphene and graphene oxide: synthesis, properties, and applications. Adv. Mater. **22**(35), 3906–3924 (2010)
9. K.S. Novoselov et al., A roadmap for graphene. Nature **490**(7419), 192–200 (2012)
10. D. Li, R.B. Kaner, Graphene-based materials. Science **320**(5880), 1170–1171 (2008)
11. H. Dai, Carbon nanotubes: opportunities and challenges. Surf. Sci. **500**(1-3), 218–241 (2002)
12. J.M. Schnorr, T.M. Swager, Emerging applications of carbon nanotubes. Chem. Mater. **23**(3), 646–657 (2010)
13. V.N. Popov, Carbon nanotubes: properties and application. Mater. Sci. Eng. R Rep. **43**(3), 61–102 (2004)
14. I. Sumio, Carbon nanotubes: past, present, and future. Phys. B Condens. Matter. **323**(1–4), 1–5 (2002)
15. P.R. Bandaru, Electrical properties and applications of carbon nanotube structures. J. Nanosci. Nanotechnol. **7**(4–5), 1239–1267 (2007)
16. H. Dai, Carbon nanotubes: synthesis, integration, and properties. Acc. Chem. Res. **35**(12), 1035–1044 (2002)
17. R.H. Baughman, A.A. Zakhidov, W.A. de Heer, Carbon nanotubesDOUBLEHYPHENthe route toward applications. Science **297**(5582), 787–792 (2002)
18. M. Shao, D.D.D. Ma, S.-T. Lee, Silicon nanowires – synthesis, properties, and applications. Eur. J. Inorg. Chem. **2010**(27), 4264–4278 (2010)
19. Y. Wu et al., Controlled growth and structures of molecular-scale silicon nanowires. Nano Lett. **4**(3), 433–436 (2004)
20. P.R. Bandaru, P. Pichanusakorn, An outline of the synthesis and properties of silicon nanowires. Semicond. Sci. Technol. **25**(2), 024003 (2010)
21. V. Schmidt, J.V. Wittemann, U. Gösele, Growth, thermodynamics, and electrical properties of silicon nanowires. Chem. Rev. **110**(1), 361–388 (2010)
22. L.J. Chen, Silicon nanowires: the key building block for future electronic devices. J. Mater. Chem. **17**(44), 4639–4643 (2007)
23. R. Rurali, Colloquium: structural, electronic and transport properties of silicon nanowires. Rev. Mod. Phys. **82**(1), 427–449 (2010)
24. Y. Zheng et al., Electronic properties of silicon nanowires. IEEE Trans. Electron Devices **52**(6), 1097–1103 (2005)
25. D.A. Giljohann et al., Gold nanoparticles for biology and medicine. Angew. Chem. Int. Ed. **49**(19), 3280–3294 (2010)
26. X. Zhang, Gold nanoparticles: recent advances in the biomedical applications. Cell Biochem. Biophys. **72**(3), 771–775 (2015)
27. H.-H. Jeong et al., Recent advances in gold nanoparticles for biomedical applications: from hybrid structures to multi-functionality. J. Mater. Chem. B **7**(22), 3480–3496 (2019)
28. J. Siegel et al., Properties of gold nanostructures sputtered on glass. Nanoscale Res. Lett. **6**(1), 96 (2011)
29. E.C. Dreaden et al., The golden age: gold nanoparticles for biomedicine. Chem. Soc. Rev. **41**(7), 2740–2779 (2012)
30. R. Sardar et al., Gold nanoparticles: past, present, and future. Langmuir **25**(24), 13840–13851 (2009)
31. R.A. Sperling et al., Biological applications of gold nanoparticles. Chem. Soc. Rev. **37**(9), 1896–1908 (2008)
32. S. Alex, A. Tiwari, Functionalized gold nanoparticles: synthesis, properties and applicationsDOUBLEHYPHENa review. J. Nanosci. Nanotechnol. **15**(3), 1869–1894 (2015)

33. G. Schmid, U. Simon, Gold nanoparticles: assembly and electrical properties in 1–3 dimensions. Chem. Commun. **6**, 697–710 (2005)
34. A.B. Afzal et al., Investigation of structural and electrical properties of polyaniline/gold nanocomposites. J. Phys. Chem. C **113**(40), 17560–17565 (2009)
35. M. Ahamed, M.S. Alsalhi, M.K. Siddiqui, Silver nanoparticle applications and human health. Clin. Chim. Acta **411**(23–24), 1841–1848 (2010)
36. X.F. Zhang et al., Silver nanoparticles: synthesis, characterization, properties, applications, and therapeutic approaches. Int. J. Mol. Sci. **17**(9), 1534 (2016)
37. J. Meng et al., Using gold nanorods core/silver shell nanostructures as model material to probe biodistribution and toxic effects of silver nanoparticles in mice. Nanotoxicology **8**(6), 686–696 (2014)
38. H. Guo et al., Intravenous administration of silver nanoparticles causes organ toxicity through intracellular ROS-related loss of inter-endothelial junction. Part. Fibre Toxicol. **13**, 21 (2016)
39. H. Li et al., In vivo metabolic response upon exposure to gold nanorod core/silver shell nanostructures: modulation of inflammation and upregulation of dopamine. Int. J. Mol. Sci. **21**(2) (2020). pii: E384
40. B. Wiley, Y. Sun, Y. Xia, Synthesis of silver nanostructures with controlled shapes and properties. Acc. Chem. Res. **40**(10), 1067–1076 (2007)
41. D. Chen et al., Synthesis and electrical properties of uniform silver nanoparticles for electronic applications. J. Mater. Sci. **44**(4), 1076–1081 (2009)
42. S.M. Adhyapak, V.R. Parachuri, Architecture of the left ventricle: insights for optimal surgical ventricular restoration. Heart Fail. Rev. **15**(1), 73–83 (2010)
43. R. Hashizume et al., Biodegradable elastic patch plasty ameliorates left ventricular adverse remodeling after ischemia–reperfusion injury: a preclinical study of a porous polyurethane material in a porcine model. J. Thorac. Cardiovasc. Surg. **146**(2), 391–399.e1 (2013)
44. D.D. Ateh, H.A. Navsaria, P. Vadgama, Polypyrrole-based conducting polymers and interactions with biological tissues. J. R. Soc. Interface **3**(11), 741–752 (2006)
45. X. Liu et al., Conducting polymers with immobilised fibrillar collagen for enhanced neural interfacing. Biomaterials **32**(30), 7309–7317 (2011)
46. A. Mihic et al., A conductive polymer hydrogel supports cell electrical signaling and improves cardiac function after implantation into myocardial infarct. Circulation **132**(8), 772–784 (2015)
47. Z. Cui et al., Polypyrrole-chitosan conductive biomaterial synchronizes cardiomyocyte contraction and improves myocardial electrical impulse propagation. Theranostics **8**(10), 2752–2764 (2018)
48. S. He et al., Preservation of conductive propagation after surgical repair of cardiac defects with a bio-engineered conductive patch. J. Heart Lung Transplant. **37**(7), 912–924 (2018)
49. A. Gelmi et al., Direct mechanical stimulation of stem cells: a beating electromechanically active scaffold for cardiac tissue engineering. Adv. Healthc. Mater. **5**(12), 1471–1480 (2016)
50. G. Kaur et al., Electrically conductive polymers and composites for biomedical applications. RSC Adv. **5**(47), 37553–37567 (2015)
51. Y. He et al., Mussel-inspired conductive nanofibrous membranes repair myocardial infarction by enhancing cardiac function and revascularization. Theranostics **8**(18), 5159–5177 (2018)
52. J.H. Tsui et al., Conductive silk–polypyrrole composite scaffolds with bioinspired nanotopographic cues for cardiac tissue engineering. J. Mater. Chem. B **6**(44), 7185–7196 (2018)
53. P.R. Bidez III et al., Polyaniline, an electroactive polymer, supports adhesion and proliferation of cardiac myoblasts. J. Biomater. Sci. Polym. Ed. **17**(1-2), 199–212 (2006)
54. M. Li et al., Electrospinning polyaniline-contained gelatin nanofibers for tissue engineering applications. Biomaterials **27**(13), 2705–2715 (2006)
55. C.-W. Hsiao et al., Electrical coupling of isolated cardiomyocyte clusters grown on aligned conductive nanofibrous meshes for their synchronized beating. Biomaterials **34**(4), 1063–1072 (2013)

56. L. Wang et al., Electrospun conductive nanofibrous scaffolds for engineering cardiac tissue and 3D bioactuators. Acta Biomater. **59**, 68–81 (2017)
57. M. Kapnisi et al., Auxetic cardiac patches with tunable mechanical and conductive properties toward treating myocardial infarction. Adv. Funct. Mater. **28**(21), 1800618 (2018)
58. P.T. Bertuoli et al., Electrospun conducting and biocompatible uniaxial and core-shell fibers having poly(lactic acid), poly(ethylene glycol), and polyaniline for cardiac tissue engineering. ACS Omega **4**(2), 3660–3672 (2019)
59. X. Zhao et al., Antibacterial and conductive injectable hydrogels based on quaternized chitosan-graft-polyaniline/oxidized dextran for tissue engineering. Acta Biomater. **26**, 236–248 (2015)
60. B. Yang et al., Development of electrically conductive double-network hydrogels via one-step facile strategy for cardiac tissue engineering. Adv. Healthc. Mater. **5**(4), 474–488 (2016)
61. J. Zhou et al., Engineering the heart: evaluation of conductive nanomaterials for improving implant integration and cardiac function. Sci. Rep. **4**(1), 3733 (2014)
62. S. Pok et al., Biocompatible carbon nanotube-chitosan scaffold matching the electrical conductivity of the heart. ACS Nano **8**(10), 9822–9832 (2014)
63. B. Peña et al., Injectable carbon nanotube-functionalized reverse thermal gel promotes cardiomyocytes survival and maturation. ACS Appl. Mater. Interfaces **9**(37), 31645–31656 (2017)
64. S. Ahadian et al., Moldable elastomeric polyester-carbon nanotube scaffolds for cardiac tissue engineering. Acta Biomater. **52**, 81–91 (2017)
65. M. Kharaziha et al., Tough and flexible CNT–polymeric hybrid scaffolds for engineering cardiac constructs. Biomaterials **35**(26), 7346–7354 (2014)
66. N. Shokraei et al., Development of electrically conductive hybrid nanofibers based on CNT-polyurethane nanocomposite for cardiac tissue engineering. Microsc. Res. Tech. **82**(8), 1316–1325 (2019)
67. J. Meng et al., Electrospun aligned nanofibrous composite of MWCNT/polyurethane to enhance vascular endothelium cells proliferation and function. J. Biomed. Mater. Res. A **95A**(1), 312–320 (2010)
68. Y. Wu et al., Interwoven aligned conductive nanofiber yarn/hydrogel composite scaffolds for engineered 3D cardiac anisotropy. ACS Nano **11**(6), 5646–5659 (2017)
69. J. Ren et al., Superaligned carbon nanotubes guide oriented cell growth and promote electrophysiological homogeneity for synthetic cardiac tissues. Adv. Mater. **29**(44) (2017). https://doi.org/10.1002/adma.201702713
70. S.R. Shin et al., Carbon-nanotube-embedded hydrogel sheets for engineering cardiac constructs and bioactuators. ACS Nano **7**(3), 2369–2380 (2013)
71. X. Li et al., A PNIPAAm-based thermosensitive hydrogel containing SWCNTs for stem cell transplantation in myocardial repair. Biomaterials **35**(22), 5679–5688 (2014)
72. J. Wang et al., Graphene sheet-induced global maturation of cardiomyocytes derived from human induced pluripotent stem cells. ACS Appl. Mater. Interfaces **9**(31), 25929–25940 (2017)
73. A.S.T. Smith et al., Micro- and nano-patterned conductive graphene–PEG hybrid scaffolds for cardiac tissue engineering. Chem. Commun. **53**(53), 7412–7415 (2017)
74. A.J. Ryan et al., Electroconductive biohybrid collagen/pristine graphene composite biomaterials with enhanced biological activity. Adv. Mater. **30**(15), e1706442 (2018)
75. M.H. Norahan et al., Electroactive graphene oxide-incorporated collagen assisting vascularization for cardiac tissue engineering. J. Biomed. Mater. Res. A **107**(1), 204–219 (2019)
76. G. Zhao et al., Reduced graphene oxide functionalized nanofibrous silk fibroin matrices for engineering excitable tissues. NPG Asia Mater. **10**(10), 982–994 (2018)
77. N. Annabi et al., Highly elastic and conductive human-based protein hybrid hydrogels. Adv. Mater. **28**, 40–49 (2016)
78. P. Hitscherich et al., Electroactive graphene composite scaffolds for cardiac tissue engineering. J. Biomed. Mater. Res. A **106**(11), 2923–2933 (2018)
79. S.R. Shin et al., Reduced graphene oxide-GelMA hybrid hydrogels as scaffolds for cardiac tissue engineering. Small **12**(27), 3677–3689 (2016)

80. J. Zhou et al., Injectable OPF/graphene oxide hydrogels provide mechanical support and enhance cell electrical signaling after implantation into myocardial infarct. Theranostics **8**(12), 3317–3330 (2018)
81. R. Bao et al., A π-π conjugation-containing soft and conductive injectable polymer hydrogel highly efficiently rebuilds cardiac function after myocardial infarction. Biomaterials **122**, 63–71 (2017)
82. S.R. Shin et al., Layer-by-layer assembly of 3D tissue constructs with functionalized graphene. Adv. Funct. Mater. **24**(39), 6136–6144 (2014)
83. S. Ahadian et al., Graphene induces spontaneous cardiac differentiation in embryoid bodies. Nanoscale **8**(13), 7075–7084 (2016)
84. J. Park et al., Graphene oxide flakes as a cellular adhesive: prevention of reactive oxygen species mediated death of implanted cells for cardiac repair. ACS Nano **9**(5), 4987–4999 (2015)
85. J.-O. You et al., Nanoengineering the heart: conductive scaffolds enhance Connexin 43 expression. Nano Lett. **11**(9), 3643–3648 (2011)
86. P. Baei et al., Electrically conductive gold nanoparticle-chitosan thermosensitive hydrogels for cardiac tissue engineering. Mater. Sci. Eng. C **63**, 131–141 (2016)
87. Y. Li et al., AuNP-collagen matrix with localized stiffness for cardiac-tissue engineering: enhancing the assembly of intercalated discs by beta1-integrin-mediated signaling. Adv. Mater. **28**(46), 10230–10235 (2016)
88. B. Peña et al., Gold nanoparticle-functionalized reverse thermal gel for tissue engineering applications. ACS Appl. Mater. Interfaces **11**(20), 18671–18680 (2019)
89. A. Navaei et al., Gold nanorod-incorporated gelatin-based conductive hydrogels for engineering cardiac tissue constructs. Acta Biomater. **41**, 133–146 (2016)
90. K. Zhu et al., Gold nanocomposite bioink for printing 3D cardiac constructs. Adv. Funct. Mater. **27**(12) (2017). pii: 1605352
91. S. Fleischer et al., Coiled fiber scaffolds embedded with gold nanoparticles improve the performance of engineered cardiac tissues. Nanoscale **6**(16), 9410–9414 (2014)
92. M. Shevach et al., Gold nanoparticle-decellularized matrix hybrids for cardiac tissue engineering. Nano Lett. **14**(10), 5792–5796 (2014)
93. S. Saravanan et al., Graphene oxide-gold nanosheets containing chitosan scaffold improves ventricular contractility and function after implantation into infarcted heart. Sci. Rep. **8**(1), 15069 (2018)
94. Y. Tan et al., Silicon nanowire-induced maturation of cardiomyocytes derived from human induced pluripotent stem cells. Nano Lett. **15**(5), 2765–2772 (2015)
95. Y. Tan et al., Cell number per spheroid and electrical conductivity of nanowires influence the function of silicon nanowired human cardiac spheroids. Acta Biomater. **51**, 495–504 (2017)
96. H. Sun et al., Carbon nanotubes enhance intercalated disc assembly in cardiac myocytes via the β1-integrin-mediated signaling pathway. Biomaterials **55**, 84–95 (2015)
97. H. Sun et al., Carbon nanotube-composite hydrogels promote intercalated disc assembly in engineered cardiac tissues through β1-integrin mediated FAK and RhoA pathway. Acta Biomater. **48**, 88–99 (2017)
98. A. Navaei et al., The influence of electrically conductive and non-conductive nanocomposite scaffolds on the maturation and excitability of engineered cardiac tissues. Biomater. Sci. **7**(2), 585–595 (2019)
99. F. Wu et al., High modulus conductive hydrogels enhance in vitro maturation and contractile function of primary cardiomyocytes for uses in drug screening. Adv. Healthc. Mater. **7**(24), e1800990 (2018)
100. C.A. Dunn, P.D. Lampe, Injury-triggered Akt phosphorylation of Cx43: a ZO-1-driven molecular switch that regulates gap junction size. J. Cell Sci. **127**(2), 455–464 (2014)
101. G. Bendig et al., Integrin-linked kinase, a novel component of the cardiac mechanical stretch sensor, controls contractility in the zebrafish heart. Genes Dev. **20**(17), 2361–2372 (2006)
102. C.H. Tang et al., Ultrasound induces hypoxia-inducible factor-1 activation and inducible nitric-oxide synthase expression through the integrin/integrin-linked kinase/Akt/mammalian target of rapamycin pathway in osteoblasts. J. Biol. Chem. **282**(35), 25406–25415 (2007)

103. S.J. Zhang, G.A. Truskey, W.E. Kraus, Effect of cyclic stretch on β1D-integrin expression and activation of FAK and RhoA. Am. J. Physiol. Cell Physiol. **292**(6), C2057–C2069 (2007)
104. C. Zhao et al., Spontaneous and specific myogenic differentiation of human mesenchymal stem cells on polyethylene glycol-linked multi-walled carbon nanotube films for skeletal muscle engineering. Nanoscale **7**(43), 18239–18249 (2015)
105. D. Mata et al., Diels–Alder functionalized carbon nanotubes for bone tissue engineering: in vitro/in vivo biocompatibility and biodegradability. Nanoscale **7**(20), 9238–9251 (2015)
106. S. Ostrovidov et al., Myotube formation on gelatin nanofibers – multi-walled carbon nanotubes hybrid scaffolds. Biomaterials **35**(24), 6268–6277 (2014)
107. S. Shao et al., Osteoblast function on electrically conductive electrospun PLA/MWCNTs nanofibers. Biomaterials **32**(11), 2821–2833 (2011)
108. B. Chaudhuri et al., Myoblast differentiation of human mesenchymal stem cells on graphene oxide and electrospun graphene oxide-polymer composite fibrous meshes: importance of graphene oxide conductivity and dielectric constant on their biocompatibility. Biofabrication **7**(1), 015009 (2015)
109. J.S. Medeiros et al., Nanohydroxyapatite/graphene nanoribbons nanocomposites induce in vitro osteogenesis and promote in vivo bone neoformation. ACS Biomater Sci. Eng. **4**, 1580–1590 (2018)
110. X. Xie et al., Graphene and hydroxyapatite self-assemble into homogeneous, free standing nanocomposite hydrogels for bone tissue engineering. Nanoscale **7**(17), 7992–8002 (2015)
111. E. Kolanthai et al., Graphene oxide—a tool for the preparation of chemically crosslinking free alginate–chitosan–collagen scaffolds for bone tissue engineering. ACS Appl. Mater. Interfaces **10**(15), 12441–12452 (2018)
112. W. Su et al., Promoting tendon to bone integration using graphene oxide-doped electrospun poly(lactic-co-glycolic acid) nanofibrous membrane. Int. J. Nanomedicine **14**, 1835–1847 (2019)
113. H. Jo et al., Electrically conductive graphene/polyacrylamide hydrogels produced by mild chemical reduction for enhanced myoblast growth and differentiation. Acta Biomater. **48**, 100–109 (2017)
114. T.H. Qazi et al., Development and characterization of novel electrically conductive PANI–PGS composites for cardiac tissue engineering applications. Acta Biomater. **10**(6), 2434–2445 (2014)
115. R. Dong et al., Biocompatible elastic conductive films significantly enhanced myogenic differentiation of myoblast for skeletal muscle regeneration. Biomacromolecules **18**(9), 2808–2819 (2017)
116. B. Guo et al., Degradable conductive self-healing hydrogels based on dextran-graft-tetraaniline and N-carboxyethyl chitosan as injectable carriers for myoblast cell therapy and muscle regeneration. Acta Biomater. **84**, 180–193 (2019)
117. M.-C. Chen, Y.-C. Sun, Y.-H. Chen, Electrically conductive nanofibers with highly oriented structures and their potential application in skeletal muscle tissue engineering. Acta Biomater. **9**(3), 5562–5572 (2013)
118. T. Zhou et al., A mussel-inspired persistent ROS-scavenging, electroactive, and osteoinductive scaffold based on electrochemical-driven in situ nanoassembly. Small **15**(25), e1805440 (2019)
119. S. Ribeiro et al., Electroactive biomaterial surface engineering effects on muscle cells differentiation. Korean J. Couns. Psychother. **92**, 868–874 (2018)
120. A. Shahini et al., 3D conductive nanocomposite scaffold for bone tissue engineering. Int. J. Nanomedicine **9**, 167–181 (2014)
121. J.D. Bronzino, *Biomedical engineering Handbook* (CRC Press, Boca Raton, 2000)
122. L. Ghasemi-Mobarakeh et al., Electrical stimulation of nerve cells using conductive nanofibrous scaffolds for nerve tissue engineering. Tissue Eng. Part A **15**(11), 3605–3619 (2009)
123. V. Guarino et al., Conductive PANi/PEGDA macroporous hydrogels for nerve regeneration. Adv. Healthc. Mater. **2**(1), 218–227 (2013)

124. H. Xu et al., Conductive PPY/PDLLA conduit for peripheral nerve regeneration. Biomaterials **35**(1), 225–235 (2014)
125. L. Jin et al., A novel fluffy conductive polypyrrole nano-layer coated PLLA fibrous scaffold for nerve tissue engineering. J. Biomed. Nanotechnol. **8**(5), 779–785 (2012)
126. L. Zhou et al., Soft conducting polymer hydrogels cross-linked and doped by tannic acid for spinal cord injury repair. ACS Nano **12**(11), 10957–10967 (2018)
127. Y. Wu et al., Electroactive biodegradable polyurethane significantly enhanced Schwann cells myelin gene expression and neurotrophin secretion for peripheral nerve tissue engineering. Biomaterials **87**, 18–31 (2016)
128. R. Guo et al., Accelerating bioelectric functional development of neural stem cells by graphene coupling: Implications for neural interfacing with conductive materials. Biomaterials **106**, 193–204 (2016)
129. W. Guo et al., Construction of a 3D rGO-collagen hybrid scaffold for enhancement of the neural differentiation of mesenchymal stem cells. Nanoscale **8**(4), 1897–1904 (2016)
130. Y. Qian et al., An integrated multi-layer 3D-fabrication of PDA/RGD coated graphene loaded PCL nanoscaffold for peripheral nerve restoration. Nat. Commun. **9**(1), 323 (2018)
131. Q. Zheng et al., Biodegradable triboelectric nanogenerator as a life-time designed implantable power source. Sci. Adv. **2**(3), e1501478 (2016)
132. W. Guo et al., Self-powered electrical stimulation for enhancing neural differentiation of mesenchymal stem cells on graphene-poly(3,4-ethylenedioxythiophene) hybrid microfibers. ACS Nano **10**(5), 5086–5095 (2016)
133. D.Y. Lewitus et al., Biohybrid carbon nanotube/agarose fibers for neural tissue engineering. Adv. Funct. Mater. **21**(14), 2624–2632 (2011)
134. J. Wang et al., The cellular response of nerve cells on poly-l-lysine coated PLGA-MWCNTs aligned nanofibers under electrical stimulation. Korean J. Couns. Psychother. **91**, 715–726 (2018)
135. N. Singh et al., Chitin and carbon nanotube composites as biocompatible scaffolds for neuron growth. Nanoscale **8**(15), 8288–8299 (2016)
136. J. Shin et al., Three-dimensional electroconductive hyaluronic acid hydrogels incorporated with carbon nanotubes and polypyrrole by catechol-mediated dispersion enhance neurogenesis of human neural stem cells. Biomacromolecules **18**(10), 3060–3072 (2017)
137. W. Liedtke et al., Highly conductive carbon nanotube matrix accelerates developmental chloride extrusion in central nervous system neurons by increased expression of chloride transporter KCC2. Small **9**(7), 1066–1075 (2013)
138. X. Zhao et al., Antibacterial anti-oxidant electroactive injectable hydrogel as self-healing wound dressing with hemostasis and adhesiveness for cutaneous wound healing. Biomaterials **122**, 34–47 (2017)
139. J. Qu et al., Degradable conductive injectable hydrogels as novel antibacterial, anti-oxidant wound dressings for wound healing. Chem. Eng. J. **362**, 548–560 (2019)
140. L. Feng, J.D. Andrade, Protein adsorption on low temperature isotropic carbon: V. How is it related to its blood compatibility? J. Biomater. Sci. Polym. Ed. **7**(5), 439–452 (1995)
141. J. Meng et al., Effects of single-walled carbon nanotubes on the functions of plasma proteins and potentials in vascular prostheses. Nanomedicine **1**(2), 136–142 (2005)
142. J. Meng et al., Preparation and biocompatibility evaluation of polyurethane filled with multiwalled carbon nanotubes. J. Nanosci. Nanotechnol. **13**(2), 1467–1471 (2013)
143. J. Meng et al., Improving the blood compatibility of polyurethane using carbon nanotubes as fillers and its implications to cardiovascular surgery. J. Biomed. Mater. Res. A **74**(2), 208–214 (2005)
144. J. Meng et al., Enhancement of nanofibrous scaffold of multiwalled carbon nanotubes/polyurethane composite to the fibroblasts growth and biosynthesis. J. Biomed. Mater. Res. A **88**(1), 105–116 (2009)
145. J. Meng et al., Using single-walled carbon nanotubes nonwoven films as scaffolds to enhance long-term cell proliferation in vitro. J. Biomed. Mater. Res. A **79**(2), 298–306 (2006)

146. P. Tang et al., Mussel-inspired electroactive and antioxidative scaffolds with incorporation of polydopamine-reduced graphene oxide for enhancing skin wound healing. ACS Appl. Mater. Interfaces **11**(8), 7703–7714 (2019)
147. Y. Liang et al., Adhesive hemostatic conducting injectable composite hydrogels with sustained drug release and photothermal antibacterial activity to promote full-thickness skin regeneration during wound healing. Small **15**(12), 1900046 (2019)
148. X. Zhao et al., Injectable antibacterial conductive nanocomposite cryogels with rapid shape recovery for noncompressible hemorrhage and wound healing. Nat. Commun. **9**(1), 2784 (2018)
149. J. Meng et al., Effects of long and short carboxylated or aminated multiwalled carbon nanotubes on blood coagulation. PLoS One **7**(7), e38995 (2012)

Chapter 3
Nanotechnology in Dental Therapy and Oral Tissue Regeneration

Zukun Yang, Liping Han, Yu Guo, Lu Jia, Cheng Yin, and Yang Xia

Abstract The emergence of nanotechnology within dental fields has sparked great interest in their potential applications. This chapter focuses on the application of nanotechnology in dental therapy and oral tissue regeneration, especially in dental materials. Nowadays, various nano-additives have been introduced into many commercially available products, making it overwhelmingly difficult for both dentists and patients to properly choose from. Actually, the choice of nanomaterials is dependent on the clinical scenario and the tooth to be restored, paying close attention to esthetic demand, loading, and the presence of any risk factors. In this chapter, we will introduce "Nanotechnology in tooth defect therapy," "Nanotechnology in oral tissue regeneration," and "Nanotechnology in antibacterial for oral disease and therapy." Future direction is to develop more efficient and cost-effective nanobiosensing materials to treat dental diseases intelligently. For example, the materials have the potential to deliver drugs to disrupt biofilm formation in order to reduce the incidence of caries and periodontal disease and also can be used for tooth defect filling. Ultimately, it may be possible to achieve the pinnacle goal, tooth regeneration. Therefore, this chapter will help the readers gain a general grasp about the current application of nanotechnology in dental fields, relative benefits and limitations, and future trends.

Keywords Tooth defect · Oral tissue regeneration · Antibacterial

Z. Yang · L. Han · Y. Guo · L. Jia · C. Yin · Y. Xia (✉)
Jiangsu Key Laboratory of Oral Diseases, Nanjing Medical University, Nanjing, Jiangsu, China
e-mail: xiayang@njmu.edu.cn

H. Xu, N. Gu (eds.), *Nanotechnology in Regenerative Medicine and Drug Delivery Therapy*, https://doi.org/10.1007/978-981-15-5386-8_3

3.1 Nanotechnology in Tooth Defect Therapy

3.1.1 Nano Tooth Filling Materials

Tooth defect is one of the main oral health problems. Its definition is that a part of a tooth is lost due to caries, trauma, or dysplasia, which will cause damage to the shape and structure of the tooth, leading to the loss of function. The most common cause of the disease is dental decay. Each year, about 200 million tooth defects are restored in the USA, costing a lot of money.

There are, of course, many details and variations that are specific to one problem. For a small defect, it is commonly restored by direct filling to restore the damaged tooth immediately. And for a large one, it is more suitable to employ prosthetic treatment like inlay and crown. This chapter mainly focuses on the materials that can be used for direct tooth filling.

With the development of science and technology, a variety of materials have been applied to restore the tooth defects, such as composite resins, glass ionomer cements, and silver amalgam. The ideal tooth filling materials should (1) be strong enough to bear the bite force, (2) have poor conductivity so as to not transmit temperature and current, (3) be operated easily, and (4) have color that closely resembles that of teeth. Despite better understanding of the materials and chemistry, and improvements in physical properties, no material has been found to be ideal for tooth filling so far [1].

For example, the silver amalgam, which is the traditional filling material, has better durability and longevity, lower incidence of cuspidian fracture occurrence and recurrence of caries compared with composite resins [2]. Hence, dental restorations have employed silver amalgam for more than a century. However, the toxicity of mercury within amalgam has posed a crucial drawback [3]. Another major concern is that the metal hue of amalgam is not suitable for esthetic tooth restoration. Due to the advances in tooth-colored restorations and adhesive technology, the use of amalgam has been increasingly replaced by alternative materials.

Currently, dental composite resins are the most commonly used material for tooth filling. Dental composite resins have been used to restore teeth since their first introduction about 50 years ago [4]. Compared with dental amalgams, they are safer and more esthetic. But the wear resistance of the composite resins is poorer than the silver amalgam. And it is easier to get food lodged between teeth due to the matrix bands. Based on the report in 2005, the composite resins were used in more than 95% of all anterior tooth direct restorations and about 50% of all posterior tooth direct restoration [4]. They are mainly composed of three chemically different components: the organic matrix (usually a resin or synthetic monomer), the inorganic matrix (fillers), and a coupling agent (usually silane) for bonding the filler onto the organic matrix. Composite resin can be classified either according to their composition or the filler particle size. A widely accepted classification based on filler particle size proposed by Lutz F et al. is: macro-filler composites (0.1–100 μm), micro-filler composites (0.04–0.1 μm), and hybrid composites (fillers of different

sizes) [5]. Later, nano-filler (1–100 nm) is developed and categorized as nano-modified composite resin. This new type of resin has the properties which the traditional one does not have, which will be discussed later.

Glass ionomer cements, which were introduced by Wilson and Kent in the 1970s as a dental filling material, are also commonly used in dentistry [6]. The milestone timeline in the development of glass ionomers cement in dentistry is described in Fig. 3.1. Currently, there is no universally accepted cement that fulfills all requirements. However, there are a variety of cements whose properties and manipulation lead them to be an appropriate choice for a specific application. Generally, glass ionomers require the mixing of the acidic powder and the basic liquid form, utilizing the principle of acid–base reactions. The powder form consists mainly of fluoroaluminosilicate (FAS) glass particles and ions such as calcium, lanthanum, and strontium, while the liquid form is a viscous fluid which consists of a copolymer of maleic acid or itaconic acid and acrylic acid. The reaction takes place after mixing these two forms, with the initial setting taking place within 3–4 min. Because of its remarkable qualities such as strong chemical bonding to tooth structures, good compatibility, and fluoride release, glass ionomers have become increasingly widespread in usage. However, the inferior mechanical properties of glass ionomers have limited their application. For traditional glass ionomers, the most intractable problem is the lack of strength and toughness. Because of its excellent performance, resins were added to the matrix to improve the clinical performance of glass ionomer cements. However, this did not significantly overcome the drawbacks. After immersing in water for 12 months, compared with traditional glass ionomers, the strength, toughness, and microhardness of the resin-modified glass ionomers were

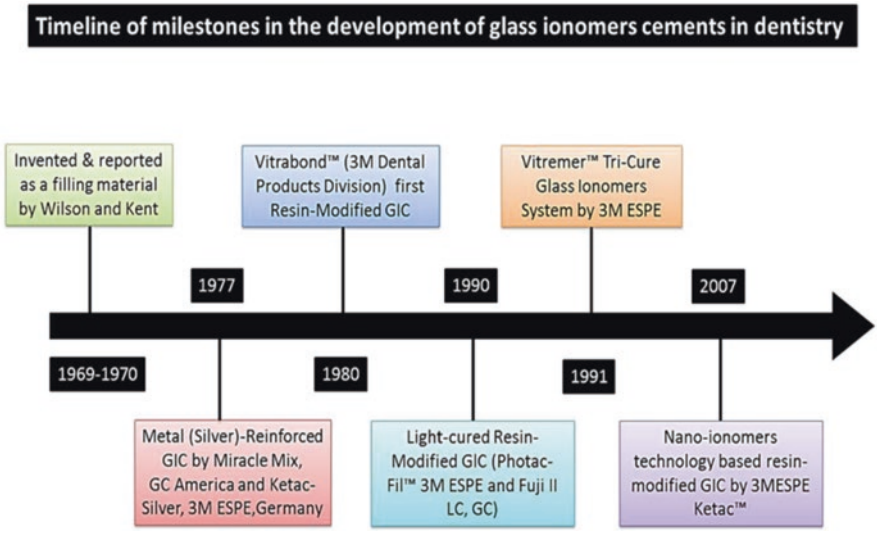

Fig. 3.1 Timeline of milestone in the development of glass ionomer cements and nano-ionomers for dental restorations [7]

not improved with the addition of resins. Alternatively, there have been extensive efforts to improve the glass ionomer cement by fluoride (F)-releasing properties. It is expected that the F ions can enrich tooth structure, promote remineralization, and inhibit demineralization. Glass ionomers, resin-modified glass ionomers, compomers, and composites have received much attention due to their release of F ions that can be incorporated into tooth mineral, resulting in fluoroapatite or F-enriched hydroxyapatite, both having reduced solubility. Moreover, nano-modified glass ionomers are developed to improve its mechanical properties.

The composite materials are promising in esthetic restoration. However, these materials are very technique sensitive, and the mechanical properties are not as good as amalgams [8]. A favorable method to increase the properties and performance of the final restorative material is by increasing the percentage and reducing the size of the filler in the matrix. By adding fillers, the mechanical properties of composites are enhanced, polymerization shrinkage is reduced, thermal expansion coefficient of the composite is modified to match that of the tooth, handling is improved, and radio-opacity as well as translucency and wear resistance are endowed in the composites [9].

Most of the current conventional composites typically range between 0.04 and 0.7 μm in filler particle size. Terry DA found that the size of these particles hinders the interaction with the nanoscale (1–10 nm) structural components of enamel and dentine, such as the enamel rods, dentinal tubules, HA crystals, and collagen fibers [10]. This results in a compromise between the restorative material and the surrounding tissue. After the introduction of nano-fillers (particle size 1–100 nm), the possibility of creating more ideal advanced composites became a reality. Ideal composite materials should have two important properties: strength and esthetics. Both the properties depend upon the size of the filler particle. The small particle size can decrease curing shrinkage, offer more uniform particle distribution, allow a higher filler load, reduce viscosity, offer better handling properties, and endow stronger mechanical properties [10].

New materials introduced in recent years, especially nano-fillers, demonstrate noteworthy advances in composites [11]. Bowen et al. generated the resins using silane couplers and bisphenol A-glycidyl dimethacrylate (bis-GMA). Circa the same era, words such as nano were conceived by the noble laureate Sir Feynman R in 1959 [12]. This breakthrough was a key milestone for the advancement of dental composites. Henceforth, composite fillings have been added as a valuable treatment in the restorative armamentarium. Rapid advances have occurred in the past decade in dental restorative materials, including the resin-based composites. Likewise, the discovery of nano-filler particles arose from the introduction of nanotechnology. Research has continuously strived to improve the physical properties of materials as well as tackle obstacles such as wear resistance, polymerization shrinkage, micro hardness, and patient dissatisfaction due to poor esthetic appearance [8, 9].

Titanium dioxide nanoparticles (TiO_2 NPs) has many excellent properties to be an inorganic filler: it is chemically stable and nontoxic and evinces a highly efficient photocatalytic effect. Furthermore, research on TiO_2 NPs as a filler in epoxy found that the addition overcomes the shortcomings of traditional toughers, such as

rubber beads and glass, by improving the strength, stiffness, and toughness of the epoxy without undermining its thermo-mechanical properties. Moreover, they are granular and can easily agglomerate, which makes it useful for practical applications. However, homogenous dispersion in organic solvent remains a challenging obstacle. To overcome this, suitable modification to the surface is needed. Coating inorganic fillers in resin-based composites with organosilane strengthens their bond to the resin matrix and prolongs the operational life of the composite. Additionally, the substance advantageously promotes the dispersal of silanated filler particles within the matrix. So, TiO_2 NPs were coated with an organosilane (namely allyltriethoxysilane, hereafter ATES) and blended into dental resin-based composites. The result showed that surface modification by the organosilane ATES improved the dispersion and linkage of TiO_2 NPs within a resin matrix, and thus improved the microhardness and flexural strength of dental composite resins [13].

In another study, the mechanical behavior of the TiO_2 nanoparticle-reinforced resin-based dental composites was predicted by using a nanoscale representative volume element (RVE): these results were then compared against those obtained the non-interaction approximation (NIA). The results illustrated that the nanoparticle-reinforced composites have a mechanical advantage over those reinforced with glass fibers. Further assessment was conducted to analyze the effects of nanoparticle aspect ratio, volume fraction, and stiffness under the criteria of yield strength of the composite and effective Young's modulus. And the result showed a mechanical advantage of nanocomposites over microcomposites. Compared with glass fiber, the reinforce effect of the nanoparticle with 3% volume fraction contains the same stiffness as at only half the volume fraction. Additionally, an approximately linear increase in effective Young's modulus and yield strength of the composite was found at volume fractions from 1% to 5%, considering perfect nanoparticle dispersion. These results provide better understanding of the mechanical behavior of nanoparticle-based resin-based dental composites and can provide insight into further optimization of the composition of dental composites [14].

Nanocomposite resins have excellent properties. However, what is the best concentration of the NPs? Can adding more nanoparticles achieve better performance? According to many in vitro studies, nano-filled materials have greater wear resistance than micro-filled materials. When 40 nm filler particles were added to a composite with 3 μm particles, wear resistance was improved until a concentration of 15% vol [15]. But determining the most appropriate concentration still needs further scientific investigation. Three experimental nanocomposites were formulated with different weight percent filler loads (25, 50, and 65%) by Lawson NC [16]. The elastic modulus, flexural strength, and hardness of the composites and the unfilled resin were measured. Notably, the wear resistance exhibited by the composites decreased as the filler content was increased beyond 25%. Comparatively, flexural strength and hardness and modulus increased with increasing filler content up to 50%. Scanning electron microscope (SEM) inspection of the worn specimens revealed that while the resin and 25% filled materials cracked and failed because of fatigue, the 50 and 65% filled materials expressed microcutting and failed as a result of abrasive wear. So, concentrations between 25 and 50% may be the best choice.

Thus, it seems that there does appear to be an optimal maximum of the percentage of nano-filler in the nanocomposite, beyond which the mechanical properties do not improve further, or even deteriorate [17]. Similar result was obtained in another study. Nanocomposite dental resins comprised mainly of polyhedral oligomeric silsesquioxane nanocomposite matrix with 0, 0.5, 1, 1.5 and 2 wt% nano SiO_2 as filler were created by light curing. Characterization of these resins were performed by compressive, three-point flexure, nanoscratch, and nanoidentation tests as well as SEM analysis and optical microscopy in order to study how different SiO_2 contents affect the resin. It was found that nano SiO_2 effectively enhanced the mechanical properties of the composite resins at low content (below 1.5 wt% SiO_2 addition). But with the increase of the nano SiO_2 content (above 2.0 wt% SiO_2 addition), the mechanical properties decreased [17]. The reason may lie in that increasing filler load beyond a high concentration led to the agglomeration of filler particles which acted as crack-initiating flaws [18].

In order to improve the properties and overcome these shortcomings of the glass ionomer cement, active research is in progress, such as in the addition of cellulose fibers, hydroxyapatite, fluoroapatite, and nanotechnologies. The application of nanotechnology is the focus here.

Novel CaF_2 NPs (56 nm) were synthesized via spray-drying and incorporated into resin. F release increased with increasing the nano-CaF_2 content and decreasing pH. Nearly threefold flexural strength was found as compared to that of resin-modified glass and also exceeded that of composite resin while exhibiting little F release. To summarize, the modified CaF_2 NPs exhibited high F release at low filler levels, making space in the resin for the reinforcement glass [19]. This relatively high F release arising from the nanocomposite was presumably due to the small size and consequently the high surface area of the NPs. Ball milling or grinding can reduce the size of these traditional particles; however, it is difficult to achieve a median particle size of 1 μm or smaller. The CaF_2 in Xu's study had a surface area of 35.5 m^2/g [20]. While Anusavice KJ's study used a traditional commercial CaF_2 powder which had a surface area of 1.9 m^2/g [21]. This is likely attributed to the high and sustained release of F ions from the nanocomposite.

Another exciting development is the Equia system, a new nano filling material. This material uses liquid dispersed inorganic silica nano-fillers (40 nm in size) to reinforce the produced polymer matrix. Shrinking the initial setting time and improving the wear resistance is accomplished by adding 15 wt% silica nano-fillers. Since these materials can better resist against dissolution, wear, and disintegration, the maintenance of a polished surface was prolonged. The translucency, optical properties, and esthetic appearance of nano glass ionomers compared with conventional ones are also improved remarkably, being claimed as good as that of natural teeth [22]. Friedl K et al. presented a retrospective study on new glass ionomer cements to evaluate their performance. They found that 151 restorations were placed in permanent molars (n = 94) and premolars (n = 57) in 43 patients. Restorations were evaluated at 4.5× magnification using modified USPHS criteria. They concluded that Equia system is good for posterior filling materials [23].

The effects of additives such as nanoscale hydroxyapatite (HA) and fluoroapatite (FA) on the properties of glass ionomers is a hot topic [24]. HA crystals are a key contributor to the chemical structure of natural enamel and dentin and are recognized for their biocompatibility. Resin-modified glass ionomers have an 8–12 MPa bond strength to tooth structures [25]. Increases in bond strength occurred after adding micro-HA (5–10 μm) and improved even further if nano-HA (100–150 nm) was added. This suggests that tooth structures with higher surface area for bonding, as with the case of nano-HA, might result in improved bond strength. Additionally, high surface area of nano-HA also improves the surface finish, while the solubility of the material helps to fill the demineralized micropores in the tooth structure. A similar research was conducted by adding ethanol-based sol-gel prepared nano-HA and nano-FA to Fuji II glass ionomers [26]. Improved mechanical properties were exhibited by these modified nano-filled glass ionomers, such as compressive strength, diametral tensile strength and biaxial flexural strength. It is a remarkable fact that different mixing methods make different results. A new nanocomposite, glass ionomer cement (GIC)-nanoSiO_2-HA-ZrO_2 was fabricated by adding zirconia to increase the hardness. Synthesis of this nanocomposite was performed using two methods, one pot and spatulation method. Within the study limitations, the one pot method produced better GIC-nanoSiO_2-HA-ZrO_2 composite [27]. The probable cause is one pot method was able to produce less agglomerated and more uniform dispersion of nanozirconia. This type of dispersion from nanozirconia improves the strength mechanism of the resulting composite. If the nanopowder is highly agglomerated, the matrix of GIC may be altered, resulting in the decreases in hardness. In comparison, less agglomerated nanopowder promotes uniform distribution of nanopowder and may strengthen the matrix by filling up the empty gap within the GIC, which results in the improvement of the GIC strength.

Modification of the existing glass ionomers using nanomaterials is an active area of current research, with many having lofty expectations. Consequentially, there is an expectation that new nano-modified GIC and the properties of existing glass ionomers will be improved significantly [28].

Recent years have produced remarkable researches on nanomaterials, which has propelled it from theoretical foundation to clinical practice. A variety of nano-products for dental applications have emerged due to all the active researches. Here is the list of available materials: Ketac™ (3M ESPE, St. Paul, MN, USA), Ketac N100; Filtek Supreme XT (3M ESPE), Nano-ionomers (3M ESPE), Nano-primer, Fuji IX GP (GC, Leuven, Belgium), Premise™ (Kerr/Sybron, Orange, CA, USA), and Ceram X™ (DENTSPLY International, Milford, CT, USA). For example, Premise is a universal nano-filled restorative composite that contains 20 nm filler. The main nano-filler very likely is silica. But this is trade secret, so we are not clear. They are all available globally. They are easy to use and are alternatives to expensive compomers and composites and in many cases amalgam. And they cure extremely hard and are very wear resistant. They have strong wear resistance, high compressive strength, and more excellent mechanical properties compared with traditional materials. Though of course, this adds a premium to the price.

True glass ionomers, such as Fuji IX GP, bonds chemically to tooth structures, has similar values for coefficient of thermal expansion as compared to tooth, and releases substantial levels of rechargeable fluoride. It is provided either in hand-mix powder-liquid form or premeasured capsules. It is the ideal product for pediatric and geriatric restorations, non-stress area final restorations, intermediate restorations (IRM), core material, and either long-term or temporary restoration.

Although there have been many types of nano products, the new nano products are pursuing better performance, more proper appearance, and lower prices.

Nano-fillers have revolutionized the field of dentistry over the past 30 years. Despite these developmental advances, some problems still limit the use of composites in dental restoration. Most improvements are focused on the reduction of polymerization shrinkage, as well as the improvement of wear resistance, mechanical properties, biocompatibility, and processing properties.

For those with hypersensitive teeth, a new nanotechnology treatment proposed by researchers in Taiwan might one day bring pain relief. Researchers have found that dentinal tubules are increased (35.6% as compared to 9.3%) and the diameter widened (0.83 μm as compared to 0.43 μm) in sensitive teeth as compared to those in non-sensitive dentine. The Chinese researchers have demonstrated that gold NPs can be used to block these tubules: viewed as the world's smallest gold fillings. One such method to close sub-micron-sized dentinal tubules was explored by Dr. Chris Wang and his team, involving the sintering the highly concentrated gold NPs which were brushed into the exposed openings of dentinal tubules. The photofusion of these gold NPs was induced by laser irradiation via photothermal conversion. Clinically, modification of the material and improvement of the techniques to achieve a better fill in-depth may be required, especially considering the normal wear rate of dentine and the filling material [29]. It may be a good decision to develop a nano gold-modified resin to solve this issue.

Although spherical nano-fillers are popular, partly because they distribute stress more uniformly across the bulk volume of the composite resin and inhibit crack formation, tube-like fillers such as carbon nanotubes (CNT) have also been tried. For example, Zhang F et al. used single-walled carbon nanotubules (SWCNTs) to fabricate a composite [30], resulting in a nanocomposite with enhanced mechanical performance. While SWCNTs are noted to have superior strength, they also have the advantage of being accepted at higher filler concentrations by resin systems owing to their unique dimensional distribution (aspect ratio > 1000). Therefore, resins accommodating CNTs should be investigated further. However, there is a problem in the application of CNTs in dentistry. In contrast with the natural color of teeth, the resin specimen prepared through the method previously described is characterized as gray black, therefore rendering it incompatible for direct oral use. Applying other inorganic additives, for example, chromorphic xerogel pigment particles or sol gel-based opalescent fillers would help in fulfilling the esthetic requirements. However, further research on this subject is still required.

3.1.2 Nano-Modified Adhesive Material

The basics of the adhesive are discussed in this section. One of the most revolutionary developments among recent advances in dentistry has been the utilization of adhesive dentistry toward treatment. As compared to traditional mechanical factors for retention, "adhesive dentistry" depends only on techniques and procedures for "adherence" to tooth structures. Such examples include the placement of composite resin restoration, resin-bonded bridgework, and porcelain and composite veneers.

The success of adhesive dental techniques hinges on the establishment of an "adhesion" or "bond" between the underlying tooth and restorative materials. A comparison between traditional and adhesive techniques can be examined through the filling of composite resin in a cavity after the removal of caries. "Traditional" restorative materials, like amalgam, require the dentist to remove substantial healthy tooth to create undercuts for maintaining mechanical retention. In contrast, "adhesive" restoration renders this unnecessary as mechanical undercuts are not necessary for retention. Since the removal of healthy tooth substance is reduced, the tooth can be maintained for a longer period [31].

Adhesives play an important role in tooth defect, dentition defect, and orthodontics. These can all be divided into two categories according to which parts of the teeth the adhesive sticks to.

Therefore, it is essential to understand the outer parts of the teeth where the adhesive "sticks" to. The external surface of the tooth, enamel, is mainly inorganic. At the microscopic level, enamel is composed of millions of prisms that adhere to each other spreading from the dentin–enamel junction (DEJ) to the tooth's exterior (imagine millions of "Toblerone" bars spreading from the DEJ to the tooth's surface). By contrast, dentine has far more organic material, such as the protein collagen. The dentine is composed of millions of dentinal tubules which each contains odontoblast extensions (tissue cell extensions from the pulp) and tissue fluid. To better visualize dentine, one can picture a block of Swiss cheese. In the Swiss cheese, the "holes" resemble the dentinal tubules, while the material in between is the dentine.

Adhesive restorative materials as well as luting cements "adhere" to a tooth via two ways. They can be described as:

- Micromechanical retention, by which the prepared tooth surface is roughened and the restorative material meshes with the created pits and crevices via retentive tags.
- Chemical adhesion, by which the restorative material or luting cement chemically bonds with the tooth substance.

3.1.2.1 Enamel Bonding

During the advent of adhesive dentistry techniques, bonding to enamel (enamel bonding) achieved greater success than bonding to dentine (dentine bonding). Enamel bonding can be achieved by the following method:

1. First, etching the cut enamel surface by 37% phosphoric acid (applied as either a liquid or a gel) for 30–40 s. This serves to dissolve the underlying enamel prisms at different rates. Since some prisms dissolve quicker than others, a roughened surface is created, with deep pits denoting where the enamel has been dissolved. Afterward, the surface is washed to remove the phosphoric acid, and then dried. The above steps result in the enamel having a familiar frosted appearance.
2. Then, a primer is etched onto the enamel surface. This allows the bonding resin (applied subsequently) to more easily seep into the roughened enamel pits.
3. Finally, application of the bonding resin is placed on the enamel. Restoration of the cavity is performed using this dilute (or runny) state of the composite resin. Then resin seeps into the etched enamel surface and set when exposed to curing light (this is due to the linking of millions of tiny molecules, called monomers, into polymer chains when shone by the curing light). These chains then fabricate the millions of minute resin tags, which eventually fill the cavity at the micromechanical level.

3.1.2.2 Dentine Bonding

Dentine bonding was difficult to achieve during the early years of adhesive dentistry. More recently, denting bonding technology has been improved. The steps required for dentine bonding are similar to enamel bonding.

- As compared to enamel etching, the etching of cut dentine surface requires less time because it contains less inorganic material. Dentine etching mainly serves to remove debris from the entrances of the dentinal tubules.
- Afterward, a primer is applied, serving to increase the flow of the bonding resin as well as encouraging the proteins appearing in dentine to chemically link with the bonding resin.
- Finally, a bonding resin is applied, entering the dentinal tubules and forming resign tags (micromechanical retention). The resin is also believed to chemically link with the dentinal proteins (chemical linkage).

The component of new adhesives is different from the traditional ones. Twenty years ago, the etch, primer, and bonding agent all existed as three separate parts. Combined primer and bonding agents were produced later, which reduced the number of steps and time needed to place composite resin restorations. Further improvements in these areas have been seen in the last 15 years due to the introduction of combined etch, prime, and bonding systems (or self-etching systems) [31].

The chemical composition of adhesives aims to fulfill all above-mentioned processes. Although dental adhesives can be classified into either the etch and rinse (E&Rs) or the self-etch adhesives (SEAs) (Table 3.1) groups, the ingredients are similar and completely independent of the number of bottles required for the adhesive. Nevertheless, these different classes differ in their proportional composition. Typically, adhesives consist of acrylic resin monomers, organic solvents, initiators and inhibitors, and occasionally filler particles. Obviously, every component has its unique function. Knowledge of the chemical properties of these components are paramount for understanding or possibly predicting their behavior.

Nano-modified adhesive material. At the resin dentin interface, the adhesive layer has the lowest elastic modulus among the components of the bonded complex and was reported to be weaker than the resin-infiltrated demineralized dentin layer (hybrid layer). When the complex encountered stresses, the adhesive layer, the component with the lowest elastic modulus, would suffer the greatest stain among all the components. If these stresses are concentrated while the polymerizing composite resin is undergoing shrinkage or during occlusal overloading of this layer, defects, cracks, or even abrupt catastrophic failure of the resin dentin bond may occur dependent on the amount of stress [32]: consequent failure may occur either in this layer or its adjacent layers [33].

The mechanical strength and viscosity of the adhesive layer might be improved with the addition of fillers [34]. These filled adhesives were predicted to serve as an intervening shock-absorbing elastic layer between the two stiff components, the composite resin and dentin, and increase the bond strength. However, when the nanoscaled fillers were added into the dentin adhesives, too much nano-filler addition increased the viscosity, hindered the penetration of the resin monomers into the interfibrillar spaces within the collagen network, and caused internal voids within the adhesives. NPs which are of the similar size to those of the polymer chain have led to good interaction between the chain/polymer due to the increased surface to volume ratio of the fillers. Thus, the method that reduces the particle size down to the nanoscale level has been widely used. Reports have also found that flexural and

Table 3.1 Etch and rinse adhesives and self-etch adhesives

Group	Sub-step	Conditioner	Primer	Adhesive resins
Etch and rinse adhesives	Two-step	Acid	Solvent mono-methacrylates + dimethacrylates HEMA + initiator + inhibitor + filler	
	Three-step	Acid	Solvent mono-methacrylates + initiator + inhibitor	Dimethacrylates HEMA + initiator + inhibitor + filler
Group	**Sub-step**	**Self-etch adhesives**		**Adhesive resins**
Self-etch adhesives	One-step	Solvent Mono-methacrylates + dimethacrylates HEMA + initiator + inhibitor + filler		–
	Two-step	Solvent acidic mono-methacrylates initiator + inhibitor		Dimethacrylates HEMA + initiator + inhibitor + filler

tensile strength can be significantly increased by incorporating 1–10 wt% silica nano-fillers into adhesive resins [35].

Recently, evidence has revealed that adding hydroxyapatite nanorods at 0.2–0.5 wt% to an experimental adhesive significantly increases its flexural strength and diametral tensile strength. Lohbauer et al. found that increasing the concentration of zirconia nano-fillers in either the primer or the adhesive greatly increased the microtensile bond strength [36]. However, different studies yield diverging conclusions regarding nanoparticle incorporation into adhesive resins, and dentin bond strength increases. Some studies found that adding filler content up to 20 wt% significantly increases the bond strength, whereas exceeding 50% results in bond strength deterioration [37]. If hydroxyapatite was used as the nano-filler, significant increases in bond strength occurred at 0.2 wt% incorporation, but decreased to the starting level with further packing [38]. Abdelaziz EM found that these exact systems also decreased viscosity while improving the microtensile bond strength [39]. On the other hand, if when these adhesive systems used 1 wt% HA-modified adhesive, the results were completely reversed. This can be explained by silane coupling having a stronger chemical-grafting on the surface of fillers at lower fill concentration, which improved stability and dispersion, and hence improved flowability while reducing the viscosity of the dental adhesives. In contrast, the particles were in closer proximity with each other at higher filler concentration, which result in greater collision probability under shear and creates aggregates. So, the mechanical strength will be the greatest at proper nanoparticle concentration.

Success of restorations are highly dependent on a durable and strong adhesion to dental hard tissues. Other challenges to dental restoration such as chewing forces and biofilm acids interact with the oral environment and limit the longevity of the restoration. Currently, the weak link in restorations can be attributed to the resin-bonded tooth interface, while secondary caries at the margins are the main impediment to longevity of restorations.

Adhesives containing CaP [$Ca_3(PO_4)_2$] particles could remineralize the remnants of tooth lesions in the cavity as well as the acid-etched dentin. Thus, they are promising to improve the longevity of the restorations. Due to the release by the adhesive of Ca and P ions, which serve as seed crystals, mineralization can be facilitated in the hybrid layer (HL) as well as the tooth-restoration margins. Furthermore, other advantages include the likely protection of the exposed collagen within the bonded interface by the CaP adhesive, which improves bonding stability and durability and the protection of the weak link of tooth restoration. However, since Ca and P ion release is only short term, lasting only weeks to a few months and then diminishing, this poses a major flaw for Ca–P containing resin. A previous study confirmed this short ion release duration for CaP resins, showing an ion release of only 1–2 months. Therefore, it would be advantageous to develop a rechargeable CaP adhesive to constantly refill the Ca and P ions to provide long-term ion release for remineralization and the ultimate inhibition of caries. Thus, nano-CaP (NACP) (116 nm) is synthesized which is rechargeable to provide long-term Ca and P ions. Because NACP has smaller particle size, it can more easily flow with the bonding agent into the dentinal tubules to result in resin tags. This adhesive can also be considered “smart”

because they released Ca and P ions, which are beneficial to combat caries, at low cariogenic pH. Among all the bonding agents tested (the NACP content from 0% to 30%), adhesive with 30% NACP appeared to be the best, considering its highest dentin bond strength, Ca and P ion release, and recharge and re-release. NACP filler levels ≥40% were not used due to a decrease in dentin bond strength in preliminary study. After recharge, the resins had continuous release of ions for at least 2–3 weeks, before another recharge would be needed [40].

Moreover, incorporating high atomic number containing particles may induce radiopacity in adhesive systems, compared to the typical radiolucent property of the adhesive layer. Regrettably, these radiolucent radiographic images might misguide dentists as they may resemble those of defective restoration and secondary caries, as a consequence, resulting in possible clinical misdiagnosis or needless replacement of restorations which cause increased cost, chair time, and patient discomfort.

To overcome these, oxides such as silicon dioxide (SiO_2), titanium dioxide, strontium oxide, zirconia dioxide, barium oxide, and barium sulfate have been incorporated as radiopacifiers. Additionally, radiopacity been satisfactorily shown by using ytterbium trifluoride (YbF_3) as a source [41], while using SiO_2 NPs improved the cohesive strength of adhesive resins.

Unfortunately, unwanted problems could arise from the additives. For instance, incorporating a large concentration of fillers into dental resin significantly reduced the inter-particle spacing, increased the number of particle collisions, and increased the suspension viscosity, thereby possibly adversely affecting the mechanical properties of the material. Beyond that, excessive fillers could also cause the composite materials to lose dimensional stability, deteriorate in bond strength, weaken in flexural strength and diametral tensile strength, and decrease elastic modulus as well as fracture toughness.

To address this problem, YbF_3 (40–80 nm average particle size, nanostructured and amorphous materials) is added into the adhesive. For nano-based materials, it is of utmost importance that NPs do not jeopardize the chemo-mechanical stability of the modified material. Compared with nanoparticle-free adhesive, the YbF_3-modified adhesive improved radiopacity and maintained the bond strength to dentin stable over time. Considering the different results of the nanoparticle-modified adhesives, gaining radiopacity without sacrificing beneficial characteristics of dental bonding agents may depend on the type of radiopacifiers added into the material. As such, YbF_3 could be considered a promising candidate to develop novel radiopaque dental adhesives [35].

Contemporary adhesives are limited by their inability to successfully infiltrate into the acid-etched or self-etched exposed collagen fibril network of the demineralized dentin [42]. Denuded dentin collagen exposure along the dentin–resin interface is the result of this incomplete infiltration of resin and the hydrolysis of the polymerized resin. Bacterial acids and enzymes, as well as activated host-derived proteases, further degrade this already defective bonded interface, thereby eroding the lifespan of the resin–dentin bond [43]. Although several methods aimed to optimize the infiltration of resin into the collagen matrix of the demineralized dentin, such as

the usage of catalysts, various solvents, and hydrophilic resin monomers, they all failed.

To solve the limited resin penetration problem, a novel solution is to develop a novel adhesive that can be actively manipulated and forced to infiltrate and penetrate the interfibrillar spaces within acid-etched dentin and the dentinal tubules. This adhesive is bis-GMA-based and doped with spherical nanoparticles. The nanoparticles are composed of an iron core, a whitening coat shell of zirconium oxide (10–20 nm), and silanized by a monolayer of vinyl groups grafted on the surface of particles to covalently bond to the resin matrix. This nanoparticle-doped resin can be actively pulled into dentin interfibrillar spaces by magnetic force (~60 s), using off-the-shelf magnets (1.2 T). We hypothesize that this magnetic nano-adhesive system can enhance resin infiltration and penetration of dentinal tissues and that tubules thus enhance the adherence and seal. Magnetic forces, unlike the passive self-diffusion, might be able to actively enhance the adhesive penetration. Under the guidance of this external force, magnetic nanoparticles (MNP) can deliver more drugs to a target than either iontophoresis or diffusion. This system should also increase the surface area of dentin available for bonding and may help counteract adhesive lift due to polymerization shrinkage of composite restorations, result in an improved bonded interface with dentin, and ultimately enhance the longevity of composite resin restorations. Furthermore, this system should not adversely affect pulpal health [44]. However, it did not have bactericidal and remineralization abilities. So, another study developed a novel magnetic nanoparticle-containing adhesive system with antibacterial and remineralization functions for the first time [43]. MNPs, dimethylaminohexadecyl methacrylate (DMAHDM), and amorphous calcium phosphate nanoparticles (NACP) were mixed into a commercially available adhesive resin (Adper ScotchBond, Multi-Purpose Adhesive, SBMP) at 2%, 5%, and 20%, respectively, by mass. The two types of magnetic nanoparticles, iron oxide nanoparticles and acrylate functionalized iron oxide nanoparticles (AINPs), each were added to the resin at 1% by mass. A commercial cube-shaped magnet was used to apply a magnetic force for 3 min for inducing dentin bonding, subsequently measurements were taken of dentin shear bond strengths. Furthermore, resins were used to grow *Streptococcus mutans* biofilms, and colony-forming units (CFU), metabolic activity, and lactic acid were measured. The phosphate (P) ion concentrations, calcium (Ca) ion concentrations, and pH of the biofilm culture were also determined. Results showed that it had greater dentin bond strength and antibacterial and remineralizing capabilities. The reason is that teeth restored using the nanoparticle-doped adhesive and magnetic pull displayed an extensive network of resin tags penetrating dentin, both vertically and horizontally, compared to control. Additionally, teeth restored by nanoparticle-doped adhesives displayed a significantly greater number of resin tags per field of view and average length of resin tags as compared to controls (Fig. 3.2).

Adhesives have been revolutionized by developments and improvements in material compositions and placement technology [40]. With the development of the nanotechnology, nano-scale adhesive is extensively studied. Here are the main nano-scale adhesives currently available: Prime&Bond NT (DENTSPLY); Adper™

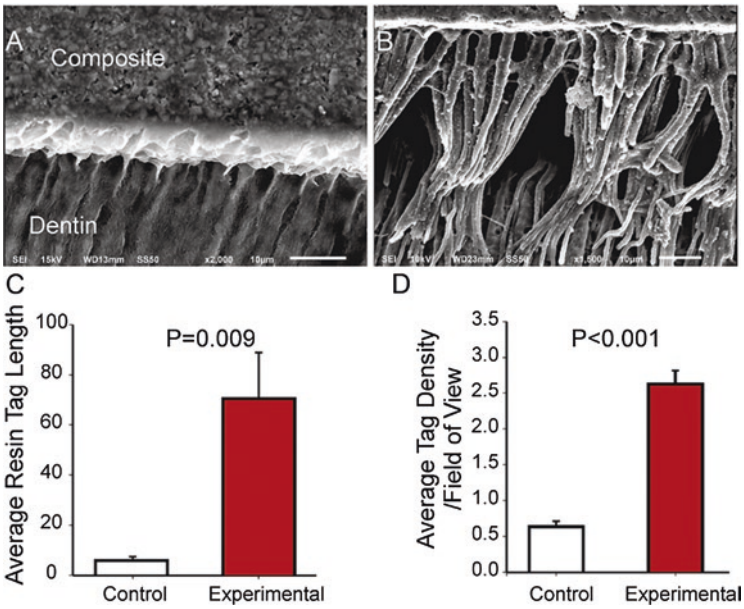

Fig. 3.2 Representative examples of SEM images from teeth restored using (**a**) control adhesive, (**b**) nano-adhesive with magnetic pull. (**c**) Quantification of average resin tag length and (**d**) density [44]

Single Bond 2 (3M ESPE); SE-BOND (kuraray). But the ingredients included are unclear. Due to its excellent adhesion strength, sealing property, desensitization effect, antibacterial property, and no significant markup in prices, nano-scale adhesive reaches a broader global market.

Above all, we know magnetic forces have a great effect on adhesive. But as yet, reports that have tested magnetic nanoparticle-doped adhesives with magnetic nanoparticle-doped adhesives have been scarce. There are still many aspects which need to be improved. For example, when the adhesive is applied, a magnetic field force should be exerted for 3 min. But the 3 min of magnet application is too long for clinical applications [45]. Therefore, further efforts are needed to investigate the incorporation of drug-loaded magnetic nanoparticles into bonding agents to help establish a new and effective strategy in conservative dentistry.

3.1.3 Nano Root Canal Filling Materials

In the human oral cavity, pulpitis and periapical periodontitis are the most common bacterial infections, with the major symptoms being pain, tooth defect, and dysfunction. The most effective treatment for pulpitis is root canal therapy (RCT) [46]. RCT, also known as endodontic treatment, an operation to treat pulp necrosis, root

infection, apical periodontitis, and endodontic retreatment in dentistry, is used to treat the infected pulp tissue that is composed of blood vessels and nerve tissue within the tooth. The aim is to eliminate inflammation and pain, while protecting the tooth against future reinfection as well as preserving its function. Conventional RCT usually applies dedicated instruments and methods to clean and restructure the root canal and appropriate drugs to disinfect and sterilize the root canal. Finally, it uses special materials to fill the root canal firmly (Fig. 3.3), thus eliminating the inflamed pulpal tissue, helping the healing of apical tissue, and preventing the development of periapical periodontitis [47]. The process requires the placement of a root canal filling with high sealing properties.

To clear the infections, a perfect root canal preparation and root canal filling are necessary. The chief criteria for the successful treatment of periapical periodontitis is the reduction or elimination of bacteria. To accomplish this, a combination of mechanical instruments, various irrigation solutions, and antibacterial dressings or medicants placed into the canal are required [48]. Before root canal preparation, the root canal wall has a dentine smear layer attached. This could negatively affect the root-filling material adhesion to the root canal wall and result in apical leakage [49, 50]. Three main factors are involved, namely the complexity of the anatomical structure of the root canal, the biofilm lifestyle, and the low permeability of the lavatory fluid into the dentinal tube. Thus, the conventional procedure rarely achieves complete roots canal disinfection and closure [51, 52]. The complexity of the anatomic root canal system enables bacteria to hide and multiply [53], limiting the elimination of microorganisms in specific areas of the root canal despite the use of high-quality instrumentation and various irrigating solutions [54]. Thus, the major problems in RCT are the inability to completely clear and restructure the canal using standard cleaning and shaping procedures. Eliminating bacterial biofilms surviving within the anatomic complexities and uninstrumented portions of the root

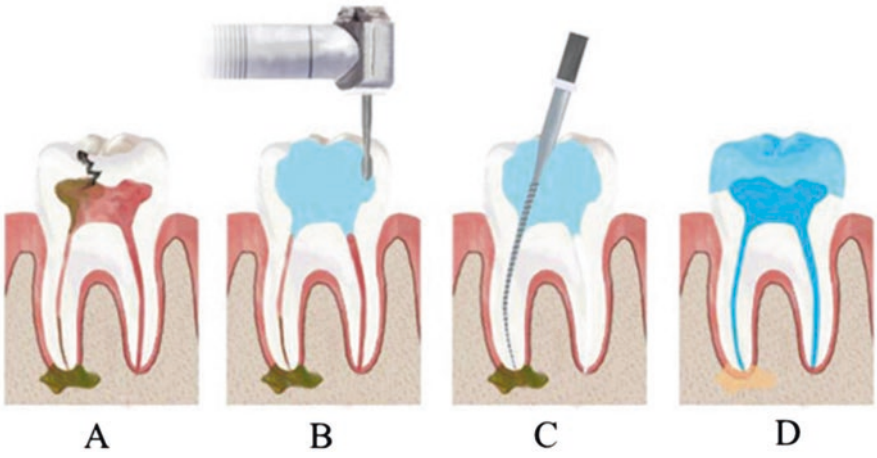

Fig. 3.3 The condition of the tooth before and after root canal therapy: (**a**) pulpitis caused by dental caries; (**b**, **c**) root canal preparation by appropriate equipment; (**d**) perfect root canal filling

canal system continue to pose a challenge [55]. Therefore, the basic root canal preparation greatly affects the success rate of RCT.

High-quality instruments are vital to root canal preparation. Some of the critical features of the instruments are now measured using the latest nano-indentation technology. Nano-indentation, also known as depth-sensing indentation and ultra-low-load indentation, is a relatively new form of sensitive mechanical testing that is appropriate to capture the incidence of localized phase changes [56]. A study by Jamleh et al. demonstrates that the nano-indentation technique can be applied to determine the performance of NiTi instrument [57]. This application has an important influence on the development of RCT.

Hermetic sealing is the primary factor associated with the success of RCT. Ingle et al. pointed out that 58% treatment failures were due to incomplete obturation [58]. Microorganisms and their byproducts are the main etiologic factors in the initiation, propagation, and persistence of pulpal and periapical infections [59]. Minimizing gap and void formation during root canal obturation is clinically relevant because as little as 1% shrinkage of the sealers may result in filling deficiencies due to the penetration of bacteria and their byproducts [60]. RCT prevents bacteria in an oral environment from entering and re-infecting the root canal. It also prevents the tissue fluid from going into the root canal, which otherwise would become the culture media for the residual bacteria and result in periapical periodontitis. The apical third is the most complex and critical area in the root canal system, not only for root canal instrumentation but also for root canal filling [61]. Thus, the apical sealing of the root canal is one of the most important indicators for a successful RCT. Therefore, complete root canal filling is another important factor in RCT.

The traditional root canal filling material refers to the material that is used to fill the root canal in RCT treatment, eliminating the dead cavity and preventing reinfection in the root canal. It includes three categories: a solid, a paste, and a liquid. The solid material includes gutta-percha points, silver cones, and plastic points. The paste material is often used in conjunction with solid materials, which is mainly used to bond the solid material with the root canal wall, while filling the gap between the solid material and the root canal wall. It includes zinc oxide lilac oil root canal filling material, root canal paste (AH-Plus), calcium hydroxide pastes, thymol paste, and iodoform paste. The liquid material is mainly phenolic resin.

The obturation of root canal system is an essential part in endodontics to close the leakage pathways from the coronal and apical directions [62]. Many types of root canal sealers have been introduced to seal the canal. But an ideal root canal sealer must have the following properties: sufficient setting time to allow enough working time, an excellent sealing and perfect dimensional stability after setting, adequate adhesion with canal walls, tissue tolerance and high biocompatibility, and insolubility to tissue fluids [63]. Decontamination and 3D obturation are essential in RCT. However, most of the obturating materials cannot provide an effective seal [64]. As a result, root canal filling materials are continuously improved, and bioactive materials are becoming increasingly popular.

Currently, commercially available sealers can be broadly categorized into the following types: zinc oxide eugenol-based, calcium hydroxide-based, glass

ionomer-based, resin-based, silicone-based, and calcium silicate-based sealers. However, none of the existing sealers fit all the criteria required to be ideal. Dissolution when contacting periapical tissues are a common drawback for zinc oxide eugenol-based [65], calcium hydroxide-based [66] and glass ionomer-based sealers. Moreover, slight shrinkage occurs during settings with zinc oxide eugenol-based sealers [60, 67].

Different materials and techniques have been investigated in order to establish the ideal root canal seal for filling the root canal space. Among these, the cold lateral condensation of gutta-percha (GP) technique in conjunction with a sealer remains one of the most popular techniques that has both been extensively investigated and employed [68]: some authors refer to it as the gold standard [69, 70]. Currently, RCT obturation uses the current standard materials: GP, an inert thermoplastic polymer consisting of the GP latex, zinc oxide, a radiopacifier which allows clinical X-ray imaging to monitor the treatment, and a plasticizer [71]. Filling the root canal space with GP is the standard of care for endodontic therapies, and it has a long history of application. It offers numerous advantages, including good biocompatibility, low cost efficiency, and easy removal. However, it also has several limitations. Conventional GP obturation may still lead to endodontic failures due to reinfection of root canals, which are in part associated with microleakage. These poorly obturated root canals create possible passages for bacteria, fluid, and chemical substance to penetrate [72, 73]. The phenomenon occurs because the sealers that are currently available, such as the widely adopted root filling material (thermoplastic GP), reveals volume shrinkage after cooling [74]. Conventional GP may be conducive to bacterial regrowth. If there are bacterial remnants in the root canal space, the tissue fluid would reestablish contact. While being frequently used, it has been previously reported to be associated with microleakage which would allow oral fluids and bacteria to access the treated root canal and suboptimal mechanical properties with respect to handling the material, potentially resulting in buckling during obturation [75]. Due to the dimensional changes and lack of adhesion from GP, it is not easy to achieve a complete filling with the current root-filling materials. Therefore, the adaptability of a sealer to the dentin is the primary method to prevent the microleakage and reinfection of the root canal.

Epoxy resin-based sealers demonstrate good dimensional stability [76] and good adhesive properties [77]. Therefore, they are good candidates to provide an adequate root canal seal. The intricate nature of their adhesion to dentin [78] and their ability to undergo slight expansion [79] may partly explain their thorough sealing properties. AH-Plus is used frequently in clinic and is commonly chosen as the control in studies of the new sealer's properties because of its good flowability, proper film thickness, and viscosity [80]. It is an epoxy resin-based sealer with good physicochemical properties [81] and antibacterial effect [82]. Previous studies suggested that AH-Plus can be considered the gold standard for root canal sealants. The combination of AH-Plus and GP is commonly used in RCT. It has many advantages in clinical practice, including permanent seal, excellent X-ray resistance, easy mixing, unapparent shrinkage after solidification, good long-term space stability and

sealing characteristics, no irritation, and non-interference with the bond strength of fiberglass posts cemented by adhesive resin cements [83].

However, the contemporary dental root-end filling materials still do not possess all desirable features, such as biocompatibility, adhesion to tooth structures, and antibacterial activity [84]. The good biocompatibility of the sealing material is needed when it is in contact with surrounding tissues to achieve a successful long-term outcome [85]. Mineral trioxide aggregate (MTA) is a kind of trioxide agglomerate and gray powder, including calcium silicate, calcium oxide, calcium phosphate, and other components. Several studies have investigated the properties of MTA, including composition, radiopacity, setting time, and biocompatibility. Since the introduction of MTA to the market, it has gained popularity due to its excellent biocompatibility [86]. Previous reports have recognized that MTA acts as a bioactive material [87] which promotes mineralization [88]. MTA serves many purposes, such as internal and external root resorption repair [89, 90], furcal perforations sealing [91], apexification [92], as a direct pulp capping agent [93], and also as a retrograde filling material [94]. MTA can also be used as root canal filling material, which is usually used for pulp capping, perforation reparation, root tip formation, and root pour filling materials. However, MTA exhibits certain disadvantages such as handling difficulty, low acidic resistance, and long setting time [95]. Long setting time increases the probability of the contamination of MTA by oral fluids before the material is completely solidified.

Hence, the ideal material for root canal filling should have favorable biocompatibility, bioactivity, antibacterial property, flowability, small particle size, no setting shrinkage, no setting dissolution, complete coverage of root canal space, adhesion to tooth structures, etc. Nanotechnology is applied to improve the performance of present dental materials.

Due to the imperfection of the existing material, the field of nanomedicine has been applied to make important clinical advances in recent years. Nanomaterials are natural, incidental, or manufactured materials containing unbound, aggregate, or agglomerate state particles in which 50% or more of the particles based on number, size, distribution, or one or more of the external dimensions is within the 1–100 nm range [71]. Nanomaterial offers enhanced physicochemical properties, such as increased chemical reactivity, ultra-small sizes, and large surface area/mass ratio, as compared to their bulk counterparts [96, 97]. Nanoparticles (NPs) have been the focus of attention in the past few decades owing to their innovative and functional properties. Particles with dimensions of 1–1000 nm made from any type of biocompatible substance can be defined as NPs (but commonly defined as 5–350 nm in diameter) [98]. The use of nanotechnology has allowed many other developments in dentistry and advances in oral-health-related nanomaterial and therapeutic methods [99]. Nanotechnology has been developed rapidly and created a myriad of biomedical applications such as drug delivery, tissue regeneration, antimicrobial application, gene transfection, and imaging [100, 101]. Moreover, nanotechnology is used to produce many dental materials, including light-cured restorative composite resins and their bonding systems, impression materials, ceramics, the covering layers of dental implants, fluoride mouthwashes, and so on.

In nanoscale, a decrease in dimensions to the atomic level leads to a considerable increase in the surface area of the agent. Therefore, the contact of NPs with dentin can effectively achieve good sealing effect. Some studies show that bacterial biofilms are considered the major cause of both primary and secondary root canal infections [102, 103]. Silver nanoparticles (AgNPs) as a medicament and not as an irrigant showed potential to eliminate residual bacterial biofilms during root canal disinfection.

The quality of the filling material affects its ability to prevent reinfection of the root canal and the healing of apical lesion. Nanotechnology makes improvements in root canal filling materials. The nanotechnology is used to modify the current materials by adding nanostructured materials to enhance its properties. It enables the material to be antibacterial and enhances the obturation in RCT. Furthermore, the application of nanomaterials in clinic is more and more extensive. In the field of endodontics, nanomaterials is mainly used to improve antimicrobial efficacy, mechanical integrity of diseased dentin matrix, and tissue regeneration [104, 105]. The research and development of nanomaterials with excellent apical sealing ability is a significant contribution to increase the success rate of RCT. The advantages of using nanoparticles in endodontic sealers include improving their physicochemical characteristics, enhancing the antibacterial property, decreasing microleakage, and increasing biocompatibility [7, 106, 107].

Nano-modified cements can help to produce ideal root-end filling materials. Attempts have been made to improve the properties of MTA by incorporating nanomaterials. For example, incorporation of silicon dioxide (SiO_2) nanoparticles has improved the microstructure of MTA and accelerated the hydration process. Alternatively, antibacterial activity can be improved by adding chitosan or silver (Ag) nanoparticles [85]. Iron disulfide (FeS_2) nano or microparticles, originating naturally from hydrothermal sources and clay in the form of iron sulfide particles, have been extensively studied [108]. Results show that the FeS_2 nanocrystals are biocompatible, indicating their potential applications in biomedicine. These nanostructures can also effectively modulate MTA's mechanical properties. At small concentrations (0.2–0.6 wt%), these nanostructures prevent volume changes, resulting in a stiffer material and reduced initial setting time than conventional MTA [109]. Thus, the addition of FeS_2 nanostructures to MTA can improve its physical and biological properties [110]. The particle size of MTA is important for its clinical applications in dentistry due to its influence in creating an adequate seal between the material and the dentin [111]. It is necessary that the particle size of the MTA should be smaller than the size of the dentinal tubules. It allows the MTA particles to penetrate the tubules and provide an adequate seal.

A nano-modification of white mineral trioxide aggregate (WMTA), mainly changes in the surface porosity, microhardness, and setting time, is a new root-end filling cement with similar composition to WMTA. However, the former was more resistance to an acidic environment and set ten times faster than WMTA [112]. The initial setting time of WMTA was approximately 40 min, while that of nano-WMTA (nano-modified with white mineral trioxide aggregate) was only about 6 min [112]. Therefore, a shorter setting time prevented the bacterial reinfection in the root canal

to a certain extent and reduced the chance of tissue fluid infiltrating into the root canal. An acidic environment had an adverse effect on the microhardness of WMTA cement, which was consistent with previous studies [113]. However, WMTA was affected much greater than nano-WMTA, which might be attributed to the greater porosity of WMTA compared with nano-WMTA. The greater porosity might accelerate the acid penetration into the surface texture and decrease the surface microhardness. Nano-WMTA revealed low surface porosity and high acid resistance. Greater porosity can also increase crack propagation. The push-out bond strength is recommended in further investigation, because WMTA has been widely applied to perforation repair materials, root canal retrograde filling materials, and the materials of the formation of the top barrier in clinical practice. The push-out bond strength of nano-WMTA is significantly higher than WMTA [114]. It is indicated that the strong adhesion between materials and the dentin tubules, which can reduce the microleakage and improve the maneuverability of root canal filling materials. The smaller particle size and uniform distribution of constituents in nano-WMTA are the two influencing factors.

Recent literatures lay strong emphasis on the prospects of nanotechnology to improve mechanical strength (e.g. nanofibers incorporation) and provide antibacterial protective effects (e.g. silver nanoparticles and chlorhexidine diacetate) to resin-based dental sealants [115]. Chitosan (CH), chitin's deacetylated form, is a nontoxic biopolymer which has garnered much attention based on its biocompatibility, antioxidant, anti-inflammatory, and antibacterial properties. While nylon is a polyamide having excellent strength, flexibility, and abrasion resistance [116]. Due to these properties, reinforcement of dental composites has used electrospun nylon-6 (N6) nanofibers [117]. Hamilton et al. successfully prepared CH and N6 nanofibers via electrospinning to improve the mechanical properties and provide an antibacterial protective effect to resin-based dental sealants [118] (Fig. 3.4). The overall results indicated that the CH groups exhibited significantly higher flexural strength (FS) and hardness than any other group. Molecular weight (MW) and degree of deacetylation (DA) vary among the different types of chitosan; these factors that independently influence the antimicrobial activity of chitosan. It has been reported that lower MW CHs have greater antimicrobial activity than high MW CHs. However, with the limitations of above in vitro study, further investigation is needed to evaluate whether chitosan with different molecular weight and degree of deacetylation may enhance the physicomechanical and antibacterial properties of the materials tested.

We have earlier discussed the merits and drawbacks of GP in RCT. While GP offers numerous advantages, it cannot provide adequate seal to prevent bacterial percolation which is a challenge in endodontic therapy. To address these challenges, clinicians have explored other root canal filling materials than GP. Detonation of nano-diamonds (NDs), which are carbon nanoparticles approximately 4–6 nm in diameter, are very attractive. They are the waste byproducts that are readily processed for biomedical applications [119–127]. NDs may offer unique advantages due to their favorable properties, particularly for dental applications. These include versatile faceted surface chemistry, biocompatibility, and their role in improving

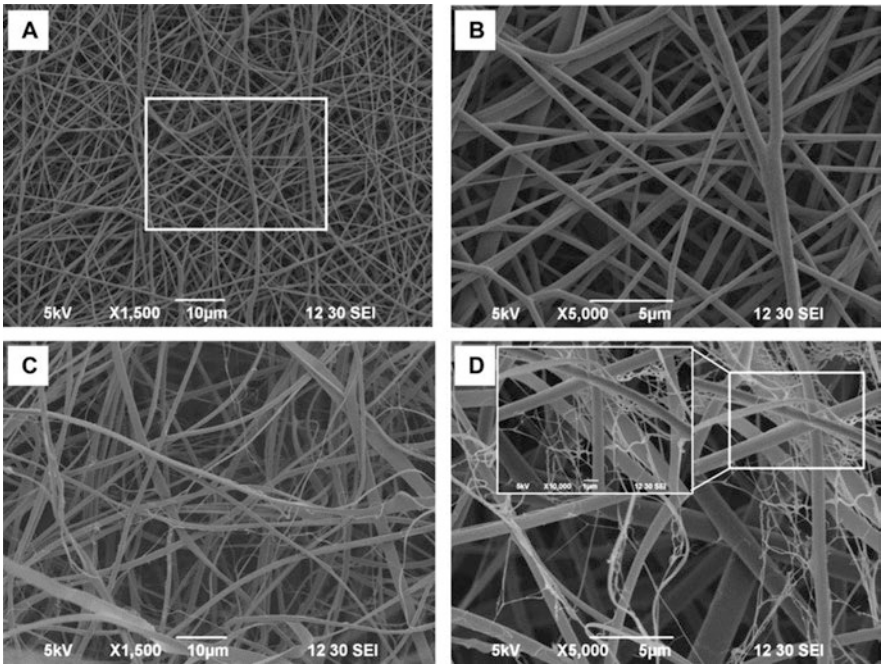

Fig. 3.4 Electrospun nylon-6 (**A**, **B**) and chitosan (**C**, **D**) nanofibers shown using representative SEM images at various magnifications. (**D**) The selected area as shown under higher magnification (5000×). (**D**) Chitosan fiber branching shown under higher magnification images (5000× and 10,000×) [119]

mechanical properties. Importantly, NDs with consistent particle size and surface chemistry properties can be largely synthesized, supporting their clinical transition [128–130]. Thus, researchers developed a nano-diamond gutta-percha composite (NDGP) embedded with nano-diamond amoxicillin (ND-AMC) conjugates (Fig. 3.5a), which can reduce the likelihood of root canal reinfection and enhance the treatment prognosis. While multiple nanoparticles have been evaluated in human studies, there remains a need to accelerate novel, nanotechnology-enabled strategies which can enhance the efficacy and safety of therapy [132, 133]. ND-containing composite materials have also been shown to exhibit superior mechanical properties compared with unmodified materials (Fig. 3.5b) [125, 131, 134]. Examination of the clinical potential of these key ND attributes [131] finds that the thermoplastic biomaterial, ND-embedded gutta-percha, could be utilized as a nonsurgical RCT filler material in preventing reinfection and enabling lesion healing. While the administration of NDGP also confers simultaneously the beneficial properties of GP with the increased mechanical strength and ND-mediated antimicrobial and/or pharmacological antimicrobial activity. Therefore, these capabilities may reduce the risk of root canal reinfection and improve the long-term treatment outcomes.

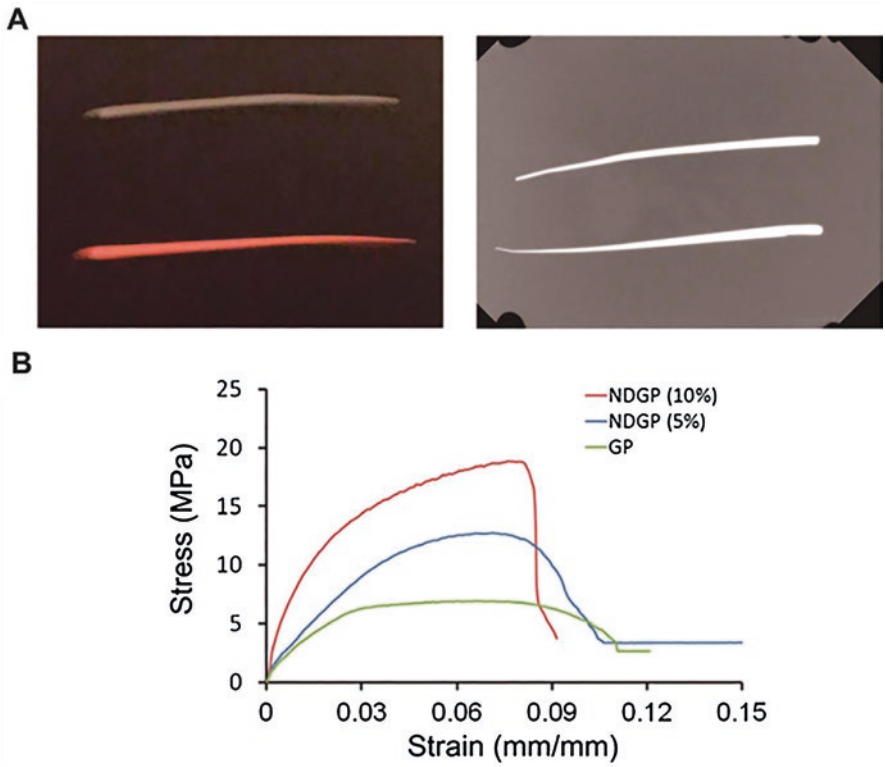

Fig. 3.5 Radiopaque and mechanical properties of NDGP. (**A**) Left: NGDP photographs (top) and unmodified GP (bottom). Right: Digital X-ray imaging showing the radiopaque property of NDGP (top) was similar to that of the unmodified GP (bottom). (**B**) Tensile test results expressed as stress–strain curves of G, and NDGP (5 wt% ND, 10 wt% ND). The tests were conducted at 0.3 cm/min strain rate with the sample gauge lengths set to 0.89 cm. Results clearly indicated the areas under the NGDPs curves (5% and 10%) were larger than the corresponding unmodified GP, suggesting the modified NGDPs were more mechanically robust [131]

Researchers fabricated bioactive mesoporous calcium–silicate (MCS) NPs (around 100 nm) with high specific surface area and pore volume to prepare the injectable materials for the filling of the root canal. The apatite mineralization ability, in vitro osteogenesis, drug delivery, and antibacterial properties of the material were evaluated. The prepared MCS was found to be easily injected. And it could fill the apical root canal successfully. MCS NPs induced apatite mineralization in DMEM solution without any cytotoxic effects [135]. Hence, it suggested that MCS NPs could be an advanced biomaterial with multiple functions due to their unique nanostructure, injectability, and antibacterial efficiency. Meanwhile, it also has the features of apatite mineralization, osteostimulation, and drug delivery [136].

Recently, a new group of sealers, bioceramic (BC) sealers, were introduced for dental practice [137]. BC materials, calcium silicate-based materials, are osteoinductive bioceramic products or components employed in medical and dental

application mainly as implants and replacements [138]. The calcium silicate-based material, which is a cement paste, has attracted considerable attention, because of its good penetration ability and flowability. The Total Fill BC sealer (FKG Dentaire, La Chaux-de-Fonds, Switzerland), one of the first commercially available sealers in Europe, contains the same chemical composition as the Endo Sequence BC sealer (Brasseler, Savannah, GA, USA), which is a nanomaterial. Endo Sequence BC sealer is one of the ideal bioactive sealants that contains nanoparticles facilitating its penetrating into dentinal tubules [139]. It is composed of calcium silicates, calcium phosphate monobasic, calcium hydroxide, zirconium oxide, other filler, and thickening agents. This is also marketed as the iRoot SP (Innovative. BioCeramix Inc., Vancouver, British Columbia, Canada) which has been provided as an ideal premixed, ready-to-use, and injectable biomaterial in dental clinic, exhibiting excellent radiopacity, insolubility, zero-shrinkage, and hydrophilic (due to using moisture from the dentinal tubules to start and complete the setting reaction) qualities [140]. The shrinkage during setting and dissolution when contacted with tissue fluid is the common problems for most of the currently available sealers [65]. Total Fill BC sealer is no exception. These shortcomings will result in the existence of gaps in the interface of sealers and root canal wall which lead to the microleakage in the root canal system. Such gaps ultimately affect the outcome of root canal treatment. Nanoparticles have improved the handling and physical properties of Total Fill BC sealer. BC sealer, due to its hydrophilic properties [108], uses the moisture within the root canal to finish the setting reaction. Hydration reactions of calcium silicates are facilitated by this moisture, which produces calcium hydroxide and silicate hydrogel. These products can partially react with the phosphate to form water and hydroxyapatite, along with the formation of a nanocomposites structure of calcium silicate and hydroxyapatite. The hydration reaction and setting time are affected by the availability of water [102]: setting time may be prolonged in overly dried canals. It sets and becomes hard in a few hours, providing excellent seal and dimensional stability. Upon setting, it forms the hydroxyapatite, providing excellent biocompatibility and bioactivity. Many in vitro studies have indicated its good biocompatibility [80], bioactivity [141, 142], antibacterial property [143, 144], and certain kinds of sealing ability [145, 146]. Moreover, it has favorable flowability, small particle size, and acceptable volume expansion [147, 148], which directly affect the root canal filling condition. The manufacturers recommend this sealer to be used together with the Total Fill BC gutta-percha (FKG Dentaire, La Chaux-de-Fonds, Switzerland), which when coated and impregnated with a nano-layer of BC particles improves the adaptation [149].

With its properties of almost no shrinkage when setting and no dissolution when in contact with tissue fluids, the new bioceramic sealer may be a promising filling material [150]. The iRoot SP penetration of sealers into dentinal tubules can form a physical barrier to prevent bacterial microleakage and recontamination of root canal system [151]. It will also generate micro-mechanical interlocking with dentine and strengthen the resistance to bacteria of the filling material, and the deep penetration into dentinal tubules can maintain their bactericidal effect [152, 153], which is favorable for the healing of the periapical lesion. In addition, the moisture

remaining in the dentinal tubules will trigger its setting reaction with the production of hydroxyapatite and create the chemical bond with root dentine [141]. A study [154] indicated that the depth of sealer penetration into dentinal tubules had no correlation with the sealability of nonbonded root fillings. However, it was of paramount clinical relevance, particularly for iRoot SP. Therefore, the sealing of the root canal is improved. It was found that bioceramic sealer iRoot SP penetrated dentinal tubules better than AH-Plus in the root tip 2 mm. The good penetration ability of iRoot SP may be one of the factors which are the reasons for the success of endodontic treatments.

Nowadays, MTA Fillapex is one of the recently developed endodontic sealers [155–157]. This endodontic sealer (MTA Fillapex; Angelus Solucoes Odontologicas, Londrina, PR, Brazil) consists of MTA, natural resin, salicylate resin, bismuth, nanoparticulated silica, and pigments. However, information about the physicochemical properties of MTA Fillapex is scarce. These properties must be further researched as they have an impact on the final quality of root filling [158]. For example, the effectiveness obturating the accessory canals and voids between master and accessory gum tips is dependent on the flow of endodontic sealers; adequate flow allows for proper filling of irregularities, whereas high could cause apical extrusion, leading to the cytotoxicity of the sealers causing periapical tissue injury [159]. Since proper fluidity has a great effect on the quality of the root canal filling, much attention has been paid to the flow properties of endodontics sealers. MTA Fillapex sealer was more flowable than the Endosequence BC sealer. An excessive flow rate increases the probability of extrusion into periodontal tissues. Moreover, the pH change of sealers, which is associated with antimicrobial effects and deposition of mineralized tissue [66, 160–162], may play a role in healing: neutralization of lactic acid produced by osteoclasts as well as the prevention of mineralized tooth dissolution can be associated with the effects of the alkaline pH of root canal sealers. Therefore, by activating alkaline phosphatases, the root canal sealers, especially bioceramic-based sealers, can assist in hard tissue formation [163]. Comparing the two novel root sealers, MTA Fillapex and the Endo sequence BC, the former although showing higher flowability and thicker film also displays shorter working time, setting time, and solubility than the latter. On the other hand, both sealers produce an alkaline pH when immersed in distilled water and even after setting, which may contribute to their osteogenic potential, biocompatibility, and antibacterial ability. All sealers satisfied the criteria for flowability, solubility, film thickness, and dimensional change. The new endodontic sealers, Endo sequence BC and MTA Fillapex, both possessed acceptable flowability and dimensional stability. But they had higher solubility, film thickness, and better sealing capability than AH Plus.

Zinc oxide-eugenol (ZOE)-based sealers have been widely used in endodontic for many years. Nanotechnology has been applied to overcome their limitations. A study showed that the incorporating zinc oxide nanoparticles enhanced the physicochemical characteristics (setting time, flowability, solubility, dimensional stability, and radiopacity) of Grossman sealer [107]. The new nano zinc oxide-eugenol (NZOE) sealer produced less microleakage than Pulpdent and AH-26 root canal sealers. NZOE has less cytotoxicity than Pulpdent sealer, suggesting that the

incorporation of zinc oxide nanoparticles can decrease the cytotoxicity of ZOE-based sealers [164].

Hydroxyl apatite nanoparticles (HAp NPs) have been used widely in medicine and dentistry. Typically, they are used as implant coatings for better biocompatibility and wear resistance [165]. They are also used for the preparation of bone graft [166]. The HAp NPs can easily integrate into the dental tubules, which is beneficial to root canal sealing. HAp NPs have greater surface area, resulting in strong binding with proteins as well as with bacterial and plaque fragments [167]. Biocompatibility studies indicated that hydroxyapatite can bind to bone, and it will not lead to any local and systemic inflammatory response. It has great significance in treatments such as root canal filling, tooth filling, and dental implant.

Another example is adding silver nanoparticles and GP powder to the silicon-based sealer (Gutta-Flow Sealer). Available in uni-dose capsule form, this material can be mixed and injected [108]. This nano-sealer has multiple advantages such as good biocompatibility, stable dimension, and short setting time. The material has also been reported to have improved sealing capability and better resistance to bacterial penetration.

Endodontic sealers are noted for their highly beneficial antibacterial activity. Recently, antibacterial quaternary ammonium polyethyleneimine (QPEI) nanoparticles have been incorporated into the existing sealers such as AH plus, Epiphany, and Gutta-flow [168]. Resin composites containing QPEI nanoparticles resulted in prolonged antibacterial activity without compromising the mechanical properties [169]. The addition of QPEI nanoparticles is very stable, leaching no byproducts in the surrounding and showing no influence on the biocompatibility.

The novel injectable self-curing polyurethane (PU)-based antibacterial root canal sealer by incorporating silver phosphate (Ag_3PO_4) particles is being developed. Ag_3PO_4 can be evenly distributed within the material. The release of Ag^+ can provide satisfactory antibacterial effects. Physical properties such as setting time, film thickness, and solubility were important indexes which were used to evaluate the properties of endodontic sealers [170]. The study showed that the setting time shortened with the increased Ag_3PO_4 content in the PU sealers. Film thickness and solubility increased with the increased Ag_3PO_4 concentration. In a study, PU was set with different concentration of Ag_3PO_4 as the amount of research such as 0 wt% (PU0), 1 wt% (PU1), 3 wt% (PU3), and 5 wt% (PU5) concentrations of Ag_3PO_4 [170]. The setting times of the PU sealers with different proportions of Ag_3PO_4 are just shorter than the setting times of AH Plus and can meet the requirement of ISO standard. These properties make fabricated PU-based sealers better than AH-Plus. As Ag_3PO_4 content is increasingly incorporated into the PU sealer, the curing time shortens, inferring that Ag_3PO_4 (or Ag+) might be a driving force for polymerization [170]. And PU0, PU1, and PU3 sealers have good flowability. Another important requirement for dental material, especially when exposed to a host environment for a prolonged period, is its resistance to solubility and degradation. The solubility of the fabricated PU-based sealers increases with the content of incorporated Ag_3PO_4. This correlation may be attributed to more Ag_3PO_4 on the surface of the material

dissolved in water [170]. More importantly, root fracture often happens after RCT. Root fracture risk is related to tangential strain, which is affected by the expansion of the material as well as the elastic modulus of the root canal sealer and dentin. Thus, sealers with low elastic modulus pose lower risk for dentin fracture compared to those with higher modulus. The low moduli of PU-based sealers can reduce the amount of damage to root dentin that is generated by volume expansion. The cytocompatibility evaluation revealed that the PU1 and PU3 sealers possess good cytocompatibility and low cytotoxicity. PU5 exhibited the highest cytotoxicity. PU3 sealer offers good physicochemical and antimicrobial properties along with acceptable cytocompatibility, which may hold great application potential in the field of root canal fillings. Therefore, the properties of PU reveal that it is an excellent candidate for root sealers.

Ideal root canal filling materials should possess good biocompatibility, mobility, X-ray radiopaque ability, antibacterial ability, and stability and can seal the root canal cavity completely. An ideal root canal sealer should be non-cytotoxic, non-mutagenic, and immunologically compatible with periapical tissues [171, 172]. Therefore, further research is required to improve the materials. Within the limit of our knowledge, we put forward several points here.

First, GP surfaces can be coated with nanoparticles. For example, optical fiber glasses tips can be covered with AgNPs, which is a polymeric material with light transmission properties and bacteriostatic qualities. Therefore, they can be a substitutive material to GP. Nanoindentation results demonstrated that the optical fibers covered by AgNPs achieved excellent nano-hardness and elastic modulus considerably. It made the material more rigid and more resistant to corrosion. And they ensure the compatibility with the glass fiber posts and resin cement materials. The main reason optical fiber-silver nanoparticles are suitable for dental root canals is due to their superior bacteriostatic properties. Another advantage is it contains optical fiber, the light transmission properties of which allows the use of light curing liquid resins in the root canal.

Second, novel new type of root canal filling materials can be designed and developed, such as nanocomposite hydrogels. Hydrogels, due to its excellent biocompatibility, swelling property, and stability, can prevent apical or coronal microleakage. Hydrogels also have the potential as root canal sealers, but still need to have certain degree of X-ray radiopaque and antibacterial ability. Nowadays, the current commercialized zirconia nanoparticles lack X-ray radiopaque property and long-lasting antibacterial function. Based on the dispersion and stability issues of water-soluble AgNPs, ZrO_2 can be diffused in the hydrogels of AgNPs to prepare ZrO_2, Ag, and ZrO_2/Ag nanocomposite hydrogels.

Third, the cold flowable GP can be improved. Gutta-flow is a novel cold flowable root canal filling system. Future work is required to improve its flowability, adjust its setting time, and deepen its penetration depth.

3.1.4 Nano Enhanced Resin-Based Materials for Dentition Restoration

The importance of healthy teeth goes beyond the practical use of teeth to chew and break down food. It also has a significant impact on a person's attractiveness, confidence, and ultimately their quality of life. The loss of dentition can have a great impact on an individual's local and systemic health including alveolar bone resorption, periodontal tilt, temporomandibular joint disorder, and digestive system dysfunction.

Therefore, the field of dentistry has put forth a significant amount of effort to restore the lost teeth. The removable partial denture (RPD) is one of the most commonly used resolutions. RPD is a type of restoration that patients can remove by themselves, which uses the natural teeth, the mucous membrane, and base tissue to underpin for support and retention. The artificial teeth are used to restore the missing teeth including the morphology and function. And the base materials are used to restore the missing alveolar bone, jaw, and its surrounding soft tissue.

RPD is composed of a denture base, artificial teeth, and retainers [173]. Artificial teeth assist in the restoration of masticatory efficiency, pronunciation, and improvement of esthetic appeal. The retainer is used to stabilize the base and improve masticatory function. The denture base is a major component of RPD, which covers the alveolar ridge in the missing tooth area and the palate. Its main function is to arrange and attach artificial teeth, conduct and disperse bite force, and connect all parts of the denture into a whole. Additionally, the denture base materials should also have good biocompatibility, good chemical and size stability, as well as rigorously tested mechanical properties such as the flexural, compressive strength, impact strength, suitable hardness, and wear resistance. The dentures also need to be easy to fix, nontoxic, and non-irritating and have low solubility in saliva. Furthermore, they should also be esthetically pleasing, cheap, and contain anti-microbial properties.

Dental acrylic resin has been widely used as denture materials since it was developed by Walter Bauer in 1936. These resins commonly consist of methyl methacrylate (MMA) and polymethyl methacrylate (PMMA) [174, 175]. MMA resin is a commonly used dental material, because it is quick to cure at low temperatures and is naturally balanced in terms of hardness and toughness. It has suitable wear resistance and maintains good transparency. PMMA is one of the most commonly used dental materials in prosthodontics due to its other desirable characteristics, such as accurate reproduction of surface details, lack of toxicity, better transparency, outstanding aging resistance, good insulation, corrosion resistance, and cost-effectiveness [174, 175].

Denture base resin can be classified according to the polymerization and curing mode into four kinds: (1) heat-curing denture base resin, (2) self-curing denture base resin, (3) light-curing denture base resin, and (4) thermoplastic injection molding denture base resin. The heat-curing resin is composed of MMA mixed with its homopolymer powder or copolymer powder. Different copolymerized powders result in different performance of the final resin. The impact strength and flexural

strength of denture base bracket are improved by MMA and butyl acrylate (BA) block copolymer. The copolymerized powder of MMA and methyl acrylate require less water for plastic filling, which improves the wear and abrasion resistance of the base support. MMA, ethyl acrylate (EA), and methyl acrylate (MA) ternary copolymerized powder improve the mechanical properties of the base resin. The graft copolymerized powder of MMA and rubber improve the impact strength of the base resin and obviously enhance its toughness. The self-curing resin refers to the base material that is polymerized by REDOX system at room temperature. It is composed of methyl methacrylate and PMMA homopolymer powder or copolymer powder, which can shorten the time that distension denture base powder is dissolved in the solution of the denture base. The light-curing denture base resin is a single component and dough-shaped plasticizer, and the resin matrix is mainly bis-GMA and isocyanate-modified bis-GMA. The material has an excellent working time before curing. Commonly used thermoplastic-injection-molding materials include polyamide (nylon), which is soft and elastic. It can be used to fabricate teeth or gum color resin clasp, which is known as the invisible denture. They are widely used in provisional prosthesis and orthodontic removable appliances, as temporary prosthetic base materials, and to repair dentures. In addition, because they are cheap and easy to make and repair, the materials are perfect for molding material [176, 177].

Full and removable partial dentures have been used widely in oral clinical applications such as traditional prosthetic methods [178]. However, current resin-based materials have some drawbacks including insufficient surface hardness, low flexural strength [179], and poor antibacterial activity [180]. It is also a common cause of abutment caries and denture stomatitis [181]. Current dentures also have relatively poor mechanical properties which can lead to the denture base fracture and affect the longevity of the dentures [175, 182, 183]. Due to these properties, these fractures are commonplace in prosthodontics and cause problems for both prosthodontists and patients. Fracture can also occur due to fatigue arising from the bending forces caused by inordinate masticatory forces or from denture deformation [184]. Another factor that determines the esthetics of denture is the transparency or transparency rate of base material. These deficiencies require special technique and material for improvements.

Recent advancement in materials science and the introduction of nanotechnology in dentistry leads to new materials, with improved esthetic, antimicrobial property, and durability. Nanotechnology [185] was coined by Japanese scientist Dr. Nori Taniguchi in 1974 and defined as the processing of separation, consolidation, and deformation of materials by one atom or one molecule [186]. Nanotechnology allows the manufacturing of products of less than 100 nm to create designs and perform functions which was impossible previously [187].

The global market for dental materials is expected to increase rapidly due to multiple factors such as improved awareness, healthier lifestyles, expanding populations and life expectancy. This demand stimulates the development of novel materials to remedy the inadequacies of current dental materials. Dentures will deteriorate over time, may fracture due to external stresses [183, 188]. The application of nanomaterials in dentistry will be helpful to improve the quality of life of the patients.

Various attempts have been undertaken to enhance the physical properties of the denture base material, such as chemically modifying poly(methyl methacrylate) (PMMA), developing alternatives to PMMA, and reinforcing PMMA with other materials, e.g., fibers and nano-fillers [189, 190]. To facilitate clinical applications, various micro- or nano-sized fillers have been incorporated into PMMA [191–194], with the aim to develop new materials or significantly improve the properties of existing materials.

Due to unique properties, nanomaterials are always the research focus of biomaterials scientists. Nanomaterials have been developing in four categories (metals, polymers, ceramics, and composites) for practical applications in health care [188]. They combine the advantages from various nanomaterials to improve the quality of life. Some studies have investigated the effect of incorporating inorganic NPs into PMMA [190, 195, 196]. The shape, size, as well as the concentration and interaction of these nanoparticles with a polymer matrix determine the properties of a polymer nanocomposite mixture [195]. The properties of the reinforced resin by nanoparticles depend on the size, shape, type, and concentration of the added nanoparticles [197]. The properties of the resin base material can be improved by dispersing nano-silica particles evenly into the resin material, including (1) improves the strength and elongation, (2) improve the abrasion resistance and the surface finish of the material, and (3) anti-aging performance.

Clinical handling has improved after nanoparticles are added to materials. As compared to amalgam, the dental resin 2,2-bis-[4-(methacryloxypropoxy)-phenyl]-propane (bis-GMA) has been commonly employed for decades as a restorative material. Since bis-GMA resin has relatively low mechanical properties, this material has been further researched through multiple studies [198]. Nanofibers are believed to have the potential to substantially improve the mechanical properties of bis-GMA resin for their ultrahigh interfacial area. Some researchers consider its self-tailoring ability to meet the requirement for the demanding mechanical properties [199]. Research has shown that the flexural properties of the post-drawn nanofibers reinforced composites were further improved by increasing the fiber fraction. Because of their superb interface adhesiveness, polyacrylonitrile (PAN)–poly (methyl methacrylate) (PMMA), a core–shell nanofiber reinforced dental composites, has been studied. Due to this property, it has the potential to be used for crown bridge material and denture base resin in the clinic. Tensile properties and flexural properties of both nanofiber membranes and nanofiber reinforced bis-GMA/TEGDMA (tri-(ethyleneglycol)dimethacrylate) composites were also studied. Adding PAN–PMMA nanofibers into bis-GMA/TEGDMA clearly demonstrated the reinforcing effect. The flexural modulus (Ey), flexural strength (Fs), and work of fracture (WOF) increases as the nanofiber mass fraction increases from 0%, 0.6%, 0.8%, 1.0% to 1.2% [200]. Moreover, the addition of nanofibers could increase the storage modulus of the composite as a merit of high nanofiber strength, good nanofiber deposition, and strong interfacial bonding between the nanofiber and the matrix [201].

Clinically, the usage of PMMA denture is widespread. Generally, dentures suffer from tensile, compressive, and shear forces as well as the hazard of sudden drop,

which might cause denture base fracture [202]. Reinforcement of the PMMA denture base by adding inorganic filler is a strategy which aims to improve these properties [203]. To improve the base material itself, several materials have been used to repair fractured denture bases, including auto-polymerized, visible light polymerized, heat polymerized, or microwave polymerized acrylic resin [204, 205]. Most (86%) of denture base repairs are made by using auto-polymerized acrylic resin [206] because of its manageable properties; it is easily manipulated, fast setting, and therefore chair-side friendly [207]. Unfortunately, its strength compared to intact heat polymerized denture resin is only 18–81% [208, 209]. Metal oxide nanoparticles have recently been investigated. Additions of nano-zirconia (ZrO_2) to PMMA denture base have been reported to increase the transverse strength due to its small size and homogenous distribution [210]. Nano-ZrO_2 is a metal oxide and may be used as a reinforcement material to improve the transverse strength of denture base resin [211, 212]. Meanwhile, nano-ZrO_2 is regularly used as particle fillers, which possess excellent properties such as high strength, high fracture toughness, excellent wear resistance, high hardness, and excellent chemical resistance. ZrO_2, also being a typical bioceramic, shows great biocompatibility and bioactivity and possesses various desirable properties, such as excellent mechanical strength and toughness, resistance to corrosion and abrasion, and biocompatibility [203, 213, 214]. The nano form also has excellent mechanical properties, allowing it to endure against crack propagation. Moreover, it has the highest hardness among any oxide nanoparticles. Therefore, nano-ZrO_2 may be considered as a new approach for denture base repair. Meanwhile, reinforcement of acrylic denture base with nano-ZrO_2 significantly increases its transverse strength [215]. The nano-ZrO_2 resin resulted in significantly higher transverse strength as compared to unreinforced repaired resin [216]. But agglomerations of nano-scale particles often reach micrometer scales. The particles need surface modification to reduce clustering and improve their dispersion throughout the resin matrix. Left unchecked, this tendency can limit improvements to the mechanical properties and translucency of the composites. On the contrary, increases in the transverse strength is possibly attributed to the increased distribution of the nano-size particles, enabling better infiltration into the spaces between polymeric chains, thereby resulting in increased interfacial shear strength between the nanoparticles and the polymeric chains [215]. Moreover, the silane coupling agents used to treat the surface of nano-ZrO_2 could eliminate its aggregation and improve its compatibility with the polymer matrix [216]. The strong adhesion formed between the coupling agent on the surface of the nano-ZrO_2 and PMMA matrix improves the mechanical properties of the nanocomposites [203, 216]. Typically, it is used mechanically to reinforce polymers and improve the strength of the reinforced PMMA matrix [215, 217]. In regard to tensile strength, the group containing nano-ZrO_2 reinforced fillers showed a significant improvement over the control group (58.07 ± 3.14 MPa). Good adhesion and homogeneous dispersion of nanoparticles within a resin matrix improved the flexural properties of a polymer/nanoparticles composite [216]. Furthermore, the large interfacial area of the nanoparticles increases the contact area between the nano-ZrO_2 and PMMA, thereby improving mechanical interlocking and changing the properties of the ZrO_2/

PMMA nanocomposite, shown by an increase in the PMMA matrix ductility and plastic deformation [218–220]. A significant increase in the tensile strength was found with increase of nano-ZrO_2 levels (specifically 2.5%, 5%, and 7.5% of nano-ZrO_2). This outcome agreed with previous studies, which found that the addition of nano-ZrO_2 significantly increases the mechanical properties, and the two were positively correlated [221]. Therefore, the amount of filler used to reinforce the acrylic resin is another important factor in affecting the mechanical properties.

Determining how nanocomposites affect hardness and strength is also critical for potential clinical use. The result of a study showed that ZrO_2/PMMA nanocomposites achieved the highest surface hardness (19.97 ± 1.62 MPa) and flexural strength (87.37 ± 4.48 MPa) when 1.5 wt% nano-ZrO_2 was added, which achieved 23% and 12% increases, respectively, when compared to the pure PMMA. Another study shows that aluminum borate whiskers (ABWs) which were first developed in 1980s can offer superior mechanical properties at a low cost [196]. The ratio of nano-ZrO_2 and ABWs added to PMMA showed that it significantly influenced the surface hardness and flexural strength of ZrO_2-ABW/PMMA nanocomposites. Achieving maximum flexural strength (increased by 52% as compared to pure PMMA) required adding the optimum ratio of nano-ZrO_2 and ABWs to reinforce PMMA (adding 2% of nano-ZrO_2 at a ZrO_2 : ABW ratio of 1:2). Whereas, achieving maximum surface hardness (increased by 27% as compared to PMMA) required adding 3% of nano-ZrO_2 with the same ZrO_2/ABW ratio [222, 223].

Furthermore, patients require prosthesis that have good esthetics. The esthetics of a removable prosthesis is dependent on the appearance of the denture base on the patient's oral mucosa, which mainly depends on the translucency [224]. Therefore, good optical properties of PMMA reinforced with inorganic fillers are vital. The filler reinforcements permitted by PMMA (Fig. 3.6) [225] may influence its translucence and, consequently, the overall esthetics. Attempts to improve PMMA properties were explored through the incorporation of filler particles (zirconia, alumina, glass, silica, fiber, tin, and copper) [226]. The translucency property of the material results from the color difference between the thickness of the examined material over a white background and the same uniform thickness of that material over a black background. Nano-ZrO_2, a material possessing a white color, has received considerable consideration because it is less prone to alter the esthetics as compared with other metal oxide nanoparticles as well as maintain excellent biocompatibility [214, 216]. As the nano-ZrO_2 concentration increased, however, translucency was reduced and therefore adversely affected. Therefore, the selection of an appropriate concentration is critical in both establishing enhanced mechanical properties of the reinforced PMMA denture base and maintaining proper esthetics.

Previous reports indicated that the rough surfaces and hydrophobic properties of oral bacteria help it to readily adhere to the surfaces of dentures. More concerningly, *C. Albicans* shows resistance to conventional antifungal medications, rendering denture stomatitis to be a major challenge for oral treatment [227]. The development of denture stomatitis hinges on the adherence of *C. albicans* to denture base resin surfaces, followed by biofilm formation. Hence, increasing the antifungal

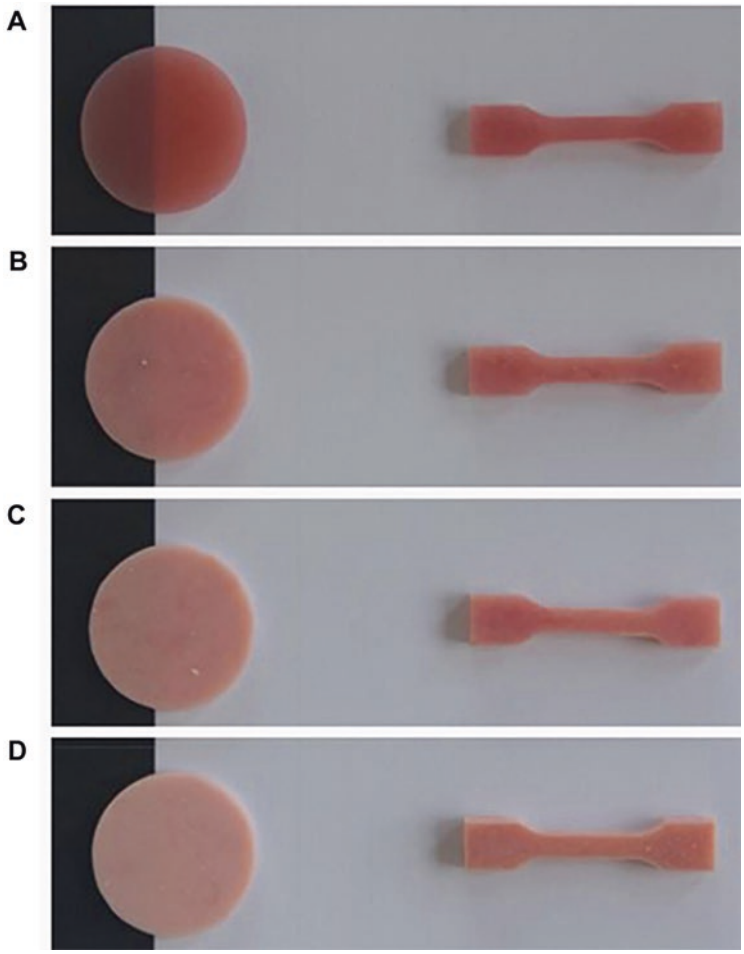

Fig. 3.6 The disc specimens are prepared for translucency tests while the dumbbell specimens are used for tensile strength test. Based on the reinforcement can be characterized as (**A**) unreinforced specimen ($n = 20$), reinforcement of the acrylic resin specimens with (**B**) 2.5% nano-ZrO_2 ($n = 20$), (**C**) 5% nano-ZrO_2 ($n = 20$), and (**D**) 7.5% nano-ZrO_2 ($n = 20$), nano-ZrO_2, zirconium oxide nanoparticles [225]

activity in denture base resins and controlling *C. albicans* adhesion and biofilm formation might efficiently control the occurrence of denture stomatitis [228, 229].

The colonization of oral fungi on denture soft lining material can result in infections and stomatitis of oral tissues. An in vitro study has confirmed that silver nanoparticles [230, 231] used as additives in denture base acrylic resins and tissue conditioners show antimicrobial effects. To incorporate these antimicrobial properties, a method was developed to integrate silver nanoparticles into silicone soft lining materials. Confirmation of fungicidal activity for these composites was established by Chladek et al. [232]. In another study, they showed that the

mechanical properties of nanocomposites reinforced by AgNPs decreased as the AgNP concentrations increased [233]. Levels from 0 to 200 ppm of AgNPs were incorporated as an antimicrobial agent into composites to reduce the microbial colonization of lining materials. Increases in the nano silver concentration resulted in increases in solubility and sorption, decreases in hardness and bond strength, and a change in the failure type for the samples. Ideally, AgNP concentrations from the 20 to 40 pm range achieve the best combination of bond strength, hardness, solubility, and sorption was achieved. Introducing AgNPs into Ufi Gel SC (UG) soft liner material also prolonged the sample cross-linking timing. As AgNP concentration increased in these composites, the cross-linking time required increased as well: at 40 ppm cross-linking took 15 min longer than that of UG, but at 80 ppm required approximately 40 min longer. Composites with AgNP concentrations up to 40 ppm presented properties that were no worse than those of the UG liner material. At these concentrations, the composites conform to the ISO standard requirements for soft lining materials (the bond strength after 24 h of soaking in distilled water, values over 1 MPa were observed in at least 8 out of the 10 samples). Starting at the 80-ppm concentration, the hardness and tensile bond strength of the composites were greatly reduced, while the absorption and solubility increased due to problems associated with the cross-linking of the composites. Although materials with a silver nanoparticle concentration of 80 ppm were classified as extra soft, they did not meet the ISO standard requirements.

Nano-ZrO_2 particles have received a great attention due to their attractive scientific, technological, and medical potentials [209]. They were also found to possess remarkable antimicrobial and antifungal effects. The antifungal effect of nano-ZrO_2 incorporated into PMMA removable prosthesis was investigated and found that it had the capability to reduce the candida counts. The antibacterial activity of nano-ZrO_2 might be attributed to active oxygen species, which in turn causes a disruption of the cell membrane of microorganisms [234]. The addition of nano-ZrO_2 to room temperature cured acrylic resin is an effective method for reducing *Candida* adhesion to polymethyl methacrylate (PMMA) denture bases and room temperature cured removable prosthesis. This is the reason why nano-ZrO_2 can actively inhibit the growth of fungal strains by interfering with cell function and causing deformation in fungal hyphae [235]. However, to fabricate a PMMA/nanocomposite that holds antimicrobial properties without affecting the physical and mechanical properties, adequate concentrations of nano-ZrO_2 should be used. The incorporation of nano-ZrO_2 in denture bases and PMMA removable prostheses is a possible way to prevent denture stomatitis [234].

Four potential inorganic antibacterial agents ((titanium dioxide (TiO_2), titanium dioxide supported by silver (Ag/TiO_2), zirconium phosphate supported by silver (Navaron), and tetrapod-like zinc oxide whiskers (T-ZnOw)) were investigated by Chen RR to determine their mechanical behaviors, antibacterial activities against oral microorganisms, and cytotoxicity [236]. The TiO_2, Ag/TiO_2, Novaron, and T-ZnOw of 3 wt% were mixed with the composites, respectively. The 3 wt% additions of various antibacterial agents had significant antibacterial activities compared to the control and blank group. Compared to the other groups, the T-ZnOW and

Novaron groups displayed higher antibacterial property against both bacteria. Adding 3% of TiO_2, Ag/TiO_2, Novaron, and T-ZnOw antibacterial agents showed a respective 30.26%, 67.82%, 61.69%, and 49.81% antibacterial rate against *S. mutans*, whereas the antibacterial rate was a respective 21.63%, 50.16%, 50.16%, and 37.62% against *C. albicans*.

The type of antibacterial agent is important to affect the composite properties. Quaternary ammonium salts are the most widely used organic antimicrobial agent before the application of nanomaterials. Recently, there are also many studies about the quaternary ammonium antimicrobial monomer usage in methyl methacrylate-based resin systems. Quaternary ammonium salts not only have desirable antimicrobial properties comparing to other antimicrobial agents but also have the added advantages of good permeability, low toxicity, minor skin irritation, stable performance, low light corrosion, and long-lasting biological effects. Therefore, they have been widespread in multiple industries and other fields [237, 238]. Researchers are expected to obtain durable antimicrobial properties by incorporating quaternary ammonium salts into a methyl methacrylate-based resin system to prevent denture stomatitis [239, 240]. A few studies have reported that denture base resins have antimicrobial activity when silver ions or quaternary ammonium antimicrobial monomers are added [241–244].

Nano poly(4-vinylpyridinium) (NPVP) is a nano-modified cationic surfactant, which can be used as antistatic agent, fungicide, etc. The poly(4-vinylpyridinium) (PVP) is used in synthetic resin coatings, which can improve the peel resistance and weather resistance. A study evaluated the antimicrobial activity of the quaternary ammonium grafted AgBr nanocomposite (AgBr/NPVP), a newly developed organic–inorganic composite antimicrobial agent, as compared to unpolymerized AgBr/NPVP and modified room temperature-cured denture base resins, against *C. albicans*. The research also confirmed that the silver ions which pass through the cell walls could interfere with cell membrane continuity (Fig. 3.7), increase cell permeability, and affect the metabolism and respiration of microbes [245–249]. Statistical analysis showed that the negative control and blank control groups had a large amount of fungal growth. The control group revealed no antifungal activity, but at the 0.1, 0.2, and 0.3 wt% dosage of AgBr/NPVP, the PMMA resin antifungal ratios were (78.22 + 1.90) %, (82.58 + 2.35) %, and (97.82 + 2.05) %, respectively, before aging (Fig. 3.8). Therefore, higher doses of AgBr/NPVP revealed significant increases in the antifungal activity of the PMMA resin. Alternatively, quaternary ammonium salts could inhibit the free movement of microbes and their breathing by attracting the negatively charged cell membrane in so-called contact killing. Quaternary ammonium salts and silver ions could exert strong antifungal effects, which have an important role in denture base.

Large-area mucosal supported denture (full denture, distal-extension absence of teeth denture, implant over-denture, etc.) continues to have issues such as insufficient retention, pain from biting, and general discomfort: all of which causes patient dissatisfaction. Traditionally, the soft lining material can only be a temporary or semi-permanent material because of the loss of softness and elasticity with time, and the failure of the bond and the difficulty of maintaining the cleanliness are due

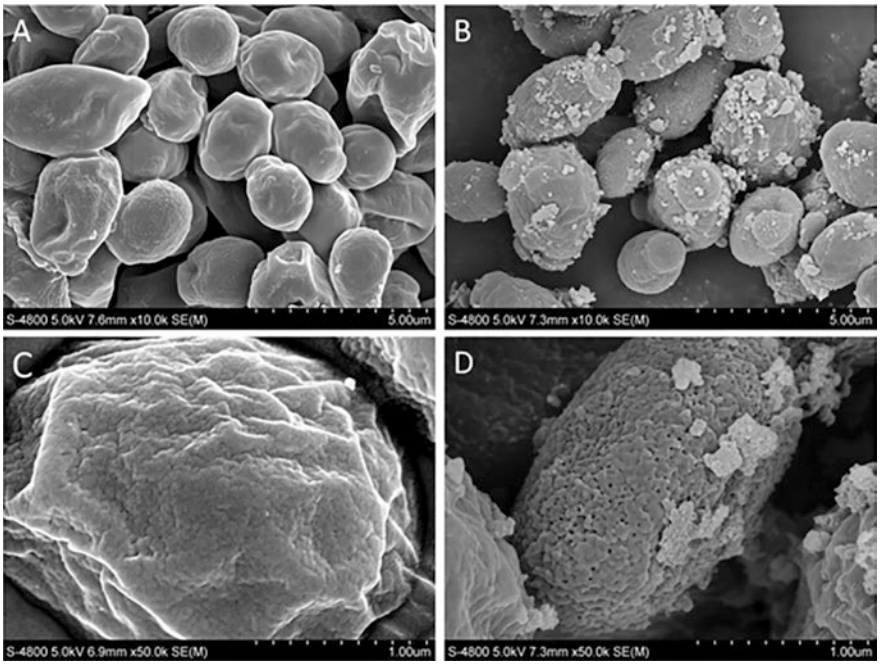

Fig. 3.7 The morphology of *C. albicans* ATCC90028 as displayed through field emission scanning electron microscopy (Fe-SEM) images after 24 h. Incubation (**A**, **C**) of *C. albicans* ATCC90028 normal morphology. (**B**, **D**) Morphology of *C. albicans* ATCC90028 after 24 h. Incubation with AgBr/NPVP suspensions (1 × MFC) [178]

to the easy adhesion of microbes. Therefore, the design and manufacture of rubber resin materials with different hardness values and rigid resin materials are urgently needed. The future trend is to explore the rubber-based resins with optimal oral mucosal tissue compatibility, the proportion of rubber-based resins to rigid resin materials which represents the thickness of "soft/hard" ratio. The "soft" rubber resin material is used as the base surface to contact the oral mucosa and the "hard" rigid resin material as the smooth surface which is exposed in the oral. The soft tissue surface has advantages in retention and can buffer and reduce local stress, which can greatly alleviate pain under masticatory force. The rigid surface has the advantages of increasing strength and stiffness, leading to a smoother and cleaner denture surface.

Therefore, the future trend is the application of nanotechnology to realize an ideal combination of soft and hard rubber resin material: (1) Nanotechnology to develop soft rubber resin material, (2) nanotechnology to develop hard rubber resin material, and (3) nanotechnology to combine soft with hard rubber resin material.

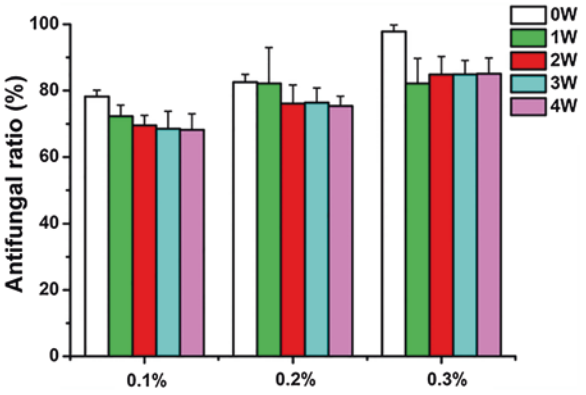

Fig. 3.8 Histogram of the antifungal ratio of PMMA resin. Each value is the mean ± SD ($n = 9$). The control group revealed no antifungal activity. As AgBr/NPVP increases, the antifungal activity of unaged PMMA resin also increases, with significant differences ($p < 0.017$) among the groups. Compared with corresponding unaged groups, the antifungal ratio at 1-week aging groups was less, especially at the 0.3 wt% group. However, the antifungal ratio for each group stabilized after 2 weeks of aging, with the 0.3 wt% group showing the best antifungal effect, achieving more than 80% [178]

3.2 Nanotechnology in Oral Tissue Regeneration

The oral and maxillofacial region refers to the complex area from the cranial base to the mandible, which includes oral organs (teeth, lip, tongue, etc.), facial soft tissue, maxillofacial bones (maxilla, mandible, etc.), temporomandibular joints, etc. Tissue defects of oral and maxillofacial regions are of high incidence due to inflammation, trauma, tumor, and atrophy after tooth extraction or a variety of genetic disorders such as cleft lip and palate, and hereditary dentine disorders (type 1). Reconstruction of these damaged tissues and organs is quite challenging due to their intricate structures, diverse functions, and highly esthetic requirements. Among many methods (e.g., autografts) to tackle these challenges, oral tissue engineering is a promising approach, which has been developed in the last three decades.

Tissue engineering focuses on the development of biological constructs to restore the function of damaged tissues and organs. The defects in oral and maxillofacial regions can also be treated by this method. There are three key factors in tissue engineering: scaffolds, seed cells, and growth factors. To date, numerous improvements have been performed to enhance tissue regeneration. Among them, nanotechnology has been applied to fabricate high-performance scaffolds with tunable physical, chemical, and biological properties, to label and track seed cells, and to deliver gene, drugs, and growth factors. Therefore, nanotechnologies and nanomaterials are of great potential to enhance oral tissue regeneration.

3.2.1 Nanotechnology to Improve Stem Cells

Stem cells are undifferentiated cells with the ability to self-replicate throughout life and to differentiate into multiple specialized cell types. Human stem cells can be found in various tissues of both epithelial and mesenchymal origin, including skin, adipose tissue, periosteum, cartilage, and teeth. Stem cells are of great importance to be applied in tissue/organ regeneration owing to their various potentials, such as (1) differentiation potential: stem cells can give rise to myogenic, adipogenic, osteogenic, and chondrogenic mesodermal lineages; (2) migration and homing capacity: stem cells can migrate to inflammation sites and injury sites under a variety of pathologic conditions; and (3) secretory ability and immunomodulatory functions: stem cells can secret a variety of paracrine and autocrine factors as well as extracellular vesicles, affect almost all cells involved in innate and adaptive immune reaction by secreting factors and cell–cell contact.

However, there are still limitations in widening the applications of stem cells. How to get isolated and purified stem cells quickly and effectively? How to achieve controllable and sustained release of bioactive molecules? How to obtain highly sensitive, real-time, noninvasive, in vivo stem cell tracking? And so forth. These problems are urgently needed to be solved. Fortunately, several techniques, such as genetic and epigenetic modifications, and nanotechnology have been performed to achieve wider application of stem cells in regenerative medicine.

Genetic modification has been generally regarded as one of the promising approaches to modify stem cells which will alter the secretion of some crucial proteins (such as cytokines and growth factors) by changing the expressions of related genes. It offers a promising potential for stem cell-based therapies. Therefore, numerous clinical benefits could be obtained. Currently, numerous viral and non-viral gene delivery techniques have been applied to deliver genes in an optimal manner for specific requirements. Just as its name implies, viral methods use virus as vectors (adenoviral vectors, retroviral vectors, and lentiviral vectors) for gene delivery. The advantages of viral methods are high transduction efficiency and long-term gene expression. However, their application is still limited due to some disadvantages, such as toxicity, immunogenicity, carcinogenicity, poor target cell specificity, high costs, and inability to transfer large size genes [250]. On the other hand, non-viral methods can be classified as physical, chemical, and inorganic nanoparticles techniques. The physical techniques include microinjection, electroporation, sonoporation, and so forth. The chemical techniques generally use cationic lipids or cationic polymers as vectors. The inorganic nanoparticle techniques involve the application of inorganic nanoparticles, which will be discussed here. The non-viral methods have been confirmed to be safe, easy to prepare, and are able to transfer large-sized genes. In addition, non-viral vectors can be modified with tissue- or cell-specific ligands for target gene delivery [251]. However, these vectors do not always lead to favorable transfection efficacy and transient transgene expression of non-viral gene delivery methods has limited their application. In addition to

genes, various micro RNAs (miRNAs) or small interfering RNAs (siRNAs) have recently been delivered into stem cells by viral or non-viral delivery systems.

Besides, epigenetic modification can also help adjusting the secretion of vital factors and proteins of stem cells. However, the gene sequence of stem cells stays unchanged after epigenetic modification. Epigenetic control is known to play a major role in transcriptional regulation of gene expression. DNA methylation and histone modification (acetylation/deacetylation) are classical control mechanism of epigenetics. It has been reported that inhibition of DNA methylation with DNA demethylating agent in human MSCs could improve their immunoregulatory capability and affect their differentiative capacity for therapeutic applications [252]. However, the epigenetic control mechanism for stem cells remains unclear. It is difficult to explain when controversial results were obtained using the same epigenetic control technique (e.g., DNA methylation) in different types of cells. This also limits the application of epigenetic modification in stem cells.

Compared with genetic and epigenetic modifications, nano modification in stem cells may provide a new sight. The application of nanotechnology on stem cells can be mainly classified into following fields: (1) separating and purifying stem cells; (2) labeling and tracking stem cells; (3) transferring biomolecules (gene, drug, growth factors, and so forth) into stem cells; (4) mimicking extracellular matrix (ECM) to promote the proliferation and differentiation of stem cells. The combination of nanotechnology with stem cells showed great potentials. For instance, stem cells can be easily separated via integrating with specific antibodies loaded on magnetic nanoparticles under magnetic field, which belongs to magnetic cell separation (MCS) techniques [253]. MCS techniques are effective and specific for stem cell separation and purification. Its advantage lies in that the application of magnetic nanoparticles (MNPs) can reduce the damage to stem cells due to their nano size compared with magnetic microparticles (such as neodymium and iron oxides). Besides, after human stem cells endocytose magnetic and/or fluorescence-labeled nanoparticles, noninvasive, and biosafety tracking stem cells can be realized both in vitro and in vivo. And it can provide important information for evaluating the efficacy of stem cell therapy. In addition, nanoparticles have shown potential as non-viral vectors for gene and drug delivery and growth factors release. Generally, nanoparticle vectors have several advantages, such as bio-safety, low immunogenicity, and good cell target specificity. And the released growth factors may influence the cell signaling pathway (such as MAPK/p38/AKT pathway and Wnt/â-catenin pathway) and regulate osteogenesis and angiogenesis in bone tissue engineering (Fig. 3.9). Furthermore, some nanomaterials, possessing similar nanostructure to natural extracellular matrix (ECM), showed the potential to enhance stem cells adhesion, migration, proliferation, and differentiation. In summary, it is of great potential to improve the stem cells using nanotechnology which can strongly promote the application of stem cells in tissue engineering.

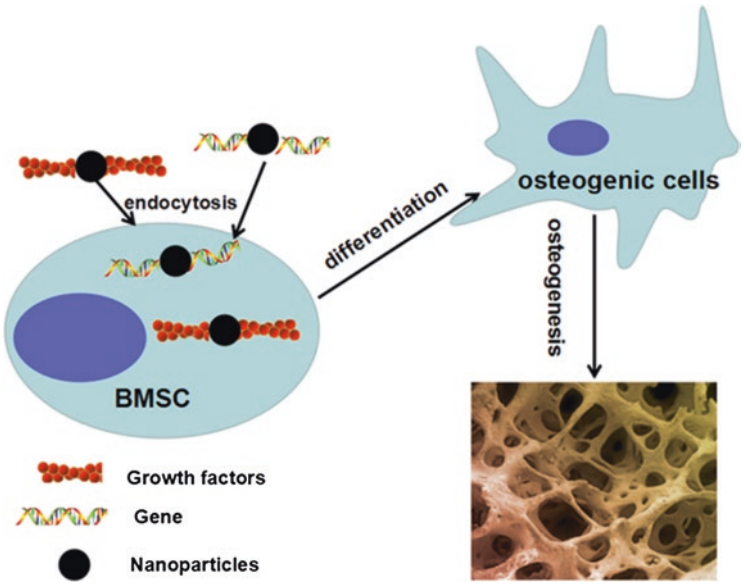

Fig. 3.9 The delivery of osteogenic gene and growth factors via nanoparticles for stem cells to promote osteogenesis

3.2.2 Nanotechnology and Dental Stem Cells

A tooth consists of the enamel, dentin, cementum, and dental pulp (composed of cells, fibers, nerves, blood vessels, and lymphatic vessels). After root development and cementum mineralization, the tooth fastens to the surrounding alveolar bone via the periodontal ligament (PDL), which contains a variety of cells such as fibroblasts, endothelial cells, and epithelial rests of Malassez (ERM) as well as extracellular matrix (ECM).

Dental mesenchymal stem cells (MSC) have been isolated from different locations within adult or post-natal dental tissues, such as the pulp of adult teeth (dental pulp stem cells, DPSCs) and deciduous teeth (stem cells from human exfoliated deciduous teeth, SHEDs), the apical part of dental papilla (stem cells from the apical papilla, SCAP) and the PDL (periodontal ligament stem cells, PDLSCs) (Fig. 3.10). These stem cells are often characterized by their ability to differentiate into the odontogenic, adipogenic, chondrogenic, or osteogenic lineages in vitro or to regenerate dental tissues in vivo. Currently, DPSCs are the most popular cells applied in oral tissue engineering among these dental stem cells due to their wide source and easy isolation. Besides, PDLSCs and SCAP also have been widely used. All these dental stem cells can be modified by nanotechnology.

DPSCs can be labeled by MNPs incorporated with growth factors to achieve patterned cell sheets and enhanced bone regeneration. For example, Zhang et al. designed new Fe_3O_4 MNPs coated with nanoscale graphene oxide (nGO-Fe_3O_4) to

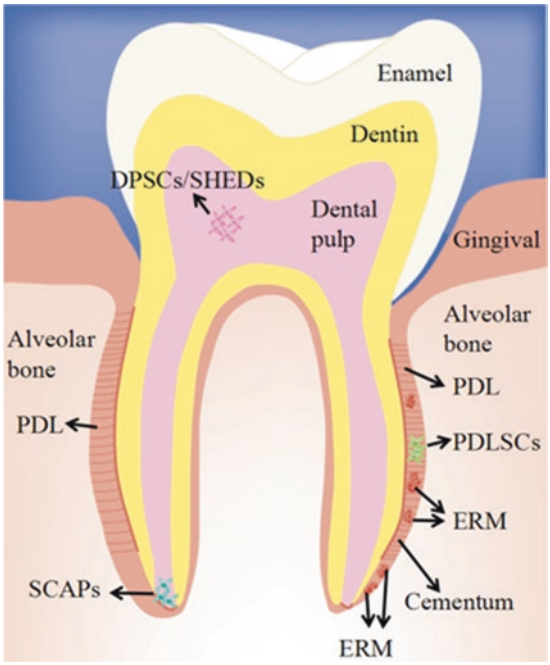

Fig. 3.10 The various dental stem cell populations within an adult human tooth. (*DPSCs* dental pulp stem cells, *ERM* epithelial cell rest of Malassez, *PDL* periodontal ligament, *PDLSCs* periodontal ligament stem cells, *SCAPs* stem cells from the apical papilla, *SHEDs* stem cells from human exfoliated deciduous teeth) [254]

label DPSCs and deliver BMP2 or TGF-â3 [255]. The nGO-Fe_3O_4 was easily swallowed by DPSCs, and these labeled DPSCs were cultured to form cell sheets. Cell sheet technology has been recently used in tissue engineering to repair tissue defect. The cell-sheet constructs, without restriction from the scaffolds, are largely maintained by the formation of cell-to-cell junctions and secretion of ECM proteins. Thus, these cell-sheet constructs are similar to the natural tissue compositions. To incorporate osteogenic growth factors into the cell sheets, the nGO-Fe_3O_4 were employed (Fig. 3.11). On the one hand, nGO-Fe_3O_4 MNP uptake into cells makes them controllable by magnetic force. On the other hand, the GO coating creates protein immobilization sites, allowing growth factors to be both incorporated into cell sheets and magnetically controlled. The arranged magnet can modulate the shape of the cell sheets with the help of nGO-Fe_3O_4 MNP. Therefore, the magnetic force can control the nGO-Fe_3O_4 MNP-labeled DPSCs precisely and prepare multilayered cell sheets with different patterns. Furthermore, the incorporation of BMP2 or TGF-â3 enhanced the osteogenic or chondrogenic differentiation of DPSCs. Given that the nGO-Fe_3O_4 nanocomposites provide a novel magnetically controlled vehicle to construct protein-immobilized DPSC sheets, other types of stem cells and growth factors can also be hired to form another kind of nanocomposite in tissue engineering. Thus, nanotechnology exhibits promising potential for future use in regenerative medicine.

Generally, there are two classical types of non-viral vectors, cationic lipids, and cationic polymers. However, sometimes, complex transferring protocols and

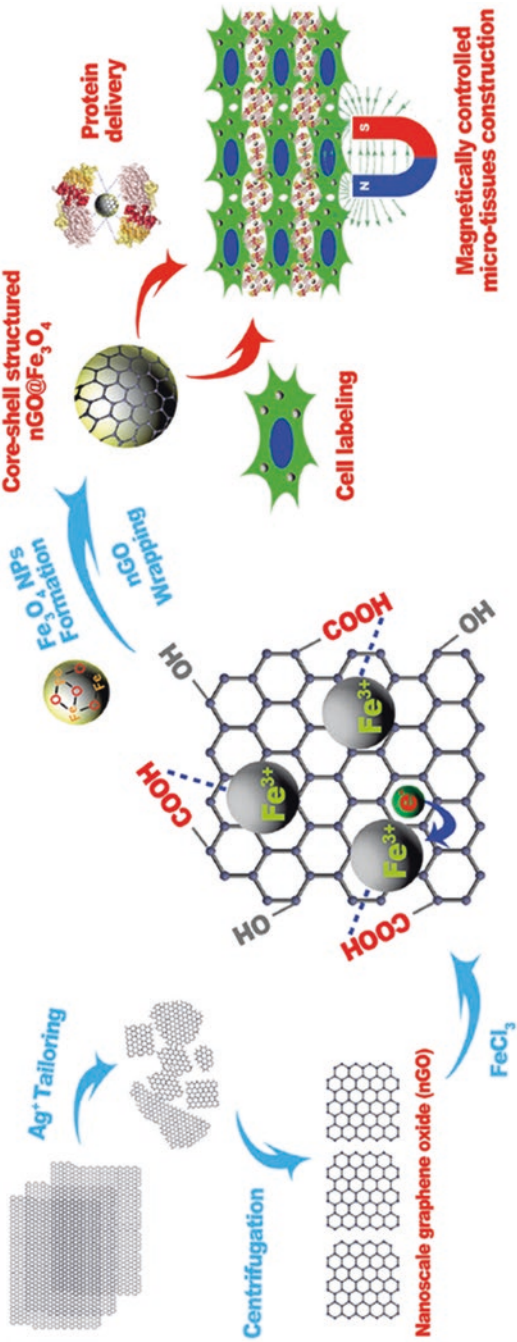

Fig. 3.11 Schematic illustration of the preparation of the nGO-Fe_3O_4 MNPs and application of these MNPs for magnetically controlled growth-factor-immobilized multilayer cell-sheet fabrication [255]

inefficient nuclear uptake of the two vectors may decrease the transfection efficacy. Comparatively, nanoparticles, which can be easily internalized by the cells, have been used as an alternative for gene delivery. For example, calcium phosphate nanoparticles, fabricated by Yang's et al. [256], were used for *hBMP2* gene delivery in rat DPSCs. These nanoparticles were less than 100 nm in diameter and can be easily taken up through endocytosis. And the DNA encapsulated in calcium phosphate nanoparticles was protected from the external DNase environment, which was benefit for DNA survival. Furthermore, it has been confirmed that calcium ions play an important role in endosomal escape, cytosolic stability and enhance nuclear uptake of DNA through nuclear pore complexes [257]. Although Lipofectamine (a kind of cationic lipid vectors used in Yang's study)-mediated cells were shown to produce higher *hBMP2* levels in the initial 4 days, the nanoparticles mediated cells reached higher levels at later time points. Furthermore, in Yang's study, the nanoparticles mediated *BMP2* gene transfected rat DPSCs (referred as NP-DPSC group), or untreated DPSCs were cultured on a fibrous 3D titanium mesh. The gene expression of dentin sialophosphoprotein (DSPP) and dentin matrix protein-1 (DMP-1) was increased in NP-DPSC group than that in untreated DPSC group. DSPP and DMP-1 proteins are two specific proteins which play a major role during dentin mineralization. These results revealed that the BMP2 secreted from the NPs-transfected rat DPSCs reached a functional level and helped to promote the odontogenic differentiation and matrix mineralization of cells. Therefore, nanoparticles were confirmed to be effective non-viral vectors for *BMP2* gene delivery and can be applied to improve the efficacy of DPSCs for odontogenic differentiation and hard tissue engineering.

Gene delivery via viral or non-viral vectors is not the only way for gene therapy. A novel type of three-dimensional nanomaterials, tetrahedral DNA nanostructures (TDNs), have garnered increasing interest and attention in biomedicine. Under certain conditions, self-assembly of the tetrahedral nanostructure by complementary base-pairing can be generated from four DNA single strands with preset programmable base sequences. Given that the original DNA is difficult to be taken up by cells without the assistance of relevant auxiliary agents, it is simple and direct for TDNs to be transported into cells by endocytosis. Therefore, the TDNs has been extensively applied in bioimaging, molecular transport, drug delivery, and molecular diagnosis due to its simple synthetic method, high yield, high stability, excellent biocompatibility, fast degradation, and low toxicity. Zhou et al. synthesized TDNs and co-cultured with DPSCs in vitro [258]. The results proved that TDNs can be successfully delivered into DPSCs without the assistance of other transfection reagents. Furthermore, TDNs can promote the proliferation and osteo/odontogenic differentiation of DPSCs by upregulating the expression of related genes and proteins. As the classical Notch signaling pathway has been confirmed to regulate the osteo/odontogenic differentiation of DPSCs by various studies, the authors also tried to explore its involvements. Their results demonstrated that proliferation and differentiation of DPSCs was driven by TDNs via activating the classical Notch signaling pathway. Therefore, the TDNs, as novel 3D DNA nanomaterials, have the

potential to be a promising and remarkable alternative approach for DPSCs-based tissue regeneration.

In addition to DPSCs, other dental stem cells like PDLSCs and SCAP also have been combined with nanomaterials and widely applied in recent decades. For example, Shrestha et al. synthesize dexamethasone (Dex)-loaded chitosan nanoparticles (CSnp) to obtain sustained release of Dex by encapsulation (Dex-CSnpI) and adsorption (Dex-CSnpII) methods [259]. The SCAPs were then co-cultured with CSnp, Dex-CSnpI, or Dex-CSnpII, and the expression of odontogenic differentiation related gene (alkaline phosphatase (ALP), DSPP, DMP-1) was evaluated. Results showed that Dex-CSnpII had faster release of Dex compared with Dex-CSnpI, but both demonstrated sustained release of Dex for 4 weeks. The sustained release of Dex resulted in enhanced odontogenic differentiation of SCAPs.

Niu et al. explored the effect of gold nanoparticles (GNPs) on human PDLSCs [260]. GNPs are attractive in regenerative medicine due to their unique physical and chemical properties. They have many prominent advantages such as excellent biocompatibility, facile synthesis method, and easy functionalization with biomolecules including growth factors, DNA, and peptides. They can promote osteogenic differentiation and inhibit adipogenic differentiation of mouse MSCs via activating the p38 mitogen-activated protein kinase (MAPK) pathway [261] and inhibit osteoclast formation of bone marrow-derived macrophages via downregulating the receptor activator of the nuclear factor-êB (NF-êB) ligand pathway. Therefore, GNPs have been developed as a new generation of osteogenic agents for bone tissue regeneration. In Niu's study, they treated PDLSCs with GNPs, and the cellular effects on the osteogenic differentiation of PDLSCs and the associated signaling pathways in cell differentiation were investigated. The results suggested that GNPs enhanced the osteogenic differentiation of human PDLSCs partially via activation of the p38 MAPK signaling pathway. This was consistent with the results of Yi et al. [261], and the two studies demonstrated that GNPs can affect stem cells via regulating signaling pathway.

Therefore, nanotechnology exhibits promising potential in modifying stem cells for application in oral tissue engineering.

With the fast development of medical technologies, the implant-supported dentures have been widely used as a restoration method to treat patients with lost teeth. However, the quality and quantity of bone at the implant site is usually unfavorable to achieve an ideal position and esthetics due to excess alveolar bone loss caused by inflammation, trauma, and physiologic atrophy. There are various methods for alveolar bone augmentation, including guided bone regeneration (GBR), sinus floor elevation, bone splitting, onlay graft and distraction osteogenesis, and so forth. GBR is regarded as the most commonly used methods by the patients due to the minimal trauma and pain among these methods.

GBR is a surgical procedure involving the use of guided bone regeneration membranes with bone grafts or bone substitutes (Fig. 3.12). A GBR membrane is placed into the surgical site, acts as the barrier to prevent fibrous connective tissue infiltration, and provides a more suitable local environment for bone regeneration. Besides, bone substitutes with osteoinductivity and/or osteoconductivity are placed under the

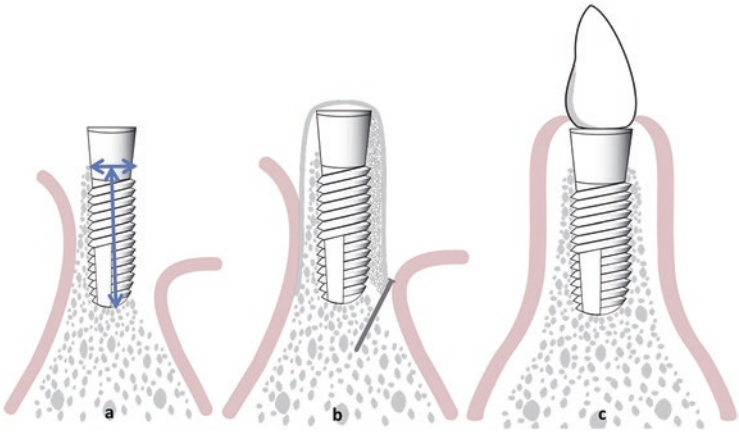

Fig. 3.12 (**a**) An adequate bone volume (height and width) is a prerequisite for successful implant treatment. (**b**) Barrier membrane and bone graft as bone substitute materials are placed to accelerate bone formation. (**c**) Final prosthesis is fabricated after the formation of new bone [262]

GBR membrane to maintain space and enhance osteogenesis. Generally, one face of the membrane is smooth to prevent the ingrowth of soft tissue, the opposite face is porous to allow the attachment and growth of osteogenic cells. And the integrity of the membrane also plays an important role in maintaining space in which the bone substitutes can be replaced by new bone and blood vessels. Both occlusive membranes (also called as GBR/GTR membranes) and bone substitutes are important for GBR and bone augmentation.

Recently, nanotechnology and nanomaterials have been applied to improving the structure and mechanical property, which is important for barrier membranes and bone substitutes.

GBR membranes are mainly divided into two types: resorbable and non-resorbable. Generally, clinicians and patients prefer the resorbable ones which do not need a second surgery. However, current resorbable membrane products still have some problems such as low osteoinduction and insufficient mechanical properties. Nanotechnology has been applied to overcome these limitations, such as insufficient mechanical strength, and poor osteoinduction.

The nanostructure of membrane surface mimic the architecture of a natural ECM and provide favorable micro-environments to improve the biological activity (such as adhesion, proliferation, odonto/osteogenic differentiation, and biomineralization) of dental stem cells and osteogenic cells.

Bachhuka et al. evaluated the role of surface nanotopography on the fate of human DPSCs (hDPSCs) [263]. They utilized density gradients of GNPs to examine, on a single substrate, the influence of nano-feature density and size on stem cell behavior. The density gradients of nanotopography were generated as follows: (1) 13 mm round coverslips were first coated with a 20-nm thin layer of plasma polymerized allylamine (AApp). (2) The modified coverslips were then immersed in a

rate-controlled fashion in a solution of GNPs of three different sizes (16, 38, or 68 nm) using a dip coating method [264]. Using this technique, the authors successfully controlled the contact time of every sector of the gold nanoparticle solution and the AApp-coated surface, resulting in nanoparticle density gradients along the surface. By using a predetermined size of the immobilized nanoparticles (16, 38 or 68 nm), the authors not only controlled spacing between nanoscale features but also generated surface nanotopography of controlled height. However, these substrates present not only variation in nanotopography but also difference in chemical composition. The underlying AApp coating is rich in amine/nitrogen while gold nanoparticles carry carboxyl acid groups on the surface. Previously, the authors demonstrated that AApp films of 5 nm are continuous and pinhole free. Thus, they provide uniform surface chemistry across the surface [265] and were able to uniquely tailor the outermost surface chemistry by overcoating the nanoparticle density gradients with a 5-nm AApp films. As a result, the GNPs were randomly distributed with an increase in nanoparticle density from region 0–12 mm (namely 0, 3, 5, 7, 10, 12 mm) and did not form aggregates. The hDPSCs cultured on GNP gradient coverslip were performed differently with changes in nanotopography. Results showed that the number of adhered DPSCs was higher, and cells proliferated faster on the sections of the gradients at certain density (e.g., 12 mm) of nanotopography features. Furthermore, greater surface nanotopography density (12 mm) could direct the differentiation of hDPSC to osteogenic lineages proving by the results of ALP staining and *ALP* gene expression. Besides, GNP diameters of 16 nm were most effective in promoting cell attachment, proliferation, and differentiation than those of 38 and 68 nm when the nanotopography density was the same among all groups. Though the mechanism was still unclear, this study provided new sight in designing the surface of biological membrane or scaffolds.

The incorporation of nano component, especially nano-hydroxyapatite (nHA), can improve the mechanical properties of GBR membranes. For example, Zeng et al. prepared new nano-hydroxyapatite/poly (vinyl alcohol) (nHA/PVA) composite membranes by solvent casting and evaporation technique. They found that the surface of composite membranes was biocompatibleand that nHA and PVA are distributed uniformly when the content of nHA is less than 20 wt%. Interestingly, the addition of nHA particles can increase the compressive strength, reduce the tensile strength and the elongation rate, and increase the Young's modulus of this composite membrane, which makes it easier for clinical practice in GBR [266].

In addition to GBR membrane, bone substitute material is another key point for GBR. Desired bone substitutes should have a 3D architecture and can promote osteogenesis and angiogenesis by allowing host osteogenic cells and vascular endothelial cells to adhere and migrate into the inner part. Furthermore, ideal bone substitutes should also possess suitable biodegradability, good biocompatibility, appropriate biomechanical strength, and beneficial osteoinduction. However, the integration of current bone substitutes with host bone suffers from long-term inefficiency due to their low osteoinductivity.

Generally, the bone substitutes are classified into three types: natural polymers, synthetic polymers, and inorganic ceramics. Natural polymers, including

fibrinogen, collagen, and polysaccharides such as alginates, chitosan and cellulose, hold similar structure as bone ECM, which are desirable to be free of immune reactions. Furthermore, as polysaccharides degrade rapidly, they could be used as porogens in composites. Synthetic polymers (such as poly(å-caprolactone) and poly(lactic-co-glycolic acid) (PLGA)) exhibit reasonable characteristics such as porosity, reproducible mechanical, physicochemical, and degradation properties, which can be modified for specific biomedical applications. Inorganic ceramics (like bioglass, tricalcium phosphate (TCP), HA, CPC, etc.) are utilized to provide a biochemical structure to enhance the osteoinductivity. However, insufficient mechanical strength, low supply, and high cost of natural polymers impede their use as bone substitutes. Besides, low osteointegration (which is due to the lack of endogenous vascular network) and lack of surface bioactivity are the main obstacle of applying synthetic polymers and ceramic scaffolds.

To design and fabricate functional bone substitutes, different nano-based strategies are employed. For instance, nanotopography can be achieved by nanoscale fabrication methods to produce nanometer features and patterns on the surface of current bone substitutes to mimic bone ECM which can guide and improve the osteointegration of bone substitutes with the native bone tissue. Besides, nanomaterials, incorporated into bone substitutes, can be used as nanocarriers to regulate the sustained release profile of biological macro-molecules and growth factors which are benefit for bone regeneration and vascularization. In addition to nanocarriers and nanocoatings, different fabrication methods such as electrospinning are used to provide 3D nanoporous structure for bone regeneration. Furthermore, the addition of MNPs, such as superparamagnetic iron oxides (SPIONs), has been proved to enhance bone regeneration by improving cell proliferation and osteogenic differentiation via activating MAPK/ERK signaling pathway [267]. There are several hypotheses to explain why the MNP-added biomaterials can stimulate cell proliferation and differentiation. One hypothesis proposes that every magnetic nanoparticle in the scaffold performs as its own nanoscale-level magnetic domain to induce micro-motions between the cell and scaffold interface, which in turn possibly affects the cell membrane ion channels, triggers the mechanotransduction pathway, and leads to enhanced cell proliferation and differentiation [268].

Surface topography of the bone substitutes is one of the major factors which can affect the osteointegration. To enhance the osteointegration, the surface of bone substitutes should trigger specific cellular responses. With the help of nanotechnology, the pore size and porosity of bone substitutes can be made more suitable to facilitate cell seeding, adhesion, migration of cells, vascular ingrowth, and tissue regeneration. Besides, the incorporation of bone substitutes with nanoparticles can lead to the increase of hydrophilicity and enable the sustainable release of growth factors. Nanoscale topographies on surfaces can be fabricated by different methods such as plasma-etching process, nanolithography, and nanoparticle/molecule grafting.

Calcium phosphate cement (CPC) is one of the promising bone substitutes due to their good injectability (owing to their self-setting and in situ hardening), acceptable mechanical properties, excellent biocompatibility, and osteoconductivity. Lee

et al. simply modulated the sizes of the initial CPC particles (the mixture of calcium hydrogen phosphate ($CaHPO_4$) and calcium carbonate ($CaCO_3$) and used two different protocols to obtain micro-CPCs and nano-CPCs samples [269]. A direct cell culture method was performed on the CPCs to assess the effect of micro or nano-CPCs in odontogenic media using human DPSCs. The ALP activity and the expression of marker genes such as *BSP*, *OPN*, *OCN*, *DSPP*, and *DMP-1* of DPSCs cultured on nano-CPCs was higher than those cells cultured on micro-CPCs with or without osteogenic media, which indicated that nano-CPCs substantially promoted odontogenic differentiation when compared to micro-CPCs. The integrin signaling pathway plays an important role in the cell–matrix interactions including cell adhesion, survival, proliferation, and differentiation. The á and â subunits of integrin are the major adhesive molecule-binding receptors in cells that form bone and dentin. The expression levels of integrin subunits á1, á2, and â1 increased significantly in nano-CPCs cultured as compared to micro-CPCs cultured cells, indicating that the hDPSCs more easily recognized the nanotopological substrate matrix receptors compared to the microtopological ones. The integrin downstream signaling might require the activation of several intracellular protein kinases, such as the focal adhesion kinase (FAK), Akt paxillin, MAPK, and NF-êB. The PCR results showed that the DPSCs on nano-CPCs expressed higher levels of *p-FAK*, *p-Akt*, *p-MAPK*, and *NF-êB*, which indicated that the nano-CPCs might act on the FAK, Akt, MAPK pathways to induce NF-êB activation in the DPSCs. Taken all these into consideration, Lee et al. claimed that nano-sized CPCs are superior to micro-sized CPCs in terms of their odontogenic differentiation in the hDPSCs through FAK, Akt, MAPK, and NF-êB signaling pathways.

Calcium phosphate cement can also be modified by other nanoparticles. Our groups designed a novel calcium phosphate cement (the mixture of tetracalcium phosphate ($Ca_4(PO_4)_2O$) and dicalcium phosphate anhydrous ($CaHPO_4$)) containing gold nanoparticles (GNP-CPC) [270]. The advantages of GNPs have been discussed in the previous paragraphs. In our study, GNPs were incorporated into CPCs via liquid to achieve a better dispersion and obtain homogenous particles. GNPs are proved to be able to enter cells through direct diffusion or endocytic pathway. Our results also showed that GNPs promoted the osteogenic differentiation of DPSCs even without the presence of CPCs. This may be due to the mechanical stresses on the cells from GNPs endocytosis through regulating the Yes-associated protein (YAP) activity [271]. Besides, we also found that the addition of GNPs improved the properties of CPCs such as wetting and protein adsorption. Furthermore, compared with CPCs, hDPSCs cultured on GNP-CPCs showed better cell attachment and larger spreading area. The osteogenic differentiation of hDPSCs on GNP-CPCs than those on CPCs were also greatly improved which was demonstrated by increases in ALP activity, osteogenic gene expressions and bone matrix mineral deposition. Interestingly, GNPs had no influence on cell adhesion and spreading without the presence of CPCs or GNP-CPCs, which may demonstrate that it is the nanosurface but not the nanoparticles themselves that played major role in cell attachment. Therefore, GNPs are promising to modify CPC with nanotopography by working as bioactive additives and enhance bone regeneration.

Instead of being used alone, the inorganic ceramics can also be utilized to fabricate composites with natural or synthetic polymers as bone substitutes to offer a nanostructured 3D network in human body. Samadikuchaksaraei et al. fabricated a nano-hydroxyapatite/gelatin (nHA/GEL) nanocomposite scaffold that mimic the natural ECM by the layer solvent casting combined with the freeze-drying and lamination techniques [272]. HA is one of the main mineral components of bone tissue, gelatin was added to mimic the organic component of the bone. The incorporation of nHA not only increased the mechanical properties of the gel scaffolds but also promoted the biocompatibility of rat BMSCs. Besides, the nHA/GEL nanocomposite scaffolds also showed better osteoinductivity in vivo than gel scaffolds alone when implanted in the calvarial critical size bone defect of SD rats. Therefore, this study indicates that nanocomposite can be a novel strategy for the development of bone tissue engineering scaffolds.

Interactions between the cells and their microenvironment determine the fate of grafted bone substitutes. Growth factors have been widely used to improve cellular bioactivity and increase stability and physiological activity of administered active compounds. Growth factors can be incorporated into bone substitutes or scaffolds for targeted, sustained, and controlled release of growth factors, to enhance osteogenesis, angiogenesis, and tissue regeneration. Growth factors which are commonly used as osteoinductive agents are bone morphogenetic proteins (BMP), platelet-derived growth factors (PDGF), and vascular endothelial growth factors (VEGF). Currently, multi-carrier structures (e.g., hierarchical structure, core–shell structure, and nanoparticle embedded structure) have been developed to incorporate growth factors within bone substitutes and scaffolds. However, the key challenge with the direct incorporation of growth factors within the scaffold is that they can be deactivated during the fabrication process (e.g., under high voltage or in contact with organic solvents [273]). Furthermore, another concern is the burst release. To address the issue, nanoparticles are used to encapsulate the proteins to preserve the bioactivity of the growth factor and provide a sustained release profile. Li et al. developed a new nanoparticle-embedded electrospun nanofiber scaffold for the controlled dual delivery of BMP-2 and DEX [274]. The preparation of this scaffold was shown in Fig. 3.13. Briefly, BMP-2 was loaded into bovine serum albumin (BSA) nanoparticles to maintain its bioactivity. Then, the BMP-2-loaded BSA nanoparticles were stabilized by a chitosan shell through electrostatic self-assembly (BNP). Encapsulation of both BNP and DEX were performed by electrospinning the blended solution of nanoparticles and PCL-poly(ethylene glycol) (PEG) copolymer (DEX was dissolved into this copolymer solution). Hydrophilic PEG was copolymerized with PCL to improve the water wet ability and degradation rate of PCL. Finally, a controlled dual delivery of BMP-2 and DEX can be acquired using this nanoparticle-derived fiber scaffold. Results showed that the bioactivity of DEX and BMP-2 was preserved in this scaffold. Besides, a controlled and sequential release pattern of the DEX and BMP-2 was achieved. Most of the DEX was released in the first 8 days, and the BMP-2 release lasted up to 35 days. Furthermore, the drug-loaded groups exhibited a strong ability to induce osteogenic differentiation both in vitro and in vivo and manifested the best repair efficacy due to a synergistic

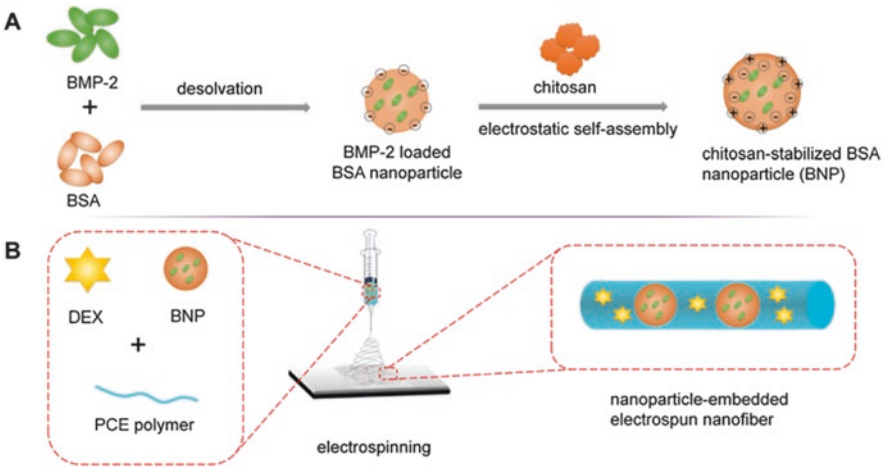

Fig. 3.13 Schematic illustration of BMP-2 and DEX-loaded electrospun nanofiber scaffold [274]

effect of BMP-2 and DEX. Therefore, the biomolecule-loaded nanofiber scaffold fabricated in this way is a strong potential candidate to repair bone defects.

Instead of biomolecules, stem cells have also been incorporated into bone substitutes in stem cell-based therapy. The incorporation of stem cells within bone substitutes have many advantages due to their differentiation potential, ability to secrete multiple bioactive molecules, and immunomodulatory functions. It is of great benefit to apply injectable scaffolds which could enable the seeding of stem cells into the deep internal space. Besides, using injectable scaffolds is advantageous when it comes to irregular bone defects.

He et al. designed a novel injectable, biodegradable, porous, and load-bearing nano-scale calcium sulfate/alginate (nCS/A) delivery system incorporated with *BMP2*-gene-modified rat MSCs in rat critical-sized craniofacial bone defects to evaluate the osteoconductivity of the system [275]. Calcium sulfate (CS) is a biocompatible, bioactive, and biodegradable material with crystalline structure whose compressive strength is greater than that of cancellous bone and has been applied to fill cysts, bone cavities, and segmental bone defects. Nano-calcium sulfate (nCS) particles (generally between 30 and 100 nm) may enhance physical properties, such as increasing the surface area to improve growth factor adsorption while potentially controlling the degradation rate, as well as mechanical strength for optimal osteoconductivity and fractures resistance. On the other hand, alginate is a natural anionic polysaccharide with good biocompatibility, mild requirement of gelation conditions, low immunogenicity, high hydrophilicity, and good biodegradability under physiological conditions and low cost (easily to be obtained from brown seaweed). It has been widely used in bone tissue engineering. Thus, they cross-linked alginate hydrogels with nCS to form the injectable nCS/A paste [275]. When the nCS/A paste was cultured in the medium, the degradation of ionically cross-linked alginate due to the loss of divalent cations (Ca^{2+}) will lead to the formation of nano pores

which enhances cell migration into the scaffold. Besides, the mechanical properties of the nCS/A paste were improved with an increased proportion of alginate. Then, a 25 μL cell suspension with 1×10^6 rat MSCs infected with *BMP2* gene was added to the nCS/A paste to form a rat MSC-based nCS/A composite as novel bone substitutes. Both rat MSCs and *BMP2* gene-modified rat MSCs in the injectable pastes remained viable, osteo-differentiated, and yielded high alkaline phosphatase activity after injection. In animal experiment, the authors found that *BMP2*-gene-modified MSCs in nCS/A (referred as nCS/A + M/B2 group) showed the best osteogenic activity and the amount of new bone formation, and vessel density was the highest in the group which grafted with nCS/A + M/B2 composite. Therefore, the overall results confirmed that the combination of injectable nCS/A paste and *BMP2*-gene-modified MSCs is a new and effective strategy to repair bone defects.

In summary, nano-modified membranes and bone substitutes have the potential to enhance osteogenesis and have been widely applied in oral bone regeneration.

3.2.3 Nanotechnology to Regenerate Keratinized Gingival

Good osteointegration is fundamental to a successful dental implant, while the connection between gingival and implant surface determines long-term success of a dental implant because bacterial invasion and infection can be prevented by a proper seal around a dental implant. It is of great importance to maintain enough keratinized gingival (KG, a part of oral mucosa covered with keratin or parakeratin) to obtain gingival seal mentioned above. It has been believed that 2 mm in width and depth of keratinized gingival is sufficient to maintain gingival health [276]. Generally, the absence of adequate keratinized mucosa around dental implants, especially in posterior area, was associated with higher plaque accumulation and gingival inflammation. Besides, wider and deeper zones of keratinized mucosa may lead to stronger resistance to the forces of mastication.

While it is practical to achieve adequate osteointegration between dental implants and host bone, the preservation of appropriate soft tissue architecture around an implant supported denture remains challenging. Several surgical techniques have been described to increase the amount of keratinized tissue around dental implants, including the free gingival graft (FGG), the connective tissue graft (CTG), apically positioned flap (APF) technique, and xenogeneic collagen matrix (XCM). However, the formation of a scar may occur occasionally while applying APF technique together with FGG or CTG, and higher postoperative morbidity, and the longer surgical time may limit the use of autogenous grafts and APF technique. Therefore, XCM has been investigated for the treatment of gingival recessions. As far as we know, the effect of available methods for keratinized gingival augmentation stays controversial, and the regenerative mechanism of keratinized gingival remains unclear. Given that nanostructure and nanomaterials are beneficial to bone regeneration, some researchers also focus on applying nanotechnology to keratinized gingival regeneration.

Nocini et al. investigated a newly designed bi-layered collagen nanostructured membrane (collagen matrix 10,826®, CM-1826) and evaluated its fundamental cell functions of human gingival keratinocytes, such as adhesion, proliferation, and interleukin 6 (IL-6) production, to assess the biocompatibility of this new membrane [277]. It has been proven that cell adhesion activates intracellular signaling pathways governing a multiplicity of cellular processes including the gene expression of cytokines, such as IL-6 and IL-6, and stimulates keratinocyte proliferation. Thus, the IL-6 production was selected to evaluate the effect of this membrane on keratinocytes. Results showed that the production of basal IL-6 doubles in the presence of CM-10826, strongly increases in the presence of collagen I, a major component of CM-10826, but appears almost unaffected in the presence of collagen IV. Besides, CM-10826 also demonstrated a positive biological activity on gingival keratinocytes growth and adhesion, without any toxic effect. However, there was no direct comparison between keratinocytes cultured with CM-10826 and collagen I. Therefore, it is hard to figure out whether the promotion of cell growth, adhesion and IL-6 production is due to the nanostructure or the major component (collagen I) of CM-10826. Further studies should be carried on.

However, Dorkhan et al. found that nanotopography of anodic oxidation-modified Ti showed no effect on adherence of keratinocytes [278]. They used titanium discs with three different surfaces. Commercially pure titanium discs (CpTi) were selected as controls (C) while the two anodically oxidized surfaces (N1 and N2) were selected as test surfaces. Preparation of N1 was performed by anoxic oxidation on CpTi, whereas the same method on titanium alloy N1 (TiAl6V4) was used to prepare N2. Results showed that the two anodically oxidized surfaces achieved nanostructuring with differing degrees of porosity. After cultured for 24 h, the keratinocytes adhered well to the nanostructured surfaces, although to a somewhat less degree than to CpTi. However, no differences in adhesion strength of keratinocyte could be observed among the two nanostructured surfaces and the CpTi. This study indicates that nanostructure may have no effect on the adhesion of keratinocytes. Thus, it is interesting to explore whether the nanostructure can influence the bioactivities of gingival keratinocytes.

3.2.4 Nanotechnology to Regenerate Tooth

As mentioned before, a tooth consists of multiple tissues. In humans, tooth loss can lead to physical and mental suffering that compromise an individual's self-esteem and quality of life. Dental caries and periodontal disease are the two major causes for the loss of teeth. In addition, facial trauma, resection of maxillofacial tumors, and some genetic disorders may also lead to tooth loss. Due to its complex structure and limited self-healing capability, it is challenging to achieve tooth regeneration.

The current restorations for tooth loss are dentures (including removable and fixed dentures) and dental implants. Poor retention and instability of a removable denture make it uncomfortable for the patient. Besides, it is inconvenient to wear,

remove, and clean the denture every day. The fixed dentures are more comfortable than the removable ones. However, it needs to grind the adjacent healthy teeth as abutments to make a fixed denture. Furthermore, the fixed denture has to be removed or refabricated once abutment teeth suffered severe damage. Dental implants have been favorite choices for both patients and dentists in recent decades. However, high price, long treatment period and the pain caused by surgery is the main concern which impede the application of dental implants. Besides, dental implants currently cannot perceive noxious stimulations such as excessive occlusal loading and trauma because the absence of neuronal innervation in the periodontal tissue. The nervous system of a natural tooth contributes to the regulation of tooth physiological functions and the perception of noxious stimulations. Therefore, tooth regeneration should be the best way to restore the lost teeth.

The focus in damaged tissue restoration has undergone significant changes, beginning as substitution, then evolving to restoration or replacement, and finally to tissue regeneration. Novel therapeutic strategies have arisen about two decades ago, sprouting from the emergence of tissue engineering and regenerative medicine, evaluated by their potential to replace, repair, maintain, and enhance tissue or organ function. The strategy encompasses numerous elements, including biomaterials, stem cells, tissue-inducing substances, or biomimetic regenerative environments. Tooth regeneration strives to (a) regenerate a structurally and functionally sound complete tooth and (b) regenerate individual tooth structures such as enamel, dentin, pulp, cementum, and periodontal ligament. Like natural teeth, bio-engineered teeth are also expected to properly contact adjacent teeth, transmit masticatory loads, provide proprioception, and restore esthetics. Generating these teeth and restoring proper morphology require precise and orderly orientation of the epithelial mesenchymal cell layers placed onto the scaffold as well as directing the interaction of cells with the extracellular matrix. To achieve this differential placement of cells and ensure proper interaction with the matrix, 3D imprinting scaffold fabrication, cell seeding techniques, and recent developments in nanotechnology can be implemented. Currently, two approaches are considered for tooth regeneration: (1) scaffold-based approach which involves using scaffolds on which cells can be seeded in vitro or by cell homing in vivo; (2) scaffold-free approach aims at directly inducing developmental processes of embryonic tooth formation by stem cells or cell sheets. These processes have to be guided by appropriate signals to produce tooth structures that mimic natural teeth in size and shape. Nanotechnology has been widely used to modify stem cells and scaffolds, and most of the researchers focused on the former approach to achieve tooth regeneration.

Enamel, the hardest tissue located in the vertebrate body, is formed through biomineralization by ameloblast cells. These cells synthesize and secrete a complex of tissue-specific proteins into the extracellular space, where a HA-patterned matrix is self-assembled by these proteins to form a tough, wear-resistant composite material. The dominant protein of mammalian enamel includes amelogenin and ameloblastin which play important role in forming enamel matrix. The mature enamel composite contains no cells, no blood vessels, and almost no proteins. Therefore, it is difficult to regenerate enamel once it is destroyed by caries or trauma. To

hopefully achieve the long-term goal of establishing cell-based strategies for tooth regeneration, Huang et al. used an in vitro cell and organ culture system to study the effect of artificial bioactive nanostructures have on ameloblasts [279]. Huang's study hired the branched peptide amphiphile molecules "BRGD-PA," which contain the peptide motif Arg-Gly-Asp, for their ability to self-assemble into nanofibers. Primary enamel organ epithelial (EOE) cells and ameloblast-like cells (line LS8) were cultured within BRGD-PA hydrogels, and then injected into the enamel organ epithelia of mouse embryonic incisors. Results of cell proliferation assay, quantitative real-time PCR, and Western blot showed that LS8 and EOE cells responded to the BRGD-PA nanostructures with enhanced proliferation and greater amelogenin, ameloblastin, and integrin expression levels compared with cells responded to culture plates. Besides, at the site of injection in the organ culture model, Huang et al. observed that EOE cell on BRGD-PA proliferated and differentiated into ameloblasts as evidenced by their expression of enamel specific proteins. The histological analysis, transmission electron microscopic examination, and immunohistochemistry results showed that the nanofibers were inside the formed ECM, contacted the EOE cells, and engaged in enamel formation and regeneration. Therefore, this research demonstrates when BRGD-PA nanofibers are presented with enamel proteins, they participate in integrin-mediated cell binding to the matrix and deliver instructive signals for enamel formation.

Dental pulp is a complex organized tissue with various types of cells and structures, providing nutrition, sensation, and defense against various pathogens. In addition, dental pulp produces dentin and maintains the biological and physiological vitality of the dentin. Pulpitis, usually caused by dental trauma and caries, is one of the most common diseases related to dental pulp. Due to the complex structure, small volume, and insufficient blood supply of dental pulp, self-repairing is difficult to initiate in pulpitis. Traditionally, pulpitis is treated by root canal therapy, whereby the inflamed pulp is removed and replaced with inorganic material; however, tooth fragility and ultimately tooth fracture can be unfortunate end results. Therefore, a better choice is if we could keep or regenerate vital tooth pulps. Recently, scaffold- and/or stem cell-based therapy has been one of the approaches to achieve pulp regeneration. Li et al. designed and synthesized a unique hierarchical growth factor-loaded nanofibrous microsphere scaffolding system to achieve successful regeneration of pulp tissues in a full-length human root with a one-end seal [280]. In this system, heparin binds to the vascular endothelial growth factor (VEGF), which is then encapsulated into heparin-conjugated gelatin (HG) nanospheres and finally immobilized in the nanofibers of an injectable poly-(L-lactic acid) (PLLA) microsphere (HG-MS) (Fig. 3.14). For comparison, gelatin without heparin was used during the fabrication process, and the hierarchical microsphere obtained was abbreviated as G-MS. The hierarchical microsphere fabricated without gelatin or heparin, referred as MS, was used as blank control. The amount and bioactivity of released VEGF was measured and evaluated, and the result indicated that microsphere system hierarchy not only protects the VEGF from degradation and denaturation but also provides superb control of its sustained release. Additionally, the HG-MS integrates the ECM-mimicking architecture with a highly porous injectable

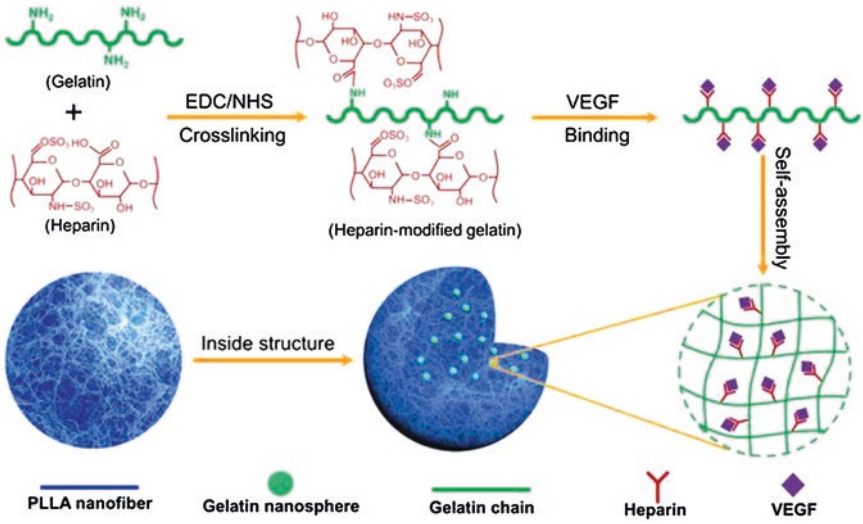

Fig. 3.14 Schematic illustration of the synthesis of heparin-conjugated gelatin (HG) and hierarchical VEGF-loaded heparin-conjugated gelatin microspheres (HG-MS) [280]

form, effectively accommodating DPSCs and assisting their proliferation and pulp tissue formation. Then freshly extracted human teeth from 18- to 30-year-old patients were collected for in vivo study. Briefly, the root for each tooth was standardized by cutting to a length of 13 mm. The root apex and coronal were processed to a length of 1.0 and 2.5 mm, respectively. During the in vivo experiment, mineral trioxide aggregate (MTA) at 2 mm into the canal space was used to seal the coronal end of the canal, leaving the remaining 11 mm of the root canal space for pulp tissue regeneration, which mimics the clinical operation. Then the pretreated roots were filled with DPSCs or HG-MS or HG-MS + DPSCs or left empty and implanted into immunocompromised nude mice. After 9 weeks, the histology and immunohistochemistry assay showed the successful regeneration of pulp-like tissues that fulfilled the entire apical and middle thirds and reached the coronal third of the full-length root canal in HG-MS + DPSCs group. In addition, many blood vessels were regenerated throughout the canal in this group. Therefore, nano-modified scaffold, together with dental stem cells, may provide new sight for dental pulp regeneration.

In regenerative endodontics, dentin and pulp are an inseparable unit because they are closely related embryologically, histologically, and functionally. Therefore, to achieve both dentin and pulp regeneration simultaneously is important to fully restore the biological and mechanical functions of the damaged tooth. Gronthos et al. combined human DPSCs with nano-hydroxyapatite/tricalcium phosphate (nHA-TCP) ceramic powder (worked as scaffolds) to explore the possibility that isolated ex vivo-expanded human DPSCs would also be capable of regenerating a dentin/pulp-like structure in vivo under similar conditions [281]. In addition, human

BMSCs were also used and compared with DPSCs to explore their potential to be applied in dentin/pulp regeneration. Immunohistochemical studies were performed to characterize the progeny of the DPSC and BMSC clonogenic populations. DPSCs and BMSCs share a similar immunophenotype in vitro according to their similar expression of markers associated with endothelium, smooth muscle, bone, and fibroblast. While functional studies revealed DPSCs produced only sporadic, densely calcified nodules without adipocyte formation, the BMSCs routinely were calcified amidst the entire adherent cell layer and had clusters of lipid-laden adipocytes. DPSCs or BMSCs were transplanted in conjunction with nHA-TCP powder into immunocompromised mice to see whether a dentin/pulp-like structure could be formed in vivo. The DPSCs produced a dentin-like structure, composed of a highly structured collagenous matrix, which lined nHA-TCP particle surfaces. Besides, a pulp-like interstitial tissue was surrounded by the odontoblast-like cells. Comparatively, BMSCs formed lamellar bone containing osteocytes and surface-lining osteoblasts, surrounding a fibrous vascular tissue with active hematopoiesis and adipocytes. This study confirmed that isolated postnatal human DPSCs combined with the nHA-TCP powder showed greater potential than BMSCs to form a dentin/pulp-like complex. It can be inferred that nanomaterials could be used as scaffolds in stem cell-based dentin/pulp regeneration.

In addition, the application of nanotechnology may provide more advantages in tooth regeneration. For example, a bio-root was regenerated by implanting pre-shaped 3D printing root-like scaffolds combined with mesenchymal stem cells into the alveolar bone. In this way, a functional root with root-like structure, periodontal ligament-like tissue, and dentin-like matrix structure was formed by Sonoyama et al. [282]. However, the bio-root showed lower compressive strength than that of natural swine root dentin, which may impede the long-time survival of the bio-root. Therefore, can we enhance its survival rate through improving the mechanical properties of the bio-root by nanotechnology? And as appropriate signals play the key role in regulating developmental processes of a tooth formation, we can try to use nanotechnology to modify stem cells and transfer growth factors in the future tooth regeneration research. Further studies are needed.

3.2.5 Shortcomings in the Current Application of Nanotechnology

Nanomaterials have unique biological activities to improve the physicochemical properties of oral stem cells, GBR membranes, and bone substitutes. Therefore, it helps with oral tissue regeneration. However, as one coin has two sides, the application of nanomaterials and nanotechnology may also have some potential problems.

One of the concerns for employing nanomaterials is their toxicity to oral tissue, which will mainly be discussed in the next part of this book. Besides, there are still other limitations when applying nanotechnology in oral tissue engineering.

When nanoparticles are used for gene delivery, lower concentration of nanoparticles is related with reduced gene loading capacity, while higher concentration is related with increased cytotoxicity. Therefore, it forms a dilemma between the two, and an optimal concentration is acquired [283]. Combining nanoparticles with other vectors, to form combo delivery system, may solve this challenge. In Zhang's study, (3-aminopropyl) triethoxysilane-modified iron oxide nanoparticles (APTES-IONPs) was designed and synthesized as gene vectors. Two other commercial vectors, Lipofectamine and TurboFect, were used as control. One gram of DNA was incubated with APTES-IONPs (weight range from 0 to 30 μg) or 1 μg Lipofectamine or 0.25 μL TurboFect for 30 min to evaluate the gene-loading capacity. Low level of APTES-IONPs failed to bind enough DNA, so did Lipofectamine or TurboFect. Comparatively, unbound DNA level was significantly decreased when high level of APTES-IONPs (30 μg) was added. However, the addition of Lipofectamine or TurboFect markedly decreased the unbound DNA level during complexation with low level of APTES-IONPs. Vice versa, 1 μg Lipofectamine or 0.25 μL TurboFect succeeded in binding enough DNA with the addition of low level of APTES-IONPs. Therefore, the commercial vectors could enhance DNA-binding capacity of the APTES-IONPs even at low concentration, and the nanoparticles could also increase the DNA-binding capacity of the commercial vectors. Besides, Zhang et al. also found that the combo gene delivery system, containing APTES-IONPs and Lipofectamine, was a time-saving method, could prevent DNA from degradation, improve gene delivery efficiencies in both adherent and suspension cells, and effectively mediate siRNA transfection. Therefore, the combination of nanoparticles with other vectors shows greater potential for gene transfection than using nanoparticles alone.

Scaffold, as one of three key factors in tissue engineering, has been modified via nanotechnology in regenerative dentistry. Magnetic nanoparticles (MNPs) have drawn great interest owing to their unique magnetic properties and have been utilized to obtain magnetomechanically functional scaffolds for bone regeneration. The simplest way to obtain magnetic scaffolds was to dip-coat the scaffolds into aqueous ferrofluids containing MNPs (such as superparamagnetic iron oxide nanoparticles, SPIONs) coated with various biopolymers. After dip-coating, the nanoparticles were integrated into the porous structure of the scaffolds. However, one concern of the magnetic scaffolds fabricated in this way is the uncontrolled and undesired release of MNPs. This concern may be addressed by designing and fabricating scaffolds with specific structure. Zeng et al. used HA powder to fabricate scaffold by the microwave-assisted foaming process [284]. This kind of HA scaffold had a specific structure with micro- and macroporosity and was shaped into disks of 12 mm diameter and 2 mm height. Then the HA disks were dip-coated with MNPs. The authors found a gradual release of magnetite over a long period in phosphate-buffered saline (PBS), simulated body fluids (SBF), and fetal bovine serum (FBS), which indicated that the integration of HA and MNPs involved an adsorption-desorption dynamic equilibrium process. At an extremely low percentage of released magnetite in the media, the release curves flattened out, suggesting that the large surface energy of HA and the specific porous structure helped for

MNPs retention in the scaffold, thereby delaying the desorption process. Therefore, specific structure of the magnetic scaffold may help to achieve desired release of MNPs.

There are many important growth factors and small molecules, such as BMPs, VEGF, platelet-derived growth factor (PDGF), and fibroblast growth factor (FGF), which can promote oral tissue regeneration. Growth factors could be stabilized by conjugation to nano-constructed materials. Usually, growth factors immobilized to nanomaterials promoted a higher growth and differentiation of the cells compared with their counterparts due to the release of growth factors [255, 285]. However, it is still difficult to get controlled and sustained release of growth factors and keep their bioactivity during release process. It seems that the combination of nanomaterials with other biomolecules as vehicles for growth factors can improve the release of growth factors. As mentioned before, Li et al. designed and synthesized a unique hierarchical growth factor-loaded nanofibrous microsphere scaffolding system HG-MS (Fig. 3.14). In this system, heparin was used to further immobilize VEGF in the PLLA nanofibers. For comparison, gelatin without heparin was used during the fabrication process and referred as G-MS, and the hierarchical microsphere fabricated without gelatin or heparin was used as blank control, referred as MS. Results showed that encapsulating VEGF into gelatin (G-MS group) and HG microspheres (HG-MS group) significantly decreased the initial burst release (shown in MS group) of the protein VEGF. In addition, binding VEGF to heparin (HG-MS group) further reduced the burst release of VEGF than that of G-MS group. Besides, the release rates of the MS and G-MS groups reached a plateau after 1 week. In contrast, the HG-MS group released VEGF consistently at a rate of approximately 1–2% per day for the last 3 weeks of the experiment. As VEGF has binding domains with heparin, it can be inferred that heparin protects VEGF from denaturation and proteolytic degradation, which subsequently prolongs its sustained release. Therefore, it may be useful to utilize other biomolecules to improve nanomaterials better for the delivery and release of growth factors.

Though shortcomings are present, there is no doubt that nanomaterials and nanotechnology bring numerous benefits and amazing perspectives to stem cell-based regenerative medicine. Recent advances in nanomaterials increase the potential to control oral stem cell bioactivity, improve gene and growth factors delivery, create functional membranes, and improve the mechanical properties and osteoconductivity of bone substitutes for the treatment of oral and maxillofacial defect. Therefore, it is of great potential to implant nanomaterials labeled oral stem cells with nanotechnology-modified scaffolds into damaged dental tissue for regeneration. Besides, the application of nanomaterials in dentistry may act as another type of personalized medicine to achieve customized treatment for different patients and different oral and dental diseases. Furthermore, for dental implants, nanotechnology can be applied to form an “osteogenic coating” which may increase the bone–implant contact and improve the osteointegration. And this may be an alternative to bone augmentation in cases whose alveolar bone in implant site is compromised.

However, some problems are imperative to be solved before further application of nanotechnology in oral tissue engineering. Most importantly, nanomaterials

require improved testing and evaluation systems to assess their potential toxicity. As such, the consideration of dose–response studies is warranted. Moreover, the underlying mechanisms of nanomaterial–cell interactions are unclear, with many hypotheses remain to be proved. Third, the exact effects of nanomaterials on cells, tissues, and organs and their metabolic pathways in vivo remain unclear and require further research.

3.3 Application of Antibacterial Nanomaterials in Dentistry

The human oral cavity is the home to over 530 different species of microorganisms. However, only some of them are related to oral disease. In the past four decades, microbial ecologists have identified the suspected pathogens which cause human dental caries and periodontal disease. Many scientists concur that the microbes which are associated with oral disease are as follows: the principal pathogenic agents of dental caries are associated with the *Mutans streptococci*, especially *Streptococcus mutans* and *Streptococcus sobrinus* and the secondarily implicated are the *Lactobacillus species* and perhaps some non-*Mutans streptococci* in coronal caries, particularly the acid-tolerant strains: *Streptococcus sanguis* and *Streptococcus gordonii* [286, 287]. In addition, *Actinobacillus actinomycetemcomitans* are associated with juvenile periodontitis, while *Prevotella, Fusobacterium*, and *Actinomyces* species are associated with gingivitis [288].

Because the infections are closely associated with bacterial biofilms, the antimicrobial susceptibility of the important pathogenic bacteria in the biofilms has been extensively investigated for many years. Antibiotics are the most common way to fight against the bacteria. However, oral administration of antibiotics results in undesirable side effects, such as inadvertent destruction of beneficial bacterial flora and development of antibiotic resistance. Instead, local polymeric-based drug delivery systems which include fibers, strips, or nanoparticles can provide appropriate drug concentrations directly to the target site.

Recently, there has been remarkable attention in the field of antimicrobial nanomaterial and nanotechnology. Several nanoparticles (e.g., zinc oxide, silver, and magnesium oxide) had been proved to be effective in inhibiting the bacterial growth and applied in several areas of dentistry, such as endodontics, dental prostheses, periodontitis, and implantology. Abou et al. found that the antimicrobial mechanisms of nanoparticles include bacterial cell membrane disruption, reactive oxygen species (ROS) generation, active transport as well as sugar metabolism inhibition, electron transport disturbance across the bacterial membrane, DNA replication prevention, and ion displacement of those required for the enzymatic activity of oral biofilms [289].

Silver (Ag) ions have strong antimicrobial effects and have been used widely in biomedical field for many years. Being a potent antimicrobial due to sustained ion release, Ag has many advantages, such as no antibiotic resistance, low toxicity, and good biocompatibility. Likewise, silver nanoparticles (AgNPs) have shown potent

antimicrobial properties, also having non-acute toxic effects on human cells. They enhance the overall biological effectiveness through fast penetration and bioavailability while reducing potential cytotoxicity, drug dosage and production costs. AgNPs in different sizes have different effects on oral bacteria: 5 nm AgNPs seem to have the highest antibacterial activity [290]. The antimicrobial mechanism of AgNPs has been extensively investigated. Seemingly, the interaction of silver ions with the peptidoglycan cell wall causes structural changes, increased membrane permeability, and ultimately leads to cell death. Furthermore, the interaction of AgNPs with the exposed sulfhydroyl groups in bacterial proteins results in the hindering of DNA replication [291, 292].

ZnO nanoparticles (ZnO NPs) are believed to be nontoxic, biosafe, and biocompatible. They have been used as drug carriers, cosmetics, and filling materials in biomedical field. ZnO NPs have a wide range of antibacterial effects on various microorganisms, including gram-positive and gram-negative bacteria under normal lighting conditions. The antibacterial activity of ZnO NPs might involve the production of ROS and the accumulation of nanoparticles in the cytoplasm or on the outer membranes [293]. Another metal oxide nanomaterial, MgO has the advantages of being cheap, readily available, and biocompatible, making it a very promising antibacterial agent. The damage to the membrane of bacterial cell likely occurs due to the attachment of the nanoparticles to the membrane, in combination with the effects of pH change, Mg^{2+} release, and ultraviolet illumination. The attachment of particles may involve phosphate groups presenting on the surface of the cells, but there are likely other adherent mechanisms contributing to the antibacterial activity [294].

Subsequently, we discuss the incorporation of nanomaterials into dental materials, highlighting the aspects regarding microorganism inhibition and potential toxicity.

The survival of pathogenic bacteria in the oral cavity depends on their successful adhesion to the dental surfaces and their ability to develop into biofilms, known as dental plaque. Bacterial plaque is the unmineralized bacterial community in the mouth that cannot be washed away by water and adheres together or to the tooth surface. Because of the self-secreted extracellular polymeric matrix, it has high recalcitrance toward antibiotics. Bacteria from the dental plaque are responsible for the development of dental caries, gingivitis, periodontitis, stomatitis, and peri implantitis. The ability of antibiotic nanoparticles with sustained release capability to penetrate the biofilm has led to its emergence as one of the premier anti-biofilm formulations in the combat against biofilm infections. Moreover, biofilm resistance can be overcome by including drug delivery systems such as lipid or polymer nanoparticles. These particles can increase the treatment efficacy by improving antibiotic delivery to bacterial cells.

Some researchers examined the antibacterial efficacies and physical characteristics of the antibiotic-loaded polymeric nanoparticle formulations, and the result showed that most ideal formulation is ciprofloxacin-loaded PLGA nanoparticles, by virtue of their high drug encapsulation efficiency and high antibacterial efficacy while maintaining a low dose to combat against the biofilm cells and biofilm-derived planktonic cells of *Escherichia coli* [295]. Likewise, Forier et al. found that in many

cases antimicrobial efficacy can be improved by using lipid and polymer nanoparticles. To maximize the biofilm exposure to the antimicrobial agent and ensure delivery of the antimicrobial agent to the vicinity of the bacterial cells, strategies which include nanoparticle targeting, antimicrobial triggered release, and fusogenic liposomes are promising [296].

Other researchers fabricated two forms (sphere and wire) of chlorhexidine (CHX)-loaded mesoporous silica nanoparticles (MSNs) and investigated their releasing capacities and anti-biofilm efficiencies. The spherical MSNs with an average diameter of 265 nm exhibited a larger surface area and faster CHX-releasing rate than the MSN wires, the spherical nanoparticle-encapsulated CHX presented with a greater anti-biofilm capacity than the wire nanoparticle-encapsulated CHX, since the entanglement of wire nanoparticle-encapsulated CHX could restrict the drug release and interactions with the microorganisms. These findings revealed that the spherical nanoparticle-encapsulated CHX could preferably enhance its anti-biofilm efficiency through an effective releasing mode and close interactions with microbes [297]. Another researcher reported the synthesis of mesoporous silica nanoparticle-encapsulated pure CHX (nano-CHX), and its antimicrobial properties against oral biofilm. The nano-CHX elicited potent antibacterial effects against mono-species biofilms and planktonic bacteria such as *Streptococcus mutans, Streptococcus sobrinus, Aggregatibacter actinomycetemcomitans, Fusobacterium nucleatum*, and *Enterococcus faecalis* at the 50–200 μg/mL concentrations. Moreover, nano-CHX successfully inhibited multi-species biofilms that include *Streptococcus mutans, Aggregatibacter actinomycetemcomitans, Fusobacterium nucleatum*, and *Porphyromonas gingivalis* until 72 h [298].

A traditional Chinese medicine, *Scutellaria baicalensis* (SB), has been used to treat infectious and inflammatory diseases. Baicalin, a flavonoid compound isolated from SB, possesses marked anti-inflammatory, antioxidative, and immunomodulating effects. It has potent antibacterial effects on oral pathogens, and it could indeed inhibit bacterial quorum sensing activity and exhibit protective effect on the development of experimental periodontitis and benefits for controlling periodontal disease. The combined use of another compound baicalein presented in SB with antibiotics has synergistic effects against oral bacteria [299–302]. It has been shown that nanoparticle-encapsulated SB enhanced the biological effectiveness via high bioavailability and fast penetration with less cytotoxicity, reduced dosage of the agents, and lowered the costs. This team also explored the synergistic effects of the combined usage of nano-MIX (nanoparticle-encapsulated SB and nano-CHX at 9:1 (w/w) ratio) with the aim to minimize the unexpected effects of CHX, against the mixed oral biofilms such as *Streptococcus mutans*, *Fusobacterium nucleatum*, *Aggregatibacter actinomycetemcomitans*, and *Porphyromonas gingivalis*. The result showed enhanced synergistic antibacterial effects of the nano-MIX on common oral bacterial biofilms, which could be developed as a novel antimicrobial agent for clinical oral/periodontal treatment [303].

Besinis et al. found that the biofilm formation occurring on dentine surfaces and the bacterial growth occurring in surrounding media can be successfully controlled by applying silver nanocoating on dentine. This nanocoating was found to be

chemically and biologically stable and also can protect the teeth from dental plaque as well as secondary caries when applied as a dentine coating [304].

Dental caries is the most common and widespread oral disease, resulting from the acidic attack of the cariogenic bacteria, such as *Streptococcus mutans* and *Lactobacillus* spp. Currently, composite resin is the most widely used restorative materials, due to their excellent esthetics and load-bearing properties. They are applied in core buildup, inlays/onlays restoration, cavity lining, and fissure sealing. However, one major drawback is that composites tend to accumulate biofilm and plaque in vivo [305, 306]. Such plaque accumulation with acid production by acidogenic bacteria could result in secondary caries. However, it has been shown that there is microleakage on the margins of the restoration. These gaps can be colonized by oral bacteria, resulting in secondary caries. To prevent or diminish biofilm accumulation, filling materials with antimicrobial properties have been developed.

In order to elicit acid neuralization ability as well as release calcium and phosphate ions, a dental composite including amorphous calcium phosphate nanoparticles (NACP) was created. Few studies have reported on antibacterial agents being incorporated into calcium phosphate composites. One study investigated the effect of AgNP mass fraction in NACP nanocomposite on mechanical properties and dental plaque microcosm biofilm. Five NACP nanocomposites were fabricated with AgNP mass fractions of 0, 0.028, 0.042, 0.088, and 0.175%, respectively. The results showed that the composites with AgNPs at 0–0.088% had the similar mechanical properties with those containing no AgNPs. The modulus of the sample containing 0.175% AgNPs was lower than the moduli of all other groups. Besides, counts of colony-forming units (CFU) containing 0.042% AgNPs for total *streptococci* were 75% less than the control group without AgNPs. A considerable antibacterial capability was imparted by the AgNPs in the NACP nanocomposite, which rose with AgNP concentration. However, increasing the mass fraction of the AgNPs to 0.175% revealed a brownish color and was accompanied by a precipitous strength drop. Therefore, to maintain both esthetics and mechanical strength, the AgNP mass fraction used must not exceed 0.042%. At 0.042%, the AgNP nanocomposites capably reduced biofilm metabolic activity greatly as well as decreased both lactic acid production and CFU counts, as compared to the commercial composite control [307].

AgNP-modified light-activated composites were evaluated by another study to determine the physical and antibacterial activity. Disks were produced with either the unmodified resin (control group) or the AGNP-modified resin at 0.3 wt% (MR03) and 0.6 wt% (MR06) concentrations. *Streptococcus mutans* and *Lactobacillus acidophilus* biofilms onto the disks were incubated and induced onto the disks in vitro. The result showed that the number of viable cells was statistically lower for MR03 and MR06 compared with control group. MR03 and MR06 showed no significant differences. MR03 was stronger in compression resistance than control group, and MR06 was statistically lower than control group and MR03. Both MR03 and MR06 inhibited the biofilm growth on their surfaces with no increase in surface roughness compared with the unmodified control resin [308].

Besides AgNPs, ZnO NPs also have antibacterial activity. It can inhibit the production of acid by the dental plaque through inhibiting *Lactobacillus* and *Streptococcus mutans*. In one study, ninety discoid tablets containing 0 wt%, 1 wt% AgNPs (20 nm), and 1 wt% ZnO NPs (50 nm) were prepared using flowable composite resin. Evaluation of the antibacterial properties of these discs were conducted using the direct contact test. 0.01 mL diluted solutions of the bacterial species *Streptococcus mutans* and *Lactobacillus* were each placed separately on the disks. The result showed that composites containing ZnO NPs and AgNPs both exhibited higher antibacterial activity against *Streptococcus mutans* and *Lactobacillus* compared with the control group. The effect of ZnO NPs on *Streptococcus mutans* was significantly higher than that of AgNPs. However, there were no significant differences in the antibacterial activity against *Lactobacillus* between composites containing AgNPs and those containing ZnO NPs [309].

Azarsina et al. added the 0.5 wt% and 1 wt% AgNPs into Z250 composite to evaluate the antibacterial properties against *Streptococcus mutans* and *Lactobacillus*, using those without AgNPs as control. And the result showed that addition of AgNPs into composite resin had a significant effect on the reduction of *Streptococcus mutans* and *Lactobacillus* colonies. The antibacterial properties of composite resins are different depending on the concentration of AgNPs. 1 wt% of AgNPs had stronger antibacterial properties than 0.5 wt% [310].

Aiming to enhance the mechanical properties and endow composite resin with high antibacterial activity, a novel composite resin was produced. Hydroxyapatite (HA) nanowires were synthesized and then coated with polydopamine (PDA) by submerging the nanowires in dopamine (DA) aqueous solution. A reduction reaction was then used to prepare AgNP-laden HA (HA-PDA-Ag) nanowires by adding glucose and silver nitrate into HA-PDA suspensions in deionized water. The loading amounts of AgNPs controlled by adjusting the feeding doses of silver nitrate and HA-PDA nanowires and then HA-PDA-Ag nanowires were readily obtained. Benefiting from the surface PDA layer, HA-PDA-Ag nanowires could successfully disperse in composite resin and form sound interfacial adhesion with the resin matrix. As compared to the neat resin, the addition of HA-PDA-Ag nanowires achieved significant increases both in modulus of cured composites and flexural strength. The distribution of AgNPs was homogeneous throughout the resin matrix in all designed groups, which endowed the composites with high antibacterial activity against *Streptococcus mutans* [311].

A lot of studies investigated the effects of AgNPs on the mechanical properties of dental resins since they are important for load-bearing dental restorative materials. Incorporation of small amounts of AgNPs (e.g., 0.02 wt%) did not significantly reduce the flexural strength [312]. However, greater amounts of AgNPs could decrease the mechanical properties of composites. The hardness of the light-cured resins containing 0.1 wt% Ag benzoate nanoparticles decreased significantly, compared with the control group [230].

Bonding agents help the adhesion of the composite restoration to the tooth structure in order to form a functional and stable construct. Generally, residual bacteria often exist in the prepared tooth cavity, and microleakage between the margins

could allow the invasion of new bacteria. Modern minimally invasive techniques are recommended for the treatment of deep caries to protect pulp vitality and preserve more tooth tissues. These techniques require to remove less-infected dentin to be the least-invasive surgical approach, possibly leaving behind the affected dentin in the cavity. Therefore, the antibacterial adhesives are needed to combat biofilms and reduce recurrent caries at the tooth-restoration margins.

Quaternary ammonium compounds which contain cationic monomers have been shown to be effective in reducing bacterial growth in a wide range of applications including the medical devices [313]. Due to the covalent bonding with the polymer network to exert "contact inhibition," the quaternary ammonium dimethacrylate (QADM) is immobilized to the resin and the adhesive [314].

Li et al. compared the antibacterial activity, contact-inhibition, and long-distance inhibition of a novel bonding agent containing QADM with that containing AgNPs. While the QADM-containing adhesive presented contact-inhibition exhibited by bacterial inhibition only on its surface, AgNP-containing adhesive had the added advantage of long-distance killing inhibiting away from its surface due to the releases of the silver ions. The novel antibacterial adhesives are promising for caries-inhibition restorations. QADM and AgNPs could cooperate and work together in inhibiting bacteria on resin surface as well as away from resin surface [315].

Since dentin primer directly contacts with the tooth structure, it would be beneficial to use antibacterial primers. QADM and AgNPs were incorporated into dentin primers (Scotchbond Multi-Purpose, "SBMP," 3M, St. Paul, USA) to investigate the effects on dentin bond strength and dental plaque microcosm biofilms. SBMP primer was the control group, and control + 10% QADM (mass), control + 0.05% AgNPs, and control + 10% QADM + 0.05% AgNPs were the modified primers. QADM + AgNP-containing primer increased the bacteria inhibition area by ninefold, compared with control primer. QADM-AgNP-containing primer reduced lactic acid production and CFU of total microorganisms (Fig. 3.15). In conclusion, novel QADM-AgNP-containing primers were strongly antibacterial. They are promising to inhibit biofilms and secondary caries [316].

Disinfection of the bacteria impregnating the dentin in vitro using extracted human teeth was researched using SBMP primer containing AgNPs and QADM. The interior of the dentin blockers was successfully impregnated by *Streptococcus mutans*. After impregnation, either an antibacterial primer or a control primer was applied to the dentin. Primer was applied to the dentin. Harvesting of the *Streptococcus mutans* CFU in dentin was then performed by sonicating from the dentin block for different groups. SBMP + 10% QADM + 0.1% AgNPs had bacteria inhibition zone eightfold that of control, and SBMP + 10% QADM + 0.1% AgNPs inhibited *Streptococcus mutans* in dentin blocks, decreasing the viable CFU in dentin by three orders of magnitude, as compared to the control dentin lacking primer. Therefore, it was more effective to use QADM + AgNPs than QADM alone. These results demonstrate that antibacterial primers were able to kill the bacteria residing inside the dentinal tubules of dentin blocks. Bonding agents containing AgNPs and QADM exerted a long-lasting effect against residual bacteria in the dentinal tubules

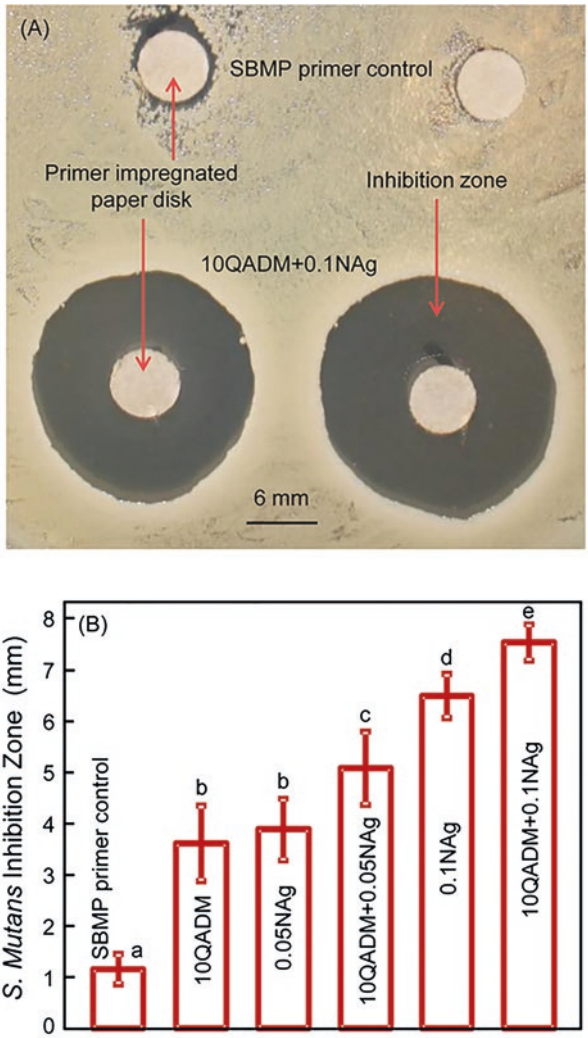

Fig. 3.15 Results of the agar disk diffusion for uncured primers against *S. mutans*: (**A**) representative specimens of SBMP control primer (top), and 10QADM + 0.1Nag added primers (bottom); (**B**) *S. mutans* inhibition zone sizes (mean ± SD; $n = 6$): dissimilar letters suggest the corresponding values are significantly different ($p < 0.05$) [316]

as well as new invading bacteria along the margins due to microleakage (Fig. 3.16) [317].

Unpolymerized 12-methacryloyloxydodecylpyridinium bromide (MDPB) has strong antibacterial activity, and the primer incorporating MDPB demonstrated bactericidal effect before cured, indicating the possible ability to kill residual bacteria in the prepared cavity [318]. A study was done to investigate the effects of dentin primer containing dual antibacterial agents, namely MDPB and AgNPs, on dentin

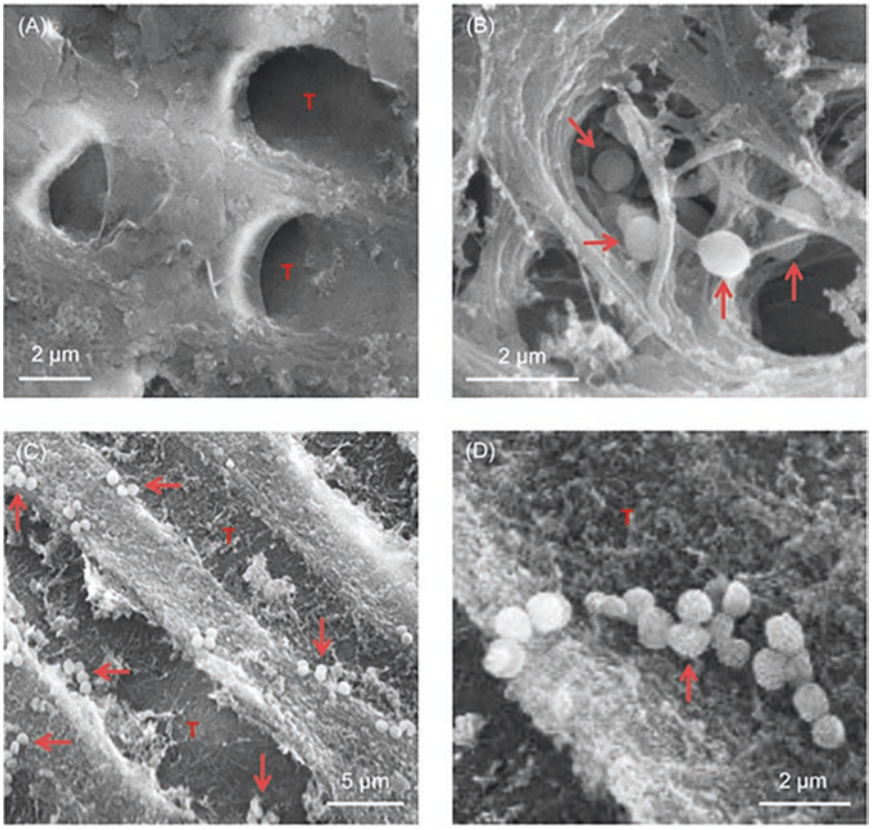

Fig. 3.16 (**A**) Dentinal tubules are shown before impregnation by *Streptococcus* and after impregnation (**B**). The dentin cross section is shown in (**C**), displaying *S. mutans* inside dentinal tubules. Shown under higher magnification (**D**). T: dentinal tubules [316]

bond strength and dental plaque microcosm biofilm response. SBMP was used as the parent bonding agent. Four primers were tested: SBMP primer control, control + 5% (mass fraction) MDPB, control + 0.05% AgNPs, and control + 5%MDPB + 0.05% AgNPs. Dentin shear bond strengths were tested utilizing extracted human teeth. The biofilms arising from the mixed saliva of ten donors were cultured to examine metabolic activity, lactic acid production, and CFU. The result showed that incorporating MDPB and AgNPs into primer did not reduce dentin bond strength, but they both greatly reduced acid production and biofilm viability was considerably diminished as measured against the control. Dual agents MDPB + AgNPs had far stronger effects than either separately, presenting as increased inhibition zone size and reduced metabolic activity, lactic acid, and CFU by an order of magnitude, as measured against the control [319].

To investigate the combined effects of antibacterial adhesive and primer on biofilm viability, metabolic activity, lactic acid, and dentin bond strength, MDPB and

AgNPs were added together into SBMP. MDPB and AgNPs were included in the SBMP primer and adhesive. Tests were conducted on five systems: SBMP adhesive, adhesive + MDPB, adhesive + AgNPs, adhesive + MDPB + AgNPs, primer + MDPB + AgNPs combined with adhesive + MDPB + AgNPs. The mixed saliva from ten donors were used to culture dental plaque microcosm biofilms. Investigations were then conducted on CFU, metabolic activity, and the lactic acid production of biofilms. The results showed that MDPB + AgNPs in the adhesive/primer did not undermine the dentin bond strength. Although MDPB or AgNPs each separately substantially decreased biofilm activities, the dual agents MDPB + AgNPs showed even more substantial decreases. But, when both the adhesive and primer incorporated MDPB + AgNPs, the inhibition of biofilms was the highest [320].

The nanoparticles of NACP were incorporated into the composites and endowed the composites with calcium ion and phosphate ion release properties. The release of calcium ions and phosphate ions were able to remineralize the tooth lesions and inhibit the secondary caries. Melo et al. incorporated NACP and AgNPs into bonding agents and explored the effects on dentin bond strength and plaque microcosm biofilms formation. AgNPs were added into primer and adhesive at 0.1% by mass. NACP were mixed into adhesive at 10%, 20%, 30%, and 40% (mass). It is found that the addition of AgNPs and NACP into adhesive did not decrease the bond strength. NACP had little antibacterial effect but could neutralize acids. SEM showed that numerous NACP infiltrated into the dentinal tubules. Dental plaque microcosm biofilm viability and acid production were greatly reduced by bonding agents containing AgNPs and NACP [321].

The antimicrobial mechanism is through silver ions that inactivate the vital enzymes of bacteria, preventing the bacteria from replicating its DNA which leads to cell death. AgNPs with the release of silver ions could generate ROS, damage the cell membrane, and interact directly with cell membranes. The NACP composite could release high levels of calcium ions and phosphate ions to neutralize cariogenic acid solutions and remineralize tooth lesions. The NACP composites with AgNPs which were able to hinder biofilm growth and acid production would be a promising method to combine three benefits, namely remineralization, acid neutralization, and antibacterial capabilities.

It has been known that the pulpal infection and periradicular lesion formation are often caused by Gram-negative anaerobes and residual bacteria in root canal. And they often lead to the treatment failure of the disease [322]. Ideally, endodontic materials should have some antimicrobial activity to improve the prognosis of endodontically treated teeth. Because the elimination of bacteria in root canal is the key to achieve the success of the treatment. Therefore, it is better that materials in root canal therapy, including root canal filling materials, root canal irrigation solution, and root canal sealing drugs, can be improved by nanomaterials to have the antibacterial properties.

One important step in the endodontic treatment is the chemomechanical debridement of pulpal tissue and pathogenic bacteria. As in every root canal system, there are spaces that cannot be cleaned mechanically. In such places, the cleaning is

dependent on thorough chemomechanical debridement of pulpal tissue, dentin debris, and infective microorganisms. At this stage, irrigant solutions should be used, for dissolving tissue and disinfecting the root canal system. As an irrigant solution, sodium hypochlorite (NaClO) has been used for many years for dissolving tissue and disinfecting the root canal system due to its effective antimicrobial activity. Its working concentration varies from 0.5% to 5.25%; however, if NaClO went beyond the apex, it would damage the periapical tissues.

The liquid form of AgNPs with particle size 35 nm was prepared using a two-step procedure. Nanoparticles were produced using a catalytic chemical vapors deposition procedure and then added to distilled water. No surfactant was used in the liquid to prepare AgNP suspensions. The mixture was prepared using an ultrasonic homogenizer. Lotfi et al. used the AgNP solution and compared its antibacterial effect with NaClO against *Enterococcus faecalis*, which is a bacterium often detected in the failed endodontic treatments. No significant differences were found between the 5.25% NaClO and 0.005% AgNPs, suggesting that although the AgNP was used at remarkably lower concentrations, its bactericidal effect was equivalent to the 5.25% NaClO. Hence, it is a potential new candidate for intracanal irrigant [323].

Yet, questions remain on how effective AgNPs are in combating *Enterococcus faecalis* biofilm. Effectiveness against *Enterococcus faecalis* biofilm was evaluated and compared for the 1% and 5% NaClO, 2% CHX, 1% AgNP suspension, and 26% ZnO NP suspensions. Seventy-six human teeth prepared biomechanically were extracted, mounted onto a specific apparatus, and sterilized. Next, an *Enterococcus* faecalis suspension in 100 μL amounts were inoculated into the root canals, and replaced at 24 h intervals for 7 days. The teeth were randomly divided into six groups according to the irrigation solution: the control 0.85% saline, 1% NaClO, 5% NaClO, 2% CHX, 1% AgNP suspension, and 26% ZnO NP suspension. After the irrigation treatment, the biofilm susceptibility to disinfecting solutions was determined by CFU quantification. The result showed that the effectiveness of 5% NaClO and 1% AgNPs against *Enterococcus faecalis* biofilm was superior than 0.85% saline solution. When compared with the control, 5% NaClO was able to reduce 100% of CFU, followed by 1% AgNPs (97.6%), 26% ZnO NPs (96.1%), 1% NaClO (94.1%), and 2% CHX (93.1%). Based on the methodology used, 5% NaClO and 1% AgNPs was excellent and effective against intracanal *Enterococcus faecalis* biofilm [324]. As NaClO will damage the periapical tissues when it is beyond the apex, 1% AgNP suspension may be a more suitable irrigant solution to intracanal biofilm.

Typically, camphorated phenol (CP), a medicant categorized in the phenolic group, has been implemented either through a paper point submerged in the root canal or on a cotton wool pellet submerged into the pulp chamber, with the expectation that the vaporization properties can elicit antimicrobial activity [325]. However, the antibacterial action of this group of medicants may not be long-lasting. Thus, some bacteria may survive and have opportunity to multiply and persist in the root canal system.

An alternative, nanosilver gel (NSG), was assessed in comparison with CHX and CP against *Enterococcus faecalis* biofilm to determine its effectiveness. NSG was in three concentrations (0.05%, 0.1%, and 0.2%). Two percent CHX was used, and CP and normal saline were used as control. Among the groups (0.05% CP and NSG, 0.1% CP and NSG, 0.2% CP and NSG, 2% CHX and 0.1% NSG, and 2% CHX and 0.2% NSG), significant differences were found. Comparatively, there was no significant difference between CHX and 0.05% NSG. Thus, it can be concluded that 0.1% and 0.2% NSG is more effective on *Enterococcus faecalis* biofilm as compared with CHX and CP [326].

Other researchers synthesized and characterized the AgNPs with different surface charges to evaluate the antibacterial and cytotoxicity activity in the presence of dentine compared with NaClO and CHX. AgNPs with positive, negative, and neutral surface charges were synthesized and characterized. AgNPs having a positive surface charge were found to have the smallest minimal inhibitory concentration (MIC) against planktonic *Enterococcus* faecalis and also were active at notably lower concentrations compared with NaClO, CHX, and other evaluated AgNPs. At 5.7×10^{-10}mol/L, the positively charged AgNPs completely prevented *Enterococcus faecalis* growth after 5 min contact, a finding that was comparable to 0.025% NaOCl. And the most positively charged AgNP solution was the least toxic solution to L929 fibroblasts. So, they concluded that the surface charge of AgNPs was significant for bactericidal efficacy against *Enterococcus faecalis*. Antibacterial results against *Enterococcus faecalis* was promisingly displayed by the positively charged imidazolium-based ionic liquid protected AgNPs, which also showed a high degree of cytocompatibility to L929 cells [327].

A variety of materials have typically been employed for root canal fillings, especially gutta-percha [328]. The zinc oxide in this material has been proven to slightly provide it with antibacterial properties. However, effective bactericidal properties are still lacking. To counter this drawback, some researchers have developed a new kind of gutta-percha coated with AgNPs to improve the antibacterial effect. The new materials showed significant effect against some sorts of germs such as *Enterococcus faecalis*, *Staphylococcus aureus*, *Candida albicans*, and *Escherichia coli* [329]. In addition, to test its biocompatibility, the cytotoxicity of nanosilver-coated gutta-percha was tested using mouse fibroblasts compared with normal gutta-percha. And the results confirmed its good biocompatibility. They found that nanosilver-coated gutta-percha presented similar cytotoxicity to normal gutta-percha after 24 h. And it reached the lowest level of cytotoxicity compared with the gutta flow and normal gutta-percha after 1 week [330].

Ideal materials for sealing root-end cavities should prevent leakage, have dimensional stability, adhere to the cavity walls, and promote healing. They should also be nontoxic and biocompatible. However, most current root-end filling materials are unable to guarantee a hermetic seal. This results in a possible microscopic space that can exist between the interface of the filling material and the root-end cavity, providing a pathway for bacteria and cytotoxic produce to possibly penetrate. Thus, in addition to other properties, antimicrobial activity must also be addressed for ideal root-end-filling materials [331].

Due to low solubility, low cytotoxicity, good biocompatibility, and excellent ability to induce hard tissue formation, the mineral trioxide aggregate (MTA) had been used in many indications such as perforations sealing, external/internal root resorption repair, and apexification. But the antimicrobial properties of MTA are controversial and seem to be limited. Aiming to improve it, some researchers modified MTA by adding 1% by weight AgNPs [85] and then evaluated its effect against fungi species and oral bacteria. Compared to unmodified MTA, the AgNP-containing MTA possess enhanced antimicrobial effects against *Candida albicans, Enterococcus faecalis*, and *Pseudomonas aeruginosa* [85, 332]. Each gram of MTA powder was mixed with 350 μL of 25, 12.5, and 6.25 ppm preparations of AgNP solution. Both AgNPs and AgNP–MTA inhibited the growth of all four anaerobic endodontic–periodontal pathogens (*Aggregatibacter actinomycetemcomitans, Fusobacterium nucleatum, Porphyromonas gingivalis,* and *Prevotella intermedia*) at 25 ppm concentration. AgNPs significantly improved the antimicrobial activity of MTA. And bacterial susceptibility to various concentrations of AgNPs was dependent on bacterial type. Overall, AgNP–MTA displayed a significant time- and dose-dependent inhibitory effect [333].

Antimicrobial effects against five microorganisms typically associated with dental infections were tested by adding two concentrations of AgNPs (100 and 200 ppm) to MTA (60 μg) and testing their effectiveness. The result showed that resultant MTA had antibacterial activities on all microorganism strains except *Enterococcus faecalis* and mixture group. These two cements in aqueous form could not inhibit the growth of *Enterococcus faecalis.* The main reason is that *Enterococcus faecalis* possibly has the ability to change its cell wall structure, whereby also increasing its resistance against temperature and high pH. Adding AgNPs, however, can significantly alter the antibacterial effects of MTA against *Enterococcus* faecalis and other assessed microorganisms. No statistically significant difference was found between two AgNP concentrations. The mechanism of the positive antimicrobial effects of AgNPs was that silver particle can decrease the attachment of microorganisms to the surface and also increase the antibacterial properties of endodontic sealer [332].

Evaluation of the inflammatory reaction of MTA and AGNPs was also performed by some researchers by comparing the subcutaneous inflammatory reaction of rat connective tissues to MTA with and without AgNPs (1 wt%). Polyethylene tubes (1.1 × 8 mm) containing experimental materials (MTA and MTA + AgNPs and empty control tubes) were implanted in subcutaneous tissues of male rats with different evaluation of time, 7 days, 15 days, 30 days, and 60 days. And it can be concluded that incorporation of 1% AgNPs into MTA does not induce the inflammatory reaction of subcutaneous tissue in rat models [334].

Endodontic treatment aims to eradicate microorganisms from the root canal space, or at least reduce microorganism levels to amounts suitable for periadicular tissue health [335]. After chemomechanical treatment of root canals, the population of microorganisms is significantly decreased. However, the microorganisms cannot be eliminated thoroughly. Therefore, endodontic sealers with high antimicrobial activity helps to decrease or prevent the growth of microorganisms and aid the repair process of apical and periapical tissues. However, fiber posts are generally

needed in endodontically treated teeth with great coronal destruction to obtain better retention of crowns or resin composite restorations. When implemented, it can help evenly distribute the stress generated by tooth function [336].

MicroMedica S.r.l. (a company in Italy) developed a new fiber post with AgNP incorporation. The purpose is to create a fiber post which combines the common elasticity, mechanical strength, adhesion, and esthetic characteristics, with the new antibacterial capacity provided by the incorporation of silver. Poggio et al. compared the antibacterial activity and the cytotoxicity effects of different fiber posts: glass fiber post, quartz fiber post, nanofiber post (glass fiber with zirconia nanoparticles), and silver fiber post (quartz fiber with AgNPs). Silver fiber post was the only one showing a fair antibacterial effect against all the three streptococcal strains, while the other posts tested did not present any antibacterial effects. The incorporation of AgNPs endows the fiber post with antibacterial activity, decreasing the development of recurrent caries and increasing the longevity of tooth restorations [337].

Dentures, mostly constituted by methyl methacrylate (MMA) and poly methyl methacrylate (PMMA) acrylic resin, have their inner surface considerably rough. The roughness, combined with other factors such as poor hygiene, xerostomia, and HIV infection, contributes to the emergence of denture stomatitis [338, 339]. This pathology mostly localized in palatal mucosa and presented in 50–70% of complete denture wearers. It is frequently associated with *Candida* species colonization. The biofilm formed by fungi is a key factor in the development of denture stomatitis [340]. The treatment of denture stomatitis is based on topical or systemic antifungal drugs, e.g., fluconazole and nystatin. However, antifungal resistance has been reported in *Candida* biofilms [341]. Therefore, this infection is often persistent. Another challenge associated with denture stomatitis is the difficulty for many geriatric prosthetic wearers in maintaining clean dentures, due to their reduced motor dexterity, cognitive impairment, and memory loss [342]. Considering the above factors, denture stomatitis represents a challenge in dentistry. And the prevention methods are urgently needed. Therefore, nanoparticles have been incorporated.

In a research, graphene-oxide nanosheets (nGO) were incorporated into PMMA to introduce sustained antimicrobial-adhesive effects by increasing the hydrophilicity of PMMA. nGO was added in quantities of 0.25, 0.5, 1.0, or 2.0% by weight relative to PMMA powder which coarsened its surface and enhanced its hydrophilicity without sacrificing surface hardness or flexural strength. The nGO-incorporated specimens showed increasing concentration-dependent levels of anti-adhesive effect after exposing 1 h to the microbials in artificial saliva, while neither producing significant cytotoxicity to oral keratinocytes nor requiring the loading of chemicals or drugs. Additionally, PMMA continuously expressed improved anti-adhesive effects against *Candida albican* for up to 28 days after nGO modification than expressed by pure PMMA as viewed through increased hydrophilicity [343].

Nano-chitosan particles, which have lasting antimicrobial activity, at concentrations of 0, 1%, 5%, and 10% (w/w), were added to the acrylic resins to study the inhibitory effect on the biofilm formation of *Candida* species. The results showed that there were significant differences between unmodified acrylic resin (control)

and acrylic resin with nano-chitosan particles in terms of biofilm formation. No significant difference was found in the formation of biofilm species on resins. With the increase in the concentration of nano-chitosan particles, the rate of biofilm formation is reduced [342].

AgNPs (100–120 nm) were incorporated into a commercial tissue conditioner, in the following concentrations: 0.1%, 0.5%, 1.0%, 2.0%, and 3.0% (vol/vol %: colloidal Ag/conditioner liquid). Their inhibitory effect was evaluated against *Staphylococcus aureus, Streptococcus mutans*, and *Candida albicans* after 24 h and 72 h. The authors reported that the modified tissue conditioner combined with AgNPs displayed antimicrobial properties against *Staphylococcus aureus*, *Streptococcus mutans* at 0.1% Ag incorporation and *Candida albicans* at 0.5% Ag incorporation after a 24 and 72 h incubation periods [344].

In another research, 2 wt% silanized zirconium dioxide nanoparticles (nano-ZrO_2) and 4 wt% silanized aluminum borate whiskers (ABWs) were mixed with PMMA powder to get ZrO_2-ABWs/PMMA composites. Titanium dioxide (TiO_2), silver-supported TiO_2 (Ag/TiO_2), Novaron, and tetrapod-like zinc oxide whiskers (T-ZnOw) antibacterial agents of 3 wt% were mixed with the composites respectively to fabricate standard specimens. Then, the composites were mixed with MMA monomer at a 2:1 powder-to-liquid ratio to test the antibacterial property against *Streptococcus mutans* and *Candida albicans*. Table 3.2 lists the groups of different composition prepared in this study. The 3 wt% addition of various antibacterial agents had significant antibacterial activities compared to the control and blank groups. The Ag/TiO_2 and Novaron groups had better antibacterial property than the other groups. As for Ag/TiO_2, it can consequently interact with O_2 and H_2O and form ROS, which can adhere to the membrane of the bacteria occurring lipid peroxidation reaction to cause the damage of cellular proteins and finally lead to cell death [236].

AgNPs have high antibactericidal activity and good biocompatibilities. They tend to aggregate spontaneously when their diameters are less than 200 nm. And their stability in air, water, or sunlight is not good enough for long-time storage. Novaron, a silver-supported inorganic antimicrobial agent, offers superb antimicrobial efficacy to a broad range of microorganisms. Presumably, the antimicrobial mechanism involves either one or both of the following steps: inhibition of the bacteria's vital metabolism by silver ions and/or the destruction of the bacteria cell membranes from the activated oxygen generated from water [181, 236].

Periodontitis is an inflammatory and infectious disease of the periodontium caused by pathogenic microorganisms. Left untreated, periodontitis destroys the

Table 3.2 PMMA composite components by group [236]

Group	Ingredients
Blank	MMA monomer, PMMA powder
Control	MMA monomer, PMMA powder, silane coupling agent: nano-ZrO_2, ABWs
TiO_2	MMA monomer, PMMA powder, silanized ABWs 3 wt% TiO_2, silanized nano-ZrO_2
Ag/TiO_2	MMA monomer, PMMA powder, silanized ABWs 3 wt% Ag/TiO_2, silanized nano-ZrO_2
Novaron	MMA monomer, PMMA powder, silanized ABWs 3 wt% Novaron, silanized nano-ZrO_2
T-ZnOw	MMA monomer, PMMA powder, silanized ABWs 3 wt% T-ZnOw, silanized nano-ZrO_2

alveolar bone of the teeth and supporting tissues. Current treatment of periodontal infections includes mechanical debridement, administration of antibiotics, and bone grafting.

The primary goal of periodontal treatment has always been the elimination of pathogen containing biofilms. Traditionally, the initial phase of treatment is using supra- and subgingival mechanical debridement. However, periodontal pathogens cannot be completely removed by this method. To augment mechanical debridement, adjunctive antimicrobial agents in forms of topical or systemic antibiotics or topical antiseptics have been employed [345, 346]. However, the systemic antibiotic therapies seem to constitute an inferior choice compared with the topical use of low-cost, broad spectrum antiseptic agents which is low in adverse reaction potentials.

To develop the high and safe antimicrobial subgingival irrigation, nanobubble water (NBW3) which is a form of gas nucleus less than 100 nm in diameter was developed by nanobubble-generating technology. The ozone concentration of NBW3 is 1.5 mg/L which is equivalent to the oxidation titer determined by electron spin resonance. In one research, mechanical therapy was completed in a single visit with an ultrasonic scaler running NBW3 or tap water as irrigant. The results showed that the NBW3 group posed significantly greater clinical attachment gain and reduction in the probing pocket depth as compared to the water group after 4 and 8 weeks. Moreover, the mean total number of bacteria in subgingival plaque showed significant reductions only in the NBW3 group during the investigation [347].

Yet, the mechanisms for how NB3 inactivates bacteria still require further research. However, one can postulate that the phenomenon might be similar to that of existing ozonated water. The ozone, as a potent oxidizing agent, in ozonated water could react with various organic substances and decompose them by free radical-mediated oxidation reactions. Ozone can be converted into oxygen when it reacts with organic substances. In this process, hydroxyl radicals are generated, which is an important ROS. These free radicals might play a role in the eradication of bacteria by NBW3 [347].

Nanoparticles have also been used in dentistry to locally deliver drugs in sufficient concentrations directly to the site of action. These delivery systems are usually injected into periodontal tissues or inserted into the periodontal pocket for enhancing the therapeutic effects while also reducing the drug effects due to systemic use and large dosage [348]. Because of their small size, nanoparticles can penetrate into areas, such as bacterial cells, alveolar bone trabeculae, and from the gingival sulcus inward to the underlying connective tissue and to the periodontal pocket areas below the gum line where may be inaccessible to other delivery systems [349].

The biogenic AgNPs, produced by *Escherichia coli* which served as a matrix preventing aggregation, were assessed for the possible inhibiting effect on a selected suspected periodontopathic bacterium, by bacterial colony counting assay. The result showed that lower concentrations of bio AgNPs (1, 3, 6, 12μM) failed to inhibit the growth of the selected bacterium, and the higher concentration (18, 30μM) showed significant bacterial inhibition effect. When the antibacterial activity of the biogenic silver, ionic silver, and chemically produced nanosilver is compared, the MIC of the former two was lower than that of the chemically produced nanosilver. It was the same in the minimal bactericidal concentration (MBC) results.

The existence of salts and organic matter reduced the antimicrobial activity of biosynthesized silver, thereby increasing the MBC and slowing the inactivation of the bacteria. Due to the high concentration of free silver ions and also the similarity in performance between both ionic silver and biogenic silver radical formation, the mechanism of biogenic silver action can mainly be attributed to silver ion release. (Fig. 3.17) [350].

Minocycline is a long-acting and bacteriostatic antibiotic, often acts against periodontal pathogens, and was chosen to be incorporated into PLGA nanoparticles by Kashi TS [351]. Novel minocycline-PEGylated PLGA nanoparticles, with an average particle size of 85–424 nm, was the best in drug loading, showing higher in vitro antibacterial activity than the free drug. The results of drug release test performed in phosphate buffer at pH 7.4 indicated slow release of minocycline lasting from 3 days to several weeks [351].

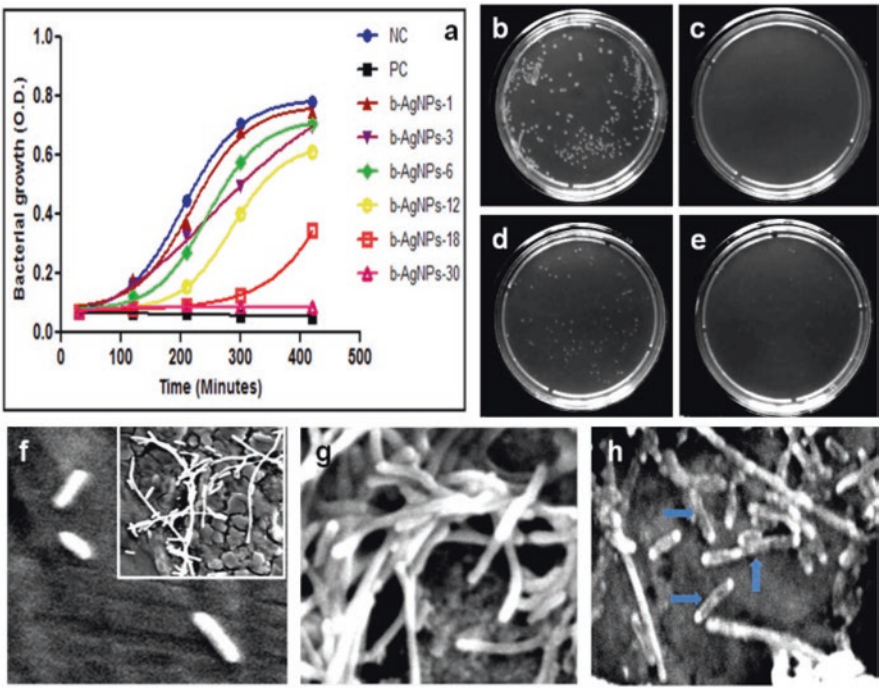

Fig. 3.17 Study of antibacterial activities: (**a**) liquid growth inhibition kinetics of *E. coli* using different concentrations of b-AgNPs. b-AgNP-30 (at 30 μM) shows almost 100% growth inhibition. Ampicillin has been used as a positive control (PC) and NC: negative control or untreated *E. coli*. The numbers indicate the concentration of b-AgNPs in μM. (**b**–**e**) optical images of bacterial colonies formed by *E. coli* cells, i.e., colony counting assay (after 24 h): (**b**) Control, (**c**) Ampicillin (100 μg/mL), (**d**) b-AgNPs (18 μM), (**e**) b-AgNPs (30 μM) and (**f**–**h**) SEM images of *E. coli* cells (**f**) without being treated (control), (**g**) treated with Olax for 1 h, (**h**) treated with b-AgNPs (30 μM) for 1 h. The SEM images show the silver nanoparticles damage the bacterial cell membrane (marked by blue arrows), whereas the bacterial membranes of untreated and treated *E. coli* with Olax are intact [350]

Some researchers developed an osteoconductive drug delivery system composed of apatite nanocarriers capable of providing sustained delivery of drugs in the periodontium. The antibacterial activity of calcium-deficient hydroxyapatite (CDHA) nanocarrier-loaded tetracycline with different Ca/P ratios was detected. CDHA nanocarriers of Ca/P = 1.61 was found to be an ideal carrier for local delivery of tetracycline with continuous release over a period of 120 h. Tetracycline showed a release profile having an initial burst release followed by a slowly prolonged releases over the next 5 days. The first stage is because of the desorption of loosely bound drug molecules on the surface while the second is from the slower dissolution of the CDHA crystal. It can be concluded that the CDHA nanocarriers are ideal drug delivery agents and have bone regenerative potential for local periodontal applications [352].

The concept of periodontal regeneration necessitates the exclusion of epithelial and connective tissue cells of the gingiva from the wound site. Therefore, it leads to the development and application of guided tissue regeneration (GTR) technique. GTR procedures using nonabsorbable and bioabsorbable membranes have been used successfully and predictably in treating various types of intrabony defects [353]. Because of the bacterial contamination of the wound site at the time of surgery or during the period of healing, the outcome of the GTR procedure could be significantly compromised. Numerous protocols, such as systemic antibiotic therapy, local application antibiotics in the form of antibiotic gel and antibiotic fiber, and irrigation with antibiotic solution, have been advocated in controlling or eliminating periodontal pathogens during GTR procedures, achieving improved outcomes during GTR therapy. Antibiotics such as amoxicillin and metronidazole have been loaded on GTR membranes for successful treatment outcomes [354–357].

AgNPs were impregnated into GTR membranes to evaluate the antibacterial activity in terms of bacterial adherence to the membranes and specific bacterial penetration through the membranes. Three sets of GTR commercial membranes used in this study were grouped as GTR-C: plain GTR membrane; GTR-NS: GTR membrane impregnated with 0.1 mg/mL 10 nm AgNPs; and GTR-DOX: GTR membrane impregnated with 25% (w/w) doxycycline hydrochloride acting. The bacterial strains used in this study were *Streptococcus mutans*, *Aggregatibacter actinomycetemcomitans*, *Fusobacterium nucleatum*, and *Porphyromonas gingivalis*. The GTR-C group showed significantly higher mean bacterial adherence scores compared to the GTR-DOX and GTR-NS groups. Highly significant lower adherence scores were found for GTR-NS as compared to GTR-DOX among all four microorganisms [358].

To combine the beneficial properties of the bioactive-glass, the gelatin, and AgNPs together, a study added various concentrations of AgNPs (0, 5, 10, 20, and 40 mM) to a macroporous scaffold for bone tissue engineering which contained hybrid gelatin/bioactive glass. Incorporating AgNPs to the scaffolds may affect physicochemical properties of the scaffolds, such as gel fraction, porosity, swelling behavior, morphology, and the antimicrobial activity. The antimicrobial activity of the scaffolds was investigated against two types of bacteria *Staphylococcus aureus* and *Escherichia coli*, presenting significant inhibition of the growth of those bacteria and the reduction of the biofilm formation on the scaffolds. The antibacterial effect was increased with increased AgNP concentrations [359].

Due to being nontoxic and having high biocompatibility, biopolymers have been widely used for scaffolding in biomedical research. However, certain limitations still arise from using polymers (e.g., pure polymers have nonbactericidal nature) which can be overcome by bioinorganic hybrid nanocomposites [360]. Typical inorganic nanomaterials used for this purpose include metals (Au, Ag, etc.) and metal oxides (ZnO, TiO_2, MgO, CaO, NiO, CoO, etc.). When they are utilized in the synthesis of polymer nanocomposites, they act as reinforcement materials. Regenerated bacterial cellulose (RBC) nanocomposites with TiO_2 NPs were prepared with the aim to enhance the bactericidal activity and tissue regeneration. The results suggested that the bactericidal activities were due to ROS and membrane stress generated by the TiO_2 NPs present in the composite membranes.

Nanoparticle-mediated oxidative stress by nanoparticles might be caused by a variety of factors, which include the generation of ROS, e.g., H_2O_2, O_2^*, O_2^-, and OH. When the ROS generation becomes excessive, the mitochondrial membrane permeability increases and the cellular respiratory chain is damaged. So, the RBC-TiO_2 nanocomposites showed impressive adhesion and proliferation capabilities on animal fibroblast cells without any toxic effects in addition to antibacterial properties [361].

Titanium implants, which are widely used in dentistry, sometimes present infections around their surface, especially where the implant connects the gingiva soft tissue. This infection is still one of the major complications in orthopedics and implantology. Several methods have been presented to combat bacterial contamination, such as aseptic surgical protocols and implant disinfection. Nonetheless, bacterial invasion still occurs frequently after surgery. Thus, antibacterial coatings have been developed and tested to prevent biofilms from forming over the implant surface. However, most exhibit inadequate long-term antibacterial action and pose the problem of generating resistant strains after the possibility of generating resistant strains after extensive use [362]. Thus, some researchers incorporated AgNPs to implant surface and expected that it would be possible to produce coatings with long-term antibacterial properties by the controlled release of AgNPs [363].

In one research, pure titanium foils underwent electrochemical anodization to form a titania nanotubular (TiO_2-NT) layer, and then the TiO_2-NTs were soaked in $AgNO_3$ solutions with four different concentrations (0.5, 1, 1.5, and 2 mol/L) for 10 min, to introduce AgNPs to the wall of the TiO_2-NTs to get the Ag-loaded TiO_2-NTs (NT-Ag), and found that TiO_2-NT-coated Ag had inhibitory effect on the planktonic bacteria in the first 4 days. In addition, the high efficacy of Ag at very low concentrations and relatively large reservoir provided by the nanotubes can give rise to long-term antibacterial effects, which can last for 30 days, and guarantee normal wound healing in the early stage. Initially, a large amount of Ag is released. But it diminishes gradually with immersion time. For dental implants, the phase right after implantation poses the greatest risk and likelihood of infection. Hence, the robust ability of NT-Ag to eliminate surrounding planktonic bacteria assists in preventing postoperational infection and guaranteeing normal wound healing at the early stage. Afterward, primary healing of the surgery site will be completed and in time osseointegration as well. A low-level Ag release can be used in the later stage in order to inhibit bacterial adhesion and biofilm formation and thereby prevent later-stage

infection conjugated with the host defense. This strategy provides both the production of a long-term antibacterial surface while also decreasing the risk of cytotoxicity by controlling the Ag release rate. Furthermore, prevention of implant-associated infection in both early and medium stages is effectively controlled by the long-term bacterial resistance presented [363].

An attractive strategy for control of peri-implantitis is posed by titanium nanoscale modifications of antibacterial implant surfaces. Silica-based composite coating containing AgNPs (AgNP/NSC) produces a strong antibacterial effect on titanium surface by not only killing the adherent bacteria but also reducing the extent of biofilm formation by more than 70% on the coated surface compared to the control. Since relatively low levels of silver release in the aqueous solution was presented by the AgNP/NSC coating, bacterial contact or adjacent to the AgNP-doped nanoporous silica surface can explain the bactericidal mechanism. Nanometer-level erosion of the silica-coating matrix can appear in the aqueous medium, resulting in the metal nanoparticle exposure and release at the material/aqueous solution interface. AgNPs with the release of silver ion could generate the ROS and damage the cell membrane happened due to the interaction between nanoscale silver and cell membranes. The silanol functional groups on the surface of silica have shown stronger antimicrobial activity. Silica has silanol functional groups on its surface which have shown more potent antimicrobial activity than that of their analogous alcohols due to the physicochemical properties of silanol, particularly based on the higher H-bond acidity and hydrophobicity as compared to alcohols. Thus, the surface chemistry of the nanoporous silica matrix and the bactericidal effect of AgNPs in conjunction may explain the antibacterial activity of the AgNP/NSC nanocomposite coating [364].

Flores et al. modify Ti/TiO_2 surfaces with citrate-capped AgNPs by immersing the Ti substrates in the AgNP solutions (3.16×10^2 mg Ag/mL) in the dark for 24 h and evaluated the antibacterial activity of AgNPs against *Pseudomonas aeruginosa*. They tested the efficiency as antimicrobial coating of AgNP on Ti/TiO_2 surfaces by checking the ability of attached bacteria to form colonies in agar. The results from early stages of biofilm formation as detected by bacterial spreading on agar plates conducted on control Ti/TiO_2 substrates after incubating 24 h in nutrient agar were 0.28 and 1.24 cm for the AgNP-covered substrate and the control, respectively. These results support that there are less viable cells found attached on the AgNP-covered surface as compared to the control. Additionally, the halo area was reduced, indicating that growth of bacteria on the agar in the vicinity of the substrate was inhibited by the diffusion of silver ions from the AgNP-covered substrate. To quantitatively assess the effectiveness of AgNP-modified Ti/TiO_2 surfaces, viability assays were carried out with the LIVE/DEAD viability kit. The result showed that the total number of bacterial cells revealed on AgNP-modified implants was only 20% of those that were attached to unmodified surfaces. These results suggest that incorporating AgNPs on Ti implants can efficiently protect the implant surface against pathogen colonization [365].

AgNPs with various diameters and distributions were immobilized on stainless steel (SS) via silver-sourced plasma immersion ion implantation (Ag-PIII), for 0.5 and 1.5 h, and their antibacterial ability was investigated with four different

bacteria, including *Escherichia coli* (Gram-negative), *Pseudomonas aeruginosa* (Gram-negative), *Staphylococcus aureus* (Gram-positive), and *Staphylococcus epidermidis* (Gram-positive). Ag-PIII treatment is effective in inhibiting bacteria adhesion and biofilm formation, and the antibacterial activity of AgNPs immobilized on SS for 1.5 h was higher than that of 0.5 h. Moreover, Ag ions were minimally released by the Ag-PIII samples, and their antibacterial activity was maintained after multiple cycles of bacterial exposure, suggesting that antibacterial action of the Ag-PIII SS was independent of Ag release and more likely from Ag and SS substrate synergy. However, further studies are needed to fully elucidate the antibacterial mechanism. The study also found that new bone formation occurred on the surface of the Ag-PIII wires, and fibrous tissue occurred only surrounding the SS wire, suggesting that the Ag-PIII SS also had good osteogenic ability (Fig. 3.18) [366].

Silver ion-containing HA nanopowder coating was evaluated for their potential to reduce bacterial colonization on titanium rods in a methicillin-resistant *Staphylococcus aureus* (MRSA)-challenged rabbit femoral implant model. Compared to the uncoated and HA-only-coated rods, the coated rods exhibited significantly less bacterial growth at 10 weeks. Organ and tissue samples showed no detectable accumulation of silver, and likewise bone cells did not exhibit cellular inflammation or the toxic effect of silver. Silver ion-doped calcium phosphate-based ceramic nanopowder coating on orthopedic implants may prevent bacterial colonization and infection in open fractures compared with those without coatings [367].

ZnO NPs were deposited alone or in mixtures with nanohydroxyapatite onto the surface of glass substrates using an electrohydrodynamic atomization process. The coatings displayed significant antimicrobial activity against *Staphylococcus aureus* in in vitro test. As the concentration of ZnO NPs increased, an increased

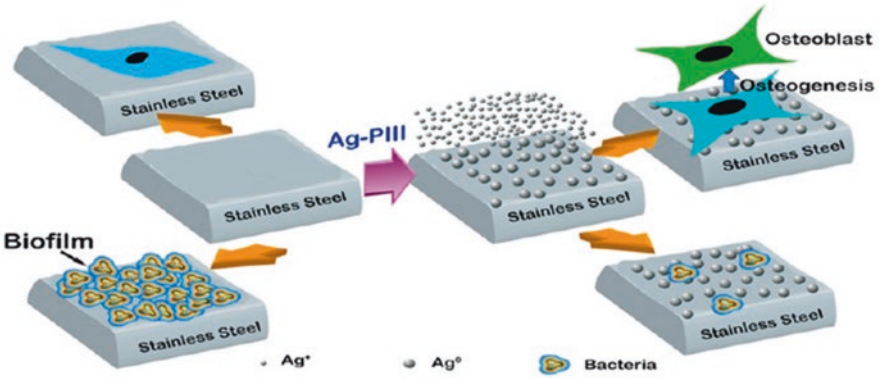

Fig. 3.18 Modification of the stainless steel surface (SS) was performed by silver-sourced plasma immersion ion implantation (Ag-PIII). Various distributions and diameters of the metallic silver nanoparticles were fabricated on the SS surfaces after treating with Ag-PIII for 0.5 and 1.5 h, respectively. In vitro and in vivo tests were used to evaluate the antimicrobial properties and osteogenic activity of SS before and after Ag-PIII treatment. The results showed that the Ag-PIII not only enhanced the antibacterial activity of SS but also promoted the osteogenic differentiation of human bone marrow stromal cells [366]

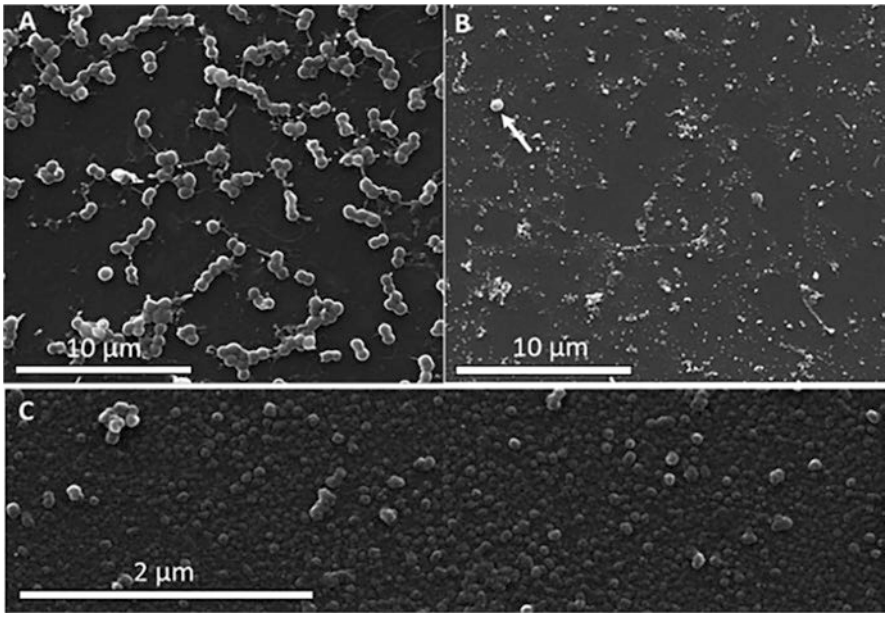

Fig. 3.19 The antimicrobial effect of nZnO-coated glass samples as compared to uncoated samples analyzed qualitatively. (**A**) Bacteria appearing on uncoated surface. (**B**) A single bacterium, as denoted by the white arrow, appearing on the coated surface. (**C**) Uniform characteristics of the coating as shown under high resolution [368]

antimicrobial activity was observed when submerged in a suspension of *Staphylococcus aureus* for a prolonged period. The coatings also demonstrated minimal toxicity to rat UMR-106, human MG-63 and human mesenchymal cells. And osteoblast cells UMR-106 showed an increase in proliferation and alkaline phosphatase activity on the coated surfaces (Fig. 3.19) [368].

To create titanium implants with potent antibacterial activity, a new "sandwich-type" structure of sulfhydrylated chitosan/gelatin polyelectrolyte multilayer films embedding AgNPs was coated onto titanium substrate through a spin-assisted layer-by-layer assembly technique. The coatings were shown to inhibit the growth and activity of *B subtilis* and *Escherichia coli* in vitro. It was indicated that Ag ions derived from AgNPs within multilayer films were released into peripheral region around titanium substrate and killed bacteria until AgNPs were completely consumed [369]. The cytotoxicity of AgNPs within multilayer films was attributed to some extent by the released Ag ion concentration [370]. To lower the cytotoxicity to osteoblasts, Ag ion release must be adjusted to a slow manner, possibly by using multilayer films, and the coordination between sulfhydrylated chitosan and Ag elements could adjust the Ag ions. On the other hand, the interaction mechanism between osteoblasts and Ag ions was different from that of bacteria and Ag ions due to their differences in size and structure. The proton-depleted region formed around AgNPs would disrupt the synthesis of adenosine triphosphate, leading to the death of bacteria [371].

Due to its small size, large surface area, and high probability of contact with pathogenic bacteria, nanomaterials have strong bacteriostatic properties to prevent and control oral infectious diseases. The nanotechnology has been exploited in dentistry for some time with significant success, particularly in the development of restorative materials. Researchers have been able to overcome the technical challenges in processing these materials and exploit the properties at nanoscale. Other areas which have significant promise to prevent and treat oral biofilms using nanotechnology are dental bonding materials, nanocoated implants, and so on. One point to note in the treatment of biofilms is that virtually all treatments have focused on killing the bacteria in the biofilm. The most commonly used dental microcosm biofilm model as the inoculum is the individual saliva. However, different individuals may have different biofilm compositions and dietary habits. Therefore, the antibacterial applications of nanomaterials in the treatment of oral disease need to be investigated in human in situ or in vivo models to get a better understanding of the underlying mechanisms.

The development of nanomaterials and nanotechnologies will become the core of the continuous progress of oral medicine and will make more remarkable contributions to maintaining oral health and improving the quality of life. We are also facing many challenges, such as the toxicity of nanomaterials to the mouth is low, but some nanoparticles may lead to the intestinal disorders and the organ lesions. So, the test of cytotoxicity and genetic aberration of nanoparticles and the biological safety of nanomaterials need the in-depth study. And these are the focus of future study.

3.3.1 The Toxicological Side Effects in Nano-Incorporated Dental Materials and Device

The benefits of nanotechnology are widely publicized. However, the discussion of the potential effects of their widespread use in consumer and industrial products is just beginning. And the knowledge on potential harmful effects of nanomaterials lags their increased usage in consumer products. Particularly, the toxicity data in the public domain on nanomaterials toward dental applications are sparse, with no information on oral toxicity from dental materials, e.g., biomaterials or implants containing nanomaterials, in animal models or patients. Therefore, the safety data on various nanomaterials applicable for risk assessment are urgently needed.

In principle, dental materials used in the oral environment must be chemically stable and inert. However, leaching of toxic compounds has always been a major concern, occurring as a result of either material instability or degradation, or clinician error due to inappropriate preparation or plication of the material [372].

Metal release such as amalgams and metal alloys from dental materials is common. Comparable to food or drink intake, reported elemental release from dental materials is usually similar or considered negligible. However, the leaching of

chemical substances released from endodontic sealers and resin composites has also been confirmed. This raises the concern that potentially toxic chemicals might be exposed to patients during and after treatment. Nanomaterials used in other fields can be discharged into the environment, which are then modified by pollutants, pH, temperature, and different biological conditions. In turn, nanomaterials also alter the atmosphere, water, and soil. These transformations and interactions can be detrimental to the environment and deleterious to human health [373, 374]. However, similar information for dental materials containing nanomaterials is lacking.

There is also a concern of toxicity to the cells and tissues of human body from the dental nanomaterials used in oral cavity. Some nanoparticles are not toxic but exhibit lack of activity. This lack of activity is presumably associated with an inability to modify the pharmacokinetics of the encapsulated drugs, as well as the rapid clearance of nanoparticles by the liver, spleen, and other organs [375]. Moreover, some nanoparticles have limited toxicity, such cationic nanoparticles. However, these nanoparticles can rapidly biodegrade, with both products and parents being able to deeply penetrate into cells and tissues, partly because of their small size, which finally results in the destabilization of the plasma membrane, cell death, tissue damage, and organ dysfunction [376].

The potential toxicities of nanomaterials on variety of target organs are attributed to various mechanisms, including oxidative stress, ROS generation, inflammatory reactions, DNA damage, protein structure alteration, and membrane integrity disruption [377]. Research has shown that several nanoparticles induce ROS and inhibit antioxidant function. Moreover, metal or metal oxide nanoparticles have consistently been revealed to induce oxidative stress in the liver, spleen, and kidneys. This can be attributed to the activation of specific stress-related cell signaling pathways, mitochondrial dysfunction, and DNA damage leading to cell cycle arrest and apoptosis [378].

Silver has raised the interest of many investigators because of its good antimicrobial activity and low toxicity. There are concerns regarding the possible toxicity of silver-related nanomedical devices. Research showed that free silver ions could affect the therapeutic and toxic properties. A study showed that impairment of hMSC vitality was detected at AgNP concentrations of 10 μg/mL and showed an inhibitory effect on tissue regeneration by repressing stem cell migration. These effects only occur at high concentrations. The migration is not influenced by AgNPs at concentrations of 0.01, 0.1, and 1 μg/mL [379]. There are also reports describing an inhibition of fibroblasts by silver-releasing wound dressings, the toxicity of AgNP-induced differentially expressed miRNAs regulated the expression of target genes and proteins, leading to fibroblasts toxicity through the destruction of cytoskeleton, reduction of intracellular ATP content, and induction of apoptosis [380]. The cytotoxic effects to cells seem to depend on dose. As reported by Tweden et al. [381], silver concentrations up to 1200 ppb showed no cytotoxic effect on fibroblasts in vitro. However, in vivo studies have not established a threshold concentration for silver that can lead to deterioration of the fibroblast. Furthermore, someone found that of 20 nm was more toxic than the larger nanoparticles in L929 fibroblasts. Altogether, these results suggest that AgNP effects on different toxic

endpoints may be due to its aptitude for inflicting cell damage. Additionally, the potency of nanoparticle-sized silver for inducing cell damage as compared to silver ions depends on both cell type and size [382].

Various works have shown that AgNPs have toxicological properties with a consensus on increased oxidative stress as the main mechanism of toxicity, but many focuses on acute, supernormal doses. Some researchers studied the toxicity of AgNPs (two different sizes 10 or 75 nm) with low dose (250 μM/kg) to key organs of rats for 4 weeks. The result showed that AgNPs were capable of entering mitochondria, which gives further strength to the fact that oxidative stress is most important in the toxicity of AgNPs. AgNPs diminished mitochondrial respiratory complex activities and affected the calcium-loading capacity of mitochondria. But the effects of AgNP exposure to cardiac and renal mitochondrial activity were hardly found. No evident changes in the typical hepatic injury serum markers were displayed, which might suggest that AgNP toxicity is a "silent" event, emphasizing that great care is required when using AgNPs for humans. Also, they found that from the two sizes of AgNPs utilized (10 and 75 nm), the smaller 10-nm ones were apparently more [383]. That was because the size of the nanoparticles determines the extent of endocytosis: internalization of smaller nanoparticles is more likely than larger ones. Also, smaller nanoparticles have a greater likelihood to produce cellular toxicities. After entering the cells, nanoparticles flow through the endosomal/lysosomal pathways and different cytoplasmic networks [383].

Studies have also found that nanoparticles can boost the quantity of several inflammatory cytokines. The intake of nanoparticles is usually performed by the macrophages in macrophage-rich organs, such as the spleen and liver, which induces the macrophages to release cytokines. The binding of nanoparticles can also be performed by specific macrophage receptors having collagenous structure. After binding, NPs are internalized and translocated inside the macrophages thru micropinocytosis or endocytosis [377].

TNF-α is known to stimulate several signaling pathways leading to inflammation, apoptosis, and tissue degradation: most importantly, AgNP phagocytosis stimulates the inflammatory signaling by generating ROS in macrophages cells, succeeded by induced secretion of TNF-α by activated macrophages cells, and resulting damage of the cell membrane ultimately leading to apoptosis [384].

To obtain information concerning the pathophysiologic effects of nanoparticles through systemic migration, acute pulmonary responses were examined after intraperitoneal administration of TiO_2 NPs (40 mg/kg) in mice, the exposure of TiO_2 NPs increased neutrophil influx, protein levels in bronchoalveolar lavage fluid, and reactive oxygen species (ROS) activity of bronchoalveolar lavage cells in 4 h. They could also activate inflammatory signaling pathways including the c-Src, p38 MAP kinase, and NF-κB pathways [385].

Iron oxide NPs (IONPs) has been widely used in the biomedical application, namely in magnetic resonance imaging, tissue repair, drug delivery, hyperthermia, transfection, and tissue soldering. However, the safety issues are still a matter of debate. Polyacrylic acid (PAA)-coated IONs and non-coated IONs were evaluated on the production of six cytokines (interleukin (IL)-6, IL-8, IL-10, IL-1β, tumor

necrosis factor (TNF)-α, and interferon (IFN)-γ) in human peripheral blood cells to establish the inflammatory pathways involved. The result indicated that PAA-coated and -uncoated IONPs induced all the evaluated cytokines and involved the activation of transforming growth factor beta (TGF-β)-activated kinase (TAK1), c-Jun N-terminal kinases, and p38 mitogen-activated protein kinases [386].

In summary, nanotechnology is one of the fastest growing fields of the last decade, with applications in the prevention, diagnosis, and treatment of oral disease. However, although there has been rapid development in the engineering and use of nanoparticles, the knowledge about its toxicity is still lacking. Therefore, further toxicological studies on nanoparticles is urgently required, especially prior clinical use. Particularly, the relationship between the structural and physio-chemical properties of nanoparticles as well as how it reacts within cells of various organs and tissues must be further explored.

Daily exposure must also be considered in the occupational health of the practitioner. For the health and safety in the workplace, safe systems should be applied with the aim to prevent the exposure, so that there is negligible risk. Potential exposure of the practitioner could arise from incidental ingestion or dermal contact. However, the clinical practice with protective device such as overalls, surgical gloves, and masks could minimize these exposure routes.

Exposure to aerosols of dental materials containing nanomaterials has not been quantified. There is an exposure from drilling or filing with nanomaterials [372]. In UK, there are limits for the exposure (10 mg m^{-3} for an 8 h exposure to dusts) to aerosol in the workplace. According to the reports from various health and safety agencies, the workers in nanomaterials manufacturing plants undergo an exposure of a few mg m^{-3} or less [387]. Most likely, by reducing the amount of dental material used at a time, the risk of aerosol exposure also reduces substantially. Intriguingly, findings on the abrasion/sanding of composites report releases of free nanomaterials that range from low to negligible; implying that the risk to the dentist by abrading/shaping a dental composite might also be low. However, distance from the exposure source is critical to the victim. In dentistry, the practitioner is inevitably very close to the patient. Therefore, further research is needed on workplace exposure to nanomaterials.

References

1. S.B. Mitra et al., An application of nanotechnology in advanced dental materials. J. Am. Dent. Assoc. **134**, 1382–1390 (2003)
2. V. Varlan et al., Performances of dental materials (amalgam versus composite). Int. Metalurgia **13**, 35–39 (2009)
3. D.W. Jones, A Canadian perspective on the dental amalgam issue. Br. Dent. J. **184**, 581–586 (1998)
4. P.S. Stein et al., Composite resin in medicine and dentistry. J. Long Term Eff. Med. Implants **15**, 641–654 (2005)
5. F. Lutz et al., A classification and evaluation of composite resin systems. J. Prosthet. Dent. **50**, 480–488 (1983)

6. R. Guggenberger et al., New trends in glass-ionomer chemistry. Biomaterials **19**, 479–483 (1998)
7. Z. Khurshid et al., Advances in nanotechnology for restorative dentistry. Materials **8**, 717–731 (2015)
8. S.A. Saunders, Current practicality of nanotechnology in dentistry. part 1: focus on nanocomposite restoratives and biomimetics. Clin. Cosmet. Investig. Dent. **1**, 47–61 (2009)
9. M.H. Chen, Update on dental nanocomposites. J. Dent. Res. **89**, 549–560 (2010)
10. N. Kumar et al., Essentials in nanoscience and nanotechnology. Appl. Nanotechnol., 361–418 (2016). https://doi.org/10.1002/9781119096122
11. N.B. Cramer et al., Recent advances and developments in composite dental restorative materials. J. Dent. Res. **90**, 402–416 (2011)
12. S.T. Ozak et al., Nanotechnology and dentistry. Eur. J. Dent. **7**, 145–151 (2013)
13. Y. Xia et al., Nanoparticle-reinforced resin-based dental composites. J. Dent. **36**, 450–455 (2008)
14. Y. Hua et al., Micromechanical analysis of nanoparticle-reinforced dental composites. Int. J. Eng. Sci. **69**, 69–76 (2013)
15. N.C. Lawson et al., Wear of nanofilled dental composites at varying filler concentrations. J. Biomed. Mater. Res. B Appl. Biomater. **103**, 424–429 (2015)
16. P. Pallav et al., The influence of admixing microfiller to small-particle composite resin on wear, tensile strength, hardness, and surface roughness. J. Dent. Res. **68**, 489–490 (1989)
17. Y. Liu et al., Effect of nano SiO2 particles on the morphology and mechanical properties of POSS nanocomposite dental resins. J. Nano Res. **16**, 2736 (2014)
18. M. Hosseinalipour et al., Investigation of mechanical properties of experimental Bis-GMA/TEGDMA dental composite resins containing various mass fractions of silica nanoparticles. J. Prosthodont. **19**, 112–117 (2010)
19. K.H.H. Xu et al., Novel CaF2 nanocomposite with high strength and fluoride ion release. J. Dent. Res. **89**, 739–745 (2010)
20. K.H.H. Xu et al., Strength and fluoride release characteristics of a calcium fluoride based dental nanocomposite. Biomaterials **29**, 4261–4267 (2008)
21. K.J. Anusavice et al., Effect of CaF2 content on rate of fluoride release from filled resins. J. Dent. Res. **84**, 440–444 (2005)
22. M. Basso, Teeth restoration using a high-viscosity glass ionomer cement: the Equia® system. J. Min. Int. Dent. **4**, 74–76 (2011)
23. K. Friedl et al., Clinical performance of a new glass ionomer-based restoration system: a retrospective cohort study. J. Dent. Mater. **27**, 1031–1037 (2011)
24. A.S. Khan et al., Synthesis and characterizations of a fluoride-releasing dental restorative material. Mater. Sci. Eng. C Mater. Biol. Appl. **33**, 3458–3464 (2013)
25. R.L. Sakaguchi et al., *Craig's restorative dental materials*, vol 213 (Elsevier Ltd, Oxford, 2012), p. 90
26. A. Moshaverinia et al., Effects of incorporation of hydroxyapatite and fluoroapatite nanobioceramics into conventional glass ionomer cements (GIC). Acta Biomater. **4**, 432–440 (2008)
27. N.A.M. Ghazali et al., Fabrication of modified GIC: GIC-nanoSiO2-HA-ZrO2 using two different mixing methods. AIP Conf. Proc. **1901**(1), 020007 (2017)
28. J.F. McCabe et al., Smart materials in dentistry--future prospects. Dent. Mater. J. **28**, 37–43 (2009)
29. M. Berger, A gold filling from the nanotechnology dentist. Nanowerk. Jan 03 (2008)
30. F. Zhang et al., Surface modification and microstructure of single-walled carbon nanotubes for dental composite resin. J. Biomed. Eng. **23**, 1279–1283 (2006)
31. C. Lynch, Vital guide to adhesive dentistry. Vital **3**, 21–24 (2006)
32. S.H. Dickens et al., Interpretation of bond failure through conversion and residual solvent measurements and Weibull analyses of flexural and microtensile bond strengths of bonding agents. Dent. Mater. **21**, 354–364 (2005)
33. B.H. Cho et al., Effects of the acetone content of single solution dentin bonding agents on the adhesive layer thickness and the microtensile bond strength. Dent. Mater. **20**, 107–115 (2004)

34. A.R. Cocco et al., Addition of nanoparticles for development of radiopaque dental adhesives. Int. J. Adhesion Adhesives **80**, 122–127 (2018)
35. J.S. Kim et al., Effect of the hydrophilic nanofiller loading on the mechanical properties and the microtensile bond strength of an ethanol-based one-bottle dentin adhesive. J. Biomed. Mater. Res. B Appl. Biomater. **72**, 284–291 (2005)
36. U. Lohbauer et al., Zirconia nanoparticles prepared by laser vaporization as fillers for dental adhesives. Acta Biomater. **6**, 4539–4546 (2010)
37. M. Miyazaki et al., Influence of filler addition to bonding agents on shear bond strength to bovine dentin. Dent. Mater. **11**, 234–238 (1995)
38. M. Sadat-Shojai et al., Hydroxyapatite nanorods as novel fillers for improving the properties of dental adhesives: synthesis and application. Dent. Mater. **26**, 471–482 (2010)
39. E.M. Abdelaziz et al., Viscosity and micro-tensile bond strength of total-etch adhesive system reinforced with hydroxyapatite nano-particles. Mansoura J. Dent. **1**, 115–118 (2014)
40. L. Zhang et al., Rechargeable dental adhesive with calcium phosphate nanoparticles for long-term ion release. J. Dent. **43**, 1587–1595 (2015)
41. N.L.V. Carreño et al., YbF3/SiO2 fillers as radiopacifiers in a dental adhesive resin. Nano-micro Lett. **4**, 3 (2012)
42. E.A. Koulaouzidou et al., Cytotoxicity of dental adhesives *in vitro*. Eur. J. Dent. **3**, 3–9 (2009)
43. Y. Li et al., Novel magnetic nanoparticle-containing adhesive with greater dentin bond strength and antibacterial and remineralizing capabilities. Dent. Mater. **34**, 1310–1322 (2018)
44. Y. Ji et al., Nanomagnetic-mediated drug delivery for the treatment of dental disease. Nanomedicine **14**, 919–927 (2018)
45. L. Breschi et al., Dental adhesion review: aging and stability of the bonded interface. Dent. Mater. **24**, 90–101 (2008)
46. F. Mingwen, *Endodontics* (People's Health Publishing House, Shelton, 2012), p. 260
47. A.A. Azim et al., The Tennessee study: factors affecting treatment outcome and healing time following nonsurgical root canal treatment. Int. Endod. J. **49**, 6–16 (2016)
48. C. Sathorn et al., Effectiveness of single-versus multiple-visit endodontic treatment of teeth with apical periodontitis: a systematic review and meta-analysis. Int. Endod. J. **38**, 347–355 (2005)
49. D.R. Violich et al., The smear layer in endodontics: a review. Int. Endod. J. **43**, 2–15 (2010)
50. A. Stabholz et al., The use of layers for cleaning and disinfecting of the root canal system. Alpha Omegan **101**, 195–201 (2008)
51. P.N.R. Nair et al., Microbial status of apical root canal system of human mandibular first molars with primary apical periodontitis after 'one-visit' endodontic treatment. Oral Surg. Oral Med. Oral Pathol. Oral Radiol. Endod. **99**, 231–252 (2005)
52. U. Romeo et al., Effectiveness of KTP laser versus 980 nm diode laser to kill enterococcus faecalis in biofilms developed in experimentally infected root canals. Aust. Endod. J. **41**, 17–23 (2015)
53. D. Orstavik et al., Disinfection by endodontic irrigants and dressings of experimentally infected dentinal tubules. Endod. Dent. Traumatol. **6**, 142–149 (1990)
54. R.E. Walton, Histologic evaluation of different methods of enlarging the pulp canal space. Aust. Endod. J. **2**, 304–311 (1976)
55. S. Annie et al., Antibacterial nanoparticles endodontics: a narrative review. Int. Endod. J. **42**(10), 1417–1426 (2016)
56. A. Sadr et al., The viscoelastic behavior of dental adhesives: a nanoindentation study. Dent. Mater. **25**, 13–19 (2009)
57. A. Jamleh et al., Nano-indentation testing of new and fractured nickel-titanium endodontic instruments. Int. Endod. J. **45**, 462–468 (2012)
58. F.W. Benenati et al., Obturation of the radicular space. Ingle's Endodont, chapter 30, 1053–1087 (2008)
59. A.C. Câmara et al., *In vitro* antimicrobial activity of 0.5%, 1%, and 2.5% sodium hypochlorite in root canal instruments with the ProTaper Universal system. Oral Surg. Oral Med. Oral Pathol. Oral Radiol. Endod. **108**, e55–e56 (2009)

60. D. Orstavik et al., Dimensional change following setting of root canal sealer materials. Dent. Mater. **17**, 512–519 (2001)
61. D. Ricucci, Apical limit of root canal instrumentation and obturation. Int. Endod. J. **31**, 384–393 (1998)
62. J.F. Siqueira et al., Coronal leakage of two root canal sealers containing calcium hydroxide after exposure to human saliva. Int. Endod. J. **25**, 14–16 (1999)
63. B.G. Tidmarsh, Preparation of the root canal. Int. Endod. J. **15**, 53–61 (1982)
64. R.S. Schwartz, Adhesive dentistry and endodontics. Part 2: bonding in the root canal system—the promise and the problems: a review. Int. Endod. J. **32**, 1125–1134 (2006)
65. Peters, Two-year *in vitro* solubility evaluation of four Gutta-percha sealer obturation techniques. Int. Endod. J. **12**, 139–145 (1986)
66. S. Desai et al., Calcium hydroxide-based root canal sealers: a review. Int. Endod. J. **35**, 475–480 (2009)
67. R.B. Kazemi et al., Dimensional changes of endodontic sealers. Oral Surg. Oral Med. Oral Pathol. **76**, 766–771 (1993)
68. J.G. Cailleteau et al., Prevalence of teaching apical patency and various instrumentation and obturation techniques in United States Dental Schools. Int. Endod. J. **23**, 394–396 (1997)
69. M.K. Wu et al., Fluid movement along the coronal two-thirds of root fillings placed by three different gutta-percha techniques. Int. Endod. J. **36**, 533–540 (2003)
70. L. Peng et al., Outcome of root canal obturation by warm gutta-percha versus cold lateral condensation: a meta-analysis. Int. Endod. J. **33**, 106–109 (2007)
71. A.S. Kishen, Nanotechnology in endodontics current and potential clinical applications. Endodontology **28**, 78 (2016)
72. F. Chen et al., Bismuth-doped injectable calcium phosphate cement with improved radiopacity and potent antimicrobial activity for root canal filling. Acta Biomater. **6**, 3199–3207 (2010)
73. J.F. Siqueira, Microbial causes of endodontic flare-ups. Int. Endod. J. **36**, 453–463 (2003)
74. A. Gesi et al., Interfacial strength of resilon and gutta-percha to intraradicular dentin. Int. Endod. J. **31**, 809–813 (2005)
75. R. Lam et al., Nanodiamond-embedded microfilm devices for localized chemotherapeutic elution. ACS Nano **2**, 2095–2102 (2008)
76. R.P. Borges et al., Changes in the surface of four calcium silicate-containing endodontic materials and an epoxy resin-based sealer after a solubility test. Int. Endod. J. **45**, 419–428 (2011)
77. N. Shokouhinejad et al., Pushout bond strength of resilon/epiphany self-etch and gutta-percha/AH26 after different irrigation protocols. Oral Surg. Oral Med. Oral Pathol. Oral Radiol. Endod. **110**, e88–e92 (2010)
78. N. Shokouhinejad et al., Penetration of epiphany, epiphany self-etch, and AH plus into dentinal tubules: a scanning electron microscopy study. Int. Endod. J. **37**, 1316–1319 (2011)
79. M.A. Fisher et al., An *in vitro* comparison of bond strength of various obturation materials to root canal dentin using a push-out test design. Int. Endod. J. **33**, 856–858 (2007)
80. H.M. Zhou et al., *In vitro* cytotoxicity of calcium silicate containing endodontic sealers. Int. Endod. J. **41**, 56–61 (2015)
81. F.R. McMichen et al., A comparative study of selected physical properties of five root-canal sealers. Int. Endod. J. **36**, 629–635 (2003)
82. M.R. Leonardo et al., *In vitro* evaluation of antimicrobial activity of sealers and pastes used in endodontics. Int. Endod. J. **26**, 391–394 (2000)
83. D. Cecchin et al., Effect of root canal sealers on bond strength of fiberglass posts cemented with self-adhesive resin cements. Int. Endod. J. **44**, 314–320 (2011)
84. M. Ceci et al., Biological and chemical-physical properties of root-end filling materials: a comparative study. Conserv. Dent. J. **18**, 94–99 (2015)
85. M. Samiei et al., Antimicrobial efficacy of mineral trioxide aggregate with and without silver nanoparticles. Iran. Endod. J. **8**, 166–170 (2013)
86. A.S. Jain et al., MTA: the new biocompatible material of choice for direct pulp capping in cariously exposed immature teeth with open apex: a case report. Indian Conserve Endod. J. **1**, 24–27 (2016)

87. E.T. Koh et al., Mineral trioxide aggregate stimulates a biological response in human osteoblasts. Biomed. Mater. Res. J. **37**, 432–439 (1997)
88. L.A.S. Dreger et al., Mineral trioxide aggregate and portland cement promote biomineralization *in vivo*. Int. Endod. J. **38**, 324–349 (2012)
89. N. Ahmed et al., External cervical resorption case report and a brief review of literature. Nat. Sci. Biol. Med. J. **5**, 210–214 (2014)
90. M. Bendyk-szeffer et al., Perforating internal root resorption repaired with mineral trioxide aggregate caused complete resolution of odontogenic sinus mucositis: a case report. Aust. Endod. J. **41**, 274–278 (2015)
91. V. Aggarwal et al., Comparative evaluation of push-out bond strength of ProRoot MTA, Biodentine, and MTA Plus in furcation perforation repair. Conserve Dent. J. **16**, 462–465 (2013)
92. E. Bonte et al., MTA versus Ca (OH)2 in apexification of non-vital immature permanent teeth: a randomized clinical trial comparison. Clin. Oral Invest. **19**, 1381–1388 (2015)
93. P. Bansal et al., Effect of mineral trioxide aggregate as a direct pulp capping agent in cariously exposed permanent teeth. Saudi Endod. J. **4**, 137–141 (2014)
94. C. Kruse et al., Periapical bone healing after apicectomy with and without retrograde root filling with mineral trioxide aggregate: a 6-year follow-up of a randomized controlled trial. Int. Endod. J. **42**, 533–537 (2016)
95. A. Prasad et al., A comparative evaluation of the effect of various additives on selected physical properties of white mineral trioxide aggregate. Conserve Dent. J **18**, 237–241 (2015)
96. M.L. Cohen, Nanotubes, nanoscience, and nanotechnology. Mater. Sci. Eng. C **15**, 1–11 (2001)
97. J.P. Thomas et al., *Nanotechnology and Biomaterials* (Boca Raton, FL, CRC Taylor and Francis, 2006)
98. S.C. Abeylath et al., Drug delivery approaches to overcome bacterial resistance to β-lactam antibiotics. Expert Opin. Drug Deliv. **5**, 931–949 (2008)
99. S.T. Ozak et al., Nanotechnology and dentistry. Eur. Dent. J. **7**, 145–151 (2013)
100. J. Venugopal et al., Nanotechnology for nanomedicine and delivery of drugs. Curr. Pharm. Des. **14**, 2184–2200 (2008)
101. B.L. Cushing et al., Recent advances in the liquid-phase syntheses of inorganic nanoparticles. Chem. Rev. **104**, 3893–3946 (2004)
102. P.N. Nair, On the causes of persistent apical periodontitis: a review. Int. Endod. J. **39**, 249–281 (2006)
103. B.P. Gomes et al., Microbiological examination of infected dental root canals. Oral Microbiol. Immunol. **19**, 71–76 (2004)
104. J.W. Costerton et al., Biofilms, the customized microniche. Bacteriol. J. **176**, 2137–2142 (1994)
105. P.J.L. Del et al., The challenge of treating biofilm-associated bacterial infections. Clin. Pharmacol. Ther. **82**, 204–209 (2007)
106. S.A. Saunders, Current practicality of nanotechnology in dentistry. Invest. Dent. **1**, 47–61 (2009)
107. M.A. Versiani et al., Zinc oxide nanoparticles enhance physicochemical characteristics of grossman sealer. Int. Endod. J. **42**, 1804–1810 (2016)
108. K. Zoufan et al., Cytotoxicity evaluation of gutta flow and endo sequence BC sealers. Oral Surg. Oral Med. Oral Pathol. Oral Radiol. Endod. **112**, 657–661 (2011)
109. L. Argueta-Figueroa et al., Mineral trioxide aggregate enriched with iron disulfide nanostructures: an evaluation of their physical and biological properties. Eur. Oral Sci. J. **126**, 1–10 (2018)
110. J. Santos-cruz et al., Colloidal synthesis of biocompatible iron disulphide nanocrystals. Nanomed. Biotechnol. **1**, 1–8 (2017)
111. S. Muliyar et al., Microleakage in endodontics. Int. Oral Health J. **6**, 99–103 (2014)
112. M.A. Saghiri et al., Nanomodification of mineral trioxide aggregate for enhanced physiochemical properties. Int. Endod. J. **45**, 979–988 (2012)

113. M.S. Namazikhah et al., The effect of pH on surface hardness and microstructure of mineral trioxide aggregate. Int. Endod. J. **41**, 108–116 (2008)
114. A. Mohammad et al., Push-out bond strength of a nano-modified mineral trioxide aggregate. Dent. Trauma **29**, 323–327 (2013)
115. K.D. Jandt et al., Future perspectives of resin-based dental materials. Dent. Mater. **25**, 1001–1006 (2009)
116. C. Silva et al., Biotransformations in synthetic fibres. Biocatal. Biotransformation **26**, 350–356 (2008)
117. M. Tian et al., Bis-GMA/TEGDMA dental composites reinforced with electrospun nylon 6 nanocomposite nanofibers containing highly aligned fibrillar silicate single crystals. Polymer **48**, 2720–2728 (2007)
118. M.F. Hamilton et al., Physicomechanical and antibacterial properties of experimental resin-based dental sealants modified with nylon-6 and chitosan nanofibers. J. Biomed. Mater. Res. Part B Appl. Biomater. **103**(8), 1560–1568 (2014)
119. L.M. Manus et al., Gd (III)-nano diamond conjugates for MRI contrast enhancement. Nano Lett. **10**, 484–489 (2010)
120. E.K. Chow et al., Nano-diamond therapeutic delivery agents mediate enhanced chemoresistant tumor treatment. Sci. Transl. Med. **3**, 73ra21 (2011)
121. A.H. Smith et al., Triggered release of therapeutic antibodies from nanodiamond complexes. Nanoscale **3**, 2844–2848 (2011)
122. E.K.H. Chow et al., Cancer nanomedicine: from drug delivery to imaging. Sci. Transl. Med. **5**, 216rv4 (2013)
123. L. Moore et al., Diamond-lipid hybrids enhance chemotherapeutic tolerance and mediate tumor regression. Adv. Mater. **25**, 3532–3541 (2013)
124. T.B. Toh et al., Nano-diamond mitoxantrone complexes enhance drug retention in chemoresistant breast cancer cells. Mol. Pharm. **11**, 2683–2691 (2014)
125. H.J. Kim et al., Diamond nanogel-embedded contact lenses mediate lysozyme-dependent therapeutic release. ACS Nano **8**, 2998–3005 (2014)
126. X. Wang et al., Epirubicin-adsorbed nanodiamonds kill chemoresistant hepatic cancer stem cells. ACS Nano **8**, 12151–12166 (2014)
127. O. Faklaris et al., Photoluminescent diamond nanoparticles for cell labeling: study of the uptake mechanism in mammalian cells. ACS Nano **3**, 3955–3962 (2009)
128. V.N. Mochalin et al., The properties and applications of nanodiamonds. Nat. Nanotechnol. **7**, 11–23 (2011)
129. Y. Liang et al., A general procedure to functionalize agglomerating nanoparticles demonstrated on nanodiamond. ACS Nano **3**, 2288–2296 (2009)
130. A. Pentecost et al., Deaggregation of nanodiamond powders using salt- and sugar-assisted milling. ACS Appl. Mater. Interfaces **2**, 3289–3294 (2010)
131. D.K. Lee et al., Nanodiamond-gutta percha composite biomaterials for root canal therapy. ACS Nano **9**, 11490–11501 (2015)
132. J. Hrkach, Preclinical development and clinical translation of a PSMA targeted docetaxel nanoparticle with a differentiated pharmacological profile. Sci. Transl. Med. **4**, 128–139 (2012)
133. M.E. Davis et al., Evidence of RNAi in humans from systemically administered siRNA via targeted nanoparticles. Nature **464**, 1067–1070 (2010)
134. Q. Zhang et al., Fluorescent PLLA-nanodiamond composites for bone tissue engineering. Biomaterials **32**, 87–94 (2011)
135. S. Mohammad et al., Nanoparticles for antimicrobial purposes in endodontics: A systematic review of in vitro studies. Mater. Sci. Eng. C **58**, 1269–1278 (2015)
136. C. Wu et al., Bioactive mesoporous calcium–silicate nanoparticles with excellent mineralization ability, osteostimulation, drug-delivery and antibacterial properties for filling apex roots of teeth. Mater. Chem. J. **22**, 16801–16809 (2012)
137. Z. Wang, Bioceramic materials in endodontics. Int. Endod. J. **32**, 3–30 (2015)
138. S. Noushin et al., Push-out bond strength of gutta-percha with a new bioceramic sealer in the presence or absence of smear layer. Aust. Endod. J. **39**, 102–106 (2013)

139. A. Al-Haddad et al., Interfacial adaptation and thickness of bioceramic-based root canal sealers. Dent. Mater. J. **34**, 516–521 (2015)
140. S. Ersahan et al., Dislocation resistance of iRoot SP, a calcium silicate-based sealer, from radicular dentine. Int. Endod. J. **36**, 2000–2002 (2010)
141. L. Han et al., Bioactivity evaluation of three calcium silicate-based endodontic materials. Int. Endod. J. **46**, 808–814 (2013)
142. E.P. Guven et al., *In vitro* comparison of induction capacity and biomineralization ability of mineral trioxide aggregate and a bioceramic root canal sealer. Int. Endod. J. **46**, 1173–1182 (2013)
143. T. Du et al., Combined antibacterial effect of sodium hypochlorite and root canal sealers against enterococcus faecalis biofilms in dentin canals. Int. Endod. J. **41**, 1294–1298 (2015)
144. H. Zhang et al., Antibacterial activity of endodontic sealers by modified direct contact test against enterococcus faecalis. Int. Endod. J. **35**, 1051–1055 (2009)
145. S. Ersahan et al., Solubility and apical sealing characteristics of a new calcium silicate-based root canal sealer in comparison to calcium hydroxide-, methacrylate resin- and epoxy resin-based sealers. Acta Odontol. Scand. **71**, 857–862 (2013)
146. W. Zhang et al., Assessment of a new root canal sealer's apical sealing ability. Oral Surg. Oral Med. Oral Pathol. Oral Radiol. Endod. **107**, e79–e82 (2009)
147. H.M. Zhou et al., Physical properties of 5 root canal sealers. Int. Endod. J. **39**, 1281–1286 (2013)
148. G.T. Candeiro et al., Evaluation of radiopacity, pH, release of calcium ions, and flow of a bioceramic root canal sealer. Int. Endod. J. **38**, 842–845 (2012)
149. A. Gartman et al., Comparison of pyrite (FeS2) synthesis mechanisms to reproduce natural FeS2 nanoparticles found at hydrothermal vents. Geochim. Cosmochim. Acta **120**, 447–458 (2013)
150. Y.H. Wang et al., *In vitro* study of dentinal tubule penetration and filling quality of bioceramic sealer. PLoS One **13**, e0192248 (2018)
151. A. Kokkas et al., The influence of the smear layer on dentinal tubule penetration depth by three different root canal sealers: an in vitro study. Int. Endod. J. **30**, 100–102 (2004)
152. I. Heling et al., The antimicrobial effect within dentinal tubules of four root canal sealers. Int. Endod. J. **22**, 257–259 (1996)
153. J. Branstetter et al., The physical properties and sealing action of endodontic sealer cements: a review of the literature. Int. Endod. J. **8**, 312–316 (1982)
154. G. De-Deus et al., Lack of correlation between sealer penetration into dentinal tubules and sealability in nonbonded root fillings. Int. Endod. J. **45**, 642–651 (2012)
155. L.P. Salles et al., Mineral trioxide aggregate-based endodontic sealer stimulates hydroxyapatite nucleation in human osteoblast-like cell culture. Int. Endod. J. **38**, 971–976 (2012)
156. C.V. Bin et al., Cytotoxicity and genotoxicity of root canal sealers based on mineral trioxide aggregate. Int. Endod. J. **38**, 495–500 (2012)
157. R.D. Morgental et al., Antibacterial activity of two MTA based root canal sealers. Int. Endod. J. **44**, 1128–1133 (2011)
158. D. Orstavik et al., Clinical performance of three endodontic sealers. Endod. Dent. Traumatol. **3**, 178–186 (1987)
159. M.A. Duarte et al., Influence of calcium hydroxide association on the physical properties of AH Plus. Int. Endod. J. **36**, 1048–1051 (2010)
160. C.P. Mchugh et al., pH required to kill Enterococcus faecalis *in vitro*. Int. Endod. J. **30**, 218–219 (2004)
161. C.H. Stuart et al., Enterococcus faecalis: its role in root canal treatment failure and current concepts in retreatment. Int. Endod. J. **32**, 93–98 (2006)
162. T. Okabe et al., Effects of pH on mineralization ability of human dental pulp cells. Int. Endod. J. **32**, 198–201 (2006)
163. C.J. Stock, Calcium hydroxide: root resorption and perio-endo lesions. Br. Dent. J. **158**, 325–334 (1985)
164. J. Maryam et al., *In vitro* cytotoxicity of a new nano root canal sealer on human gingival fibroblasts. Iran. Endod. J **12**, 220–225 (2017)

165. J. Ma et al., Biomimetic processing of nanocrystallite bioactive apatite coating on titanium. Nanotechnology **14**, 619 (2003)
166. R.A. McIntyre, Common nano-materials and their use in real world applications. Sci. Prog. **95**, 1–22 (2012)
167. P. Subhashree et al., Nanoparticles used in dentistry: a review. J. Oral Biol. Craniofac. Res. **8**(1), 58–67 (2018)
168. I. Abramovitz et al., In vitro biocompatibility of endodontic sealers incorporating antibacterial nanoparticles. Nanomater. J., **2012**, 1–9 (2012)
169. N. Beyth et al., Surface antimicrobial activity and biocompatibility of incorporated polyethylenimine nanoparticles. Biomaterials **29**, 4157–4163 (2008)
170. J. Wang et al., Physicochemical and biological properties of a novel injectable polyurethane system for root canal filling. Int. J. Nanomed. **10**, 697–709 (2015)
171. G.P. Badole et al., A comparative evaluation of cytotoxicity of root canal sealers: an in vitro study. Restor. Dent. Endod. **38**, 204–209 (2013)
172. A. Kaur et al., Biotoxicity of commonly used root canal sealers: a meta-analysis. Conserve Dent. J. **18**, 83 (2015)
173. S. Imamura et al., Effect of filler type and polishing on the discoloration of composite resin artificial teeth. Dent. Mater. J. **27**, 802–808 (2008)
174. G. Zarb et al., *Prosthodontic treatment for edentulous patients: complete dentures and implant-supported prostheses* (Mosby, Maryland Heights, 2013), p. 135
175. K. Katja et al., Flexural fatigue of denture base polymer with fiber-reinforced composite reinforcement. Compos. Part A Appl. Sci. Manuf. **36**, 1177–1324 (2005)
176. N. Murakami et al., Effect of high-pressure polymerization on mechanical properties of PMMA denture base resin. Mech. Behav. Biomed. Mater. J. **20**, 98–104 (2013)
177. A. Al-Haddad et al., Fracture toughness of heat cured denture base acrylic resin modified with chlorhexidine and fluconazole as bioactive compounds. Dent. J. **42**, 180–184 (2014)
178. Y. Zhang et al., The antifungal effects and mechanical properties of silver bromide/cationic polymer nanocomposite-modified poly-methyl methacrylate-based dental resin. Sci. Rep. **7**, 1547 (2017)
179. N.M. Ajaj-Alkordy et al., Elastic modulus and flexural strength comparisons of high-impact and traditional denture base acrylic resins. Saudi Dent. J. **26**, 15–18 (2014)
180. D.T. Castro et al., *In vitro* study of the antibacterial properties and impact strength of dental acrylic resins modified with a nanomaterial. Prosthet. Dent. J. **115**, 238–246 (2016)
181. Z. Han et al., Effect of silver-supported materials on the mechanical and antibacterial properties of reinforced acrylic resin composites. Mater. Des. **65**, 1245–1252 (2015)
182. P. Franklin et al., Reinforcement of poly (methyl methacrylate) denture base with glass flake. Dent. Mater. J. **21**, 365–370 (2005)
183. E. Nagai et al., Repair of denture base resin using woven metal and glass fiber: effect of methylene chloride pretreatment. Prosthet. Dent. J. **85**, 496–500 (2001)
184. U.R. Darbar et al., Denture fracture: a survey. Br. Dent. J. **176**, 342–345 (1994)
185. M. Eshed et al., MgF2 nanoparticle-coated teeth inhibit Streptococcus mutans biofilm formation on a tooth model. Mater. Chem. B J. **1**, 3985–3991 (2013)
186. G.A. Silva, Introduction to nanotechnology and its applications to medicine. Surg. Neurol. **61**, 216–220 (2004)
187. A. Mnyusiwalla et al., Mind the gap: science and ethics in nanotechnology. Nanotechnology **14**, R9–R13 (2003)
188. V. Asopa et al., A comparative evaluation of properties of zirconia reinforced high impact acrylic resin with that of high impact acrylic resin. Saudi Dent. Res. J. **2**, 146–151 (2015)
189. N.W. Elshereksi et al., Studies on the effects of titanate and silane coupling agents on the performance of poly (methyl methacrylate)/barium titanate denture base nanocomposites. Dent. J. **56**, 121–132 (2017)
190. H.Z. Mahross et al., Effect of silver nanoparticles incorporation on viscoelastic properties of acrylic resin denture base material. Eur. Dent. J. **9**, 207–212 (2015)

191. K.Y. Nam et al., Antifungal and physical characteristics of modified denture base acrylic incorporated with silver nanoparticles. Gerodontology **29**, 413–419 (2012)
192. M. Atai et al., Nano-porous thermally sintered nano silica as novel fillers for dental composites. Dent. Mater. J. **28**, 133–145 (2012)
193. Q.Q. Wang et al., Surface modification of PMMA/O-MMT composite microfibers by TiO2 coating. Appl. Surf. Sci. **258**, 98–102 (2011)
194. Y. Gao et al., Preparation of poly (methyl methacrylate) grafted titanate nanotubes by *in situ* atom transfer radical polymerization. Nanotechnology **19**, 495604 (2008)
195. J. Jordan et al., Experimental trends in polymer nano composites – a review. Mater. Sci. Eng. **393**, 1–11 (2005)
196. M.A. Compagnoni et al., The effect of polymerization cycles on porosity of microwave-processed denture base resin. Prosthet. Dent. J. **91**, 281–285 (2004)
197. I.N. Safi, Evaluation the effect of nano—fillers (TiO2, AL2O3, SiO2) addition on glass transition temperature, e-modulus and coefficient of thermal expansion of acrylic denture base material. Baghdad Coll. Dent. J. **26**, 37–41 (2014)
198. M. Tian et al., Fabrication and evaluation of BIS-GMA/TEGDMA dental resins/composites containing nano fibrillar silicate. Dent. Mater. J. **24**, 235–243 (2008)
199. H.C.C. Van et al., Fiber reinforced dental composites in beam testing. Dent. Mater. J. **24**, 1435–1443 (2008)
200. W. Sun et al., Post-draw PAN–PMMA nanofiber reinforced and toughened Bis-GMA dental restorative composite. Dent. Mater. J. **26**, 873–880 (2010)
201. S. Subramani et al., Crosslinked aqueous dispersion of silylated poly(urethane-urea)/clay nanocomposites. Compos. Sci. Technol. **67**, 1561–1573 (2007)
202. G. Zappini et al., Comparison of fracture tests of denture base materials. Prosthet. Dent. J. **90**, 578–585 (2003)
203. N.M. Ayad et al., Effect of reinforcement of high impact acrylic resin with micro-zirconia on some physical and mechanical properties. Rev. Clin. Pesq. Odontol. **4**, 145–151 (2008)
204. F.J.N. Arioli et al., Flexural strength of acrylic resin repairs processed by different methods: water bath, microwave energy and chemical polymerization. Appl. Oral Sci. J. **19**, 249–253 (2011)
205. S. Suvarna et al., Residual monomer content of repair autopolymerizing resin after microwave postpolymerization treatment. Eur. J. Prosthodont. **2**, 28–32 (2014)
206. A.I. Zissis et al., Repairs in complete dentures: results of a survey. Quint. Dent. Technol. **20**, 149–155 (1997)
207. C. Bural et al., Flexural properties of repaired heat-polymerizing acrylic resin after wetting with monomer and acetone. Gerodontology **27**, 217–223 (2010)
208. G.L. Polyzois et al., Fracture force, deflection at fracture, and toughness of repaired denture resin subjected to microwave polymerization or reinforced with wire or glass fiber. Prosthodont. Dent. J. **86**, 613–619 (2001)
209. I. Kostoulas et al., Fracture force, deflection, and toughness of acrylic denture repairs involving glass fiber reinforcement. Aust. Prosthodont. J. **17**, 257–261 (2008)
210. N.S. Ihab et al., Evaluation the effect of modified nano-fillers addition on some properties of heat cured acrylic denture base material. Baghdad Coll. Dent. J. **23**, 23–29 (2011)
211. N.V. Asar et al., Influence of various metal oxides on mechanical and physical properties of heat-cured polymethylmethacrylate denture base resins. Adv. Prosthodont. J. **5**, 241–247 (2013)
212. A.O. Alhareb et al., Effect of Al2O3/ZrO2 reinforcement on the mechanical properties of PMMA denture base. Reinf. Plast. Compos. J. **30**, 86–93 (2011)
213. S. Skukla et al., Phase stabilization in nanocrystalline zirconia. Rev. Adv. Mater. **5**, 117–120 (2003)
214. M. Gad et al., The reinforcement effect of nano-zirconia on the transverse strength of repaired acrylic denture base. Int. Dent. J. **2016**, 7094056 (2016)
215. M.A. Ahmed et al., Effect of zirconium oxide nano-fillers addition on the flexural strength fracture toughness, and hardness of heat-polymerized acrylic resin. World Nano Sci. Eng. J. **4**, 50–57 (2014)

216. M.M. Gad et al., Influence of incorporation of ZrO2 nanoparticles on the repair strength of polymethyl methacrylate denture bases. Int. J. Nanomed. **11**, 5633–5643 (2016)
217. M.M. Gad et al., PMMA denture base material enhancement: a review of fiber, filler, and nanofiller addition. Int. J. Nanomed. **12**, 3801–3812 (2017)
218. F. Haupert et al., Reinforcement of thermosetting polymers by the incorporation of micro- and nanoparticles. Polym. Compos. **5**, 45–62 (2005)
219. A.O. Alhareb et al., Impact strength, fracture toughness and hardness improvement of PMMA denture base through addition of nitrile rubber/ceramic fillers. Saudi Dent. Res. J. **8**, 26–34 (2017)
220. A.O. Alhareb et al., Poly (methyl methacrylate) denture base composites enhancement by various combinations of nitrile butadiene rubber/treated ceramic fillers. Thermoplast. Compos. Mater. J. **28**, 1–22 (2015)
221. L. Cheng et al., Antibacterial amorphous calcium phosphate nanocomposites with a quaternary ammonium dimethacrylate and silver nanoparticles. Dent. Mater. J. **28**, 561–572 (2012)
222. X. Zhang et al., Mechanical and thermal properties of denture PMMA reinforced with silanized aluminum borate whiskers. Dent. Mater. J. **31**, 903–908 (2012)
223. X.Y. Zhang et al., Hybrid effects of zirconia nanoparticles with aluminum borate whiskers on mechanical properties of denture base resin PMMA. Dent. Mater. J. **33**, 141–146 (2014)
224. W.M. Johnston et al., Translucency parameter of colorants for maxillofacial prostheses. Aust. Intellect. Prop. J. **8**, 79–86 (1995)
225. M.M. Gad et al., Effect of zirconium oxide nanoparticles addition on the optical and tensile properties of polymethyl methacrylate denture base material. Int. J. Nanomed. **13**, 283–292 (2018)
226. H.K. Hameed et al., The effect of addition nano particle ZrO2 on some properties of autoclave processed heat cure acrylic denture base material. Baghdad Coll. Dent. J. **27**, 32–39 (2015)
227. A. Almaroof et al., Influence of a polymerizable eugenol derivative on the antibacterial activity and wettability of a resin composite for intracanal post cementation and core build-up restoration. Dent. Mater. J. **32**, 929–939 (2016)
228. J.A. Skupien et al., Prevention and treatment of Candida colonization on denture liners: a systematic review. Prosthodont. Dent. J. **110**, 356–362 (2013)
229. A. Falah-Tafti et al., A comparison of the efficacy of nystatin and fluconazole incorporated into tissue conditioner on the *in vitro* attachment and colonization of *Candida albicans*. Dent. Res. J. **7**, 18–22 (2010)
230. C. Fan et al., Development of an antimicrobial resin—a pilot study. Dent. Mater. J. **27**, 322–328 (2011)
231. K.Y. Nam, *In vitro* antimicrobial effect of the tissue conditioner containing silver nanoparticles. Adv. Prosthodont. J. **3**, 20–24 (2011)
232. G. Chladek et al., Antifungal activity of denture soft lining material modified by silver nanoparticles—a pilot study. Int. J. Mol. Sci. **12**, 4735–4744 (2011)
233. G. Chladek et al., Sorption, solubility, bond strength and hardness of denture soft lining incorporated with silver nanoparticles. Int. J. Mol. Sci. **14**, 563–574 (2013)
234. M.M. Gad et al., Inhibitory effect of zirconium oxide nanoparticles on Candida albicans adhesion to repaired polymethyl methacrylate denture bases and interim removable prostheses: a new approach for denture stomatitis prevention. Int. J. Nanomed. **12**, 5409–5419 (2017)
235. S. Veeraapandian et al., Antibacterial and antioxidant activity of protein capped silver and gold nanoparticles synthesized with *Escherichia coli*. Biomed. Nanotechnol. J. **8**, 140–148 (2012)
236. R.R. Chen et al., Antibacterial activity, cytotoxicity and mechanical behavior of nano-enhanced denture base resin with different kinds of inorganic antibacterial agents. Dent. Mater. J. **36**, 693–699 (2017)
237. B.S. Buffet et al., Emergence of resistance to antibacterial agents: the role of quaternary ammonium compounds–a critical review. Int. J. Antimicrob. Agents **39**, 381–389 (2010)
238. P. Gilbert et al., Cationic antiseptics: diversity of action under a common epithet. Appl. Microbiol. J. **99**, 703–715 (2005)

239. C. Pesci-Bardon et al., *In vitro* new dialysis protocol to assay the antiseptic properties of a quaternary ammonium compound polymerized with denture acrylic resin. Lett. Appl. Microbiol. **39**, 226–231 (2004)
240. C. Pesci-Bardon et al., *In vitro* antiseptic properties of an ammonium compound combined with denture base acrylic resin. Gerodontology **23**, 111–116 (2006)
241. L. Caillier et al., Synthesis and antimicrobial properties of polymerizable quaternary ammoniums. Eur. J. Med. Chem. **44**, 3201–3208 (2009)
242. G. McDonnell et al., Antiseptics and disinfectants: activity, action, and resistance. Clin. Microbiol. Rev. **12**, 147–179 (1999)
243. M. Balkenhol et al., Provisional crown and fixed partial denture materials: mechanical properties and degree of conversion. Dent. Mater. J. **23**, 1574–1583 (2007)
244. J.L. Ferracane, Correlation between hardness and degree of conversion during the setting reaction of unfilled dental restorative resins. Dent. Mater. J. **1**, 11–14 (1985)
245. S. Galdiero et al., Silver nanoparticles as potential antiviral agents. Molecules **16**, 8894–8918 (2011)
246. J.R. Morones et al., The bactericidal effect of silver nanoparticles. Nanotechnology **16**, 2346–2353 (2005)
247. Q. Feng et al., A mechanistic study of the antibacterial effect of silver ions on Escherichia coli and Staphylococcus aureus. Biomed. Mater. Res. J. **52**, 662–668 (2000)
248. J. Jain et al., Silver nanoparticles in therapeutics: development of an antimicrobial gel formulation for topical use. Mol. Pharm. **6**, 1388–1401 (2009)
249. J.S. Kim et al., Antimicrobial effects of silver nanoparticles. NanoBiotechnology **3**, 95–101 (2007)
250. W. Wang et al., Genetic engineering of mesenchymal stem cells by non-viral gene delivery. Clin. Hemorheol. Micro. **58**, 19–48 (2014)
251. H. Boulaiz et al., Non-viral and viral vectors for gene therapy. Cell. Mol. Biol. **51**, 3–22 (2005)
252. T. Teklemariam et al., Inhibition of DNA methylation enhances HLA-G expression in human mesenchymal stem cells. Biochem. Biophys. Res. Commun. **452**, 753–759 (2014)
253. M. Kamihira et al., Development of separation technique for stem cells. Adv. Biochem. Eng. Biotechnol. **106**, 173–193 (2007)
254. A.M. Thimios et al., Nanodentistry: combining nanostructured materials and stem cells for dental tissue regeneration. Nanomedicine **7**, 1743–1753 (2012)
255. W. Zhang et al., Magnetically controlled growth-factor-immobilized multilayer cell sheets for complex tissue regeneration. Adv. Mater. **29**, 1703795 (2017)
256. X. Yang et al., Non-viral bone morphogenetic protein 2 transfection of rat dental pulp stem cells using calcium phosphate nanoparticles as carriers. Tissue Eng. Part A **14**, 71–81 (2008)
257. S.V. Dorozhkin, Nanosized and nanocrystalline calcium orthophosphates. Acta Biomater. **6**, 715–734 (2010)
258. M. Zhou et al., Effect of tetrahedral DNA nanostructures on proliferation and osteo/odontogenic differentiation of dental pulp stem cells via activation of the Notch signaling pathway. Nanomedicine **14**, 1227–1236 (2018)
259. S. Shrestha et al., Temporal-controlled dexamethasone releasing chitosan nanoparticle system enhances odontogenic differentiation of stem cells from apical papilla. Int. Endod. J. **41**, 1253–1258 (2015)
260. C. Niu et al., Gold nanoparticles promote osteogenic differentiation of human periodontal ligament stem cells via the p38 MAPK signaling pathway. Mol. Med. Rep. **16**, 4879–4886 (2017)
261. C. Yi et al., Gold nanoparticles promote osteogenic differentiation of mesenchymal stem cells through p38 MAPK pathway. ACS Nano **4**, 6439–6448 (2010)
262. Y.D. Rakhmatia et al., Current barrier membranes: titanium mesh and other membranes for guided bone regeneration in dental applications. J. Prosthodont. Res. **57**, 3–14 (2013)
263. A. Bachhuka et al., Nanotopography mediated osteogenic differentiation of human dental pulp derived stem cells. Nanoscale **9**, 14248–14258 (2017)
264. R.V. Goreham et al., Small surface nanotopography encourages fibroblast and osteoblast cell adhesion. RSC Adv. **3**, 10309–10317 (2013)

265. K. Vasilev et al., Early stages of growth of plasma polymer coatings deposited from nitrogen- and oxygen-containing monomers. Plasma Process. Polym. **7**, 824–835 (2010)
266. S. Zeng et al., Preparation and characterization of nano-hydroxyapatite/poly (vinyl alcohol) composite membranes for guided bone regeneration. J. Biomed. Nanotechnol. **7**, 549–557 (2011)
267. Y. Zhu et al., Protein corona of magnetic hydroxyapatite scaffold improves cell proliferation via activation of mitogen-activated protein kinase signaling pathway. ACS Nano **11**, 3690–3704 (2017)
268. C.F. Adams et al., Magnetic nanoparticle mediated transfection of neural stem cell suspension cultures is enhanced by applied oscillating magnetic fields. Nanomedicine **9**, 737–741 (2013)
269. S.Y. Lee et al., Nanotopological-tailored calcium phosphate cements for the odontogenic stimulation of human dental pulp stem cells through integrin signaling. RSC Adv. **5**, 63363–63371 (2015)
270. Y. Xia et al., Gold nanoparticles in injectable calcium phosphate cement enhance osteogenic differentiation of human dental pulp stem cells. Nanomedicine **14**, 35–45 (2018)
271. Q. Yu et al., Inhibition of gold nanoparticles (AuNPs) on pathogenic biofilm formation and invasion to host cells. Sci. Rep. **6**, 26667 (2016)
272. A. Samadikuchaksaraei et al., Fabrication and in vivo evaluation of an osteoblast-conditioned nano-hydroxyapatite/gelatin composite scaffold for bone tissue regeneration. J. Biomed. Mater. Res. A **104**, 2001–2010 (2016)
273. W. Liu et al., Electrospun nanofibers for regenerative medicine. Adv. Health Mater. **1**, 10–25 (2012)
274. L. Li et al., Controlled dual delivery of BMP-2 and dexamethasone by nanoparticle-embedded electrospun nanofibers for the efficient repair of critical-sized rat calvarial defect. Biomaterials **37**, 218–229 (2015)
275. X. He et al., Integration of a novel injectable nano calcium sulfate/alginate scaffold and BMP2 gene-modified mesenchymal stem cells for bone regeneration. Tissue Eng. A **19**, 508–518 (2013)
276. J. Kissa et al., Augmentation of keratinized gingiva around dental implants. J. Stomatol. Oral Maxillofac. Surg. **118**, 156–160 (2017)
277. P.F. Nocini et al., Bi-layered collagen nano-structured membrane prototype (collagen matrix 10826(®)) for oral soft tissue regeneration: an "in vitro" study. Clin. Oral Implants Res. **24**, 612–617 (2013)
278. M. Dorkhan et al., Adherence of human oral keratinocytes and gingival fibroblasts to nano-structured titanium surfaces. BMC Oral Health **21**, 75 (2014)
279. Z. Huang et al., Bioactive nanofibers instruct cells to proliferate and differentiate during enamel regeneration. J. Bone Miner. Res. **23**, 1995–2006 (2008)
280. X. Li et al., Pulp regeneration in a full-length human tooth root using a hierarchical nanofibrous microsphere system. Acta Biomater. **35**, 57–67 (2016)
281. S. Gronthos et al., Postnatal human dental pulp stem cells (DPSCs) *in vitro* and *in vivo*. Proc. Natl. Acad. Sci. U. S. A. **97**, 13625–13630 (2000)
282. W. Sonoyama et al., Mesenchymal stem cell-mediated functional tooth regeneration in swine. PLoS One **1**, e79 (2006)
283. Z. Zhang et al., A promising combo gene delivery system developed from (3-Aminopropyl) triethoxysilane-modified iron oxide nanoparticles and cationic polymers. J. Nanopart. Res. **15**, 1–11 (2013)
284. X. Zeng et al., Magnetic responsive hydroxyapatite composite scaffolds construction for bone defect reparation. Int. J. Nanomed. **7**, 3365–3378 (2012)
285. I. Levy et al., Bioactive magnetic near Infra-Red fluorescent core-shell iron oxide/human serum albumin nanoparticles for controlled release of growth factors for augmentation of human mesenchymal stem cell growth and differentiation. J. Nanobiotechnol. **13**, 34 (2015)
286. R.P. Ellen et al., Longitudinal microbiological investigation of a hospitalized population of older adults with a high root surface caries risk. J. Dent. Res. **64**, 1377–1381 (1985)

287. W.F. Liljemark et al., Human oral microbial ecology and dental caries and periodontal diseases. Crit. Rev. Oral Biol. Med. **7**, 180–198 (1996)
288. S.S. Socransky et al., The bacterial etiology of destructive periodontal disease: current concepts. J. Periodontol. **63**, 322–331 (1992)
289. N.E.A. Abou et al., Nanotechnology in dentistry: prevention, diagnosis, and therapy. Int. J. Nanomedicine **10**, 6371–6394 (2015)
290. Z. Lu et al., Size-dependent antibacterial activities of silver nanoparticles against oral anaerobic pathogenic bacteria. J. Mater. Sci. Mater. Med. **24**, 1465–1471 (2013)
291. K. Chaloupka et al., Nanosilver as a new generation of nanoproduct in biomedical applications. Trends Biotechnol. **28**, 580–588 (2010)
292. D. Seth et al., Nature-inspired novel drug design paradigm using nanosilver: efficacy on multi-drug-resistant clinical isolates of tuberculosis. Curr. Microbiol. **62**, 715–726 (2011)
293. K.R. Raghupathi et al., Size-dependent bacterial growth inhibition and mechanism of antibacterial activity of zinc oxide nanoparticles. Langmuir **27**, 4020–4028 (2011)
294. Y.H. Leung et al., Mechanisms of antibacterial activity of MgO: non-ROS mediated toxicity of MgO nanoparticles towards Escherichia coli. Small **10**, 1171–1183 (2014)
295. W.S. Cheow et al., Antibacterial efficacy of inhalable antibiotic-encapsulated biodegradable polymeric nanoparticles against *E. coli* biofilm cells. J. Biomed. Nanotechnol. **6**, 391–403 (2010)
296. K. Forier et al., Lipid and polymer nanoparticles for drug delivery to bacterial biofilms. J. Control. Release **190**, 607–623 (2014)
297. X. Li et al., The spherical nanoparticle-encapsulated chlorhexidine enhances anti-biofilm efficiency through an effective releasing mode and close microbial interactions. Int. J. Nanomedicine **11**, 2471–2480 (2016)
298. C.J. Seneviratne et al., Nanoparticle-encapsulated chlorhexidine against oral bacterial biofilms. PLoS One **9**, e103234 (2014)
299. X. Cai et al., Protective effects of baicalin on ligature-induced periodontitis in rats. J. Periodontal Res. **43**, 14–21 (2008)
300. W. Luo et al., Baicalin downregulates porphyromonas gingivalis lipopolysaccharide-upregulated IL-6 and IL-8 expression in human oral keratinocytes by negative regulation of TLR signaling. PLoS One **7**, e51008 (2012)
301. C. Song et al., Inhibition of quorum sensing activity by ethanol extract of scutellaria baicalensis Georgi. J. Plant Pathol. Microbiol. **S7**, 1 (2012)
302. E.J. Jang et al., Combination effects of baicalein with antibiotics against oral pathogens. Arch. Oral Biol. **59**, 1233–1241 (2014)
303. K.C. Leung et al., Synergistic antibacterial effects of nanoparticles encapsulated with scutellaria baicalensis and pure chlorhexidine on oral bacterial biofilms. Nanomaterials (Basel) **6**(4), 61 (2016)
304. A. Besinis et al., Inhibition of biofilm formation and antibacterial properties of a silver nanocoating on human dentine. Nanotoxicology **8**, 745–754 (2014)
305. S. Imazato et al., Incorporation of bacterial inhibitor into resin composite. J. Dent. Res. **73**, 1437–1443 (1994)
306. N. Beyth et al., An *in vitro* quantitative antibacterial analysis of amalgam and composite resins. J. Dent. **35**, 201–206 (2007)
307. L. Cheng et al., Effect of amorphous calcium phosphate and silver nanocomposites on dental plaque microcosm biofilms. J. Biomed. Mater. Res. B Appl. Biomater. **100**, 1378–1386 (2012)
308. P.B. das Neves et al., Addition of silver nanoparticles to composite resin: effect on physical and bactericidal properties *in vitro*. Braz. Dent. J. **25**, 141–145 (2014)
309. S. Kasraei et al., Antibacterial properties of composite resins incorporating silver and zinc oxide nanoparticles on streptococcus mutans and lactobacillus. Restor. Dent. Endod. **39**, 109–114 (2014)
310. M. Azarsina et al., The antibacterial properties of composite resin containing nanosilver against streptococcus mutans and lactobacillus. J. Contemp. Dent. Pract. **14**, 1014–1018 (2013)

311. M. Ai et al., Composite resin reinforced with silver nanoparticles-laden hydroxyapatite nanowires for dental application. Dent. Mater. J. **33**, 12–22 (2017)
312. Y.J. Cheng et al., In situ formation of silver nanoparticles in photocross linking polymers. J. Biomed. Mater. Res. B Appl. Biomater. **97**, 124–131 (2011)
313. S. Imazato, Antibacterial properties of resin composites and dentin bonding systems. Dent. Mater. J. **19**, 449–457 (2003)
314. J.M. Antonucci et al., Synthesis and characterization of dimethacrylates containing quaternary ammonium functionalities for dental applications. Dent. Mater. **28**, 219–228 (2012)
315. F. Li et al., Comparison of quaternary ammonium-containing with nano-silver-containing adhesive in antibacterial properties and cytotoxicity. Dent. Mater. J. **29**, 450–461 (2013)
316. L. Cheng et al., Effects of antibacterial primers with quaternary ammonium and nano-silver on Streptococcus mutans impregnated in human dentin blocks. Dent. Mater. J. **29**, 462–472 (2013)
317. L. Cheng et al., Anti-biofilm dentin primer with quaternary ammonium and silver nanoparticles. J. Dent. Res. **91**, 598–604 (2012)
318. S. Imazato et al., Incorporation of antibacterial monomer MDPB in dentin primer. J. Dent. Res. **76**, 768–772 (1997)
319. K. Zhang et al., Effects of dual antibacterial agents MDPB and nano-silver in primer on microcosm biofilm, cytotoxicity and dentine bond properties. J. Dent. **41**, 464–474 (2013)
320. K. Zhang et al., Dual antibacterial agents of nano-silver and 12-methacryloyloxydodecylpyri dinium bromide in dental adhesive to inhibit caries. J. Biomed. Mater. Res. B Appl. Biomater. **101**, 929–938 (2013)
321. M.A. Melo et al., Novel dental adhesives containing nanoparticles of silver and amorphous calcium phosphate. Dent. Mater. J. **29**, 199–210 (2013)
322. A. Byström et al., Bacteriologic evaluation of the efficacy of mechanical root canal instrumentation in endodontic therapy. Scand. J. Dent. Res. **89**, 321–328 (1981)
323. M. Lotfi et al., Antimicrobial efficacy of nanosilver, sodium hypochlorite and chlorhexidine gluconate against Enterococcus faecalis. African J. Biotechnol. **10**, 6799–6803 (2011)
324. J. Almeida et al., Treatment of the Enterococcus faecalis root canal biofilm with nanoparticle suspensions and conventional irrigants. Arq. Odontol. Belo Horizonte **51**, 32–38 (2015)
325. S.W.S. Larz et al., Rationale and efficacy of root canal medicaments and root filling materials with emphasis on treatment outcome. J. Endodont. Top. **2**, 35–58 (2002)
326. D. Bo et al., Effect of nanosilver gel, chlorhexidine gluconate, and camphorated phenol on enterococcus faecalis biofilm. Int. Sch. Res. Notices **2014**, 380278 (2014)
327. A. Abbaszadegan et al., Positively charged imidazolium-based ionic liquid-protected silver nanoparticles: a promising disinfectant in root canal treatment. Int. Endod. J. **48**, 790–800 (2015)
328. J. Kreth et al., The antimicrobial effect of silver ion impregnation into endodontic sealer against streptococcus mutans. Open Dent. J. **2**, 18–23 (2008)
329. O. Dianat, et al., Gutta-percha coated with nanosilver particles. Invention registered number: 56019 (2008)
330. Y. Shantiaee et al., Cytotoxicity comparison of nanosilver coated gutta-percha with Guttaflow and normal gutta-percha on L929 fibroblast with MTT assay. Beheshti Univ. Dent. J. **29**, 62–68 (2011)
331. M. Torabinejad et al., Comparative investigation of marginal adaptation of mineral trioxide aggregate and other commonly used root-end filling materials. Int. Endod. J. **21**, 295–299 (1995)
332. N. Jonaidi-Jafari et al., The effects of silver nanoparticles on antimicrobial activity of ProRoot mineral trioxide aggregate (MTA) and calcium enriched mixture (CEM). J. Clin. Exp. Dent. **8**, e22–e26 (2016)
333. A. Bahador et al., *In vitro* evaluation of the antimicrobial activity of nanosilver-mineral trioxide aggregate against frequent anaerobic oral pathogens by a membrane-enclosed immersion test. Biom. J. **38**, 77–83 (2015)

334. V. Zand et al., Tissue reaction and biocompatibility of implanted mineral trioxide aggregate with silver nanoparticles in a rat model. Iran. Endod. J. **11**, 13–16 (2016)
335. L. Bazvand et al., Antibacterial effect of triantibiotic mixture, chlorhexidine gel, and two natural materials propolis and aloe vera against enterococcus faecalis: an ex vivo study. Dent. Res. J. (Isfahan) **11**, 469–474 (2014)
336. B. Sagsen et al., *In vitro* fracture resistance of endodontically treated roots filled with a bonded filling material or different types of posts. J. Endod. **39**, 1435–1437 (2013)
337. C. Poggio et al., Biological and antibacterial properties of a new silver fiber post: *in vitro* evaluation. J. Clin. Exp. Dent. **9**, e387–e393 (2017)
338. K. Bulad et al., Colonization and penetration of denture soft lining materials by Candida albicans. Dent. Mater. **20**, 167–175 (2004)
339. H.F. Paranhos et al., Effect of three methods for cleaning dentures on biofilms formed in vitro on acrylic resin. J. Prosthodont. **18**, 427–431 (2009)
340. E. Budtz-Jłrgensen et al., Oral candidiasis in long-term hospital care: comparison of edentulous and dentate subjects. Oral Dis. **2**, 285–290 (1996)
341. R. Rowan et al., Analysis of the response of Candida albicans cells to silver(I). Med. Mycol. **48**, 498–505 (2010)
342. A.Z. Sadeghi et al., The effect of nanochitosans particles on Candida biofilm formation. Curr. Med. Mycol. **2**, 28–33 (2016)
343. J.H. Lee et al., Nano-graphene oxide incorporated into PMMA resin to prevent microbial adhesion. Dent. Mater. **34**, e63–e72 (2018)
344. K.Y. Nam, *In vitro* antimicrobial effect of the tissue conditioner containing silver nanoparticles. J. Adv. Prosthodont. **3**, 20–24 (2011)
345. G. Greenstein et al., The role of controlled drug delivery for periodontitis. J. Periodontol. **71**, 125–140 (2000)
346. J. Staehelin et al., Decomposition of ozone in water in the presence of organic solutes acting as promoters and inhibitors of radical chain reactions. Environ. Sci. Technol. **19**, 1206–1213 (1985)
347. S. Hayakumo et al., Clinical and microbiological effects of ozone nano-bubble water irrigation as an adjunct to mechanical subgingival debridement in periodontitis patients in a randomized controlled trial. Clin. Oral Investig. **17**, 379–388 (2013)
348. J.M. Corrêa et al., Silver nanoparticles in dental biomaterials. Int. J. Biomater. **2015**, 485275 (2015)
349. A. Chwalibog et al., Visualization of interaction between inorganic nanoparticles and bacteria or fungi. Int. J. Nanomedicine **5**, 1085–1094 (2010)
350. S. Mukherjee et al., Potential theranostics application of bio-synthesized silver nanoparticles (4-in-1 system). Theranostics. **4**, 316–335 (2014)
351. T.S.J. Kashi et al., Improved drug loading and antibacterial activity of minocycline-loaded PLGA nanoparticles prepared by solid/oil/water ion paring method. Int. J. Nanomedicine **7**, 221–234 (2012)
352. K. Madhumathi et al., Regenerative potential and antibacterial activity of tetracycline loaded apatitic nanocarriers for the treatment of periodontitis. Biomed. Mater. **9**, 035002 (2014)
353. A.H. Melcher, On the repair potential of periodontal tissues. J. Periodontol. **47**, 256–260 (1976)
354. I.A. Demolon et al., Effects of antibiotic treatment on clinical conditions and bacterial growth with guided tissue regeneration. J. Periodontol. **64**, 609–616 (1993)
355. E.E. Machtei et al., Guided tissue regeneration and anti-infective therapy in the treatment of class II furcation defects. J. Periodontol. **64**, 968–973 (1993)
356. D.W. Chen et al., Preclinical experiments on the release behavior of biodegradable nanofibrous multipharmaceutical membranes in a model of four-wall intrabony defect. Antimicrob. Agents Chemother. **57**, 9–14 (2013)
357. J. Xue et al., Drug loaded homogeneous electrospun PCL/gelatin hybrid nanofiber structures for anti-infective tissue regeneration membranes. Biomaterials **35**, 9395–9405 (2014)

358. S. Rani et al., Evaluation of the antibacterial effect of silver nanoparticles on guided tissue regeneration membrane colonization—an *in vitro* study. J. Int. Acad. Periodontol. **17**, 66–76 (2015)
359. M. Yazdimamaghani et al., Hybrid macroporous gelatin/bioactive-glass/nanosilver scaffolds with controlled degradation behavior and antimicrobial activity for bone tissue engineering. J. Biomed. Nanotechnol. **10**, 911–931 (2014)
360. M. Ul-Islam et al., Nanoreinforced bacterial cellulose–montmorillonite composites for biomedical applications. Carbohydr. Polym. **89**, 1189–1197 (2012)
361. S. Khan et al., Bacterial cellulose-titanium dioxide nanocomposites: nanostructural characteristics, antibacterial mechanism and biocompatibility. Cellulose **22**, 565–579 (2015)
362. C.R. Arciola et al., Strong biofilm production, antibiotic multi-resistance and high gelE expression in epidemic clones of enterococcus faecalis from orthopedic implant infections. Biomaterials **29**, 580–586 (2008)
363. L. Zhao et al., Antibacterial nano-structured titania coating incorporated with silver nanoparticles. Biomaterials **32**, 5706–5716 (2011)
364. M.A. Massa et al., Synthesis of new antibacterial composite coating for titanium based on highly ordered nanoporous silica and silver nanoparticles. Mater. Sci. Eng. C Mater. Biol. Appl. **45**, 146–153 (2014)
365. C.Y. Flores et al., Spontaneous adsorption of silver nanoparticles on Ti/TiO2 surfaces. J. Colloid Interface Sci. **350**, 402–408 (2010)
366. H. Qin et al., Antimicrobial and osteogenic properties of silver-ion-implanted stainless steel. ACS Appl. Mater. Interfaces **7**, 10785–10794 (2015)
367. N. Kose et al., Silver ion doped ceramic nano-powder coated nails prevent infection in open fractures: *in vivo* study. Injury **47**, 320–324 (2016)
368. K. Memarzadeh et al., Nanoparticulate zinc oxide as a coating material for orthopedic and dental implants. J. Biomed. Mater. Res. A **103**, 981–989 (2015)
369. W. Li et al., Surface modification of titanium substrates with silver nanoparticles embedded sulfhydrylated chitosan/gelatin polyelectrolyte multilayer films for antibacterial application. J. Mater. Sci. Mater. Med. **25**, 1435–1448 (2014)
370. A. Peetsch et al., Silver-doped calcium phosphate nanoparticles: synthesis, characterization, and toxic effects toward mammalian and prokaryotic cells. Colloids Surf. B Biointerfaces **102**, 724–729 (2013)
371. H. Cao et al., Biological actions of silver nanoparticles embedded in titanium controlled by micro-galvanic effects. Biomaterials **32**, 693–705 (2011)
372. A. Besinis et al., Review of nanomaterials in dentistry: interactions with the oral microenvironment, clinical applications, hazards, and benefits. ACS Nano **9**, 2255–2289 (2015)
373. A.S. Barnard, Nanohazards: knowledge is our first defense. Nat. Mater. **5**, 245–248 (2006)
374. L. Tijana et al., Nanotechnology in dentistry—current state and future perspectives. Serb. Dent. J. **59**, 44–50 (2012)
375. Y.N. Zhang et al., Nanoparticle liver interactions: cellular uptake and hepatobiliary elimination. J. Control. Release **240**, 332–348 (2016)
376. K.I. McConnell et al., Reduced cationic nanoparticle cytotoxicity based on serum masking of surface potential. J. Biomed. Nanotechnol. **12**, 154–164 (2016)
377. W.N. Missaoui et al., Toxicological status of nanoparticles: what we know and what we don't know. Chem. Biol. Interact. **295**, 1–12 (2018)
378. P. Khanna et al., Nanotoxicity: an interplay of oxidative stress, inflammation and cell death. Nanomaterials (Basel) **5**, 1163–1180 (2015)
379. S. Hackenberg et al., Silver nanoparticles: evaluation of DNA damage, toxicity and functional impairment in human mesenchymal stem cells. Toxicol. Lett. **201**, 27–33 (2011)
380. Y. Huang et al., Toxicity of silver nanoparticles to human dermal fibroblasts on microRNA level. J. Biomed. Nanotechnol. **10**, 3304–3317 (2014)
381. K.S. Tweden et al., Biocompatibility of silver-modified polyester for antimicrobial protection of prosthetic valves. J. Heart Valve Dis. **6**, 553–561 (1997)

382. M.V. Park et al., The effect of particle size on the cytotoxicity, inflammation, developmental toxicity and genotoxicity of silver nanoparticles. Biomaterials **32**, 9810–9817 (2011)
383. J.S. Teodoro et al., Low-dose, subchronic exposure to silver nanoparticles causes mitochondrial alterations in Sprague-Dawley rats. Nanomedicine (Lond.) **11**, 1359–1375 (2016)
384. S. Haider et al., Human tumor necrosis factor: physiological and pathological roles in placenta and endometrium. Placenta **30**, 111–123 (2009)
385. C. Moon et al., Pulmonary inflammation after intraperitoneal administration of ultrafine titanium dioxide (TiO2) at rest or in lungs primed with lipopolysaccharide. J. Toxicol. Environ. Health A **73**, 396–409 (2010)
386. D. Couto et al., Polyacrylic acid-coated and non-coated iron oxide nanoparticles induce cytokine activation in human blood cells through TAK1, p38 MAPK and JNK pro-inflammatory pathways. Arch. Toxicol. **89**, 1759–1769 (2015)
387. M.G.M. Berges, Exposure during production and handling of manufactured nanomaterials. Nanomaterials, 25–31 (2013)

Chapter 4
Next Generation of Cancer Immunotherapy: Targeting the Cancer-Immunity Cycle with Nanotechnology

Yifan Ma and Lintao Cai

Abstract Although cancer immunotherapy has made great progress in treating a variety of malignances, its clinical efficacy is often dampened by tumor heterogeneity, tumor microenvironment, and immune cell dysfunction. An effective antitumor immune response involves a series of immunological events called the "cancer-immunity cycle," which provides the rationale for designing new therapeutic approaches. Nanotechnology demonstrates great potentials of immunomodulation, offering new opportunities to accelerate the development of next generation of cancer immunotherapy. We herein review current applications of nanotechnology, which effectively boost anticancer immune responses through targeting each step of the cancer-immunity cycle, thereby enhancing the potency and minimizing the toxicity of cancer immunotherapy.

Keywords Nanotechnology · Cancer immunotherapy · Dendritic cell · Cytotoxic T cell · Immunogenic cell death · Lymph nodes · Tumor microenvironment

Y. Ma (✉)
Guangdong Key Laboratory of Nanomedicine, Shenzhen engineering Laboratory of nanomedicine and nanoformulations, CAS-HK Joint Lab of Biomaterials, Institute of Biomedicine and Biotechnology, Shenzhen Institutes of Advanced Technology, Chinese Academy of Sciences, Shenzhen, People's Republic of China

HRYZ Biotech. Co., Shenzhen, People's Republic of China
e-mail: yf.ma@siat.ac.cn

L. Cai
Guangdong Key Laboratory of Nanomedicine, Key Lab of Health Informatics of Chinese Academy of Sciences, Shenzhen Institutes of Advanced Technology, Chinese Academy of Sciences, Shenzhen, People's Republic of China

H. Xu, N. Gu (eds.), *Nanotechnology in Regenerative Medicine and Drug Delivery Therapy*, https://doi.org/10.1007/978-981-15-5386-8_4

4.1 Antitumor Immune Responses and Cancer Immunotherapy

In 1891, immunotherapy was first applied to treat a sarcoma patient using intratumoral injection of streptococcal organisms (so-called Coley toxin). Since then, cancer immunotherapy has emerged as a plausible therapeutic strategy and attracted a lot of attention, Compared with conventional chemotherapy and radiotherapy, which directly kill cancer cells, immunotherapy eliminates cancer cells through activating adaptive and innate immunity of patients with higher specificity and less toxicity, thereby being considered as the new generation of cancer therapy.

An effective antitumor immune response involves a series of immunological events called the "cancer-immunity cycle" initiated by tumor antigen releasing from dead tumor cells (step 1, Fig. 4.1). The released tumor antigens are captured and processed into antigenic epitopes by antigen presenting cells (APCs), such as dendritic cells (DCs) and macrophages, and then presented by MHC class I (MHC I) and MHC class II (MHC II) molecules onto cell surface (step 2). MHC-presented antigenic epitopes are recognized by T cell receptors (TCRs) on T cells in lymphoid tissues, triggering the proliferation and activation of tumor-specific $CD4^+$ and $CD8^+$ T cells (step 3). The tumor-specific T cells can infiltrate into tumor microenvironment through the blood circulation (steps 4, 5) and recognize tumor cells through the interaction of TCR-antigen-MHC I (step 6), which subsequently leads to antitumor cytotoxic killing (step 7) and tumor antigen releasing (step 1 again), thereby initiating the next round of cancer-immunity cycle for broader and stronger antitumor immunity [1]. Unfortunately, the cancer-immunity cycle is often inactivated in cancer patients due to dysfunctional immune cells and immune escape of tumor cells. Moreover, the tumor microenvironment contains a variety of immunosuppressive molecules, such as IL-10, TGF-β, VEGF, PGE_2, and different types of immunosuppressive cells, such as regulatory T (Treg) cells, myeloid-derived suppressor cells (MDSCs), and tumor-associated macrophages (TAMs), which directly inhibit the cancer-immunity cycle. Hence, the goal of cancer immunotherapies is to generate effective and sustained antitumor immunity through re-activating the cancer-immunity cycle, which could not only ablate primary tumors but also prevent tumor recurrence and metastasis [1].

Cancer immunotherapy includes cancer vaccines, adoptive T cell therapy (ACT), checkpoint inhibitors, oncolytic viruses, etc. Immune checkpoint-blocking antibodies, such as anti-CTLA-4, anti-PD-1, and anti-PD-L1, are the most successful immuno-oncology (IO) therapies, which block either inhibitory molecules on tumor-infiltrating T cells or their ligands expressed on tumor cells, thereby re-activating T cell-mediated cytotoxicity against cancer. To date, several monoclonal antibodies targeting cytotoxic T lymphocyte antigen-4 (CTLA-4), programmed cell death protein 1 (PD-1), and the PD-1 ligand (PD-L1) have obtained regulatory approvals for treating a variety of malignancies. However, their clinical efficacy is often dampened by a series of immunotoxic effects and drug resistance [2]. Cancer vaccines are another therapeutic approach that is aimed to deliver tumor antigens to APCs and

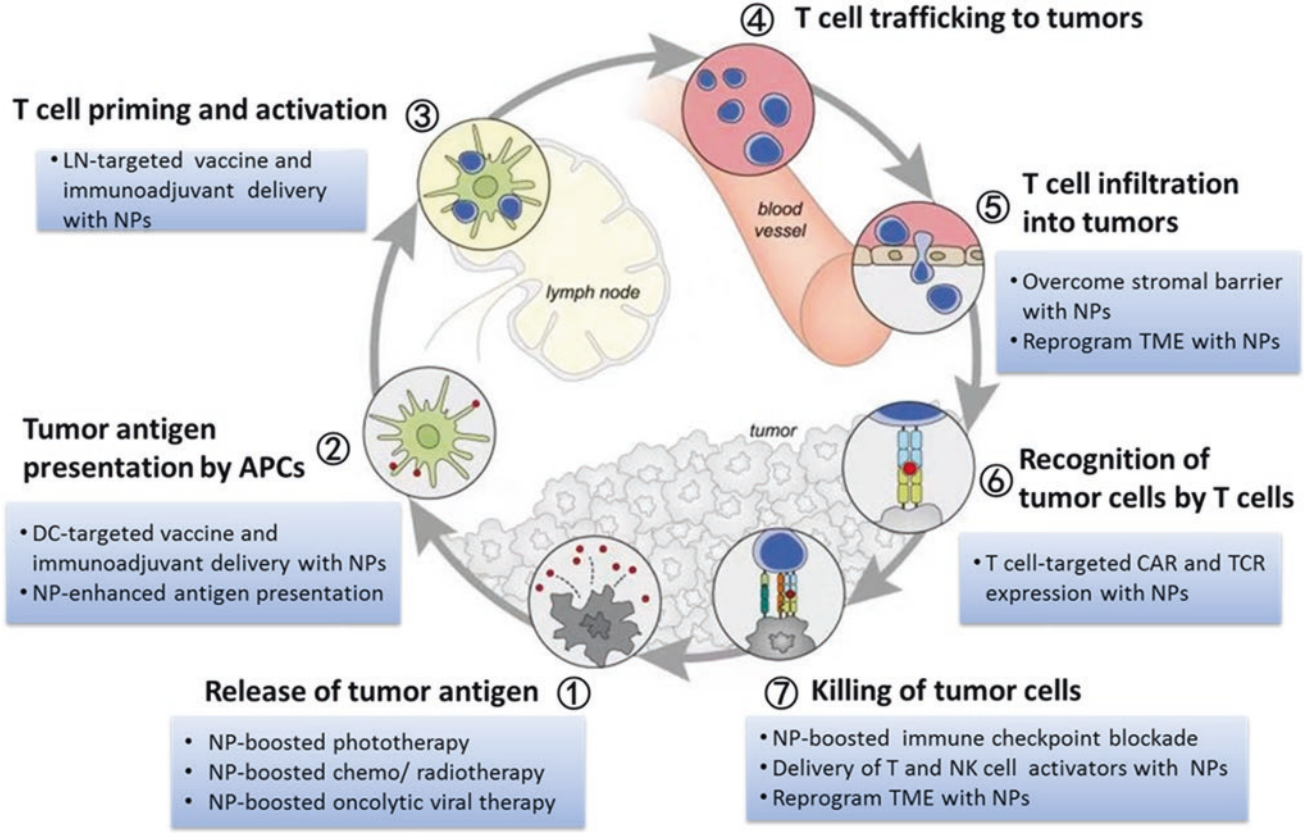

Fig. 4.1 Nanotechnology improves the efficacy of cancer immunotherapy through targeting the cancer-immunity cycle. *NPs* nanoparticles, *DC* dendritic cells, *APCs* antigen-presenting cells, *LN* lymph node, *TME* tumor microenvironment. Adapted from [1] with copyright permission

evoke antitumor immune responses. Despite the great safety of cancer vaccines, their therapeutic efficacy remains unsatisfied due to the poor immunogenicity of tumor antigens and failure of overcoming tumor-derived immunosuppression [3]. In contrast to cancer vaccines, adoptive cell therapy (ACT) is designed to eliminate tumors through directly infusing antitumor effector cells, such as tumor-specific cytotoxic T cells (CTLs), NK cells, NK T cells, and γδT cells [4]. More recently, genetically engineered effector T cells with chimeric antibody receptors (CAR) or with T cell receptors (TCR) have demonstrated a great potential for cancer treatment. In 2017, the US FDA approved two chimeric antigen receptor T (CAR-T) cell products to treat lymphoblastic leukemia and B cell lymphoma, further highlighting the promising future of genetically engineered T cells [5]. With the first oncolytic virus (OV) approved by US FDA in 2017, OV therapy has become another important tool for cancer therapy. OA can not only directly infect and lysis tumor cells but also trigger tumor antigen release, eliciting systemic anticancer immunity [6].

Despite the promising results in cancer patients, cancer immunotherapies still face many challenges, especially for treating solid tumors, which could be primarily attributable to tumor heterogeneity, immune cell dysfunction, tumor microenvironment, acquired resistance to immunotherapy, and immune toxicity [7]. Hence, new technologies are highly desirable to improve the potency and safety of cancer immunotherapy.

4.2 Nanomaterials for Immunomodulation and Cancer Immunotherapy

Nanomaterials are well recognized as a potent and versatile tool for disease diagnosis, molecular imaging, as well as drug and gene delivery. In the meantime, a variety of nanomaterials, including synthetic and biological-derived nanomaterials, also demonstrate great potential of immunomodulation, thereby offering new opportunities to cancer immunotherapy. The immunomodulatory effects of nanomaterials primarily include several aspects: (1) to form a depot of antigens, immunoadjuvants, and cytokines to generate persistent stimulation to the immune system; (2) to stimulate a variety of signaling pathways due to the intrinsic immunogenicity; (3) to facilitate immune cell-targeted vaccine and drug delivery; (4) promoting antigen cross-presentation for $CD8^+$ T cell activation; (5) to increase the accumulation of immunomodulatory molecules in tumors and lymphoid organs [8].

4.2.1 Synthetic Nanomaterials

Synthetic nanomaterials, including organic nanoparticles, inorganic nanoparticles, and organic-inorganic hybrid nanoparticles, have been developed to modulate the immune system and enhance antitumor immunity (Table 4.1).

Table 4.1 Synthetic nanomaterials for cancer immunotherapy

Delivery system	Materials	Payload	Major immunomodulatory effects
Organic nanoparticles			
Lipid-based nanoparticles (NPs)	• Cationic liposomes • Stealth liposomes	• Protein/peptide antigens [9, 10] • DNA/mRNA antigens [11–13] • Immunoadjuvant (TLR agonists, iNKT agonist, cytokines) [14] • Small molecules (IDO inhibitor) [15]	• Facilitate antigen uptake [14] • Enhance the potency of immunoadjuvants [14] • Promote DC maturation, MHC I antigen presentation and cytokine/chemokine production [10, 16] • Boost tumor-specific CTL responses [17]
Polymeric NPs	• PLGA NPs [18, 19] • Chitosan NPs [20]	• Protein/peptide antigen [18, 19] • siRNA/miRNA [21] • Immunoadjuvant (TLR agonists, iNKT agonist, cytokines) [22] • Antibodies [23]	• Facilitate antigen uptake and control antigen release [18, 19] • Enhance the potency of immunoadjuvants [22] • Promote DC maturation, MHC I antigen presentation, and cytokine/chemokine production [24] • Boost tumor-specific CTL responses [23, 25]
Polymeric micelles	• Block copolymer micelles [26–29] • Polypeptide micelles [30–33]	• Protein/peptide antigen [26, 29] • siRNA/micro RNA [31, 33] • Immunoadjuvants [26, 30, 34] • Small molecules (STAT3 inhibitor, curcumin) [29, 35] • Oncolytic virus [36]	• Lymph node (LN)-targeting ability [26, 27] • Enhance antigen uptake, DC maturation, and MHC I antigen presentation [26, 27] • Enhance the potency of immunoadjuvants [26, 30] • Boost tumor-specific CTL responses [23, 25, 27]
Dendrimer	• PAMAM dendrimer [37, 38] • Polyamidoamine dendrimers [39, 40] • Glycopeptide dendrimers [41]	• Protein/peptide antigen [40, 42], tumor-associated carbohydrate antigens [41] • DNA/RNA [37, 43] • Antibodies [44] • Virus [38, 39]	• High loading capacity of multiple antigens • Enhance cellular uptake by DC and antigen presentation [44, 45]

(continued)

Table 4.1 (continued)

Delivery system	Materials	Payload	Major immunomodulatory effects
Hydrogel NPs	• Beta glucan nanogel [46] • pHEMA-pyridine nanogel [47] • Polysaccharide nanogel [48–50]	• Protein/peptide antigens [48, 51] • siRNA [52] • Immunoadjuvant (TLR agonist, cytokines) [46, 50]	• LN-targeting ability [51] • Facilitate antigen uptake by APCs[48, 51] • Promote DC maturation and MHC I/II antigen presentation; boost tumor-specific CTL responses [48, 49, 53] • Sustained release of payload [50]
Lipid-polymeric hybrid NPs	• Lipid-PLGA nanoparticles [54, 55] • Lipid-protamine-DNA (LPD) NPs [56]	• Protein and peptide antigens [54] • DNA antigen, siRNA [56, 57] • Trap DNA [58]	• High loading capacity • High stability and biocompatibility, controlled release properties [54] • Facilitate antigen uptake by DCs • Enhance antigen-specific antibody and Th1/Th17 immune responses [54]
Inorganic nanoparticles			
Au NPs	• Au NP/nanorod/nanocluster	• Protein/peptide antigen [59] • DNA/siRNA [60] • Immunoadjuvant (CpG) • Cytokines (TNF, GM-CSF) [61]	• Intrinsic immunoregulatory effect, such as inducing macrophage activation, attenuating immunosuppressive IL-10 and TGF-β1 [61, 62]
Silica NPs	• Mesoporous silica (MS) • Hollow mesoporous silica (HMS) • Mesoporous silica rod scaffold	• Protein/peptide antigen [63] • Immunoadjuvant (CpG) [64] • Cytokines (IL-2, GM-CSF) • Small molecules (IDO inhibitor) [65]	• High porosity and loading capacity [25, 66] • Enhance antigen uptake by DC and macrophages • Promote DC maturation, antigen presentation, and cytokine/chemokine production • Enhance Th1/Th2 immunity and memory T cell population [67, 68]
Carbon NPs	• Multi-wall carbon nanotubes (MWCNT) [69–71] • Single-wall carbon nanotubes (sWCNT) [72, 73] • Nanodiamonds (NDs)[74] • Graphene oxide [75]	• Protein/peptide antigen [69] • DNA antigen [76] • Immunoadjuvant (CpG, anti-CD40) [75, 77]	• Large surface area [69–71] • Promote antigen uptake and DC maturation [73] • Activate complement system [70] • Induce proinflammatory cytokines [78] • Delete M2 macrophages [70, 71, 77]

Organic-inorganic hybrid NPs			
Lipid-inorganic hybrid NPs	• Lipid calcium phosphate (LCP) NPs [79–83] • Lipid-coated silica microparticles [84, 85] • Lipid-coated IONPs [86]	•Peptide antigen [80] • mRNA antigen [81] • Immunoadjuvants (TLR agonists) [82, 83] • T cell-stimulating antibodies [84, 85]	• LN-targeting ability [86] • Facilitate antigen uptake by DCs [80, 81] • Stimulate T cell proliferation and boost tumor-specific CTL responses [84, 85] • Elevated ratio of M1 to M2 macrophages [82] • Enhance the immunopotency of immunoadjuvants [83]
Other metal-organic NPs	• Metal-organic frameworks (MOFs) [87, 88] • Polyelectrolyte multilayer-gold nanoparticles [89]	• Peptide/protein antigens [88] • Immunoadjuvants (TLR agonists) [87] [89]	• Facilitate antigen uptake and antigen presentation [88] • Enhance the potency of immunoadjuvants [87, 89] • Boost tumor-specific CTL responses [88]

4.2.1.1 Organic Nanoparticles

Organic nanoparticles (NPs), such as lipid-based NPs [17], polymeric NPs [23, 25], polymeric micelles [26–33], lipid-enveloped polymeric NPs [54, 56–58] dendrimers [37, 42–44, 90], and hydrogel NPs [48–50, 53], are well-known delivery systems for cancer immunotherapy due to their biocompatibility, biodegradability, high loading capacity of hydrophilic or hydrophobic molecules, tunable size and charge, as well as easy surface functionalization. The organic nanoparticle-based delivery system can not only deliver their payloads to certain immune cells and regulate their functions but also ameliorate immunosuppression in tumor microenvironment, thereby enhancing immunotherapeutic efficacy [17, 23, 25, 27, 44, 45, 48, 49, 53].

4.2.1.2 Inorganic Nanoparticles

Some of inorganic NPs, such as gold nanoparticles (Au NPs) [59–61], silica NPs [63–65, 91], and carbon nanotubes [69, 76, 77], have been applied for cancer immunotherapy due to their biocompatibility and easy surface functionalization. These inorganic NPs can load antigens and immunoregulatory molecules through physical absorption or chemical conjugation and deliver them to immune cells to boost cancer immunotherapy. Moreover, some inorganic NPs also demonstrate intrinsic immunoregulatory effects [61, 62, 70, 71, 77], which could further enhance antitumor immune responses.

4.2.1.3 Organic-Inorganic Hybrid Nanoparticles

Organic-inorganic hybrid nanoparticles, which integrate advantages of organic and inorganic counterparts, are multifunctional platforms for cancer theranostics. Typically, the organic-inorganic hybrid nanoparticles consist of inorganic nanoparticles (e.g., gold, magnetic iron oxide, carbon nanotubes, mesoporous silica) as the core, and organic materials (e.g., polymers, lipids, dendrimers, peptides, and cell membranes) as the shell, which allow to simultaneously achieve cancer therapy and cancer diagnosis [92].

Lipid-calcium-phosphate (LCP) nanoparticle is a versatile delivery system with great biocompatibility and high loading capacity of encapsulating different therapeutic agents, such as siRNA, DNA, antigen peptides, chemotherapeutic agents, and radionuclides, therefore being applied for anticancer gene therapy, immunotherapy, chemotherapy, radiation therapy, and cancer imaging [79–83]. Lipid-coated silica particles (e.g., silica microparticles and mesoporous silica micro-rods) were developed as artificial antigen presenting cell (aAPC) systems, which presented T cell-stimulating antibodies on their surface, thereby effectively stimulating $CD4^+$ and $CD8^+$ T cell expansion as well as antitumor CTL responses [84, 85]. Iron oxide nanoparticles (IONPs) coated with self-assembled lipid shells not only demonstrated much higher loading capacity of bio-macromolecules, such as antigen peptides and immunoadjuvants, than non-coated IONPs, but also demonstrated superior

LN-targeting ability for boosted cancer immunotherapy and imaging monitoring [86]. Polyelectrolyte multilayer (PEM)-gold nanoparticles were successfully loaded with antigen peptides and Poly I:C (a TLR3 agonist) through stepwise electrostatic interactions, which effectively induced DC maturation and robustly elicited $CD8^+$ T cell responses in vivo [89].

Metal-organic frameworks (MOFs) are emerging as a new type of porous crystalline materials assembled from metal ions and organic linkers via coordination chemistry. Because of the tunable pore size and high surface area, MOFs have high loading capacity of both small molecules and bio-macromolecules, thereby being considered as a potent multifunctional platform for cancer theranostics [93]. A pH-responsive MOF utilizing lanthanide ions ($Eu3^+$) and guanine monophosphate (GMP) as coordinating partners was developed for vaccine delivery. In the acidic endo/lysosomes, the coordination of $Eu3^+$ and GMP was dissociated, which promoted antigen releasing and cross-presentation. Immunization of OVA-loaded GMP/Eu MOFs induced antitumor immune responses and effectively inhibited tumor growth [87]. Zeolitic imidazole frameworks (ZIF-8) containing zinc ions and 2-methylimidazole (MeIM) were incorporated with aluminum ions to generate aluminum-nanoZIF-8 nanoparticles (ZANPs) for cancer vaccine delivery. The results showed that ZANPs were an effective platform, which not only effectively codelivered OVA antigens and CpG (a TLR9 agonist), but also released their payload in a pH-dependent manner due to protonation. The immunization of CpG/ZANPs robustly elicited antigen-specific humoral and T cell responses, thereby inhibiting tumor growth [88].

4.2.2 Biologically Derived Nanomaterials

In addition to the synthetic nanomaterials, the biomimetic drug delivery system using biologically derived materials, such as caged protein NPs, cell membrane-based NPs, and live cells, also holds great potential for boosting cancer immunotherapy (Table 4.2).

4.2.2.1 Caged Protein-Based Nanoparticles

Caged protein nanoparticles, such as virus-like particles (VLPs), enzymes, the ferritin superfamily, and heat shock proteins, are self-assembling natural nanocapsules with great biocompatibility and biodegradability. A previous study showed that protein nanoparticles effectively targeted LNs due to slightly negative charge and appropriate hydrodynamic sizes, thereby eliciting robust CTL responses against tumors [94]. Moreover, caged protein nanoparticles can be easily modified through protein engineering for vaccine delivery [97, 98]. Molino et al. conjugated Pyruvate dehydrogenase-derived protein nanoparticles (E2 nanoparticles) with CpG and antigen peptides to obtain pH-sensitive CpG-E2 nanovaccines. Compared with free CpG, CpG-E2 more effectively targeted DC and induced DC maturation, robustly enhancing MHC I antigen presentation and $CD8^+$ T cell activation. Moreover,

Table 4.2 Biologically derived nanomaterials for cancer immunotherapy

Delivery system	Materials	Payload	Major immunomodulatory effects
Caged protein-based NPs	• Virus-like particles (VLPs) [94] • Pyruvate dehydrogenase-derived caged protein [95, 96] • Encapsulin [97] • Ferritin [94]	• Peptide antigen [94, 97] • Immunoadjuvants (CpG) [96]	• Enhance antigen and adjuvant uptake by APCs (DC and macrophage)[95, 96, 98] • Enhance antigen presentation [95, 97] • LN targeting and prolong LN retention [94]
Cell membrane-coated NPs	• RBC membrane [99, 100] • Platelet membrane [101] • Cancer cell membrane [102, 103] • NK cell membrane [104, 105] • Azide-modified T cells [106]	• Bacterial toxoid [99] • Peptide antigen [100] • Immunoadjuvants (MPLA, CpG) [100, 102] • Anti-PD-L1 [101] • Photosensitizer [105]	• Biocompatibility and non-immunogenic • Prolonged circulation and LN targeting [103, 107] • Enhance the uptake by DCs and macrophages [102] • Tumor-targeting ability [104, 105] • Induce the polarization of TAM to M1 type [105]
Immune cell-based drug delivery	• Antigen-specific CTLs [108–110] • CAR-T cells [111] • CIK cells [111] [112]	• siRNA [108] • Cytokine (IL-15) [110, 111] • Prussian blue NPs (PBNPs) [109] • Photosensitizer [112]	• Intrinsic tumor-targeting ability [112] • Specifically enhanced antitumor effect of T cell therapy [108–110] • Boost combinational therapy [112]
Live attenuated bacteria	• Salmonella [113]	• DNA vaccine [113]	• Colonize the gut-associated lymphoid tissue • Induce tumor-specific $CD8^+$ T cell activation

CpG-E2 prolonged LN retention time of nanovaccine, which could potentially promote the anticancer efficacy of nanovaccines [95, 96]. Choi et al. reported Encapsulin (Encap), another self-assembled protein nanoparticle, as a vaccine delivery system, which could be loaded with protein or peptide antigens through genetic modification, thereby enhancing antigen presentation and CTL response against tumors [97].

4.2.2.2 Cell Membrane-Based Nanoparticles

Cell membrane-cloaked nanoparticles are emerging as a novel delivery system integrated with certain advantages of live cells. For example, red blood cells (RBC) are the most abundant blood cell population with long circulation time due to their ability to avoid reticuloendothelial system. Surface coating with RBC membranes has been shown as a plausible strategy to prolong the blood circulation and enhance targeting ability of nanoparticles. Zhang's group loaded RBC membrane-coated

PLGA nanoparticles with Staphylococcal α hemolysin (Hla) to obtain nanotoxoid, which elicited roust and sustained Hla-specific antibody responses due to enhanced LN-targeting ability and prolonged circulation time [99]. Another study coated antigen peptide-loaded PLGA with RBC membrane to obtain nanovaccine. The results showed that coating with RBC membrane, especially mannosylated RBC membrane, significantly enhanced DC capture and LN-targeting ability of nanovaccines. The incorporation of monophosphoryl lipid (MPLA), a TLR4 agonist, into the PLGA core of nanovaccines further promoted DC maturation and proinflammatory cytokine production, thereby effectively inhibited tumor growth and tumor metastasis [100].

Platelets have been reported as another biological delivery system due to their long circulation time and ability of targeting wound sites and recognizing CTCs. Anti-PD-L1-functionalized platelets (P–aPDL1) not only demonstrated longer blood circulating time than anti-PD-L1 antibody but also enhanced antibody accumulation in residual tumors after surgical resection, which subsequently decreased tumor-infiltrating Treg cells and robustly induced $CD8^+$ T cell responses, thereby preventing cancer recurrence and metastasis after surgery [101].

Cancer cell membranes carry on a lot of tumor antigens and have been utilized for cancer vaccine development. Two studies loaded PLGA nanoparticles with TLR agonists (NP-TLR) followed by cancer cell membrane coating to generate biomimetic nanovaccine (NP-TLR@M). The results showed that cancer cell membrane not only enhanced vaccine uptake and TLR-induced DC maturation but also augmented vaccine-elicited T cell responses and tumor regression [102, 103]. Surface modification of NP-TLR@M with PEG or mannose further improved LN targeting of nanovaccines, which consequently boosted antitumor immune responses and led to tumor regression [103, 107].

More recent studies utilized cell membranes of antitumor effector cells, such as NK cells and T cells, to achieve tumor-targeted drug delivery and cancer immunotherapy. NK cells, as cytolytic effector cells of the innate immunity, can recognize and kill tumor cells through a variety of surface active receptor, such as natural cytotoxicity receptors, Fc receptor, and NKG2D and SLAM family. Pitchaimani et al. isolated activated NK-92 cell membranes line and fused them with liposome-encapsulated DOX to generate NK cell membrane-infused liposome (NKsome). The NKsomes preserved surface receptors of NK cell, such as NKG-2D, NKp30, and CD56, which not only facilitated the cellular uptake of DOX by MCF-7 cells in vitro but also enhanced tumor-targeted DOX delivery in vivo, thereby leading to dramatic tumor regression [104]. Our group developed photosensitizer TCPP-loaded nanoparticles (T-NPs) and cloaked them with NK cell membranes to obtain NK-NPs for anticancer photodynamic therapy. Compared with T-NPs, NK-NPs not only demonstrated superior tumor-targeting ability but also significantly induced M1 macrophages polarization, which should be attributable to the presence of NK cell membrane proteins. With NIR laser radiation, NK-NPs robustly induced tumor cell apoptosis and antitumor immune responses, thereby effectively suppressing both primary and distal tumor growth [105]. In another study, PLGA-encapsulated

ICG nanoparticles (INP) were wrapped with T cell membrane to generate TINPs for antitumor PTT. Compared with INP, TINP significantly enhanced the cellular uptake and tumor accumulation of ICG, which could be partially due to TCR-mediated tumor cell recognition. The tumor-targeting ability of TINPs was further enhanced by in vivo bioorthogonal reaction between N3 groups on T cell membranes and BCN group on tumor cell surfaces, which consequently led to superior PTT effect for tumor ablation [106].

4.2.2.3 Immune Cell-Based Drug Delivery for Cancer Immunotherapy

A group of immune cells, such as cytotoxic T cells (CTLs), NK cells, and macrophages, have been recently applied as a "live" delivery system for cancer immunotherapy due to their tumor-infiltrating ability and intrinsic oncolytic machinery. To improve antitumor efficacy of adoptive T cell therapy, drug (e.g., cytokine, siRNA)-loaded nanoparticles were successfully conjugated onto the surface of antigen-specific CTLs, which did not interfere with T cell proliferation or antitumor cytotoxicity [108–110]. Interbilayer-crosslinked multilamellar vesicles (ICMVs) were developed to release their payload in response to perforin, a membrane pore-forming protein. Jones et al. conjugated IL15-loaded ICMVs onto CTLs and observed significant enrichment of ICMVs in the immunological synapse of CTLs and tumor cells, where CTL-released perforin ruptured ICMVs and triggered the release of IL-15, thereby boosting antiviral effect of CTLs in vivo [110]. A recent study reported significantly elevated reduction activity on cell surface upon T cell activation. Therefore, bioreducible protein drug nanogels (NG) functionalized with anti-CD45 were developed, which not only effectively bound to CD45 on T cell surface but also selectively released their payloads upon T cell activation. Compared with soluble IL-15, T cell-conjugated IL15-NGs more effectively promoted tumor-specific T cell expansion and activation without causing systemic immunotoxicity, thereby robustly enhancing the antitumor effect of CTL and CAR-T therapy in vivo [111].

T cells can also serve as a promising delivery system for boosted antitumor PTT and PDT. With NIR laser radiation, Prussian blue nanoparticle (PBNP)-conjugated CTLs more potently induced cancer cell death than either CTL or PBNP alone, indicating a synergistic anticancer effect of PTT and T cell immunotherapy [109]. Cytokine-induced killer (CIK) cells, another type of tumor-killing cells, were loaded with Ce6 gold nanoclusters (Ce6-GNCs) through anti-CD3 antibodies, which was shown to effectively enhance tumor-targeted Ce6 delivery. Compared with Ce6+laser or CIK cells alone, CIK-loaded Ce6-GNCs with laser radiation more robustly inhibited tumor growth, indicating synergistic effect of CIK-mediated immunotherapy and Ce6-GNC-based PDT [112].

4.3 Next Generation of Cancer Immunotherapy: Targeting the Cancer-Immunity Cycle with Nanotechnology

Immunomodulatory nanomaterials hold great potentials to accelerate the development of next generation of cancer immunotherapy. However, to achieve more potent and safe immunotherapy, nanomaterials must be further optimized in order to target each single step or multiple steps of cancer-immunity cycle, thereby enabling broader and more sustained antitumor immune responses.

4.3.1 Enhancing Immunogenic Antigen Release with Nanomaterials (Step 1)

Immunogenic cell death (ICD) is a mode of tumor cell death triggering both innate and adaptive immune responses against tumors. Tumor cell ICD can be induced by photodynamic therapy (PDT), hyperthermia (HT) and photothermal therapy (PTT), radiotherapy (RT), and certain chemotherapeutics [114]. Tumor cells undergoing ICD expose danger molecules, such as calreticulin (CRT) and heat shock proteins (Hsp90 and Hsp70), on pre-apoptotic cell surfaces, which are essential for dying cell engulfment and antigen uptake by APCs. Moreover, ICD of tumor cells also results in the release of intracellular danger signals, such as high-mobility group protein B1 (HMBG1), ATP, DNA, and RNA, which consequently induce DC maturation through activating NF-κB, MAPK, and IFN-regulatory factor (IRF) pathways, thereby evoking antitumor immune responses [115, 116]. Hence, promoting immunogenic antigen release is an important strategy to activate the cancer-immunity cycle.

4.3.1.1 PDT-Triggered Immunogenic Antigen Release

Photodynamic therapy (PDT) is a therapeutic strategy using photosensitizer and a particular type of light for cancer therapy. Upon exposed to the light, the photosensitizer generates reactive oxygen species (ROS), which not only directly disrupt tumor cells but also cause microvasculature damage, vessel constriction, and thrombus formation, leading to tumor regression. In addition, PDT can induce tumor cell ICD and subsequently elicit antitumor immune responses to prevent tumor metastasis and reoccurrence [117]. However, the therapeutic efficacy of PDT is often dampened due to inefficient tumor-target ability and hypoxia in tumor microenvironment.

Nanoparticle-based delivery systems have been reported as an effective tool to improve the therapeutic efficacy of PDT through increasing tumor-targeting ability of photosensitizers. More recent studies have shown that nanoparticle-based PDT

systems can also be equipped with the ability of oxygen supply to overcome hypoxia in tumor microenvironment. Fe-TBP is a nanoscale metal-organic framework containing porphyrin, a photosensitizer, and Fe_3O clusters, an inorganic catalase decomposing H_2O_2 to generate O_2 with the laser radiation. Upon laser radiation, Fe-TBP rather than the nano-frameworks without Fe_3O effectively ameliorated tumor hypoxia and significantly inhibited primary tumor growth. Moreover, Fe-TBP-based PDT significantly induced tumor ICD, thereby eliciting systemic antitumor immune responses and significant abscopal anticancer effects [118]. Hollow silica nanoparticles were loaded with catalase (CAT), a H_2O_2-decomposing enzyme and a photosensitizer chlorine e6 (Ce6) to obtain CAT@S/Ce6 nanoparticles, followed by modification with mitochondria-targeted (3-carboxypropyl) triphenylphosphonium bromide (CTPP) and surface coating with pH-responsive charge reversible polymers to generate multi-responsive CAT@S/Ce6-CTPP/DPEG nanoparticles for boosted PDT. Catalase could convert tumor endogenous H_2O_2 to O_2 to overcome tumor hypoxia. CTPP on nanoparticles could enhance drug delivery to mitochondria, the organelle most sensitive to ROS stress, which would further enhance the anticancer effect of PDT. The in vitro study showed that CAT@S/Ce6-CTPP/DPEG effectively delivered Ce6 into the mitochondria through CTPP. Moreover, CAT@S/Ce6-CTPP/DPEG effectively ameliorated tumor hypoxia and robustly inhibited tumor growth, confirming the crucial role of oxygen supply for effective anticancer PDT [119].

4.3.1.2 PTT-Triggered Immunogenic Antigen Release

Photothermal therapy (PTT) is an anticancer strategy that utilizes photo-absorbing agent to produce hyperthermia for tumor killing. Compared with conventional cancer treatments, PTT is more attractive because of its tumor specificity, safety, non-invasiveness, and remote-controllable properties. Moreover, PTT could induce ICD and evoke systemic anticancer immune responses for preventing tumor metastasis and reoccurrence [120, 121]. For example, gold nanoshell-enabled photothermal therapy (NEPTT) dose-dependently induced tumor cell ICD through inducing the release of adenosine triphosphate (ATP), adenosine diphosphate (ADP), and uric acid [122]. Intratumoral injection of SWNTs with NIR laser radiation significantly induced DC maturation and proinflammatory cytokine production in tumor draining lymph nodes (DLNs), which subsequently led to robust antitumor immune responses, thereby inhibiting the growth of distant tumors (so-called abscopal effect) [72]. Gd:CuS@BSA hybrid theranostic nanoparticles not only demonstrated potent PTT effect against tumors but also slightly increased tumor-infiltrating $CD8^+$ T cell, indicating the mild immune responses induced by PTT [123].

The immunostimulatory effect of PTT appeared to be related with tumor temperatures. Although PTT-induced tumor cell death is directly correlated with the local temperature, only medium PTT (tumor temperature 50–60 °C) rather than low PTT (<40 °C) or high PTT (>80 °C) effectively elicited ICD of tumor cells, as indicated with decreased intracellular ATP and HMGB1 and increased surface

calreticulin. [124]. In vivo immunization of tumor cells treated with medium PPT more effectively inhibited tumor growth than the cells treated with low or high PPT, consistent with the results of PPT-induced ICD. These results indicate a thermal dose window of PPT, which is crucial for effectively triggering robust anticancer immune response to prevent tumor recurrence and metastasis [124].

In addition to inducing tumor cell ICD, PPT-induced local heating was shown to enhance macrophage-targeted immunoadjuvant delivery. Cationic graphene oxide was functionalized with PEG and PEI to obtain GO-PEG-PEI nanovector for CpG delivery as well as the combination of PTT and immunotherapy. Interestingly, GO-PEG-PEI-CpG-mediated PTT enhanced cellular uptake of CpG by macrophages and promoted CpG-induced cytokine production by 2–3-folds through elevating the temperature of culture medium [75]. Similar results were observed in MoS2 nanosheet-based PTT. MoS2 single layer was conjugated with PEG and CpG to obtain MoS2-PEG-CpG nanosheets. Although MoS2-PEG-CpG effectively enhanced cellular uptake of CpG by macrophages, MoS2-PEG-CpG with NIR laser radiation further enhanced the internalization of CpG by macrophages, which might be due to heat-induced cell membrane permeability [125].

4.3.1.3 Chemotherapy-Triggered Immunogenic Antigen Release

Although conventional chemotherapy is often associated with immunosuppression, some of chemotherapeutic drugs, such as doxorubicin (DOX), mitoxantrone (MIT), cyclophosphamide(CSA), oxaliplatin (OXA), shikonin, and the proteasome inhibitor, have been reported to induce tumor cell ICD and stimulate both innate and adaptive immune responses against tumor. Moreover, chemotherapy can overcome tumor-derived immunosuppression through inducing lymphopenia or depleting immunosuppressive cells, such as Treg cells and MDSCs, further enhancing antitumor immunity [126, 127].

Nanotechnology is an important strategy to improve the therapeutic efficacy and safety of chemotherapy through facilitating tumor-targeted drug delivery. Increasing evidence showed that nanoparticles also enhanced the immunoregulatory effects of cytotoxic agents, which could be a novel mechanism improving the therapeutic efficacy of chemotherapy. OXA was encapsulated with mPEG-PLGA to obtain NP-OXA nanoparticles. Compared with free OXA, NP-OXA not only more significantly inhibited tumor cell growth but also more potently induced tumor cell ICD, which consequently elicited more robust DC maturation and anticancer CTL responses. Notably, the antitumor effect of NP-OXA was significantly diminished in immunodeficient nude mice, confirming the involvement of anticancer immune responses in tumor regression [88]. Similar results were observed in a study of DOX-conjugated chimeric polypeptides nanoparticles (CP-DOX), which more potently increased tumor-infiltrating T cells and inhibited tumor growth in BALB/c mice than free DOX did. However, $CD8^+$ T cell depletion dramatically attenuated antitumor effect of CP-DOX nanoparticles, further confirming the contribution of tumor-specific $CD8^+$ T cell responses in the anticancer effect of CP-Dox [128].

Zheng et al. load DOX into integrated mesoporous silica nanoparticles (IMSN) to generate DOX@HIMSNs theranostic system for imaging-guided therapy. Compared with free DOX and DOX@IMSN, DOX@HIMSN demonstrated superior anticancer effect due to its superior tumor-targeting ability. Moreover, DOX@HIMSN significantly induced DC maturation and proinflammatory cytokine release (TNF, IFN, IL-6), evoking robust antitumor CTL responses in tumors [129].

4.3.1.4 Radiotherapy-Triggered Immunogenic Antigen Release

Radiotherapy was initially designed to selectively kill tumor cells in the irradiated field. However, emerging evidence indicates that radiotherapy can also activate immune system to eliminate tumor cells through inducing tumor cell ICD [130]. Unfortunately, the efficacy of radiotherapy is often limited by tumor radiation resistance. Nanotechnology holds a great potential to sensitize tumor cells to radiotherapy. Core–shell PLGA nanoparticles were loaded with catalase (Cat) in the core and R837 (a TLR 7/8 agonist) in the shell to obtain PLGA-R837@Cat nanoparticles. Cat can degrade H_2O_2 to generate O_2, which significantly alleviated hypoxia in tumor microenvironment, whereas R837 was incorporated to overcome tumor-derived immunosuppression. The administration of PLGA-R837@Cat nanoparticles significantly enhanced radiotherapy-induced tumor ICD, thereby effectively improving the antitumor efficacy of radiotherapy [131]. Lu et al. developed a hybrid nanoscale metal-organic framework (nMOF) using Hf clusters, an X-ray scintillator, and porphyrin photosensitizer, which would enable radiotherapy–radiodynamic therapy (RT–RDT) with low-dose X-rays. The results showed that low-dose X-ray irradiation did not inhibit tumor growth, while the combination of low-dose X-rays with nMOF not only completely eliminated tumors but also triggered tumor cell ICD and systemic antitumor immune responses, thereby leading to effective tumor ablation [132].

4.3.1.5 Oncolytic Virus-Triggered Immunogenic Antigen Release

Oncolytic virus (OV) therapy is another promising approach that not only directly destroys tumor cells but also triggers immunogenic tumor antigen release, eliciting systemic antitumor immunity. However, the therapeutic efficacy of OV is still limited due to in vivo antiviral immune responses and poor tumor penetration [6]. To avoid the recognition and rapid clearance by the immune system, OV has to be administrated through intratumoral injection, which is not feasible for metastatic cancer patients. Moreover, the therapeutic efficacy of OVA could also be dampened by its poor tumor retention, impersistent viral infectivity in situ, and nonspecific virion shedding into normal tissue, and so on [133].

Nanotechnology has been reported to enhance the potency of OV through enhancing tumor-specific virus infection and cytotoxicity, blocking neutralizing antibody binding [134], prolonging circulation time, and reducing potential toxicity in livers and other normal tissues [38, 135]. For example, virus coating with cationic

nanomaterials (e.g., PEI and PEI-based copolymers) effectively enhances the internalization, transduction efficacy, and tumor lysis effect of oncolytic adenovirus (Ad) [133]. Coating Ad with poly(amidoamine) (PAMAM) dendrimers not only protected virus from neutralizing antibodies but also enhanced viral transduction efficacy in hepatoma cells both in vitro and vivo, improving the survival of tumor-bearing mice [135]. PEGylated PAMAM dendrimers with EGFR-specific antibody conjugation further enhanced Ad infection in EGFR-positive cancer cells (A549) rather than in EGFR-negative cancer cells (MCF-7) with more potent anticancer killing effect than naked Ad did. Furthermore, anti-EGFR antibody-conjugated dendrimers enhanced Ad virus accumulation in tumors, prolonged viral circulation time, while reducing the immunogenicity and toxicity of virus, thereby robustly inhibiting EGFR-positive orthotopic lung tumors [38].

Nanotechnology-based imaging guiding is another effective strategy to enhance the potency of OV. Oncolytic Ad virus was coated with PEGylated and crosslinked iron oxide nanoparticles (PCION) to generate Ad-PCION complexes. Upon exposure to a magnetic field, PCION dramatically enhanced viral transduction efficacy and anticancer killing in multiple cancer cell lines. Administration of Ad-PCION complexes selectively facilitated virus accumulation and replication in tumors and reduced virus burden in the liver, thereby effectively inhibiting tumor growth [136]. Another study conjugated PEGylated gold nanoparticles onto Ad virus to obtain Ad–gold–PEG complexes, which aimed to explore the effect of ultrasound-guided OV therapy. Compared with naked Ad virus, Ad–gold–PEG showed significantly reduced antibody binding and attenuated infectivity. However, the presence of ultrasound increased virus accumulation in tumors over 100-folds compared with naked Ad did, thereby leading to robust tumor regression [137].

4.3.2 Promoting Dendritic Cell-Targeted Immunotherapy with Nanomaterials (Step 2)

Dendritic cells (DCs) are the most potent APCs playing a central role in initiating and regulating antitumor immunity. DCs capture and process tumor antigens into short peptides, and then present them through MHC class I or II molecules to $CD8^+$ and $CD4^+$ T cells, eliciting anticancer adaptive immunity. In the meantime, DCs also secrete a variety of cytokines and chemokines to modulate T cell activation, CTL response, and memory cell differentiation. Hence, DCs are certainly the major target cell of cancer immunotherapy. DC-targeted immunotherapy includes in vitro DC targeting (so-called DC vaccines) and in vivo DC targeting using cancer vaccines. Increasing evidences have demonstrated nanotechnology as an effective strategy to boost DC-targeted immunotherapy through several aspects: (1) to enhance antigen uptake by DCs; (2) to enhance antigen presentation through MHC I molecule; (3) to directly stimulate DC maturation through a variety of receptors and downstream signaling pathways; (4) to improve the potency and safety of immunoadjuvants (Fig. 4.2).

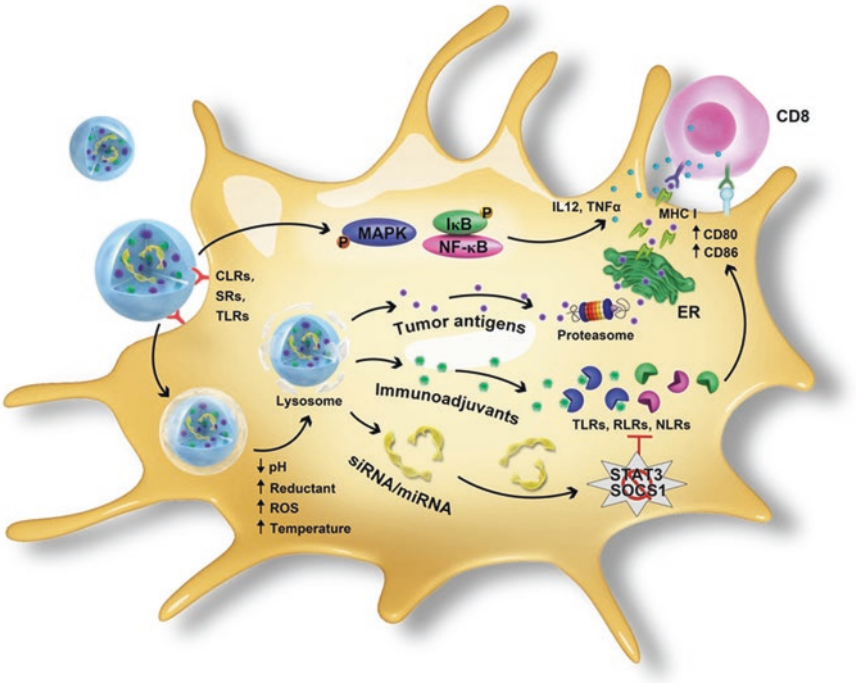

Fig. 4.2 Dendritic cell-targeted cancer immunotherapy with nanotechnology. Nanoparticles can boost DC-targeted immunotherapy through several aspects: (1) enhancing antigen uptake by DCs via surface receptors, such as C-type lectin receptors (CLR), Toll-like receptors (TLRs), scavenger receptors (SRs), etc.; (2) inducing DC maturation through stimulating multiple intracellular signaling pathways; (3) enhancing MHC class I antigen presentation through facilitating lysosomal escape; (4) enhancing the potency of immunoadjuvants through promoting their binding with corresponding receptors, such as TLRs, RIG-I-like receptors (RLRs), NOD-like receptors (NLRs); (5) silencing immunosuppressive factors (STAT3, SOCS1) through codelivering siRNA or miRNA

4.3.2.1 Nanomaterial-Based Cancer Vaccines

Nanomaterials for peptide vaccine delivery. Synthetic peptide vaccines containing single or multiple small fragments of tumor-derived antigen proteins are the major type of cancer vaccines; however their therapeutic efficacy is often limited due to the poor immunogenicity and rapid clearance.

Organic nanoparticles have been reported to improve the efficacy of peptide vaccines through controlling antigen releasing, facilitating antigen uptake and antigen presentation by DCs. For example, PLGA nanoparticles can effectively encapsulate both hydrophilic and hydrophobic antigen peptides and facilitate their uptake by DCs, thereby eliciting robust T cell responses and tumor regression [54, 138]. Liposomes can effectively load antigen peptides through encapsulation or chemical conjugation, enhancing the immunogenicity of peptide vaccines [9, 139, 140]. In addition to the organic nanovectors, inorganic nanoparticles are also developed for

peptide vaccine delivery. OVA peptide-conjugated Au NP (Au NP-OVA) robustly evoked OVA-specific T cell activation and tumor regression in mice [59]. The peptide loading capacity of hollow mesoporous silica nanoparticles (HMSNs) with large pore size could be significantly improved by NH_2 modification on the inner hollow core and COOH modification in the porous channels [141]. Phospholipid-enveloped zinc phosphate hybrid (LZnP NPs) demonstrated superior loading capacity of antigen peptides over 60–70% due to the specific interaction between $Zn2^+$ and protein molecules, which robustly facilitated the antigen uptake by DC both in vitro and in vivo [66].

Nanomaterials for nucleotide vaccine delivery. In addition to peptide vaccines, DNA and RNA vaccines have emerged as a practical and attractive approach for cancer immunotherapy. Compared with peptide vaccines, DNA and RNA vaccines are more easily engineered and produced in a large scale. However, the poor immunogenicity is a major hurdle limiting their clinical benefits, which could be attributable to inefficient uptake and presentation by APCs. Although RNA vaccines do not require genomic integration, which could be a benefit compared with DNA vaccine, their half-life is short due to the rapid degradation by ubiquitous RNAases [36, 142].

Synthetic nanoparticles, such as cationic liposomes, cationic polymers (e.g., PEI, PEI/PGA, chitosan), graphene and carbon nanotubes, as well as hybrid particles, are promising delivery platforms of nucleotide vaccines due to their ability of condensing DNA/RNA, preventing nuclease degradation, and promoting the cellular uptake and endosomal escape of nucleotides [76]. Cationic *B*ranched *A*mphiphilic *P*eptide *C*apsules (BAPCs) were shown to effectively condense DNA plasmid and facilitate gene expression in vitro. Moreover, BAPC-formulated DNA vaccine significantly induced DC maturation and tumor-specific $CD8^+$ T cell response, effectively inhibiting tumor growth [143]. Cationic DOTMA/DOPE liposome-encapsulated RNA vaccine (RNA-LPX) not only protected RNA from ribonuclease degradation but also effectively delivered RNA into splenic APCs (DC and macrophages) simply by adjusting net charge RNA-LPX around −30 mV. The immunization of RNA-LPX robustly induced tumor-specific T cell responses both in mice and in melanoma patients, indicating its great potential for boosting cancer immunotherapy [11]. Lipid nanoparticles (LNPs) consisting of an ionizable lipid, a PEGylated lipid, phospholipid, and cholesterol were developed for mRNA vaccine delivery. In an acidic condition, the ionizable lipid could be converted to be positively charged, which was not only essential for mRNA condensation but also could promote the cellular uptake and endosomal escape of mRNA vaccine. The s.c. injection of LNP-formulated mRNA vaccines successfully led to gene transfection in multiple immune cells, such as macrophages, dendritic cells, and neutrophils. A single dose of LNP/mRNA vaccines robustly evoked $CD8^+$ T cell activation and tumor regression with prolonged overall survival in mice [12].

In addition to synthetic nanoparticles, live attenuated bacteria are emerging as a novel vector to facilitate APC-targeted vaccine delivery due to their ability to colonize the gut-associated lymphoid tissue. However, the acidic environment in stomach often dampens bacteria colonization and vaccination efficacy. To overcome the acidic condition, salmonella (SAL) was coated with crosslinked

β-cyclodextrin-PEI_{600} encapsulated DNA nanocomplexes (NP) to generate NP/SAL, which aimed to improve the bacterial tolerance to acidic condition and enhanced bacterial infection of peritoneal macrophage. The results showed that the blood bacterial level of NP/SAL group was about 2–20-fold higher than that of SAL group 1–2 h after oral administration, indicating enhanced bacteria dissemination into blood circulation. Oral delivery of VEGFR2 DNA vaccines using NP/SAL elicited remarkable $CD8^+$ T cell activation and consequently inhibited tumor growth by angiogenesis suppression in tumor neovasculature. Hence coating live bacterial cells with synthetic nanoparticles represents a promising strategy to engineer efficient and versatile DNA vaccines for the era of immunotherapy [113].

4.3.2.2 Facilitating APC-Targeted Vaccine Delivery with Nanomaterials

To generate potent anticancer immune responses, tumor antigens must be effectively delivered to APCs (DCs and macrophages) for antigen process and presentation, which subsequently triggers downstream antitumor $CD4^+$ and $CD8^+$ T cell responses. The poor immunogenicity of vaccines is often due to the insufficient antigen uptake by APCs, thereby dampening the therapeutic efficacy of cancer vaccines. Hence, it is very necessary to enhance APC-targeted vaccine delivery in order to improve vaccination efficacy.

A variety of surface receptors on APCs, such as C-type lectin receptors (CLR), Toll-like receptors (TLRs), Fc receptors (FcR), and scavenger receptors (SRs), have been discovered to be responsible for antigen recognition, internalization, and APC activation [144]. Therefore, targeting these surface receptors could be a plausible strategy to enhance APC-targeted vaccine delivery. The family of CLRs, including mannose receptor (CD206), DEC-205(CD205), DC-SIGN (CD209), langerin (CD207), macrophage galactose-type C-type lectin (MGL, CD301), DCIR, and dectin-1/2, are the major endocytic receptors that can effectively bind to carbohydrates and facilitate antigen uptake [145]. DC-SIGN antibody-functionalized Au NPs not only effectively enhanced the cellular uptake by DCs but also induced DC activation through targeting DC-SIGN [146]. PLGA NPs were loaded with OVA and MPLA (a TLR4 agonist), and then functionalized with anti-CD205 to obtain DC-targeted nanovaccines. The results showed that the presence of anti-CD205 significantly enhanced vaccine uptake by DCs. Moreover, the functionalization of PLGA nanovaccines with anti-DCIR, anti-DEC205, anti-BDCA-2, anti-CD32 (FcR), or anti-DC-SIGN not only effectively facilitated vaccine uptake by myeloid DC and plasmacytoid DC (pDC) but also promoted DC maturation, thereby enhancing MHC I/II antigen presentation to $CD4^+$ and $CD8^+$ T cells [147, 148]. Chitosan-encapsulated tumor cell lysate nanoparticles (CTS-TCL NPs) were coated with mannose-modified alginate to obtain Man-CTS-TCL nanovaccines. The in vitro study showed that mannose moieties effectively promoted antigen uptake and presentation as well as DC maturation. Moreover, Man-CTS-TCL nanovaccines also demonstrated lymphatic-targeting ability through targeting mannose receptors,

thereby eliciting robust tumor-specific T cell responses and tumor regression [20]. Curdlan (Curd) and mannan (Man) are polysaccharides that can be recognized by Dectin-1 and 2 on DC and macrophages. Functionalization of liposomal vaccines with pH-sensitive Curd or Man not only significantly enhanced vaccine uptake by DCs via dectin-1 and scavenger receptors but also enhanced DC maturation. In vivo immunization of MGlu-Curd or MGlu-Man liposomal vaccines effectively induced tumor-specific T cell activation and CTL responses, thereby inhibiting tumor growth [149].

In addition to CLRs, other receptors are also involved in antigen capture and processing. Scavenger receptor class B1(SR-B1) is a natural HDL receptor selectively expressing on mature DCs but not on immature DCs. Alpha-helical peptide, a HDL-mimicking peptide, was linked to tumor antigen peptides to obtain α-Ap fusion protein, which were incorporated into ultra-small (~20 nm) core-shell lipid nanoparticles to generate DC-targeted nanovaccine (α-Ap-FNP). Upon injection, α-Ap-FNP effectively accumulated in LNs and enhanced the uptake of antigen peptide by DCs, especially mature DCs. Mature DC pulsed with α-Ap-FNP effectively induced T cell proliferation and tumor-specific CTL responses in vitro. Although the immunization of α-Ap-FNP moderately inhibited tumor growth in mice, further incorporation of CpG into α-Ap-FNP robustly inhibited tumor growth and prolonged the overall survival [150]. HSP70 is a protein chaperone that can bind and deliver unfolded protein or peptides into APCs. Hsp70-coated SPIONs effectively delivered antigen peptides into DCs through the endo/lysosomal pathway. Moreover, DCs co-treated with Hsp70-SPIONs and tumor cell lysates effectively induced tumor-specific T cell activation and CTL response, confirming the ability of Hsp70-SPIONs to chaperone tumor antigens into DCs [151].

The antigen uptake by DCs and macrophages can also be enhanced by fine tuning the surface chemistry (e.g., surface charge and hydrophobicity) of vaccine delivery systems. Positively charged nanoparticles were reported to more effectively enhance antigen uptake by DCs and macrophages than those with neutral or negative charge did [76], and could be positively correlated with their surface charge density [152]. Cationic liposome-formulated RNA vaccine complexes (RNA-LPX) were reported to primarily deliver RNA vaccine into the lung, whereas anionic RNA-LPX was primarily captured by splenic DC and macrophages after i.v. injection [11]. Fromen et al. observed that alveolar macrophages preferably captured anionic nanovaccines after pulmonary instillation. On the other hand, although lung DCs significantly captured both anionic and cationic nanovaccines, the cellular uptake of cationic nanovaccines was higher than that of anionic vaccines [153].

The hydrophobicity is another important factor affecting vaccine internalization by APCs. Compared with less hydrophobic polymeric microparticles (MPs), the MPs with higher hydrophobicity more effectively promoted antigen uptake by DCs [154]. Similarly, the uptake of amphiphilic γ-PGA-Phe formulated nanovaccines by DCs effect was positively correlated with their hydrophobicity [155]. Min et al. reported an improved cancer immunotherapy approach, which utilized antigen-capturing nanoparticles (AC-NPs) to capture and present in vivo tumor antigens to APCs. Herein, a series of PLGA AC-NPs with different physiochemical properties

were prepared in order to acquire tumor antigen capture ability. Among different AC-NPs, the unmodified PLGA AC-NPs most effectively bound to tumor proteins (e.g., neoantigens and DAMPs) through hydrophobic-hydrophobic interactions, whereas methoxy-PEG-coated PLGA AC-NPs showed minimal ability to bind proteins. Maleimide-modified AC-NPs (Mal AC-NPs) were observed to moderately bind to proteins through stable thioether bonds. Although AC-NPs coated with cationic phospholipid DOTAP (DOTAP AC-NPs) or amine PEG (NH_2 AC-NPs) both effectively bound to tumor proteins via electrostatic interactions, DOTAP AC-NP demonstrated more potent protein capture ability than NH_2 AC-NPs did. These results indicated that the protein capture ability of AC-NPs relied on their surface properties. The in vivo study showed that the unmodified PLGA AC-NPs and Mal AC-NPs both effectively delivered tumor proteins to DCs and macrophages in TDLNs, which subsequently improved the therapeutic efficacy of local radiotherapy combined with anti-PD-1 treatment [156].

Wrapping nanoparticles with cell membranes has been recently reported as a novel strategy for DC-targeted vaccine delivery. PLGA-encapsulated Staphylococcal toxoid wrapped with RBC membrane not only demonstrated superior LN-targeting ability but also effectively facilitated toxoid uptake by DCs [99]. In another study, antigen peptide ($hgp100_{25–33}$) conjugated-PLGA nanoparticles were coated with mannosylated RBC membrane to obtain Man-RBC-NP_{hpg} nanovaccine. Compared with naked PLGA NPs, Man-RBC-NP_{hpg} more effectively accumulated in draining LNs and facilitated antigen capture by DCs [100]. Tumor cell membranes, as a good source of tumor antigens, have been reported to facilitate DC-targeted vaccine delivery. Two studies generated cancer cell membrane-coated nanovaccines (NP@M), which consisted a core of PLGA nanoparticles loaded with TLR agonists (R837 or CpG) and a shell of tumor cell membrane. Compared with PLGA-encapsulated TLR nanoparticles (NP), NP@M more effectively facilitated vaccine uptake by DCs and induced DC maturation as well as proinflammatory cytokine production. More importantly, NP@M rather than NP alone robustly induced anticancer T cell responses, thereby leading to tumor regression [102, 103]. These data suggest the codelivery of antigen and immunoadjuvant using cancer cell membrane-coated NP can be a promising strategy for enhancing cancer vaccine efficacy.

4.3.2.3 Promoting Antigen Cross-Presentation with Nanomaterials

Tumor antigen presentation by MHC class I molecules on APCs and tumor cells is the most critical step to trigger $CD8^+$ T cell activation and elicit anticancer cytotoxic T lymphocyte (CTL) responses. Typically, MHC I is responsible for presenting endogenous antigens to $CD8^+$ T cells, whereas extracellular antigens (protein and peptide antigens) are primarily presented by MHC class II for $CD4^+$ T cell activation. To enhance the anticancer effect of vaccines, protein and peptides must be transported from endo/lysosomes into the cytosol, enabling proteasome-mediated degradation into short peptides. The resulted peptides are then transported into ERs

or early endosomes for MHC class I presentation (so-called cross-presentation) [157, 158].

Nanomaterials have been demonstrated as a promising strategy to enhance the cross-presentation of protein and peptide antigens through multiple mechanisms. For example, Poly (γ-glutamic acid)-based nanoparticles (γ-PGA NPs) enhanced antigen cross-presentation and evoked robust antitumor immunity, which involved the participant of cytoplasmic proteasomes and TAP. γ-PGA also triggers ER-endosome fusion, facilitating antigen transportation into the cytoplasm [159]. Cationic liposome-induced cross-presentation was related with elevated lysosomal pH, which subsequently limited lysosomal degradation of antigen, thereby enhancing cross-presentation and $CD8^+$ T cell responses [16].

Stimuli-responsive nanoparticles can be designed to facilitate the lysosome escape of antigens, thereby being considered as an effective approach to enhance MHC I antigen presentation. The pH-responsive nanoparticles can be dissociated in the acidic endo/lysosome compartment, which subsequently caused lysosome rupture and induced antigen escape from lysosomes [19, 49, 87, 160]. The pH-sensitive OVA-alginate (ALG) conjugates (ALG = OVA) and mannosylated alginate (MAN-ALG) were crosslinked to generate DC-targeted pH-sensitive nanovaccines, which effectively promoted cytosolic release of OVA and augmented MCH class I antigen presentation, evoking robust $CD8^+$ T cell responses against tumor [160]. The pH-responsive PLGA NPs containing ammonium bicarbonate (NH_4HCO_3) were developed for OVA vaccine delivery. In acidic endo/lysosomes, NH_4HCO_3 reacted with H^+ to generate NH_3 and CO_2, which effectively facilitated lysosome escape and cross-presentation of OVA [19]. A pH-responsive endosomolytic metal-organic framework (MOF) consisting of lanthanide ions (Eu^{3+}) and guanine monophosphate (GMP) was developed for vaccine delivery. In the acidic endo/lysosome, the Eu^{3+} and GMP were dissociated, which promoted antigen releasing from MOFs and antigen transportation into the cytosol, thereby enhancing the cross-presentation [87]. Our group developed bioreducible alginate-polyethylenimine nanogels (AP-SS) for vaccine delivery. Upon internalization, AP-SS nanogels were quickly disassembled, which accelerated cytosolic antigen releasing and degradation, and enhanced both MHC class I and II antigen presentation, thereby leading to robust antitumor CTL responses [48]. A recent study conjugated Au NPs with hyaluronic acid (HA) and OVA to generate NIR-responsive nanovaccines. The results showed that PTT-caused local heat triggered endo/lysosome disruption and cytosolic antigen release, which consequently enhanced cross-presentation and evoked anticancer CTL upon laser irradiation [161].

Reactive oxygen species (ROS), the by-products of intracellular oxidative phosphorylation, not only act as a "danger" signal to induce DC maturation but also play a critical role in antigen cross-presentation. ROS-caused oxidative damage could induce ubiquitination and degradation of antigen peptides by immunoproteasomes, providing sufficient peptide supply for MHC class I antigen presentation [162]. Hence, elevating ROS could be a potential strategy to enhance antigen cross-presentation. Our group developed a pH-responsive galactosyl dextran-retinal (GDR) nanogel for cancer vaccine delivery. The results showed that GDR nanogel

effectively triggered lysosomal rupture and promoted cytosolic antigen release, significantly enhancing MHC I antigen presentation. More interestingly, GDR-triggered lysosomal rupture also induced ROS production, which was shown to contribute to enhanced proteasome activity and downstream MHC I antigen presentation [49]. Biodegradable glutathione (GSH)-depletion dendritic mesoporous organosilica nanoparticles (GDMON) incorporated with tetra-sulfide bonds were generated for cancer vaccine delivery. The results showed that GDMON effectively codelivered OVA and CpG into draining LNs. More importantly, GDMON depleted intracellular GSH through the -S-S-/GSH redox chemistry and significantly elevated ROS in LNs, resulting in robust antitumor CTL responses and tumor regression [163].

Modification with membrane-fusogenic peptides, such as octaarginine (R8) and KALA peptide, is another effective strategy to facilitate lysosome escape and cross-presentation of antigens. Octaarginine-modified liposome (R8-Lip) significantly enhanced cellular uptake, endosomal escape, and cross-presentation of OVA. Moreover, R8-Lip enhanced the C-terminal cleavage of antigen-derived peptides essential for MHC class I antigen presentation [36]. KALA peptide is an amphiphilic peptide that has an α-helical structure at physiological pH, but converts to random coil for membrane destabilization. A recent study reported that KALA-modified liposomes (KALA-LPs) also significantly enhanced MHC class I antigen presentation in DCs. The in vivo study showed that OVA-loaded KALA-LPs elicited OVA-specific CTL response and antitumor effect more potently R8-LPs did [10].

Targeting different receptors on APCs could trigger different antigen internalization routes, and direct antigens into different endo-lysosomal compartments for antigen processing and presentation. For example, the pinocytosis or scavenger receptor-mediated endocytosis were reported to rapidly direct antigens towards lysosomal compartments, leading to poor cross-presentation. In contrast, antigen internalization through MR and CD40 could direct antigens into early endosomes and avoided rapid lysosome degradation, thereby enhancing cross-presentation [157]. Liposomes were modified with DC-SIGN-binding glycans Lewis (Le)(B) or Le(X) for DC-targeted vaccine delivery. The results showed that glycan modification effectively increased liposomes binding and uptake by BMDCs expressing human DC-SIGN. Moreover, glycan-liposomes rather than unmodified liposomes significantly enhanced the cross-presentation of OVA and MART-1 antigen presentation, eliciting antigen-specific $CD8^+$ T cell response [164].

Autophagy is a self-degradative process involving lysosomal degradation of damaged cellular components and recycling of different cytoplasmic components. Increasing evidences have revealed the crucial role of autophagy in MCH I/II antigen presenting machinery. In APCs, the autophagosome-lysosome fusion allows the access of endogenous antigens to the MHC II molecules, triggering $CD4^+$ T cell activation. On the other hand, autophagy also contributes to the cross-presentation of soluble antigen. An α-Al_2O_3 nanoparticle was conjugated with OVA protein to generate α-Al_2O_3-OVA nanovaccines. The in vitro study showed that α-Al_2O_3-OVA effectively enhanced cross-presentation of OVA by DCs, which consequently

triggered OVA-specific $CD8^+$ T cell activation and effectively inhibited tumor growth in mice. More interestingly, upon internalization by DCs, α-Al_2O_3-OVA were primarily localized in autophagosomes rather than in the endo/lysosome compartment, indicating nanovaccine-induced autophagy in DCs. Blocking autophagy of DCs significantly abolished the cross-presentation of α-Al_2O_3-OVA but not soluble OVA. These results demonstrated the essential role of autophagy in the enhanced cross-presentation of OVA by α-Al_2O_3-OVA nanovaccines [165]. Wang et al. prepared OVA-doped hierarchical $CaCO_3$ nanoparticles (OVA@NP) for vaccine delivery. In the lysosomes, $CaCO_3$ reacted with acid and generated large amounts of CO_2 to disrupt lysosomes, facilitating OVA release and lysosomal escape into the cytosol for MCH I presentation. In the meantime, the lysosome rupture and CO_2 release triggered autophagosome formation through the LC3/Beclin-1 pathways, which also contributed to MCH I antigen presentation. Immunization of OVA@NP effectively elicited $CD8^+$ T cell proliferation, antitumor CTL responses, and tumor regression [166]. Umlauf et al. developed PEGylated stealth liposome vaccine with a MHC I epitope from measles (H250) encapsulated inside and a cancer-specific targeting peptide (H1299.3) displayed on its surface. The goal of this design was to enhance MHC I presentation of H250 in tumor cells in order to facilitate tumor recognition and killing by T cells. The results showed that liposomes vaccines successfully enhanced the MHC I presentation of H250 antigen in lung cancer cells, which consequently induced $CD8^+$ T cell activation and resulting tumor regression. The enhanced MHC I presentation required the presence of H1299.3 peptide and relied on autophagy. The perturbation of autophagy significantly dampened H1299.3 facilitated MHC I presentation of H250 [167].

4.3.2.4 Intrinsic Immunostimulatory Effect of Nanomaterials

A variety of organic nanomaterials, such as liposomes [152], chitosan [24], poly(beta-amino esters)(PBAE) [168], polypeptide micelles [32], and inorganic nanoparticles, such as gold nanoparticle (Au NPs) [169], carbon nanotubes [78], and silica NPs [63, 170], have been reported to stimulate innate and adaptive immunity directly. The intrinsic immunogenicity of nanomaterials is primarily related with their morphology (size, shape) and surface features (charge, hydrophobicity, surface functionality).

The size and shape of nanoparticles not only affect their cellular uptake, trafficking, in vitro bio-distribution, and targeting ability but also affect their intrinsic immunogenicity [171]. The cellular uptake of gold nanoclusters (Au NCs) with smaller size (<3 nm) by DCs was 300–400-folds higher than that of Au NPs with larger size (>12 nm) [169]. The intermediate chitin (IC, 40–70 μm) and small chitin (SC, 2–10 μm) rather than the big chitin (BC, 70–100 μm) or super small chitin (SSC, <2 μm) significantly induced TNF production by mouse macrophages through activating NF-κB and tyrosine kinase (syk) signaling pathways [172]. Spherical and rod-shaped polystyrene particles were conjugated with OVA antigen for vaccine delivery. Despite different shapes, the smaller particles more effectively enhanced

the production of OVA-specific antibodies and IFN γ, a Th1 signature cytokine, than the larger particles did. For smaller particles, the spheres induced higher OVA-specific IgG, IgG1, and IgG2a than the rods did. However, for larger particles, the rods induced higher levels of IgG and IgG1 than spheres did [173]. Hence, the size and shape could modulate the immunogenicity of nanoparticles.

The surface charge of nanoparticles is an important physiochemical property not only contributing to the stability, the cellular uptake, cytotoxicity, and biodistribution of nanoparticles but also contributing to their intrinsic immunogenicity [17]. The positive charge rather than negative charge has been reported to significantly enhance the intrinsic immunogenicity of nanoparticles. The i.v. injection of cationic liposomes robustly elevated mRNA expression of proinflammatory cytokines, such as IL-2, IL-6, IL-17, IFN, TNF, as well as IFN responsive genes about 15–75-fold higher than neutral and anionic liposomes did, which involved TLR4 signaling [174]. Moreover, the cationic liposomes with higher charge density more effectively enhanced DC maturation, OVA-specific antibody response, and IFN-γ production than those with lower charge density did [152]. Although anionic and cationic charged nanoparticles both entered into the draining lymph nodes and were captured by alveolar macrophages and lung DCs after pulmonary instillation, only cationic nanoparticles significantly induced CCL2 and CXC10, thereby recruiting CD11b DCs to lung tissues [153]. In addition to direct stimulation of the immune system, the positive surface charge also prolonged the retention of nanovaccine at the site of injection, which subsequently promoted monocyte infiltration into the vaccination site and enhanced vaccine-induced Th1 immune response [175].

The hydrophobic moieties may serve as danger signals stimulating innate and adaptive immunity. Moyano et al. modified gold nanoparticles (Au NP) with different functional groups to obtain a series of Au NPs with uniform structure but different hydrophobicity. The in vitro study showed a positive correlation between the hydrophobicity of Au NP and TNF production in splenocytes [176]. Another study investigated the relationship between hydrophobicity and intrinsic immunostimulatory effects using three types of PLA microparticles (MPs), which had similar size and structure but different hydrophobicity. Compared with MPs with lower hydrophobicity, MPs with higher hydrophobicity more potently enhanced antigen uptake and promoted DC maturation, which could be attributable to MP hydrophobicity-caused stronger interaction force between MPs and cell membranes. The in vivo study showed that increased MP hydrophobicity significantly enhanced LN-targeting ability of MP vaccines and augmented MP vaccine-induced T cell responses but not antibody responses [154]. Shima et al. showed that the hydrophobicity of γ-PGA-Phe nanoparticles was positively correlated with their ability of facilitating DC-targeted antigen, promoting DC maturation, and eliciting T cell responses [155]. Kakizawa et al. coated monodisperse silica NPs with different poly(amino acid)s (PAAs) to obtain delivery platform for vaccine and immunoadjuvants. Regarding the anionic PAA-Si NPs, the induction of IL-1β in vitro and OVA-specific IFN-γ in vivo was both positively correlated with the hydrophobicity of NPs [177]. These results suggest that increasing the hydrophobicity of nanoparticles could be an effective strategy to augment their immunogenicity.

Surface chemical moieties have been reported to participate in the cellular uptake and immunomodulatory effect of nanoparticles. Gold nanoclusters (Au NCs) functionalized with zwitterionic ligands robustly induced DC maturation and cytokine production, whereas the PEGylation dramatically attenuated Au NC-triggered DC maturation and T cell activation [169]. Our group investigated the effect of PEGylation and its terminal functional groups (–COOH, $–NH_2$, –OH, and –OCH3) on the proinflammatory property of polymer-coated CdSe/ZnS QDs (pQDs). Among four PEGylated pQDs, COOH-PEG-pQDs elicited highest levels of proinflammatory cytokines in macrophages through activating scavenger receptor/lipid raft/NF-kB pathway, whereas NH_2-PEG-pQDs and HO-PEG-pQDs moderately induced cytokine production through MAPK/p38 signaling cascades [178]. Thermally oxidized porous silicon (PSi) (TOPSi) and thermally hydrocarbonized PSi (THCPSi) NPs were reported to induce DC maturation and enhance Th1/Th2 cytokines. However, thermally carbonized PSi (TCPSi) and (3-aminopropyl) triethoxysilane-functionalized TCPSi (APSTCPSi) NPs failed to activate DC and T cells [170]. Lee et al. prepared radionuclide-embedded gold nanoparticles (Poly-Y-RIe-AuNPs) using oligotyrosine-modified AuNPs with additional Au shell for in vivo monitoring of DC migration. The in vitro results showed that Poly-Y-RIe-AuNPs significantly induced DC Maturation. Moreover, the immunization of Poly-Y-RIe-AuNPs-labeled DCs without antigen pulsing effectively elevated TNF and IL-6 both in the spleen and TDLNs and elicited antitumor CTL responses, thereby inhibiting tumor growth [179].

Although the molecular mechanism remains unclear, the immunogenicity of nanomaterials appears to involve the participant of multiple surface receptors and signaling pathways. TLR4 was involved in DC maturation induced by cationic lipid-like material (lipidoids) and DiC14-amidine cationic liposomes [180, 181]. Cationic DOTAP liposome-induced DC maturation was mediated by ERK and p38 signaling pathways and required optimal amount of ROS production [152, 182]. Chitosan-induced DC maturation and type I IFN productions relied on the cytoplasmic DNA sensor cGAS and STING [24]. Poly(beta-amino esters)-induced macrophage activation relied on IRF signaling rather than NF-κB or TLR3/7/9 signaling pathways [168]. Single-walled CNTs (SWCNTs) induced chemokine productions in human monocyte-derived macrophages through targeting activating the TLR4/MyD88/NF-κB pathway [78]. The varied proinflammatory effects of PEG-pQDs relied on lipid raft- and/or SRA-mediated endocytosis, which sequentially triggered downstream NF-kB and MAPK signaling cascades for proinflammatory cytokine production [178]. Gadolinium endohedral metallofullerenols ($Gd@C_{82}(OH)_{22}$) significantly induced IL-1β in mouse macrophages through activating NLRP3 inflammasomes, $P2X_7$ receptor activation and potassium efflux. Moreover, the TLR4/MyD88 pathway rather than TLR2 also mediated $Gd@C_{82}(OH)_{22}$-induced IL-1β secretion [183]. Cationic and anionic cellulose nanocrystals (CNCs) both induced IL-1β secretion in macrophages through activating NLRP3 inflammasomes [184]. Recent studies have revealed the critical role of autophagy in the immunogenicity of nanoparticles. Superparamagnetic iron oxide nanoparticles (SPIONs) interacted with TLR4 on macrophages, which

subsequently induced proinflammatory cytokine production and autophagy in macrophages [185]. Another study demonstrated an essential role of autophagy in DC maturation induced by lactosylated N-Alkyl polyethylenimine-coated SPIO (N-Alkyl-PEI2k-LAC/SPIO) [186].

4.3.2.5 Enhancing the Potency of Immunoadjuvants with Nanomaterials

Immunoadjuvants are the key component of cancer vaccines and responsible for enhancing the magnitude, breadth, and longevity of antitumor immune responses. Although oil in water emulsions and alum have successfully improved the effectiveness of prophylactic vaccines against certain pathogens, their effect on cancer vaccines remains unsatisfied. In the past decades, a variety of immunostimulatory compounds targeting pattern recognition receptors (PRRs) of the innate immunity, such as Toll-like receptors (TLRs), NOD-Like receptors (NLRs), RIG-I-Like receptors (RLRs), and the stimulator of IFN genes (STING), have been reported as promising adjuvant candidates for cancer vaccine development due to their superior ability to induce cellular immune responses. However, these PRR ligands may trigger multiple signaling pathways and influence various cell types, leading to systemic immunotoxicity [158]. Nanomaterial-based delivery system has been demonstrated as a promising approach that could not only facilitate DC-targeted immunoadjuvant delivery and strengthen their downstream signaling transduction but also reduce the systemic immunotoxicity, thereby improving the potency and safety of immunoadjuvant.

TLR3. Poly I:C, a synthetic double strand RNA and agonist of endosomal TLR3, is a potent immunoadjuvant to induce tumor-specific CTL and NK/NKT cell responses against tumors [187]. Poly I:C can be effectively encapsulated or absorbed by cationic nanoparticles through the electrostatic interaction, which subsequently facilitate the cellular uptake by DCs. Poly I:C-loaded DOTAP liposomes not only enhanced the cellular uptake of Poly I:C by BMDCs but also promoted the colocalization of Poly I:C with TLR3, thereby robustly eliciting CTL response and NK cell activation to inhibit tumor growth [188]. OVA and Poly I:C were coencapsulated with cationic PEG-PLL-PLLeu polypeptide micelles to generate polypeptide micelle-Poly I:C (PMP) nanovaccines, which induced OVA-specific CTL response more potently than soluble Poly I:C + OVA did [32]. Antigen peptide and Poly I:C can also be layer-by-layer (LbL) assembled on gold nanoparticles through electrostatic interactions to generate immune-polyelectrolyte multilayer (iPEM) for vaccine delivery. The iPEM-coated gold nanoparticles (iPEM-AuNPs) were effectively captured by dendritic cells (DCs) and robustly induced DC maturation through TLR3 signaling, and promoted MHC I antigen presentation. Immunization of iPEM-AuNP not only effectively induced antigen-specific $CD8^+$ T activation but also evoked a more potent recall response with antigen-specific $CD8^+$ T cells than soluble peptide+PIC did [89].

TLR4. Monophosphoryl lipid A (MPLA), a nontoxic derivative of LPS, is the only TLR4 agonist approved for human application [187]. Due to the amphiphilic

structure, MPLA can be incorporated into the hydrophobic compartment of nanoparticles. For example, phospholipid-enveloped ZnP hybrid nanoparticles (LZnP NPs) were loaded with multiple antigen peptides and MPLA to generate LZnP/HTM nanovaccines. Compared with LZnP vaccine, LZnP/HTM with MPLA incorporation more effectively induced DC maturation and cytokine production, robustly evoking T cell responses against tumors [66]. Antigen peptide-loaded hollow mesoporous silica nanoparticles (HMSNs) were coated with MPLA-entrapped lipid bilayer to obtain HTM@HMLB nanovaccines, which effectively induced DC maturation and tumor-specific $CD8^+$ and $CD4^+$ T cell activation, inhibiting tumor growth and metastasis with good safety profiles [141].

TLR7/8. Imidazoquinoline derivatives, such as resiquimod (R848), imiquimod (R837), and CL075, are synthetic agonist of endosomal TLR7 [187]. R837-loaded PLGA nanoparticles were coated by mannosylated cancer cell membranes to obtain NP-R@M-M nanovaccines, which were effectively internalized by DCs and stimulated DC maturation, thereby eliciting antitumor immune responses and inhibiting tumor growth [103]. Peritumoral administration of nanoparticle-conjugated R837 induced DC activation in draining LNs and evoked antigen-specific $CD8^+$ T cell proliferation without inducing systemic type I IFN production, indicating great efficacy and biosafety of nanoparticle-based localized immunotherapy [189]. Gold nanoparticles were coated with the mixture of 1-octanethiol and 11-mercaptoundecane sulfonic acid to obtain pH-sensitive amphiphilic nanoparticles (AmpNPs) for R848 delivery. The results showed that R848 could be effectively loaded in the hydrophobic pockets of AmpNPs without further chemical modification. Moreover R848-AmpNPs could quickly release R848 at an acidic condition (pH 5.5) due to the protonation of amine groups, while retaining particle stability and minimal drug release at pH 7.2 despite the presence of serum. Compared with R848 alone, R848-AmpNPs elicited more robust antitumor T cell responses, leading to more significant tumor regression [190].

TLR9. CpG oligonucleotides (ODNs), the agonist of endosomal TLR9, are synthetic short single-stranded DNA molecules containing unmethylated CpG motifs [187]. Multi-walled carbon nanotubes (MWNTs) were loaded with the conjugation of OVA and CpG (OVA-CpG) to obtain OVA-CpG/MWNT vaccines. Compared with soluble OVA+CpG, OVA-CpG/MWNT more effectively induced BMDC maturation and MHC class I/II antigen presentation, robustly evoking OVA-specific antibody production and CTL responses [77]. Concatemer CpG analogs and magnesium pyrophosphate (Mg_2PPi) were co-precipitated to form DNA-inorganic hybrid nanovaccines (hNVs). Although hNVs and free CpG both effectively induced DC maturation and macrophage activation, hNVs significantly prolonged tumor retention of CpG analogs, thereby leading to robust tumor regression and reduced systemic immunotoxicity of CpG [191]. Magnetite-filled PEGylated phospholipid micelles (IONP micelles) loaded with OVA antigen or CpG ODNs not only facilitated the co-localization of the endo/lysosomal compartment with CpG and OVA but also enhanced CpG-induced DC maturation and IL-6/TNF production. Compared with free CpG ODNs, CpG-IONP more effectively induced DC maturation and NK cell activation in the spleen and LNs without eliciting systemic IL-6

production. These results indicated enhanced immunogenicity and diminished systemic immunotoxicity of CpG, which should be due to the LN-targeted delivery by IONP micelles [192]. A recent study conjugated immunogenically dying tumor cells with CpG-loaded multilamellar lipid-polymer nanodepots (CpG-NPs) to obtain CpG-loaded whole tumor cell vaccines, which elicited robust antigen-specific $CD8^+$ T cells and tumor regression [193].

STING. The *c*yclic *G*MP-*A*MP *s*ynthase (cGAS)-stimulator of *in*terferon *g*ene (STING) pathway has been recently identified as an important PRR for sensing cytosolic dsDNA. First, cGAS binds to cytosolic dsDNA and catalyzes the formation of cyclic GMP-AMP (cGAMP), a cyclic dinucleotide (CDN). Next, cGAMP activates STING, an endoplasmic reticulum-resident adaptor molecule, triggering the TBK1–IRF3 and NF-κB pathways to induce type I IFN production. Hence, the cGAS-STING pathway can be an ideal target for boosting cancer immunotherapy [194]. However, it remains a challenge to effectively deliver cGAS-STING agonist into the cytosol. Wilson et al. mixed anionic cGAMP, a STING agonist, with cationic poly(beta-amino ester) (PBAE) polymers to generate PBAE/CDN nanoparticles, which not only facilitated the internalization of CNDs by macrophages but also enhanced CND-triggered IRF3 activation with the dosage of 100-fold less than that of free CNDs did [195]. More recent study encapsulated cGAMP with endosomolytic polymersomes with pH-responsive and membrane-destabilizing activity, which aimed to facilitate intracellular release and endosomal escape of cGAMP. The results showed that polymersomes-encapsulated cGAMP (STING-NPs) significantly enhanced cellular uptake and immunopotency of cGAMP. Compared with free cGAMP, the injection of STING-NPs more effectively ameliorated immunosuppressive TME and enhanced T cell tumor infiltration and activation, thereby robustly inhibiting tumor growth and metastasis [196].

RIG-I. Retinoic acid-inducible gene I (RIG-I)-like receptors (RLRs) are a class of cytosolic PRRs that detect double-stranded RNA (dsRNA) and single-stranded RNA (ssRNA) with a triphosphate group at the 5′ end, triggering downstream production of type I interferons and other proinflammatory cytokines. Despite the potent immunostimulatory potential, RLR-targeted therapy could be a challenge due to RNA degradation, poor cellular uptake, and minimal access to cytosolic RLRs as well as potential immunotoxicity. A pH-responsive, endosomolytic polymer nanoparticle was developed to deliver short double-stranded RNA with 5′ triphosphate (NP/3pRNA), a ligand of RLR. These nanoparticles were composed of amphiphilic diblock copolymers with dimethylaminoethyl methacrylate (DMAEMA), a cationic segment for RNA condensation, and terpolymer block of DMAEMA, butyl methacrylate (BMA), and propylacrylic acid (PAA), an endosome-destabilizing segment to enhance the cytosolic delivery of RNA with a cationic first block for facile electrostatic complexation and protection of nucleic acid cargo, and an endosome-destabilizing terpolymer block comprising DMAEMA, butyl methacrylate (BMA), and propylacrylic acid (PAA) act cooperatively to mediate efficient cytosolic delivery. The in vitro study showed that NP/3pRNA significantly induced the activation of APCs (DC and macrophages) and triggered the production of type I IFNs and proinflammatory cytokines/chemokines, both of which were essential

for eliciting antitumor immune responses. On the other hand, NP/3pRNA also effectively upregulated RIG-I expression, induced production of type I IFNs, and activated downstream STAT1 and IRF3 signaling pathways in multiple tumor cell lines. The activation of RIG-I pathway in tumor cells subsequently led to tumor cell ICD, thereby enhancing $CD8^+$ T cell activation and tumoral infiltration. The intratumoral (IT) injection of NP/3pRNA not only inhibited tumor growth but also significantly enhanced the therapeutic efficacy of anti-PD-1 [197]. Das et al. designed a dual-functional ppp dsRNA, which could not only silence Bcl-2 gene to induce tumor apoptosis but also activate RLRs to evoke antitumor immune responses. After i.v. injection, lipid calcium phosphate nanoparticles (LCP-AEAA)–encapsulated ppp dsRNA rather than free ppp dsRNA significantly decreased Bcl-2 expression and suppressed tumor growth through inducing cell apoptosis. More importantly, LCP-AEAA–encapsulated ppp dsRNA effectively induced tumor-specific T cell activation and ameliorated immunosuppression through decreasing M2 macrophages, B regulatory cells, and plasma cells in tumor microenvironment, both of which further contributed to tumor regression [198].

4.3.3 Lymph Node-Targeted Cancer Immunotherapy with Nanomaterials (Step 3)

The lymphatic system consists of lymphatic organs (e.g., spleens, lymph nodes, tonsils, Peyer's patches) and lymphatic vessel network, playing a central role in transporting exogenous/endogenous antigens and immune cells from peripheral tissues into lymphoid organs [199, 200]. Lymph nodes (LNs) are major lymphoid organs for trapping lymph-borne antigens from peripheral tissues and generating adaptive immunity, thereby being considered as a critical target organ for cancer immunotherapy. Compared with peripheral DC-targeted vaccine, LN-targeted vaccine delivery can accelerate the generation of antigen-specific immune responses, which could be due to the quick LN drainage and cellular uptake of antigens by APCs [199–201]. Moreover, the lymphatic targeted delivery of immunostimulators, such as TLR agonists and cytokines, also effectively enhances antitumor immune responses through selectively modulating the microenvironment in LNs without causing systemic immunotoxicity [192, 202], thereby enhancing the potency and biosafety of immunostimulatory compounds.

Appropriate particle size is critical for LN-targeted drug delivery. Particle sizes between 10 and 100 nm are more effective than the larger size (>100 nm) for lymphatic transfer due to the size limitation of the lymphatic interstitium (~100 nm). On the other hand, the smaller particles (<10 nm) are primarily absorbed via the blood capillaries [203]. Amine group-modified poly(γ-glutamic acid) (γ-PGA-CH-NH_2) were mixed with OVA antigen or poly I:C to obtain SVNP-OVA nanovaccine and SVNP-IC nanoadjuvant, respectively. The sizes of SVNP-OVA and SVNP-IC were around 20–70 nm, which allowed them to effectively drain into LNs and be captured

by lymphatic APCs (macrophages and DCs), thereby leading to robust antitumor T cell responses and tumor regression [202]. Phospholipid-enveloped zinc phosphate hybrid nanoparticles (LZnP NPs) were loaded with multiple antigen peptides and MPLA to generate LZnP/HTM nanovaccines, which demonstrated superior LN-targeting ability due to their appropriate particle size (~30 nm) [66]. PEGylated phospholipid-coated magnetite micelles (IONP micelles) were loaded with CpG to generate CpG-IONP with the size around 40 nm. Compared with free CpG, CpG-IONP more effectively accumulated in LNs, thereby inducing DC maturation and NK cell activation in spleens and LNs without eliciting systemic cytokine storm [192]. Amphiphilic polymer-coated gold nanoparticles were loaded with R848, a TLR7 ligand to generate R848-AmpNPs, which were negatively charged with the hydrodynamic size around 5 nm. Upon s.c. injection, R848-AmpNPs primarily accumulated in ipsilateral draining LNs but were barely detected in contralateral LNs and in the spleen. Moreover, R848-AmpNPs selectively induced cytokine production in ipsilateral draining LNs, whereas free R848 significantly induced cytokine production in both ipsilateral and contralateral LNs. Although R848 and R848-AmpNPs equally induced DC maturation and cytokine production in vitro, R848-AmpNPs inhibited tumor growth more effectively than free R848 did. These results showed that the LN-targeted delivery of vaccines and immunoadjuvants with nanoparticles not only avoided severe systemic immunotoxicity but also significantly enhanced their antitumor effect [190].

Surface charge certainly plays a critical role in modulating LN-targeting ability of nanoparticles [204]. Positive charge was previously considered as a negative factor to diminish LN-targeting ability of nanoparticles. Cationic nanoparticles were shown to be trapped by negatively charged extracellular matrix around the injection sites, whereas the anionic and neutral NPs drain into LNs from injection sites more effectively [205]. However, a recent study showed positive charge as a double-edged sword for LN-targeted drug delivery. Polymeric hybrid micelles (PHMs) with varied proportions of polycaprolactone-polyethylenimine (PCL-PEI) and polycaprolactone-polyethyleneglycol (PCL-PEG) were prepared for LN-targeted codelivery of tumor antigen and vaccine adjuvant (CpG). The results showed that the appropriate amount of cationic PCL-PEI (10%) was essential for vaccine accumulation in LNs. When PCL-PEI was less than 10%, PHM/CpG nanovaccines quickly dispersed throughout the body, which could potentially cause systemic immunotoxicity. On the other hand, high proportions of cationic PCL-PEI (25–50%) caused nanovaccine entrapment at the injection site, thereby dampening their antitumor effect [26]. PEGylation was reported as another strategy to enhance LN targeting of cationic liposomes through reducing nonspecific binding by extracellular matrix. Incorporating 1 mol% of DSPE-PEG_{2000} into OVA-loaded DOTAP vaccines (DOTAP-1%PEG) not only accelerated liposomal drainage into draining LNs with a few minutes but also enhanced liposome uptake by APCs, thereby accelerating primary OVA-specific antibody production [201].

Surface functionalization of nanoparticles with APC-targeted molecules is another effective strategy to facilitate LN-targeted drug delivery. Mannosylated DSPE-PEG_{2000} was incorporated into DOTAP to generate mannosylated DOTAP

(LP-Man), which not only significantly accumulated in LNs with prolonged LN retention time but also was effectively captured by APCs in LNs, thereby leading to robust antigen-specific IFN production and long-term immunological memory [206]. Mannosylated lipid/calcium/phosphate (Man-LCP) NPs was loaded with MUC1 mRNA to obtain Man-LCP-MUC1 nanovaccines with the size around 50 nm. The injection of Man-LCP-MUC1 nanovaccine significantly induced MUC1 expression in mouse draining LNs, thereby inducing robust tumor-specific CTL responses and tumor regression [81]. Incorporation of monosialoldihexosylganglioside (GM3), a ligand of CD169 expressed on DCs and macrophages, effectively facilitated the enrichment of lipid membrane-wrapped NPs in LNs [207].

Natural cell membrane coating is emerging as a promising strategy to facilitate LN-targeted cancer immunotherapy. For example, RBC membrane-coated PLGA nanoparticles not only demonstrated prolonged circulation time but also showed superior lymphatic-targeting ability, which enabled their payload to be enriched in the spleen and LNs within 1 h after s.c. injection [99]. Surface coating with mannosylated RBC membranes effectively enhanced LN-targeted delivery of MPLA-adjuvanted nanovaccines, which consequently elicited robust antitumor immune responses and tumor regression with minimal systemic immunotoxicity [100]. Cancer cell membrane, as a good source of cancer antigens, has been recently applied for cancer vaccine development. Cancer cell membrane-coated PLGA nanoparticles (CM-PLGA NPs) not only demonstrated LN-targeting ability, which directly contributed to enhanced antitumor $CD8^+$ T cell responses, but also were capable of inhibiting cancer cell migration towards fibroblasts due to the presence of membrane-associated proteins (e.g., CXCR4 and CD44), thereby effectively preventing tumor metastasis [208]. Further modification of CM with PEG or mannose more significantly improved LN targeting of nanovaccines, which consequently led to boosted antitumor immune responses and tumor regression [103, 107].

Tumor draining LNs (TDLNs) are special LNs with immunosuppressive microenvironment but high levels of tumor-associated antigens due to the direct connection with tumor tissues. TDLNs not only play a role in tumor metastasis but also are important anatomic sites for initiating antitumor immune responses [200]. Several studies investigated whether TDLN-targeted cancer immunotherapy would be more effective than those targeting non-tumor-associated LNs. After intradermal injection, CpG-loaded poly(propylene sulfide) (PPS) nanoparticles (CpG-NPs) with the size around 30 nm were effectively captured by DCs in DTLNs or non-tumor LNs, depending on the injection sites. Compared with non-tumor LN-targeted CpG delivery, TDLN-targeted CpG delivery more effectively induced DC maturation and reversed immunosuppression in TDLNs, leading to more robust tumor-specific T cell responses and tumor regression [209]. The same group also codelivered CpG-NPs and tumor antigen-conjugated NPs into TDLNs or non-tumor LNs using similar strategy. Compared with non-tumor LN-targeted vaccination, TDLN-targeted vaccination induced much stronger CTL responses both locally and systemically, leading to robust tumor regression and host survival [210]. These data implicate TDLNs of solid tumor as a potential target organ for cancer immunotherapy.

Direct intra-lymph node (iLN) injection offers a new opportunity for modulating the microenvironment on LNs. Upon iLN injection, TLR agonists and tumor antigen peptide-loaded PLGA microparticles (MPs) served as a vaccine depot in LNs, which not only induced DC maturation and macrophage activation but also recruited $CD4^+$ T cells, $CD8^+$ T cells, DCs, and macrophages into LNs, thereby robustly eliciting T cells responses and tumor regression [211].

4.3.4 Reprogramming the Tumor Microenvironment with Nanomaterials (Steps 5 and 7)

The tumor microenvironment is a network of cells and tumor-surrounded structures, including blood vessels, stromal cells, fibroblast cells, immune cells, the extracellular matrix, and signaling molecules. Immunosuppressive cells (e.g., TAMs, TIDCs, MDSCs, Tregs, and CAFs) and tumor-derived immunosuppressive molecules (e.g., TGF-β, IL-10, IDO, Arg1, ROS, and NO) in tumor microenvironment directly contribute to immune evasion and immunosuppression of antitumor response [212, 213]. Moreover, dysfunctional tumor vasculature and aberrant metabolic activity of tumor cells, such as high glucose consumption and lactate secretion, lead to hypoxic and acidic tumor microenvironment, which not only enhances the accumulation of TAMs, MDSCs and Treg cells but also inhibits antitumor T cell activities [214]. Hence, overcoming the immunosuppression in tumor microenvironment is an important strategy to improve the clinical efficacy of cancer immunotherapy.

4.3.4.1 Repolarizing Tumor-Associated Dendritic Cells with Nanomaterials

Tumor-associated DC dysfunction plays an important role in tumor-derived immunosuppression. Compared with normal DCs, tumor-associated dendritic cells (TADCs) demonstrate less mature but more immunosuppressive phenotype with reduced costimulatory signals (such as CD40 and CD86) and elevated immune inhibitory molecules (PD-L1), which directly inhibit antitumor T cell responses. Moreover, TADCs are resistant to immunoadjuvant stimulation, which is a major obstacle for cancer vaccine-based immunotherapy [215].

Immunosuppressive effect of TADCs is associated with aberrantly overexpressed immunosuppressive genes, such as STAT3, FOXO3, and suppressor of cytokine signaling 1 (SOCS1), and can be regulated by multiple microRNAs from tumor cells [215]. To sensitize TADCs to TLR stimulation, a multifunctional envelope-type nano device (MEND) containing YSK12-C4, an ionizable-cationic lipid, was developed for DC-targeted SOCS-1 siRNA delivery. The delivery of SOCS-1 siRNA into DCs using YSK12-MEND reduced the expression of

immunosuppressive SOCS-1 about 80%, which was accompanied with enhanced TNF and IL-6 production. Furthermore, the immunization with YSK12-MEND/SOCS1 siRNA-treated BMDCs resulted in more significant tumor regression than untreated BMDCs [216]. Our group co-encapsulated Poly I:C and OVA antigen with STAT3 siRNA by cationic polypeptide micelles (PMP) to generate PMP/OVA/siRNA nanovaccines, which aimed to simultaneously activate TLR3 and block immunosuppressive STAT3 signal. The results showed that PMP/OVA/siRNA not only decreased STAT3 expression in TADCs but also effectively induced TADC maturation by elevating CD86 and CD40 expression as well as IL-12 production. Vaccination of PMP/OVA/siRNA effectively evoked robust tumor-specific CTL responses and ameliorated tumor-derived immunosuppression by decreasing immunosuppressive Treg cells and MDSCs in tumor draining LNs, thereby leading to dramatic tumor regression [33]. Another study reported a dysregulated miR-148a/DNA methyltransferase (DNMT)1/SOCS 1 axis contributing to the poor responsiveness of TADCs to TLR stimulation. Therefore, miR-148a inhibitor (miR-148ai) was co-encapsulated with PMP/OVA to generate PMP/OVA/148ai nanovaccines, which were shown to effectively rescue the responsiveness of TADCs to TLR3 and TLR4 agonists through elevating DNMT1 and decreasing SOCS1, thereby reprogramming immunosuppressive TADCs into immunogenic DCs. Moreover, PMP/OVA/148ai nanovaccine effectively reversed tumor-derived immunosuppression, leading to robust anticancer immune responses and tumor regression [31].

4.3.4.2 Targeting Tumor-Associated Macrophages with Nanomaterials

Tumor-associated macrophages (TAMs), the dominant inflammatory cell population in tumor microenvironment, primarily polarize the “alternatively activated” M2-like macrophages and play an important role in promoting tumor growth, metastasis, angiogenesis, and immunosuppression. Removing or depleting TAMs is considered as a promising strategy to overcome tumor-derived immunosuppression and enhance antitumor immune responses. To effectively remove TAMs, therapeutic agents must be specifically delivered into TAMs in tumor tissues. Nanovectors have been reported to specifically deliver their cargo into TAMs through actively targeting a variety of surface receptors on TAMs, such as macrophage galactose-type C-type lectin (MGL) receptor [30], mannose receptor (CD206), folate receptor beta (FRβ), transferrin receptor [217], and scavenger receptors (SR) [60, 218]. M2 macrophage-targeting peptide (M2pep) is a peptide that preferentially binds to M2 macrophages and M2-like TAMs. Gold nanoparticles (Au NPs) functionalized with M2pep effectively delivered VEGF siRNA into TAMs and significantly decreased VEGF expression. Intratracheal administration of VEGF siRNA-loaded M2pep-AuNPs selectively delivered siRNA into TAMs of lung cancers, which consequently reduced VEGF expression and TAM number in lungs, inhibiting lung cancer progression [60]. To further enhance TAM-targeting ability, M2pep was conjugated with α-peptide (a scavenger receptor B type 1 (SR-B1)) to generate a fusion peptide α-M2pep with dual TAM-targeting ability. The

in vivo study showed that α-M2pep-functionalized lipid nanoparticles (M2NPs) specifically delivered siRNA of CSF-1R(CD115) to M2-like TAMs and reduced M2-like TAMs in mouse tumors over 50%, which subsequently increased tumor-infiltrated $CD8^+$ T cells and IFN-γ production, leading to robust tumor regression [218].

In addition to TAM depletion, reprogramming pro-tumoral M2-like TAMs to antitumor M1 macrophages is another plausible strategy of cancer immunotherapy. R848 is a potent immunoadjuvant to promote the differentiation of M1 macrophages. Rodell et al. developed R848-loaded β-cyclodextrin nanoparticles (CDNP-R848) for TAM-targeted immunotherapy. The in vivo results showed that CDNP-R848 not only accumulated in tumors and tumor draining LNs after i.v. injection but also was effectively captured by TAMs, which consequently promoted TAM differentiation towards M1 phenotype, inhibiting tumor growth [219]. Overexpression of certain microRNA (miR), such as miR-125b and miR-155, is another strategy to reprogram TAMs into M1 macrophages. However, it remains a challenge to selectively deliver miR into TAMs without affecting the macrophages in normal tissues. Our group reported redox/pH dual-responsive polypeptide nanovectors consisting of self-crosslinked galactose functionalized polypeptides (GLC) coated with sheddable PEG-PLL (sPEG) copolymers. The charge reversible sPEG covered cationic GLC core at physiological pH to avoid nonspecific binding by normal macrophages, but quickly shed off at pH 6.5 to re-expose GLC for TAM targeting. The injection of miR155-loaded sPEG/GLC robustly elevated miR155 expression in TAMs and repolarized them to antitumor M1 macrophages, which were accompanied with increased tumor infiltration of T cells and NK cells, thereby leading to robust tumor regression [220]. Parayath et al. encapsulated miR-125b with hyaluronic acid-poly(ethylenimine) (HA-PEI), which was expected to target $CD44^+$ macrophages. The i.p. injection of HA-PEI/miR-125b selectively elevated miR-125b in peritoneal macrophages over 100-folds and repolarized them from M2 to antitumor M1 phenotype. More interestingly, activated peritoneal macrophages effectively migrated into mouse lung cancer and significantly elevated lung M1 macrophages, suggesting its potential to boost cancer immunotherapy [221].

In recent studies, nanovectors with intrinsic ability of repolarizing TAMs have been developed for TAM-targeted cancer immunotherapy. Polyhydroxylated fullerenols ($C_{60}(OH)_{22}$ and $Gd@C_{82}(OH)_{22}$) were reported to directly induce macrophage activation and enhance their cytotoxic effect against tumor cells through activating NF-kB signaling pathway [222]. Reactive oxygen species (ROS) play an important role in promoting M1 macrophage differentiation through activating MAPK and NF-κB signal pathways. Hence, elevating intracellular ROS appears to be a plausible strategy to repolarize TAM to M1 macrophages. Our groups reported TAM-targeted polypeptide micelles grafted with Zinc protoporphyrin IX (ZnPP), an ROS inducer, to obtain ZnPP PM nanoparticles. The results showed that ZnPP PM significantly elevated ROS production and attenuated immunosuppressive STAT3 signaling in TAMs, which consequently re-sensitized TAMs to TLR stimulation. Poly I:C-loaded ZnPP PM (ZnPP PM/PIC) effectively repolarized TAMs to M1 macrophages and elevated tumor-infiltrating NK cells and T lymphocytes, thereby leading to robust

tumor regression [30]. Another study developed TAM-targeted nanoparticles loaded with photosensitizers (e.g., ICG, titanium dioxide), which significantly elevated ROS in TAMs through PDT effect, thereby promoting M1 macrophage repolarization and enhancing their antitumor effects [223]. M1 macrophages can induce tumor cell death through NO production using L-arginine as a substrate. Based on this mechanism, Kudo et al. developed poly(L-arginine)-based micelles ((PEG-b-P(l-Arg)/m) for NO induction and anticancer immunotherapy. The results showed that PEG-b-P(l-Arg) but not PEG-b-P(D-Arg) or PEG-b-poly(L-ε-guanidium lysine) robustly induced NO production in macrophages. The systemic administration of PEG-b-P(l-Arg)/m dose dependently suppressed the tumor growth in vivo [28].

4.3.4.3 Targeting Myeloid-Derived Suppressor Cells with Nanomaterials

Myeloid-derived suppressor cells (MDSCs), including myeloid MDSCs (M-MDSCs) and granulocytic MDSCs (PMN-MDSCs), are major immunosuppressive cell population in tumor microenvironment [224]. Therefore, depleting MDSCs could be a promising strategy to overcome tumor-derived immunosuppression and restore anticancer immunity. Gemcitabine (Gem), a nucleoside analog of chemotherapy, has been shown to reduce MDSCs in vivo at a low dose. The s.c. injection of lipid nanocapsule-formulated gemcitabine (GemC12) led to significant drug accumulation in the spleen and effectively reduced splenic and tumor-infiltrating M-MDSCs in mice. The pretreatment with GemC12-LNCs a day before adoptive T cell therapy effectively increased the number and activity of tumor-infiltrating $CD8^+$ T cells, which should be attributed to decreased M-MDSCs in tumor microenvironment [225]. Another study encapsulated Gem with lipid-coated calcium phosphate (LCP) nanoparticles for cancer therapy. Compared with free Gem, LCP-Gem more effectively induced tumor cell apoptosis, but also more significantly attenuated tumor-derived immunosuppression through depleting MDSCs, promoting M1 macrophage differentiation, and attenuating PD-L1 expression in tumor tissues, which consequently led to boosted antitumor $CD8^+$ T cell responses and robust tumor regression [226]. The purine analog 6-thioguanine (TG), a cytotoxic drug for myeloid leukemia treatment, is another reagent for MDSC depletion. Herein, TG was conjugated to PEG–PPS chain via a disulfide bond to generate ultra-small micelles (MC-TG) (~25 nm). MC-TG micelles were effectively captured by MDSC in both tumors and lymphatic systems after i.d. injection, which subsequently depleted M-MDSCs and G-MDSCs in the spleen and LNs and selectively depleted M-MDSCs in tumors. Although MC-TG alone did not inhibit tumor growth, the administration of MC-TG prior to adoptive $CD8^+$ T cell transfer more effectively inhibited tumor growth than T cell transfer alone, which could be attributable to ameliorated immunosuppression through MDSC depletion in tumors. Moreover, the pretreatment of MC-TG also elevated tumor infiltration of endogenous T cells and increased the proportion of effector memory cells in transferred T cells, thereby leading to more effective tumor inhibition [227]. These results suggest that MDSC depletion could be a promising strategy to improve the therapeutic efficacy of T cell therapy.

4.3.4.4 Targeting Regulatory T Cells with Nanomaterials

$FOXP3^+CD25^+CD4^+$ regulatory T (Treg) cells, as the major immunosuppressive cell population in tumor microenvironment, have a broad range of immunosuppressive activities, such as inhibiting tumor-specific T cell activation and expansion, dampening APC function, ect. Targeting Treg cells has been considered as a plausible immunotherapeutic strategy to rescue antitumor immunity [228]. Currently, Treg-targeted therapy can be achieved by Treg depletion using anti-CD25 or chemotherapeutic drugs (cyclophosphamide and fludarabine). Since CTLA-4 and PD-1 are highly expressed on Treg cells, immune checkpoint blockade with anti-CTLA4 and anti-PD1 is also an effective strategy to attenuate Treg cell activity [177]. Nanotechnology offers great opportunities for Treg-targeted immunotherapy [229]. Li et al. encapsulated CTLA-4 siRNA with PEG-PLA and cationic lipid BHEM-Chol to obtain NPsiCTLA-4 nanocomplexes, which effectively decreased CTLA-4 expression in active T cells about 60–70%. The i.v. injection of NPsiCTLA-4 not only reduced CTLA-4 expression over 60% in $CD4^+$ and $CD8^+$ TILs but also significantly decreased Treg cells in tumors, which consequently enhanced frequency and CTL activity of tumor-infiltrating T cells, leading to robust tumor regression [230]. Imatinib (IMT) is a tyrosine kinase inhibitor that has been reported to decrease Treg cell viability and activity through blocking STAT3 and STAT5 signaling. Ou et al. developed IMT-loaded lipid-PLGA hybrid nanoparticles functionalized with a tLyp1 peptide (IMT/tLyp1-NP) to achieve Treg cell-targeting through Neuropilin-1 (Nrp1) receptor. The results showed that IMT-loaded tLyp1 nanoparticles (IMT/tLyp1-NP) not only suppressed Treg cell differentiation and expansion in vitro but also decreased tumor-infiltrating Treg cells over 30% in mice [231]. The functionalization of PLGA NPs with glucocorticoid-induced TNF receptor family-related protein (GITR) antibody was reported as another effective strategy to enhance the inhibitory effect of IMT on Treg cells [232]. The combination of IMT/tLyp1-NP and anti-CTLA-4 further decreased Treg cells in tumors over 50%, while increasing tumor-infiltrating $CD8^+$ T cells, thereby synergistically inhibiting tumor growth [231]. These studies demonstrate the great potential of nanoparticle-based drug delivery system for modulating Treg cells in tumor microenvironment and improving antitumor immunotherapy.

4.3.4.5 Targeting Immunosuppressive Factors with Nanomaterials

In addition to immunosuppressive cells, a variety of immunosuppressive factors in tumor microenvironment play an important role in attenuating antitumor immune responses, thereby acting as promising targets of cancer immunotherapy. For example, programmed death-ligand 1 (PD-L1), a surface molecule on tumor cells and APCs, inhibits the antitumor immune responses through binding to PD-1 on T cells and NK cells. Hence, PD-1/PD-L1 blockade is emerging as the most potent immunotherapeutic strategy to treat a variety of cancers. Folic acid (FA)-functionalized polyethylenimine (PEI) was reported to effectively deliver PD-L1 siRNA into FA

receptor-positive tumor cells and decreased PD-L1 protein expression about 40–50%, thereby sensitizing the tumor cells to T cell killing [233]. Hyaluronic acid (HA), as the major component of extracellular matrix, is a major barrier dampening drug penetration into tumors. Hyaluronidase (HAase) is the enzyme to degrade the overexpressed HA in tumor tissues. The in vivo study showed that the pretreatment of HAase significantly increased tumor accumulation and tissue penetration of NP-encapsulated PD-L1 shRNA, which consequently improved gene silencing efficacy of PD-L1 shRNA, leading to robust tumor regression [234]. Wang et al. conjugated anti-PD-L1 antibody onto the platelet surface to obtain anti-PD-L1-conjugated platelets (P–aPDL1). Compared with anti-PD-L1, P-aPDL1 not only demonstrated longer blood circulating time but also more significantly accumulated in residual tumors after surgical resection. Moreover, P-aPDL1 significantly decreased tumor-infiltrating Treg cells but robustly boosted antitumor $CD8^+$ T cell responses, thereby preventing cancer recurrence and metastasis after surgery [101]. A recent study generated PD-1^+ cell membrane-derived nanovesicles (PD-1 NVs) for tumor-targeted drug delivery. As expected, PD-1 NVs effectively bond to PD-L1 on melanoma cancer cells, which not only facilitated tumor-targeted drug delivery but also blocked PD1/PD-L1 axis to rescue T cell exhaustion, thereby effectively inhibiting tumor growth. Moreover, PD-1 NVs were further loaded with 1-methyl-tryptophan (1-MT), an indoleamine 2,3-dioxygenase (IDO) inhibitor, in order to simultaneously block immunosuppressive PD1/PD-L1 and IDO signaling pathways in tumor microenvironment. Compared with PD-1 NVs and 1-MT, 1-MT-loaded PD-1 NVs more remarkably enhanced CD8+ activation and tumor infiltration, robustly leading to tumor regression [235].

Despite great success of PD1/PD-L1 blockade in a variety of cancers, patients with low tumor antigens often poorly respond to the therapy. Hypomethylation agents (HMAs), an epigenetic modulator, are able to induce the expression of tumor antigens, which might potentially improve the therapeutic efficacy of PD1/PD-L1 blockade. To test this hypothesis, anti-PD1 was formulated with pH-sensitive $CaCO_3$ nanoparticles to obtain aPD1-NPs. The aPD1-NPs were then co-encapsulated with Zebularine (Zeb), a HMA, into a pH-ROS dual-responsive gel depot, which was designed to utilize low pH and high ROS in tumor microenvironment to trigger controlled release of the payload. The peritumoral injection of Zeb-loaded gel (Zeb-gel) significantly elevated the immunogenicity of tumors by increasing tumor antigen expression, which consequently triggered DC maturation and upregulated tumor PD-L1 expression but reduced immunosuppressive MDSCs in tumor microenvironment. Although aPD1-NP loaded gel (aPD1-gel) moderately inhibited tumors, the codelivery of aPD1 and Zeb with aPD1-Zeb-gel significantly boosted antitumor T cell responses and promoted T cell infiltration into tumors, thereby effectively inhibiting both primary and distant tumors [236].

Indoleamine 2,3-dioxygenase (IDO) is a tryptophan catabolic enzyme that breakdown tryptophan (TRP) to kynurenine for tumor progression and tumor immunosuppression [237]. Melanoma antigen Trp2 epitope-expressed S. cerevisiae yeast (yeast-Trp2) was coated with PEI_{25k} and IDO siRNA to generate yeast-Trp2-siRNA nanocomplexes (YCP), which simultaneously induced DC maturation and inhibited

IDO expression in DCs over 60%. Immunization of YCP robustly elicited Trp2-specific $CD8^+$ T cell responses but decreased Treg cells, thereby leading to dramatic tumor regression [238]. Dual-responsive peptide nanoparticles were developed to codeliver a short peptide antagonist of PD-L1 (DPPA-1) and an inhibitor of IDO (NLG919) for combinational cancer immunotherapy. Although DPPA-1 nanoparticle alone significantly induced antitumor T cells response and inhibited tumor growth, the codelivery of DPPA-1 and NLG919 more effectively induced antitumor CTL responses and inhibited tumor regression with significantly prolonged overall survival [239].

In addition to PD-L1 and IDO, several immunosuppressive molecules in TEM were also investigated for cancer immunotherapy. CD73, a surface molecule expressed on tumor and immune cells, is responsible for the production of adenosine, a soluble factor promoting tumor growth and immunosuppression. CD73 siRNA-loaded chitosan-lactate nanoparticles (ChLa NPs) significantly decreased CD73 expression on tumor cells and moderately reduced tumor-infiltrating Treg and MDSCs. The combination of NP/CD73 siRNA with tumor lysate-loaded DC vaccines further reduced immunosuppressive Treg, MDSCs, and TAMs, evoking robust anticancer T cell responses and tumor regression [21]. Wnt family member 5A (Wnt5a) is a signaling protein in tumor microenvironment, inducing DC tolerance and tumor fibrosis. The expression of Wnt5a trap protein in tumors with cationic lipid protamine-DNA (LPD) nanoparticles effectively reduced Wnt5a protein level in tumors over 70%, which subsequently elevated tumor-infiltrating DCs but decreased immunosuppressive cells, such as MDSCs, M2 macrophages, and $PD\text{-}L1^+$ cells, thereby promoting antitumor immunity [56].

4.3.4.6 Ameliorating Hypoxia in Tumor Microenvironment with Nanotechnology

Hypoxia in tumor microenvironment not only promotes tumor progression and metastasis but also triggers multiple signaling pathways and metabolic switch to aerobic glycolysis, leading to immunosuppression and resistance to cancer therapy [214]. Therefore, alleviating hypoxia is highly desirable to enhance the efficacy of cancer therapy. Nanomaterials provide great opportunities to achieve tumor-targeted O_2 delivery and O_2 supply. For example, nanoparticles incorporated with hemoglobin [240] or perfluorocarbon [183, 241] have been reported as a potent O_2 carrier to improve the therapeutic efficacy of PDT and radiotherapy through alleviating hypoxia in tumor microenvironment. Our group developed human serum albumin (HSA)-hemoglobin (Hb) hybrid protein nanocarriers, which were designed to codeliver O_2 and Ce6 (C@HPOC) for oxygen-boosted PDT. Compared with conventional PDT, C@HPOC-mediated oxygen-boosted PDT more effectively induced tumor cell ICD, thereby leading to tumor regression and preventing tumor metastasis [242].

Nanoparticles can also be incorporated with manganese dioxide (MnO_2), which reacts with H_2O_2 at acidic conditions to spontaneously generate O_2, alleviating tumor hypoxia [243–245]. Our group developed core-shell gold nanocage@manganese dioxide (AuNC@Mn O_2, AM) nanoparticles for oxygen-boosted immunogenic PDT against triple-negative breast cancer. In this platform, MnO_2 shell degraded in the acidic and oxidative TEM to generate O_2, which subsequently boosted the PDT effect of AM nanoparticles for tumor ablation. More importantly, O_2-boosted PDT elicited tumor cell ICD with damage-associated molecular patterns (DAMPs) release, which subsequently induced DC maturation and evoked systematic antitumor immune responses, leading to tumor regression [244]. A recent study reported a photosynthetic leaf-inspired abiotic/biotic nano-thylakoid (PLANT) system, which fused natural thylakoid membrane (the site of photosynthesis) with synthetic nanoparticles (e.g., Ag nanoparticles, SiO_2 nanoparticles, and ZnO nanoparticles) for efficient O_2 generation in vivo. With 660 nm laser irradiation, the PLANT system elevated intracellular O_2 generation in tumor cells, which subsequently switched tumor cell metabolism from anaerobic respiration to mitochondrial respiration, and effectively normalized tumor glucose metabolism, thereby enhancing the efficacy of phototherapy [246]. Hence, nanoparticle-based O_2 supply can not only improve the efficacy of conventional cancer therapy but also evoke systemic antitumor immunity for preventing tumor metastases and reoccurrence.

4.3.5 Targeting Antitumor Effector Cells with Nanomaterials (Step 6 and 7)

Antitumor effector cells, such as T cells, NK cells, and NK T cells, are cytotoxic lymphocytes responsible for tumor cell elimination. T cell-mediated tumor eradiation is highly specific, requiring the recognition of MHC-presented tumor antigen with TCRs. In contrast, the antitumor cytotoxic effects of NK cells and NK T cells are less specific and do not rely on the recognition of MHC-presented tumor antigen. Currently, adoptive cell therapy with in vitro expanded antitumor effector cells is an important strategy for treating both hematological and solid malignancies. Moreover, a variety of antibody drugs and immunostimulators are also developed to directly activate effector cells in vivo to eliminate tumors.

4.3.5.1 T Cell-Targeted Immunotherapy

The antitumor effect of adoptive T cell therapy can be enhanced by genetic modification of T cells with chimeric antigen receptor (CAR) or T cell receptor (TCR), the aim of which is to enhance tumor recognition by T cells. However, the poor gene transduction efficiency in primary T cells often limits the therapeutic efficacy of CAR-T and TCR-T cells. We recently developed a glycometabolic

bioorthogonal chemistry approach to facilitate viral transduction of T cells. Briefly, human T cells were first labeled with azide (-N3) groups on cell membrane via glycometabolic labeling, followed by incubation with the PEI-DBCO-coated lentivirus. The bioorthogonal reaction between DBCOs and azide groups strengthened the virus-T cell interaction, which consequently enhanced viral transduction and CAR expression in human T cells, thereby robustly boosting their antitumor effect in vivo [247]. Alternatively, Smith et al. utilized anti-CD3 modified nanovector to directly deliver CAR DNA into circulating T cells. The result showed that CD3-coated DNA-carrying nanoparticles successfully introduced CAR genes into circulating T cells, which effectively killed tumor cells and led to long-term disease remission [248]. In addition to genetic modification, we recently showed bioorthogonal click chemistry as a plausible strategy to facilitate tumor cell recognition and killing by cytotoxic T cells. Briefly, bicyclo [6.1.0] nonyne (BCN) groups and their complementary bioorthogonal groups (e.g., $-N_3$ groups) were metabolically incorporated onto the cell membranes of tumors and cytotoxic T cells through intracellular glycan biosynthetic pathways. The bioorthogonal reaction between BNC groups on tumor cells and $-N_3$ groups was highly efficient and specific, which not only promoted T cell migration towards tumor cells but also enhanced the interaction of T cells and tumor cells, thereby leading to robust antitumor cytotoxicity [249].

To achieve T cell-mediated tumor eradication, effector T cells must migrate into tumor tissues from lymphoid tissues through the blood circulation. Unfortunately, tumor tissues often exclude T cell infiltration through immunosuppressive chemokine signals and stromal barriers [250]. Chemokines and their cognate receptors play a crucial role in modulating immune cell recruitment into tumors [251]. For example, interferon-γ-inducible protein-10 (IP-10) is a member of CXC chemokine family essential for recruiting $CD8^+$ T cells into tumors. IP-10 gene DNA was encapsulated with FA-modified chitosan nanoparticles to generate FA-CS-mIP-10 nanoparticle. The combinational therapy of FA-CS-mIP-10 and TRP2-specific T cells dramatically increased tumor-infiltrated $CD8^+$ T cells but reduced immunosuppressive MDSCs and Treg in tumor microenvironment, both of which contributed to boosted anticancer immune responses [252]. CXCL12 is a key chemokine in tumor microenvironment inhibiting tumor infiltration of effector T cells through CXCL12/CXCR4 axis. Plasmid DNA of small trapping proteins against CXCL12 and PD-L1 was encapsulated with liposome−protamine−DNA (LPD) NPs to obtain pPDL1-trap LPD and pCXCL12-trap LPD, which were shown to successfully decrease the expression of PDL1 and CXCL12 in tumors, respectively. Although CXCL12 trap alone effectively increased tumor-infiltrating $CD8^+$ T cells and reduced Treg, the combination of pPDL1-trap LPD and pCXCL12-trap LPD more effectively increased $CD8^+$ T cell infiltration but reduced Treg cells and MDSCs, leading to robust tumor regression [58].

Abnormal tumor vasculature and extracellular matrix also play a critical role in T cell exclusion [250, 253]. Hence, overcoming tumor stromal barriers could be another feasible strategy to promote T cell infiltration into tumors. Chen et al. reported that mild PTT with local temperature around 45° C not only ameliorated

hypoxia in tumor microenvironment through destroying extracellular matrix and expanding tumor blood vessels but also induced local production of chemokines, such as CCL2, 3, 4 and CXCL13, which consequently enhanced tumor infiltration and antitumor cytotoxicity of CAR-T cells, thereby leading to significant tumor regression [254]. Recent studies revealed a crucial role of platelets in maintaining tumor vessel barriers to inhibit T cell infiltration. Albumin-based perfluorotributylamine nanoparticles (PFTBA@Alb) were reported to dramatically inhibit platelet adhesion and aggregation as well as platelet granule content release in vitro. The injection of PFTBA@Alb effectively increased the permeability of tumor blood vessels without affecting normal blood vessels, which consequently increased tumor-infiltrating $CD8^+$ and $CD4^+$ T cells showing an obvious rising trend. Although PFTBA@Alb alone did not significantly suppress tumor growth, it sensitized mice to anti-PD-L1-mediated immunotherapy, leading to a high tumor inhibition rate around 90%. These findings suggest that enhancing T cell infiltration could be a plausible strategy to boost the potency of PD-1/PD-L1 immunotherapy [255].

T cells express a variety of costimulatory receptors (e.g., CD3, CD4, CD8, CD28, 4-1BB, and OX40) and inhibitory receptors (so-called immune checkpoints), such as CTLA-4 and PD-1, which can be utilized for T cell-targeted cancer immunotherapy [256]. Yang et al. reported amphiphilic organic ligand-coated gold nanoparticles (amph-NPs) that could effectively load small molecule drugs (e.g., TGF-β inhibitor) within the hydrophobic pockets. The amph-NPs were functionalized with anti-CD8 nanobody in order to achieve $CD8^+$ T cell-targeted drug delivery. The results showed that anti-CD8-functionalized amph-NPs were selectively captured by $CD8^+$ T cells rather than by $CD4^+$ T cells or other immune cell populations both in vitro and in vivo. Moreover, the functionalization of anti-CD8 enhanced the uptake of amph-NPs by $CD8^+$ T cells over 40-folds than naked amph-NPs, which enabled successful delivery of TGF-β inhibitor into $CD8^+$ T cells, thereby augmenting tumor-specific $CD8^+$ T cell responses in vivo [257]. Schmid et al. generated anti-PD1-functionalized PLGA nanoparticles, which not only delivered TGF-β inhibitor into PD-1^+ T cells to augment antitumor T cell response in vivo but also effectively delivered R848 (a TLR7/8 agonist) into tumors to overcome immunosuppression [258]. Inflammation-responsive CpG DNA nanoparticles were developed to codeliver CpG (a TLR9 agonist) and anti-PD-1 (aPD1) into postsurgical tumor bed. Briefly, CpG DNA nano-cocoons, a synthetic long-chain single-stranded DNA (ssDNA) containing repeated CpG sequence and cutting sites of restriction enzyme HhaI, were loaded with anti-PD1 antibody and triglycerol monostearate (TGMS) nanoparticle-caged HhaI enzyme to obtain HhaI-TGMS-DNCs-aPD1 nanoparticles. The enzymes in inflammatory sites, such as esterases and matrix metalloproteinases (MMPs), could cleave TGMS nanoparticles and release HhaI, which would sequentially digest DNCs to generate CpG ODNs and release anti-PD1. Local injection of HhaI-TGMS-DNCs-aPD1 nanoparticles at postsurgical sites not only effectively induced systemic antitumor T cell responses but also prevented tumor recurrence and metastasis, thereby significantly prolonging the overall survival [259].

Multiple antibody-functionalized nanoparticles have been recently developed in order to simultaneously trigger T cell costimulatory signals and block immunosuppressive signals. For example, dual antibody-functionalized PLGA NPs with anti-PD1 and anti-OX40 synergistically induced antitumor T cell activation through simultaneously blocking PD1 signaling and activating OX40 signaling on T cells, leading to robust tumor regression [260]. Iron-dextran particles conjugated with anti-PD-L1 and anti-41BB antibodies (so-called immunoswitch nanoparticles) more significantly induced $CD8^+$ T cell activation and anticancer CTL responses than the nanoparticles with single antibody did. The administration of the immunoswitch not only induced tumor-specific $CD8^+$ T cell activation, clone expansion, cytotoxicity, and tumoral infiltration but also enhanced antitumor efficacy of adoptive T cell therapy, thereby effectively suppressing tumor growth [261]. To further improve the therapeutic efficacy and safety, anti-PD-L1 and T cell activators (anti-CD3 and anti-CD28) were conjugated onto fucoidan (Fu)-loaded iron oxide nanoparticles to generate triple antibody-conjugated magnetic nanomedicine (IO@$FuDex^3$). The results showed that IO@$FuDex^3$ alone not only induced tumoral T cell expansion and activation but also decreased immunosuppressive TAMs and Treg cells, inhibiting tumor growth. Notably, the magnetic navigation further increased tumoral accumulation of IO@$FuDex^3$, leading to more robust antitumor T cell activation and tumor regression. Compared with IO@$FuDex^3$ alone, magnetic navigated-IO@$FuDex^3$ induced less systemic immunotoxicity. These data indicate the potential benefit of the magnetic navigation to improve the efficacy and safety of cancer immunotherapy [262].

4.3.5.2 NK Cell-Targeted Immunotherapy

Natural killer (NK) cells, as the antitumor effectors of innate immunity, are another important target cell population for cancer immunotherapy. Poly (phosphorhydrazone) dendrimers with amino-bis(methylene phosphonate) end groups (ABP dendrimer) were shown to effectively induce proliferation and activation of NK cells in vitro [263]. Anti-GD2-conjugated gold nanoparticles (HGNP) not only effectively recognized and internalized by GD2-positive tumor cells, such as neuroblastoma (NB1691) and melanoma (M21) cells, but also effectively elicited NK-mediated antibody-dependent cellular cytotoxicity (ADCC) against tumor cells [264]. Nanoscale graphene oxide (NGO) was functionalized with anti-CD16 to generate nanoclusters of anti-CD16. Compared with soluble anti-CD16, nanoclustered anti-CD16 more effectively induced NK cell activation, degranulation, and IFN-γ secretion [265]. Wu et al. labeled NK cells with polydopamine (PDA)-coated magnetic Fe_3O_4 nanoparticles through a simple incubation, which facilitated the internalization of nanoparticles by NK cells. Under a magnetic field, the labeling of Fe_3O_4 nanoparticles not only enhanced antitumor cytotoxicity of NK cells but also facilitated NK cell infiltration into tumors, thereby effectively improving the efficacy of NK cell therapy [266].

4.3.6 Nanotechnology for Combinational Cancer Therapy

Despite the encouraging data from animal models and clinical trials, the therapeutic efficacy of cancer immunotherapy is often dampened by tumor heterogeneity, primary and acquired therapy resistance, tumor-derived immunosuppression, and immune evasion. Increasing evidence from clinical trials highlights the significance of combining immunotherapy with conventional cancer therapy, such as chemotherapy, radiotherapy, and phototherapy. Conventional cancer therapy has been reported to modulate immune systems through multiple mechanisms, such as triggering tumor antigen releasing, inducing tumor ICD, increasing tumor mutation and neoantigen loading, enhancing tumor antigen presentation, activating immune effector cells against tumors, depleting immunosuppressive MDSC and Tregs, and blocking immunosuppressive signals [267–269]. On the other hand, immunotherapy enables abscopal effects of local radiotherapy and thermotherapy to inhibit distal tumor growth and prevent tumor metastasis through evoking systemic antitumor immune responses. Moreover, the administration of immunoadjuvant or INF-γ was reported to reverse chemoresistance of tumors both in vivo and in vitro [270]. Hence, it is plausible to combine immunotherapy with conventional cancer therapy in order to improve the efficacy and safety of cancer therapy.

Nanotechnology-based chemo-immunotherapy. The combination of ICD-inducing chemotherapeutic agents, such as DOX and OXA, with immunotherapeutic agents, such as immunoadjuvants, vaccines, and checkpoint blockade, has demonstrated great potential for cancer therapy. For example, Dox and R848 (a TLR7/8 agonist) were co-encapsulated with pH-sensitive poly(L-histidine) (PHIS) to obtain multifunctional nanoparticles, which not only directly killed tumor cells but also evoked robust antitumor immunity, effectively inhibiting tumor growth and metastasis in mice [271]. The codelivery of DOX, all-trans retinoic acid (ATRA), and interleukin-2 (IL-2) using biodegradable hollow mesoporous silica nanoparticles (dHMSN) robustly inhibited tumor growth and prevented lung metastasis, which could be attributable to ATRA-alleviated immunosuppression in tumor microenvironment. Moreover. ATRA and IL-2 also synergistically elicited antitumor immunity through enhancing tumor infiltration and activation of T cells and NK cells, thereby leading to robust tumor regression [65]. Several studies reported that the codelivery of oxaliplatin (OxP) with IDO inhibitor, such as indoximod (IND) and NLG919, using nanoparticles not only induced antitumor T cell responses by triggering ICD of cancer cells but also attenuated IDO-1-mediated immunosuppression and reduced Treg cells, thereby synergistically inhibiting tumor growth and preventing tumor metastasis [272, 273]. Low dosages of paclitaxel (PTX) have been recently reported to induce tumor ICD and selectively deplete Treg cells. Zhao et al. developed thermosponge nanoparticles (TSNs) with core-shell structure, which encapsulated PTX in the core and entrapped IL-2 in the shell using the temperature-responsive swelling/deswelling feature. As compared with TSNs loaded with PTX or IL-2 alone, codelivery of PTX and IL-2 with TSN more effectively stimulated antitumor immune responses and decreased Treg cells, thereby

robustly suppressing tumor growth and preventing metastasis [274]. A recent study reported biomimetic nanoparticles (S-CM-HPAD) consisting of DOX-loaded polyethyleneimine-modified (2-hydroxypropyl)-γ-cyclodextrin (HPAD) as the core, and cancer cell membranes assembled with lactobacilli-derived S-layer proteins as the shell. Cancer cell membranes not only are a good source of tumor antigens but also show homotypic tumor-targeting ability, whereas S-layer proteins reported an immunoadjuvant with the ability to protect tumor antigens from degradation. As expected, S-CM-HPAD NPs effectively delivered DOX to the homotypic tumors and effectively induced tumor cell death. More importantly, S-CM-HPAD NPs evoked robust antitumor T cell response and tumoral T cell infiltration, which could be due to the synergistic effects of codelivered DOX, cancer antigens, and S-layer proteins, thereby effectively inhibiting tumor growth and preventing tumor metastasis [275].

Nanotechnology-based photo-immunotherapy. Local phototherapy, such as PTT and PDT, has demonstrated superior therapeutic effect on primary tumor; however, their effects on distal tumors are limited. The combination of PTT and PDT with immunotherapy was reported as a promising strategy to enhance the abscopal effect of phototherapy, inhibit distal tumors, and prevent tumor metastasis through eliciting systemic antitumor immune response. A previous study showed that although conventional PTT using liposome-encapsulated IR-7 (IR-7-lipo), Prussian blue nanoparticle (PBNP), or SWNT effectively suppressed tumor growth, they failed to inhibit or prevent tumor reoccurrence due to PTT-elevated immunosuppressive MDSCs and Treg cells in tumor tissues [72, 276, 277]. The combination of PTT with immunoadjuvant CpG or CTLA-4 blockade not only effectively alleviated immunosuppression by reducing MDSCs and Treg cells but also increased tumor-infiltrated $CD8^+$ T cells, thereby eliminating secondary tumors and preventing reoccurrence [72, 276, 277]. Another study co-encapsulated ICG and TLR7 agonist imiquimod (R837) with PLGA to generate PLGA-ICG-R837 nanoparticles, which moderately suppressed primary and secondary tumor growth with laser radiation. The further combination of PLGA-ICG-R837 and CTLA-4 checkpoint inhibitor (pre/post) not only eliminated primary tumors but also effectively induced robust tumor-specific T cell responses and immunological memory, thereby providing a long-term protection against tumor reoccurrence and tumor metastasis [278]. Ou et al. developed layer-by-layer pH-sensitive hybrid nanoparticles (LBL hNPs) to codeliver IR-780 and IMT in order to simultaneously achieve PTT and Treg cell inhibition. As compared with either IR-780 or IMT alone, LBL hNP-mediated photoimmunotherapy much more robustly induced antitumor immune responses and suppressed tumor growth, indicating synergistic antitumor effect of PTT and Treg cell inhibition [232].

Similar to PTT, PDT can be combined with immunotherapy to boost cancer therapy. Amphiphilic polymer-coated upconversion nanoparticles (UCNPs) were loaded with a photosensitizer chlorin e6 (Ce6) and R837 to generate multifunctional UCNP-Ce6-R837 nanoparticles. With laser irradiation, UCNP-Ce6-R837 nanoparticles not only demonstrated potent PDT effect against tumor cells but also effectively induced DC maturation and anticancer CTL responses, which consequently

led to robust tumor regression. However, local PDT with UCNP-Ce6-R837 failed to inhibit distant tumor growth, which could be related with elevated Treg cells in tumors. The further combination of UCNP-Ce6-R837 with CTLA-4 blockade significantly decreased Tregs and enhanced tumor infiltration of $CD8^+$, suppressing distant tumors [279]. Another study coated upconversion nanoparticles (UCNPs) with large-pore mesoporous silica to obtain UCMSs with the broadened pore size range from 3.4 to 30 nm. Compared with conventional mesoporous silica-coated UCNPs, UCMSs demonstrated superior loading capacity of photosensitizers (MC540) and tumor antigen proteins (tumor cell fragment, TF) due to their larger pore sizes. MC540-loaded UCMSs moderately elicited antitumor immune responses upon 980 nm NIR laser irradiation; the codelivery of MC540 and TF with UCMSs more effectively induced Th1/Th2 responses and promoted tumor infiltration of T cells, suggesting synergistic effect of PDT and cancer vaccines on evoking antitumor immune responses. Moreover, UCMS–MC540–TF with NIR laser radiation more robustly inhibited tumor growth than PDT or vaccine alone, effectively prolonging the survival of tumor-bearing mice [280]. Song et al. developed caspase-responsive chimeric peptides C16-K(PpIX)-PEG 8-KDEVD-1MT (PpIX-1MT) containing photosensitizer PpIX and IDO inhibitor 1MT for combinational therapy. PpIX-1MT not only demonstrated PDT effect against tumors but also induced tumor-specific $CD8^+$ T cell proliferation both in vitro and in vivo. PpIX-1MT-induced PDT also elevated caspase-3 to trigger 1MT release, which subsequently blocked immunosuppressive IDO and further enhanced antitumor immunity, thereby inhibiting tumor growth and lung metastasis [281].

Nanotechnology-based multimodal cancer therapy. Recent studies explored therapeutic efficacy of multimodal cancer therapy. Photosensitizer Ce6 and DOX were codelivered with pH-sensitive hollow manganese dioxide nanoparticles (H-MnO_2) to obtain H-MnO_2-PEG/C&D nanoparticles for combinational chemophototherapy. At pH 5.5, H-MnO_2-PEG/C&D could be degraded to release Ce6 and DOX to mediate PDT and chemotherapy, respectively. Moreover, MnO_2 could trigger a quick O_2 generation from H_2O_2, thereby alleviating tumoral hypoxia. H-MnO_2-PEG/C&D without laser radiation decreased pretumoral M2-like TAMs in tumor microenvironment, which could be attributed to alleviated hypoxia and DOX-induced tumor cell ICD. With laser radiation, H-MnO_2-PEG/C&D nanoshells not only robustly ablated primary tumors but also significantly reprogrammed TAM to antitumor M1 macrophages, resulting in systemic antitumor responses for inhibiting distant tumor growth and tumor metastasis [282]. A pH-sensitive DOX-copper complex (CuDox) was encapsulated with temperature-sensitive liposomes (TSL) to obtain ultrasound (US)-releasable CuDox-TSL for cancer treatment. Although the i.v. injection of CuDox-TSL with the US treatment (CuDox+US) caused local hyperthermia in tumors and effectively inhibited primary tumor growth, it failed to inhibit contralateral tumors. However, the combination of CuDox+US and intratumor injection of CpG not only inhibited primary tumors but also induced anticancer effects, including enhanced T cell activation and tumor infiltration as well as MDSCs, which consequently prevented contralateral tumor growth [283]. Nanoscale coordination polymer (NCP) nanoparticles were loaded with OX in the core and

pyropheophorbide-lipid conjugate (pyrolipid), a photosensitizer, in the shell to generate NCP@pyrolipid nanoparticles for combinational photodynamic-chemotherapy. With the laser radiation, NCP@pyrolipid significantly decreased the IC50 of oxaliplatin and pyrolipid around 4–5-folds and over 2-folds, respectively, indicating synergistic antitumor effect of OX and PDT. Compared with OX-loaded NCP, NCP@pyrolipid+laser more effectively induced antitumor immune responses and eliminated primary tumors, confirming the critical role of PDT in eliciting antitumor immunity. Furthermore, the combination of NCP@pyrolipid+laser with anti-PD-L1 further boosted systemic anticancer T cell response and enhanced tumor infiltration of $CD4^+$ and $CD8^+$ T cells in both primary and distant tumors, thereby leading to robust tumor regression [284]. Ruthenium nanoparticles (RuNPs) are multifunctional nanomaterials with high photothermal conversion rate and multiple oxidation states. PEGylated hollow mesoporous ruthenium nanoparticles were loaded with a fluorescent antitumor complex ($[Ru(bpy)2(tip)]2^+$, RBT) to generate HMRu@RBT nanoparticles, followed by surface functionalization with anti-CEA/anti-CD16 bispecific antibodies (CEA-CD16-SS-Fc) for combinational immune-chemo-photothermal therapy. The in vitro study showed that HMRu@RBT-SS-Fc not only effectively delivered their payload to CEA^+ tumor cells but also recruited NK cells towards tumor cells, which should be due to the presence of CEA-CD16-SS-Fc. After i.v. injection, HMRu@RBT-SS-Fc more significantly accumulated in tumor tissues and enhanced NK cell infiltration than HMRu@RBT did. With NIR laser radiation, HMRu@RBT-SS-Fc completely ablated primary tumors and effectively inhibited distant tumors, indicating superior and systemic antitumor effects of the multimodality cancer therapy [285].

4.4 Perspectives

Immune checkpoint blockades have made great progress in treating a variety of malignances. Unfortunately, only a small subset of the patients respond to the treatment due to multiple mechanisms, such as immune cell dysfunction, immunosuppressive cells and soluble factors, development of cancer resistance to immunotherapy, distinct metabolic pathways, and secretion of metabolites in tumor microenvironment [286]. The combinational therapy has been reported as an effective strategy to improve the therapeutic efficacy of immune checkpoint blockades. For example, the combination of anti-PD1/PD-L1 and anti-CTLA4 has demonstrated synergistic antitumor effect through targeting different inhibitory signals on T cells and has been approved to treat advanced renal cell carcinoma and metastatic colorectal cancer. The combination of immune checkpoint blockades can also be combined with conventional cancer therapies (e.g., chemotherapy and radiotherapy) or with other immunotherapies (e.g., cancer vaccines, immunoadjuvants, and oncolytic viruses), and some of them have been approved for clinical application [286, 287]. Nanomaterials hold a great potential to enhance the potency and safety of combinational therapies; however, they still need to be further optimized in terms of

the codelivery and programmed release of different agents, tumor-targeting and retention ability, immune cell-targeting ability, intrinsic immunogenicity, and toxicity of component compounds in order to improve the clinical benefit and safety.

Adoptive cell therapy with genetically engineered T cells, such as CAR-T and TCR-T cells, has been considered as an important strategy to treat a variety of malignances. Despite the encouraging results, insufficient gene transfection efficacy can directly limit their clinical outcome. Although viral vector (e.g., lentivirus and retrovirus) systems have been widely applied to facilitate gene editing in T cells, the potential insertional oncogenesis of viral vectors also raises a safety concern [288]. Several recent studies have shown the potential of nanomaterials to enhance T cell-targeted gene editing; therefore, it would be necessary to further explore the application of nanomaterials for T cell gene editing. In addition, the therapeutic efficacy of CAR-T and TCR-T cells in solid tumors is often dampened by poor tumor infiltration and on-target off-tumor toxicity. Moreover, a variety of immunosuppressive factors in tumor microenvironment, such as immunosuppressive cells and cytokines, immune checkpoints, as well as hypoxia and acidic environment, could lead to T cell exhaustion and dysfunction, dampening their therapeutic efficacy [289]. Although nanotechnology has demonstrated the ability of enhancing tumor specificity of cancer therapy and overcoming tumor-derived immune suppression, how to improve the potency and safety of CAR-T and TCR-T therapy using nanotechnology is still in infancy.

Antitumor immune responses are controlled by multiple metabolic pathways in immune cells (so-called immunometabolism). For example, naïve and memory T cells primarily utilize oxidative phosphorylation to generate ATP because of low metabolic demands. Upon activation, T cells increase nutrient uptake and switch to glycolysis for rapid energy production in order to support clonal expansion and effector functions. Compared with effector T cells, memory T cells also maintain substantial mitochondrial spare respiratory capacity (SRC) for long-term survival and rapid recall upon antigen challenge [290]. On the other hand, the altered metabolic status in tumor microenvironment, such as glucose and amino acids deprivation, suppresses T cell glycolysis, which subsequently leads to T cell dysfunction and dampens antitumor immune responses. Additionally, immune checkpoint receptors (e.g., PD-1 and CTLA-4) and cell signaling pathways (e.g., Akt/mTORC1) can inhibit antitumor T cell responses through manipulating T cell metabolism [291–293]. Based on these observations, reprogramming immunometabolic pathways appears to be a plausible approach to enhance the potency of cancer immunotherapy. A variety of organic nanoparticles (e.g., PAMAM dendrimer, polystyrene nanoparticles) and inorganic nanoparticles (e.g., iron oxide, gold nanoparticles, SWNCT, selenium nanoparticles) have been shown to regulate Akt/mTORC1 signaling pathway [294, 295], implying their potential capability of regulating metabolic pathways. Therefore, understanding the regulatory effect of different nanomaterials on metabolic pathways would allow us to integrate metabolic regulation into immunotherapy or combinational therapy for boosted anticancer effect.

Increasing evidences have revealed the association between gut microbiota and clinical responses to chemotherapy and immunotherapy. Using prebiotics is an

effective approach to modulate intestinal microbiota through increasing beneficial bacteria (e.g., Lactobacilli and Bifidobacteria) and decreasing pathogenic bacteria (e.g., Clostridia and Enterobacteriaceae), which are not only essential for improving bowel function but also beneficial for chemotherapy and immunotherapy [296]. Previous studies showed that gut microbiota may be altered by the exposure of NPs, such as silver NPs, gold nanoclusters, and metal oxide NPs (e.g., ZnONPs, TiO_2NPs, CeO_2NPs) [297, 298]. A latest research reported a phage-guided biotic–abiotic hybrid nanosystem, in which a strain of phage against pro-tumoral Fusobacterium was conjugated with dextran nanoparticles (DNPs)-encapsulated irinotecan (IRT) for colorectal cancer (CRC) treatment. The results showed that the phage-guided nanosystem not only increased IRT accumulation in tumors but also rebalanced intestinal microbiota, thereby augmenting the effects of chemotherapy against CRC [299]. The potential of nanotechnology to simultaneously rebalance gut microbiota and achieve cancer immunotherapy needs to be further explored in future studies.

4.5 Conclusions

Nanotechnology holds great potentials to boost cancer immunotherapy through targeting each step of the cancer-immunity cycle (Fig. 4.1). To accelerate the clinical application, nanomaterials must be further optimized to enhance the potency and minimize potential toxicity of cancer immunotherapy. The future application of nanotechnology should be able to target multiple steps of the cancer-immunity cycle with the integration of multiple therapeutic components to achieve synergistic multimodal cancer therapy.

References

1. D.S. Chen, I. Mellman, Oncology meets immunology: the cancer-immunity cycle. Immunity **39**(1), 1–10 (2013)
2. R. Anderson, B.L. Rapoport, Immune dysregulation in cancer patients undergoing immune checkpoint inhibitor treatment and potential predictive strategies for future clinical practice. Front. Oncol. **8**, 80 (2018)
3. L.H. Butterfield, Cancer vaccines. BMJ **350**, h988 (2015)
4. E.N. Baruch et al., Adoptive T cell therapy: an overview of obstacles and opportunities. Cancer **123**(S11), 2154–2162 (2017)
5. B. Ye et al., Engineering chimeric antigen receptor-T cells for cancer treatment. Mol. Cancer **17**(1), 32–47 (2018)
6. G. Marelli et al., Oncolytic viral therapy and the immune system: a double-edged sword against cancer. Front. Immunol. **9**, 866 (2018)
7. E. Hong, M.A. Dobrovolskaia, Addressing barriers to effective cancer immunotherapy with nanotechnology: achievements, challenges, and roadmap to the next generation of nanoimmunotherapeutics. Adv. Drug Deliv. Rev. **141**, 3–22 (2018)

8. D.M. Smith, J.K. Simon, J.R. Baker Jr., Applications of nanotechnology for immunology. Nat. Rev. Immunol. **13**(8), 592–605 (2013)
9. T. Iwama et al., Vaccination with liposome-coupled glypican-3-derived epitope peptide stimulates cytotoxic T lymphocytes and inhibits GPC3-expressing tumor growth in mice. Biochem. Biophys. Res. Commun. **469**(1), 138–143 (2016)
10. N. Miura et al., Modifying antigen-encapsulating liposomes with KALA facilitates MHC class I antigen presentation and enhances anti-tumor effects. Mol. Ther. **25**(4), 1003–1013 (2017)
11. L.M. Kranz et al., Systemic RNA delivery to dendritic cells exploits antiviral defence for cancer immunotherapy. Nature **534**(7607), 396–401 (2016)
12. M.A. Oberli et al., Lipid nanoparticle assisted mRNA delivery for potent cancer immunotherapy. Nano Lett. **17**(3), 1326–1335 (2017)
13. A. Garu et al., Genetic immunization with in vivo dendritic cell-targeting liposomal DNA vaccine carrier induces long-lasting antitumor immune response. Mol. Ther. **24**(2), 385–397 (2016)
14. C. Lai et al., The enhanced antitumor-specific immune response with mannose- and CpG-ODN-coated liposomes delivering TRP2 peptide. Theranostics **8**(6), 1723–1739 (2018)
15. J. Lu et al., Breast cancer chemo-immunotherapy through liposomal delivery of an immunogenic cell death stimulus plus interference in the IDO-1 pathway. ACS Nano **12**(11), 11041–11061 (2018)
16. J. Gao et al., Cationic liposomes promote antigen cross-presentation in dendritic cells by alkalizing the lysosomal pH and limiting the degradation of antigens. Int. J. Nanomedicine **12**, 1251–1264 (2017)
17. S. Mizrahy et al., Advanced strategies in immune modulation of cancer using lipid-based nanoparticles. Front. Immunol. **8**, 69 (2017)
18. E.M. Varypataki et al., Synthetic long peptide-based vaccine formulations for induction of cell mediated immunity: a comparative study of cationic liposomes and PLGA nanoparticles. J. Control. Release **226**, 98–106 (2016)
19. Q. Liu et al., pH-responsive poly(D,L-lactic-co-glycolic acid) nanoparticles with rapid antigen release behavior promote immune response. ACS Nano **9**(5), 4925–4938 (2015)
20. G.N. Shi et al., Enhanced antitumor immunity by targeting dendritic cells with tumor cell lysate-loaded chitosan nanoparticles vaccine. Biomaterials **113**, 191–202 (2017)
21. F. Jadidi-Niaragh et al., CD73 specific siRNA loaded chitosan lactate nanoparticles potentiate the antitumor effect of a dendritic cell vaccine in 4T1 breast cancer bearing mice. J. Control. Release **246**, 46–59 (2017)
22. L.J. Cruz et al., Targeting nanoparticles to CD40, DEC-205 or CD11c molecules on dendritic cells for efficient CD8(+) T cell response: a comparative study. J. Control. Release **192**, 209–218 (2014)
23. J. Conniot et al., Cancer immunotherapy: nanodelivery approaches for immune cell targeting and tracking. Front. Chem. **2**, 105 (2014)
24. E.C. Carroll et al., The vaccine adjuvant chitosan promotes cellular immunity via DNA sensor cGAS-STING-dependent induction of type I interferons. Immunity **44**(3), 597–608 (2016)
25. F. Fontana et al., Delivery of therapeutics with nanoparticles: what's new in cancer immunotherapy? Wiley Interdiscip. Rev. Nanomed. Nanobiotechnol. **9**(1) (2017)
26. H. Li et al., Rational design of polymeric hybrid micelles to overcome lymphatic and intracellular delivery barriers in cancer immunotherapy. Theranostics **7**(18), 4383–4398 (2017)
27. C. Li et al., Synthetic polymeric mixed micelles targeting lymph nodes trigger enhanced cellular and humoral immune responses. ACS Appl. Mater. Interfaces **10**(3), 2874–2889 (2018)
28. S. Kudo, Y. Nagasaki, A novel nitric oxide-based anticancer therapeutics by macrophage-targeted poly(l-arginine)-based nanoparticles. J. Control. Release **217**, 256–262 (2015)
29. Y. Lu et al., Curcumin micelles remodel tumor microenvironment and enhance vaccine activity in an advanced melanoma model. Mol. Ther. **24**(2), 364–374 (2016)
30. L. Liu et al., ROS-inducing micelles sensitize tumor-associated macrophages to TLR3 stimulation for potent immunotherapy. Biomacromolecules **19**(6), 2146–2155 (2018)

31. L. Liu et al., Integrated nanovaccine with microRNA-148a inhibition reprograms tumor-associated dendritic cells by modulating miR-148a/DNMT1/SOCS1 axis. J. Immunol. **197**(4), 1231–1241 (2016)
32. Z. Luo et al., Cationic polypeptide micelle-based antigen delivery system: a simple and robust adjuvant to improve vaccine efficacy. J. Control. Release **170**(2), 259–267 (2013)
33. Z. Luo et al., Nanovaccine loaded with poly I:C and STAT3 siRNA robustly elicits anti-tumor immune responses through modulating tumor-associated dendritic cells in vivo. Biomaterials **38**, 50–60 (2015)
34. K. Miki et al., Combination therapy with dendritic cell vaccine and IL-2 encapsulating polymeric micelles enhances intra-tumoral accumulation of antigen-specific CTLs. Int. Immunopharmacol. **23**(2), 499–504 (2014)
35. S.M. Garg et al., Self-associating poly(ethylene oxide)-block-poly(alpha-carboxyl-epsilon-caprolactone) drug conjugates for the delivery of STAT3 inhibitor JSI-124: potential application in cancer immunotherapy. Mol. Pharm. **14**(8), 2570–2584 (2017)
36. B. Yang et al., DNA vaccine for cancer immunotherapy. Hum. Vaccin. Immunother. **10**(11), 3153–3164 (2014)
37. P. Daftarian et al., Peptide-conjugated PAMAM dendrimer as a universal DNA vaccine platform to target antigen-presenting cells. Cancer Res. **71**(24), 7452–7462 (2011)
38. A.R. Yoon et al., Antitumor effect and safety profile of systemically delivered oncolytic adenovirus complexed with EGFR-targeted PAMAM-based dendrimer in orthotopic lung tumor model. J. Control. Release **231**, 2–16 (2016)
39. A.E. Czapar et al., Slow-release formulation of cowpea mosaic virus for in situ vaccine delivery to treat ovarian cancer. Adv. Sci. (Weinh) **5**(5), 1700991–1700998 (2018)
40. J. Xu et al., Nanovaccine based on a protein-delivering dendrimer for effective antigen cross-presentation and cancer immunotherapy. Biomaterials **207**, 1–9 (2019)
41. P. Niederhafner et al., Glycopeptide dendrimers, part III: a review. Use of glycopeptide dendrimers in immunotherapy and diagnosis of cancer and viral diseases. J. Pept. Sci. **14**(5), 556–587 (2008)
42. W.M. Hussein et al., Multiantigenic peptide-polymer conjugates as therapeutic vaccines against cervical cancer. Bioorg. Med. Chem. **24**(18), 4372–4380 (2016)
43. Y.H. Roh et al., Multivalent DNA-based vectors for DNA vaccine delivery. Methods Mol. Biol. **1143**, 159–179 (2014)
44. H. Yang, Targeted nanosystems: advances in targeted dendrimers for cancer therapy. Nanomedicine **12**(2), 309–316 (2016)
45. I. Corraliza-Gorjon et al., New strategies using antibody combinations to increase cancer treatment effectiveness. Front. Immunol. **8**, 1804 (2017)
46. N. Miyamoto et al., Adjuvant activity enhanced by cross-linked CpG-oligonucleotides in beta-Glucan nanogel and its antitumor effect. Bioconjug. Chem. **28**(2), 565–573 (2017)
47. A. Purwada et al., Self-assembly protein nanogels for safer cancer immunotherapy. Adv. Healthc. Mater. **5**(12), 1413–1419 (2016)
48. P. Li et al., Bioreducible alginate-poly(ethylenimine) nanogels as an antigen-delivery system robustly enhance vaccine-elicited humoral and cellular immune responses. J. Control. Release **168**(3), 271–279 (2013)
49. C. Wang et al., Self-adjuvanted nanovaccine for cancer immunotherapy: role of lysosomal rupture-induced ROS in MHC class I antigen presentation. Biomaterials **79**, 88–100 (2016)
50. T. Shimizu et al., Nanogel DDS enables sustained release of IL-12 for tumor immunotherapy. Biochem. Biophys. Res. Commun. **367**(2), 330–335 (2008)
51. D. Muraoka et al., Nanogel-based immunologically stealth vaccine targets macrophages in the medulla of lymph node and induces potent antitumor immunity. ACS Nano **8**(9), 9209–9218 (2014)
52. S.Z. Khaled et al., One-pot synthesis of pH-responsive hybrid nanogel particles for the intracellular delivery of small interfering RNA. Biomaterials **87**, 57–68 (2016)
53. Y. Tahara, K. Akiyoshi, Current advances in self-assembled nanogel delivery systems for immunotherapy. Adv. Drug Deliv. Rev. **95**, 65–76 (2015)

54. S. Tan et al., Combinational delivery of lipid-enveloped polymeric nanoparticles carrying different peptides for anti-tumor immunotherapy. Nanomedicine (Lond.) **9**(5), 635–647 (2014)
55. F. Rose et al., Engineering of a novel adjuvant based on lipid-polymer hybrid nanoparticles: a quality-by-design approach. J. Control. Release **210**, 48–57 (2015)
56. Q. Liu et al., Nanoparticle-mediated trapping of Wnt family member 5A in tumor microenvironments enhances immunotherapy for B-Raf proto-oncogene mutant melanoma. ACS Nano **12**(2), 1250–1261 (2018)
57. K. Thanki et al., Engineering of small interfering RNA-loaded lipidoid-poly(DL-lactic-co-glycolic acid) hybrid nanoparticles for highly efficient and safe gene silencing: a quality by design-based approach. Eur. J. Pharm. Biopharm. **120**, 22–33 (2017)
58. L. Miao et al., Transient and local expression of chemokine and immune checkpoint traps to treat pancreatic cancer. ACS Nano **11**(9), 8690–8706 (2017)
59. J.P.M. Almeida et al., In vivo gold nanoparticle delivery of peptide vaccine induces anti-tumor immune response in prophylactic and therapeutic tumor models. Small **11**(12), 1453–1459 (2015)
60. J. Conde et al., Dual targeted immunotherapy via in vivo delivery of biohybrid RNAi-peptide nanoparticles to tumour-associated macrophages and cancer cells. Adv. Funct. Mater. **25**(27), 4183–4194 (2015)
61. J.P. Almeida, E.R. Figueroa, R.A. Drezek, Gold nanoparticle mediated cancer immunotherapy. Nanomedicine **10**(3), 503–514 (2014)
62. S. Fogli et al., Inorganic nanoparticles as potential regulators of immune response in dendritic cells. Nanomedicine (Lond.) **12**(14), 1647–1660 (2017)
63. X. Wang et al., Comprehensive mechanism analysis of mesoporous-silica-nanoparticle-induced cancer immunotherapy. Adv. Healthc. Mater. **5**(10), 1169–1176 (2016)
64. J. Kim et al., Injectable, spontaneously assembling, inorganic scaffolds modulate immune cells in vivo and increase vaccine efficacy. Nat. Biotechnol. **33**(1), 64–72 (2015)
65. M. Kong et al., Biodegradable hollow mesoporous silica nanoparticles for regulating tumor microenvironment and enhancing antitumor efficiency. Theranostics **7**(13), 3276–3292 (2017)
66. X. Zhuang et al., Lipid-enveloped zinc phosphate hybrid nanoparticles for codelivery of H-2K(b) and H-2D(b)-restricted antigenic peptides and monophosphoryl lipid A to induce antitumor immunity against melanoma. J. Control. Release **228**, 26–37 (2016)
67. X. Xia et al., Porous silicon microparticle potentiates anti-tumor immunity by enhancing cross-presentation and inducing type I interferon response. Cell Rep. **11**(6), 957–966 (2015)
68. X. Wang et al., Stimulation of in vivo antitumor immunity with hollow mesoporous silica nanospheres. Angew. Chem. Int. Ed. Engl. **55**(5), 1899–1903 (2016)
69. J. Meng et al., Carbon nanotubes conjugated to tumor lysate protein enhance the efficacy of an antitumor immunotherapy. Small **4**(9), 1364–1370 (2008)
70. J. Meng et al., Subcutaneous injection of water-soluble multi-walled carbon nanotubes in tumor-bearing mice boosts the host immune activity. Nanotechnology **21**(14), 145104–145112 (2010)
71. M. Yang et al., Multiwalled carbon nanotubes interact with macrophages and influence tumor progression and metastasis. Theranostics **2**(3), 258–270 (2012)
72. C. Wang et al., Immunological responses triggered by photothermal therapy with carbon nanotubes in combination with anti-CTLA-4 therapy to inhibit cancer metastasis. Adv. Mater. **26**(48), 8154–8162 (2014)
73. C.H. Villa et al., Single-walled carbon nanotubes deliver peptide antigen into dendritic cells and enhance IgG responses to tumor-associated antigens. ACS Nano **5**(7), 5300–5311 (2011)
74. Y. Zhang et al., One-shot immunomodulatory nanodiamond agents for cancer immunotherapy. Adv. Mater. **28**(14), 2699–2708 (2016)
75. Y. Tao et al., Immunostimulatory oligonucleotides-loaded cationic graphene oxide with photothermally enhanced immunogenicity for photothermal/immune cancer therapy. Biomaterials **35**(37), 9963–9971 (2014)
76. W. Song, S.N. Musetti, L. Huang, Nanomaterials for cancer immunotherapy. Biomaterials **148**, 16–30 (2017)

77. H.A. Hassan et al., Dual stimulation of antigen presenting cells using carbon nanotube-based vaccine delivery system for cancer immunotherapy. Biomaterials **104**, 310–322 (2016)
78. S.P. Mukherjee et al., Macrophage sensing of single-walled carbon nanotubes via toll-like receptors. Sci. Rep. **8**(1), 1115–1132 (2018)
79. A.B. Satterlee, L. Huang, Current and future theranostic applications of the lipid-calcium-phosphate nanoparticle platform. Theranostics **6**(7), 918–929 (2016)
80. M. Huo et al., Tumor-targeted delivery of sunitinib base enhances vaccine therapy for advanced melanoma by remodeling the tumor microenvironment. J. Control. Release **245**, 81–94 (2017)
81. L. Liu et al., Combination immunotherapy of MUC1 mRNA nano-vaccine and CTLA-4 blockade effectively inhibits growth of triple negative breast cancer. Mol. Ther. **26**(1), 45–55 (2018)
82. Q. Liu et al., BRAF peptide vaccine facilitates therapy of murine BRAF-mutant melanoma. Cancer Immunol. Immunother. **67**(2), 299–310 (2018)
83. T.J. Goodwin, L. Huang, Investigation of phosphorylated adjuvants co-encapsulated with a model cancer peptide antigen for the treatment of colorectal cancer and liver metastasis. Vaccine **35**(19), 2550–2557 (2017)
84. B.R. Olden et al., Cell-templated silica microparticles with supported lipid bilayers as artificial antigen-presenting cells for T cell activation. Adv. Healthc. Mater. **8**(2), e1801188 (2019)
85. A.S. Cheung et al., Scaffolds that mimic antigen-presenting cells enable ex vivo expansion of primary T cells. Nat. Biotechnol. **36**(2), 160–169 (2018)
86. R.M. Clauson et al., Size-controlled iron oxide nanoplatforms with lipidoid-stabilized shells for efficient magnetic resonance imaging-trackable lymph node targeting and high-capacity biomolecule display. ACS Appl. Mater. Interfaces **10**(24), 20281–20295 (2018)
87. F. Duan et al., A simple and powerful co-delivery system based on pH-responsive metal-organic frameworks for enhanced cancer immunotherapy. Biomaterials **122**, 23–33 (2017)
88. X. Zhong et al., An aluminum adjuvant-integrated nano-MOF as antigen delivery system to induce strong humoral and cellular immune responses. J. Control. Release **300**, 81–92 (2019)
89. P. Zhang et al., Polyelectrolyte multilayers assembled entirely from immune signals on gold nanoparticle templates promote antigen-specific T cell response. ACS Nano **9**(6), 6465–6477 (2015)
90. A. Jurj et al., The new era of nanotechnology, an alternative to change cancer treatment. Drug Des. Devel. Ther. **11**, 2871–2890 (2017)
91. W. Li et al., Tailoring porous silicon for biomedical applications: from drug delivery to cancer immunotherapy. Adv. Mater. (2018)
92. S.T. Haque, E.H. Chowdhury, Recent progress in delivery of therapeutic and imaging agents utilizing organic-inorganic hybrid nanoparticles. Curr. Drug Deliv. **15**(4), 485–496 (2018)
93. Y. Liu, Y. Zhao, X. Chen, Bioengineering of metal-organic frameworks for nanomedicine. Theranostics **9**(11), 3122–3133 (2019)
94. B.R. Lee et al., Engineered human ferritin nanoparticles for direct delivery of tumor antigens to lymph node and cancer immunotherapy. Sci. Rep. **6**, 35182 (2016)
95. N.M. Molino et al., Display of DNA on nanoparticles for targeting antigen presenting cells. ACS Biomater Sci. Eng. **3**(4), 496–501 (2017)
96. N.M. Molino et al., Biomimetic protein nanoparticles facilitate enhanced dendritic cell activation and cross-presentation. ACS Nano **7**(11), 9743–9752 (2013)
97. B. Choi et al., Effective delivery of antigen-Encapsulin nanoparticle fusions to dendritic cells leads to antigen-specific cytotoxic T cell activation and tumor rejection. ACS Nano **10**(8), 7339–7350 (2016)
98. N.M. Molino, S.W. Wang, Caged protein nanoparticles for drug delivery. Curr. Opin. Biotechnol. **28**, 75–82 (2014)
99. C.M. Hu et al., Nanoparticle-detained toxins for safe and effective vaccination. Nat. Nanotechnol. **8**(12), 933–938 (2013)

100. Y. Guo et al., Erythrocyte membrane-enveloped polymeric nanoparticles as nanovaccine for induction of antitumor immunity against melanoma. ACS Nano **9**(7), 6918–6933 (2015)
101. C. Wang et al., In situ activation of platelets with checkpoint inhibitors for post-surgical cancer immunotherapy. Nat. Biomed. Eng. **1**(0011), 1–10 (2017)
102. A.V. Kroll et al., Nanoparticulate delivery of cancer cell membrane elicits multiantigenic antitumor immunity. Adv. Mater. **29**(47), 1703969–1703977 (2017)
103. R. Yang et al., Cancer cell membrane-coated adjuvant nanoparticles with mannose modification for effective anticancer vaccination. ACS Nano **12**(6), 5121–5129 (2018)
104. A. Pitchaimani, T.D.T. Nguyen, S. Aryal, Natural killer cell membrane infused biomimetic liposomes for targeted tumor therapy. Biomaterials **160**, 124–137 (2018)
105. G. Deng et al., Cell-membrane immunotherapy based on natural killer cell membrane coated nanoparticles for the effective inhibition of primary and Abscopal tumor growth. ACS Nano **12**(12), 12096–12108 (2018)
106. Y. Han et al., T cell membrane mimicking nanoparticles with bioorthogonal targeting and immune recognition for enhanced photothermal therapy. Adv. Sci. (Weinh) **6**(15), 1900251 (2019)
107. L.J. Ochyl et al., PEGylated tumor cell membrane vesicles as a new vaccine platform for cancer immunotherapy. Biomaterials **182**, 157–166 (2018)
108. L. Wayteck et al., Hitchhiking nanoparticles: reversible coupling of lipid-based nanoparticles to cytotoxic T lymphocytes. Biomaterials **77**, 243–254 (2016)
109. R.A. Burga et al., Conjugating Prussian blue nanoparticles onto antigen-specific T cells as a combined nanoimmunotherapy. Nanomedicine (Lond.) **11**(14), 1759–1767 (2016)
110. R.B. Jones et al., Antigen recognition-triggered drug delivery mediated by nanocapsule-functionalized cytotoxic T-cells. Biomaterials **117**, 44–53 (2017)
111. L. Tang et al., Enhancing T cell therapy through TCR-signaling-responsive nanoparticle drug delivery. Nat. Biotechnol. **36**(8), 707–716 (2018)
112. F. Xia et al., Cytokine induced killer cells-assisted delivery of chlorin e6 mediated self-assembled gold nanoclusters to tumors for imaging and immuno-photodynamic therapy. Biomaterials **170**, 1–11 (2018)
113. Q. Hu et al., Engineering nanoparticle-coated bacteria as oral DNA vaccines for cancer immunotherapy. Nano Lett. **15**(4), 2732–2739 (2015)
114. X. Duan, C. Chan, W. Lin, Nanoparticle-mediated immunogenic cell death enables and potentiates cancer immunotherapy. Angew. Chem. Int. Ed. Engl. **58**(3), 670–680 (2019)
115. B. Montico et al., Immunogenic apoptosis as a novel tool for anticancer vaccine development. Int. J. Mol. Sci. **19**(2), 594 (2018)
116. I. Adkins et al., Physical modalities inducing immunogenic tumor cell death for cancer immunotherapy. Onco. Targets. Ther. **3**(12), e968434 (2014)
117. M. Olivo et al., Targeted therapy of cancer using photodynamic therapy in combination with multi-faceted anti-tumor modalities. Pharmaceuticals (Basel) **3**(5), 1507–1529 (2010)
118. G. Lan et al., Nanoscale metal-organic framework overcomes hypoxia for photodynamic therapy primed cancer immunotherapy. J. Am. Chem. Soc. **140**(17), 5670–5673 (2018)
119. G. Yang et al., Smart nanoreactors for pH-responsive tumor homing, mitochondria-targeting, and enhanced photodynamic-immunotherapy of cancer. Nano Lett. **18**(4), 2475–2484 (2018)
120. D.S. Pellosi, P. De Jesus, A.C. Tedesco, Spotlight on the delivery of photosensitizers: different approaches for photodynamic-based therapies. Expert Opin. Drug Deliv. **14**(12), 1395–1406 (2017)
121. W.R. Chen et al., Laser-photosensitizer assisted immunotherapy: a novel modality for cancer treatment. Cancer Lett. **115**(1), 25–30 (1997)
122. H.T. Nguyen et al., Activation of inflammasomes by tumor cell death mediated by gold nanoshells. Biomaterials **33**(7), 2197–2205 (2012)
123. W. Yang et al., Albumin-bioinspired Gd:CuS nanotheranostic agent for in vivo photoacoustic/magnetic resonance imaging-guided tumor-targeted photothermal therapy. ACS Nano **10**(11), 10245–10257 (2016)

124. E.E. Sweeney, J. Cano-Mejia, R. Fernandes, Photothermal therapy generates a thermal window of immunogenic cell death in neuroblastoma. Small, 1800678–1800686 (2018)
125. Q. Han et al., CpG loaded MoS2 nanosheets as multifunctional agents for photothermal enhanced cancer immunotherapy. Nanoscale **9**(18), 5927–5934 (2017)
126. J. Wu, D.J. Waxman, Immunogenic chemotherapy: dose and schedule dependence and combination with immunotherapy. Cancer Lett. **419**, 210–221 (2018)
127. L. Zitvogel et al., Immunological aspects of cancer chemotherapy. Nat. Rev. Immunol. **8**(1), 59–73 (2008)
128. E.M. Mastria et al., Nanoparticle formulation improves doxorubicin efficacy by enhancing host antitumor immunity. J. Control. Release **269**, 364–373 (2018)
129. D.W. Zheng et al., Highly integrated nano-platform for breaking the barrier between chemotherapy and immunotherapy. Nano Lett. **16**(7), 4341–4347 (2016)
130. E.B. Golden, L. Apetoh, Radiotherapy and immunogenic cell death. Semin. Radiat. Oncol. **25**(1), 11–17 (2015)
131. Q. Chen et al., Nanoparticle-enhanced radiotherapy to trigger robust cancer immunotherapy. Adv. Mater. **31**(10), 1802228–1802239 (2019)
132. K. Lu et al., Low-dose X-ray radiotherapy-radiodynamic therapy via nanoscale metal-organic frameworks enhances checkpoint blockade immunotherapy. Nat. Biomed. Eng. **2**(8), 600–610 (2018)
133. J. Hong, C. Yun, Overcoming the limitations of locally administered oncolytic virotherapy. BMC. Biomed. Eng. **1**, 1–11 (2019)
134. I.R. Khalil et al., Poly-gamma-glutamic acid (gamma-PGA)-based encapsulation of adenovirus to evade neutralizing antibodies. Molecules **23**(10), 2565 (2018)
135. G.K. Grunwald et al., Systemic image-guided liver cancer radiovirotherapy using dendrimer-coated adenovirus encoding the sodium iodide symporter as theranostic gene. J. Nucl. Med. **54**(8), 1450–1457 (2013)
136. J.W. Choi et al., Using a magnetic field to redirect an oncolytic adenovirus complexed with iron oxide augments gene therapy efficacy. Biomaterials **65**, 163–174 (2015)
137. S. Mo et al., Increasing the density of nanomedicines improves their ultrasound-mediated delivery to tumours. J. Control. Release **210**, 10–18 (2015)
138. Z. Zhang et al., Induction of anti-tumor cytotoxic T cell responses through PLGA-nanoparticle mediated antigen delivery. Biomaterials **32**(14), 3666–3678 (2011)
139. Y. Horiuchi et al., Targeting cryptic epitope with modified antigen coupled to the surface of liposomes induces strong antitumor CD8 T-cell immune responses in vivo. Oncol. Rep. **34**(6), 2827–2836 (2015)
140. G. Alipour Talesh et al., Poly (I:C)-DOTAP cationic nanoliposome containing multi-epitope HER2-derived peptide promotes vaccine-elicited anti-tumor immunity in a murine model. Immunol. Lett. **176**, 57–64 (2016)
141. J. Xie et al., Encapsulation of hydrophilic and hydrophobic peptides into hollow mesoporous silica nanoparticles for enhancement of antitumor immune response. Small **13**(40), 1701741–1701758 (2017)
142. M.A. McNamara, S.K. Nair, E.K. Holl, RNA-based vaccines in cancer immunotherapy. J. Immunol. Res. **2015**, 794528–794537 (2015)
143. L.A. Avila et al., Gene delivery and immunomodulatory effects of plasmid DNA associated with branched amphiphilic peptide capsules. J. Control. Release **241**, 15–24 (2016)
144. K. Sehgal, K.M. Dhodapkar, M.V. Dhodapkar, Targeting human dendritic cells in situ to improve vaccines. Immunol. Lett. **162**(1 Pt A), 59–67 (2014)
145. C.G. Figdor, Y. van Kooyk, G.J. Adema, C-type lectin receptors on dendritic cells and Langerhans cells. Nat. Rev. Immunol. **2**(2), 77–84 (2002)
146. K. Fytianos et al., Aerosol delivery of functionalized gold nanoparticles target and activate dendritic cells in a 3D lung cellular model. ACS Nano **11**(1), 375–383 (2017)
147. S.T. Jahan, S.M. Sadat, A. Haddadi, Design and immunological evaluation of anti-CD205-tailored PLGA-based nanoparticulate cancer vaccine. Int. J. Nanomedicine **13**, 367–386 (2018)

148. J. Tel et al., Targeting uptake receptors on human plasmacytoid dendritic cells triggers antigen cross-presentation and robust type I IFN secretion. J. Immunol. **191**(10), 5005–5012 (2013)
149. E. Yuba et al., Bioactive polysaccharide-based pH-sensitive polymers for cytoplasmic delivery of antigen and activation of antigen-specific immunity. Biomaterials **120**, 32–45 (2017)
150. Y. Qian et al., Targeting dendritic cells in lymph node with an antigen peptide-based nanovaccine for cancer immunotherapy. Biomaterials **98**, 171–183 (2016)
151. M.A. Shevtsov et al., 70-kDa heat shock protein coated magnetic nanocarriers as a nanovaccine for induction of anti-tumor immune response in experimental glioma. J. Control. Release **220**(Pt A), 329–340 (2015)
152. Y. Ma et al., The role of surface charge density in cationic liposome-promoted dendritic cell maturation and vaccine-induced immune responses. Nanoscale **3**(5), 2307–2314 (2011)
153. C.A. Fromen et al., Nanoparticle surface charge impacts distribution, uptake and lymph node trafficking by pulmonary antigen-presenting cells. Nanomedicine **12**(3), 677–687 (2016)
154. Y. Li et al., Surface hydrophobicity of microparticles modulates adjuvanticity. J. Mater. Chem. B **1**(32), 3888–3896 (2013)
155. F. Shima et al., Manipulating the antigen-specific immune response by the hydrophobicity of amphiphilic poly(gamma-glutamic acid) nanoparticles. Biomaterials **34**(37), 9709–9716 (2013)
156. Y. Min et al., Antigen-capturing nanoparticles improve the abscopal effect and cancer immunotherapy. Nat. Nanotechnol. **12**(9), 877–882 (2017)
157. V. Schuette, S. Burgdorf, The ins-and-outs of endosomal antigens for cross-presentation. Curr. Opin. Immunol. **26**, 63–68 (2014)
158. N.I. Ho et al., Adjuvants enhancing cross-presentation by dendritic cells: the key to more effective vaccines? Front. Immunol. **9**, 2874 (2018)
159. Y. Mukai et al., Induction of endoplasmic reticulum-endosome fusion for antigen cross-presentation induced by poly (gamma-glutamic acid) nanoparticles. J. Immunol. **187**(12), 6249–6255 (2011)
160. C. Zhang et al., Targeted antigen delivery to dendritic cell via functionalized alginate nanoparticles for cancer immunotherapy. J. Control. Release **256**, 170–181 (2017)
161. F. Cao et al., Photothermally controlled MHC class I restricted CD8(+) T-cell responses elicited by hyaluronic acid decorated gold nanoparticles as a vaccine for cancer immunotherapy. Adv. Healthc. Mater. **7**(10), 1701439–1701451 (2018)
162. A. Warnatsch, T. Bergann, E. Kruger, Oxidation matters: the ubiquitin proteasome system connects innate immune mechanisms with MHC class I antigen presentation. Mol. Immunol. **55**(2), 106–109 (2013)
163. Y. Lu et al., Glutathione-depletion mesoporous organosilica nanoparticles as a self-adjuvant and co-delivery platform for enhanced cancer immunotherapy. Biomaterials **175**, 82–92 (2018)
164. W.W. Unger et al., Glycan-modified liposomes boost CD4+ and CD8+ T-cell responses by targeting DC-SIGN on dendritic cells. J. Control. Release **160**(1), 88–95 (2012)
165. H. Li et al., Alpha-alumina nanoparticles induce efficient autophagy-dependent cross-presentation and potent antitumour response. Nat. Nanotechnol. **6**(10), 645–650 (2011)
166. S. Wang et al., Exploration of antigen induced CaCO3 nanoparticles for therapeutic vaccine. Small **14**(14), 1704272–1704280 (2018)
167. B.J. Umlauf, C.Y. Chung, K.C. Brown, Modular three-component delivery system facilitates HLA class I antigen presentation and CD8(+) T-cell activation against tumors. Mol. Ther. **23**(6), 1092–1102 (2015)
168. N.M. Dold et al., A poly(beta-amino ester) activates macrophages independent of NF-kappaB signaling. Acta Biomater. **68**, 168–177 (2018)
169. T.D. Fernandez et al., Intracellular accumulation and immunological properties of fluorescent gold nanoclusters in human dendritic cells. Biomaterials **43**, 1–12 (2015)
170. M.A. Shahbazi et al., Surface chemistry dependent immunostimulative potential of porous silicon nanoplatforms. Biomaterials **35**(33), 9224–9235 (2014)

171. J.I. Andorko, C.M. Jewell, Designing biomaterials with immunomodulatory properties for tissue engineering and regenerative medicine. Bioeng. Transl. Med. **2**(2), 139–155 (2017)
172. C.A. Da Silva et al., Chitin is a size-dependent regulator of macrophage TNF and IL-10 production. J. Immunol. **182**(6), 3573–3582 (2009)
173. S. Kumar et al., Shape and size-dependent immune response to antigen-carrying nanoparticles. J. Control. Release **220**(Pt A), 141–148 (2015)
174. R. Kedmi, N. Ben-Arie, D. Peer, The systemic toxicity of positively charged lipid nanoparticles and the role of toll-like receptor 4 in immune activation. Biomaterials **31**(26), 6867–6875 (2010)
175. M. Henriksen-Lacey et al., Comparison of the depot effect and immunogenicity of liposomes based on dimethyldioctadecylammonium (DDA), 3beta-[N-(N',N'-Dimethylaminoethane)carbomyl] cholesterol (DC-Chol), and 1,2-Dioleoyl-3-trimethylammonium propane (DOTAP): prolonged liposome retention mediates stronger Th1 responses. Mol. Pharm. **8**(1), 153–161 (2011)
176. D.F. Moyano et al., Nanoparticle hydrophobicity dictates immune response. J. Am. Chem. Soc. **134**(9), 3965–3967 (2012)
177. Y. Kakizawa et al., Precise manipulation of biophysical particle parameters enables control of proinflammatory cytokine production in presence of TLR 3 and 4 ligands. Acta Biomater. **57**, 136–145 (2017)
178. Y. Zhang et al., Functionalized quantum dots induce proinflammatory responses in vitro: the role of terminal functional group-associated endocytic pathways. Nanoscale **5**(13), 5919–5929 (2013)
179. S.B. Lee et al., Antigen-free radionuclide-embedded gold nanoparticles for dendritic cell maturation, tracking, and strong antitumor immunity. Adv. Healthc. Mater., 1701369–1701379 (2018)
180. A.M. de Groot et al., Immunogenicity testing of lipidoids in vitro and in silico: modulating lipidoid-mediated TLR4 activation by nanoparticle design. Mol. Ther. Nucl. Acids **11**, 159–169 (2018)
181. T. Tanaka et al., DiC14-amidine cationic liposomes stimulate myeloid dendritic cells through toll-like receptor 4. Eur. J. Immunol. **38**(5), 1351–1357 (2008)
182. W. Yan, W. Chen, L. Huang, Reactive oxygen species play a central role in the activity of cationic liposome based cancer vaccine. J. Control. Release **130**(1), 22–28 (2008)
183. Z. Chen et al., Polyhydroxylated metallofullerenols stimulate IL-1β secretion of macrophage through TLRs/MyD88/NF-κB pathway and $NLRP_3$ inflammasome activation. Small. 10 (12), 2362–2372 (2014)
184. H.W. Despres et al., Mechanisms of the immune response cause by cationic and anionic surface functionalized cellulose nanocrystals using cell-based assays. Toxicol. In Vitro **55**, 124–133 (2019)
185. R. Jin et al., Iron oxide nanoparticles promote macrophage autophagy and inflammatory response through activation of toll-like receptor-4 signaling. Biomaterials **203**, 23–30 (2019)
186. T. Shen et al., Lactosylated N-alkyl polyethylenimine coated iron oxide nanoparticles induced autophagy in mouse dendritic cells. Regen. Biomater. **5**(3), 141–149 (2018)
187. C. Gouttefangeas, H.G. Rammensee, Personalized cancer vaccines: adjuvants are important, too. Cancer Immunol. Immunother. **67**(12), 1911–1918 (2018)
188. C. Wang et al., Toll-like receptor 3 agonist complexed with cationic liposome augments vaccine-elicited antitumor immunity by enhancing TLR3-IRF3 signaling and type I interferons in dendritic cells. Vaccine **30**(32), 4790–4799 (2012)
189. L. Nuhn et al., Nanoparticle-conjugate TLR7/8 agonist localized immunotherapy provokes safe antitumoral responses. Adv. Mater. **30**(45), 1803397–1803406 (2018)
190. I. Mottas et al., Amphiphilic nanoparticle delivery enhances the anticancer efficacy of a TLR7 ligand via local immune activation. Biomaterials **190-191**, 111–120 (2019)
191. G. Zhu et al., DNA-inorganic hybrid nanovaccine for cancer immunotherapy. Nanoscale **8**(12), 6684–6692 (2016)

192. A. Ruiz-de-Angulo et al., Microdosed lipid-coated (67)Ga-magnetite enhances antigen-specific immunity by image tracked delivery of antigen and CpG to lymph nodes. ACS Nano **10**(1), 1602–1618 (2016)
193. Y. Fan et al., Immunogenic cell death amplified by co-localized adjuvant delivery for cancer immunotherapy. Nano Lett. **17**(12), 7387–7393 (2017)
194. A. Li et al., Activating cGAS-STING pathway for the optimal effect of cancer immunotherapy. J. Hematol. Oncol. **12**(1), 35–42 (2019)
195. D.R. Wilson et al., Biodegradable STING agonist nanoparticles for enhanced cancer immunotherapy. Nanomedicine **14**(2), 237–246 (2018)
196. D. Shae et al., Endosomolytic polymersomes increase the activity of cyclic dinucleotide STING agonists to enhance cancer immunotherapy. Nat. Nanotechnol. **14**(3), 269–278 (2019)
197. M.E. Jacobson et al., Delivery of 5′-triphosphate RNA with endosomolytic nanoparticles potently activates RIG-I to improve cancer immunotherapy. Biomater. Sci. **7**(2), 547–559 (2019)
198. M. Das et al., Nanoparticle delivery of RIG-I agonist enables effective and safe adjuvant therapy in pancreatic cancer. Mol. Ther. **27**(3), 507–517 (2019)
199. K. Maisel et al., Exploiting lymphatic vessels for immunomodulation: rationale, opportunities, and challenges. Adv. Drug Deliv. Rev. **114**, 43–59 (2017)
200. S.N. Thomas, N.A. Rohner, E.E. Edwards, Implications of lymphatic transport to lymph nodes in immunity and immunotherapy. Annu. Rev. Biomed. Eng. **18**, 207–233 (2016)
201. Y. Zhuang et al., PEGylated cationic liposomes robustly augment vaccine-induced immune responses: role of lymphatic trafficking and biodistribution. J. Control. Release **159**(1), 135–142 (2012)
202. S.Y. Kim et al., Synthetic vaccine nanoparticles target to lymph node triggering enhanced innate and adaptive antitumor immunity. Biomaterials **130**, 56–66 (2017)
203. N.L. Trevaskis, L.M. Kaminskas, C.J. Porter, From sewer to saviour—targeting the lymphatic system to promote drug exposure and activity. Nat. Rev. Drug Discov. **14**(11), 781–803 (2015)
204. I. Singh et al., Lymphatic system: a prospective area for advanced targeting of particulate drug carriers. Expert Opin. Drug Deliv. **11**(2), 211–229 (2014)
205. M. Henriksen-Lacey et al., Liposomal cationic charge and antigen adsorption are important properties for the efficient deposition of antigen at the injection site and ability of the vaccine to induce a CMI response. J. Control. Release **145**(2), 102–108 (2010)
206. C. Wang et al., Lymphatic-targeted cationic liposomes: a robust vaccine adjuvant for promoting long-term immunological memory. Vaccine **32**(42), 5475–5483 (2014)
207. F. Xu et al., Lipid-mediated targeting with membrane-wrapped nanoparticles in the presence of Corona formation. ACS Nano **10**(1), 1189–1200 (2016)
208. J. Jin et al., Human cancer cell membrane-coated biomimetic nanoparticles reduce fibroblast-mediated invasion and metastasis and induce T-cells. ACS Appl. Mater. Interfaces **11**(8), 7850–7861 (2019)
209. S.N. Thomas et al., Targeting the tumor-draining lymph node with adjuvanted nanoparticles reshapes the anti-tumor immune response. Biomaterials **35**(2), 814–824 (2014)
210. L. Jeanbart et al., Enhancing efficacy of anticancer vaccines by targeted delivery to tumor-draining lymph nodes. Cancer Immunol. Res. **2**(5), 436–447 (2014)
211. J.I. Andorko et al., Targeted programming of the lymph node environment causes evolution of local and systemic immunity. Cell. Mol. Bioeng. **9**, 418–432 (2016)
212. A.J. Oliver et al., Tissue-dependent tumor microenvironments and their impact on immunotherapy responses. Front. Immunol. **9**, 70 (2018)
213. L. Labanieh, R.G. Majzner, C.L. Mackall, Programming CAR-T cells to kill cancer. Nat. Biomed. Eng. **2**(6), 377–392 (2017)
214. B. Wegiel et al., Metabolic switch in the tumor microenvironment determines immune responses to anti-cancer therapy. Front. Oncol. **8**, 284 (2018)

215. J.M. Tran Janco et al., Tumor-infiltrating dendritic cells in cancer pathogenesis. J. Immunol. **194**(7), 2985–2991 (2015)
216. S. Warashina et al., A lipid nanoparticle for the efficient delivery of siRNA to dendritic cells. J. Control. Release **225**, 183–191 (2016)
217. C. Ngambenjawong, H.H. Gustafson, S.H. Pun, Progress in tumor-associated macrophage (TAM)-targeted therapeutics. Adv. Drug Deliv. Rev. **114**, 206–221 (2017)
218. Y. Qian et al., Molecular-targeted immunotherapeutic strategy for melanoma via dual-targeting nanoparticles delivering small interfering RNA to tumor-associated macrophages. ACS Nano **11**(9), 9536–9549 (2017)
219. C.B. Rodell et al., TLR7/8-agonist-loaded nanoparticles promote the polarization of tumour-associated macrophages to enhance cancer immunotherapy. Nat. Biomed. Eng. **2**(8), 578–588 (2018)
220. L. Liu et al., Tumor associated macrophage-targeted microRNA delivery with dual-responsive polypeptide nanovectors for anti-cancer therapy. Biomaterials **134**, 166–179 (2017)
221. N.N. Parayath, A. Parikh, M.M. Amiji, Repolarization of tumor-associated macrophages in a genetically engineered nonsmall cell lung cancer model by intraperitoneal administration of hyaluronic acid-based nanoparticles encapsulating microRNA-125b. Nano Lett. **18**(6), 3571–3579 (2018)
222. J. Tang et al., Polyhydroxylated fullerenols regulate macrophage for cancer adoptive immunotherapy and greatly inhibit the tumor metastasis. Nanomedicine **12**(4), 945–954 (2016)
223. C. Shi et al., Reprogramming tumor-associated macrophages by nanoparticle-based reactive oxygen species photogeneration. Nano Lett. **18**(11), 7330–7342 (2018)
224. Y. Liu et al., Targeting myeloid-derived suppressor cells for cancer immunotherapy. Cancer Immunol. Immunother. **67**(8), 1181–1195 (2018)
225. M.S. Sasso et al., Low dose gemcitabine-loaded lipid nanocapsules target monocytic myeloid-derived suppressor cells and potentiate cancer immunotherapy. Biomaterials **96**, 47–62 (2016)
226. Y. Zhang et al., Gemcitabine nanoparticles promote antitumor immunity against melanoma. Biomaterials **189**, 48–59 (2019)
227. L. Jeanbart et al., 6-Thioguanine-loaded polymeric micelles deplete myeloid-derived suppressor cells and enhance the efficacy of T cell immunotherapy in tumor-bearing mice. Cancer Immunol. Immunother. **64**(8), 1033–1046 (2015)
228. H. Nishikawa, S. Sakaguchi, Regulatory T cells in cancer immunotherapy. Curr. Opin. Immunol. **27**, 1–7 (2014)
229. H. Jonuleit, T. Bopp, C. Becker, Treg cells as potential cellular targets for functionalized nanoparticles in cancer therapy. Nanomedicine (Lond.) **11**(20), 2699–2709 (2016)
230. S.Y. Li et al., Restoring anti-tumor functions of T cells via nanoparticle-mediated immune checkpoint modulation. J. Control. Release **231**, 17–28 (2016)
231. W. Ou et al., Regulatory T cell-targeted hybrid nanoparticles combined with immunocheckpoint blockage for cancer immunotherapy. J. Control. Release **281**, 84–96 (2018)
232. W. Ou et al., Combination of NIR therapy and regulatory T cell modulation using layer-by-layer hybrid nanoparticles for effective cancer photoimmunotherapy. Theranostics **8**(17), 4574–4590 (2018)
233. P.Y. Teo et al., Ovarian cancer immunotherapy using PD-L1 siRNA targeted delivery from folic acid-functionalized polyethylenimine: strategies to enhance T cell killing. Adv. Healthc. Mater. **4**(8), 1180–1189 (2015)
234. X. Guan et al., Efficient PD-L1 gene silence promoted by hyaluronidase for cancer immunotherapy. J. Control. Release **293**, 104–112 (2019)
235. X. Zhang et al., PD-1 blockade cellular vesicles for cancer immunotherapy. Adv. Mater. **30**(22), 1707112–1707122 (2018)
236. H. Ruan et al., A dual-bioresponsive drug-delivery depot for combination of epigenetic modulation and immune checkpoint blockade. Adv. Mater. **31**(17), 1806957–1806965 (2019)
237. G.C. Prendergast et al., Indoleamine 2,3-dioxygenase pathways of pathogenic inflammation and immune escape in cancer. Cancer Immunol. Immunother. **63**(7), 721–735 (2014)

238. D.Q. Liu et al., An indoleamine 2, 3-dioxygenase siRNA nanoparticle-coated and Trp2-displayed recombinant yeast vaccine inhibits melanoma tumor growth in mice. J. Control. Release **273**, 1–12 (2018)
239. K. Cheng et al., Sequentially responsive therapeutic peptide assembling nanoparticles for dual-targeted cancer immunotherapy. Nano Lett. **18**(5), 3250–3258 (2018)
240. Z. Luo et al., Self-monitoring artificial red cells with sufficient oxygen supply for enhanced photodynamic therapy. Sci. Rep. **6**, 23393 (2016)
241. G. Song et al., Perfluorocarbon-loaded hollow Bi2Se3 nanoparticles for timely supply of oxygen under near-infrared light to enhance the radiotherapy of cancer. Adv. Mater. **28**(14), 2716–2723 (2016)
242. Z. Chen et al., Bioinspired hybrid protein oxygen nanocarrier amplified photodynamic therapy for eliciting anti-tumor immunity and Abscopal effect. ACS Nano **12**(8), 8633–8645 (2018)
243. H. Inoue, K. Tani, Multimodal immunogenic cancer cell death as a consequence of anticancer cytotoxic treatments. Cell Death Differ. **21**(1), 39–49 (2014)
244. R. Liang et al., Oxygen-boosted immunogenic photodynamic therapy with gold nanocages@ manganese dioxide to inhibit tumor growth and metastases. Biomaterials **177**, 149–160 (2018)
245. H. Zhu et al., Oxygenic hybrid semiconducting nanoparticles for enhanced photodynamic therapy. Nano Lett. **18**(1), 586–594 (2018)
246. D. Zheng et al., Normalizing tumor microenvironment based on photosynthetic abiotic/biotic nanoparticles. ACS Nano **12**(6), 6218–6227 (2018)
247. H. Pan et al., Glycometabolic bioorthogonal chemistry-guided viral transduction for robust human T cell engineering. Adv. Funct. Mater. **1807528**, 1–9 (2019)
248. T.T. Smith et al., In situ programming of leukaemia-specific T cells using synthetic DNA nanocarriers. Nat. Nanotechnol. **12**(8), 813–820 (2017)
249. W. Li et al., Bio-orthogonal T cell targeting strategy for robustly enhancing cytotoxicity against tumor cells. Small **15**(4), 1804383–1804389 (2019)
250. E. Lanitis et al., Mechanisms regulating T-cell infiltration and activity in solid tumors. Ann. Oncol. **28**(suppl_12), xii18–xii32 (2017)
251. V. Mollica Poeta et al., Chemokines and chemokine receptors: new targets for cancer immunotherapy. Front. Immunol. **10**, 379 (2019)
252. J. He et al., Folate-modified chitosan nanoparticles containing the IP-10 gene enhance melanoma-specific cytotoxic CD8(+)CD28(+) T lymphocyte responses. Theranostics **6**(5), 752–761 (2016)
253. J.A. Joyce, D.T. Fearon, T cell exclusion, immune privilege, and the tumor microenvironment. Science **348**(6230), 74–80 (2015)
254. Q. Chen et al., Photothermal therapy promotes tumor infiltration and antitumor activity of CAR T cells. Adv. Mater. **31**(23), 1900192–1900199 (2019)
255. Z. Zhou et al., Perfluorocarbon nanoparticle-mediated platelet inhibition promotes intratumoral infiltration of T cells and boosts immunotherapy. Proc. Natl. Acad. Sci. U. S. A. **116**(24), 11972–11977 (2019)
256. I. Mellman, G. Coukos, G. Dranoff, Cancer immunotherapy comes of age. Nature **480**(7378), 480–489 (2011)
257. Y.S. Yang et al., Targeting small molecule drugs to T cells with antibody-directed cell-penetrating gold nanoparticles. Biomater. Sci. **7**(1), 113–124 (2018)
258. D. Schmid et al., T cell-targeting nanoparticles focus delivery of immunotherapy to improve antitumor immunity. Nat. Commun. **8**(18), 1747–1759 (2017)
259. C. Wang et al., Inflammation-triggered cancer immunotherapy by programmed delivery of CpG and anti-PD1 antibody. Adv. Mater. **28**(40), 8912–8920 (2016)
260. Y. Mi et al., A dual immunotherapy nanoparticle improves T-cell activation and cancer immunotherapy. Adv. Mater. **30**(25), 1706098–1706107 (2018)
261. A.K. Kosmides et al., Dual targeting nanoparticle stimulates the immune system to inhibit tumor growth. ACS Nano **11**(6), 5417–5429 (2017)
262. C.S. Chiang et al., Combination of fucoidan-based magnetic nanoparticles and immunomodulators enhances tumour-localized immunotherapy. Nat. Nanotechnol. **13**, 746–754 (2018)

263. M. Poupot et al., Poly(phosphorhydrazone) dendrimers: Yin and Yang of monocyte activation for human NK cell amplification applied to immunotherapy against multiple myeloma. Nanomedicine **12**(8), 2321–2330 (2016)
264. P. Jiao et al., Enhancing both CT imaging and natural killer cell-mediated cancer cell killing by a GD2-targeting nanoconstruct. J. Mater. Chem. B **4**(3), 513–520 (2016)
265. C. Loftus et al., Activation of human natural killer cells by graphene oxide-templated antibody nanoclusters. Nano Lett. **18**(5), 3282–3289 (2018)
266. L. Wu et al., Magnetic delivery of Fe3O4@polydopamine nanoparticle-loaded natural killer cells suggest a promising anticancer treatment. Biomater. Sci. **6**(10), 2714–2725 (2018)
267. C.G. Drake, Combination immunotherapy approaches. Ann. Oncol. **23**(Suppl 8), viii41–viii46 (2012)
268. A.G. Dalgleish, Rationale for combining immunotherapy with chemotherapy. Immunotherapy **7**(3), 309–316 (2015)
269. X.T. Li et al., Toward innovative combinational immunotherapy: a systems biology perspective. Cancer Treat. Rev. **68**, 1–8 (2018)
270. W. Wang et al., Effector T cells abrogate stroma-mediated chemoresistance in ovarian cancer. Cell **165**(5), 1092–1105 (2016)
271. Y. Liu et al., Dual pH-responsive multifunctional nanoparticles for targeted treatment of breast cancer by combining immunotherapy and chemotherapy. Acta Biomater. **66**, 310–324 (2018)
272. J. Lu et al., Nano-enabled pancreas cancer immunotherapy using immunogenic cell death and reversing immunosuppression. Nat. Commun. **8**(1), 1811–1824 (2017)
273. B. Feng et al., Binary cooperative prodrug nanoparticles improve immunotherapy by synergistically modulating immune tumor microenvironment. Adv. Mater. **30**(38), 1803001–1803010 (2018)
274. Y. Zhao et al., Immunochemotherapy mediated by thermosponge nanoparticles for synergistic anti-tumor effects. J. Control. Release **269**, 322–336 (2018)
275. M. Wu et al., Surface-layer protein-enhanced immunotherapy based on cell membrane-coated nanoparticles for the effective inhibition of tumor growth and metastasis. ACS Appl. Mater. Interfaces **11**(10), 9850–9859 (2019)
276. L. Li et al., An endogenous vaccine based on fluorophores and multivalent immunoadjuvants regulates tumor micro-environment for synergistic photothermal and immunotherapy. Theranostics **8**(3), 860–873 (2018)
277. J. Cano-Mejia et al., Prussian blue nanoparticle-based photothermal therapy combined with checkpoint inhibition for photothermal immunotherapy of neuroblastoma. Nanomedicine **13**(2), 771–781 (2017)
278. Q. Chen et al., Photothermal therapy with immune-adjuvant nanoparticles together with checkpoint blockade for effective cancer immunotherapy. Nat. Commun. **7**, 13193 (2016)
279. J. Xu et al., Near-infrared-triggered photodynamic therapy with multitasking upconversion nanoparticles in combination with checkpoint blockade for immunotherapy of colorectal cancer. ACS Nano **11**(5), 4463–4474 (2017)
280. B. Ding et al., Large-pore mesoporous-silica-coated upconversion nanoparticles as multifunctional immunoadjuvants with ultrahigh photosensitizer and antigen loading efficiency for improved cancer photodynamic immunotherapy. Adv. Mater. **30**(52), 1802479–1802488 (2018)
281. W. Song et al., Enhanced immunotherapy based on photodynamic therapy for both primary and lung metastasis tumor eradication. ACS Nano **12**(2), 1978–1989 (2018)
282. G. Yang et al., Hollow MnO2 as a tumor-microenvironment-responsive biodegradable nanoplatform for combination therapy favoring antitumor immune responses. Nat. Commun. **8**(1), 902–915 (2017)
283. A. Kheirolomoom et al., CpG expedites regression of local and systemic tumors when combined with activatable nanodelivery. J. Control. Release **220**(Pt A), 253–264 (2015)
284. C. He et al., Core-shell nanoscale coordination polymers combine chemotherapy and photodynamic therapy to potentiate checkpoint blockade cancer immunotherapy. Nat. Commun. **7**, 12499–12511 (2016)

285. M. Xu et al., Hollow mesoporous ruthenium nanoparticles conjugated bispecific antibody for targeted anti-colorectal cancer response of combination therapy. Nanoscale **11**(19), 9661–9678 (2019)
286. A.L. Shergold, R. Millar, R.J.B. Nibbs, Understanding and overcoming the resistance of cancer to PD-1/PD-L1 blockade. Pharmacol. Res. **145**, 104258–104279 (2019)
287. J. van den Bulk, E.M. Verdegaal, N.F. de Miranda, Cancer immunotherapy: broadening the scope of targetable tumours. Open Biol. **8**(6), 180037–180046 (2018)
288. K.T. Marcucci et al., Retroviral and Lentiviral safety analysis of gene-modified T cell products and infused HIV and oncology patients. Mol. Ther. **26**(1), 269–279 (2018)
289. S. Tahmasebi, R. Elahi, A. Esmaeilzadeh, Solid tumors challenges and new insights of CAR T cell engineering. Stem Cell Rev. Rep. **15**(5), 619–636 (2019)
290. C.H. Chang, E.L. Pearce, Emerging concepts of T cell metabolism as a target of immunotherapy. Nat. Immunol. **17**(4), 364–368 (2016)
291. H.C. Hope, R.J. Salmond, Targeting the tumor microenvironment and T cell metabolism for effective cancer immunotherapy. Eur. J. Immunol. **49**(8), 1147–1152 (2019)
292. P.C. Ho, S.M. Kaech, Reenergizing T cell anti-tumor immunity by harnessing immunometabolic checkpoints and machineries. Curr. Opin. Immunol. **46**, 38–44 (2017)
293. N. Assmann, D.K. Finlay, Metabolic regulation of immune responses: therapeutic opportunities. J. Clin. Invest. **126**(6), 2031–2039 (2016)
294. M. Lunova et al., Targeting the mTOR signaling pathway utilizing nanoparticles: a critical overview. Cancers (Basel) **11**(1), 82–90 (2019)
295. H. Amani et al., Selenium nanoparticles for targeted stroke therapy through modulation of inflammatory and metabolic signaling. Sci. Rep. **9**(1), 6044–6053 (2019)
296. M. Sambi, L. Bagheri, M.R. Szewczuk, Current challenges in cancer immunotherapy: multimodal approaches to improve efficacy and patient response rates. J. Oncol. **2019**(4508794), 1–12 (2019)
297. J. Tsiaoussis et al., Effects of single and combined toxic exposures on the gut microbiome: current knowledge and future directions. Toxicol. Lett. **312**, 72–97 (2019)
298. L. Wang et al., Impact of short-term exposure of AuNCs on the gut microbiota of BALB/c mice. J. Biomed. Nanotechnol. **15**(4), 779–789 (2019)
299. D.W. Zheng et al., Phage-guided modulation of the gut microbiota of mouse models of colorectal cancer augments their responses to chemotherapy. Nat. Biomed. Eng. **3**(9), 717–728 (2019)

Chapter 5
Molecular Studies of Peptide Assemblies and Related Applications in Tumor Therapy and Diagnosis

Huayi Wang, Xiaocui Fang, Yanlian Yang, and Chen Wang

Abstract Peptides and proteins are known to form a variety of aggregate forms via assembling processes with significant dependence on sequences, which is characteristic for amyloid-like structures. Such peptides could be explored as diagnostic probes targeting tumor antigens. Nanostructured peptide aggregates have been shown to improve the binding affinity and selectivity to the tumor-associated antigens, and can also enhance the antitumor efficacy. The insight of the aggregation and assembly propensities of peptide and protein structures could provide a basis for developing diagnosis and therapeutics for a variety of diseases. An important subject under study is the formation mechanism of peptide assemblies at the level of individual amino acids. This effort could lead to the insight of assembly propensity of peptide molecules. In this chapter, we will review the representative progress on studying aggregation propensity of peptides based on the high-resolution structural analysis of peptide assemblies. It will be presented that these efforts could advance our insight into the peptide assembly mechanisms, as well as provide potential venues for developing peptide-aggregate-based tumor therapeutic strategies.

Huayi Wang and Xiaocui Fang contributed equally to this work.

H. Wang
CAS Key Laboratory of Standardization and Measurement for Nanotechnology, CAS Key Laboratory of Biological Effects of Nanomaterials and Nanosafety, CAS Center for Excellence in Nanoscience, National Center for Nanoscience and Technology, Beijing, People's Republic of China

Department of Chemistry, Tsinghua University, Beijing, People's Republic of China

University of Chinese Academy of Sciences, Beijing, People's Republic of China

X. Fang · Y. Yang (✉) · C. Wang (✉)
CAS Key Laboratory of Standardization and Measurement for Nanotechnology, CAS Key Laboratory of Biological Effects of Nanomaterials and Nanosafety, CAS Center for Excellence in Nanoscience, National Center for Nanoscience and Technology, Beijing, People's Republic of China

University of Chinese Academy of Sciences, Beijing, People's Republic of China
e-mail: yangyl@nanoctr.cn; wangch@nanoctr.cn

H. Xu, N. Gu (eds.), *Nanotechnology in Regenerative Medicine and Drug Delivery Therapy*, https://doi.org/10.1007/978-981-15-5386-8_5

Keywords Peptide assembly · Peptide-based biomaterial · Drug delivery system · Tumor therapy

5.1 Structures and Formation of Amyloid-Like Fibrils

The tendency for proteins to form various aggregate forms was predicted in a number of pioneering studies [1, 2]. About 50 proteins and peptides have been reported to be associated with human diseases [3, 4]. These natural peptides or proteins have the ability to self-assemble into fibrils under specific conditions, and may accumulate into plaques and deposit in different organs like brain or kidney with aging, and related with the progression of lots of different diseases [3–6]. It has been widely demonstrated that proteins with amyloid-like segments are capable of triggering amyloid formation [7]. The revelation of the formation of amyloid fibrils, including the structure and kinetic process, could promote the understanding of the toxicity mechanism of these amyloid peptides, which benefits the design and utilization of amyloid peptide assemblies.

In a very closely related research field, nanostructured peptide aggregates have been shown to improve the binding affinity and selectivity to the tumor-associated antigens, and can also enhance the antitumor efficacy. The insight of the aggregation and assembly propensities of peptide and protein structures could provide a basis for developing diagnosis and therapeutics for a variety of diseases. An important subject under study is the formation mechanism of peptide assemblies at the level of individual amino acids. This effort could lead to the insight of assembly propensity of peptide molecules. In this chapter, we will review the representative progress on studying aggregation propensity of peptides based on the high-resolution structural analysis of peptide assemblies. The presented efforts could serve to advance our insight into the peptide assembly mechanisms, as well as provide potential venues for developing peptide-aggregate-based tumor therapeutic strategies.

5.1.1 Structures of Amyloid-Like Fibrils

The fibrillar structures are representative of amyloid aggregates and have been the focus of extensive investigations. With tremendous breakthroughs in the micro- and nano-characterization technologies, such as cryo-electron microscope (cryo-EM), scanning tunneling microscopy (STM), and solid-state nuclear magnetic resonance (NMR), the structural analytical capabilities have been greatly enhanced to gain molecular level insight of fibrillar structures of amyloids. The progression of amyloid structure studies over the 400 years and highlighted recent breakthroughs have been comprehensively summarized in literatures [4]. The development of cryo-EM promotes amyloid fibrils analysis into atomic resolution [8–10]. Gremer et al. achieved a 4.0 Å resolution of the structure of an $A\beta_{1\text{-}42}$ fibril composed of two

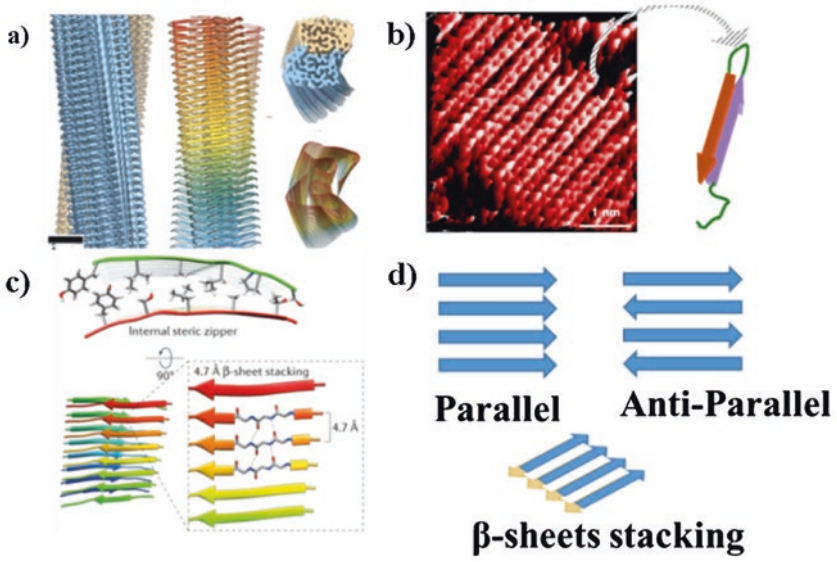

Fig. 5.1 (**a**) Three-dimensional (3D) reconstruction from cryo-EM images showing the density of two proto-filaments (brown and blue) and the clear separation of the β strands [10]. Copyright 2017, AAAS. (**b**) 3D high-resolution STM image of $A\beta_{42}$ assemblies, and proposed structural model of a folded single $A\beta_{42}$ molecule [11]. Copyright 2009, Elsevier. (**c**) A ten-residue peptide from transthyretin (TTR), showing β-sheet stacking in which each β-strand "rung" is stabilized by hydrogen bonds (denoted by fine black dotted lines) between the polypeptide backbones of precursors, which are separated by the canonical 4.7–4.8 Å repeat of the cross-β amyloid fold. Further stabilization is provided by a steric zipper between the β-sheets, which stabilizes the fibril core [4]. (**d**) Multiple secondary structural units organizing to form cross-β and stacking of β-sheets

intertwined proto-filaments, and the backbone of all 42 residues and nearly all side chains are well resolved in the EM density map (Fig. 5.1a) [10]. Besides cryo-EM, due to the submolecular structural resolution, STM has also been widely exploited to probe the assembly behavior and single-molecular structure of small molecules on surfaces. Compared to the complicated sample preparation, the micro-technologies of cryo-EM and STM show their advantages of easy sample preparation, easy-analysis, and visualized single-molecule resolution. Ma et al. demonstrated the molecular observation of core regions of $A\beta_{42}$ hairpins and unfolded peptide and confirmed the parallel assembling characteristics of $A\beta_{42}$ hairpins (Fig. 5.1b) [11]. STM has been utilized for investigating peptide assemblies ranging from complex disease-related peptides to model peptide for better understanding of peptide–peptide interactions [11–14].

The reported structural analyses reveal that amyloid fibrils share a common underlying structure: β-strand align into parallel or antiparallel β-sheet, and thus form proto-filament with the β-strand perpendicular to the axis of the fibril and about ~4.7–4.8 Å distance between each β-strands repeating running down the fibril axis (Fig. 5.1c, d) [4]. Understanding the structures and formation of amyloid fibrils

can not only help us discover the reason for the toxicity of amyloid fibrils, but also provide molecular information for predictive design of self-assembled peptides. Rational design of β-sheet peptide assemblies relies on the deep understanding of the structure and formation of natural amyloid fibrils, digging the regularities of amyloid molecular and interactions between strand to strand, and sheet to sheet.

5.1.2 Formation of Amyloid-Like Aggregates

The formation of amyloid fibrils involves three phases: nucleation phase, elongation phase, and stationary phase, as shown in Fig. 5.2a. The first step of amyloid fibrils formation is nucleation. Monomeric molecules aggregate into oligomers, which is a complicated process with varied structures of the nucleation. Models proposed to describe the nucleation process mainly include "classical nucleation" characterized by an one-step nucleation and "non-classical nucleation" characterized by a two-step nucleation [15]. In the formation of the amyloid fibril, a β-strand rich secondary structure was formed and the cross β-structure will recruit the monomers and prolong the amyloid fibril. The kinetic process is commonly measured by thioflavin T (ThT), a dye that is able to emit fluorescence when it binds to amyloid fibril and was widely used for the investigation of the influencing factors in amyloid fibril formation processes [5, 16].

Additionally, atomic force microscopy (AFM) has also been used to track the formation kinetics of oligomers and fibrils of amyloid peptides [17–19]. Yang's group recently observed the amyloid aggregation dynamics of $amylin_{1\text{-}37}$-nucleation to fibrillation under real liquid condition using Fast scan AFM and proposed a tentative model (Fig. 5.2b) [19]. They found that in the initial phase of aggregation, $amylin_{1\text{-}37}$ monomers developed into the oligomeric nucleus, then, the active region of amyloid oligomers began to recruit monomers and formed β-structures, but the opposite ends of amyloid oligomers were passivated due to the low β-sheet content.

In general, understanding of dynamic progress of amyloid aggregation is essential in investigating how the peptide monomers assemble into amyloid fibrils. On the other hand, the structure analysis of amyloid fibrils can illustrate why the peptide monomers aggregate into amyloid fibrils.

5.2 Structural Perspectives of Peptide-Based Aggregates

Peptides are short chains of amino acid linked by amide bonds and show high biocompatibility and bioactivity due to these amino acids are widely existed throughout the human body. Rational design of self-assembled peptide is based on the deep understanding of the interactions between peptides, along with the ability to scaffold multiple interactions with precise location. Some common interaction motifs utilized in the biomolecular assembly include hydrophobic interaction, π–π

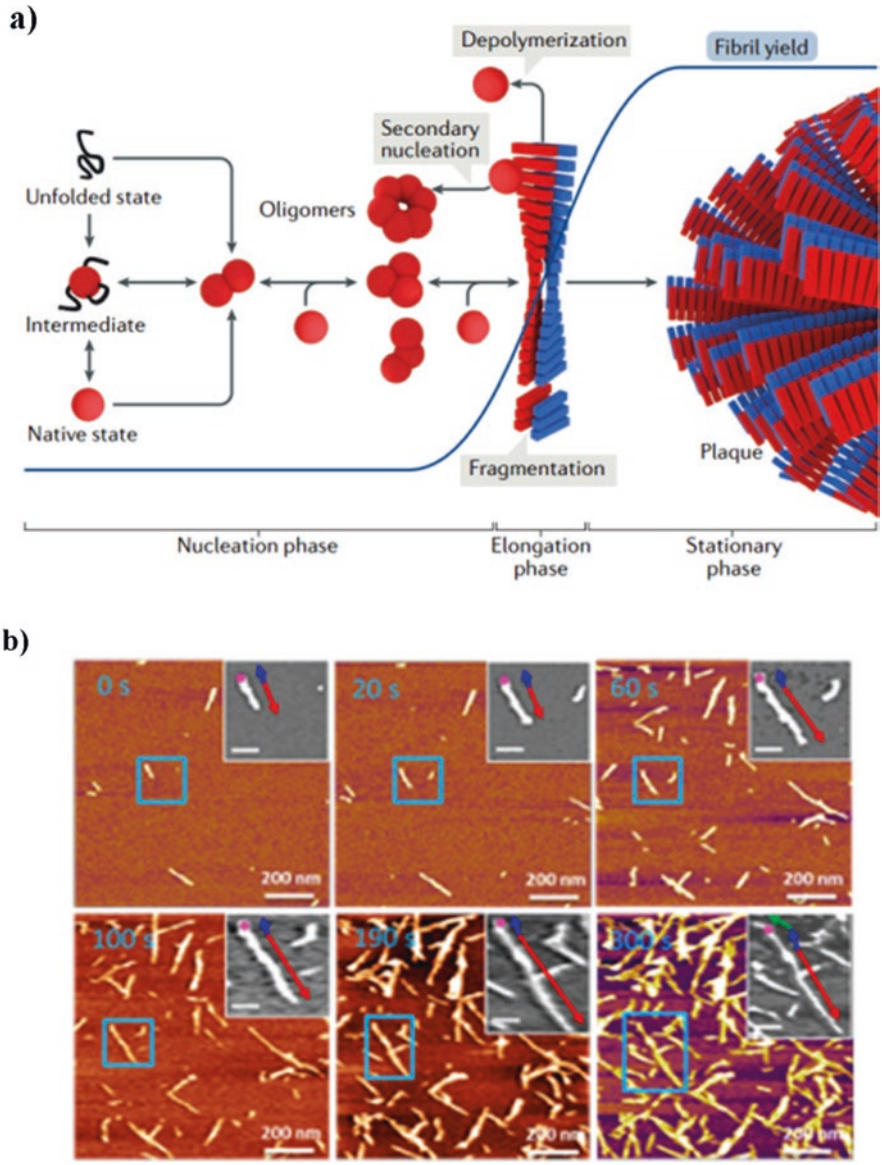

Fig. 5.2 (**a**) Schematic of amyloid formation [4]. (**b**) In situ AFM imaging of amylin$_{1\text{-}37}$ fibrillation. AFM imaging was performed immediately after sample deposition. Time lapsed images were captured at 0 s, 20 s, 60 s, 100 s, 190 s, and 300 s after AFM imaging, respectively. *Z* scale: 15 nm. Inset: zoomed-in AFM images of the blue squares marked in the panels. Scale bar: 50 nm [19]. Copyright 2019, ACS

stacking, hydrogen bonding, and cation–π interaction. Many efforts have been made available for investigating the interactions between amino acid sequence and peptide structures. Examples of widely explored strategies of peptide-based nanomaterials based on self-assembled β-sheet may include designing the amino acid sequence in the formation of β-strand, controlling the interactions between β-strand with β-sheet, or controlling the β-sheet assembly with β-sheet.

5.2.1 Primary Peptide Structures with Aggregation Propensity

Peptide assemblies are predominantly influenced by the interactions between side chains of the amino acids, especially the hydrophobic, charged, and polar residues. For example, Zhang et al. found residue repeats with $(HP)_n$ (hydrophilic-polar/charged) side chains in a yeast protein zuotin that can self-assemble into β-strand in vitro [20, 21]. Some similar patterns have been found in different peptide/protein with the self-assembled ability (Table 5.1) [15]. Many designed peptides were inspired by this discovery especially in designing nanofibrils (NFs) [22–27], including the famous peptide RADA16-I (RADARADARADARADA) which have been widely used in 3D cell culture, slow drug release and tissue engineering (Fig. 5.3a) [26]. Besides NFs, nanosheets can also be well designed utilizing the electrostatic interactions, which leads to the design of two-dimension peptide assemblies (Fig. 5.3b) [28]. Furthermore, this design strategy was also used for peptoid-based self-assembly nanomaterials [29, 30]. Nam et al. demonstrated growing extremely thin peptoid self-assembly nanosheets by periodic amphiphilicity, electrostatic recognition, and aromatic interactions of peptoid molecules (Fig. 5.3c, d) [29].

The usage and modification of natural β-strand amino acid sequences was also an efficient method to form β-strand. Table 5.1 listed some key sequences of β-strand protein or peptides segment [15]. Among them, KLVFFAE, a hydrophobic central domain (HCD) of $A\beta_{42}$, is widely studied and plays a key role in the formation of

Table 5.1 Key sequences of some amyloid peptides or proteins [15] Copyright 2018, ACS

Peptide or Protein Segment	*Amino Acid Sequence*
zuotin (306-339)	**EGARAEAEAKAKAEAEAKAKAESEAKANASAKAD**
RADA16-I	**CH_3CO-RADARADARADARADA-NH_2**
DN1	**QQRFQWQFEQQ**
Q11	**CH_3CO-QQKFQFQFEQQ-NH_2**
MAX1	**VKVKVKVKV^{D}PPTKVEVKVKV-NH_2**
p1/p2	**EEFKWKFKEE / KKFEWEFEKK**
CATCH+/CATCH-	**CH_3CO-QQKFKFKFKQQ-NH_2**
	CH_3CO-QQEFEFEFEQE-NH_2
amyloid-β	**KLVFFAE**

Note: black, green, blue, and red letters indicated amino acids having hydrophobic, polar, positively charged, and negatively charged side chains, respectively

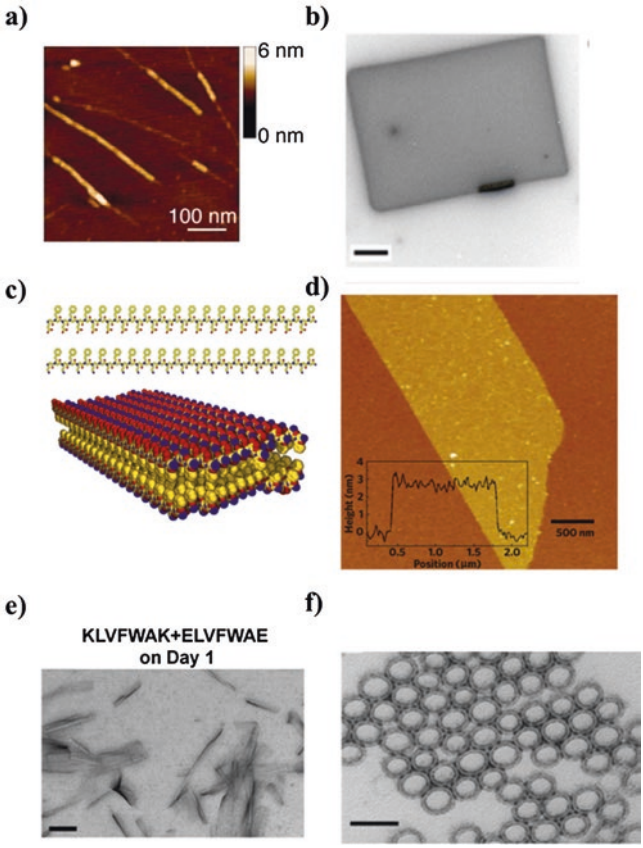

Fig. 5.3 (**a**) AFM image of RADA16-I nanofiber scaffold (0.5 × 0.5 μm) [26]. Copyright 2005, National Academy of Sciences, U.S.A. (**b**) TEM image of an individual NSI nanosheet (scale bar: 1 μm), and the amino acid sequence of NSI is $(Pro\text{-}Amp\text{-}Gly)_4$-$(Pro\text{-}Hyp\text{-}Gly)_4$-$(Glu\text{-}Hyp\text{-}Gly)_4$ [28]. Copyright 2014, ACS. (**c**) 2D crystalline sheets formed from two oppositely charged peptoid polymers (carbon, yellow; nitrogen, blue; oxygen, red). The modeled conformation shows that hydrophobic groups face each other in the interior of the sheet and oppositely charged hydrophilic groups are alternating and surface-exposed [29]. (**d**) Height-mode AFM image of a peptoid nanosheet (*Z* range: 20 nm) [29]. (**e**) TEM images of peptides mixtures (KLVFWAK and ELVFWAE, scale bar: 200 nm) [31]. Copyright 2018, RSC. (**f**) Cross-section of dried and flattened KLVFFAL nanotubes (scale bar: 100 nm) [32]. Copyright 2010, John Wiley and Sons

amyloid fibrils as mentioned above. Candreva et al. achieved hetero-assembly using two peptides of KLVFWAK and ELVFWAE, derived from KLVFFAE [31]. These peptides of KLVFWAK and ELVFWAE do not self-assemble but form flat nanotapes upon mixing and incubating for 24 h. The growth of the amyloid fibrils is stationary until the addition of the partners (Fig. 5.3e) [31]. Another congener of KLVFFAE, KLVFFAL can self-assembly as bilayer membranes, and formed nanotubes with (4 ± 1) nm wall thickness and (45 ± 10) nm diameter (Fig. 5.3f) [32].

The extensive analysis of aggregation propensity of amyloidal peptides may provide supportive evidences of the self-complementary interactions between amino acids at the level of individual residues [33–35]. In the parallel β structure, the side chains of individual amino acid interact with the identical ones in their vicinity. Thus one could qualitatively correlate the contributions to aggregation propensity from individual amino acid with the self-similar binding affinity of self-similar amino acids presented above. For example, phenylalanine (F) in Aβ and IAPP, and alanine (A) in myoglobin are identified to induce high aggregation propensity [35].

The full-fledged analysis of affinity would need to take into account contributions from all types of interactions that have been acknowledged in previous literatures. Rigorous consideration of the interaction characteristics will need systematic analysis of cooperativity in heterogeneous sequence peptides. Furthermore, binding kinetics should be considered to clarify the origins of such interaction characteristics. It should be noted that binding kinetics are depend on the chemical structures of side chains associated with varied types of interactions. For example, simulation analysis of association kinetics of polar peptide GNNQQNY (a N-terminal segment from the yeast prion Sup35) and hydrophobic peptide GGVVIA (a C-terminal segment of $A\beta_{42}$) revealed that the hydrophobic peptides form fibrils at a rate 1000 times faster than the polar peptide [36]. It is plausible to believe that inter-peptide binding kinetics will be keen to reveal the multiplicity of interactions in binding affinity.

As part of the endeavor to pursue the impacts of interactions between different amino acids to the overall inter-peptide interactions, a microbead-based flow cytometry method was used to determine the inter-amino acid interaction with homogeneous oligopeptides. Utilizing this method, a complete binding affinity matrix of 20×20 pairs of homo-octapeptides consisting of the 20 common amino acids can be obtained [37]. The results manifested that the side–side chain interaction and side–main chain interaction dominated the recognition of amino acid interaction, and provided a foundation for the study of amino acid specificity and selectivity of amino acids and the basis for peptide design of hydrophobic, charged, and polar side chains with specific secondary structures. This effort could provide a basis for analyzing specificity, polymorphisms, and selectivity of inter-amino-acid interactions, and understanding of binding interactions between the amino acids which are keen for peptide designs.

5.2.2 Nanostructures of Peptide Aggregates

Regulating the inter-amino-acid interactions is essential for designing strategy for peptide assemblies designing. Amyloid fibrils can be formed in either parallel β-sheet or antiparallel β-sheet as mentioned above [6]. Regulating the cross-strand pairing interaction can influence the arrangement of β-strand within β-sheet and achieve parallel or antiparallel β-sheet assembly. Researchers designed the

complementary peptides p1 (EEFKWKFKEE) and p2 (KKFEWEFEKK) with markedly different isoelectric point (pI) values based on a simple "*hphphp*" repeating pattern (*h* = hydrophobic residue, *p* = polar residue) that is known to favor β-sheet formation [38, 39]. With different placements of lysine (K) and glutamic acid (E) in two peptide segments, p1 and p2 can each solve in water but co-assemble into fibrils composed of antiparallel β-sheet structures (Fig. 5.4a) [39]. Under physiological conditions (pH 7.4), the termini of p1 and p2 should carry opposite charges, and the edges of fibrils will be patterned, which facilitates higher-order assembly into thicker fibrils, such as self-supporting hydrogels (Fig. 5.4b) [39]. In addition, utilizing the β-turn or a double proline hinge-V^{D}PPT is another strategy to achieve antiparallel β-sheet assembly [40, 41].

Changing the interaction of β-sheet to control the assembly of amyloid fibrils is another peptide design strategy in higher order. Achievement of designing the β-sheet into different specific morphologies like nanotubes or nanosheets should be

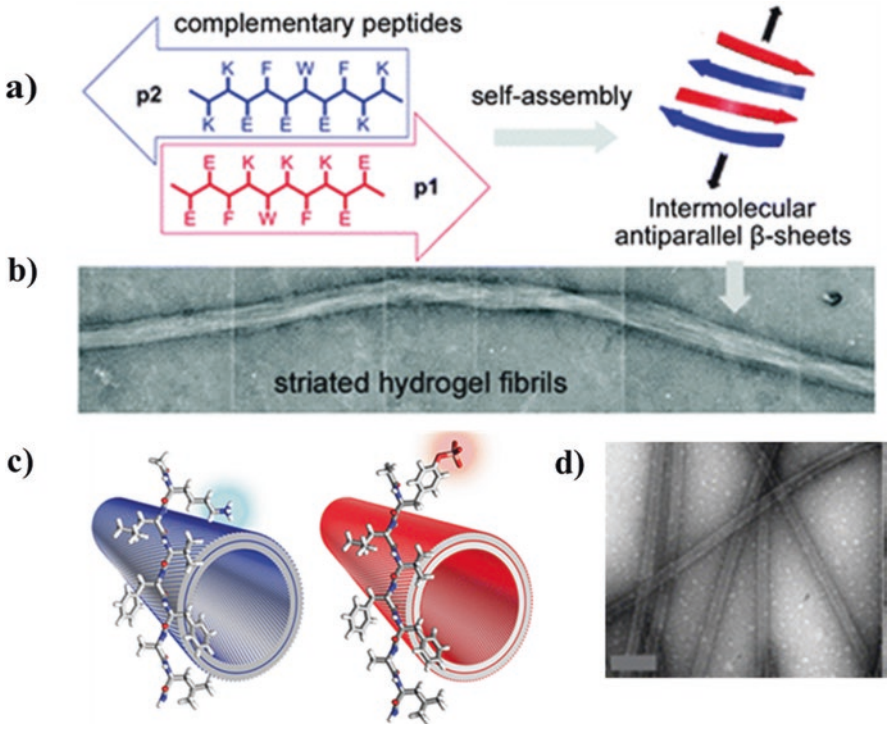

Fig. 5.4 (**a**) Schematic representation showing the proposed assembly of peptides of p1 (pI = 4.7) and p2 (pI = 9.7) into β-sheet structures, including an expanded view of each peptide showing their one-letter amino acid sequences [39]. Copyright 2016, RSC. (**b**) TEM image of fibrils observed in p1 and p2 self-supporting hydrogels [39]. Copyright 2016, RSC. (**c**) Model of (K16pY)(E22L) bilayer nanotubes, in which the N-terminal phosphotyrosine (pY) repeats every nanometer along each row [42]. Copyright 2014, ACS. (**d**) TEM image of (K16pY)(E22L) nanotubes without additional salts [42]. Copyright 2014, ACS

a challenge of such strategies. For example, Li et al. demonstrated that $A\beta_{(16-22)}$, Ac-KLVFFAE-NH_2, and Ac-KLVFFAL-NH_2 (E22L), can assemble into peptide bilayer nanotubes with diameters of 54 ± 3 nm and 32 ± 5 nm, respectively [42]. In this study, the authors synthesized the phosphotyrosine Ac-(pY) LVFFAL-NH_2 peptide (K16pY)(E22L), and found that this kind of peptide can form bilayer nanotubes with a diameter of 32 ± 3 nm (Fig. 5.4c, d) [42].

5.3 Self-Assembled Peptide-Based Biomaterials

Peptide-based fibrous structures, such as amyloid fibrils, have been developed as potential biomaterials with broad applications including 3D cell culture, tissue regeneration, and controlled-release [43, 44]. The amyloid-based biomaterials are distinguished from other synthetic polymeric materials due to their assumed biodegradability and biocompatibility. Also, rational design of the peptide sequence can be used to regulate folding patterns of amyloid peptide assemblies, while chemical modification of peptides can confer their structural diversity and functionality. Therefore, in some respects, amyloid-inspired bioactive materials usually may have higher efficacy in disease diagnosis and therapeutics than synthetic polymeric materials. For instance, the documented experimental results have revealed that amyloid peptides have been explored as important probes targeting tumor antigens and showed the improved binding affinity and selectivity to the tumor-associated antigens [45].

According to different applications in disease treatment, many efforts for constructing various amyloid-based nanostructures have been reported over the past 30 years. We will summarize some of the self-assembled peptide-inspired bioactive materials and their related applications. It should be noted that because this field is advancing rapidly, it is nearly unlikely to cover the entire field within this limited space. We therefore only outline the most talented approaches in the elaborate designs of amyloid peptide assemblies and related applications in tumor diagnosis and therapeutics. In order to have a comprehensive view, interested readers are encouraged to consult other related reviews and articles in this issue.

5.3.1 In Vitro Self-Assembled Peptide-Based Nanomaterials

In the closely related studies, self-assembled peptide-based nanomaterials have great advantages of higher stability and better performance than peptide monomers, which has widely been used in different kinds of fields. For instance, amyloid-based nanomaterials have been widely studied in vaccine development for epithelial tumors. In vaccine engineering, a major obstacle is low immunogenicity of the short peptides. To overcome this obstacle, researchers designed an amyloid-based vaccine strategy for tumor therapy [46, 47]. MUC1 proteins, which have a variable number of tandem repeats (VNTR) that bearing tumor-associated carbohydrate

antigens, normally overexpressed on almost all types of epithelial tumors [48]. Researchers therefore have a great interest in the development of antitumor vaccines based on MUC1 proteins. However, the VNTR sequence of MUC1 proteins, HGVTSAPDTRPAPGSTAPPA, has several potential glycosylation sites at Ser/Thr residues, but has low immunogenicity for vaccine development [48].

To solve this problem, a number of research groups synthesized MUC1 glycopeptides bearing T and Tn antigens conjugated to bovine serum albumin (BSA) at threonine 9 (T9) and/or serine 15 (S15) of the VNTR sequence [49, 50]. Immunization of Balb/c mice with these vaccines candidates indicated that the glycosylation of the VNTR sequence successfully enhanced the immune response. In 2012, Li's group constructed a totally synthetic, self-assembling, adjuvant-free MUC1 glycopeptide vaccine for tumor therapy [51]. Specifically, for this case, they designed four vaccine candidates H1, H2, H3, and H4, and these vaccine candidates contained full-length MUC1 VNTR domains (M1, M2, M3, and M4, respectively) conjugated to a Q11 domain (Ac-QQKFQFQFEQQ-Am) (Fig. 5.5a). The Q11 domain worked as both an adjuvant and a vaccine carrier because it can assemble into fibrils under mild condition (Fig. 5.5b). Immunization of mice with these self-assembly vaccine candidates revealed that, H3 and H4 elicited a higher immune response than H1 and H2. Compared to H4, H3 elicited the highest immune response, and the highest IgG titer was about 6400 (Fig. 5.5c). This study indicated that glycosylation of Tn antigen at threonine 9 (T9) residue in MUC1 VNTR was necessary for an effective immune response, which was agreement with the previous findings [48, 50]. Moreover, the self-assembling, glutamine-rich H3 and H4 showed more biocompatible and biodegradable than other vaccine carriers and delivery systems [51]. Consequently, these synthetic MUC1 glycopeptide-Q11 conjugates may represent novel vaccine candidates with well-defined formulation.

Also, researchers are interested in the development of antitumor self-assembly vaccine candidates based on chemical intramolecular reactions. For example, Mariusz et al. initiated an isopeptide strategy to obtain a variety of vaccine carrier systems based on "parent" peptides via the pH-triggered O-N acyl migration reaction (Fig. 5.5d) [52]. These "parent" peptides aggregated into the active form in a pH-controlled manner, which induced desired conformation structures of antigens (peptide epitopes) with reduced vaccine-associated side effects.

5.3.2 In Vivo Peptide Assemblies for Tumor Diagnosis and Therapeutics

From the above studies, we could identify that the assembly processes of amyloid-inspired bioactive materials for tumor-associated vaccine development were occurred under "in tube" and "in vitro" conditions. Recently, an "in vivo" self-assembly strategies have emerged, which displayed that peptides can self-assemble "in vivo" into bioinspired nanostructures for biomedical application [53–55].

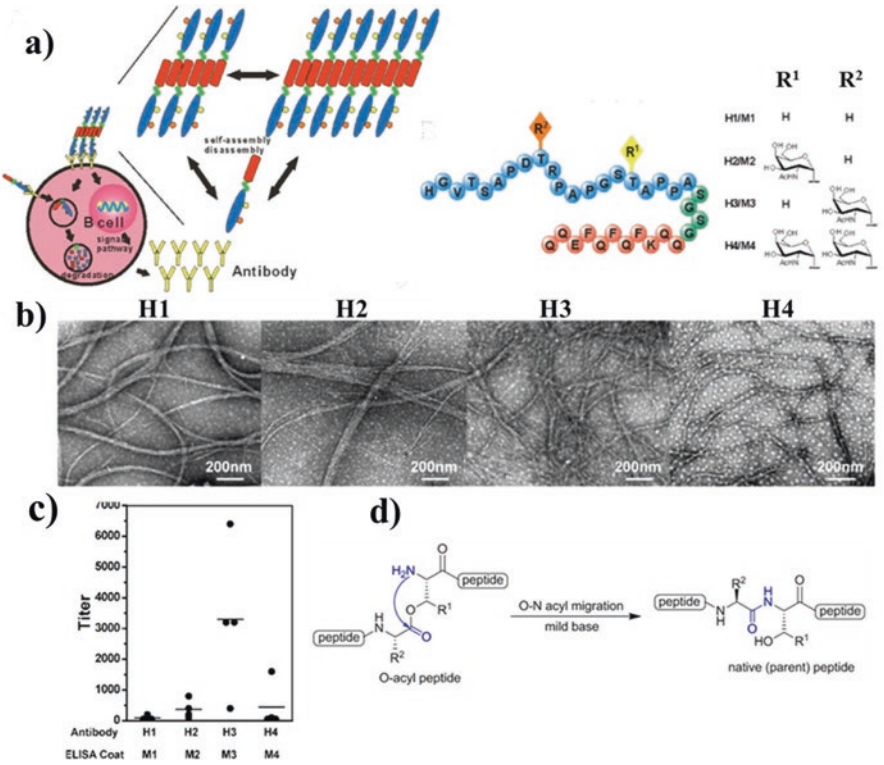

Fig. 5.5 (**a**) Schematic of designed vaccine candidates (H1, H2, H3, and H4) that can aggregate into fibrils and elicit activation of B cells [51]. Copyright 2012, ACS. (**b**) Four vaccine candidates aggregated into fibrils. Briefly, H1, H2, H3, and H4 (400 μM) samples were incubated at room temperature for 8 h, and imaged with a transmission electron microscope [51]. Copyright 2012, ACS. (**c**) ELISA results of anti-MUC1 IgG titers elicited by H1, H2, H3, and H4. Each black spot represented the titer value of serum of one mouse after the fifth immunization, and each black line represented the average value in each group [51]. Copyright 2012, ACS. (**d**) The pH-triggered O-N acyl migration reaction for "parent" peptide-vaccine design

Self-assembly of peptides can be modulated by pre-designed building blocks. In order to monitor the self-assembly process of peptides in vivo, researchers proposed a bispyrene (BP) molecule as a multifunctional building block (Fig. 5.6a, b). BP molecules show non-fluorescence in the monomeric state, but can self-assemble into nanoaggregates with the fluorescence emission (Fig. 5.6c, d) [56, 57]. BP and its derivatives can self-assemble in the physiological environment into various nanostructures arise from the hydrophobic and π–π interactions [57], which are successfully employed as ideal fluorescence nanoprobes [58]. Based on this optical property, the self-assembly process of peptide aggregates can be observed by BP nanoaggregates.

Natural peptides in biological systems support precision control with ordered secondary structures through hydrophobic and π–π interactions to form amyloid

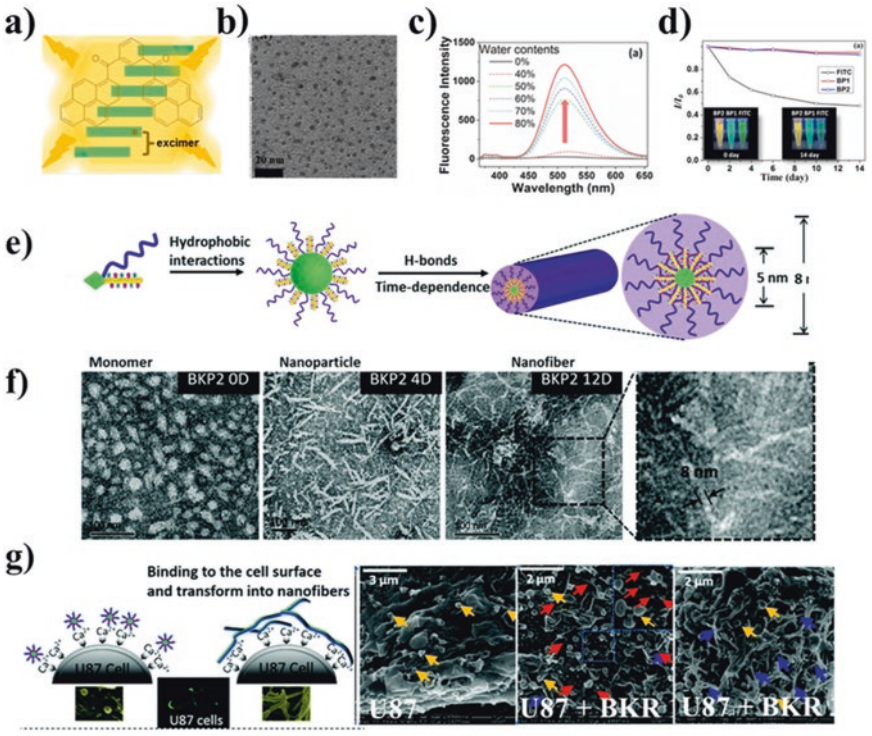

Fig. 5.6 (**a**) The structure of a BP molecule [57]. Copyright 2013, ACS. (**b**) The TEM image of the self-assembled BP nanoaggregates in mixed solvent of DMSO and H_2O [57]. Copyright 2013, ACS. (**c**) The fluorescence spectra of BP (25 μM) in the mixed DMSO/H_2O solution with different volume fractions of H_2O. The excitation wavelength is 340 nm [57]. Copyright 2013, ACS. (**d**) Time courses of fluorescence intensity change of BP (BP1 and BP2) nanoaggregates during 14 days, and fluorescence intensity change of FITC was shown for comparison [57]. Copyright 2013, ACS. (**e**) Schematic illustration of the self-assembled morphological transformation processes of BKP [62]. Copyright 2016, RSC. (**f**) The morphological transformation of BKP2 (25 μM) from NPs into NFs, which was monitored by TEM with time, scale bar: 100 nm [62]. Copyright 2016, RSC. (**g**) Schematic models (left) and SEM images (right) of BKR transformation from NPs into NFs over U87 tumor cell surfaces with different incubation times (left to right: 0 h, 1 h, and 3 h). Yellow arrows: irregular protrusions of U87 cell membranes, red arrows: BKR NPs, and blue arrows: BKR NFs [65]. Copyright 2016, RSC

oligomers and fibrils. This prompted the researchers to create and modify self-assembled peptide-based bioactive materials with a variety of biological applications. Unlike natural self-assembly process of peptides and proteins to form fibrils, the designed artificial amyloid-based materials display more abundant structures and morphologies, which determine their broad bio-applications. These peptide-based self-assemblies show the structure transformation under appropriate stimuli, such as photo-irradiation [59], pH [60], enzyme [61], and so on. This kind of morphologies transformation can be utilized to exhibit the advantages of each structure to realize ideal biological applications. However, due to the fact that in vivo

physiological conditions are very complicated, the precise transformation control by internal stimuli is difficult.

To solve this problem, researchers applied many methods to modulate the peptide structure transformation by molecular design. For instance, Wang et al. chose BP molecules functionalized with active moieties such carboxylic acid, amide, and bromide to modulate the self-assembly peptides [62]. The conjunction of BPs with KLVFF and PEG (BP-KLVFFG-PEG, BKP) can lead to transformation of NFs (Fig. 5.6e, f) [62]. The transformation into NFs in situ was faster with the increasing hydrophilic chain length [62], which meant that hydrophilic-lipophilic balance (HLB) played a central role in the morphology transformation of BKP [63, 64].

Additionally, researchers have found that ligand–receptor interactions could induce the further morphology transformation of peptide-based nanomaterials [65]. Wang et al. reported metal ion induced structural evolution of peptide-based nanostructures on specific tumor cell surfaces for inhibiting cellular viability [65]. Briefly, RGD has a high binding activity to integrin $\alpha_v\beta_3$, which is contributed by the interactions between RGD and the metal ions (Mg^{2+} and Ca^{2+}) at "metal ion-dependent adhesion site" (MIDAS) [66]. Due to the reason that BPs could form *J*-type aggregates in water and show strong fluorescence emission, BPs therefore were chosen as hydrophobic cores to not only induce self-assembly process but also monitor the aggregation by fluorescence. Also, The KLVFF sequence was chosen as a building block to induce fibrils formation [67]. As a result, the BP-KLVFF-RGD (BKR) self-assembled into NPs and further transformed into NFs in situ in the presence of Ca^{2+} metal ions, which could light up integrin $\alpha_v\beta_3$ overexpressed U87 tumor cells and inhibit their viabilities (Fig. 5.6g) [65]. This phenomenon is named as a transformation-enhanced accumulation and retention (TEAR) effect. It has been demonstrated that the transformation of NPs into NFs can be induced by different stimuli, such as pH, ligand, redox, and so on. Usually, NFs show better biological effects than NPs, including improved blood circulation, targeting, and accumulation behaviors [55].

In conclusion, a variety of physiological-stimuli-mediated regulations of self-assembled peptides on specific cell surfaces have been reported. These studies provide the insight how intermolecular interactions effect on the peptide-based superstructures in solutions and living cells, and show the potential how to utilize structural evolutions of peptides under specific physiological and pathological conditions for tumor diagnosis and therapeutics.

5.3.3 De Novo Design of Biologically Active Amyloid

"Almost every human protein has segments that can form amyloids, and the sticky aggregates known for their roles in diseases," says Jim Schnabel [7]. There are about 50 human proteins that known to be involved in the amyloid-associated pathologies [3, 4, 68]. More and more evidences indicate that amyloid aggregation of peptides and proteins are driven by short amyloidogenic sequence segments that

have the potential to self-assemble into amyloid structures [69–71]. In order to investigate whether endogenously expressed proteins that possess amyloidogenic potential but aggregate under specific physiological and pathological conditions could be induced to do so by seeding with a peptide consisting amyloidogenic fragments of their own sequences. Generally, compared to cross-seeding, it has been reported that amyloidogenic peptides and proteins are much more efficient at seeding aggregation of homotypic sequences [72]. This seeding concept is suitable for both in vitro and in vivo, even for these non-prion aggregation-associated peptides and proteins, which have since been termed as "prionoids" [73].

In 2016, Gallardo and collaborators chose vascular endothelial growth factor receptor 2 (VEGFR2) as a target protein due to the function of this protein is well characterized. We have known that VEGFR2 protein is not associated with amyloidosis. In order to ensure efficient seeding, Gallardo et al. designed and synthesized a synthetic amyloid peptide called vascin consisting of a tandem repeat of an amyloidogenic fragment of VEGFR2 signal peptide [45]. As shown in Fig. 5.7a, the amyloidogenic nature of the vascin peptide was observed by TEM, which revealed that vascin is a bona fide amyloidogenic peptide that forms typical amyloid fibrils of ~10 nm in width after 24 h of incubation time. Vascin fibrils can bind amyloid sensor dyes, including the amyloid-specific oligothiophene h-HTAA and ThT (Fig. 5.7b), which also confirmed that vascin is an amyloidogenic peptide that readily forms β-structured oligomeric aggregates that mature into amyloid fibrils. Co-immunoprecipitation of VEGFR2 protein from lysates of vascin- and scrambled vascin-treated HUVECs, and the data demonstrated that vascin could directly interact with VEGFR2 (Fig. 5.7c).

In order to confirm that vascin-mediated aggregation of VEGFR2 leads to dysfunction in HUVECs, authors determined the dose–response curve of vascin on ERK phosphorylation and VEGFR2 autophosphorylation after stimulating HUVECs with VEGF. As shown in Fig. 5.7d, e, HUVECs displayed a distinct dose-dependent inhibition with a median inhibitory concentration (IC_{50}) of 8.3 μM for ERK phosphorylation and 6.8 μM for VEGFR2 autophosphorylation. These data showed that vascin was internalized by HUVECs and directly bound to VEGFR2, resulting in the functional inactivation through VEGFR2 aggregation.

Also, to test the inhibitory effect of vascin on tumor growth, B16 melanoma cells were injected subcutaneously in the right dorsal flank of C57BL/6 mice. From the 4th day after tumor injection, mice were treated daily with vascin, scrambled vascin, vehicle (Tris-HCl) and kinase inhibitor PTK787. As shown in Fig. 5.7f, the curves of tumor growth volume were similar in C57BL/6 mice treated with scrambled vascin and Tris-HCl. However, the tumor growth was markedly reduced in mice that received the kinase inhibitor PTK787 orally. Specifically, compared with the PTK787-treated group, vascin-treated group showed comparable inhibition effect on tumor growth. The artificial amyloid model in this work provided an opportunity to discuss the relationship between the specific protein loss of function and amyloid toxicity. Although the mechanism of the tumor antigen recognition effect of amyloids is still not very clear, it is also attractive to develop amyloid-inspired bioactive materials for diseases treatment through improving the affinity and selectivity of

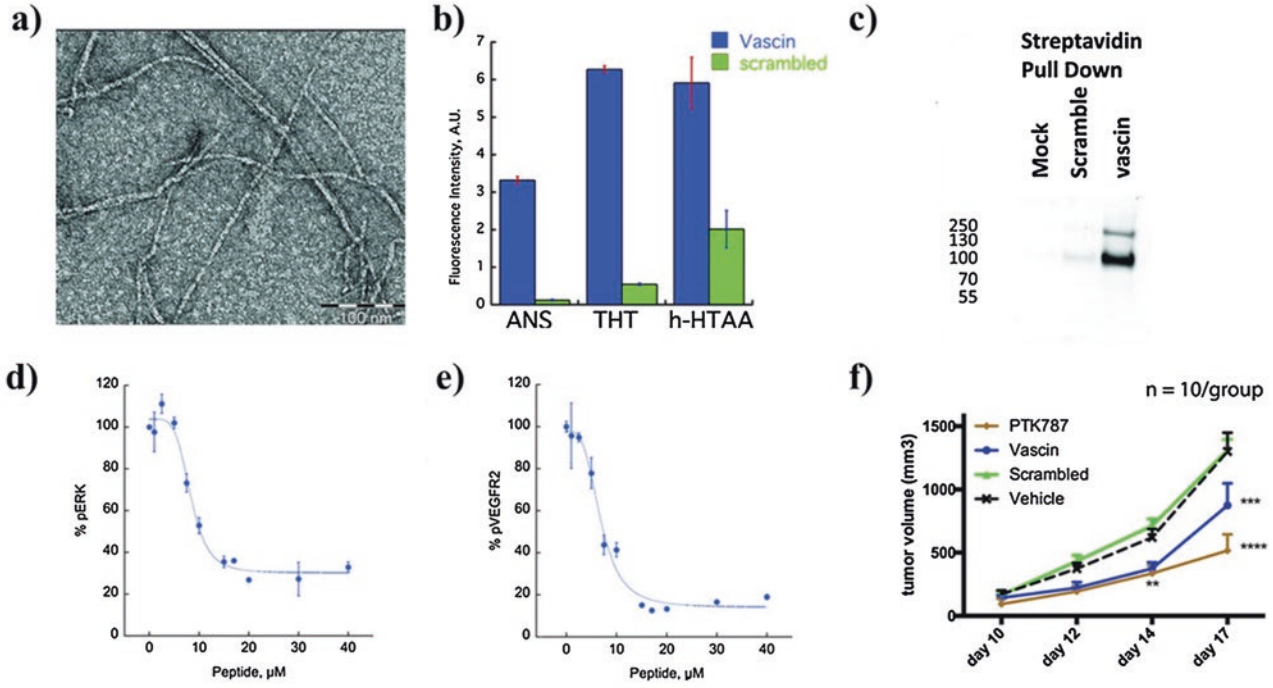

Fig. 5.7 (**a**) TEM image of 300 μM vascin in 1% (w/v) NH_4CO_3 and negatively stained with 2% (w/v) uranyl acetate. (**b**) Three different tinctorial analysis methods of vascin fibrils (300 μM). The bars show the mean of three measurements, and the error bars show the standard deviation (SD). (**c**) Western blot analysis for VEGFR2 co-immunoprecipitation in HUVECs after treatment with 20 μM PEG-biotin-labeled vascin for 4 h. (**d**) The effect of 2.5–40 μM vascin on VEGF stimulation of ERK phosphorylation in HUVECs. (**e**) The effect of 2.5–40 μM vascin on VEGF stimulation of VEGFR2 autophosphorylation in HUVECs. The data of (**d**) and (**e**) were shown as the mean of four replicates and the SD. (**f**) Tumor growth curves of C57BL/6 mice treated with 10 mg/kg PEG-biotin vascin. VEGFR2 tyrosine kinase inhibitor (PTK787) was chose as a positive control, and scrambled vascin and vehicle were chose as negative controls. Statistically significant differences were evaluated by ANOVA and Tukey multiple comparison testing [45]. Copyright 2016, AAAS

peptides to tumor antigens with molecular modulation and ration peptide design technologies.

Generally, in this chapter, starting from literatures related peptide-based fibrous structures via assembling processes and rational peptide design technologies developed for overcoming the intrinsic weaknesses of peptide-based amyloid, we also give a concise description of the recent advances of amyloid-inspired bioactive materials for tumor therapy based on in vivo self-assembly peptides, and de novo design of biologically active amyloid.

5.4 Peptide-Based Drug Delivery Systems

Therapeutic peptides have significantly impacted the development of the modern pharmaceutical industry and have contributed profoundly to the advancement of biological and chemical science. Over the past years, peptides are recognized for being highly selective and efficacious, and also relatively safe and well tolerated. Since peptide therapeutics are typically associated with lower production complexity and immunogenicity compared with protein-based pharmaceuticals, together with the possible higher selectivity and activity compared with small molecule-based drugs, peptides have gained a wide range of applications in disease diagnosis and therapies [74]. There is an increased interest in peptides in pharmaceutical research and development in recent 20 years [74]. According to the statistics, approximately 70 peptide drugs have been approved by Food and Drug Administration (FDA), and >170 peptide candidates are currently being evaluated in various stages of clinical development by 2017 [75].

However, even if many peptides have been widely investigated as potential drug candidates, both with in vitro and in vivo experiments, frequently they showed unfavorable physicochemical properties for clinical administration (such as low solubility and stability, nonspecific toxicity, and short circulating plasma half-life, etc.) [76]. In order to overcome these obstacles, peptide-based drug delivery systems (such as polymeric nanoparticles, micelles, liposomes, dendrimers, etc.) have been explored and shown to stabilize and modulate the transport and release of peptide monomers and assemblies. Such strategy was applied to emphasize the biological effects of these peptide monomers and assemblies, by means of encapsulating or even chemically conjugating these molecules over their surface with proper ligands, thus exhibiting targeting molecules with significant gain.

5.4.1 De Novo Designed Peptides for Drug Delivery Systems

In addition to the rational design techniques to improve the physicochemical stability in vitro and bioavailability in vivo of peptide therapeutics, the intrinsic weaknesses of conventional tumor therapies prompted the development and application

of a series of nanotechnologies for more effective and safer tumor therapies. Such therapeutic strategy is aimed to overcome the pharmacokinetic limitations of conventional drugs due to their ability to preferentially accumulate into tumor tissues through tumors' enhanced permeability and retention (EPR) effect as the result of their poor lymphatic drainage and pathologically leaky vasculature [77]. Literature survey revealed that, until now, more than 200,000 scientific research articles had been published on the theme of nanomedicines [78]. Several examples of nanomedicines that have been commercialized for tumor treatment, such as liposomal doxorubicin (Doxil®) and albumin-bound paclitaxel (Abraxane®) [79], and a large amount of nanomedicines are currently being evaluated in various stages of clinical development.

However, current nanomedicines could only mitigate adverse side effects but fail to enhance therapeutic efficacies of conventional drugs. Peptide-based molecular design and targeted therapy are attracting more and more attention due to their receptor selectivity and specificity. In recent years, therapeutic peptides have been utilized as targeting moieties of nanocarriers for the delivery of cargos (e.g., antitumor and anti-inflammatory) to specific organs, tissues, and cells with limited toxicity and unexpected biomedical effects. Herein, in this part, we will provide a brief introduction of nanomedicines by using targeted nanocarriers modified in composition and/or on surface with different kinds of peptides. Generally, possible strategies for peptide-based nanomedicine approaches that aim to enhance their therapeutic efficacies could be obtained:

1. ***by developing physical strategies*** capable of regulating the conformations and assembly structures of peptides for modulating their biological activity by introduction of nanostructures.
2. ***by developing active-targeting drug delivery strategies*** through peptide modification over nanocarrier surfaces, which is capable of binding specifically to the surfaces of target cells both in vitro and in vivo.
3. ***by developing effective prodrug strategies*** based on peptide-drug conjugates (PDCs) or nanostructures of self-assembling PDCs for targeted drug delivery**.**

Molecular chaperones, as an important part of the cellular quality control system in vivo, play pivotal roles in controlling undesired proteins (or peptides) misfolding and maintaining intricate proteostasis [80]. Inspired by nature, it is very compelling and promising to develop nanoparticles that represent molecular chaperones analogs to sequester the peptides and to prevent the formation of aggregates. Peptide molecules are incorporated into nanoparticles in a separate way, which can overcome formulation difficulties such as poor solubility and bioavailability.

Sterically stabilized micelle (SSM) is a self-assembled nanostructure of about 15–20 nm in diameter composed of PEGylated phospholipids [81]. The most frequently used phospholipid is the1,2-distearoyl-*sn*-glycero-3-phosphoethanolamine-*N*-[methoxy(polyethyleneglycol)-2000] (DSPE-PEG_{2000}, also termed as PEG-PE in this chapter), a biocompatible stealth material present in an already FDA-approved marketed product, Doxil® [82]. Liang's group found that PEG-PE micelle has a hydrophilic nano-cage with a negative charge layer in physiological environment,

which is similar to the 3D structure of GroEL [80, 83, 84]. GroEL-GroES has an ability to control undesired protein misfolding and aggregation, and promote efficient protein folding in vivo [80, 85]. Based on the perspective that similar structural characteristics may share general effects, PEG-PE micelle may have a potential to assist non-native protein (or peptide) refolding and avoid its aggregation.

To illustrate the refolding effects of micelle structures, Fang et al. investigated the renaturation effect of PEG-PE micelle on dithiothreitol (DTT)-denatured insulin [83]. As shown in Fig. 5.8a, when PEG-PE micelle and DTT were simultaneously added into insulin solution, the solution gradually became transparent with the increased molar ratios of PEG-PE micelle: insulin. Circular dichroism (CD) spectra results indicated that PEG-PE micelle could hinder the secondary structures transition of DTT-denatured insulin from α-helix to β-sheet, thus facilitating the formation of native insulin conformation in the presence of PEG-PE micelle (Fig. 5.8b). Mass spectrometric analysis exhibited that the peak of DTT-denatured insulin aggregates transformed into several peaks (Fig. 5.8c), including a peak of double A chains (MW: 4781 D), a peak of double B chains (MW: 6813 D) and a peak of mismatched A/B chains (MW: 5797 D). However, a distinct peak of native insulin was detected (MW: 5775 D, Fig. 5.8d) in the presence of PEG-PE micelle. Compared to DTT-induced insulin aggregates, the reduced insulin A and B chains in the presence of PEG-PE micelles are capable of recognizing each other and form native insulin molecules with yields of ~30% as measured by hypoglycemic activity analysis in mice (Fig. 5.8e). In another work, Fang and coworkers demonstrated that PEG-PE micelles-based molecular chaperones were also applicable for amyloid polypeptides, such as human islet amyloid polypeptide (hIAPP) [84].

The introduction of PEG-PE micelles was able to decrease the monomeric peptide concentration in solution, which disturbed the dynamic equilibrium between monomeric and oligomeric species and shifted the aggregation pathway from an "on-pathway" to an "off-pathway" mechanism. In another word, the ability to organize and encapsulate multiple active peptides into defined objects and spaces at the nanoscale has potential applications in biotechnology and nanotechnology.

Nanoparticle-based targeted delivery systems mainly include passive targeting such as EPR effect and active targeting such as specific-receptor-mediated targeting. Actually, nanomedicine delivery based on EPR has limitations due to EPR varies not only across different tumor types but also within different subregions of a single tumor tissue [79, 86]. Moreover, a dense fibrotic microenvironment may hinder the deep penetration of nanomedicines. Thus, depending on their size and surface properties, many peptide-encapsulated nanoparticles tend to accumulate in the perivascular space of target tissues trough EPR effect, but fail to reach the target cells. Therefore, this is only possible if the size of nanomedicines allows for deep tissue penetration and if the target is accessible. To solve it, active targeting is necessary to improve the permeation behavior of nanomedicines based on specific cellular uptake.

To achieve active targeting of nanomedicines, many approaches have been developed for conjugating targeting moieties onto nanoparticles, including antibodies, aptamers, and ligands [87]. Among them, peptide-conjugation is advantageous

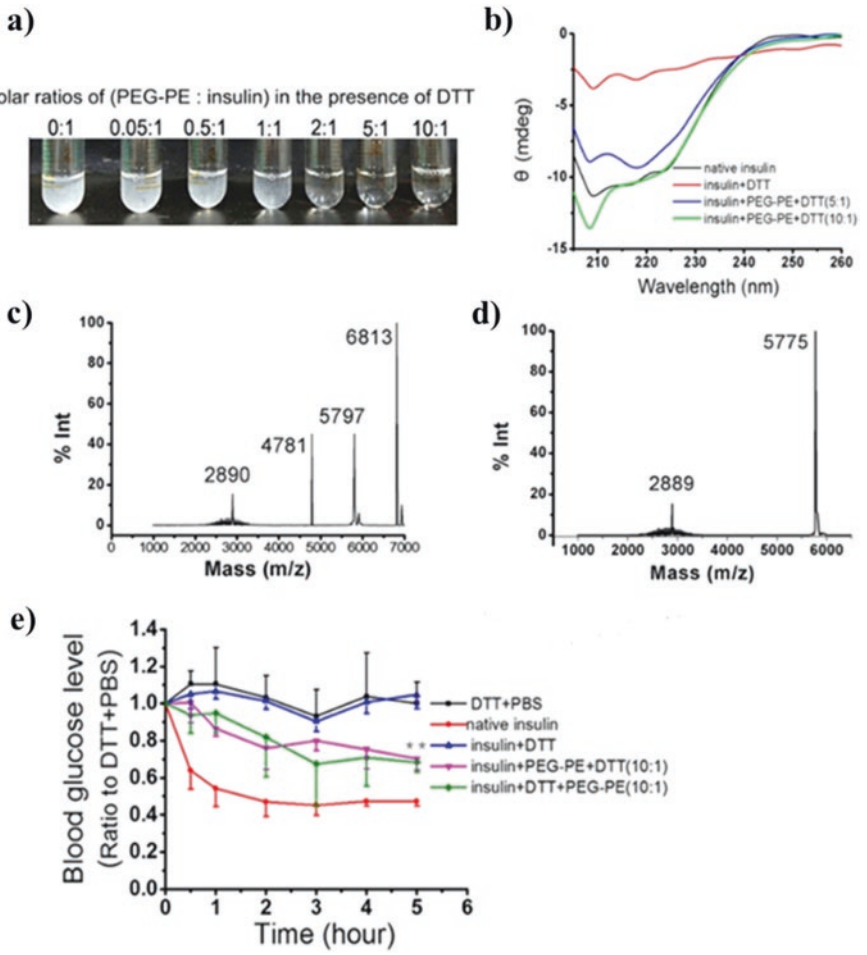

Fig. 5.8 (**a**) A photograph of the mixed solution of insulin (100 mM) and DTT (15 mM) in the absence and presence of PEG-PE micelles at different molar ratios of PEG-PE: insulin (varies from 0:1 to 10:1), after incubation at 37 °C for 24 h. (**b**) CD spectroscopy of insulin solutions in the absence and presence of DTT and PEG-PE micelles. (**c**) MALDI-TOF mass spectra of DTT-induced insulin aggregates. (**d**) MALDI-TOF mass spectra of DTT-induced insulin aggregates after PEG-PE treatment. (**e**) Hypoglycemic activity of insulin in BALB/c mice (5 U/kg body weight) with different treatments ($**p < 0.01$ by two-tailed Student's *T*-test) [83]. Copyright 2016, Elsevier

compared to other bioconjugation-based strategies because peptides have a higher or equal binding affinity and specificity to receptors than small molecules and proteins [88]. Compared with proteins, it is much easier to optimize peptide amino acid sequences to obtain an ideal targeting ligand. Importantly, peptides are readily made by good manufacturing practice because they do not require humanization.

Therefore, peptide-modified nanoparticles have been widely investigated for improving their active-targeting abilities.

As an example, vemurafenib is a chemotherapeutic drug approved by FDA to treat melanoma [89], but the oral administration of this drug readily causes severe side effects with limited therapeutic efficacy. Although liposomes were supposed to enhance the solubility in vitro and bioavailability in vivo of vemurafenib [90, 91], however, the low skin permeability of liposome formulation limits its widespread application through transdermal administration [92]. Zou et al. developed a peptide-modified vemurafenib-loaded liposome (Vem-TD-Lip) for the targeted inhibition of subcutaneous melanoma via the skin (Fig. 5.9a) [93]. The peptide of TD (ACSSSPSKHCG) has an advantage to open the paracellular pathway temporarily, which facilitates vemurafenib penetrate the skin and reduces undesired damages to normal organs [94]. As shown in Fig. 5.9b, c, the antitumor efficiency of Vem-TD-Lip delivered through the skin was significantly much better than through intravenous injection and oral administration. This work provided a strategy to achieve targeted delivery of nanoparticles by modifying liposomes with biologically inspired peptides.

In another work, Wei et al. used a new tumor-penetrating peptide, CRGDK, to conjugate onto the surface of doxorubicin-encapsulated nanomicelles (TPFM-Dox, Fig. 5.9d) [95]. As shown in Fig. 5.9e, f, the peptide-conjugated nanomicelles can effectively target MDA-MB-231 tumor cells that overexpressing neuropilin-1 (Nrp-1) receptors associated with tumor angiogenesis and tumor growth [96, 97]. Compared with doxorubicin-encapsulated nanomicelles (M-Dox) without CRGDK peptide, TPFM-Dox can specifically bind to MDA-MB-231 cells, which leads to the enhanced cellular uptake and cytotoxicity in vitro (Fig. 5.9g). Also, as shown in Fig. 5.9h, TPFM-DiR showed higher tumor targeting and penetrating efficiency than M-DiR in vivo with the assistance of tumor-penetrating peptide. The primary goal of effective drug delivery in tumor therapy is to transport sufficient drugs to target disease sites while minimizing their exposure to healthy tissues. The above results demonstrated that peptide-modified nanoparticles could improve the penetration and biological effects of encapsulated-drugs both in vitro and in vivo.

Compared with the active-targeting delivery vehicle strategy, the prodrug method features minimized premature drug liberation and fewer amounts of inert materials, both of which can lighten the metabolic burden of the patients and in turn enhance their therapeutic efficacy [98–100]. PDCs are an emerging class of prodrugs, formed through the conjugation of a specific peptide to a drug via a chemical linker. The utilization of peptides allows for the incorporation of great degree of functionality into PDCs, as the amino acid sequence can be chosen both to control the physicochemical properties, and also to achieve active targeting with particular receptors on tumor cells. The diversity of amino acid combinations enables the facile preparation of different PDCs, and the control over the amino acid sequence allows tuning of the overall conjugate hydrophobicity and ionization, both of which increases solubility and improves selectivity to target tumor cells [101, 102]. More significantly, an emerging subset of PDCs seeks to combine the advantages of peptide-based prodrugs with delivery vehicle strategy, giving rise to self-assembling PDCs in which

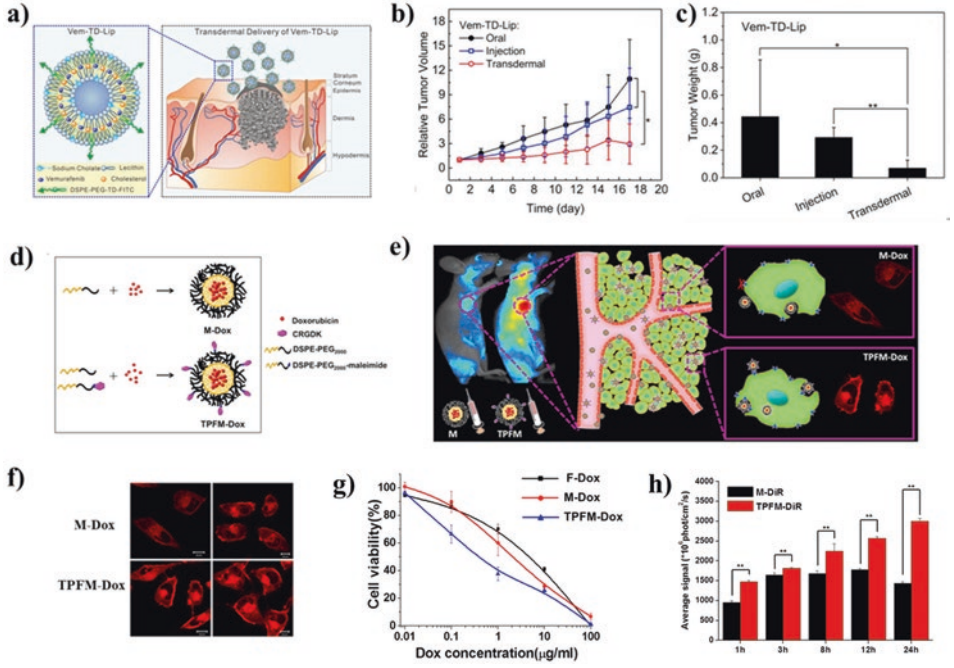

Fig. 5.9 (**a**) Schematic illustrations of Vem-TD-Lip [93]. Copyright 2018, Elsevier. (**b**) The changes in relative tumor volume over time (0–17 days) through three different administration routes (oral, injection, and transdermal) [93]. Copyright 2018, Elsevier. (**c**) Comparison of tumor weights after Vem-TD-Lip treatment through three different administration routes after 18 days [93]. Copyright 2018, Elsevier. (**d**) Schematic illustrations of the preparation of M-Dox and TPFM-Dox [95]. Copyright 2013, ACS. (**e**) Schematic diagram of M-Dox transport behaviors in the absence and presence of tumor-penetrating peptide (CRGDK) [95]. Copyright 2013, ACS. (**f**) Confocal images of MDA-MB-231 cells treated with M-Dox and TPFM-Dox at 10 μg/mL for 0.5 h (left) and 1 h (right) [95]. Copyright 2013, ACS. (**g**) In vitro cytotoxicity of free Dox, M-Dox, and TPFM-Dox against MDA-MB-231 cells, which were tested using MTT assay [95]. Copyright 2013, ACS. (**h**) Average fluorescence signals of tumor tissues at different time points of 1, 3, 8, 12, and 24 h after M-DiR and TPFM-DiR treatment. The asterisk (∗∗) represents data points that have highly significant differences ($p < 0.01$, two-tailed Student's t tests) [95]. Copyright 2013, ACS

the individual conjugates possess the ability to form nanostructures with physicochemical properties unique to those of the components.

Typically an amphiphilic PDC contains three essential components: the therapeutic agent, the rationally designed or chosen peptide, and the chemical linker that bridges the two. Figure 5.10a represents PDC bearing one drug (1) or two different types of drugs (2), and the amphiphilic PDCs (APDCs) are designed to spontaneously associate in aqueous solutions into a variety of stable nanostructures (such as NFs) (3) [103]. As an example, Liang and coworkers synthesized four amphiphilic PDCs using maytansinoid (DM1) as a cytotoxic drug, cRGDfK as a homing peptide, and disulfide (SS) or thioether (SMCC) as a chemical linker [104]. Owing to their amphiphilicity, the amphiphilic PDCs could self-assemble into nanoparticles (APDC@NPs) (Fig. 5.10b). The authors evaluated the antitumor effects of different kinds of APDC@NPs by different cell lines (in vitro) and in tumor-bearing C57BL/6 mice (in vivo). Lots of evidences confirmed that cRGDfK is able to specifically target $\alpha_v\beta_3$ integrin-overexpressing tumor cells and display excellent therapeutic efficacy. As indicated in Fig. 5.10c, in $\alpha_v\beta_3$-positive melanoma B16 tumor cells and tissues, APDC@NPs were effectively accumulated at the tumor sites by EPR effect, and their uptakes by B16 tumor cells were significantly improved via $\alpha_v\beta_3$ receptor-mediated endocytosis. Thanks to the dual targeting strategies that contributed by cRGDfK-mediated active targeting and nanoparticles-mediated passive targeting, APDC@NPs did significantly decrease the toxicity of free DM1 and greatly improve their therapeutic outcome (Fig. 5.10d, e). Specifically, the active APDC@NPs (RCCD@NPs & RSSD@NPs) showed better antitumor effects than the passive ones (QCCD@NPs & QSSD@NPs), which implied that peptide-mediated active targeting played a central role in the improvement of antitumor effect. Although their formulation remains challenging, PDCs and APDC-based self-assembled nanomaterials provide an insight for the design and development of active-targeting nanomedicines to treat tumor conditions in the future.

5.4.2 Peptide-Aggregate-Based Drug Delivery Systems

Atomic and molecular level studies have showed that, amyloid formation is driven by short amyloidogenic fragments within a protein that have the potential to self-assemble into β-sheet ribbons to form the characteristic cross-β-structured spine of amyloid structures [7, 69–71]. Compared with single peptide molecule, amyloid have a higher binding affinity to tumor-associated antigens due to their molecule cluster effects. However, frequently they displayed unfavorable chemical and physical properties as medicine candidates for diseases treatment, such as poor solubility, low bioavailability, uncontrollable toxicity, and so on. Nanomedicine strategy may have the ability to stabilize spatial conformation and improve biological effects of amyloid. Literatures have reported that the nanoparticles can enhance the local topographic interactions between the nanostructures and nanoscaled components of the cellular surface, such as folopodia and lamellipodia [105–107].

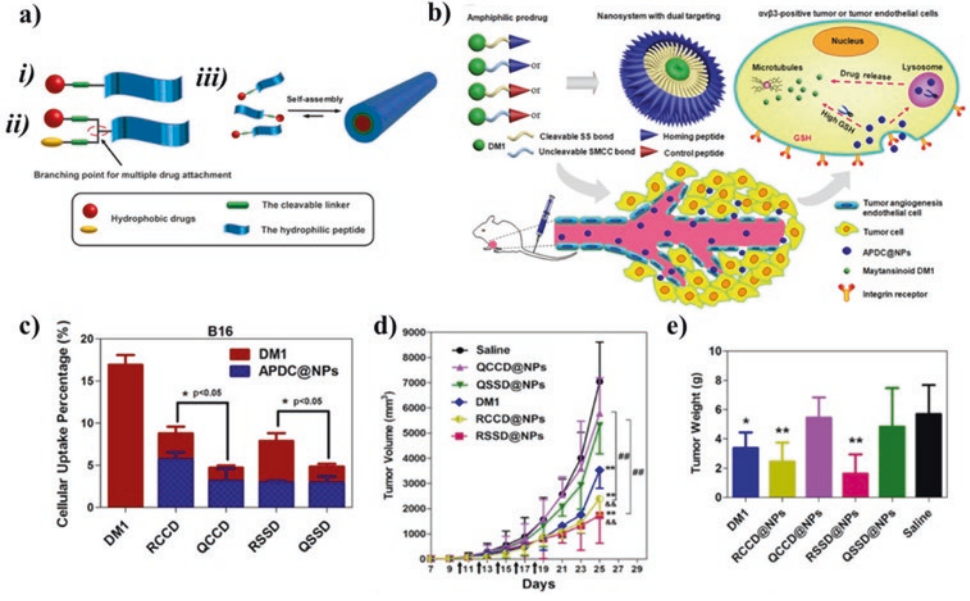

Fig. 5.10 (**a**) Scheme of PDCs bearing one drug (*i*) or two different types of drugs (*ii*), and APDC-based self-assembled nanostructures (*iii*) [103]. Copyright 2017, Elsevier. (**b**) Schematic illustrations of the self-assembly and in vivo delivery behaviors of APDC@NPs based on four APDCs molecules: cRGD-SMCC-DM1 (RCCD), cRGD-SS-DM1 (RSSD), cRPQ-SMCC-DM1 (QCCD), and cRPQ-SS-DM1 (QSSD) [104]. Copyright 2017, IIP. (**c**) Intracellular concentrations of DM1 determined by high performance liquid chromatography (HPLC) in B16 tumor cells after treatments with different APDC@NPs at a drug dose of 100 nM (calculated by free DM1, $*p < 0.05$, p = ns versus the uptake of passive cRPQfK group) [104]. Copyright 2017, IIP. (**d**) Tumor growth curves of B16 tumor-bearing C57BL/6 mice after intravenous administrations of saline, DM1, and different APDC@NPs. All formulations were given every other day for a total of five times via tail vein at the dosage of 400 μg/kg (calculated by free DM1). Black arrows indicate the injection time after tumor cell inoculation ($**p < 0.01$ versus the saline control, $^{\&\&}p < 0.01$ versus the free DM1 group and $^{\#\#}p < 0.01$ versus the passive cRPQfK group) [104]. Copyright 2017, IIP. **(e)** The weight of the excised tumor masses from different groups of DM1, and different APDC@NPs treatment. Each bar represents mean ± SD ($n = 6$). $*p < 0.05$ and $**p$ <7#x00A0;0.01 versus the saline control [104]. Copyright 2017, IIP

As an example, an isolation method was developed for circulating tumor cells (CTCs) with high efficiency by using the EpCAM recognition peptide functionalized iron oxide magnetic nanoparticles (MNPs) (Pep@MNPs) (Fig. 5.11a) [108]. The de novo designed peptide (VRRDAPRFSMQGLDACGGNNCNN) was modified on the surfaces of MNPs via biotin–avidin interaction. The kinetic parameters of the peptide binding to EpCAM were investigated with anti-EpCAM as a positive control, using the surface plasma resonance (SPR) technique. As shown in Fig. 5.11b, Pep@MNPs exhibited comparable binding affinity K_D (1.98×10^{-9} mol/L) to that of the anti-EpCAM (2.69×10^{-10} mol/L). To further determine the interactions between tumor cells and Pep@MNPs, many Pep@MNPs (as shown in red rings) can still be observed to attach on the surface of MCF-7 cells (Fig. 5.11c). Interestingly, MCF-7 cells captured by the Pep@MNPs exhibited more filopodia (Fig. 5.11c, below) than cells without Pep@MNP treatment. Authors deduce that, in addition of the high binding ability of peptide aggregates to EpCAM, MNPs-induced nanoscaled components of folopodia and lamellipodia also contribute to an improved interaction between tumor cells and Pep@MNPs.

In another work, the layer-by-layer (LbL) approach for multilayer assembly provides an excellent way to build up desired films using a range of functional materials, including DNA, proteins, nanoparticles, and nanowires [109–111]. In order to effectively control glycemic stability in patients with type 2 diabetes, Lin and collaborators developed multilayer nano-films incorporating insulin nanoparticles through pH-shift precipitation and crystal disassembly at room temperature [112]. As shown in Fig. 5.11d, LbL multilayer film incorporating insulin nanoparticles was fabricated with poly(allylamine hydrochloride) (PAH) and poly(acrylic acid) (PAA), which was indicated herein as Si/$(PAH/PAA)_5$(PAH/PAA-insulin NPs)n. At a pH of 4.5, the positively charged insulin NPs were encapsulated into the LbL film to form PAA-insulin NP aggregates and were released in PBS buffer (pH 7.4) through electrostatic interactions. Additionally, the insulin-incorporated multilayer was swollen due to different ionic environments, which led to insulin release. To determine insulin release behaviors from LbL multilayer films, about 80% of the insulin was released from the LBL film in PBS buffer solution in the first stage of 3 h, and the sustained long-term release could be observed to last for up to approximate 7 days (Fig. 5.11e). These findings could provide novel directions in establishing insulin-based amyloid delivery systems for type 2 diabetes treatment.

Although most neurodegenerative diseases are related to the deposition in tissues of pathogenic aggregates that are composed of misfolded proteins in the form of amyloid fibrils and plaques [68, 113–115], numerous hormones, such as prolactin, growth hormone, and chromogranin, are stored in self-assembled aggregates (e.g., hydrogels) and released slowly into the systemic circulation in vivo [116, 117]. Inspired by nature, with tunable numbers and sequences of amino acids, peptides show significant importance in self-assembly materials due to their designability and biocompatibility [118]. The defining feature of amyloid peptide assemblies is the utilization of synthetic chemistry to make nanoscale peptide building blocks of different shape and size, composition and surface charge, structure, and functionality. This effort is also representative of the advances in nanoscience which is

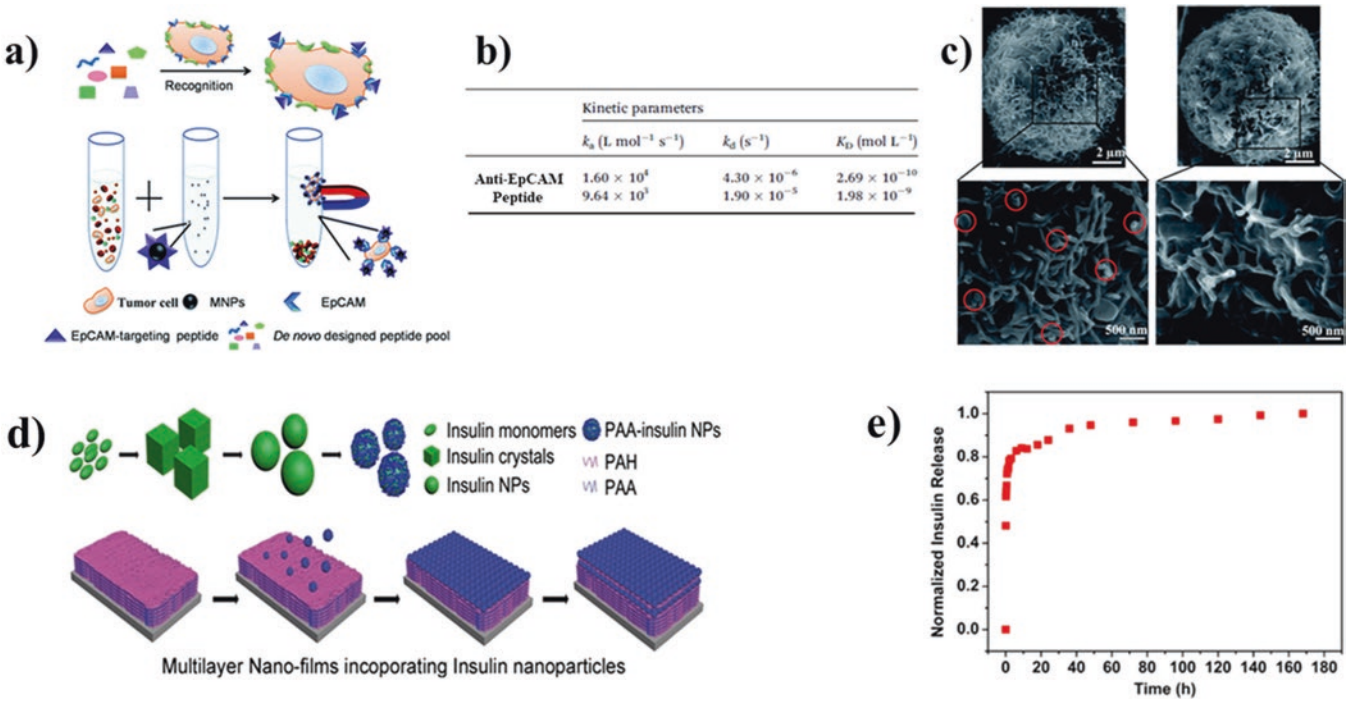

Fig. 5.11 (**a**) Schematic diagram of CTC isolation with MNPs modified with an EpCAM targeting peptide [108]. Copyright 2014, RSC. (**b**) Kinetic parameters for the binding of EpCAM targeting antibody and peptide to EpCAM by SPR [108]. Copyright 2014, RSC. (**c**) Environmental scanning electron microscopy (ESEM) images (top) and enlarged ESEM images (below) of the MCF-7 tumor cells captured by Pep@MNPs (left) or without MNPs (right) [108]. Copyright 2014, RSC. (**d**) Schematic diagram of the film assembly of Si/(PAH/PAA)$_3$/(PAH/PAA-insulin NPs)n using LbL technique [112]. Copyright 2015, Elsevier. (**e**) Normalized insulin release profile obtained in PBS buffer at 37 °C by fluorescence intensity detection of FITC-labeled insulin [112]. Copyright 2015, Elsevier

concerned with making, manipulating, and imaging materials having at least one spatial dimension in the size range of 1–1000 nm [119]. Assembly of such architectures may be achieved through spontaneous or templated self-assembly, or may be obtained by lithographically or chemically directed.

5.5 Conclusions

Many peptides and proteins have been demonstrated to form amyloids via assembly. This chapter highlighted the remarkable progresses in structure analysis and assembly mechanisms of amyloid peptides at the level of individual amino acids. With the stable nanostructures formed by conjugation-induced assembly and self-assembly, amyloid peptide assemblies are able to achieve a long circulation time with high selectivity and specificity for tumor-associated antigens, which can enhance the antitumor effect both in vivo and in vitro.

References

1. W.T. Astbury et al., The X-ray interpretation of denaturation and the structure of the seed globulins. Biochem. J. **29**(10), 2351–2361 (1935)
2. L. Goldschmidt et al., Identifying the amylome, proteins capable of forming amyloid-like fibrils. Proc. Natl. Acad. Sci. U. S. A. **107**(8), 3487–3492 (2010)
3. J.D. Sipe et al., Amyloid fibril proteins and amyloidosis: Chemical Identification and Clinical Classification International Society of Amyloidosis 2016 Nomenclature guidelines. Amyloid **23**(4), 209–213 (2016)
4. M.G. Iadanza et al., A new era for understanding amyloid structures and disease. Nat. Rev. Mol. Cell Biol. **19**(12), 755–773 (2018)
5. M. Goedert et al., Cloning and sequencing of the cDNA encoding a core protein of the paired helical filament of Alzheimer disease: Identification as the microtubule-associated protein tau. Proc. Natl. Acad. Sci. U. S. A. **85**(11), 4051–4055 (1988)
6. T. Robert, R.B. Wickner, Molecular structures of amyloid and prion fibrils: consensus versus controversy. Acc. Chem. Res. **46**(7), 1487–1496 (2013)
7. S. Jim, Protein folding: the dark side of proteins. Nature **464**(7290), 828–829 (2010)
8. M.H. Tattum et al., Elongated oligomers assemble into mammalian PrP amyloid fibrils. J. Mol. Biol. **357**(3), 975–985 (2006)
9. S. Carsten, F.N. Marcus, G. Nikolaus, Paired beta-sheet structure of an Abeta(1-40) amyloid fibril revealed by electron microscopy. Proc. Natl. Acad. Sci. U. S. A. **105**(21), 7462–7466 (2008)
10. L. Gremer et al., Fibril structure of amyloid-β(1-42) by cryo-electron microscopy. Science **358**(6359), 116–119 (2017)
11. X. Ma et al., Amyloid β (1–42) folding multiplicity and single-molecule binding behavior studied with STM. J. Mol. Biol. **388**(4), 894–901 (2009)
12. L. Liu et al., Chaperon-mediated single molecular approach toward modulating Aβ peptide aggregation. Nano Lett. **9**(12), 4066–4072 (2009)
13. I. Stensgaard, Adsorption of di-l-alanine on Cu(110 ja:math) investigated with scanning tunneling microscopy. Surf. Sci. **545**(1-2), L747–L752 (2003)

14. M. Xiaobo et al., Sequence effects on peptide assembly characteristics observed by using scanning tunneling microscopy. J. Am. Chem. Soc. **135**(6), 2181–2187 (2013)
15. C.J. Wilson et al., Biomolecular assemblies: moving from observation to predictive design. Chem. Rev. **118**(24), 11519–11574 (2018)
16. L.V.H. Rd, Thioflavine T interaction with synthetic Alzheimer's disease beta-amyloid peptides: detection of amyloid aggregation in solution. Protein Sci. **2**(3), 404–410 (1993)
17. N.M. Kad et al., Hierarchical assembly of β 2 -microglobulin amyloid in vitro revealed by atomic force microscopy. J. Mol. Biol. **330**(4), 785–797 (2003)
18. T. Watanabe-Nakayama et al., High-speed atomic force microscopy reveals structural dynamics of amyloid Î²1-42 aggregates. Proc. Natl. Acad. Sci. U. S. A. **113**(21), 5835–5840 (2016)
19. Q. Huang et al., In situ observation of amyloid nucleation and fibrillation by FastScan atomic force microscopy. J. Phys. Chem. Lett. **10**(2), 214–222 (2019)
20. S. Zhang et al., Zuotin, a putative Z-DNA binding protein in Saccharomyces cerevisiae. EMBO J. **11**(10), 3787–3796 (1992)
21. S. Zhang et al., Spontaneous assembly of a self-complementary oligopeptide to form a stable macroscopic membrane. Proc. Natl. Acad. Sci. U. S. A. **90**(8), 3334–3338 (1953)
22. R. Shyam et al., D-periodic collagen-mimetic microfibers. J. Am. Chem. Soc. **129**(47), 14780–14787 (2007)
23. L.E. O'Leary et al., Multi-hierarchical self-assembly of a collagen mimetic peptide from triple helix to nanofibre and hydrogel. Nat. Chem. **3**(10), 821–828 (2011)
24. X. Fei et al., Compositional control of higher order assembly using synthetic collagen peptides. J. Am. Chem. Soc. **134**(1), 47–50 (2012)
25. R.J. Swanekamp et al., Coassembly of enantiomeric amphipathic peptides into amyloid-inspired rippled β-sheet fibrils. J. Am. Chem. Soc. **134**(12), 5556–5559 (2012)
26. H. Yokoi et al., Dynamic reassembly of peptide RADA16 nanofiber scaffold. Proc. Natl. Acad. Sci. U. S. A. **102**(24), 8414–8419 (2005)
27. L. Wang et al., Designed graphene-peptide nanocomposites for biosensor applications: a review. Anal. Chim. Acta **985**, 24–40 (2017)
28. T. Jiang et al., Structurally defined nanoscale sheets from self-assembly of collagen-mimetic peptides. J. Am. Chem. Soc. **136**(11), 4300–4308 (2014)
29. K.T. Nam et al., Free-floating ultrathin two-dimensional crystals from sequence-specific peptoid polymers. Nat. Mater. **9**(5), 454–460 (2010)
30. R. Kudirka et al., Folding of a single-chain, information-rich polypeptoid sequence into a highly ordered nanosheet. Biopolymers **96**(5), 586–595 (2011)
31. J. Candreva et al., Hetero-assembly of a dual beta-amyloid variant peptide system. Chem. Commun. (Camb.) **54**(49), 6380–6383 (2018)
32. W.S. Childers et al., Peptides organized as bilayer membranes. Angew. Chem. Int. Ed. Engl. **49**(24), 4104–4107 (2010)
33. M.R. Sawaya et al., Atomic structures of amyloid cross-beta spines reveal varied steric zippers. Nature **447**(7143), 453–457 (2007)
34. J.J. Wiltzius et al., Molecular mechanisms for protein-encoded inheritance. Nat. Struct. Mol. Biol. **16**(9), 973–978 (2009)
35. G.G. Tartaglia et al., Prediction of aggregation-prone regions in structured proteins. J. Mol. Biol. **380**(2), 425–436 (2008)
36. G. Reddy, J.E. Straub, D. Thirumalai, Dry amyloid fibril assembly in a yeast prion peptide is mediated by long-lived structures containing water wires. Proc. Natl. Acad. Sci. U. S. A. **107**(50), 21459–21464 (2010)
37. H. Du et al., Principles of inter-amino-acid recognition revealed by binding energies between homogeneous oligopeptides. ACS Cent. Sci. **5**(1), 97–108 (2019)
38. C.E. MacPhee et al., Engineered and designed peptide-based fibrous biomaterials. Curr. Opin. Solid State Mater. Sci. **8**(2), 141–149 (2004)
39. P.J. King et al., A modular self-assembly approach to functionalised beta-sheet peptide hydrogel biomaterials. Soft Matter **12**(6), 1915–1923 (2016)

40. R.V. Rughani et al., Folding, self-assembly, and bulk material properties of a de novo designed three-stranded beta-sheet hydrogel. Biomacromolecules **10**(5), 1295–1304 (2009)
41. C. Sinthuvanich et al., Triggered formation of anionic hydrogels from self-assembling acidic peptide amphiphiles. Macromolecules **50**(15), 5643–5651 (2017)
42. S. Li et al., Neurofibrillar tangle surrogates: histone H1 binding to patterned phosphotyrosine peptide nanotubes. Biochemistry **53**(26), 4225–4227 (2014)
43. S. Zhang, Designer self-assembling peptide nanofiber scaffolds for study of 3-D cell biology and beyond. Adv. Cancer Res. **99**, 335–362 (2008)
44. Y. Yanlian et al., Designer self-assembling peptide nanomaterials. Nano. Today **4**(2), 193–210 (2009)
45. R. Gallardo et al., De novo design of a biologically active amyloid. Science **354**(6313), aah4949 (2016)
46. J. Chen et al., The use of self-adjuvanting nanofiber vaccines to elicit high-affinity B cell responses to peptide antigens without inflammation. Biomaterials **34**(34), 8776–8785 (2013)
47. C.B. Chesson et al., Antigenic peptide nanofibers elicit adjuvant-free CD8+ T cell responses. Vaccine **32**(10), 1174–1180 (2014)
48. R. Singh et al., MUC1: a target molecule for cancer therapy. Cancer Biol. Ther. **6**(4), 481–486 (2007)
49. H. Cai et al., Towards a fully synthetic MUC1-based anticancer vaccine: efficient conjugation of glycopeptides with mono-, di-, and tetravalent lipopeptides using click chemistry. Chemistry **17**(23), 6396–6406 (2011)
50. H. Cai et al., Variation of the glycosylation pattern in MUC1 glycopeptide BSA vaccines and its influence on the immune response. Angew. Chem. Int. Ed. Engl. **51**(7), 1719–1723 (2012)
51. Z.H. Huang et al., A totally synthetic, self-assembling, adjuvant-free MUC1 glycopeptide vaccine for cancer therapy. J. Am. Chem. Soc. **134**(21), 8730–8733 (2012)
52. M. Skwarczynski et al., pH-triggered peptide self-assembly into fibrils: a potential peptide-based subunit vaccine delivery platform. Bio. Chem. Comp. **1**(1), 2 (2013)
53. W. Du et al., Intracellular peptide self-assembly: a biomimetic approach for in situ nanodrug preparation. Bioconjug. Chem. **29**(4), 826–837 (2018)
54. L. Wang et al., Self-assembled nanomaterials for photoacoustic imaging. Nanoscale **8**(5), 2488–2509 (2016)
55. P. He et al., Bispyrene-based self-assembled nanomaterials: In vivo self-assembly, transformation, and biomedical effects. Acc. Chem. Res. **52**(2), 367–378 (2019)
56. J.D. Tovar et al., Probing the interior of peptide amphiphile supramolecular aggregates. J. Am. Chem. Soc. **127**(20), 7337–7345 (2005)
57. L. Wang et al., Supramolecular nano-aggregates based on Bis(pyrene) derivatives for lysosome-targeted cell imaging. J. Phys. Chem. C **117**(50), 26811–26820 (2013)
58. X. Hu et al., Transformable nanomaterials as an artificial extracellular matrix for inhibiting tumor invasion and metastasis. ACS Nano **11**(4), 4086–4096 (2017)
59. H.L. Sun et al., Photocontrolled reversible conversion of nanotube and nanoparticle mediated by beta-Cyclodextrin dimers. Angew. Chem. Int. Ed. Engl. **54**(32), 9376–9380 (2015)
60. T.J. Moyer et al., pH and amphiphilic structure direct supramolecular behavior in biofunctional assemblies. J. Am. Chem. Soc. **136**(42), 14746–14752 (2014)
61. C.E. Callmann et al., Therapeutic enzyme-responsive nanoparticles for targeted delivery and accumulation in tumors. Adv. Mater. **27**(31), 4611–4615 (2015)
62. P. Yang et al., Reorganization of self-assembled supramolecular materials controlled by hydrogen bonding and hydrophilic–lipophilic balance. J. Mater. Chem. B **4**(15), 2662–2668 (2016)
63. J. Zhuang et al., Multi-stimuli responsive macromolecules and their assemblies. Chem. Soc. Rev. **42**(17), 7421–7435 (2013)
64. M. Abbas et al., Self-assembled peptide- and protein-based nanomaterials for antitumor photodynamic and Photothermal therapy. Adv. Mater. **29**(12), 1605021 (2017)
65. A.P. Xu et al., Bio-inspired metal ions regulate the structure evolution of self-assembled peptide-based nanoparticles. Nanoscale **8**(29), 14078–14083 (2016)

66. Y.P. Yu et al., Molecular basis for the targeted binding of RGD-containing peptide to integrin alphaVbeta3. Biomaterials **35**(5), 1667–1675 (2014)
67. J.D. Pham et al., A fibril-like assembly of oligomers of a peptide derived from beta-amyloid. J. Am. Chem. Soc. **136**(36), 12682–12690 (2014)
68. C.M. Dobson, Protein misfolding, evolution and disease. Trends Biochem. Sci. **24**(9), 329–332 (1999)
69. S. Ventura et al., Short amino acid stretches can mediate amyloid formation in globular proteins: the Src homology 3 (SH3) case. Proc. Natl. Acad. Sci. U. S. A. **101**(19), 7258–7263 (2004)
70. K. Dudgeon et al., Sequence determinants of protein aggregation in human VH domains. Protein Eng. Des. Sel. **22**(3), 217–220 (2009)
71. O.S. Makin et al., Structures for amyloid fibrils. FEBS J. **272**(23), 5950–5961 (2005)
72. M.R. Krebs et al., Observation of sequence specificity in the seeding of protein amyloid fibrils. Protein Sci. **13**(7), 1933–1938 (2004)
73. K.H. Ashe, A. Aguzzi, Prions, prionoids and pathogenic proteins in Alzheimer disease. Prion **7**(1), 55–59 (2014)
74. A. Henninot et al., The current state of peptide drug discovery: back to the future? J. Med. Chem. **61**(4), 1382–1414 (2018)
75. J.L. Lau et al., Therapeutic peptides: Historical perspectives, current development trends, and future directions. Bioorg. Med. Chem. **26**(10), 2700–2707 (2018)
76. K. Fosgerau et al., Peptide therapeutics: current status and future directions. Drug Discov. Today **20**(1), 122–128 (2015)
77. Q. Sun et al., Rational design of cancer nanomedicine: nanoproperty integration and synchronization. Adv. Mater. **29**(14), 1606628 (2017)
78. K. Greish et al., Nanomedicine: is it lost in translation? Ther. Deliv. **9**(4), 269–285 (2018)
79. J. Shi et al., Cancer nanomedicine: progress, challenges and opportunities. Nat. Rev. Cancer **17**(1), 20–37 (2017)
80. F.U. Hartl et al., Molecular chaperones in protein folding and proteostasis. Nature **475**(7356), 324–332 (2011)
81. K. Esparza et al., Phospholipid micelles for peptide drug delivery. Methods Mol. Biol. **2000**, 43–57 (2019)
82. Y. Barenholz, Doxil(R)—the first FDA-approved nano-drug: lessons learned. J. Control. Release **160**(2), 117–134 (2012)
83. X. Fang et al., Nano-cage-mediated refolding of insulin by PEG-PE micelle. Biomaterials **77**, 139–148 (2016)
84. X. Fang et al., Dual effect of PEG-PE micelle over the oligomerization and fibrillation of human islet amyloid polypeptide. Sci. Rep. **8**(1), 4463–4474 (2018)
85. B. Christian et al., The heat shock protein HSP70 and heat shock cognate protein HSC70 contribute to antimony tolerance in the protozoan parasite leishmania. Cell Stress Chaperones **9**(3), 294–303 (2004)
86. Y. Tsvetkova et al., Balancing passive and active targeting to different tumor compartments using riboflavin-functionalized polymeric nanocarriers. Nano Lett. **17**(8), 4665–4674 (2017)
87. A.M. Smith et al., Bioconjugated quantum dots for in vivo molecular and cellular imaging. Adv. Drug Deliv. Rev. **60**(11), 1226–1240 (2008)
88. W. Poon et al., Targeting B16 tumors in vivo with peptide-conjugated gold nanoparticles. Nanotechnology **26**(28), 285101 (2015)
89. G. Bollag et al., Vemurafenib: the first drug approved for BRAF-mutant cancer. Nat. Rev. Drug Discov. **11**(11), 873–886 (2012)
90. W. Zhou et al., Storage stability and skin permeation of vitamin C liposomes improved by pectin coating. Colloids Surf. B Biointerfaces **117**, 330–337 (2014)
91. X. Wang et al., Sensitivity to antitubulin chemotherapeutics is potentiated by a photoactivable nanoliposome. Biomaterials **141**, 50–62 (2017)

92. S. Patra et al., The next generation cell-penetrating peptide and carbon dot conjugated nanoliposome for transdermal delivery of curcumin. Biomater. Sci. **4**(3), 418–429 (2016)
93. L. Zou et al., Peptide-modified vemurafenib-loaded liposomes for targeted inhibition of melanoma via the skin. Biomaterials **182**, 1–12 (2018)
94. R. Ruan et al., Peptide-chaperone-directed transdermal protein delivery requires energy. Mol. Pharm. **11**(11), 4015–4022 (2014)
95. T. Wei et al., Functionalized nanoscale micelles improve drug delivery for cancer therapy in vitro and in vivo. Nano Lett. **13**(6), 2528–2534 (2013)
96. N. Guttmann-Raviv et al., The neuropilins and their role in tumorigenesis and tumor progression. Cancer Lett. **231**(1), 1–11 (2006)
97. P. Frankel et al., Chondroitin sulphate-modified neuropilin 1 is expressed in human tumour cells and modulates 3D invasion in the U87MG human glioblastoma cell line through a p130Cas-mediated pathway. EMBO Rep. **9**(10), 983–989 (2008)
98. S. Youqing et al., Prodrugs forming high drug loading multifunctional nanocapsules for intracellular cancer drug delivery. J. Am. Chem. Soc. **132**(12), 4259–4265 (2010)
99. T. Aida et al., Functional supramolecular polymers. Science **335**(6070), 813–817 (2012)
100. R.G. Ellis-Behnke et al., Nano neuro knitting: peptide nanofiber scaffold for brain repair and axon regeneration with functional return of vision. Proc. Natl. Acad. Sci. U. S. A. **103**(13), 5054–5059 (2006)
101. H. Su et al., One-component nanomedicine. J. Control. Release **219**, 383–395 (2015)
102. W. Ma et al., Building nanostructures with drugs. Nano. Today **11**(1), 13–30 (2016)
103. Y. Wang et al., Peptide-drug conjugates as effective prodrug strategies for targeted delivery. Adv. Drug Deliv. Rev. **110-111**, 112–126 (2017)
104. Y. Liang et al., A nanosystem of amphiphilic oligopeptide-drug conjugate actualizing both alphavbeta3 targeting and reduction-triggered release for Maytansinoid. Theranostics **7**(13), 3306–3318 (2017)
105. G. Yang et al., Underwater-transparent nanodendritic coatings for directly monitoring cancer cells. Adv. Healthc. Mater. **3**(3), 332–337 (2014)
106. P. Zhang et al., Programmable fractal nanostructured interfaces for specific recognition and electrochemical release of cancer cells. Adv. Mater. **25**(26), 3566–3570 (2013)
107. H. Liu et al., Hydrophobic interaction-mediated capture and release of cancer cells on thermoresponsive nanostructured surfaces. Adv. Mater. **25**(6), 922–927 (2013)
108. L. Bai et al., Peptide-based isolation of circulating tumor cells by magnetic nanoparticles. J. Mater. Chem. B **2**(26), 4080–4088 (2014)
109. H. Yang et al., A new strategy for effective construction of protein stacks by using cucurbit[8]uril as a glue molecule. Chem. Commun. (Camb.) **48**(86), 10633–10635 (2012)
110. Y. Cho et al., Controlled release of an anti-cancer drug from DNA structured nano-films. Sci. Rep. **4**(2), 4078–4082 (2014)
111. S. Srivastava et al., Composite layer-by-layer (LBL) assembly with inorganic nanoparticles and nanowires. Acc. Chem. Res. **41**(12), 1831–1841 (2008)
112. X. Lin et al., Insulin particles as building blocks for controlled insulin release multilayer nano-films. Korean J. Couns. Psychother. **54**, 239–244 (2015)
113. G. Invernizzi et al., Protein aggregation: mechanisms and functional consequences. Int. J. Biochem. Cell Biol. **44**(9), 1541–1554 (2012)
114. Z. Zhao et al., Antiamyloidogenic activity of Aβ42-binding peptoid in modulating amyloid oligomerization. Small **13**(1), 1602857 (2017)
115. L. Zhu et al., Antibody-mimetic peptoid nanosheet for label-free serum-based diagnosis of Alzheimer's disease. Adv. Mater. **29**(30), 1700057 (2017)
116. K. Ariga et al., Layer-by-layer self-assembled shells for drug delivery. Adv. Drug Deliv. Rev. **63**(9), 762–771 (2011)

117. H.S. Won et al., Systematic peptide engineering and structural characterization to search for the shortest antimicrobial peptide analogue of gaegurin 5. J. Biol. Chem. **279**(15), 14784–14791 (2004)
118. X. Zhao et al., Molecular self-assembly and applications of designer peptide amphiphiles. Chem. Soc. Rev. **39**(9), 3480–3498 (2010)
119. G.A. Ozin, Nanochemistry: synthesis in diminishing dimensions. Adv. Mater. **4**(10), 612–649 (1992)

Chapter 6
Rationally Designed DNA Assemblies for Biomedical Application

Qiao Jiang, Qing Liu, Zhaoran Wang, and Baoquan Ding

Abstract Based on Watson–Crick base pairing rules, DNA molecules can work as building blocks to fabricate programmable and functional nanostructures. In recent decades, DNA nanotechnology has been developed to construct sophisticated structures and artificial mechanical devices, giving rise to a variety of desired functions and fascinating applications. Featured with rationally designed geometries, precise spatial addressability, as well as marked biocompatibility, DNA-based nanostructures provide promising candidates for drug delivery. In this chapter, we summarize the recent advances of self-assembled DNA-base nanomaterials for the biomedical applications, including molecular imaging and drug delivery both in vitro and in vivo. The remaining challenges and open opportunities are also discussed.

Keywords Self-assembly · DNA nanomaterials · Drug delivery · Cancer treatment

6.1 Introduction

Deoxyribonucleic acid (DNA) molecules work as genetic information carriers and play a central role in expressing and regulating the biological functions of most living organisms. In 1982, Seeman proposed structural DNA nanotechnology that changed the genetic roles of DNA molecules [1]. The specific Watson–Crick base pairing between multiple DNA strands allows the design and fabrication of geometrically

Q. Jiang · Q. Liu
CAS Key Laboratory of Nanosystem and Hierarchical Fabrication, CAS Center for Excellence in Nanoscience, National Center for Nanoscience and Technology, Beijing, People's Republic of China

Z. Wang · B. Ding (✉)
CAS Key Laboratory of Nanosystem and Hierarchical Fabrication, CAS Center for Excellence in Nanoscience, National Center for Nanoscience and Technology, Beijing, People's Republic of China

University of Chinese Academy of Sciences, Beijing, People's Republic of China
e-mail: dingbq@nanoctr.cn

H. Xu, N. Gu (eds.), *Nanotechnology in Regenerative Medicine and Drug Delivery Therapy*, https://doi.org/10.1007/978-981-15-5386-8_6

defined objects, as well as the arrangement of components and functions at the nanoscale with high programmability. After decades of development, a variety of sophisticated self-assemblies have been designed and constructed, including various DNA polyhedral wireframe cages [2–4], rolling circle application (RCA)-derived materials [5], single-stranded tiles (SST)-based structures [6–9], DNA origami architectures [10], etc. DNA nanotechnology is now being utilized to develop nanomaterials with various functionalities [11–13]. These successful efforts have triggered the biological application of DNA nanostructures, most notably employing them as imaging probes or drug delivery nanovehicles in vitro and in vivo.

6.2 Self-Assembled DNA Nanostructures

For their wide application prospect, nanoscale engineering of DNA structures has attracted great interest. Taking advantage of the self-recognition properties of appropriate oligonucleotides (ODNs), DNA molecules serving as stick and glue spontaneously assemble into predesigned 2D or 3D objects with nanoscale features (Fig. 6.1). Tile-based DNA nanostructures such as multi-arm junctions [1], crossovers (double-crossover [14], DX; triple-crossover [15, 16], TX), lattices [1, 17], hydrogels [9, 18], dendrimers [8, 19], and wire-framed polyhedra [2–4] with various geometries (~10–100 nm) were fabricated by hybridization of multiple DNA strands containing carefully designed sequences. With high yields and uniform sizes, these assemblies can be reliably constructed by enzyme-free annealing processes involving DNA strands with exact stoichiometric and purity control. Alternatively, rolling circle amplification (RCA) as an isothermal enzymatic strategy [5] can be used to create larger DNA-based structures (>200 nm nm)

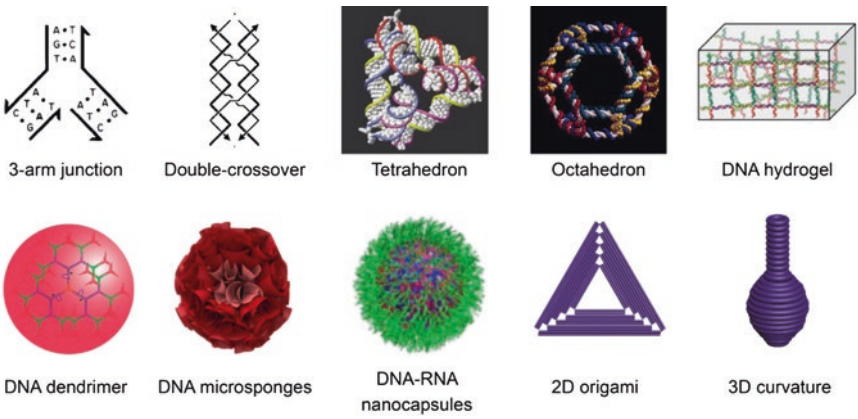

Fig. 6.1 Various self-assembled DNA nanostructures. Three-arm junction [1]. Double-crossover [14]. Tetrahedron [3]. Octahedron [4]. DNA hydrogels [18]. DNA dendrimer [19]. DNA microsponge [20]. DNA-RNA nanocapsule [24]. Triangular origami [12]. 3D curvature [12]

including microsponges [20], nanoflowers [21, 22], nanoclews [23], nanocapsules [24], etc. Easy to large-scale production by enzymatic-based processes, those RCA-derived self-assemblies displayed optimal stability under physiological environments, making it a highly desirable and scalable strategy for biomedical applications. In 2006, DNA origami technique was introduced by Rothemund [10]. This revolutionary breakthrough of DNA nanotechnology can fold a long single-stranded DNA (ssDNA) scaffold into a predesigned architecture using hundreds of staple strands that fix the scaffold's conformation. Until now, the origami approach has provided various well-formed uniform nanostructures, such as 2D origami, [10] multilayer 3D origami [25], 3D curvature [26, 27], single-stranded origami [28], and DNA-protein hybrid origami [29]. Another important strategy in fabrication of DNA nanostructures is single-stranded tile (SST) assembly [30, 31]. Each DNA "brick" as a molecular Lego comprises an ssDNA with four short binding domains only hybridizing with specific and predefined partners, enabling individual brick to assemble through the formation of DNA duplexes at the tile/tile interface.

These self-assembly processes enable rational design and construction of various DNA nanostructures with well-defined homogenous geometries ranging from 10 to 400 nm, which are appropriate for drug delivery to malignant tumors displaying enhanced permeability and retention (EPR) effects [32, 33]. DNA nanostructure can work as a molecular pegboard, on which one can precisely organize desired functional elements (including targeting aptamers, anticancer drug molecules, gene sequences, protein payloads, etc.) with designed numbers and patterns anywhere on the entire addressable nanostructure. Dynamic nanostructures can be easily fabricated through those assembly approaches [34–40], enabling controllable therapeutics release or fluorescence turn-on imaging at desired sites. Composed by biological molecules, DNA nanostructures show marked biocompatibility. All these unique advantages of DNA nanostructures have conferred them various biomedical applications.

6.3 DNA-Based Nanovehicles for Biomedical Application In Vitro and In Vivo

A variety of moieties can be integrated into DNA architectures to realize the particular biomedical functionalities, including specific tumor targeting, efficient delivery of therapeutic agents, and controllable drug release. Functional elements (such as several chemotherapeutic drugs or imaging agents) can be directly loaded into DNA nanovehicles via intercalation or covalent linkage. Hybridization between ssDNA strands attached with payloads and capture strands of DNA nanostructures offers a vital approach for site-selective arrangement of a collection of cargos (such as functional nucleic acids and DNA-modified biomolecules or nanoparticles). Aptamer sequence-targeted binding and biotin–streptavidin interaction provide alternative ways for cargo loading by specific recognition and anchoring. The subsequent sections will focus on the recent advances of self-assembled DNA

nanovehicles for delivery various types of cargos, including small molecular drugs, functional nucleic acid, metal nanoparticles, proteins, and peptides. Dynamic DNA nanodevices and DNA machines for stimuli-triggered structural reconfiguration and controlled drug release are summarized.

6.3.1 Chemotherapeutic Drugs

Doxorubicin and daunorubicin are broad-spectrum chemotherapeutic drugs that kill malignant cells through DNA intercalation and macromolecular biosynthesis inhibition. Ding and colleagues exploited the potency of the drug molecules by loading them into triangular and tubular DNA origami delivery systems [41]. After doxorubicin non-covalently attachment to DNA origami nanostructures via intercalation, drug-loaded DNA architectures were administrated to drug-sensitive or -resistant human breast cancer cell lines (regular MCF-7 or drug-resistant MCF-7). Working as "Trojan horses," DNA origami nanovehicles enhanced doxorubicin accumulation in the diseased cells and exhibited marked cytotoxicity not only to regular MCF-7 but importantly to drug-resistant cancer cells, inducing a remarkable reversal of resistance phenotype (Fig. 6.2a). In a similar fashion, Castro and his colleagues fabricated rod-like DNA origami nanoarchitectures for daunorubicin incorporation and cancer therapy [42]. As another type of DNA "Trojan horse," the DNA nanocarrier enhanced drug efficacy in leukemia cells displaying multidrug resistance (MDR), providing a rationale for exploring DNA origami as a drug delivery vehicle in leukemia and other hematologic malignancies. Hogberg and his colleagues introduced another doxorubicin-loaded DNA nanotube delivery system for cancer cell killing [43]. They designed several types of DNA tubes with varying degrees of global twist. Encapsulation efficiency and the release rate of doxorubicin were controlled by tuning the DNA nanostructure design. Compared to free drug molecules, doxorubicin-loaded DNA tubes showed enhanced cytotoxicity and lowered the intracellular elimination rate in several breast cancer cell lines (MDA-MB-231, MDA-MB-468, and MCF-7, Fig. 6.2b).

The in vitro endeavors described above have yielded new DNA nanovehicle designs with different biologically active payloads and for further in vivo application. Ding and colleagues first investigated the shape-dependent tumor accumulation by testing different DNA origami nanostructures and DNA controls (mixture of the p7249 scaffold and the biotin-containing staple strands) in tumor xenografted mice [44]. After intravenous injection, all the DNA nanostructures (tubes, triangles, rectangles) displayed enhanced passive targeting efficacy in tumor region, and the triangular DNA origami exhibited optimal tumor accumulation. Compared to free drug molecules, doxorubicin-loaded DNA origami showed more specific antitumor efficacy without any observable systemic side effects in nude mice bearing human MDA-MB-231 orthotopic breast tumors (Fig. 6.2c).

Besides anthracyclines (doxorubicin and daunorubicin), other types of chemotherapeutic drugs have been considered to load in DNA nanovehicles for cancer

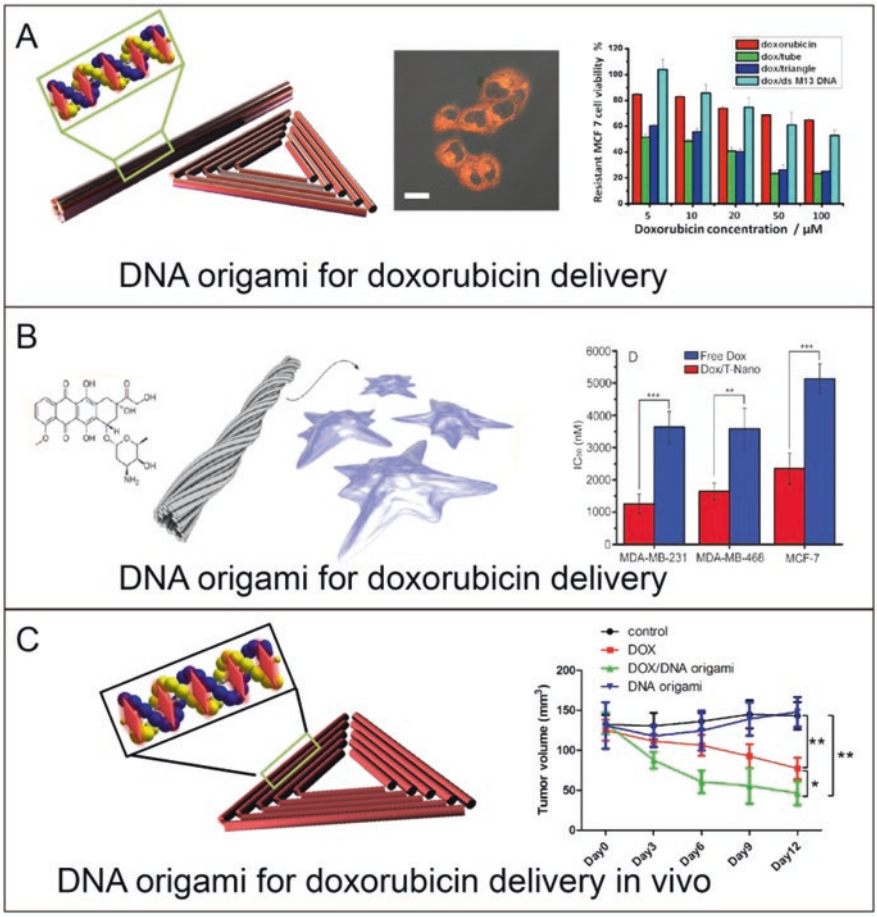

Fig. 6.2 Examples of DNA nanostructures for anthracyclines delivery. (**a**) Triangular and tubular DNA origami structures used as doxorubicin carriers for efficient inhibition of drug-resistant MCF-7 cell proliferation [41]. (**b**) Twisted doxorubicin-loaded DNA nanotubes with tunable drug release properties [43]. (**c**) Triangular DNA origami as an in vivo doxorubicin delivery nanovehicle [44]

therapy both in vitro and in vivo. Floxuridine is a pyrimidine analogue that is most often used in cancer therapy. Zhang and his colleagues synthesized floxuridine-integrated DNA strands and constructed DNA polyhedra (tetrahedra, dodecahedra, and buckyballs) with definite drug-loading ratios as well as varied sizes and morphologies [45]. In their work, floxuridine-containing DNA polyhedra exhibited robust anticancer capability. Floxuridine-DNA buckyball architecture showed superior tumor inhibition over the free drug and other formulations. Camptothecin is an inhibitor DNA topoisomerase I that has been widely applied in the treatment of cancer. Zhang and his colleagues applied carbonethyl bromide-modified camptothecin to react with phosphorothioate-modified DNA strands and produced

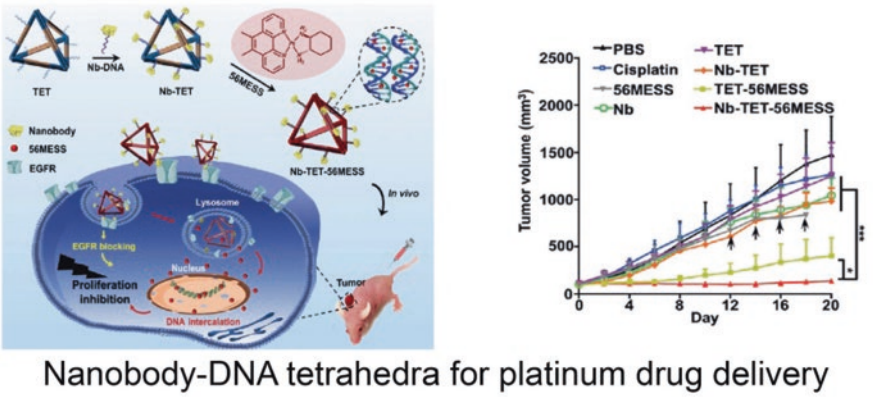

Fig. 6.3 Nanobody-conjugated double-bundle DNA tetrahedra for platinum-based DNA intercalator (56MESS) delivery [47]

drug-integrated DNA with a GSH-responsive disulfide linkage [46]. They next used these drug-modified ssDNA to fold camptothecin-containing DNA tetrahedra. In contrast to free drugs, these camptothecin-containing DNA tetrahedra exhibited higher cytotoxicity to tumor cells and better suppression of tumor growth. Cisplatin and related platinum-based drugs have been widely employed in the clinic as first-line chemotherapeutic drugs for the various type of cancer. Ding and colleagues utilized double-bundle DNA tetrahedron as a nanovehicle to load platinum-based DNA intercalator (56MESS) via intercalation with the DNA duplex [47]. Integrated with nanobodies that targeted and blocked epidermal growth factor receptor (EGFR), the dual-functional DNA tetrahedral vehicles showed targeted platinum-drug delivery and combined tumor therapy without obvious systemic toxicity (Fig. 6.3).

6.3.2 Functional Nucleic Acids

Functional oligodeoxynucleotides (ODNs) and large nucleic acids are able to be integrated with the DNA nanovehicles by direct extension or hybridization. Unmethylated cytosine-phosphate-guanine (CpG) ODNs can specifically be recognized by endosomal toll-like receptor 9 (TLR 9) and induce an immune response, which has been actively explored in both basic research and clinical trials as a type of potent vaccine adjuvant in immunotherapy for cancer [48]. Fan and colleagues described an approach to develop CpG-containing DNA tetrahedra for efficient CpG ONDs delivery and immunostimulation [49]. Through a simple annealing procedure, CpG-decorating DNA tetrahedra with a different valence number of functional ODNs were assembled. Compared to free CpG ODNs, the tetrahedron loading CpG ODNs showed improved stability and can efficiently produce the

pro-inflammatory cytokines including tumor necrosis factor (TNF)-α, interleukin (IL)-6, and IL-12 (Fig. 6.4a). In another example, Liedl and colleagues provided a DNA origami nanocarrier for CpG delivery and immune stimulation [50]. They constructed 30-helix DNA nanotube that hybridized with 62 CpG payloads at predesigned binding sites. The DNA constructs served as efficient vehicles to enhance internalization in splenic macrophages of CpG payloads. These CpG-loaded nanotubes were observed in the endosome of immune cells, stimulating effective production of cytokines (Fig. 6.4b). Ding and colleagues used a self-assembled DNA dendrimer to delivery CpG payloads [51]. TAT peptides and loop-structured-CpG motifs were incorporated into DNA dendrimers at various binding sites, and the CpG delivery was analyzed in vitro. In contrast to free CpG-containing hairpin loops, DNA nanovehicles led more functional payloads into raw264.7 macrophages. Moreover, DNA dendrimers decorated with CpG loops and TAT peptides triggered stronger pro-inflammatory cytokine production compared to DNA constructs without peptide modification, indicating that the TAT-DNA dendrimers could serve as efficient vehicles for delivery of CpG motifs (Fig. 6.4c).

Besides those in vitro investigations of CpG decorating DNA nanovehicles, Rehberg and colleagues utilized DNA nanotubes as CpG delivery systems and investigated their effects on immune cells in vivo and in real time [52]. They designed and fabricated an 8-helix DNA nanotube using the SST methods and the 24 tiles in tubes were extended by CpG motifs. After incubation with raw 264.7 macrophages, the CpG-loading DNA tubes showed enhanced cellular internalization and TNF-α response. In a mouse model, CpG-DNA tubes were observed to be internalized by tissue-resident macrophages and localized in their endosomes utilizing in vivo microscopy. Through microinjection into skeletal muscle of anesthetized mice, CpG-DNA tubes induced a significant recruitment of leukocytes into the muscle tissue as well as activation of the NF-κB pathway in surrounding cells in contrast to naked DNA nanotubes or unloaded CpG ODNs. The above examples nicely demonstrate how the defined DNA nanostructures can be used advantageously to deliver CpG ODNs to stimulate immune responses (Fig. 6.4d).

Antisense oligonucleotides (ASOs) are synthetic DNA/RNA-like ODNs that can be used for regulating gene expression. Typically, ASOs comprise 16–21 nucleotides, which bind to mRNA through sequence-specific interactions and disrupt target gene expression [53]. A series of ASO delivery application of DNA nanomaterials were investigated. Sleiman and colleagues used DNA cage vehicles for ASO delivery and investigated target gene knockdown [54]. Phosphorothioated firefly luciferase ASO (PS-TOP4005) was chosen to represent in their model system. They constructed 3D DNA nanocages that were elongated with 1, 2, 4, and 6 ASOs. After incubation with mammalian cells by these ASO-DNA cages, significant and robust gene knockdown was observed. Compared to single- and double-stranded controls, the ASO-DNA cages displayed much higher gene knockdown level according to their increased stability of bound antisense units. Tan and colleagues introduced a size-controllable and stimuli-responsive DNA nanohydrogel as a vehicle for efficient ASO delivery and gene therapy [55]. These DNA hydrogel particles were synthesized by three types of Y-shaped DNA building blocks, incorporating targeting

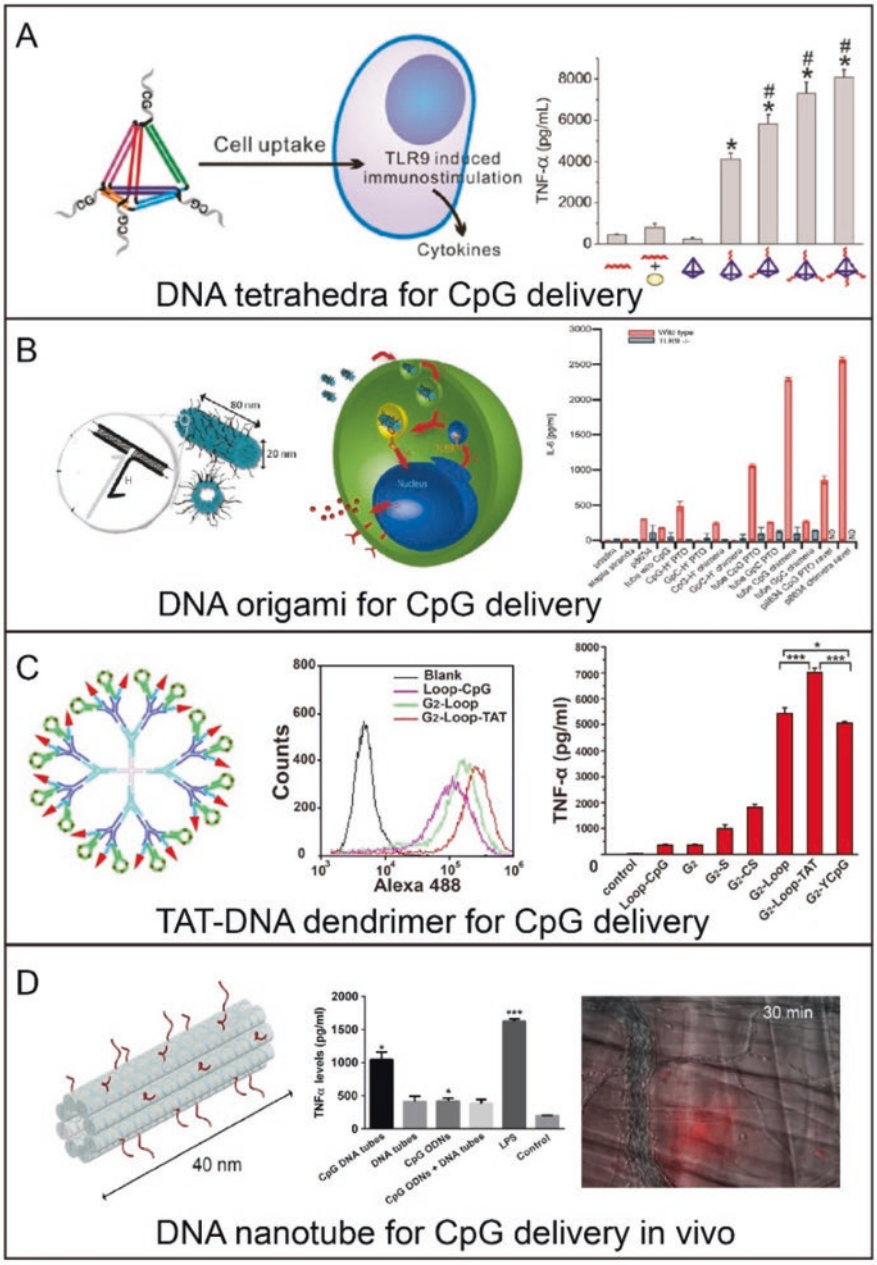

Fig. 6.4 DNA nanostructures for CpG delivery and immunostimulation. (**a**) DNA tetrahedra for CpG delivery to raw264.7 macrophage cell line [49]. (**b**) CpG-coated DNA origami for cellular delivery and immunostimulation of isolated splenic macrophages [50]. (**c**) TAT peptide-conjugated DNA dendrimer for efficient CpG delivery to raw264.7 cells [51]. (**d**) DNA nanotube folded by the SST methods for CpG delivery in vivo and in real time [52]

aptamers S6, disulfide linkages, and therapeutic ASO (ISIS5132) silencing proto-oncogene *c-raf*. After incubation with S6 targeted human lung adenocarcinoma epithelial A549 cells, DNA nanohydrogels resulted in targeted tumor cell uptake, efficient inhibition of cell growth, and stimuli-responsive gene therapy (Fig. 6.5a). For another example, Ding and colleagues constructed a double-bundle DNA tetrahedron consisting of nuclear localization signal (NLS) peptide and therapeutic ISIS5132 ASO and studied the delivery system in A549 cells [56]. They found that functionalized DNA tetrahedron assisted the delivery of ISIS5132 into the cells and

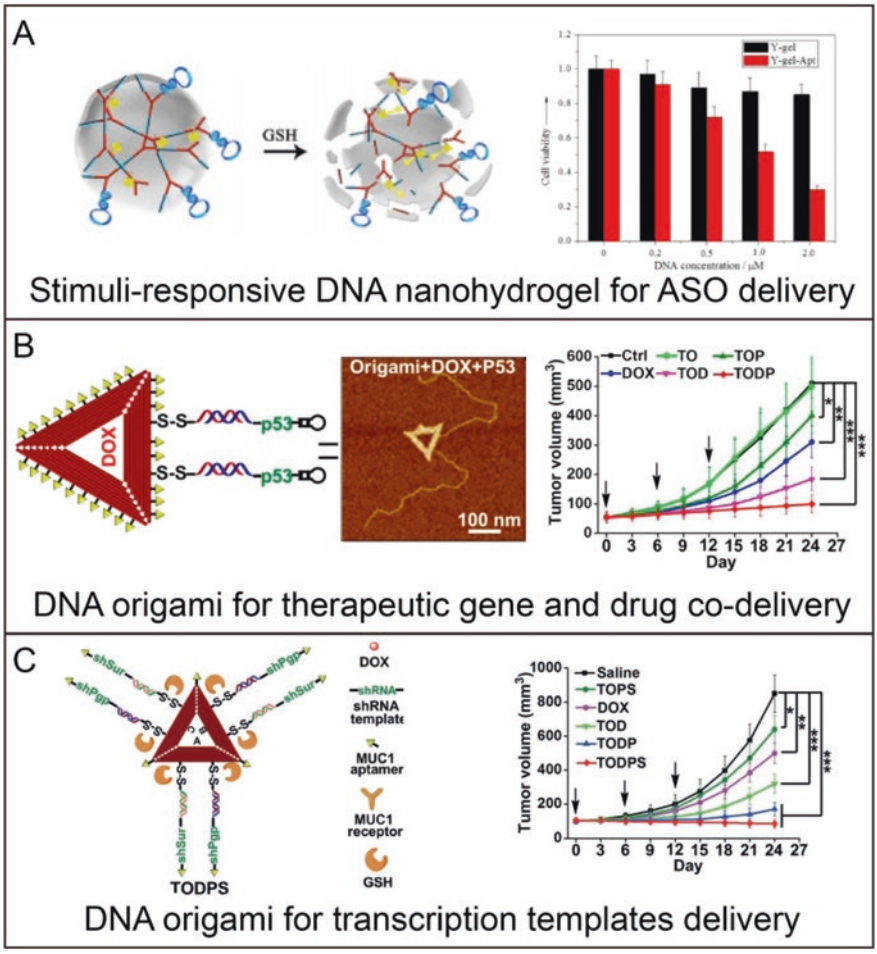

Fig. 6.5 Examples of DNA nanovehicles for therapeutic ASOs, RNAi, and genes. (**a**) DNA nanohydrogels incorporated with aptamers S6, disulfide linkage, and therapeutic ASO (ISIS5132) [55]. (**b**) MUC-1 modified DNA origami for doxorubicin and p53 gene co-delivery [61]. (**c**) DNA origami decorated with two type of linear small hairpin RNA (shRNA) transcription templates for cancer therapy [62]

increased the chance to downregulate target mRNA in nucleus and cytoplasm. In response to the intracellular reducing environment, therapeutic ASOs were released from DNA vehicles, triggering efficient knockdown of *c-raf* gene and malignant cells inhibition.

RNA interference (RNAi) that induces target gene silencing is a powerful and selective gene therapeutic strategy. Small interference RNAs (siRNAs) are synthetic mediators of RNAi, which are dsRNA molecules (21–23 base pairs in length) used to silence the expression of genes. Sleiman and colleagues developed another DNA cage structure to carry siRNA payloads and facilitate controllable release upon specific ODN triggers [57]. After recognizing the trigger strand (usually was mRNA or miRNA in malignant cells), siRNA-containing DNA cage unwind by strand displacement and releasing the corresponded siRNA cargo. This DNA cage delivery system showed a high production yield (~100%) and can sustain biological conditions and remain responsive at the molecular level in a complex cellular environment. Anderson and colleagues developed multifunctional DNA tetrahedron that decorated with siRNAs and tumor targeting moieties for in vivo gene therapy [58]. By designing the overhang of the DNA vehicle, the spatial orientation and density of cancer-targeting ligands on the tetrahedron surface can be controlled. Integrated with folic acid molecules for KB tumor cell targeting, the FA-DNA tetrahedral constructs displayed longer blood circulation time ($t_{1/2} \approx 24.2$ min) compared to the unloaded siRNA ($t_{1/2} \approx 6$ min) and enhanced tumor accumulation in vivo. After systemic injection of a tetrahedron with FA-conjugated anti-luciferase siRNAs in KB tumor xenograft mice, robust gene silencing efficacy was observed without detectable immune response. Ju and colleagues present a "dual lock-and-key" system to achieve cell-subtype-specific siRNA delivery [59]. They fabricated siRNA-containing triangular ring units and subsequently RCA-derived oligonucleotide vehicle (siRNA-ONV), which is modified with a hairpin structure to act as both the "smart key." The auto-cleavable hairpin structure used in the siRNA-ONV was activated when reacting with two aptamers (sgc8c and sgc4f) appearing at target cell membrane as "dual locks." The sequential recognition led to cell-subtype discrimination and precise siRNA delivery for efficient gene silencing in vitro and in vivo. Next, siRNAs decorating SST-based DNA nanovehicles for in vivo use were also described recently. Ke and colleagues arranged siRNAs that targeted anti-apoptotic protein Bcl2 (siBcl2) on the surface of a variety of SST-DNA nanostructures (20–100 nm) [60]. Both in vitro and in vivo evaluation confirmed the optimal tumor inhibition of the siBcl2-DNA nanovehicles. The suppressed tumor growth in xenograft mice was specifically correlated with *bcl2* downregulation.

Recently, a series of gene delivery by DNA origami nanostructures was reported by Ding and colleagues. They constructed a triangular origami platform to carry liner tumor therapeutic gene sequences (p53) and chemotherapeutic drug (doxorubicin) molecules for combined therapy of multidrug-resistant (MDR) tumors [61]. Utilizing the gene/drug-coloaded DNA vehicles, potent tumor inhibition in drug-resistant tumor xenografts was observed (Fig. 6.5b). They next fabricated another type of codelivery vector of RNAi and drugs for MDR cancer therapy [62].

Two types of linear small hairpin RNA (shRNA) transcription templates targeting MDR-associated genes (genes of P-glycoprotein and survivin) were hybridized with doxorubicin loaded-triangular DNA origami template. Integrating with tumor-targeting MUC1 aptamer and GSH-responsive disulfide linkage, these multifunctional DNA vehicles were observed to enter MDR-MCF-7 cells and synergistically inhibit tumor growth without apparent systemic toxicity (Fig. 6.5c).

6.3.3 Nanoparticle

Krishnan and colleagues designed a fluorescein isothiocyanate (FITC)-dextran (FD) encapsulated DNA icosahedral structure for in vivo imaging in *Caenorhabditis elegans* (*C. elegans)*, which was the first report of in vivo study by using DNA nanostructures [63]. Integrating with quantum dot in the core and functionalized with endocytic ligands on the DNA shell, a similar DNA icosahedron was fabricated [64]. They next deployed the multifunctional DNA particles for monitoring compartmental dynamics and endocytic pathways, resulting in a new class of molecular probes for quantitative functional imaging. Another example of nanoparticle decoration was reported by Ke and colleagues for the study of cellular uptake and trafficking process of DNA origami [65]. They provided a general method by locating gold nanoparticles (GNPs) onto the DNA origami nanostructures via hybridization for tracking origami in vitro. GNP attachment on the origami nanostructures enabled high-resolution cellular imaging at a single particle level by transmission electron microscopy (TEM), which led Ke and colleagues to assess cellular uptake efficiency of origami nanostructures influenced by sizes, shapes, and cell lines (Fig. 6.6a).

Gold nanorods (GNRs) have attracted significant research interest in cancer imaging and therapy, owing to their unique optical absorption properties and photothermal effects. Ding and colleagues represent several examples of GNRs loaded with DNA origami [66–68]. They constructed DNA origami templates with extending capture strands, which were used to anchor GNRs to pre-designed binding sites via their modified complementary DNA handles. The GNR-containing DNA origami nanostructures were applied in tumor cells and tumor-bearing animals to test their efficacy as dual-functional nanotheranostics. In contrast to bare GNRs, DNA origami loading GNR complexes showed increased tumor cell uptake and enhanced photothermal ablation [66]. As an efficient optoacoustic imaging (OAI) probe, both improved imaging quality and decreased necessary dose of GNR-DNA origami assemblies were achieved when the complex was administrated to tumor-bearing mice [67]. Besides imaging functions, GNR-DNA origami assemblies responded to external NIR irradiation (for the photothermal therapy) and effectively inhibited tumor growth, prolonging the survival of xenograft mice (Fig. 6.6b). Based on those studies, Ding and colleagues generated a DNA origami capable of assembling GNRs, doxorubicin, and MUC1 aptamers, introducing a universal strategy for origami vehicle-based co-delivery platform [68]. Rationally fabricated

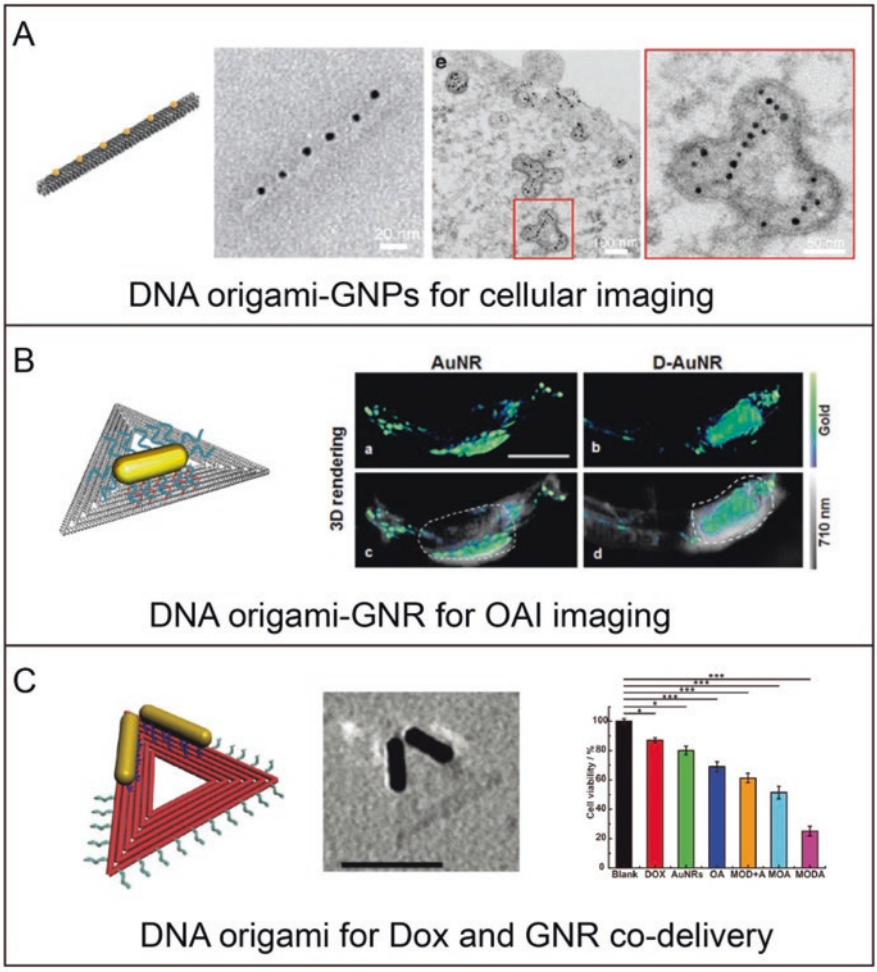

Fig. 6.6 DNA vehicles for nanoparticle delivery. (**a**) GNP-DNA origami nanostructures for in vitro tracking [65]. (**b**) GNR-containing DNA triangular origami for in vivo OAI imaging [67]. (**c**) GNR-dox-DNA origami systems for synergistic tumor cell inhibition [68]

to GNRs and drug molecules, the co-delivery DNA origami triangles were used in cancer therapy. The GNR-dox-DNA origami systems displayed increased delivery of drugs and nanoparticles in MDR-MCF-7 cell after combining tumor-cell targeting aptamers. Upon near-infrared (NIR) laser irradiation, GNR-dox-DNA origami co-delivery platforms showed downregulated expression of P-glycoprotein, a multidrug resistance pump on the cell surface of MDR-MCF-7 cells, eliciting synergistic tumor cells inhibition by chemotherapeutic drugs and photothermal agents (Fig. 6.6c).

6.3.4 Proteins and Peptides

Delivery of proteins and peptides that carry out desired biological functions is a direct approach for disease treatment. Highly programmable DNA structures have been used to engineer nanoscaled vehicles for these biological macromolecules. As demonstrated by Chang and colleagues, a double-bundle DNA tetrahedron can be assembled as a platform to hold streptavidin molecules (STVs, model antigens) and CpG ODNs (adjuvants) at the same time [69]. In contrast to a simple mixture of antigen and adjuvants (STV + CpG), the co-assembled STV-CpG-DNA tetrahedron elicited stronger and long-term immune responses in mouse models without undesirable effects against the DNA scaffold itself (Fig. 6.7a). A different approach of peptide-integrated vehicles as a nanovaccine was introduced by Chen and colleagues [24]. They utilized RCA-derived DNA-RNA nanocapsules to incorporate CpG, *Stat*3 short hairpin RNA adjuvants, and tumor-specific peptide for synergistic cancer vaccination. In this work, the RCA process produced tandem CpG and shRNA that were folded into DNA-RNA hybridized spheres. Then the DNA-RNA spheres were wrapped tightly by PPT-g-PEG (a PEGylated cationic polypeptide) to shrink the sizes and further loaded neoantigen peptide via hydrophobic interactions. As synergistic nanovaccine, these nanocapsules were used to co-deliver large amount of neoantigen and adjuvant into antigen-presenting cells (APCs) in draining lymph nodes (LNs), triggering durable neoantigen-specific T-cell responses and robust tumor growth inhibition (Fig. 6.7b).

Besides the nanovaccines mentioned above, anti-programmed cell death protein 1 antibodies (aPD1) were also used as a functional protein for cancer immunotherapy. Gu and colleagues designed an RCA-derived DNA particle that co-encapsulated aPD1 and CpG ODNs for synergistic induction of cytotoxic T-cell responses in a melanoma model [70]. Through RCA reaction specifically based on a template encoded with the CpG ODNs, CpG-containing nanoclews were fabricated, and aPD1 antibodies were co-loaded in DNA particles by ultrasonication. The DNA nanoclews were self-assembled by long-chain ssDNA repeatedly containing interval CpG ODNs and cutting sites of restriction enzyme HhaI. For conditional release of functional payloads, the corresponding enzymes were coated by triglycerol monostearate [TGMS that can be cleavage by esterases and matrix metalloproteinases (MMPs)] to form nanoparticles (TGMS-HhaI NPs) and attach to CpG/aPD1-containing nanovehicles. After local injection into incompletely removed tumors, the whole constructs were triggered by upregulated MMPs that cleaved TGMS. The uncovered HhaI further digested DNA particles and released CpG ODNs and aPD1. In contrast to a free aPD1/free CpG ODNs treatment, this microenvironment-responsive formulation of the DNA nanoclews displayed more effective tumor inhibition, preventing the potential risk of toxic peak dosage of aPD1 in the body. Using a similar assembling approach, Gu and colleagues constructed another RCA-derived DNA nanoclews for co-delivery of Cas9 nuclease and single-guide RNA (sgRNA) [71]. The DNA nanoclew structure was synthesized by RCA reaction with sequences partially complementary to the sgRNA. Cas9/sgRNA complexes were loaded via

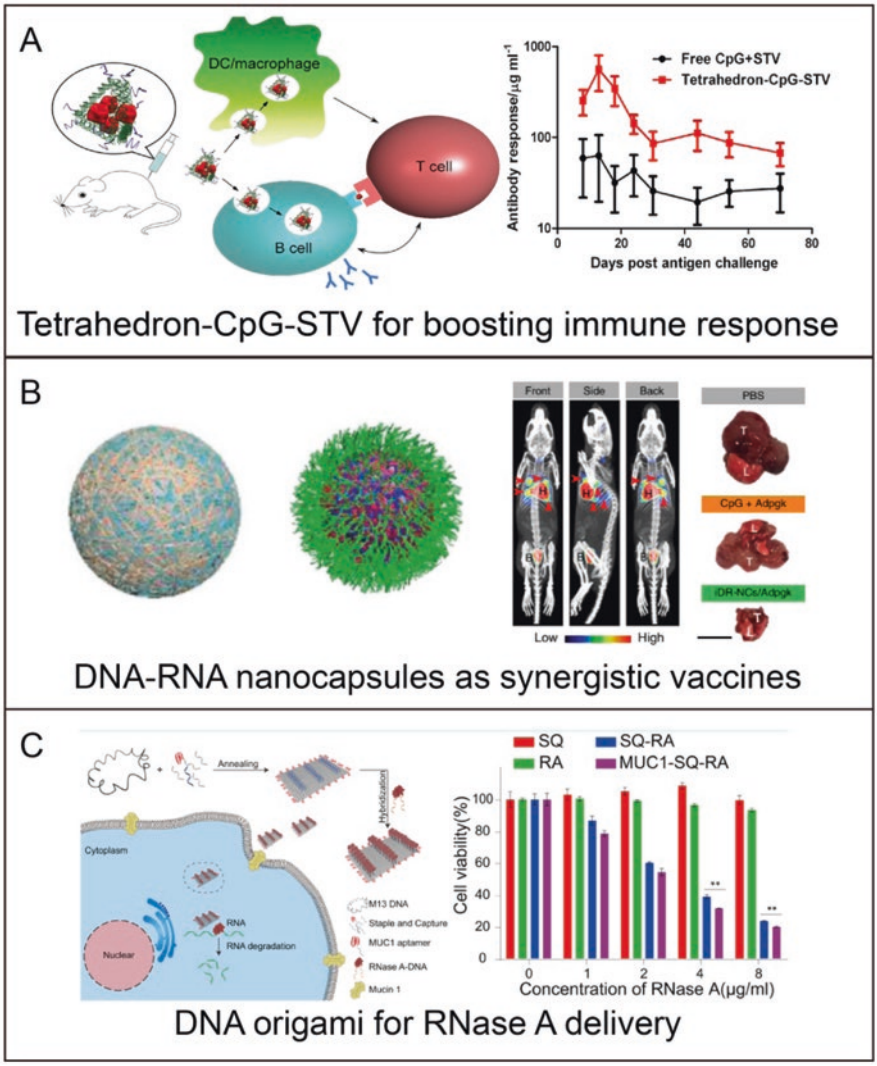

Fig. 6.7 Examples of DNA nanostructures for protein or peptide delivery. (**a**) DNA tetrahedron for co-delivery STV and CpG to elicit stronger and long-term immune responses in vivo [69]. (**b**) RCA-derived DNA-RNA nanocapsule for incorporating CpG, *Stat3* short hairpin RNA adjuvants and tumor-specific peptide as a nanovaccine [24]. (**c**) DNA rectangular origami for RNase A delivery and cancer therapy [73]

hybridization. As a result of the coating by cationic polymer polyethylenimine (PEI) for stabilization and enhanced endosomal escape, the Cas9/sgRNA co-loaded DNA nanoclews showed enhanced delivery to the nuclei of human cells, enabling targeted gene editing in vitro and in vivo.

Cytotoxic proteins ribonuclease (RNase) A can be utilized for cancer therapy. Stevens and colleagues developed multiple protein-encapsulated DNA nanoflowers derived by RCA approach [72]. They used RNase A as a model protein cargo to be delivered by nanoflower to cells without a loss in its biological function and structural integrity. The RNase A containing nanoflowers achieved protein delivery efficiency, thereby inducing significant cytotoxic effects compared to the free enzyme. Ding and colleagues utilized DNA origami nanostructures as containers for protein delivery [73]. They arranged RNase A molecules on rectangular DNA origami nanosheets, which served as nanovehicles to carry RNase A to the cytoplasm and execute their cell-killing function inside the tumor cells. Tumor-specific MUC1 aptamers were also integrated onto the DNA origami-based nanoplatform to enhance its targeting effect. Compared to free RNase A molecules, the DNA origami-protein co-assembling vehicles showed their prominent anti-tumor performance in MCF-7 cells (Fig. 6.7c).

Transferrin (Tf) is a key protein of iron transportation and delivery to cells, which is usually used as a ligand for targeting drug delivery [74]. Kjem and colleagues constructed a rectangular DNA origami functionalized with transferrin-oligodeoxynucleotide conjugates (Tf-ODN) for efficient cellular uptake. Tf-ODN was synthesized by DNA-templated protein conjugation, which kept biological activity of the conjugated Tf molecules. Tf-ODNs were then incubated with rectangular origami structures at room temperature overnight for efficient incorporation. The in vitro assessment of Tf-loaded DNA rectangles showed that Tf modification significantly enhanced the internalization of DNA origami into KB carcinoma cell line (possessing highly expressed Tf receptor) in a ligand dose-dependent manner.

6.3.5 Dynamic DNA Nanodevices and Machines for Biomedical Application

Natural macromolecular systems with stimuli-responsive properties have evolved to play various essential roles in biological systems. Inspired by natural macromolecular systems such as molecular motor proteins found in living cells, people committed in developing the artificial devices and machines. The bottom-up design, construction, and operation of these devices and machines on the molecular scale are popular topics in nanoscience and technology [75].

As excellent building blocks for design and construction of molecular devices, DNA molecules can be fabricated into various artificial, machine-like nanostructure, including tweezers, walkers, nanorobots, etc., to sense, actuate, and exert critical functions [38–40]. Besides those developments, DNA-based devices and machines as imaging probes and cargo delivery vehicles have been constructed and applied in vitro and in vivo.

Krishnan and colleagues provided a series of interesting applications for quantitative imaging and cargo delivery based on DNA nanodevices. In the first example,

they constructed a DNA nanomachine named I-switch to map pH gradients within subcellular environments [76]. Consisting cytosine-rich oligonucleotides for sensing protons and reporter molecules for fluorescence resonance energy transfer (FRET), the nanomachine was a robust pH-triggered nanoswitch, which was in "open" state (low FRET) at pH 7.3 and in "closed" state (high FRET) at pH 5.0. They tested the DNA nanomachine inside living cells and mapped spatial/temporal pH changes associated with endosome maturation. Further, they utilized two DNA nanomachines to simultaneously monitor intracellular pH changes via different pathways (the furin for retrograde endocytic pathway and the transferrin for endocytic/recycling pathway) [77]. To track the furin pathway, they fabricated type 1 DNA machine named I^{Fu}. With a similar working principle as I-switch, I^{Fu} also consisted of a dsDNA domain to specifically recognize a recombinant antibody along the furin pathway. They engineered a duplex DNA nanomachine (I^{Tf}) that contained a pH-sensitive element (forming an intramolecular i-motif at low pH) and conjugated transferrin along the transferrin receptor pathway. They demonstrated that each DNA nanomachine can localize into organelle and track pH of its targeted pathway; two nanomachines can be applied in a same cell to map pH changes along both pathways. Next, Krishnan and colleagues designed a pH-independent DNA nanomachine for detection of chloride ions in the cytoplasm and subcellular organelles [78]. In this work, the DNA nanodevice as chloride sensor was composed by sensing module (peptide nucleic acid conjugated with Cl^--sensitive fluorophore), normalizing module (DNA sequence bearing Cl^--insensitive Alexa 647) and targeting module (DNA sequence expending with Tf-targeting RNA aptamer). Through targeting delivery to organelles along the transferrin pathway, this chloride sensor enabled a precise measurement of the activity and location of subcellular chloride channels and transporters in living cells. Consisting of normalizing and sensing moieties in one DNA device, the sensor was successfully applied in quantitating the resting chloride concentration in the lumen of acidic organelles in *Drosophila melanogaster*.

In their follow-up work, they used a single DNA nanomachine integrated with quantitative pH and chloride reporting functions to investigate lysosome subpopulations [79]. Following the similar design principle to their previous work, the dual-functional nanomachine was constructed with pH-reporter containing i-motif sequence, Cl^--sensitive moiety, and normalizing fluorophore. Consequently, the measurement of two types of ions within single endosome was achieved by the combination nanomachine, enabling chemical resolving lysosome populations and evaluation of therapeutic efficacy. In their recent work, they also used the modular design of DNA nanomachine to quantitatively monitor intra-endosomal disulfide reduction in situ in coelomocytes *C. elegans* [80].

Besides those nanodevices for intracellular imaging, Krishnan and colleagues introduced encapsulating strategy of molecular cargos within DNA polyhedral vehicles [63, 64] that were mentioned above. Next, they composed conditional release moieties into their DNA polyhedral for spatiotemporal release of caged bioactive small molecules [81]. Photoactivated polymers bearing the small-molecule payload were synthesized and constructed into DNA icosahedra. Once receiving photo

irradiation, chemically modified dextrans entrapped in icosahedral nanocapsule-released fluorophores that diffused out of the nanocapsule, or released a non-fluorescent protecting group leaving behind a fluorescent cargo within the nanocapsules. DNA icosahedra as imaging agents showed cytosolic delivery with the spatial resolution of single endosomes within a single cell in *C. elegans*. Similar DNA nanocapsules were also applied to the photo-responsive release of dehydroepiandrosterone (DHEA, a neurosteroid that promotes neurogenesis and neuron survival) and determined the timescale of neuronal activation.

The DNA nanodevices and machines working in cells and *C. elegans* were all small assemblies (<20 nm) consisting of several DNA strands. Based on DNA origami techniques, several large and dynamic DNA assemblies with sophisticated functions have been fabricated and utilized in vitro and in vivo.

Douglas and colleagues described a DNA nanorobot that can transport molecular payloads to specific cells, sense cell surface inputs, and trigger activation in a programmed fashion [82]. They engineered a hexagonal DNA origami barrel (~40 nm) that was fastened by two DNA aptamer-based "locks." Inspired by structure-switching aptamer beacons, these two DNA "locks" were designed to open once binding with their corresponded antigen "keys." Molecular payloads (including DNA-modified gold nanoparticles or antibody Fab' fragments) were loaded in the cavities of nanorobots via hybridization. When confronted to human leukocytes with antigens (cell surface inputs), the DNA nanorobots were capable to open and expose the inside payloads. Subsequently, the antibody Fab' fragments were allowed to bind to cell surface receptors, inhibiting the growth of the target cells or inducing cell signaling. Moreover, the two aptamer locks could also be programmed to recognize two different inputs (thus equivalent to a logical AND gate), and both keys were needed to activate the DNA nanorobot. Andersen and colleagues employed a dynamic DNA origami nanovault to cage enzyme and control over reaction [83]. A single enzyme with an azide handle was loaded at the alkyne-exposing cargo-anchoring site (CAS) of the open DNA nanovault via click chemistry. After enzyme loading, the open DNA vault was then closed by adding sequence-specific closing strands. Once receiving a specific DNA signal (8-nt hinge) in solution, closed DNA vaults converted to fully opened structures, exposing the encapsulated enzyme molecules. The enzyme-substrate interaction and enzyme activity were controlled by the dynamic DNA nanovault with the unique properties of reversible opening/closing, cargo loading, and wall porosity (Fig. 6.8a).

The DNA robotic strategy inspired new designs with different biologically active payloads and applications. Bachelet and colleagues studied aptamer-controlled barrel-shaped DNA nanorobots and exploited a bio-computing application in living cockroaches (*Blaberus discoidalis*) [84]. They utilized the aptamers (recognized platelet-derived growth factor, PDGF; and vascular endothelial growth factor, VEGF) conjugated nanorobots to create various logic gates (AND, OR, XOR, NAND, NOT, CNOT and a half adder). When specific inputs (PDGF and VEGF) were present, Boolean computations by these logic gated DNA robots were successfully performed in living insects. In their further study, Bachelet and colleagues showed that DNA robots inside cockroaches were temporally controlled by human

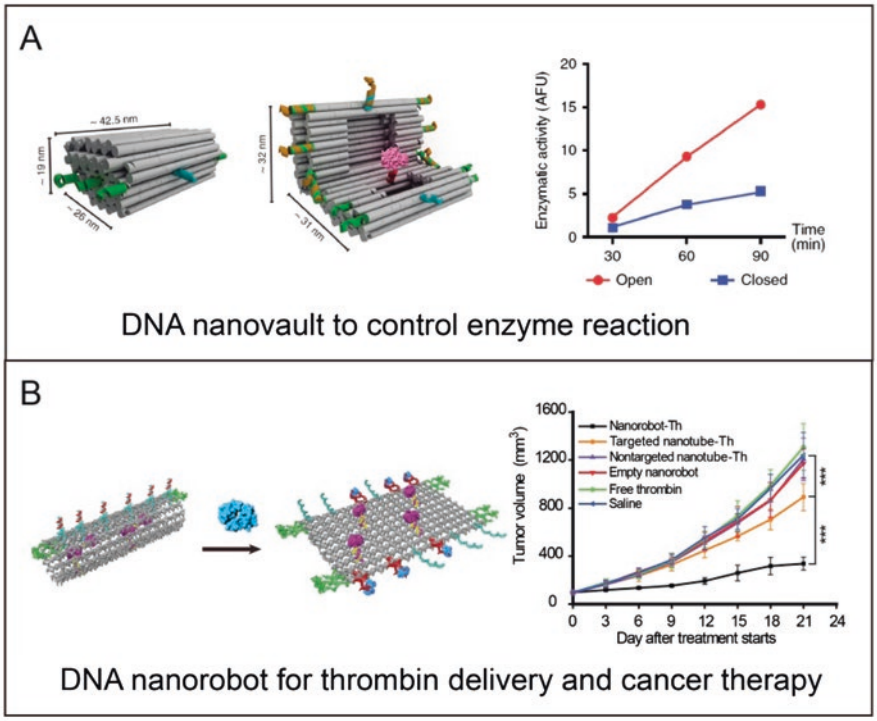

Fig. 6.8 Examples of DNA-based nanodevices for biological applications. (**a**) Reconfigurable DNA nanovault for controlling enzyme reactions [83]. (**b**) Thrombin-loaded DNA nanorobot for tumor vessel-specific coagulation and in vivo cancer therapy [86]

thoughts [85]. They recorded cognitive states associated with EEG patterns and utilized them to control states of an electromagnetic field, which was generating local thermal effects to unlock the metal nanoparticle-conjugated DNA nanorobots.

Besides applications in cells and insects, Zhao and colleagues recently used tumor-bearing mice as model animals to investigate an engineered DNA nanorobot and its therapeutic efficacy [86]. They fabricated a tube-shaped DNA nanorobot that was customized to position blood coagulation protease thrombin molecules in its cavity as payloads and nucleolin-specific DNA aptamers as locking moieties. Once confronted to tumor vascular endothelial cells highly expressing nucleolin, the mechanical opening of the DNA nanorobot was triggered. The exposed thrombin molecules in the unrolled DNA nanorobots activated localized coagulation in tumor blood vessels, inducing the tumor to "starve to death." In several tumor-bearing mouse models (breast cancer, ovarian cancer, melanoma, and lung cancer), the thrombin-loaded DNA nanorobot initiated tumor-specific thrombosis and vessel occlusion, eliciting robust tumor growth inhibition. The nanorobots were safe and immunologically inert in normal mice and Bama miniature pigs, without detectable changes in blood coagulation indices or histological morphology in either model (Fig. 6.8b).

6.4 Summary and Outlook

DNA nanotechnology enables design and fabrication of versatile drug vehicles with arbitrary structures and controllable functions. In this chapter, we have summarized recent advances of DNA-based nanomaterials according to their structural properties and functionalities. DNA assemblies can be engineered with a variety of functional payloads, enabling predesigned imaging or therapeutic applications. In recent years, DNA-based nanomachines and nanorobots with biological functions have also been introduced. These intelligent DNA nanodevices enable the targeted delivery and controllable release of bioactive payloads at the desired sites in various cellular and animal models. In contrast to nanocarriers (including liposomal or polymeric nanoparticles) composed by traditional well-defined materials, DNA-based nanomaterials are featured with predesigned sizes and shapes, addressable and programmable structures, as well as marked biocompatibility, offering an alternative promising candidate for precise and on-demand drug delivery.

Although several DNA-based nanomaterials clearly demonstrated the in vitro and in vivo therapeutic potentials, further advances of biomedical applications of DNA nanotechnology still face several roadblocks. The size- and shape-dependent properties of DNA nanostructures need to be investigated when they interact with (diseased and healthy) cells and traffic through systematic circulation. Shih and colleagues showed that large and compact origami structures were preferentially internalized by cells in contrast to elongated, high-aspect-ratio structures [87]. Ke and his colleagues published results that geometries of DNA origami assemblies affect their cellular uptake [65]. Cell types also influence the internalization of DNA origami. Recently, Fan and colleagues reported a “like-charge attraction” mechanism of DNA nanostructure at the interface of cytoplasmic membranes, providing new clues for rational design of nanovehicles for therapeutics [88].

Additionally, detailed in vivo characteristics of DNA-based nanomaterials including their circulating half-life, pharmacokinetics and clearance mechanisms must be elucidated. In a recent study, Cai and colleagues evaluated the biodistribution of ^{64}Cu-DNA origami nanostructures via positron emission tomography (PET) and discovered predominant renal uptake of origami in healthy mice [89]. They hypothesized that active kidney accumulation of origami structures might be attributed to their compact structures, negatively charged surfaces, morphologies, and sizes. Several studies from Shih and colleagues revealed PEGylated lipid bilayer enveloping of DNA octahedron [90] or oligolysine polyethylene glycol coating of DNA origami nanostructures [91] exhibited modest increase in pharmacokinetic bioavailability. Schmidt and colleagues confirmed that the PEGylated protection strategy of DNA nanostructures did not hamper the hybridization with DNA-modified gold nanoparticles or the interaction with streptavidin-modified quantum dots [92]. However, this strategy was based on electrostatic interaction, which changed the hydrodynamic radius and surface charge of DNA origami, leading to a different biodistribution pattern and altering the renal accumulation [89]. More investigation and experiments are still needed to determine the impact of

geometries, morphologies and surface charges on the in vivo behaviors of DNA nanostructures. How the DNA nanostructures and coating strategies interact with the corona proteins in the circulation should be carefully studied.

Further understanding of potential immune response of DNA nanostructures is also needed. Most biological studies need the immunogenic inert nanomaterials, which indicate their safety for in vivo application. Currently, M13mp18 phage genome DNA strands are used as scaffolds for assembling DNA origami structures in more than 90% of studies. This particular sequence may elicit weak immune responses [50]. The mentioned PEGylated strategies showed attenuated immune stimulation of DNA nanostructures [90]. On the other hand, immunotherapy needs materials to manipulate the immune system to efficiently eradicate malignant cells. Arrangement of immunostimulatory moieties (antigens and adjuvants) onto the DNA template has been used to tune the immunogenicity of DNA nanostructures, which can work as nanovaccines [24]. DNA nanomaterials generating custom-designed immune responses can be further fabricated for different applications.

Mass production (milligram-scale and even gram-scale amounts) of DNA nanostructure is another concern. Dietz and colleagues recently introduced a biotechnological method for highly efficient production of DNA origami nanostructures [93]. Growing such phages in the fermenters to produce DNA strands rather than chemical synthesis makes it much easier to pursue really large-scale production of medicinal and industrial DNA nanostructures. They also estimate production costs of folded DNA structures around €0.18/mg, which has been greatly reduced, compared to solid-phase chemical synthesis.

Though DNA nanotechnology has not yet been translated into the clinic, clear demonstrations of the targeting delivery and diseases therapy by various DNA nanomaterials have shown great potential in biological applications. We envision that the sophisticated and programmable DNA assemblies will play an increasingly important role in biomedical field, especially for intelligent drug delivery, nanomedicine-tumor interaction studies and possible clinical applications in the future.

References

1. N.C. Seeman, Nucleic-acid junctions and lattices. J. Theor. Biol. **99**(2), 237–247 (1982)
2. J.H. Chen, N.C. Seeman, Synthesis from DNA of a molecule with the connectivity of a cube. Nature **350**(6319), 631–633 (1991)
3. R.P. Goodman, R.M. Berry, A.J. Turberfield, The single-step synthesis of a DNA tetrahedron. Chem. Commun. **12**, 1372–1373 (2004)
4. Y.W. Zhang, N.C. Seeman, Construction of a DNA-truncated octahedron. J. Am. Chem. Soc. **116**(5), 1661–1669 (1994)
5. M.M. Ali et al., Rolling circle amplification: a versatile tool for chemical biology, materials science and medicine. Chem. Soc. Rev. **43**(10), 3324–3341 (2014)
6. C. Lin et al., DNA tile based self-assembly: building complex nanoarchitectures. ChemPhysChem **7**(8), 1641–1647 (2006)

7. F. Zhang, Y. Liu, H. Yan, Complex Archimedean tiling self-assembled from DNA nanostructures. J. Am. Chem. Soc. **135**(20), 7458–7461 (2013)
8. Y.G. Li et al., Controlled assembly of dendrimer-like DNA. Nat. Mater. **3**(1), 38–42 (2004)
9. S.H. Um et al., Enzyme-catalysed assembly of DNA hydrogel. Nat. Mater. **5**(10), 797–801 (2006)
10. P.W.K. Rothemund, Folding DNA to create nanoscale shapes and patterns. Nature **440**(7082), 297–302 (2006)
11. A.V. Pinheiro et al., Challenges and opportunities for structural DNA nanotechnology. Nat. Nanotechnol. **6**(12), 763–772 (2011)
12. F. Hong et al., DNA origami: scaffolds for creating higher order structures. Chem. Rev. **117**(20), 12584–12640 (2017)
13. N.C. Seeman, H.F. Sleiman, DNA nanotechnology. Nat. Rev. Mater. **3**(1), 17068 (2018)
14. T.J. Fu, N.C. Seeman, DNA double-crossover molecules. Biochemistry **32**(13), 3211–3220 (1993)
15. T.H. LaBean et al., Construction, analysis, ligation, and self-assembly of DNA triple crossover complexes. J. Am. Chem. Soc. **122**(9), 1848–1860 (2000)
16. C.D. Mao et al., Logical computation using algorithmic self-assembly of DNA triple-crossover molecules. Nature **407**(6803), 493–496 (2000)
17. H. Yan et al., Directed nucleation assembly of DNA tile complexes for barcode-patterned lattices. Proc. Natl. Acad. Sci. U. S. A. **100**(14), 8103–8108 (2003)
18. D.Y. Yang et al., DNA materials: bridging nanotechnology and biotechnology. Acc. Chem. Res. **47**(6), 1902–1911 (2014)
19. H.-M. Meng et al., DNA dendrimer: an efficient nanocarrier of functional nucleic acids for intracellular molecular sensing. ACS Nano **8**(6), 6171–6181 (2014)
20. Y.H. Roh et al., Layer-by-layer assembled antisense DNA microsponge particles for efficient delivery of cancer therapeutics. ACS Nano **8**(10), 9767–9780 (2014)
21. R. Hu et al., DNA nanoflowers for multiplexed cellular imaging and traceable targeted drug delivery. Angew. Chem. Int. Ed. **53**(23), 5821–5826 (2014)
22. G.Z. Zhu et al., Noncanonical self-assembly of multifunctional DNA nanoflowers for biomedical applications. J. Am. Chem. Soc. **135**(44), 16438–16445 (2013)
23. W.J. Sun et al., Cocoon-like self-degradable DNA Nanoclew for anticancer drug delivery. J. Am. Chem. Soc. **136**(42), 14722–14725 (2014)
24. G.Z. Zhu et al., Intertwining DNA-RNA nanocapsules loaded with tumor neoantigens as synergistic nanovaccines for cancer immunotherapy. Nat. Commun. **8**, 1482 (2017)
25. S.M. Douglas et al., Self-assembly of DNA into nanoscale three-dimensional shapes. Nature **459**(7245), 414–418 (2009)
26. D.R. Han et al., DNA origami with complex curvatures in three-dimensional space. Science **332**(6027), 342–346 (2011)
27. H. Dietz, S.M. Douglas, W.M. Shih, Folding DNA into twisted and curved nanoscale shapes. Science **325**(5941), 725–730 (2009)
28. D.R. Han et al., Single-stranded DNA and RNA origami. Science **358**(6369), eaao4648 (2017)
29. F. Praetorius, H. Dietz, Self-assembly of genetically encoded DNA-protein hybrid nanoscale shapes. Science **355**(6331), eaam5488 (2017)
30. B. Wei, M.J. Dai, P. Yin, Complex shapes self-assembled from single-stranded DNA tiles. Nature **485**(7400), 623–626 (2012)
31. Y.G. Ke et al., Three-dimensional structures self-assembled from DNA bricks. Science **338**(6111), 1177–1183 (2012)
32. V.P. Chauhan, R.K. Jain, Strategies for advancing cancer nanomedicine. Nat. Mater. **12**(11), 958–962 (2013)
33. A.S. Thakor, S.S. Gambhir, Nanooncology: the future of cancer diagnosis and therapy. CA Cancer J. Clin. **63**(6), 395–418 (2013)
34. B. Yurke et al., A DNA-fuelled molecular machine made of DNA. Nature **406**, 605–608 (2000)
35. H. Yan et al., A robust DNA mechanical device controlled by hybridization topology. Nature **415**, 62–65 (2002)

36. T. Omabegho, R. Sha, N.C. Seeman, A bipedal DNA Brownian motor with coordinated legs. Science **324**(5923), 67–71 (2009)
37. S.F.J. Wickham et al., A DNA-based molecular motor that can navigate a network of tracks. Nat. Nanotechnol. **7**, 169–173 (2012)
38. T. Gerling et al., Dynamic DNA devices and assemblies formed by shape-complementary, non-base pairing 3D components. Science **347**(6229), 1446–1452 (2015)
39. A.J. Thubagere et al., A cargo-sorting DNA robot. Science **357**(6356), eaan6558 (2017)
40. E. Kopperger et al., A self-assembled nanoscale robotic arm controlled by electric fields. Science **359**(6373), 296–301 (2018)
41. Q. Jiang et al., DNA origami as a carrier for circumvention of drug resistance. J. Am. Chem. Soc. **134**(32), 13396–13403 (2012)
42. P.D. Halley et al., Daunorubicin-loaded DNA origami nanostructures circumvent drug-resistance mechanisms in a leukemia model. Small **12**(3), 308–320 (2016)
43. L. Xu et al., Surface-engineered gold nanorods: promising DNA vaccine adjuvant for HIV-1 treatment. Nano Lett. **12**(4), 2003–2012 (2012)
44. Q. Zhang et al., DNA origami as an in vivo drug delivery vehicle for cancer therapy. ACS Nano **8**(7), 6633–6643 (2014)
45. Q. Mou et al., DNA Trojan horses: self-assembled floxuridine-containing DNA polyhedra for cancer therapy. Angew. Chem. **129**(41), 12702–12706 (2017)
46. J. Zhang et al., A Camptothecin-grafted DNA tetrahedron as a precise nanomedicine to inhibit tumor growth. Angew. Chem. Int. Ed. **58**(39)
47. T. Wu et al., A nanobody-conjugated DNA nanoplatform for targeted platinum-drug delivery. Angew. Chem. Int. Ed. Engl. **58**(40), 14224–14228 (2019)
48. S. Surana, A.R. Shenoy, Y. Krishnan, Designing DNA nanodevices for compatibility with the immune system of higher organisms. Nat. Nanotechnol. **10**(9), 741–747 (2015)
49. J. Li et al., Self-assembled multivalent DNA nanostructures for noninvasive intracellular delivery of immunostimulatory CpG oligonucleotides. ACS Nano **5**(11), 8783–8789 (2011)
50. V.J. Schüller et al., Cellular immunostimulation by CpG-sequence-coated DNA origami structures. ACS Nano **5**(12), 9696–9702 (2011)
51. Y. Qu et al., Self-assembled DNA dendrimer nanoparticle for efficient delivery of Immunostimulatory CpG motifs. ACS Appl. Mater. Interfaces **9**(24), 20324–20329 (2017)
52. S. Sellner et al., DNA nanotubes as intracellular delivery vehicles in vivo. Biomaterials **53**, 453–463 (2015)
53. Y. Liu et al., Responsive nanocarriers as an emerging platform for cascaded delivery of nucleic acids to cancer. Adv. Drug Deliv. Rev. **115**, 98–114 (2017)
54. J.J. Fakhoury et al., Development and characterization of gene silencing DNA cages. Biomacromolecules **15**(1), 276–282 (2014)
55. J. Li et al., Self-assembly of DNA nanohydrogels with controllable size and stimuli-responsive property for targeted gene regulation therapy. J. Am. Chem. Soc. **137**(4), 1412–1415 (2015)
56. J. Yang et al., Self-assembled double-bundle DNA tetrahedron for efficient antisense delivery. ACS Appl. Mater. Interfaces **10**(28), 23693–23699 (2018)
57. K.E. Bujold, J.C.C. Hsu, H.F. Sleiman, Optimized DNA "Nanosuitcases" for encapsulation and conditional release of siRNA. J. Am. Chem. Soc. **138**(42), 14030–14038 (2016)
58. H. Lee et al., Molecularly self-assembled nucleic acid nanoparticles for targeted in vivo siRNA delivery. Nat. Nanotechnol. **7**, 389–393 (2012)
59. K. Ren et al., A DNA dual lock-and-key strategy for cell-subtype-specific siRNA delivery. Nat. Commun. **7**, 13580 (2016)
60. M.A. Rahman et al., Systemic delivery of Bc12-targeting siRNA by DNA nanoparticles suppresses cancer cell growth. Angew. Chem. Int. Ed. **56**(50), 16023–16027 (2017)
61. J. Liu et al., A DNA-based nanocarrier for efficient gene delivery and combined cancer therapy. Nano Lett. **18**, 3328–3334 (2018)
62. J. Liu et al., A tailored DNA nanoplatform for synergistic RNAi-/chemotherapy of multidrug-resistant tumors. Angew. Chem. Int. Ed. **57**(47), 15486–15490 (2018)

63. D. Bhatia et al., A synthetic icosahedral DNA-based host-cargo complex for functional in vivo imaging. Nat. Commun. **2**, 339 (2011)
64. D. Bhatia et al., Quantum dot-loaded monofunctionalized DNA icosahedra for single-particle tracking of endocytic pathways. Nat. Nanotechnol. **11**, 1112–1119 (2016)
65. P. Wang et al., Visualization of the cellular uptake and trafficking of DNA origami nanostructures in cancer cells. J. Am. Chem. Soc. **140**(7), 2478–2484 (2018)
66. Q. Jiang et al., A self-assembled DNA origami-gold nanorod complex for cancer theranostics. Small **11**(38), 5134–5141 (2015)
67. Y. Du et al., DNA-nanostructure–gold-nanorod hybrids for enhanced in vivo optoacoustic imaging and photothermal therapy. Adv. Mater. **28**(45), 10000–10007 (2016)
68. L. Song et al., DNA origami/gold nanorod hybrid nanostructures for the circumvention of drug resistance. Nanoscale **9**(23), 7750–7754 (2017)
69. Y. Xie et al., Real-time observations on crystallization of gold nanorods into spiral or lamellar superlattices. Chem. Commun. (Camb.) **48**(15), 2128–2130 (2012)
70. C. Wang et al., Inflammation-triggered cancer immunotherapy by programmed delivery of CpG and anti-PD1 antibody. Adv. Mater. **28**(40), 8912–8920 (2016)
71. W. Sun et al., Self-assembled DNA Nanoclews for the efficient delivery of CRISPR–Cas9 for genome editing. Angew. Chem. Int. Ed. **54**(41), 12029–12033 (2015)
72. E. Kim et al., One-pot synthesis of multiple protein-encapsulated DNA flowers and their application in intracellular protein delivery. Adv. Mater. **29**(26), 1701086 (2017)
73. S. Zhao et al., Efficient intracellular delivery of RNase a using DNA origami carriers. ACS Appl. Mater. Interfaces **11**(12), 11112–11118 (2019)
74. D.H. Schaffert et al., Intracellular delivery of a planar DNA origami structure by the transferrin-receptor internalization pathway. Small **12**(19), 2634–2640 (2016)
75. J. Li et al., Micro/nanorobots for biomedicine: delivery, surgery, sensing, and detoxification. Sci. Robot. **2**(4), eaam6431 (2017)
76. S. Modi et al., A DNA nanomachine that maps spatial and temporal pH changes inside living cells. Nat. Nanotechnol. **4**, 325–330 (2009)
77. S. Modi et al., Two DNA nanomachines map pH changes along intersecting endocytic pathways inside the same cell. Nat. Nanotechnol. **8**(6), 459–467 (2013)
78. S. Saha et al., A pH-independent DNA nanodevice for quantifying chloride transport in organelles of living cells. Nat. Nanotechnol. **10**, 645 (2015)
79. K. Leung et al., A DNA nanomachine chemically resolves lysosomes in live cells. Nat. Nanotechnol. **14**(2), 176–183 (2019)
80. K. Dan et al., DNA nanodevices map enzymatic activity in organelles. Nat. Nanotechnol. **14**(3), 252–259 (2019)
81. A.T. Veetil et al., Cell-targetable DNA nanocapsules for spatiotemporal release of caged bioactive small molecules. Nat. Nanotechnol. **12**, 1183–1189 (2017)
82. S.M. Douglas, I. Bachelet, G.M. Church, A logic-gated nanorobot for targeted transport of molecular payloads. Science **335**(6070), 831–834 (2012)
83. G. Grossi et al., Control of enzyme reactions by a reconfigurable DNA nanovault. Nat. Commun. **8**(1), 992 (2017)
84. Y. Amir et al., Universal compting by DNA origami robots in a living animal. Nat. Nanotechnol. **9**(5), 353–357 (2014)
85. S. Arnon et al., Thought-controlled nanoscale robots in a living host. PLoS One **11**(8), e0161227 (2016)
86. S. Li et al., A DNA nanorobot functions as a cancer therapeutic in response to a molecular trigger in vivo. Nat. Biotechnol. **36**(3), 258–264 (2018)
87. M.M.C. Bastings et al., Modulation of the cellular uptake of DNA origami through control over mass and shape. Nano Lett. **18**(6), 3557–3564 (2018)
88. H. Ding et al., DNA nanostructure-programmed like-charge attraction at the cell-membrane interface. ACS Central Sci. **4**(10), 1344–1351 (2018)
89. D. Jiang et al., DNA origami nanostructures can exhibit preferential renal uptake and alleviate acute kidney injury. Nat. Biomed. Eng. **2**(11), 865–877 (2018)

90. S.D. Perrault, W.M. Shih, Virus-inspired membrane encapsulation of DNA nanostructures to achieve in vivo stability. ACS Nano **8**(5), 5132–5140 (2014)
91. N. Ponnuswamy et al., Oligolysine-based coating protects DNA nanostructures from low-salt denaturation and nuclease degradation. Nat. Commun. **8**, 15654 (2017)
92. N.P. Agarwal et al., Block copolymer Micellization as a protection strategy for DNA origami. Angew. Chem. Int. Ed. **56**(20), 5460–5464 (2017)
93. F. Praetorius et al., Biotechnological mass production of DNA origami. Nature **552**(7683), 84–87 (2017)

Chapter 7
Intermolecular Interactions and Self-Assembly of Peptide-Based Nanomaterials Against Human Pathogenic Bacteria

Wenbo Zhang, Lanlan Yu, and Chenxuan Wang

Abstract Nanomaterial systems composed of polypeptides are inherently hierarchical in their organization: non-covalent interactions displayed by peptide building blocks engender well-ordered structures with broad applications. This chapter is intended to reflect on the recent progress made in the development of functionalized peptide self-assembling nanomaterials and their therapeutic applications against pathogenic bacteria. We review recent efforts directed to the creation of structurally defined supramolecular assemblies derived from either peptides or synthetic oligomers mimicking the folding and organization of polypeptides. We elucidate the roles of non-covalent interactions, which are encoded by peptide primary amino acid sequence, on the folding and self-assembly of peptides, which in turn gives rise to biological function (e.g., antibacterial activity). Overall, the capability to build peptide-based nanomaterials and tune their functional properties presents exciting opportunities for future research and applications.

Keywords Protein folding · Self-assembled nanostructures · Antimicrobial · Intermolecular interaction · β-peptide

7.1 Introduction

A delicate balance between the host innate immune system and microbes is required to maintain human health. Perturbation of this balance can cause various microbial infectious diseases. Multicellular organisms have evolved immune response mechanisms to defend against the invasion of microorganisms. Host defense peptides are a diverse group of peptides with broad-spectrum activity against gram-positive

W. Zhang · L. Yu · C. Wang (✉)
State Key Laboratory of Medical Molecular Biology, Institute of Basic Medical Sciences, Department of Biophysics and Structural Biology, Chinese Academy of Medical Sciences and Peking Union Medical College, Beijing, China
e-mail: wangcx@ibms.pumc.edu.cn

H. Xu, N. Gu (eds.), *Nanotechnology in Regenerative Medicine and Drug Delivery Therapy*, https://doi.org/10.1007/978-981-15-5386-8_7

bacteria, gram-negative bacteria, and fungi, serving as an evolutionarily conserved mechanism against the infection of microbes [1].

Most host defense peptides adopt one of the following conformations: α-helix (magainin, LL-37, melittin, cecropin), β-sheet (arenicin, PMAP-23, lacidophilin, human β-defensin-2), extended (indolicidin, Bac-5, PR-39, omiganan) [2]. Upon contact with cell membranes, host defense peptides fold and spatially segregate cationic and hydrophobic amino acid residues on opposite faces of the molecule, resulting in amphiphilicity [1, 2]. The amphiphilic nature of host defense peptides thereby allows them to partition into bacterial cell membranes and disintegrate the lipid bilayer structure [3]. Several distinguishable hypotheses have been proposed to interpret the action mechanisms of membrane permeabilization by host defense peptides: barrel-stave, toroidal pore, and carpet [1, 4–6]. In the barrel-stave model, peptides reach the membrane as monomers or oligomers and assemble on the surface of the membrane. In the next step, they insert perpendicularly into the plane of the membrane bilayer and then recruit more peptide monomers to form a transmembrane pore of bundled peptides [1, 5, 6]. In the toroidal pore model, host defense peptides are oriented parallel to the bilayer plane at low peptide concentration. When peptides reach a critical concentration, they co-assemble with lipid molecules and translocate into the membrane. This action disintegrates the membrane and releases micelles composed of a peptide-lipid supramolecular dynamic complex [1, 4]. In the carpet mode, amphiphilic peptides cover the surface of lipid membrane at a high density. When the concentration of host defense peptide is high enough, the membrane curvature of bacterial cell is changed. It leads to the collapse of the structure of the plasma membrane and the formation of peptide-lipid micelles [1, 6].

In view of the prevalence of microbial resistance to commonly used antibiotics, there is a growing interest to develop peptide antibiotics as potential therapeutic applications. Due to their membrane-lytic activity against bacteria, host defense peptides have a low propensity to induce microbial resistance [1, 2, 4]. However, several factors prevent the clinical application of host defense peptides. One of the major limitations of peptides is their high susceptibility to proteolytic degradation and elimination by the reticuloendothelial system and renal filtration [7, 8]. The rapid metabolism and elimination of host defense peptides results in an insufficient lifetime in vivo to reach their therapeutic targets. Another limitation is that high concentrations of defense peptides produce cytotoxicity to host cells. Some host defense peptides are capable of disrupting mammalian membranes and causing mammalian cell lysis. To overcome problems associated with the failure of host defense peptide in application, substantial efforts have been made to improve the bioavailability of peptide drugs by creating nanostructured materials derived from peptides or peptide synthetic analogs [9, 10]. The strategies that develop nanostructured peptide materials, which include building self-assembled peptide-based nanostructures, encapsulating peptides in a delivery system, and chemical modification, have been shown to improve the peptide stability and delivery to the target [9, 10]. This chapter reviews the recent approaches on the development of new self-assembled peptide-based materials that may challenge the medical fight against pathogenic bacteria.

7.2 Development of Peptide-Based Materials with Antibacterial Activity

Peptide-based building blocks serve as applicable platforms to construct supramolecular nanostructures with high order and complexity. Peptide nanostructures exhibit promising features for broad therapeutic applications, such as nanofiber scaffolds, regenerative medicine and tissue engineering, scaffolds for three-dimensional (3D) cell cultures and 3D cell migration, and to stabilize diverse membrane proteins [11–14]. Herein, we focus on the discussion of peptide-based supramolecular assemblies from the perspective of their designs, characterizations, and potential medical applications against pathogenic bacteria.

7.2.1 Peptide Structures

Prior to the introduction of polypeptide self-assembly-based nanomaterials, it is necessary to give a brief introduction to the basic components of polypeptide structures. Polypeptide chains are formed by linearly linked amino acids in a definite sequence. The amino acid sequence determines protein secondary structure, which reflects the 3D arrangement of protein local segments. The two most common polypeptide secondary structures are α-helices and β structures, though coils and tight turns occur as well. Physicochemical properties of residues determine the characteristics of a protein, including, but not limited to, its 3D structure and its biological function. For example, proline has only one rather than two variable backbone angles and lacks the normal backbone NH. It has stronger stereo chemical constraints to disrupt the regular secondary structures that cause a turn along a protein chain relative to other types of amino acids. Thus, proline is usually located at the edges of a protein although it has hydrophobic properties to some extent. As for glycine, which has the smallest side group that puts little stereochemical constraints on the flexibility of backbone conformation, it is frequently found in a region where main chains are packed close to each other and have a potential to switch backbone conformation. As for other residues, the hydrophobic residues provide relatively strong driving forces for protein folding and are usually buried in the protein interiors, whereas residues with charged side chains (e.g., arginine, lysine, aspartic acid, and glutamic acid) are relatively hydrophilic and are often exposed on the surface of a protein.

7.2.1.1 Helices

α-Helix is a classic element of protein structure. It was first described by Pauling in 1951 as 3.6_{13}-helix in which every backbone NH group donates a hydrogen bond to the backbone CO group of an amino acid located four residues earlier along the

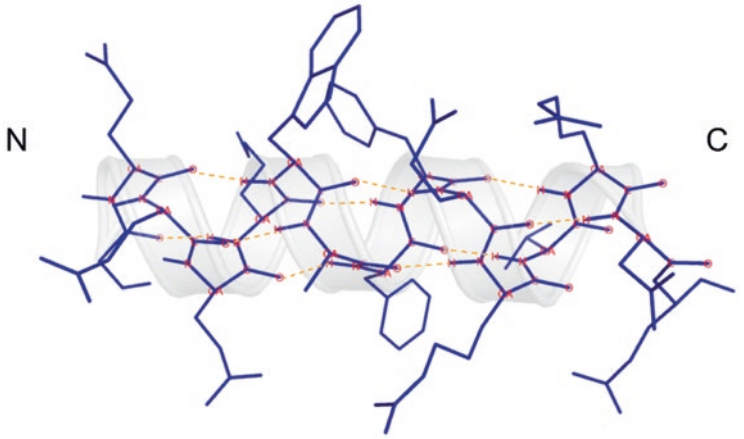

Fig. 7.1 A typical α-helix, residues 114–126 of the arsenate reductase from *Bacillus subtilis* (*B. subtilis*) [16]. The hydrogen bonds between the NH group of residue *n* and the CO group of residue *n-4* are shown as dotted lines in orange. The N- and C-termini of the peptide segment are labeled in the diagram. The direction of view is from the solvent. The front face of the helix contains hydrophilic residues whereas the back side is predominant by hydrophobic residues

protein sequence [15]. Including the hydrogen, the average atomic number per turn is 13 atoms, constructing a closed loop formed by the hydrogen bond. With 3.6 residues per turn, the side chains protrude from the α-helix at about every 100° in azimuth, and the rise per residue along the helix axis is 1.5 Å (Fig. 7.1) [15].

Based on the statistical results from a protein structural databank, α-helices are the most abundant form of secondary structure in globular proteins and are widely distributed on the surface of a protein [15]. Figure 7.2 shows the structure of an arsenate reductase which contains several α-helices [16]. Seven helices and four-stranded β-sheet (see below) are packed into an α/β-domain containing a central twisted β-sheet flanked by four α-helices. It is noteworthy that the axis of a helix may be slightly bent. The most common cause of such a bend is the presence of proline. 3_{10}-Helices are also found at either N- or C-terminal motifs of arsenate reductase. 3_{10}-Helix is a right-handed helical structure with a three-residue repeated segment and a hydrogen bond between the NH group of residue *n* and the CO group of residue *n-3*, instead of *n-4*. The average atomic number per turn is 10 atoms, which are involved in the closed loop formed by the hydrogen bond. With only 3 residues per turn, the side chains protrude from the α-helix at about every 120° in azimuth and a translation of 2 Å along the axis (Fig. 7.2). Long 3_{10}-helices are rare, but short segments of 3_{10}-helices are frequently found in globular proteins and polypeptides. However, the 3_{10}-helix is considerably less favorable than the 3.6_{13}-helix for a long periodic structure, in connection with the hydrogen bond configuration energy and local conformational energy.

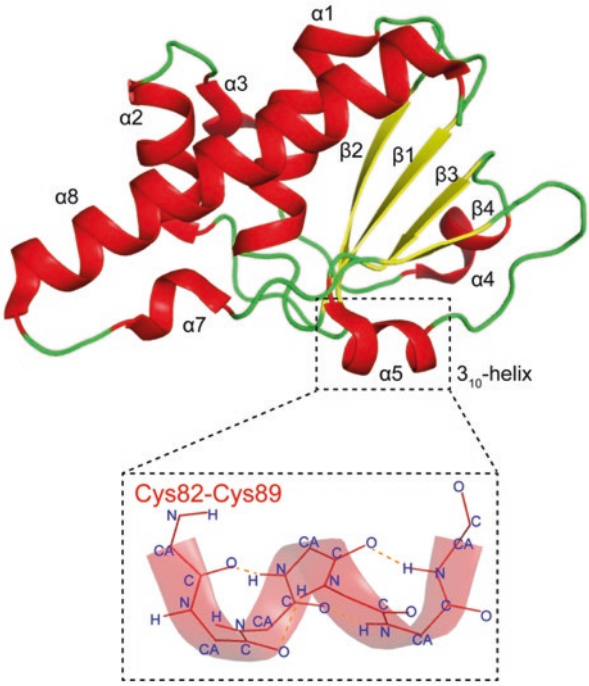

Fig. 7.2 Schematic illustration of the reduced state of arsenate reductase from *B. subtilis*. The seven α-helices and four-stranded β-sheet are colored red and green, respectively. The 3_{10}-helix formed by Cys82-Cys89 are emphasized. Hydrogen bonds between the NH group of residue *n* and the CO group of residue *n-3* are shown as dotted lines in orange

7.2.1.2 β Structure

β-Sheet is another representative structural element that is commonly found in globular proteins. In 1933, β structures were first described by William Astbury as straight, extended chains with alternating side chain directions and hydrogen bonds between the adjacent antiparallel chains. However, Astbury did not have enough data to build a correct model, since whether the peptide bond was planar or not is unclear. In 1951, Linus Pauling and Robert Corey proposed a revised model which described the distinctive patterns of the hydrogen bonding for both antiparallel and parallel β-sheet. This model described the planarity of the peptide bond and revealed that the β-sheets are pleated. β-Sheets consist of several β-strands connected by two or three backbone hydrogen bonds, forming a generally pleated sheet. In the antiparallel β-sheet arrangement, hydrogen bonds are perpendicular to the strands. Successive β-strands alternate directions, and thus the inter-strand hydrogen bonds between the CO groups and NH groups are in a plane, which is their preferred orientation and contributes to the strongest inter-strand stability. This model suggests that the narrowly spaced bond pairs alternate with widely spaced pairs. In the parallel β-sheet

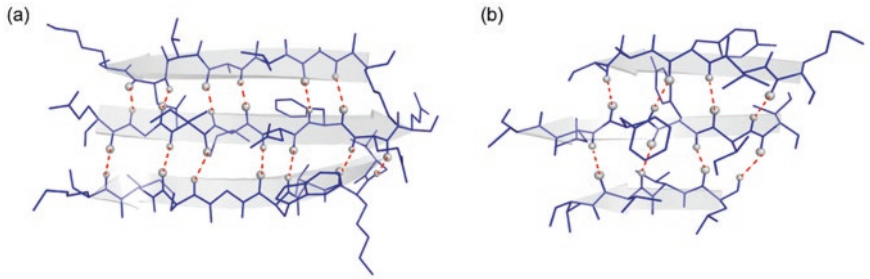

Fig. 7.3 Representative antiparallel and parallel β-sheets. (**a**) An example of antiparallel β-sheet from arsenate reductase (PDB code: 1Z2D) (residues 5–10, 33–37, and 77–80). (**b**) An example of parallel β-sheet from Cu/Zn superoxide dismutase (PDB code: 1DSW) (residues 3–9, 15–22, and 29–36). The directions of each strand are shown by arrows. The hydrogen bonds are shown by dotted lines and the atoms involved are shown as spheres

arrangement, successive β-strands are oriented in the same direction and generate nonplanarity in the inter-strand hydrogen-bonding networks. Figure 7.3 is a schematic illustration of the antiparallel and parallel β-sheets from real proteins.

β-Strands can form a pure antiparallel sheet, a pure parallel sheet, or a mixed sheet composed of both antiparallel and parallel strand pairs. Mixed sheets are relatively instable because the formation of two types of hydrogen bonds requires different backbone orientations, and the standard free energy of formation is relatively unfavorable. In general, a parallel β-sheet is more regular than an antiparallel sheet. It is difficult to find a β-sheet consisting of less than five strands, suggesting that a planar sheet composed of smaller number of strands is unfavorable in energy. However, there are some exceptions. For example, in the structure of arsenate reductase in Fig. 7.2, four β-strands form a parallel sheet exhibiting a twist conformation. Parallel β-sheets and the parallel portions of mixed sheets are always completely buried, with two surfaces of a sheet protected by other main chains (often α-helices). In contrast, an antiparallel β-sheet usually possesses an alternative pattern of hydrophobic/hydrophilic residues in sequence, and thus it exposes one surface to the solvent and keeps one surface in contact with another protein motif. It is notable that large antiparallel sheets can roll up partially or even form a cylinder or a barrel. For example, 5 to 13 β-strands can make up a β barrel, which consists of tandem β-strands twists and coils composed of hydrogen bonds between the first strand and the last strand. Within a β barrel, hydrophobic side chains are pointed toward the interior of barrel, and the barrel can be stabilized by hydrophobic forces. The side chains of hydrophilic residues are always oriented toward the outside of barrel and interact with solvent.

7.2.1.3 Other Nonrepetitive Structures

Helix, β structure, and coil are regular classifications used to describe protein structures. The main feature of coil structure is its nonrepetition in backbone conformation. Coil, commonly referred to as random coil, is a class of conformations without

regular secondary structure. We comment that peptide segments folded to ordered but irregular structures should be distinguished from random coil. For example, β turn, β bend, reverse turn, hairpin bend, kink, and widget are prevalent in protein's non-regular secondary structures. A β turn usually consists of 4 residues (*n*, *n + 1*, *n + 2*, and *n + 3*) and possesses an intra-backbone hydrogen bond between the CO of residue *n* and the NH of residue *n + 3*. The role of β turn is to connect successive β-strands, but sometimes it also appears at the ends of α-helices [15]. Relative to β turn, random coil is a kind of simple unfolded polypeptide chain conformation without any 3D structure.

7.2.2 Self-Assembly of Peptides to Nanostructures

This section focuses on introducing the formation of different self-assembled nanostructures, including their 3D structures, the driving force of the self-assembly, and some manually designed assembly materials. Self-assembly is a process in which the disordered pre-existing components form highly ordered structures controlled by the local interactions among the components' molecules. In aqueous environments, the self-assembly process is mediated through non-covalent forces, including van der Waals interactions, hydrophobic interactions, electrostatic interactions, and hydrogen bonds. Temperature, pH, and solute concentration also influence the self-assembly processes [17].

Many self-assembled molecules possess both hydrophobic and hydrophilic moieties and display amphiphilicity. In a biological system, the most well-known self-assembly structure is the lipid bilayer structure composed of amphiphilic phospholipids which have a hydrophilic phosphate head and a hydrophobic fatty acid tail. In aqueous solution, the nonpolar domains presented by the fatty acid chains engage in hydrophobic interactions to drive self-assembly. The phosphate head groups are largely deprotonated under physiological conditions and thus provide charge-related repulsions. As a result, phospholipids assemble into a two-layered sheet in which the hydrophobic tails point toward the center of the sheet and phosphate head exposed to water. The self-assembly of polypeptides or proteins is more complicated due to their complex amphiphilicity. For example, the side chains exposed on two faces of a β-pleated sheets can be either hydrophilic or hydrophobic. The folding and assembly of polypeptides is governed by the non-covalent networks that arise from side chain properties, such as charge, hydrophobicity, size, and polarity. Therefore, the chemical and structural principles encoded by amino acid identity provide an invaluable handle for manipulating and designing self-assembled polypeptide structures and peptide-peptide interactions. Here, we discuss a few representative supramolecular arrays by using peptides or proteins and unveil the principles of designing polypeptide building blocks (Fig. 7.4).

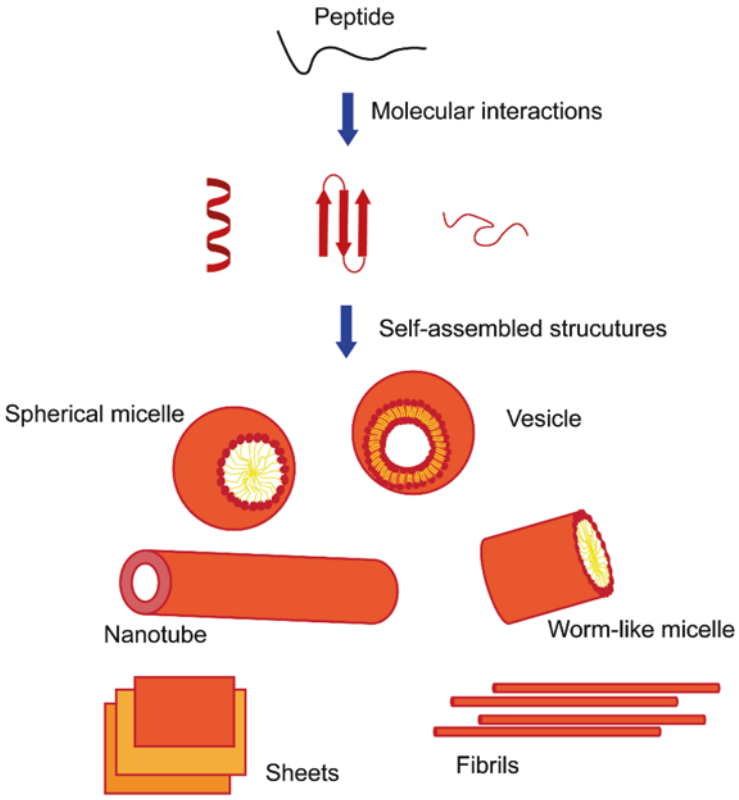

Fig. 7.4 Representative self-assembled structures, including spherical micelle, vesicle, worm-like micelle, nanotube, sheet, and fibril. The hydrophilic head and hydrophobic tail are represented as red spheres and yellow sticks, respectively

7.2.2.1 Tubular Nanostructures

Nanotubes are elongated tube-like structures and have a defined inner hole. The driving forces of nanotube growth originate from hydrogen bonds and π–π stacking of aromatic residues (cyclic peptides), as well as hydrophobic interactions (peptide amphiphiles).

Ghadiri and coworkers demonstrated a strategy to rationally design hollow nanotubes by using heterochiral cyclic peptides [18]. They used D- and L-amino acids to synthesize a cyclic heterochiral octapeptide cyclo[-(D-Ala-Glu-D-Ala-Gln)$_2$-] that self-assembled through hydrogen bonds. When the side chain of E is protonated, cyclic peptides are stacked into an antiparallel β-sheet like conformation, via hydrogen bonds between peptide backbones, and crystallize into tubular structures about hundreds of nanometers long with a 0.7–0.8 nm pore size. The hollow nanotubes made up of cyclic peptides adopt a specific orientation where

side chains are pointed outward from the nanotube surface, and intermolecular hydrogen bonds are parallel to the long-axis of the tube (Fig. 7.5) [18]. The biological functions of cyclic peptide hollow nanotubes were exploited by Fernandez-Lopez and coworkers [19]. The cyclic peptide family was found to potentially self-assemble in bacterial membranes and increase the membrane permeability. As a result, this kind of β-sheet-like tubular architecture exhibits promising antibacterial activity against gram-positive bacteria (*Bacillus subtilis*, *Bacillus cereus*, *Staphylococcus aureus*, *Listeria monocytogenes*) and gram-negative bacteria (*Enterococcus faecalis*, *Streptococcus pneumoniae*) [19].

Nanotubular structures can also be achieved by using peptide amphiphiles which have a hydrophobic tail and a hydrophilic head. Usually a bioactive peptide amphiphile also has a section of charged amino acids to promote solubility and bioactive functional peptide epitope (Fig. 7.6) [20]. The hydrophobic tails can be oligomers

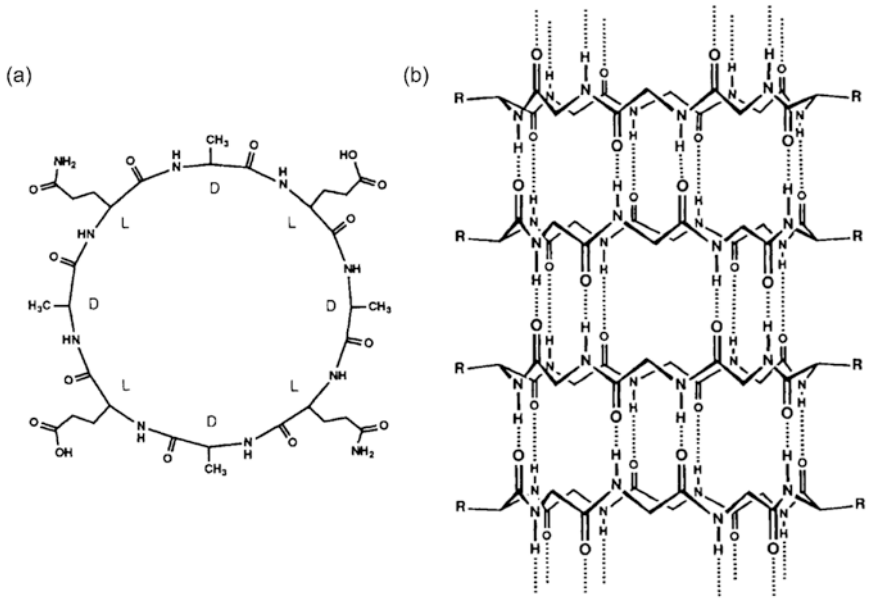

Fig. 7.5 (**a**) The chemical structure of cyclo[-(D-Ala-Glu-D-Ala-Gln)$_2$-]. The "D" or "L" represents the amino acid chirality. (**b**) Peptide subunits are shown as self-assembled tubular structures. The antiparallel stacking and the hydrogen-bonding interactions network are emphasized [18]

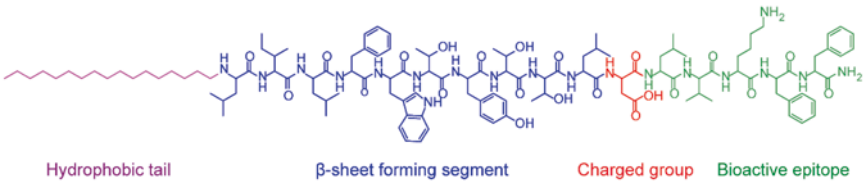

Fig. 7.6 A typical structure of peptide amphiphile. The four domains incorporate into the bioactive β-sheet peptide amphiphile [20]

of nonpolar amino acids (G, A, V, I, L, P, and F), while the heads are normally composed of positively charged amino acids (H, K and R) or negatively charged amino acids (D and E). Both the hydrophobic interactions generated by nonpolar tails as well as the hydrogen bonds between peptides provide attractive interactions for the assembly of peptide amphiphiles. For example, A_mK (where m = 3, 6, and 9) is a typical kind of peptide amphiphile. A_3K forms β-pleated sheet structure via hydrogen bonds, whereas A_6K forms long nanotubes and A_9K forms short nanorods which are driven by hydrophobic interactions [21, 22].

7.2.2.2 Nanofibers

Fibers with a diameter size of less than 100 nm are called nanofibers. The main difference between the nanofibers and nanotubes is that nanotubes include hollow structures while nanofibers do not. Under some specific solution conditions (temperature, pH, and ionic strength), peptides assemble into nanofibers via interpeptide hydrogen bonds and hydrophobic interactions. Stupp and coworkers created a broad class of 3D networks composed of nanofibers by using amphiphilic peptides, such as IKVAV [23]. Hamley and coworkers found that an alanine-rich peptide $A_{12}R_2$ can form twisted nanofibrils by stacking polyalanine domains [24]. Peptides in β-sheet conformation with alternating hydrophobic and hydrophilic residues can also form nanofibers. For example, alkylated peptide amphiphiles $C_{16}H_{31}$OVEVE, consisting of hydrophobic and negatively charged residues and an alkyl chain, can self-assemble into flat nanobelt structures (Fig. 7.7) [20].

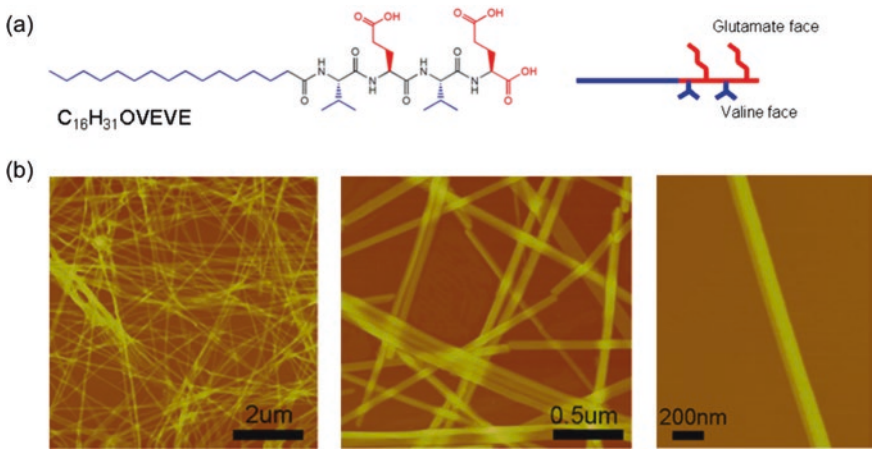

Fig. 7.7 Nanobelts assembled from a peptide amphiphile $C_{16}H_{31}$OVEVE. (**a**) Chemical structure of the peptide amphiphile. (**b**) AFM images of peptide nanobelts. Reprinted with permission from [20]. Copyright 2009 American Chemical Society

7.2.2.3 Spherical/Vesicle Structures

In aqueous solution at neutral pH, amphiphilic oligopeptides consisting of different proportions of hydrophilic to hydrophobic block length can self-assemble into spherical or vesicular structures. The peptides that self-assembled into vesicles were proline-rich peptides, copolypeptides, and cyclic peptides. Deming and coworkers showed that the poly(L-lysine)-b-poly(L-leucine), poly(L-glutamic acid)-b-poly(L-leucine), and poly(L-arginine)-b-poly(L-leucine) diblock polypeptides (where "b" refers to block) exhibit self-assembly behaviors, and stable vesicles and micelles are formed by the charged amphiphilic block copolypeptides [25]. The α-helical hydrophobic rod formation of the poly(L-leucine) block contributes to the formation of diblock polypeptides. Dreher and coworkers reported that self-assembly of elastin-like polypeptides, which were temperature triggered, can form spherical micelle architecture. Elastin-like polypeptides (ELPs) in a linear AB diblock architecture exhibit temperature-triggered self-assembly through a small increase in temperature between 37 and 42 °C [26]. While 37–42 °C is commonly used for clinical application of hyperthermia, spherical micelles formed by ELPs are used in drug therapy. Besides, both the length of the copolymer and the hydrophilic/hydrophobic block ratio control the size of the micelle. Lee and coworkers designed a block polypeptide of polyproline and an arginine oligomer, $P_{10}R_3$, which can form vesicles rather than micelles [26].

7.2.3 Structural Characterization of Self-Assembled Peptides

A series of experimental approaches, such as X-ray diffraction, nuclear magnetic resonance (NMR) spectroscopy, and cryo-electron microscopy (Cryo-EM), have been used to characterize polypeptide self-assembly structures under various conditions and study the interactions among peptides and proteins.

7.2.3.1 X-Ray Diffraction

Single crystal X-ray diffraction is the most unambiguous method for determining the arrays of atoms and molecules within a protein, which is based on the scattering of X-ray waves by electrons in the crystal. X-rays are electromagnetic waves with a wavelength of only around 1 Å. In 1895, Wilhelm Conrad Röntgen developed the method of protein crystallography inspired by the discovery of X-ray. In 1912, Max von Laue observed the diffraction of X-rays by a crystal and demonstrated that the scattering pattern would mark out the symmetrical arrangements of atoms in the crystal. These discoveries were followed by William and Lawrence Bragg, father and son, who invented the X-ray spectrometer and founded X-ray crystallography for the analysis of crystal structure. After 45 years of hard work, John Cowdery

Kendrew and Max Perutz solved the first crystal structure of a protein (the sperm whale myoglobin). They shared the Nobel Prize in Chemistry in 1962. So far, over 150,000 protein crystal structures have been deposited in the PDB databank, as well as the nucleic acids and other biological molecules. Several protein crystallographic structure studies have been awarded the Nobel Prize, illustrating the high level of recognition these outstanding works hold in the academic world. Some examples include the prize awarded to Dorothy Hodgkin (Chemistry Prize of 1964) for the determination of the structures of vitamin B_{12} and insulin; Johann Deisenhofer, Robert Huber, and Hartmut Michel (Chemistry Prize of 1988) for their efforts in solving the structure of the photosynthetic reaction center (first membrane protein); John E Walker (Chemistry Prize of 1997) for the structure of ATP synthase; Peter Agre and Roderick MacKinnon (Chemistry Prize of 2003) for their research on ion channels in cell membranes; Roger Kornberg (Chemistry Prize of 2006) for his protein crystallography-related study of molecular basis or RNA transcription machinery; Venki Ramakrishnan, Thomas A. Steitz, and Ada Yonath (Chemistry Prize of 2009) for the determination of the structure of the ribosome; and Brian Kobilka and Robert Lefkowitz (Chemistry Prize, 2012) for revealing the function and structures of GPCR proteins.

Figure 7.8 illustrates the workflow of protein crystallography. When using X-rays to detect the structures of proteins, the protein or polypeptides need to be first purified and crystallized. The preparation of well-diffracting single crystals is a time-limiting step. Hundreds to thousands of conditions need to be screened to optimize the expression, purification, and crystallization conditions of a specific polypeptide. Once appropriate protein crystals are obtained, it is necessary to submit them to the diffraction data collection process. The crystal is repeatedly exposed to X-ray beams in different orientations. Depending on the type of protein or polypeptide crystal (the cell size and symmetry), different strategies are employed for data collection, and different amounts of scattered X-rays are collected. When an X-ray beam hit a crystal, the X-ray diffraction occurs. All of the electrons in a crystal are hit with an X-ray and all of these electrons then diffract X-ray waves in all directions. Each electron in the sample can also become a small X-ray source. When the scattered waves from all electrons of each atom are added, they can either interfere constructively or destructively. The diffracted waves which get stronger are recorded by X-ray detectors. Finally, by measuring the angles and intensities of these diffracted beams, a 3D image of the density of electrons within the crystal is produced by a crystallographer, with each compound having a unique diffraction pattern. Flexible portions of a protein are often invisible in crystallographic electron density maps, because their electron density is smeared out over a large volume, which is known as a truncated error. The diffraction data is processed by using specialized computer programs, which provide the phase information of the X-ray wave in each spot and the electrons distribution in protein. The processed electron density map is informative, demonstrating positions of atoms, chemical bonds, and other valuable information in a crystal. Finally, one can reconstruct the position of each atom in a crystal by observing the diffraction pattern and build the 3D map of macromolecule. The protein or polypeptide structures are available to all scientists in a public database

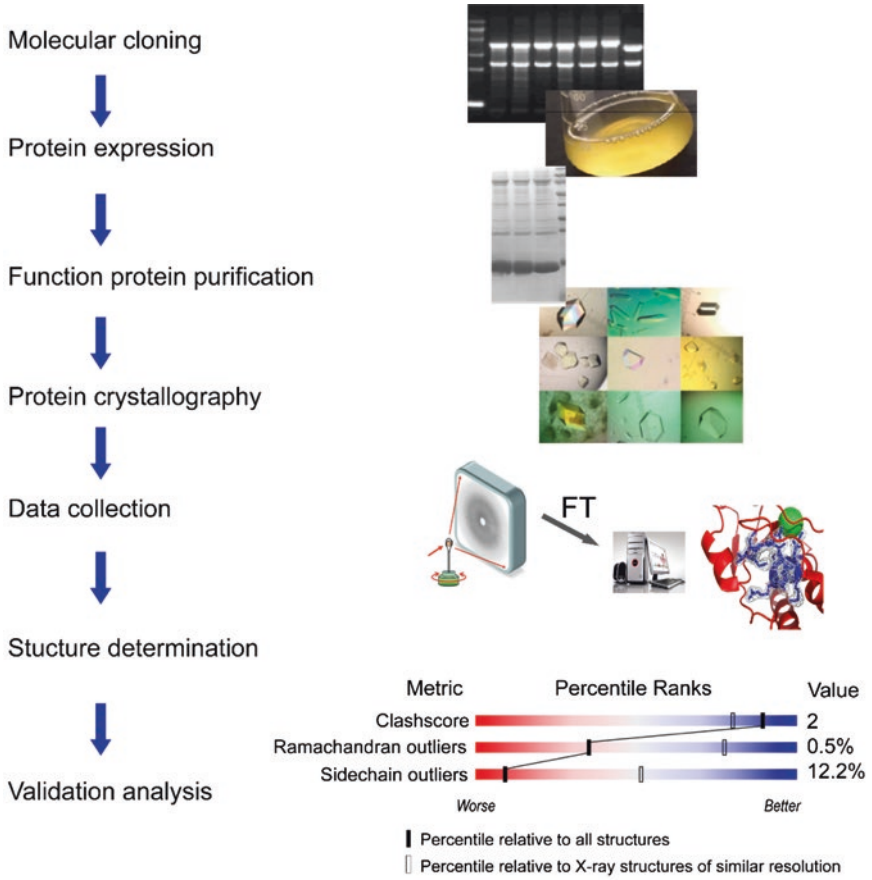

Fig. 7.8 The workflow of protein crystallography

called the "Protein Data Bank" (PDB) with detailed coordinate information and research methods.

Using X-ray crystallography, Eisenberg and coworkers studied the molecular mechanism of insulin amyloid fibrosis. A variety of amyloid fibrils are proteins that are misfolded into β-sheet conformation and form aggregated filaments 6–12 nm in diameter with variable lengths. Researchers obtained the fibril-like microcrystalline aggregates of the segment from insulin B-chain (LVEALYL) and determined the atomic arrays within the LVEALYL microcrystals. X-Ray crystallography yielded a resolution of about 1 Å, which provides information about the peptide structure and the fibrillization process of amyloidal peptide (Fig. 7.9). The peptide adopts a hydrogen-bonded cross-β-conformation, like a continuous stack of β-sheet ladders. Segments LVEALYL with extended strands conformation pack into parallel β-sheets, and each pair shows the dry steric zipper interface typical of amyloid-like fibrils [27].

Fig. 7.9 Atomic structure of the insulin dimer (PDB code: 1GUJ) [27]

By using similar methodology, Eisenberg and coworkers revealed two potential mechanisms for prion strain propagation based on the structure determination of the segments from prion and other amyloid proteins [28]. Prions are a kind of infectious proteins that can cause transmissible neurodegenerative diseases in mammals and produce heritable and sometimes beneficial phenotypes in fungi. In the inheritance and transmission of prions, strains are phenotypic variants encoded by protein conformations. Structural conversion from soluble to amyloid-like structure rich in β-sheets (aggregated) is involved in the process of prion formation. The aggregated prion accelerates the conversion of identical soluble protein molecules to the status of aggregation. However, the mechanism of maintaining protein structure stability in enduring transmission between cells or organisms is still unclear. Conformational differences that give rise to polymorphic amyloid fibrils and prion strains at atomic level are poorly understood. Researchers have determined that the steric zipper structures of fibril-like amyloidal protein segments are polymorphous (Fig. 7.10a). The different phenotypes of prion strains reflect changes in the conformations of steric zippers (Fig. 7.10b). Prion strains can be encoded by alternative packing arrangements of β-sheets, which are formed by the same segment. At the same time, prion strains can also be encoded by distinct β-sheets of different segments. The above two forms of polymorphism produce combinatorial conformations and transfer protein-encoded information into prion strains.

The X-ray crystallography progress to explore polypeptide assembly structures is evident, while challenges still remain relating to the flexible portions of protein. A polypeptide that is highly dynamic in solution with a nearly free rotation and tilt angle is difficult to be studied by X-ray crystallography, since the electron density in highly flexible regions is largely weakened in X-ray diffraction. To gain information with such a system, NMR spectroscopy can be used as a suitable characterization technology.

7.2.3.2 NMR Spectroscopy

NMR spectroscopy is the second method for determining protein structures with atomic resolution and has led to a substantial increase in the number of known protein structures. NMR is a nuclei-specific spectroscopy that measures the energy gap

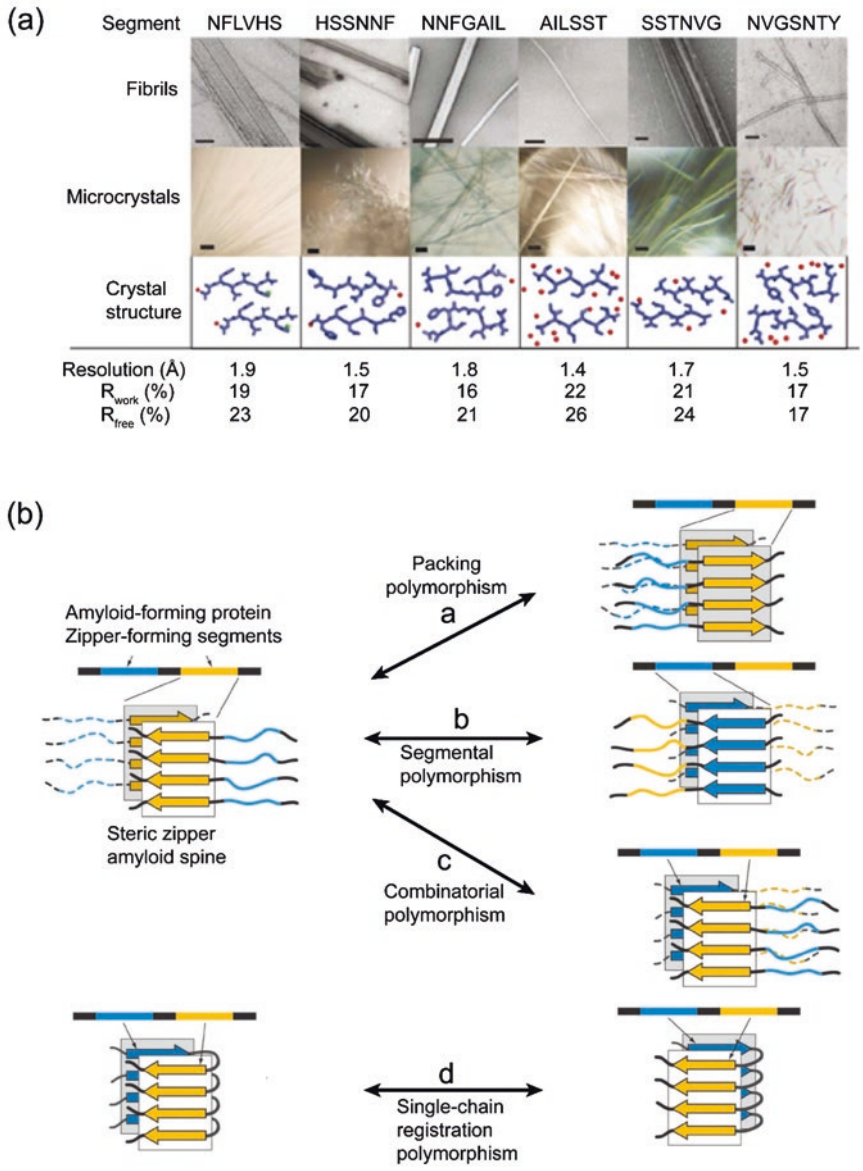

Fig. 7.10 Polymorphism in islet amyloid polypeptide (**a**) and the schematic diagram of steric zipper mechanisms for amyloid and prion polymorphism (**b**). (**a**) Peptide segments were detected to form fibrils, as shown in the electron micrographs above (scale bars are 100 nm). The segments also form microcrystals, as shown in the center (scale bars are 50 μm) of light micrographs. Crystal structures of the segments were also determined, and the resolutions and *R* factors are represented below. (**b**) Two segments in an amyloid-forming protein are respectively depicted in blue and yellow. Reproduced from [28]

between spin-up and spin-down states of nuclei in an external magnetic field. NMR techniques can provide many complementary information to those obtained from X-ray crystallography, including the atomic local structures of highly flexible regions and protein dynamic properties. Thus, NMR techniques broaden our view of molecules and give us a profound insight into the relation between structure, dynamics, and biological function. In the late 1960s and the early 1970s, with the rapid development of modern NMR techniques, including Fourier transform spectroscopy, superconducting magnets, new pulse programs, and computer control of the instrumentation, NMR spectroscopy has emerged as a powerful technique to characterize protein structures in solution. NMR has been used to study protein internal mobility, conformational changes, folding processes, pH titration of individual amino acids in protein-protein or protein-ligand interactions, and the atomic resolution structure of proteins.

Figure 7.11 presents an outline of the NMR method, including protein sample preparation, NMR experiment data collection, atom assignment, and structure calculation. The protein of interest is usually dissolved in aqueous solution (0.4–0.5 mL) under near-physiological conditions. The appropriate protein concentration is higher than 0.3 mM, ideally around 1 mM. For proteins larger than 12 kDa, samples should be ^{15}N and/or ^{13}C labeled. To collect NMR spectra of proteins, two-dimensional (2D), three-dimensional (3D), or even four-dimensional (4D) experiments are used to avoid extremely crowded and overlapped regions within the one-dimensional ^{1}H NMR spectrum generated by the larger number of hydrogen atoms in a protein. As shown in Fig. 7.11, the cross-peaks, which indicate couplings between nuclei pairs, have been further spread out along the third frequency axis, corresponding to the NMR frequencies of labeled spins. Routine experiments include 2D ^{1}H-^{15}N, ^{1}H-^{13}C HSQC, 3D HNCA, HNCO, HN(CA)CO, HN(CO)CA, HNCACB, CBCA(CO)NH, HBHA(CO)NH, (H)CCH-COSY, HCCH-COSY, and ^{15}N-edited TOCSY-HSQC spectra. Using these spectra, one can assign the frequencies at which energy absorption occurs for each of the specific NMR active nuclei in the sample. For a de novo structure determination, NMR distance constraints are obtained from nuclear Overhauser enhancement (NOE) spectroscopy, called NOESY. In the NOESY experiment, a cross-peak between two hydrogen atoms is observed only if the distance between the two protons is shorter than 6 Å. As the NOE depends on distance, one can use these distance constraints to build protein structure. Other NMR experiments can also provide distance or angle constraints, such as residual dipolar couplings (RDCs) and paramagnetic resonance enhancement (PRE) experiments. A RDCs experiment measures weakly aligned macromolecules dissolved in dilute liquid crystalline media and provides long-range orientational information that leads to significant increases in coordinate accuracy [29, 30]. The PRE effect, arising from unpaired electrons with an isotropic *g*-tenser (such as EDTA-Mn^{2+}/EDTA-Cu^{2+} or a nitroxide spin label), provides long distance (10–35 Å) restraints according to the PRE between the paramagnetic center and the nucleus [31]. PRE structures are calculated using specific computational programs. Dihedral angles (φ and ψ) can be predicted from chemical shifts using the program TALOS. The CANDID module of CYANA was used to generate the initial structure. About 20 structures with the lowest target functions are selected as models for

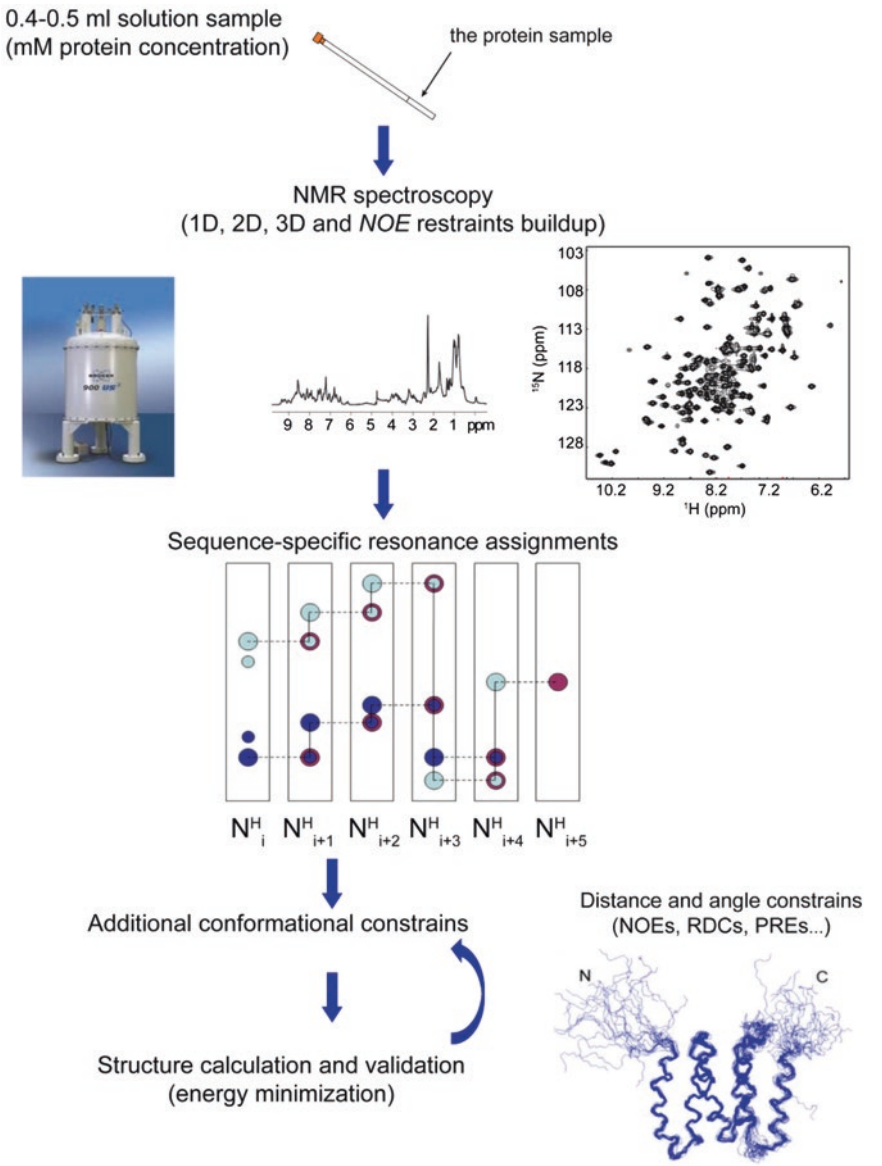

Fig. 7.11 The workflow of using the solution NMR to detect proteins structures

the program SANE to extend the NOE assignments. 200 structures are first calculated by CYANA interactively, and the 100 lowest energy structures then selected for further refinement by AMBER. Finally, 10–20 conformers with the lowest energy are selected to represent the solution structure. The quality of calculated conformers can be checked by analyzing the violations using PROCHECK software programs.

^{1}H, ^{13}C, ^{15}N triple resonance 3D and 4D spectroscopy have extended the size limit of protein NMR to 25 kDa. However, compared with other techniques, the molecular size of proteins that can be studied by NMR is relatively small. The main reasons are as follows: (1) NMR signals rapidly decay during the multitude of transfer steps in an NMR experiment; (2) The spectra become too crowded as protein molecular weight increases; (3) Cross-peaks in NOE-type spectra increase rapidly with size. These problems can be generally eliminated by employing novel techniques, such as the transverse relaxation-optimized spectroscopy (TROSY), PRE, RDCs, and pseudo-contact shifts (PCS). Labeling strategies involving perdeuteration and methyl-specific labeling of ILVs also allow researchers to obtain key structural restraints for larger proteins.

The methods mentioned above are NMR methodologies working in solution. Another type of NMR technique is solid-state NMR (ssNMR). The principle of ssNMR is the same as that of solution NMR. The ssNMR is widely used in analyzing membrane proteins inserted into lipid bilayers, which provides crucial structural and functional information of the membrane proteins. The orientation dependence of NMR interactions under non-spinning condition is exploited. The rigid-body structure of a peptide nanotube adopts a unique orientation when it is supported on glass slides. Thus, it is feasible to probe the orientation of peptides within a nanotube framework. Hamley and coworkers provided structural insights into the conformation of nanotube forming peptide H_2N-AAAAAAK-COOH (A_6K) via ssNMR. By using the unoriented A_6K nanotubes sample labeled with 1-^{13}C Ala at residue 2 and 2-^{13}C Ala at residue 6, they found that A_6K peptides are arranged in an antiparallel β-sheet within the nanotubes. Their results demonstrated that A_6K nanotubes are 20 nm in diameter and consist of β-strands with a 4.7 Å spacing in the hydrogen-bonding direction. By combining the results from ssNMR experiments and simulations, a series of structural models was proposed to be that A_6K β-strands are packed perpendicular to the nanotube axis to form a belt with a twisted angle θ in the range of 65–70° (Fig. 7.12) [32].

7.2.3.3 Cryogenic Electron Microscopy

Cryo-EM provides a feasible method to study the structures of large or heterogeneous proteins and biological macromolecular assemblies, which are difficult to be investigated by using conventional X-ray crystallography or NMR techniques. In a

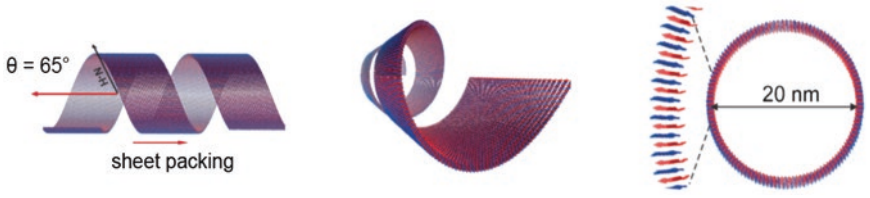

Fig. 7.12 Three perspectives of the nanotubes formed by peptide A_6K. Reprinted with permission from [32]. Copyright 2013 Wiley Publishing Group

cryo-EM experiment, biological specimens are frozen-hydrated at cryogenic temperatures and remain in their native state without the use of dyes, fixatives, or crystallization. It provides high-resolution structures of cells, viruses, and protein complexes. In the 1960s, scientists were faced with the problem that when using electron microscopy to study the structures of biomolecules, the high energy electron beams damaged the specimen. To overcome this problem, cryo-EM was invented, as it was expected to reduce the beam damage due to the low environment temperatures. In 1975, Joachim Frank proposed algorithms that can analyze 2D images and reconstruct them into 3D structures. In the early 1980s, Jacques Dubochet devoted himself to vitrify water by quickly cooling samples. This process allows the biomolecules to retain their shape in a vacuum. In the 1990s, Richard Henderson used electron microscopy to generate the first 3D image of a protein at atomic resolution. The Nobel Prize in Chemistry in 2017 was awarded to these three researchers for their efforts in developing cryo-EM.

Figure 7.13 shows the workflow of cryo-EM to detect protein structures. In the sample preparation step, an aqueous protein solution is dropped onto a carbon film-coated transmission electron microscopy (TEM) grid blotted by using a FEI Vitrobot, and then the grid with the sample is rapidly plunged into the mixture of liquid nitrogen and ethane. Frozen proteins are embedded in a thin layer of amorphous ice with a thickness of around 100 nm, which can preserve proteins in a near-native environment. The samples are quickly transferred to a TEM with cryogenic capability, maintaining low temperatures during experimentation (~90 K cooled by

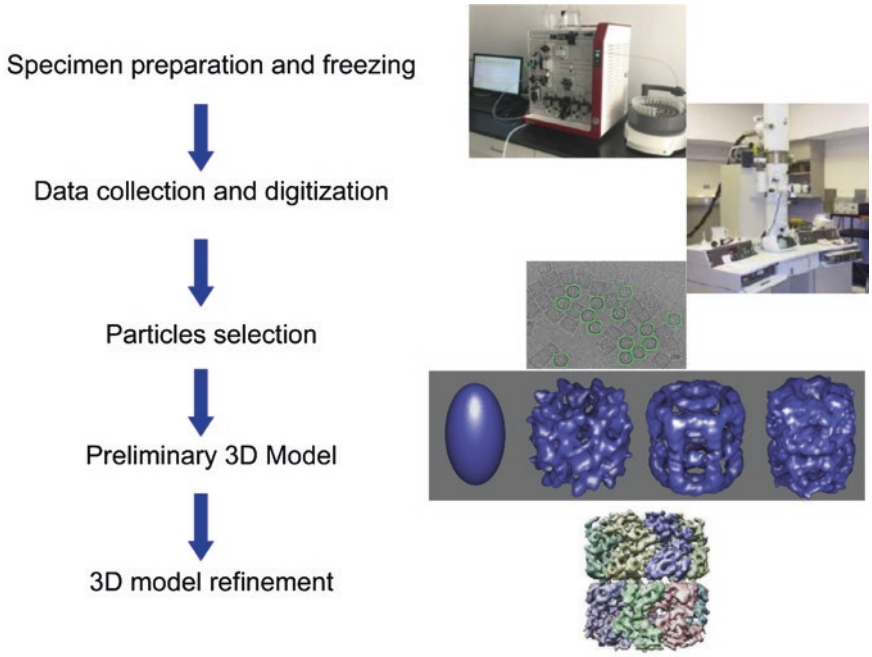

Fig. 7.13 The workflow of using electron cryo-microscopy to detect protein structures

liquid nitrogen, or ~ 4 K cooled by liquid helium). Thus, the protein samples are fixed in a hydrated state in vacuum. Images with high noise level and low contrast are recorded by using electron exposures low enough at low temperature to avoid destroying samples. To get high-resolution structural information, multiple 2D images of the specimen are collected and averaged. To reconstruct the 3D structure of a biomolecule, the single-particle analysis (SPA) procedure was developed by Frank and coworkers [33]. In the SPA procedure, thousands of 2D images of a biomolecule in different orientations are combined to generate a 3D reconstruction. Software packages that are being used in the field of SPA (e.g., EMAN, IMAGIC, Bsoft, Frealign, and RELION) are based on the SPIDER program created by Frank and coworkers in 1981. Any reconstruction process by SPA is built on the assumption that the imaged sample is a homogeneous population of structurally identical and chemically identical objects. However, not all the biological samples are truly homogeneous. Such instances of heterogeneity include the simultaneous presence of multiple biomolecule conformations and the variable nature of a bound ligand. In such cases, one should divide these 2D images into multiple homogeneous sets, and then generate multiple 3D models.

Stupp and coworkers used cryo-EM technique to investigate the structure of cylindrical nanofibers formed by alkylated peptide amphiphiles, $C_{16}H_{31}$OVVEE, which consist of hydrophobic and negatively charged residues (V and E) and a hexadecane tail [20]. Previous works demonstrate that the VEVE segment in a similar peptide $C_{16}H_{31}$OVEVE flips the hydrophilic and hydrophobic side chains to the opposite sides of extended peptide β-strand. The hydrophobic valine residues in the peptide sequence are expected to exhibit a tendency to form a dimer to limit exposure to water. Thus, researchers hypothesized that the alternation of peptide sequence from VEVE to VVEE would lead to a more effective peptide chain packing. Consistent with their prediction, the replacement of the VEVE structural motif by VVEE converts the topology of the peptide self-assembly nanostructure from flat nanobelt to the cylindrical nanofiber (Fig. 7.14).

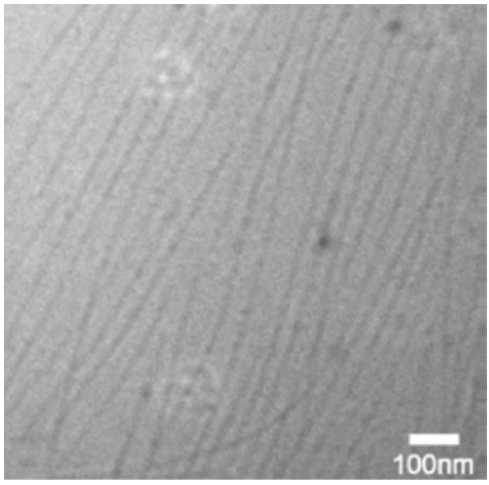

Fig. 7.14 Cylindrical nanofibers in cryo-EM image of 0.1 wt% $C_{16}H_{31}$OVVEE aqueous solution. Reprinted with permission from [20]. Copyright 2009 American Chemical Society

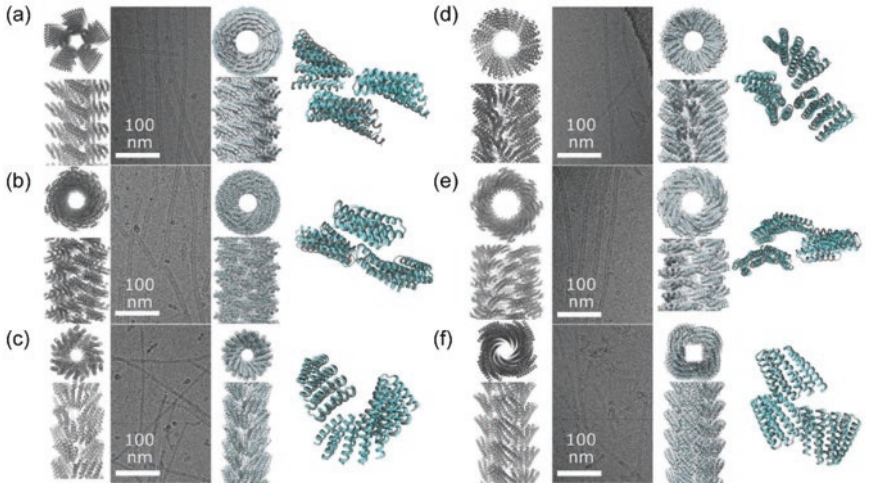

Fig. 7.15 Cryo-EM structures of de novo peptide assembled structures. (**a**–**f**) Computational model, representative filaments in cryo-EM micrographs, cryo-EM structure, and overlay between the model and structure are arranged from left to right. (**a**) DHF58, (**b**) DHF119, (**c**) DHF91, (**d**) DHF46, (**e**) DHF79, and (**f**) DHF38 [34]. Reprinted with permission from [34]. Copyright 2018 The American Association for the Advancement of Science

Cryo-EM techniques are also used to characterize the nanostructures formed by de novo peptides. In 2018, Baker and coworkers described a general computational approach to design self-assembled helical filaments from monomeric proteins [34]. Using this approach, they designed proteins that assemble into micrometer-scale filaments in vivo and in vitro. A set of 15 de novo-designed helical repeat proteins with various geometries was selected as the monomeric building blocks. By using these 15 building blocks, 6 different types of supramolecular architectures with longer persistence lengths were generated (Fig. 7.15). Within these assembly architectures, the overall orientations and packing modes of the monomers in filaments were determined by cryo-EM.

7.2.3.4 Other Methods

A series of other spectroscopic and microscopic technologies also provides us important information about polypeptide assembled structures, including scanning tunneling microscopy (STM), small-angle scattering (SAS), circular dichroism (CD), and multi-angle light scattering (MALS).

The STM works by scanning a surface with a very sharp metal wire tip. When a conducting tip is brought <1 nm to the surface to be examined, a bias applied between the two allows electrons to tunnel through the medium between them. As a result, the surface can be imaged with submolecular resolution by documenting the local density of states. Due to its high structural resolution and adaptability to

various environments, STM has been applied to study the molecular structures of peptides, especially for amyloid peptides that are difficult to be crystallized. In the past decade, STM has provided important details to allow us to gain insights into the assemblies of amyloid-forming peptides, such as human islet amyloid polypeptide, amyloid beta 40 and 42, the key aggregation segment of prion protein, as well as the binding sites of single-drug molecules on peptides [35–38].

SAS, including small-angle X-ray scattering (SAXS) and small-angle neutron scattering (SANS), is used in the structure characterization of biological macromolecules, nanocomposites, synthetic polymers, and alloys. Relative to solution NMR, which is limited by protein size, and X-ray crystallography, which is time-consuming, the SAS measurement is quick and has no significant molecular weight limitation. When combined with other high-resolution analysis methods, SAS provides 3D structures via ab initio reconstructions and hybrid modeling, which can be used in characterizing equilibrium mixtures and flexible systems.

CD is a kind of dichroism that involves circularly polarized light, such as the differential absorption of left- and right-handed light. CD is exhibited by biological molecules due to their dextrorotary and levorotary components. As a consequence, protein secondary structures have distinct CD spectral signatures representative of their structures, making CD a powerful tool in characterizing the structures of polypeptides.

MALS measures the hydrodynamic size of a particle or a protein assembly in Brownian motion from the scattered light intensity collected at multiple scattering angles. This measurement can be used to provide important insights into protein self-assembled structures, protein-protein interactions, and the aggregation status of proteins.

In conclusion, there are many techniques available to study the self-assembly structure of biomolecules. During the research process, scientists sometimes combine various technologies to obtain profound structural insights.

7.2.4 The Application of Self-Assembled Peptide-Based Nanomaterials in the Diagnosis of Bacterial Infection

Speedy diagnosis of a bacterial infection is crucial to the treatment of infectious diseases. Because of the infection complications in the bloodstream, every hour of delay in antibiotic treatment increases mortality rates by nearly 8%. However, the existing physical examination methods, such as microorganism culture and histopathology, and tests for antibodies, antigens, DNA, and RNA, are time-consuming, typically taking up to 2–5 days to obtain accurate and reliable results. Thus, new diagnostic methods are needed to detect the early stage of infection. Self-assembled peptide-based nanomaterials possess distinct biological properties, such as molecular recognition of pathogen attack, biodegradability, and biocompatibility that suggest these materials may be used as sensitive and specific sensors for bacterial detection and infection therapy.

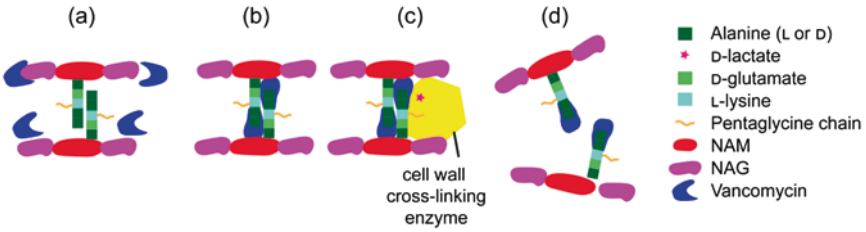

Fig. 7.16 Mechanism of vancomycin action. (**a**) Vancomycin is added to the bacterial environment while bacteria are metabolically active and synthesizing new cell wall. (**b**) Vancomycin recognizes and binds to the D-alanyl-D-alanine moieties on the end of the peptide chains. (**c**) Vancomycin interacts with the peptide chains and prevents them to bind to the cell wall cross-linking enzyme. (**d**) Cross-links cannot be formed and the bacterial cell wall is disrupted

Vancomycin is an antibiotic which is used to treat gram-positive bacterial infections as it can inhibit the proper cell wall synthesis. It is recommended as a first-line treatment for bloodstream infections, endocarditis, skin infections, and meningitis caused by gram-positive bacteria [39, 40]. The gram-positive bacterial cell wall, composed of cross-linked peptidoglycan, is constructed of a repeating disaccharide unit of *N*-acetylglucosamine (NAG) and *N*-acetylmuramic acid (NAM). The NAM bears a peptide moiety L-alanyl-D-isoglutaminyl-L-lysyl-D-alanyl-D-alanine. Vancomycin has been proved to prevent the incorporation of NAM/NAG peptide subunits into the peptidoglycan matrix and thereby inhibits cell wall polymerization by forming hydrogen bonds with the terminal D-alanyl-D-alanine moieties of NAM/NAG peptides (Fig. 7.16).

Inspired by this observation, researchers attempted to develop biotriggered materials with responsive retention and targeting accumulation property. Vancomycin is covalently conjugated with self-assembled peptides or peptide mimetics to design various biosurface-induced supramolecular assemblies for the diagnosis and therapy of bacterial infections.

In 2014, Yang and coworkers reported self-assembled vancomycin derivatives for simultaneous bacterial detection and inhibition [41]. They developed NBD-FFYEGK [Van] and NBD-FFYEEGK [Van] (NBD represents 4-nitro-2,1,3-benzoxadiazole and Van represents vancomycin), which can self-assemble induced by the bacterial surface. While the NBD exhibits the environment-sensitive fluorescence property, the NBD-Van conjugates can be used in bacterial detection and inhibition in vitro. They studied the self-assembly behaviors of these compounds by dynamic light scattering and transmission electron microscopy. The results showed that the critical micelle concentration (CMC) of NBD-FFYEGK [Van] and NBD-FFYEEGK [Van] was 75 and 190 μg/mL, respectively. TEM images of the compound in aqueous solution at pH 7.4 showed that when their concentration was higher than their respective CMC value, both NBD-FFYEGK [Van] and NBD-FFYEEGK [Van] formed nanoparticles. To test their bacterial inhibition capacity, the vancomycin-sensitive strain of *Bacillus subtilis* (ATCC 33677, *B. subtilis*) and vancomycin-resistant enterococci of *Enterococcus faecalis* (VanB genotype, ATCC

51299, *E. faecalis*) were used as model organisms. The antibacterial activity of the two peptide-conjugated compounds was investigated by standard broth microdilution assays. For *B. subtilis*, the minimum inhibitory concentration (MIC) of NBD-FFYEGK [Van] was 4.5 μM, while the MIC of NBD-FFYEEGK [Van] was 22.4 μM. NBD-FFYEGK [Van] (MIC = 90 μM) and NBD-FFYEEGK [Van] (MIC = 213 μM) exhibited more effective antimicrobial activities against *E. faecalis* than the parent vancomycin molecule (MIC = 728 μM). By measuring the local fluorescence intensity of NBD moiety at the bacterial surface, they observed that the formation of NBD peptide self-assembled nanostructures around bacteria increased the fluorescence intensity relative to the environment. It is an interesting observation that bacterial surface functions as an active substrate to recruit free NBD peptides from solution and triggered the onset of assembly of NBD peptides at the bacterial surface.

In 2015, Wang and his group designed a new photoacoustic contrast peptide agent that is capable of self-aggregation triggered by an enzyme in bioenvironments and can be used as a sensitive and specific image sensor for bacterial infection in vivo [42]. The building block is Ppa-PLGVRG-Van 1 (Ppa stands for pyropheophorbide-α, Van stands for vancomycin), where Ppa is a light-sensitive reagent to provide photoacoustic signal and PLGVRG is an enzyme-sensitive peptide linker. Ppa-PLGVRG-Van 1 binds to the gram-positive bacterial cell walls via the hydrogen bonds between vancomycin and D-alanyl-D-alanine moieties. Vancomycin leads Ppa-PLGVRG-Van to accumulate at the site of infection caused by bacteria in vivo. Gelatinase secreted by gelatinase-positive bacteria cuts the PLGVRG peptide linker and releases Ppa to self-aggregate in situ (Fig. 7.17). The aggregates of Ppa are hierarchically twisted fibers with high thermal conversion efficiency for photoacoustic imaging. Hence, the accumulation and aggregation of Ppa-PLGVRG-Van induced by bacterial infection leads to an amplification of the Ppa signal in situ, which can be used as the basis of a highly sensitive and specific system for imaging the bacterial infections. In this research, the self-aggregation and characterization of the supramolecular aggregates were studied by UV-vis absorption spectra, TEM, and CD spectra. To test the function of Ppa-PLGVRG-Van in vivo, a dose of 10^3 to 10^8 bacterial colony-forming units was added to induce muscle inflammation for 24 h. Then Ppa-PLGVRG-Van was intravenously injected (5.0 mg/kg, 200 μL) and the photoacoustic signal was acquired after a further 24 h. The results showed that Ppa-PLGVRG-Van exhibited target accumulation effect in muscles and other organs. Finally, cell viability assays were carried out to examine the toxicity of Ppa-PLGVRG-Van. The experimental data showed that this photoacoustic contrast agent has high biocompatibility as negligible cytotoxicity toward the human embryonic kidney (A293) and human hepatocyte (LO2) cells was observed.

Inspired by the potential of constructing supramolecular self-assemblies in vivo, Liu and coworkers designed a dual fluorescent-radioisotope probe for imaging gram-positive bacterial infection [43]. A vancomycin- and rhodamine-modified peptide derivative (Rho-FF-Van) was synthesized as an imaging reagent and was bound to the D-alanyl-D-alanine motif of the methicillin-resistant *Staphylococcus*

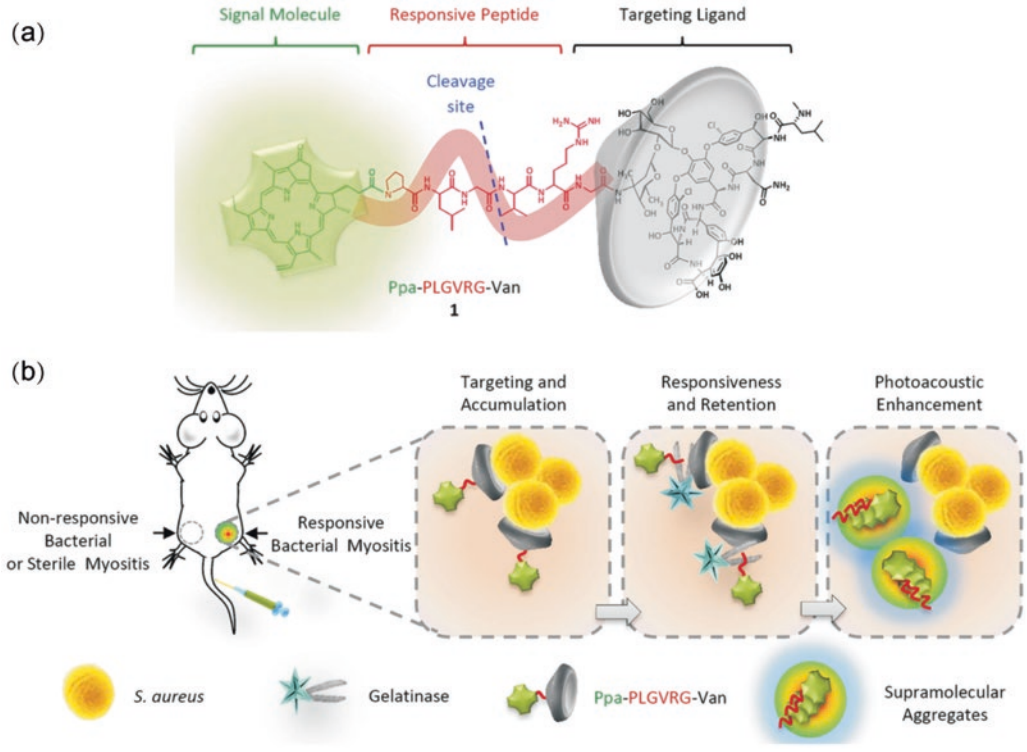

Fig. 7.17 Schematic diagrams of bacterial infection imaging based on an in vivo aggregation strategy. (**a**) The building block Ppa-PLGVRG-Van. (**b**) First, Ppa-PLGVRG-Van accumulates at the site of responsive bacterial myositis with the help of the targeting molecule vancomycin; then, the gelatinase produced by gelatinase-positive bacteria cleaves the peptide linker and triggers self-aggregation in situ; finally, the supramolecular aggregates and makes great contribution to enhance the photoacoustic signal so that the bacterial infection can be detected. Reprinted with permission from [42]. Copyright 2016 Wiley Publishing Group

aureus (MRSA) cell walls. The peptide self-assembled to form nanoaggregates on the surface of MRSA, which resulted in an increased fluorescence intensity at the site of MRSA infection. By measuring the radioactive signal released by the iodine-125 labeled peptide, ^{125}I-Rho-FF-Van, researchers probed bacterial infection in MRSA-infected lung models. Their work provides a novel way to image bacterial infection in vivo. They also synthesized Rho-GG-Van as a control group. To evaluate the self-association potency of Rho-FF-Van versus Rho-GG-Van and determine the appropriate concentration of peptide probes in vitro and in vivo, they compared the CMC values of these peptide probes in PBS buffer. The results revealed that the CMC value of Rho-FF-Van (about 78 μg/mL) is 2.4-fold lower than that of Rho-GG-Van. Similar CMC measurements were conducted with non-rhodamine control groups, Ac-FF-Van and Ac-FF-Van. The presence of rhodamine aromatic ring was observed to facilitate the self-assembly tendency of the peptide. To evaluate the bacterial surface-induced self-assembly of peptide probes, in situ self-assembly of Rho-FF-Van surrounding MRSA surface was visualized by using confocal microscopy and TEM. The results showed that the outer membrane of MRSA treated with Rho-FF-Van exhibited apparent formation of nanoaggregates. In contrast, there was no obvious aggregates formed at the outer membrane of MRSA treated by Rho-GG-Van. These results further confirm that Rho-FF-Van exhibits high sensitivity for the detection of gram-positive bacteria in vitro. Finally, they used myositis-bearing mice that have MRSA on left hind leg and *Escherichia coli* (*E. coli*) on the right hind leg to investigate the ability of Rho-FF-Van for detecting gram-positive bacterial infection in vivo. Rho-FF-Van was administered in the mice intravenously for fluorescence imaging and showed significant fluorescence only on the MRSA-induced infection sites, 2 h post-injection both in vivo and ex vivo.

7.2.5 Application of Self-Assembled Peptide-Based Nanomaterials in the Treatment of Bacterial Infection

The overuse of antibiotics have stimulated the emergence of antibiotic-resistant bacteria; thus, the conventional antibiotics that target individual intracellular processes are facing the barrier of reduced therapeutic potential against pathogens. There are four important pathways leading to bacterial resistance: (1) alteration in the target site of antimicrobial agents to reduce binding affinity, (2) reducing drug accessibility via increasing efflux or decreasing influx, (3) inactivation of a drug by releasing enzymes, and (4) tolerance that results in the survival of bacteria [44, 45]. With traditional search paradigms being exhausted, novel approaches including the creation of antimicrobial peptides and peptide mimetics may offer promising and creative solutions. Naturally occurring antimicrobial peptides are evolutionarily conserved and found in many living organisms. They serve as defense components in the innate immune system against a variety of pathogens. Antimicrobial peptides have some common characteristics as they fold into amphipathic structures in

response to membrane binding. They are cationic and bind to negatively charged bacterial cell membranes by nonspecific physical interactions and cause disrupting pores, channels, or carpets in microbial phospholipid bilayers [1, 4–6]. Although some peptides isolated from natural sources show early success as alternatives to conventional antibiotics, their therapeutic applications are limited by high costs, their low stability to enzymatic degradation in vivo, and off-target cytotoxicity. To overcome these challenges, one possible solution is to use antimicrobial peptides as building blocks and develop three-dimensional hierarchical nanomaterials with wider therapeutic windows.

Webster and coworkers designed a self-assembled Cardin antimicrobial peptide amphiphiles (ACA-PA) with the sequence of C_{16}-V4K_4G(AKKARA)$_2$ to combat bacterial drug resistance [46]. ACA-PA forms spontaneous aggregates induced by hydrophobic collapse when the peptide concentration is above 45 μM. Structural experiments revealed that the amphiphilic Cardin antimicrobial peptide can fold into β-sheet secondary conformation and self-assemble into cylindrical supramolecular structures. TEM imaging revealed that the self-assembled structures of ACA-PA are nanorods with diameters in the range of 7–10 nm at the concentration of 1 mg/mL. 40 μM ACA-PA caused bacterial cytoplasmic leakage, local membrane disruption in gram-positive bacteria, and disorganization of gram-negative bacterial membrane. Thus, the nanoparticles formed by ACA-PA are potentially promising candidates to be used as antimicrobial agents [46]. To investigate the bactericidal effects of the ACA-PA-based nanomaterial, a viable colony count assay and the live/dead staining assay were conducted against gram-positive and gram-negative bacteria, *S. aureus*, MRSA, *E. coli*, and MDR *E. coli*. At concentrations higher than 80 μM, the ACA-PA nanorods possessed significant toxicity against all the bacteria and decreased colony-forming units for both *S. aureus* and MRSA by two logs. As for gram-negative *E. coli* and MDR *E. coli*, ACA-PA nanorods had potent bactericidal effects. Drug-resistant bacterial strains were exposed to ACA-PA at concentrations below (40 μM) and above (80 μM) the CMC, and then were visualized by TEM to reveal the damage in bacterial cell envelopes caused by the ACA-PA treatment. After the treatment with 40 μM of ACA-PA, the peptidoglycan layer of MRSA was partially damaged and the cytoplasmic membrane was no longer attached to the outer membrane, resulting in cytoplasmic leakage. By using 80 μM of ACA-PA, the disintegration of the bacterial cell wall became apparent in TEM images, which is indicative of local disruption of the cell membrane and complete leakage of the cytoplasm.

Self-assembled peptide-based nanomaterials can also be used as drug delivery carriers against bacteria. For example, the resistance of bacteria to the relatively nontoxic first-line antibiotics makes it necessary to treat infections with some powerful antibiotics. However, these antibiotics are kept in reserve due to their toxicity, which can lead to symptoms worse than the infection itself, such as fever, kidney damage, thrombophlebitis, and red man syndrome. Researchers are trying to find new and safer antibiotics, which can be delivered to the infected tissues and organs to increase drug potency and reduce their side effects. In order to achieve this purpose, one approach is to package the drug into nanoparticles, which prolongs the

half-life time of the payload antibiotic. Another strategy is targeting an antibiotic to bacteria in an infected tissue. Nanoparticle delivery with specific targeting drugs is an effective means of improving drug delivery. Ruoslahti and coworkers designed and synthesized a kind of vancomycin-loaded nanoparticles with the cyclic 9-amino-acid peptide CARG peptide, cyclo(CARGGLKSC). This designed drug increases the antibacterial activity of nanoparticles in *S. aureus*-infected tissues and reduces the side effects (Fig. 7.18) [47]. The nanoparticles have a porous silicon core which

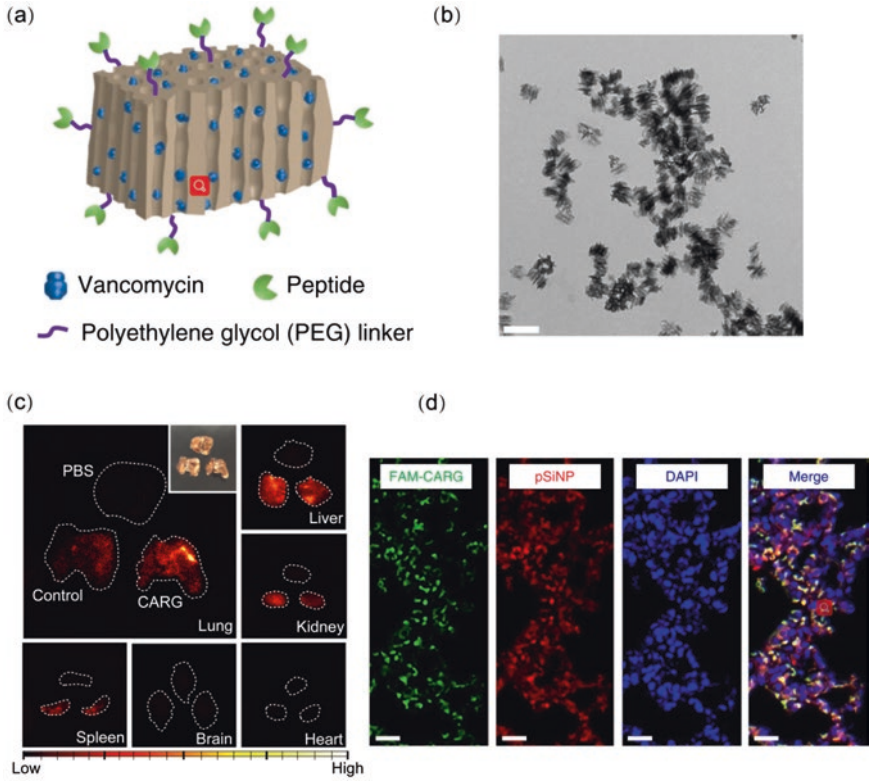

Fig. 7.18 Targeted drugs delivery to *S. aureus*-infected lungs in vivo. (**a**) A schematic illustration of the therapeutic nanoparticle system. (**b**) TEM image of vancomycin-loaded pSiNP (the scale bar is 200 nm). (**c**) Time-gated luminescence images of pSiNPs in mice after 1 h of circulation ($\lambda_e = 500$ nm). Nanoparticles were intravenously injected into infected mice 24 h post intratracheal administration of *S. aureus*. White dashed line indicates the outer boundary of each organ. The pSiNPs grafted with polyethylene glycol only (no targeting peptide) were the control nanoparticles; negative control: 50 μL corresponding volume of PBS was injected to mice intravenously. The inset is the white light photograph of lung tissues corresponding to the time-gated luminescence image. (**d**) Confocal fluorescence microscope images of the infected lung tissue of mice with CARG-pSiNPs. Green, red, and blue represent the CARG peptide labeled with FAM, intrinsic photoluminescence of pSiNPs, and DAPI nuclear stain, respectively (scale bars are 20 μm). Reproduced from [47]

provides high loading capacity for drugs and easily modified surface to accommodate targeting groups. The cyclic 9-amino-acid peptide cyclo(CARGGLKSC) that specifically binds to *S. aureus*-infected tissues was selected via a phage display peptide library screen in the mice with *S. aureus*-induced lung infections. In vivo and in vitro study results revealed that cyclo(CARGGLKSC) binds specifically to *S. aureus* bacteria and selectively accumulates in *S. aureus*-infected lungs and skin of mice. Thus, it significantly enhanced the local accumulation of intravenously injected vancomycin-loaded porous silicon nanoparticles to the infected area. Compared with vancomycin nanoparticles not labeled with cyclo(CARGGLKSC) and free vancomycin, these targeted nanoparticles more effectively suppressed staphylococcal infections in vivo. This development indicated a powerful and unbiased way to discover peptides that specifically accumulate in diseased tissues [47].

Another application of a peptide self-assembled nanomaterial against infection is the incorporation into pharmaceutical formulations that can continuously release hydrophobic and low-soluble antibiotics and provide a means of maintaining drug concentrations above the minimum inhibitory concentration for the pathogen. For example, ciprofloxacin is a gold standard for various topical applications, such as eye and skin infection. However, ciprofloxacin is sparingly soluble, and it is difficult to maintain dosing at a certain concentration. Hartley and coworkers reported the self-assembly of ciprofloxacin and a tripeptide (D-Leu-Phe-Phe) into supramolecular nanostructures, which were used in solving this solubility problem [48]. The soluble ciprofloxacin and the hydrophobic D-Leu-Phe-Phe can form supramolecular nanostructures that form macroscopic hydrogels at physiological pH (Fig. 7.19). The presence of non-covalent interactions between ciprofloxacin and the peptide hydrogel was confirmed by fluorescence spectroscopy and CD spectroscopy. Ciprofloxacin-loaded peptide hydrogel showed an antimicrobial efficacy against several bacteria, including *Escherichia coli*, *Staphylococcus aureus*, and *Klebsiella pneumonia*. No obvious cytotoxicity was found in lytic assays against human red blood cells or mouse fibroblast cell cultures. This work demonstrates the potential clinical applications of a peptide hydrogel as cost-effective wound dressings and novel antimicrobial formulations [48].

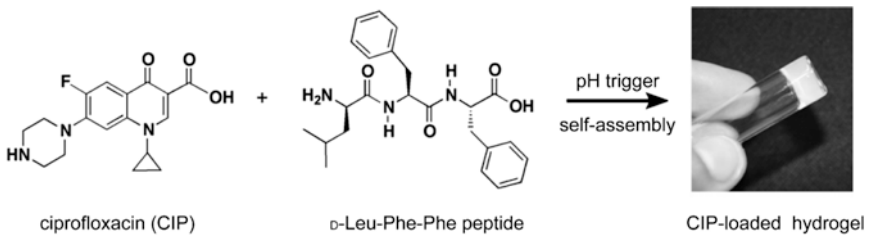

Fig. 7.19 Structures of ciprofloxacin (CIP) and peptide D-Leu-Phe-Phe that self-assemble into a hydrogel after being triggered by pH. Reprinted with permission from [48]. Copyright 2013 Elsevier

7.2.6 *Encapsulation of Peptide by Nanomaterials Against Bacteria*

Generation of nanomaterial delivery systems has been reported to be a promising strategy to improve peptide bioavailability. Nanomaterials can act as target-specific carriers to deliver therapeutic cargo for diagnosis and therapy, protect a peptide drug from proteolytic degradation, and alter the rapid peptide metabolism and elimination timescales in vivo [7–10]. Herein, we provide several recent examples demonstrating the applications of nanomaterials with encapsulated peptides in the context of treating bacterial infections.

Kwon and coworkers designed a bifunctional peptide that displays a killing domain (D-Asp-Lys-Lys) and a microbial *Pseudomonas* localization domain (a membrane-active peptide which is *Pseudomonas*-specific) and kills *Pseudomonas aeruginosa* at sub-micromolar concentrations [49]. Histological examinations of the lungs of mice treated with free peptide revealed that treatment resulted in bronchitis, sloughing of the bronchial epithelium, and interstitial pneumonitis; all of these symptoms developed in response to the toxicity of the antimicrobial peptide. When the bifunctional peptide was loaded into the pores of a biocompatible porous silicon nanoparticle (pSiNP) by electrostatic interactions and then dosed in mice, the peptide-pSiNP exhibited a better biodistribution and decreased the side effects of antimicrobial peptide in vivo. The encapsulation of the peptide by the nanoparticle significantly weakened the damage to the lung tissue. To examine the utility of peptide-pSiNP in vivo, this co-assembly material was delivered to the lungs of mice and tested for its potency against *P. aeruginosa* infection. The treatment of a lung infection model of *P. aeruginosa* (2×10^5 colony-forming unit (CFU) per mouse) with peptide-pSiNP (a mouse was given two doses of 1.5 nmol peptide and 30 μg porous silicon nanoparticle) resulted in an improved survival at 24-h post-infection from 10 to 20% (vehicle control) to 100%. To determine the effect of peptide nanoparticle on bacteria in vivo, mice were intratracheally instilled with 1×10^3 CFU *P. aeruginosa* per mouse to establish an infection model with near 100% 24-h survival and treated with peptide-pSiNPs. The utility of peptide-loaded nanoparticles markedly reduced the average bacterial number recovered from lungs from $1 \times 10^{5.2}$ CFU per lung (untreated mice) to $1 \times 10^{2.7}$ CFU per lung.

Other nanomaterials such as gold nanoparticles [9, 50] and graphene oxide [51] have also been shown to be efficient platforms to conjugate with antimicrobial peptides, increasing peptide proteolytic stability and decreasing peptide mammalian cell cytotoxicity. Rai et al. incorporated a cysteine residue to the C-terminus of an antimicrobial peptide, Cecropin-melittin, and covalently immobilized this peptide onto the surfaces of gold nanoparticles via Au-S bonds (Fig. 7.20) [50]. Cecropin-melittin modified gold nanoparticles at a concentration of 50 μg/mL exhibited high antimicrobial activity in human serum against gram-positive bacteria (*S. aureus*) and gram-negative bacteria (*E. coli*, *K. pneumoniae*, and *P. aeruginosa*). In addition, peptide-gold nanoparticles had higher resistance to enzymatic degradation than free peptides when they were treated with trypsin, *S. aureus* V8 protease, and human neutrophil elastase, respectively.

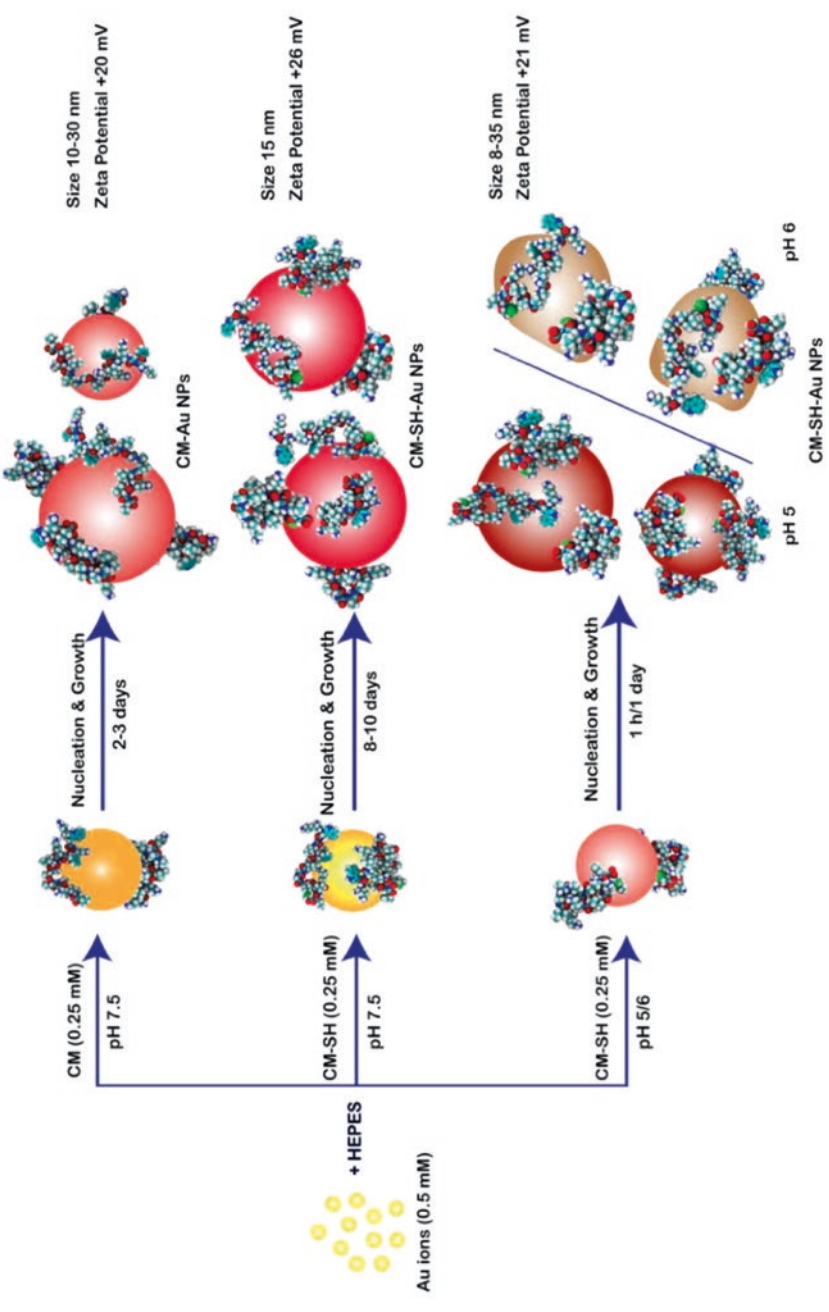

Fig. 7.20 Schematic illustration of Au nanoparticles synthesis in the presence of Cecropin-melittin (CM) peptides and CM-SH, under different experimental conditions. Reprinted with permission from [50]. Copyright 2016 Elsevier

Chen et al. non-covalently deposited an antimicrobial lipopeptide, surfactin, on the surfaces of dodecanethiol-capped gold nanodots via the hydrophobic interactions formed between the nonpolar tails of surfactin and dodecanethiol [9]. The minimal inhibitory concentration values of surfactin/dodecanethiol/gold nanodots against *E. coli*, *P. vulgaris*, MRSA, *S. aureus*, and *S. enteritidis* were much lower (less than 25 μM) than that of free surfactin (200–250 μM). Cytotoxicity evaluation using MCF-10A, NIH-3T3, and HMEC-1 cells and the hemolysis analyses using human red blood cells revealed superior biocompatibility of surfactin/dodecanethiol/gold nanodots relative to surfactin. To test the clinical applicability of this surfactin-gold nanodot material, histological analysis was carried out to evaluate the antibacterial ability in healing of skin wounds of rats exposed to MRSA. When compared to the untreated group, a greater migration for keratinocytes, higher fibroblast formation and collagen secretion, more blood vessels, and hair follicles were observed in the surfactin-gold nanodot-treated wound site relative to controls. Taken together, encapsulating peptides by nanomaterials has been demonstrated as a powerful strategy to improve the preclinical applications of antimicrobial peptides in the treatment of infections.

7.3 Development of Peptide Mimetic Materials with Antibacterial Activity

A key point that emerges from the progress described above is that diverse natural amino acid building blocks lie at the heart of the polypeptide assembly world. When appropriately coupled through amide linkages, these subunits direct folding into a particular type of secondary structure. The resulting structure provides a scaffold for the three-dimensional display of side chains. The spatial organization of side chains facilitates the non-covalent interactions between adjacent secondary structures to form both tertiary structure and quaternary structure, and then finally, a functional peptide assembly is achieved. In the past decade, increasing work has been devoted to exploring the diversity within the polypeptide backbone by using unnatural amino acids for molecular design. Alternative to the α-peptide scaffold, the β-peptide provides a new direction toward mimicking nature's molecular assemblies and antibacterial function.

7.3.1 β-Peptide: Molecular Structure and Conformational Stability

β-Peptides are oligomers composed of unnatural β-amino acids that mimic various aspects of the folding and organization of polypeptides. β-Amino acids contain an extra carbon in the backbone relative to α-amino acids (Fig. 7.21a). The

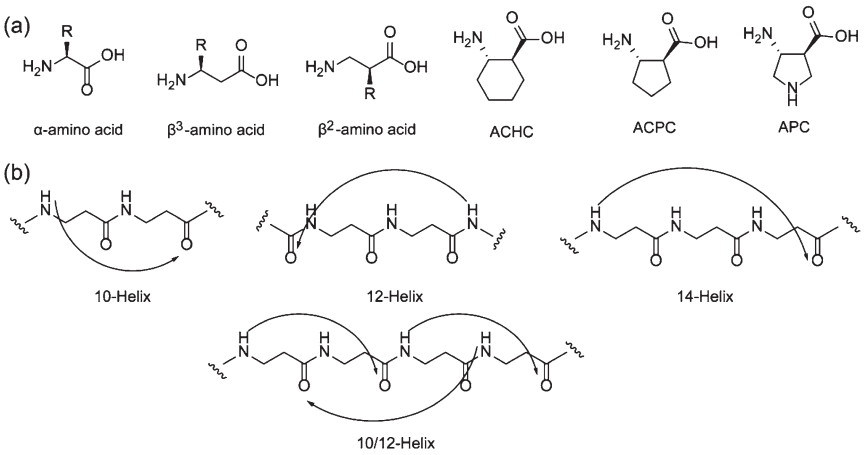

Fig. 7.21 (**a**) α- and β-amino acids. (**b**) Hydrogen-bonding patterns of β-peptide helices are shown with arrows

introduction of an additional carbon atom into the peptide backbone leads to an increase of a peptide's proteolytic stability [52]. Like α-peptides, hydrogen bonding between amino groups and carboxyl groups in neighboring regions of backbone folds β-peptide into specific secondary structures, including helices, sheets, and turns. Helices have been the most intensively studied.

The backbones of β-peptides are longer than those of peptides that consist of α-amino acids; thus β-peptides form different secondary structures (Fig. 7.21b) [52]. β-Peptides that consist exclusively of β^3-, β^2-, or cyclically constraint *trans*-2-aminocyclohexanecarboxylic acid (ACHC) residues form a 14-helix. The structure of the 14-helix is stabilized by hydrogen bonds between amides at position *n* and a main chain carbonyl group at position $n + 2$. Different from an α-helix, the 14-helix has a 3.6-residue repeat. Altering the cyclically constrained residue from 6-membered ring, ACHC, to a 5-membered ring residue, *trans*-2-aminocyclopentanecarboxylic acid (ACPC) or *trans*-3-aminopyrrolidine-4-carboxylic acid (APC), facilitates the formation of a 12-helix. β-Peptides composed entirely of a 4-membered ring constraint display a 10-helix secondary structure. β-Peptides composed of the repeated β^2- and β^3-residue units, such as poly(β^2-homoalanine-β^3-homoalanine), adopt a 10/12-helix conformation.

7.3.2 Intermolecular Interactions Encoded by β-Peptides

Understanding the origins of intermolecular interactions leading to self-assembly is one of the key challenges underlying the rational design of novel nanostructured functional materials. In particular, the association of nonpolar groups in water through "hydrophobic interactions" has been widely recognized as a key driving

force for nanoscale self-assembly [53]. Hydrophobic interactions are water-mediated interactions between nonpolar molecules or surfaces [53]. These interactions provide a principal driving force for polypeptide folding, protein assembly, and biomacromolecule-ligand association in aqueous solution and at aqueous interfaces. Hydrophobic interactions are influenced by other non-covalent interactions that are mediated by adjacent functional groups, engendering highly specific tertiary and quaternary structures observed among proteins and other biomolecular structures and complexes. To date, simulations rather than experiments have been used to explore the ways in which nanoscale chemical heterogeneity impacts hydrophobic interactions [53]. Experimental strategies for addressing this challenging topic are necessary in order to test computationally derived predictions. Contemporary simulations often ignore key features of real molecules, such as the polarizability of atoms and dissociation of water, which sharpens the need for incisive experimental approaches.

In order to study the influence of nanoscale chemical heterogeneity on hydrophobic interactions, Ma and coworkers reported single-molecule force measurements performed using a β-peptide that adopted a rigid and predictable conformation [54]. Relatively short β-peptides (7–12 residues) in which at least 30% of the residues contain the cyclohexyl constraint are fully helical in aqueous solution. The β-peptide helical structures display well-defined nano-domains of hydrophobic and hydrophilic groups, allowing for precise tailoring of the three-dimensional presentation of chemical groups via specification of the β-amino acid sequence. β-Peptides provide a rigid platform to mimic chemical heterogeneity that is more in tune with realistic biological systems. The experimental system was based on β-peptides that fold into globally amphiphilic (GA) helices (Fig. 7.22a) [54]. These helices contain 14-atom hydrogen-bonded rings, each with about three residues per turn. One side of the helix displayed an array of six cyclohexyl side chains, introduced as ACHC residues, which constituted a nonpolar domain ~1 nm^2 in size. In addition to providing a nonpolar domain, the ACHC residues strongly preorganize the β-peptide backbone for 14-helical folding. The opposing face of the helix presented three cationic side chains, from either β^3-homolysine (β^3-hLys) or β^3-homoarginine (β^3-hArg), ~1 nm from the nonpolar domain. The sequences and the predicted globally amphiphilic conformations, GA-KKK and GA-RRR, are shown in Fig. 7.22. Each β-peptide was immobilized onto a surface, and the influence of the cationic groups on hydrophobic adhesion was quantified between the ACHC-rich face of single oligopeptides and the tip of an atomic force microscope (AFM) that was made nonpolar by a coating with gold and adsorbing a monolayer of dodecanethiol (Fig. 7.22b). Hydrophobic interactions were quantified by comparing adhesive forces measured between a single surface-immobilized β-peptide molecule and a nonpolar AFM tip in either aqueous triethylammonium (TEA) buffer or TEA with 60 vol% MeOH (Fig. 7.22c). 85% of hydrophobic interactions are eliminated by 60 vol% MeOH, but its use does not measurably change screened Coulomb (electrical double layer) interactions. Accordingly, pull-off forces measured in the 60 vol% MeOH/40 vol% 10 mM TEA buffer are identified as being van der Waals interactions and electrostatic interactions in origin. Short β-peptides containing more than 30% ACHC

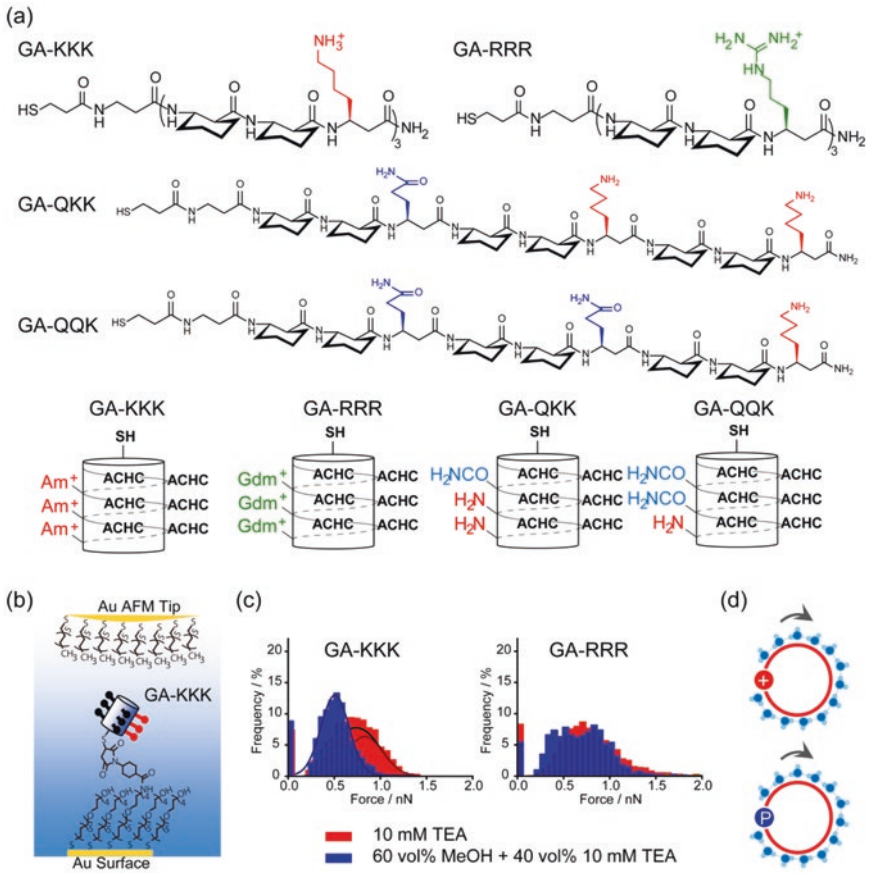

Fig. 7.22 (**a**) Chemical structures and helical cartoons for the β-peptides. (**b**) Schematic illustration of single-molecule force measurements with β-peptides. (**c**) Histograms of adhesion forces measured between an alkyl-terminated AFM tip and immobilized GA-KKK (left) or GA-RRR (right) peptides in either 10 mM TEA, pH 7 (red), or 60 vol% MeOH, pH 7 containing TEA solution (blue). (**d**) Influence of charged and polar side chains on the interfacial water structures of globally amphiphilic β-peptides. The solid red disk represents the side chains of β^3-homolysine residues. The blue disk with a white "P" sign represents the side chains of β^3-homoglutamine residues. Light blue spheres represent the interfacial water molecules [54, 55]. (**a**), (**c**), and (**d**) reprinted with permission from [55]. Copyright 2017 American Chemical Society

exhibit stable 14-helical conformations in aqueous solution and aqueous methanol, which allows for identification of hydrophobic interactions via addition of methanol. Conventional peptides, comprised of α-amino acid residues, lack sufficient α-helix stability to allow this experimental design. For the lysine-containing β-peptides (GA-KKK), adhesive interactions with the AFM tip are dependent on pH when measured in aqueous TEA. The addition of 60 vol% methanol causes the distribution of adhesive interactions. To quantify the hydrophobic component of the adhesive interactions between GA-KKK and the nonpolar AFM tip, a single

Gaussian function was fitted to each histogram measured in the presence of methanol (non-hydrophobic interactions). Two Gaussian functions were used to fit the histograms measured in aqueous TEA, one of which coincided with the Gaussian function fit in the presence of methanol (Fig. 7.22c). The forces described by the Gaussian function in aqueous TEA that were eliminated by the addition of methanol are the hydrophobic interactions between the ACHC domain of GA-KKK and the AFM tip. The methanol-independent forces arise from non-hydrophobic interactions, such as direct interactions of the β^3-hLys residues of GA-KKK with the AFM tip. This analysis led to the conclusion that the charge of the β^3-hLys side chain amino groups strengthens hydrophobic interactions between the nonpolar domain of GA-KKK and the AFM tip. The mean pull-off forces arising from hydrophobic interactions between the nonpolar ACHC-rich domains of GA-KKK and the alkyl-terminated AFM tip were determined to be 0.61 ± 0.04 nN at pH 10.5, and increased to 1.07 ± 0.01 nN at pH 7. To explore the role of the cationic residues in modulating the hydrophobic adhesion mediated by the nonpolar domains of the β-peptide, the β^3-hLys residues were substituted by β^3-hArg residues to generate GA-RRR. In striking contrast to the behavior of GA-KKK, adhesive interactions measured between GA-RRR and the AFM tip were largely unaffected by the addition of methanol (Fig. 7.22c). These observations suggest that the adhesive interactions measured with GA-Arg are not of hydrophobic origin. As a summary, when using GA-KKK, protonation of the side chains of β^3-hLys was measured to increase the strength of the hydrophobic adhesion between the AFM tip and the ACHC-rich domain. As a contrast, results of GA-RRR study showed that the guanidinium-containing β^3-hArg side chains eliminated measurable hydrophobic interactions. This observation indicates that charged groups immobilized within ~1 nm of a nonpolar domain can modulate the strength of the hydrophobic interaction mediated by the domain, and that the structure of the cationic group (ammonium vs. guanidinium) rather than net charge was crucial to the mode of action.

It is proposed that a possible mechanism by which proximal charged groups might influence hydrophobic interactions is that perturbations to the structure of interfacial water near charged groups on one face of the helix propagate, via water-water interactions (e.g., hydrogen bonding), from the site of the immobilized charges to the water adjacent to the nonpolar domain (Fig. 7.22d). These perturbations may include local fluctuations in the density of water. If this mechanism is dominated by the propagation of perturbations to solvent structure, immobilized polar but non-ionic groups might also modulate hydrophobic interactions in a group-specific manner (Fig. 7.22d). To test this hypothesis, AFM measurements with GA-QKK and GA-QQK were carried out to monitor the influence of replacing β^3-hLys residues in GA-KKK with β^3-homoglutamine (β^3-hGln or Q) residues on the hydrophobic interactions of globally amphiphilic β-peptides (Fig. 7.22a) [55]. The adhesive forces generated by GA-QKK and GA-QQK in aqueous TEA and then in 60 vol% MeOH in 40 vol% TEA were measured using the methodology described above for GA-KKK. For GA-QKK, the mean pull-off force in 60 vol% MeOH was 0.30 ± 0.17 nN at pH 10.5 and increased to 0.37 ± 0.01 nN at pH 7, whereas the hydrophobic force was 0.54 ± 0.01 nN at pH 10.5 and increased to

0.73 ± 0.03 nN at pH 7. When an additional β^3-hLys was further substituted by β^3-hGln, to generate GA-QQK, the adhesion forces mediated by a single GA-QQK molecule were measured to be the same in 60 vol% MeOH and aqueous TEA. This result indicates that GA-QQK does not generate a measurable hydrophobic force. At pH 10.5, where the degree of protonation of the K side chain is low, hydrophobic adhesive interactions mediated by GA-KKK were measured to be 0.61 ± 0.04 nN, by GA-QKK to be 0.54 ± 0.01 nN, and by GA-QQK to be 0 ± 0.01 nN. This finding suggests that replacing an amine group (β^3-hLys side chain) with a primary amide group (β^3-hGln side chain) weakens the hydrophobic interaction generated by the six cyclohexyl side chains. The differential impact of primary amine vs. primary amide on hydrophobic interactions of neighboring nonpolar surfaces reflects changes in the structure of water in the vicinity of the peptide, which in turn is influenced by hydrogen bonding and van der Waals interactions between the water and polar groups on the peptide side chains. The permanent dipole of the amine group is 1.31 D (methylamine in gas) and the amide group is 3.76 D (acetamide in gas). The geometries of the two groups are different because the amine nitrogen is sp^3-hybridized, while the amide nitrogen atom is sp^2-hybridized. Primary amine and primary amide groups have distinct abilities to form hydrogen bonds with the surrounding water molecules. The hydration free energy of acetamide (−39.9 kJ/mol) is larger relative to the *n*-butylamine (−18.0 kJ/mol). The hydration free energies are different because a primary amide likely forms more hydrogen bonds than a primary amine to water. In particular, the primary amide N-H are better hydrogen bond donors than primary amine N-H. The resonance stabilization of amides results in a partial negative charge on O and partial positive charge on N. This interaction enhances the proton accepting ability of O and makes the N-H group a stronger hydrogen bond donor (the free energy of HCOHN-H…OH_2 is −28.4 kJ/mol) than the N-H group of an amine (the free energy of H_2N-H…OH_2 is −6.3 kJ/mol). Overall, compared to an amine group, an amide group is expected to possess a stronger ability to form hydrogen bonds with nearby water, which will decrease the interfacial energy and perturb the structure of water adjacent to the nonpolar domain. It highlights the nonadditive nature of the interactions mediated by water at chemically heterogeneous surfaces.

The study mentioned above reveals the correlation between the hydration free energy of polar group and the impact of polar group on hydrophobic interactions of neighboring nonpolar surfaces. It provides a possible mechanism to interpret the influence of proximal cation identity on hydrophobic interactions. Specifically, the differential impacts of β^3-hLys versus β^3-hArg on peptide hydrophobicity reflect changes in the structure of water in the vicinity of the peptide, which is influenced by hydrogen bonding and van der Waals interactions between the water and charged groups on the peptide side chains in turn. Chemical properties of ammonium (β^3-hLys) and guanidinium (β^3-hArg) ions are distinct. The geometries of the two ions are distinct because the ammonium nitrogen is sp^3-hybridized while the guanidinium nitrogen atom is sp^2-hybridized. Ammonium and guanidinium ions have different abilities to form hydrogen bonds with surrounding water molecules. The hydration free energy of guanidinium (−583 kJ/mol) is larger relative to ammonium

(−285 kJ/mol). The hydration free energies are different because a guanidinium group likely forms more hydrogen bonds to water than an ammonium group because guanidinium contains more hydrogen bond donors than ammonium. Overall, when compared to ammonium (β^3-hLys side chain), a guanidinium group (β^3-hArg side chain) is expected to possess a stronger ability to form hydrogen bonds with nearby water, which will decrease the interfacial energy and perturb the structure of water adjacent to the nonpolar domain of peptide. This finding that the effective hydrophobicity of a nonpolar surface can be strongly influenced by the identity of proximal cationic groups, rather than simply by the presence of proximal charge, raises important questions about the impact of the identity of a charged group on noncovalent associations involving biomolecules. For example, mutation of lysine to arginine, or vice versa, is generally regarded as a conservative change in a protein. These results suggest that this assumption may require re-evaluation. If differences between the effects of proximal guanidinium and ammonium groups on hydrophobicity are mediated by cation-water hydrogen bonding, then N-methylation of lysine or arginine side chains, a common form of post-translational modification, may have previously unanticipated consequences on protein interactions. N-methylation of either side chain influences hydrogen bond donor capacity without altering net charge at neutral pH. These prospects should motivate future studies.

7.3.3 β-Peptide: Hierarchic Assemblies and Functional Properties

The well-defined three-dimensional structure of the robust β-peptide helix provides a platform to display a wide array of functional properties. Past studies have demonstrated that two- and three-dimensional hierarchical self-assembly and functionalities can be accessed through subtle changes in the presentation of chemical groups on the periphery of the β-peptide 14-helix, which is controlled by the β-peptide linear sequence.

To create unnatural β-peptides that adopt discrete quaternary structures, Raguse and coworkers designed a series of amphiphilic β-peptides containing ACHC and β^3-hLys residues [56]. Cyclic constraints in sequence promote the formation of 14-helix. Thus, the β-peptide helix has all three β^3-hLys side chains aligned on one side of the helix and the six cyclohexyl rings defining a hydrophobic helical face (Fig. 7.23a). The hydrophobic interactions displayed by the hydrophobic helical face drive self-assembly of β-peptides in bulk solution. A β^3-homotyrosine (β^3-hTyr) was put at the N-terminus to facilitate peptide concentration determination. NMR was used to interrogate β-peptide aggregation status in solution. At a concentration below 1.4 mM in 100 mM CD_3CO_2H/CD_3CO_2Na, 9:1 H_2O:D_2O at pH 3.8, the β-peptide displayed sharp NMR lines, indicating that the β-peptides remained in monomeric form at low concentration. As peptide concentrations in aqueous solutions were increased, the NMR peaks of the β-peptide solution broadened and coalesced due to the formation of peptide aggregates. The presence of β-peptide

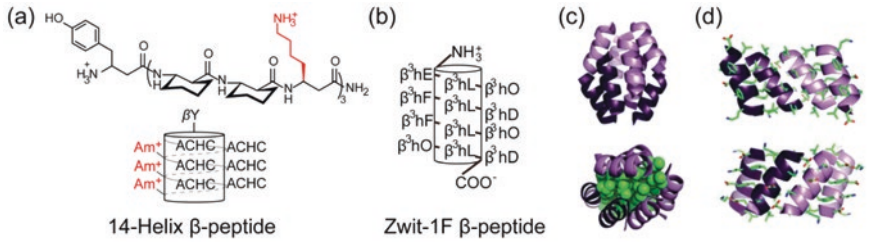

Fig. 7.23 (**a**) Chemical structure and helical cartoon for globally amphiphilic β-peptide. (**b**) Helical presentation for β-peptide Zwit-1F. (**c**) Ribbon diagram of the Zwit-1F octamer (top). Space-filling rendering of β^3-homoleucine side chains in green illustrates the well-packed hydrophobic core (bottom). (**d**) Interior (top) and exterior (bottom) views of each half show the hydrophobic and electrostatic interactions of the Zwit-1F assembly. (**c**) and (**d**) reprinted with permission from [58]. Copyright 2007 American Chemical Society

aggregates in solution was confirmed by using analytical ultracentrifugation (AUC) measurement. AUC studies were performed with the β-peptides at different concentrations in aqueous 10 mM Tris, pH 8.0, at several rotor speeds ranging from 35 to 60 krpm. Through AUC analysis, the amphiphilic β-peptide was observed to be monomeric at concentrations of 0.3 and 0.6 mM in 10 mM Tris, pH 8.0, but the radial distance spectra indicated that at least one aggregated state coexisted with the monomer when concentration was above 0.6 mM. To understand the aggregation states of the β-peptide in solution, the aggregation number of the peptide assemblies was calculated. According to the monomer/n-mer equilibrium model, 30–40% of the β-peptide was estimated to be hexameric at 1.7 mM. This finding led to the discovery that the β-peptides self-associated into a helix bundle quaternary structure, in which multiple helices associate with their long axes approximately aligned. Later, Pomerantz and coworkers identified a distinctive CD signature for self-assembled 14-helical β-peptides [57]. They found that the self-assembly of 14-helical β-peptides induces a diagnostic change in CD signature relative to monomeric 14-helices. Specifically, monomeric β-peptide 14-helices displayed a distinct CD minimum at 214 nm. Self-assembly of 14-helices leads to a shift in CD minimum from 214 nm to 205 nm. The onset of assembly is indicated by $[\theta]_{205}/[\theta]_{214} > 0.7$.

To investigate the structure of a β-peptide bundle, Daniels and coworkers designed a β-dodecapeptide (Zwit-1F) that self-assembles into a highly thermostable β-peptide octamer in aqueous solution and determined its structure by using X-ray crystallography (Fig. 7.23b) [58, 59]. Zwit-1F, composed of β^3-amino acids, favors a 14-helix secondary structure. Residues along one helical face are exclusively nonpolar residues (β^3-homoleucine, β^3-hLeu), providing a source of hydrophobic attractions for the self-association of β-peptides. This hydrophobic core is flanked by positively charged residues (β^3-homoornithine, β^3-hO) and negatively charged residues (β^3-homoaspartic acid, β^3-hD; β^3-homoglutamic acid, β^3-hE). Coulombic interactions generated by the complementary charges across the interface formed between different Zwit-1F helices can modulate assembly stability,

pairing preference, and helix orientation. At a concentration higher than 50 μM in phosphate buffer at pH 7.1, Zwit-1F peptide displayed a CD minimum at 205 nm, which indicates adoption of 14-helix bundle structure. To define the assembly state of Zwit-1F and detail the interactions within the assembly, its structure was determined by X-ray crystallography. Crystallographic analysis revealed that the Zwit-1F peptides assembled into what was defined as a β-peptide octamer model. The Zwit-1F octamer contains two pairs of tetrameric peptides, each composed of four 14 helices cupped at approximately a 90° angle to each other. The two halves of each tetramer are composed of symmetry-equivalent parallel dimers oriented in an antiparallel way. The 14-helical interfaces display association of β^3-hLeu faces, generating a solvent-excluded hydrophobic core in the octameric structure of Zwit-1F. Additionally, extensive inter-helical electrostatic interactions define the homo-oligomerization of Zwit-1F.

Supramolecular quaternary structures achieved by β-peptides encompass a set of novel three-dimensional hierarchical self-assembly materials with operational functionality. Pomerantz and coworkers found that globally amphiphilic β-peptides form liquid crystalline (LC) phases in water at β-peptide concentrations in the tens of mM range [60]. Polarized optical microscopy was used to monitor the formation of LC phases based on the observation of birefringence. To characterize the nanostructures of β-peptides that form in aqueous solutions, Cryo-EM was used to identify two different types of nanostructures, nanofibers, and globular aggregates. The nanofibers formed from the amphiphilic β-peptides were at least hundreds of nanometers in length and 10 nm in diameter. The high aspect ratio of nanofibers seems to be consistent with the length of mesogen required for LC phase formation. In contrast, globular aggregates were in the tens of nm in diameter and incapable of forming LC phases in water. Pomerantz and coworkers suggested that there is a concentration-dependent equilibrium between the two distinct types of nanostructures. At low β-peptide concentrations, the equilibrium favored formation of globular aggregates. Increasing the concentration of the β-peptide led to the coexistence of globular aggregates and nanofibers. At sufficiently high concentrations, nanofibers were the dominant aggregate form. Small bundles of β-peptides were expected to stack end-to-end forming micrometer-long nanofibers, and β-peptides were shown to form a dense, ordered nanofiber network in solution. Together, this study demonstrated that β-peptide hierarchical self-assembly can generate many types of aggregation.

Great progress has been made in the last decade toward the generation of protein-like architectures, including both secondary and quaternary structures with unnatural backbones. Biological activity has been achieved based on the formation of specific foldamer secondary structure. For example, inspired by the amphiphilic, helical, and cationic properties of α-helical host defense α-peptides, important progress has been made toward finding therapeutic use of 14-helix β-peptides against bacteria that are resistant to conventional antibiotics. Raguse and coworkers designed two series of cationic 9- and 10-residue β-peptides which form flexible amphiphilic 14-helices with analogs that have been rigidified by incorporation of the cyclohexyl-constrained ACHC residues [61]. By measuring the minimal

inhibitory concentration against gram-positive (*Bacillus subtilis*, *Staphylococcus aureus*, and *Enterococcus faecium*) and gram-negative (*E. coli*) bacteria, these β-peptides were found to possess antimicrobial activity comparable to or more potent than that of the conventional host defense α-peptides, melittin and magainin II amide [61]. Of particular significance, the biological activity of the β-peptides was specific for bacteria relative to mammalian cells. This selectivity profile was hypothesized to be dependent on the amphiphilic nature of the β-peptides, as globally amphiphilic β-peptides displayed low hemolytic activity at the corresponding bacterial minimum inhibitory concentrations, while non-globally amphiphilic β-peptides possessed antimicrobial activity at high concentrations also associated with high hemolytic activity. The mechanism of β-peptide antimicrobial activity is hypothesized to involve cell membrane disruption: cationic charge directs the peptides to anionic bacterial membranes, and hydrophobic side chains interact with the core of the lipid bilayer, ultimately destroying the barrier function of the membrane. Different from α-helical host defense peptides whose antibacterial activity decreases with increased α-helical stabilization, the antimicrobial activity of β-peptides is proposed to be independent of 14-helix propensity. ACHC-rich β-peptides were also reported to function as antifungal agents under conditions that render host defense α-peptides inactive against fungal pathogens. Karlsson and coworkers found that the β-peptide (ACHC-β^3-hVal-β^3-hLys)$_3$ displays antifungal activity against *Candida albicans* with a MIC at 17 μg/mL, which is significantly lower than that of conventional host defense peptide magainin (>128 μg/mL) [62].

β-Peptides bearing guanidinium groups in their side chains have been shown to mimic the cell penetration behavior of arginine-rich peptides, such as TAT peptides. TAT peptides are a set of peptides derived from the anti-human immunodeficiency virus (HIV) tat protein and possesses the ability to inhibit virus entry. For instance, one TAT peptide, GRKKRRQRRR, blocks HSV-1 infection at the entry step in cell culture with a 50% effective concentration (EC_{50}) of 1 μM. These findings indicated that β-peptides could be engineered to display antiviral activity against herpes simplex virus type 1 (HSV-1) infection. Akkarawongsa and coworkers designed a 14-helix β-peptide, β^3-hTyr-(ACHC-β^3-hArg-β^3-hArg)$_3$, and determined the inhibition of virus infection by the β-peptide [63]. Recombinant HSV-1 KOS mutant hrR3 virus was employed as a model system. HSV-1 hrR3 virus expresses a reporter β-galactosidase after the virus has entered the cell and released its genome to the nucleus, where transcription is activated. Thus, it allows the determination of virus infectivity by measuring the expression of β-galactosidase in cell. To determine whether the β-peptide was efficient at preventing HSV-1 infection, the β-peptide was added into Vero and HK320 mammalian cells before, during, and after HSV infection. The result demonstrates that β-peptide β^3-hTyr-(ACHC-β^3-hArg-β^3-hArg)$_3$ blocked HSV-1 infection at the postattachment entry step in cell culture (EC_{50} = 3 μM). This result suggests the potential use of cationic β-peptides as antiviral agents. To test whether the β-peptide inactivates virus, recombinant hrR3 virus was incubated with the β-peptides for a time course of 1 h and diluted 1000-fold into cell culture medium supplemented with β-peptide-free serum. To quantify the remaining infectious virus in cell cultures, the expression of β-galactosidase was

measured. The β-peptide was found to be incapable of inactivating virions in solution. Previous studies with TAT peptides revealed that they bind to sialic acids of HSV-1 glycoproteins, which in turn results in the disability of HSV-1 entry. Thus, as a mimic of TAT peptides, the underlying mechanism of these β-peptides at preventing virus infection might be related to its interactions with sialic acids [63].

7.3.4 Nylon-3 Polymers Against Pathogens

We have reviewed the structures and biological activities of β-peptides, which are oligomers composed of β-amino acids that mimic polypeptides. Next, we turn to introduce the progress of developing nylon-3 polymers. Nylon-3 polymers are polydisperse polymers whose subunit is a β-amino acid; the backbone of nylon-3 polymers thereby features periodic secondary amide groups [64]. These polymers resemble natural peptides and proteins, which are sequence-specific polymers composed of α-amino acid subunits. In comparison to natural peptides and proteins, nylon-3 polymers are faster and cheaper to synthesize and stable to hydrolysis by natural protease enzymes. The ability of nylon-3 polymers to form globally amphiphilic structures when in contact with biomembranes is believed to underlie their ability to compromise bacterial membrane barrier function and thus kill or inhibit the growth of prokaryotes. The remainder of this chapter will focus on the use of these polymers against human pathogenic bacteria.

For instance, Mowery and coworkers synthesized nylon-3 copolymers composed of cationic and hydrophobic subunits and tested their antibacterial activity [64]. Specifically, the nylon-3 copolymer, $MM_{60}CH_{40}$, which was composed of nonpolar six-membered ring side chains and positively charged ammonium-terminated side chains, was synthesized via the ring-opening copolymerization of two racemic β-lactams: 60% cationic subunits (monomethyl β-lactam, MM) and 40% hydrophobic subunits (*cis*-cyclohexyl β-lactam, CH) (Fig. 7.24a). The average molecular weight of $MM_{60}CH_{40}$ was determined by gel permeation chromatography (GPC) to be between 3000 and 3800 g/mol, which corresponds to an average polymer chain length of 16–20 subunits. The dispersity index of the copolymer was measured to be in the range of 1.3 to 1.7. The antibacterial activity of $MM_{60}CH_{40}$ was tested using standard broth dilution methods. The MIC of the MM60CH40 copolymer was 12.5 μg/mL (*E. faecium*), whereas the minimum hemolytic concentration (MHC) of $MM_{60}CH_{40}$ toward human red blood cells was measured to be 100 μg/mL. Parallel measurements were conducted with antimicrobial α-peptides, magainin 2 and cecropin A. For magainin 2, the MIC for *E. coli* was determined to be 100 μg/mL, and the MHC was higher than 400 μg/mL. For cecropin A, the MIC for *E. coli* was 0.78 μg/mL, and the MHC was higher than 400 μg/mL. Taken together, relative to the conventional antibacterial peptides, $MM_{60}CH_{40}$ possessed antimicrobial activity against a panel of bacteria at concentrations that were nontoxic to mammalian cells.

To understand the antibacterial mechanism of nylon-3 polymers, Lee and coworkers examined how nylon-3 copolymers induced membrane deformation on

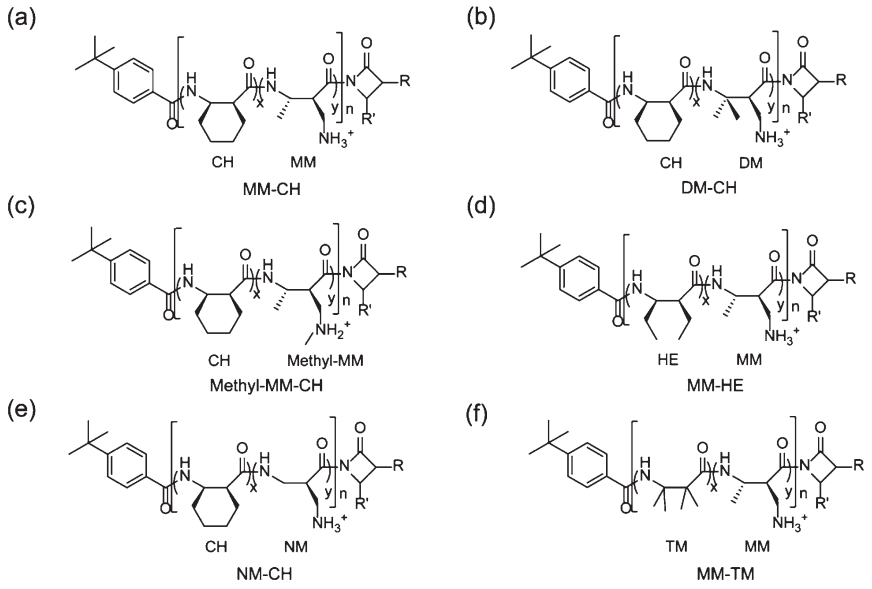

Fig. 7.24 Chemical structures for the nylon-3 polymers

synthetic vesicles and bacteria cell membranes [65]. They synthesized a nylon-3 copolymer, $DM_{50}CH_{50}$, by polymerizing cationic subunits (dimethyl β-lactam, DM) and hydrophobic CH subunits in a 1:1 molar ratio (Fig. 7.24b). The average molecular weight of $DM_{50}CH_{50}$ was determined to be 5129 g/mol, equivalent to 27 subunits. To test the impact of $DM_{50}CH_{50}$ on lipid membranes, vesicle dye leakage experiments were carried out. Unilamellar vesicles composed of DOPS/DOPE/DOPC = 20/60/20 were encapsulated with calcein dye in aqueous solution. Upon cleavage, calcein is released into solution, producing an increase in the fluorescence intensity at 510 nm. In the experiment, $DM_{50}CH_{50}$ was exposed to synthesized vesicles and observed to induce vesicle leakage. In parallel, a membrane permeability assay was performed with *E. coli* ML-35 strain to investigate the impact of DM50CH50 on a bacterial membrane. *E. coli* ML-35 strain possesses β-galactosidase activity but is lactose permease deficient. Hence, it is unable to uptake the lactose analog *o*-nitrophenyl-β-D-galactopyranoside (ONPG) unless it is permeabilized by membrane-disruptive agents. Upon membrane permeation, ONPG diffuses into the bacterial cell cytoplasm and is hydrolyzed by β-galactosidase to yield *o*-nitrophenol (ONP), which can be measured by absorbance at 405 nm. Increased absorbance was immediately observed after addition of a culture of *E. coli* ML-35, which suggests that $DM_{50}CH_{50}$ is a potent bacterial membrane permeabilization agent. The results from these two sets of independent systems, synthetic vesicles and *E. coli* ML-35 strain, demonstrate that the antibacterial mechanism of nylon-3 copolymer is correlated with its biomembrane disruption potency.

The studies mentioned above suggest that nylon-3 polymers represent a new class of promising antimicrobial agents that mimic the bacterial membrane disruption activity of natural host defense peptides. The general mechanism by which nylon-3 polymers lyse bacterial membranes first involves the coulombic attraction of the cationic side chains of nylon-3 polymers and the anionic surfaces of the bacterial cell, followed by the insertion of hydrophobic side chains of polymers into the nonpolar interior of the lipid membrane bilayer. The negative charge density of the external eukaryotic cell surfaces is lower than that of prokaryotic cell surfaces, which underlies the selectivity of nylon-3 polymer for targeting prokaryotic cells. The activity of conventional antimicrobial α-peptides is proposed to be that α-peptide forms a globally amphiphilic helical conformation upon the interactions with a biomembrane surface. In contrast, nylon-3 polymers are hypothesized to adopt specific but irregular conformations when in a micellar environment that results in global segregation of hydrophilic and lipophilic side chains. This hypothesis suggests that random sequences of cationic and nonpolar residues might be able to mimic host defense peptides [66].

To develop nylon-3 copolymers analogs with improved therapeutic properties, substantial efforts have been made to understand the structure-activity relationships in this polymer family. Several studies have focused on how varying structural parameters of nylon-3 polymers affects their minimum inhibitory concentrations against bacterial species and their hemolytic activity. Structural parameters such as nonpolar/cationic proportion, nonpolar subunit identity, length, cationic subunit identity, and end group on the antibacterial and hemolytic activities of nylon-3 copolymers have been evaluated for their impact on biological activity.

To explore the effects of nonpolar/cationic proportion on nylon-3 polymer activity, variations in the polymer composition were synthesized to include exclusively cationic MM subunits (MM_{100}), and cationic MM/nonpolar CH mixtures from $MM_{30}CH_{70}$ to $MM_{90}CH_{10}$. Homopolymer MM_{100} shows weak antibacterial activity toward *E. coli*, *S. aureus*, and *E. faecium* (MIC >50 μg/mL) and low hemolytic activity (MHC >1000 μg/mL) [66]. An increase in the proportion of nonpolar residue CH leads to improvement in antibacterial activity (MIC <50 μg/mL), until the nonpolar/cationic proportion reaches 50/50 ($MM_{50}CH_{50}$). Hemolytic activity remains very weak (MHC >800 μg/mL) until the nonpolar/cationic proportion reaches 40/60 ($MM_{60}CH_{40}$). A further decrease in the proportion of cationic residue MM results in an increase in hemolytic activity. Nylon-3 polymers composed of less than 50% cationic residues are hemolytic [66].

To explore the effects of nylon-3 polymer length on biological activity, a set of $MM_{63}CH_{37}$ copolymers with different chain lengths (10 to 60 subunits) were synthesized [66]. The MICs of $MM_{63}CH_{37}$ against *E. coli*, *B. subtilis*, *S. aureus*, and *E. faecium* are independent of the number of subunits in polymer chain, which reveals that nylon-3 antibacterial activity is not strongly affected by polymer chain length. In contrast to the trends in antibacterial activity, nylon-3 hemolytic activity is dependent on polymer chain length. Polymers containing an average of 10–30 subunits exhibit a very weak tendency to induce hemolysis, with MHC values in the vicinity of 1000 μg/mL. $MM_{63}CH_{37}$ copolymers with average chain lengths less than 30

subunits inhibited the growth of bacteria at much lower concentrations (1–100 μg/mL) than that required for human red blood cells (1000 μg/mL). The MHCs of polymers containing more than 30 subunits decreased to 1–10 μg/mL. $MM_{63}CH_{37}$ copolymers composed of more than 30 subunits were more hemolytic than their shorter analogs, with bacterial growth inhibitory concentration roughly equivalent to concentrations that induce hemolysis [66].

Substantial structure-activity relationship studies with nylon-3 polymers have been performed to evaluate the effects of residue side chain identity on the biological activity of these materials. The impact of primary amine versus secondary amine on the antibacterial activity has been examined via the direct comparison of the effects of two copolymers, $MM_{50}CH_{50}$ (number of subunits = 18) versus Methyl-$MM_{50}CH_{50}$ (number of subunits = 20) (Fig. 7.24c) [67]. $MM_{50}CH_{50}$ is cationic/nonpolar polymer presenting primary amine side chains, whereas Methyl-$MM_{50}CH_{50}$ incorporates *N*-methylated secondary amines. Relative to the nylon-3 polymer composed of primary amines, the addition of a methyl group to the side chain amines led to a decrease in antibacterial activity against a panel of bacteria (*E. coli*, *B. subtilis*, *S. aureus*), as well as a decrease in hemolytic activity. Charkraborty and coworkers demonstrated that differences in the antibacterial activities of nylon-3 polymers with cyclic versus acyclic side chains are correlated with their local backbone flexibilities [67]. The effects of cyclic versus acyclic nonpolar subunits were examined by comparing $MM_{60}CH_{40}$ (number of subunits = 15) versus $MM_{60}HE_{40}$ (number of subunits = 16) (Fig. 7.24d). Flexible polymer $MM_{60}HE_{40}$ containing acyclic nonpolar side chains displayed weak antibacterial property toward *E. coli* (MIC >200 μg/mL), relative to rigid polymer $MM_{60}CH_{40}$ containing the analogous cyclic subunit (MIC = 50 μg/mL). The impact of cyclic nonpolar side chain on the biological activities of nylon-3 polymers was further evaluated by varying the substitution pattern of the hydrophobic subunit. Mowery and coworkers synthesized copolymers containing cyclic nonpolar side chains of different ring sizes by copolymerizing CP (5-membered ring), CH (6-membered ring), CHp (7-membered ring), or CO (8-membered ring) to copolymerize with MM [66]. Comparison of these copolymers probed how variations in side chain size affected biological properties. They found that the hemolytic propensity of copolymer generally increases as the cycloalkyl ring size increases, but the correlation between cycloalkyl ring size and antibacterial activity is not clear.

The impact of end-group identity was explored by using a series of polymers containing N-terminal linear acyl units from acetyl (C_2) to octadecanoyl (C_{18}) [66]. These polymers contained 27–35 subunits and were prepared from a β-lactam mixture containing 63% MM and 37% CH. An increased terminal chain length from C_2 to C_{12} moderately decreased the MICs of copolymers against *E. coli*, *B. subtilis*, *S. aureus*, and *E. faecium.* Further increases in tail length from C_{12} to C_{18} significantly increased MIC values. This decrease in antibacterial efficacy is likely due to the increased aggregation tendency of polymers with the elongated nonpolar alkyl chain lengths. The hemolytic trends imply the N-terminal carbon tail enhances the ability of these polymers to lyse human red blood cells.

More recently, Liu and coworkers found that nylon-3 polymers displayed potent antifungal activity against *Candida albicans*, beyond strains *E. coli*, *B. subtilis*, and *S. aureus* [68]. *C. albicans* is part of our natural microflora and is the most common cause of fungal urinary tract infections. Cationic NM (no methyl β-lactam) was copolymerized with CH to obtain the nylon-3 polymers CH-NM (Fig. 7.24e). The antifungal activity against *C. albicans* increased as the proportion of CH decreased, and no detectable hemolytic activity. Cationic homopolymer displayed antifungal activity comparable to that of the most active CH-NM copolymers. Currently, therapeutic agents available to treat fungi are very limited and are plagued with rising levels of resistance. Thus, the discovery of new antifungal agents is a significant concern to clinicians responsible for treating invasive fungal infections. The finding that nylon-3 polymers are active against *C. albicans* represents an important prelude to new antifungal therapeutic strategy. To improve antifungal activity among nylon-3 materials, Rank and coworkers examined nylon-3 copolymers containing the nonpolar TM (tetramethyl β-lactam) subunit paired with either the MM or DM cationic unit with an average chain length of 20 subunits [69]. The MM-TM copolymer (Fig. 7.24f) showed activity against multiple species of *Cryptococcus* (*C. neoformans*, *C. gattii*) and Candida (*C. albicans*, *C. lusitaniae*) comparable to or more potent than clinically relevant drugs, amphotericin B and fluconazole. This polymer acted synergistically with azoles against different species of *Aspergillus* (*A. fumigatus*, *A. terreus*), including some azole-resistant strains. The activity of nylon-3 polymers against fungi from 18 pathogenic genera composed of 41 species and 72 isolates was further characterized [70]. Three types of nylon-3 polymers, DM-TM, MM-TM, and NM, show high efficacy against diverse fungi, including yeasts, dermatophytes, dimorphic fungi, molds, and even fungi that are intrinsically resistant to current antifungal drugs.

7.4 Conclusions

Self-assembly is an important process in nature. This chapter presents a brief overview of the diverse methods available to study self-assembled peptides, including the peptide amphiphiles and peptide mimetics that self-assemble into complex stable nanostructures. The examples introduced above include materials that elicit an array of biological activities in vitro and in vivo, and in this chapter, particular emphasis is placed on systems with antimicrobial activity. Despite promising activity, however, many hurdles still exist that limit the application of peptide-based nanomaterials in the fight against human pathogenic bacteria. The first is the safety of these nanomaterials. Toxic effects due to administration of these materials have been documented at the pulmonary, reproductive, cardiac, cutaneous, renal, and cellular levels. It is yet to be proven scientifically that the toxicity of nanomaterials was regulated by shape, size, area, and surface chemistry. Increased production and intentional or unintentional exposure to nanomaterials is likely to increase the probability of uncovering their adverse health effects. It is crucial that novel

nanomaterials be biologically characterized for their health hazards to ensure risk-free and sustainable implementation of nanotechnology. The second limitation is the controllability of the nanomaterial assembly. Relative to peptide-based self-assembled nanomaterials, DNA and RNA origami are more controllable in that individual molecules inherently assemble into intricate shapes and structures at the nanoscale. Improving the design method to build a well-ordered peptide self-assembled nanomaterial remains an important challenge at present. The clinical application of peptide self-assembled nanomaterials is also hindered by the poor druggability of peptides. Improvement of the oral availability and stability of peptide continues to be an area of future research.

References

1. A.A. Bahar, D. Ren, Antimicrobial peptides. Pharmaceuticals (Basel) **6**(12), 1543–1575 (2013)
2. M. Zasloff, Antimicrobial peptides of multicellular organisms: my perspective. Adv. Exp. Med. Biol. **1117**, 3–6 (2019)
3. M. Fernandez-Vidal et al., Folding amphipathic helices into membranes: amphiphilicity trumps hydrophobicity. J. Mol. Biol. **370**(3), 459–470 (2007)
4. K.A. Brogden, Antimicrobial peptides: pore formers or metabolic inhibitors in bacteria? Nat. Rev. Microbiol. **3**(3), 238–250 (2005)
5. K. Shimazaki et al., Properties of a heparin-binding peptide derived from bovine lactoferrin. J. Dairy Sci. **81**(11), 2841–2849 (1998)
6. L. Zhang, A. Rozek, R.E. Hancock, Interaction of cationic antimicrobial peptides with model membranes. J. Biol. Chem. **276**(38), 35714–35722 (2001)
7. D. Mandal, A. Nasrolahi Shirazi, K. Parang, Self-assembly of peptides to nanostructures. Org. Biomol. Chem. **12**(22), 3544–3561 (2014)
8. D.M. Raymond, B.L. Nilsson, Multicomponent peptide assemblies. Chem. Soc. Rev. **47**(10), 3659–3720 (2018)
9. W.-Y. Chen et al., Self-assembly of antimicrobial peptides on gold nanodots: against multidrug-resistant bacteria and wound-healing application. Adv. Funct. Mater. **25**(46), 7189–7199 (2015)
10. R.Y. Pelgrift, A.J. Friedman, Nanotechnology as a therapeutic tool to combat microbial resistance. Adv. Drug Deliv. Rev. **65**(13-14), 1803–1815 (2013)
11. R.G. Ellis-Behnke et al., Nano neuro knitting: peptide nanofiber scaffold for brain repair and axon regeneration with functional return of vision. Proc. Natl. Acad. Sci. U. S. A. **103**(13), 5054–5059 (2006)
12. T.C. Holmes et al., Extensive neurite outgrowth and active synapse formation on self-assembling peptide scaffolds. Proc. Natl. Acad. Sci. U. S. A. **97**(12), 6728–6733 (2000)
13. J. Kisiday et al., Self-assembling peptide hydrogel fosters chondrocyte extracellular matrix production and cell division: implications for cartilage tissue repair. Proc. Natl. Acad. Sci. U. S. A. **99**(15), 9996–10001 (2002)
14. S. Koutsopoulos et al., Controlled release of functional proteins through designer self-assembling peptide nanofiber hydrogel scaffold. Proc. Natl. Acad. Sci. U. S. A. **106**(12), 4623–4628 (2009)
15. J.S. Richardson, The anatomy and taxonomy of protein structure. Adv. Protein Chem. **34**, 167–339 (1981)
16. X. Guo et al., Solution structures and backbone dynamics of arsenate reductase from Bacillus subtilis: reversible conformational switch associated with arsenate reduction. J. Biol. Chem. **280**(47), 39601–39608 (2005)

17. C.J.C. Edwards-Gayle, I.W. Hamley, Self-assembly of bioactive peptides, peptide conjugates, and peptide mimetic materials. Org. Biomol. Chem. **15**(28), 5867–5876 (2017)
18. M.R. Ghadiri et al., Self-assembling organic nanotubes based on a cyclic peptide architecture. Nature **366**(6453), 324–327 (1993)
19. S. Fernandez-Lopez et al., Antibacterial agents based on the cyclic D,L-alpha-peptide architecture. Nature **412**(6845), 452–455 (2001)
20. H. Cui et al., Self-assembly of giant peptide nanobelts. Nano Lett. **9**(3), 945–951 (2009)
21. J. Wang et al., Dynamic self-assembly of surfactant-like peptides A(6)K and A(9)K. Soft Matter **5**(20), 3870–3878 (2009)
22. H. Xu et al., Hydrophobic-region-induced transitions in self-assembled peptide nanostructures. Langmuir **25**(7), 4115–4123 (2009)
23. G.A. Silva et al., Selective differentiation of neural progenitor cells by high-epitope density nanofibers. Science **303**(5662), 1352–1355 (2004)
24. I.W. Hamley et al., Self-assembly of a model amphiphilic oligopeptide incorporating an arginine headgroup. Soft Matter **9**(19), 4794–4801 (2013)
25. E.G. Bellomo et al., Stimuli-responsive polypeptide vesicles by conformation-specific assembly. Nat. Mater. **3**(4), 244–248 (2004)
26. M.R. Dreher et al., Temperature triggered self-assembly of polypeptides into multivalent spherical micelles. J. Am. Chem. Soc. **130**(2), 687–694 (2008)
27. M.I. Ivanova et al., Molecular basis for insulin fibril assembly. Proc. Natl. Acad. Sci. U. S. A. **106**(45), 18990–18995 (2009)
28. J.J. Wiltzius et al., Molecular mechanisms for protein-encoded inheritance. Nat. Struct. Mol. Biol. **16**(9), 973–978 (2009)
29. G.M. Clore, M.R. Starich, A.M. Gronenborn, Measurement of residual dipolar couplings of macromolecules aligned in the nematic phase of a colloidal suspension of rod-shaped viruses. J. Am. Chem. Soc. **120**(40), 10571–10572 (1998)
30. N. Tjandra, A. Bax, Direct measurement of distances and angles in biomolecules by NMR in a dilute liquid crystalline medium (vol 278, pg 1111, 1997). Science **278**(5344), 1697–1697 (1997)
31. G.M. Clore, J. Iwahara, Theory, practice, and applications of paramagnetic relaxation enhancement for the characterization of transient low-population states of biological macromolecules and their complexes. Chem. Rev. **109**(9), 4108–4139 (2009)
32. D.A. Middleton et al., Insights into the molecular architecture of a peptide nanotube using FTIR and solid-state NMR spectroscopic measurements on an aligned sample. Angew. Chem. Int. Ed. Engl. **52**(40), 10537–10540 (2013)
33. J. Frank, Averaging of low exposure electron-micrographs of non-periodic objects. Ultramicroscopy **1**(2), 159–162 (1975)
34. H. Shen et al., De novo design of self-assembling helical protein filaments. Science **362**(6415), 705–709 (2018)
35. X.J. Ma et al., Amyloid beta (1-42) folding multiplicity and single-molecule binding behavior studied with STM. J. Mol. Biol. **388**(4), 894–901 (2009)
36. X.B. Mao et al., Beta structure motifs of islet amyloid polypeptides identified through surface-mediated assemblies. Proc. Natl. Acad. Sci. U. S. A. **108**(49), 19605–19610 (2011)
37. X.B. Mao et al., Binding modes of Thioflavin T molecules to prion peptide assemblies identified by using scanning tunneling microscopy. ACS Chem. Nerosci. **2**(6), 281–287 (2011)
38. C.X. Wang et al., Determination of relative binding affinities of labeling molecules with amino acids by using scanning tunneling microscopy. Chem. Commun. **47**(38), 10638–10640 (2011)
39. C. Walsh, Molecular mechanisms that confer antibacterial drug resistance. Nature **406**(6797), 775–781 (2000)
40. D.H. Williams et al., An analysis of the origins of a cooperative binding energy of dimerization. Science **280**(5364), 711–714 (1998)
41. C. Ren et al., Interfacial self-assembly leads to formation of fluorescent nanoparticles for simultaneous bacterial detection and inhibition. Chem. Commun. (Camb.) **50**(26), 3473–3475 (2014)

42. L.L. Li et al., Pathological-condition-driven construction of supramolecular nanoassemblies for bacterial infection detection. Adv. Mater. **28**(2), 254–262 (2016)
43. C. Yang et al., Dual fluorescent- and isotopic-labelled self-assembling vancomycin for in vivo imaging of bacterial infections. Angew. Chem. Int. Ed. Engl. **56**(9), 2356–2360 (2017)
44. I. Acebron et al., The allosteric site for the nascent cell wall in penicillin-binding protein 2a: an Achilles' heel of methicillin-resistant Staphylococcus aureus. Curr. Med. Chem. **22**(14), 1678–1686 (2015)
45. M.T.G. Holden et al., Complete genomes of two clinical Staphylococcus aureus strains: evidence for the rapid evolution of virulence and drug resistance. Proc. Natl. Acad. Sci. U. S. A. **101**(26), 9786–9791 (2004)
46. R. Chang et al., Enhanced antibacterial properties of self-assembling peptide Amphiphiles functionalized with heparin-binding Cardin-motifs. ACS Appl. Mater. Interfaces **9**(27), 22350–22360 (2017)
47. S. Hussain et al., Antibiotic-loaded nanoparticles targeted to the site of infection enhance antibacterial efficacy. Nat. Biomed. Eng. **2**(2), 95–103 (2018)
48. S. Marchesan et al., Self-assembly of ciprofloxacin and a tripeptide into an antimicrobial nanostructured hydrogel. Biomaterials **34**(14), 3678–3687 (2013)
49. E.J. Kwon et al., Porous silicon nanoparticle delivery of tandem peptide anti-infectives for the treatment of Pseudomonas aeruginosa lung infections. Adv. Mater. **29**(35), 1701527 (2017)
50. A. Rai et al., One-step synthesis of high-density peptide-conjugated gold nanoparticles with antimicrobial efficacy in a systemic infection model. Biomaterials **85**, 99–110 (2016)
51. R. Kanchanapally et al., Antimicrobial peptide-conjugated graphene oxide membrane for efficient removal and effective killing of multiple drug resistant bacteria. RSC Adv. **5**(24), 18881–18887 (2015)
52. R.P. Cheng, S.H. Gellman, W.F. DeGrado, Beta-peptides: from structure to function. Chem. Rev. **101**(10), 3219–3232 (2001)
53. S. Garde, Hydrophobic interactions in context. Nature **517**(7534), 277–279 (2015)
54. C.D. Ma et al., Modulation of hydrophobic interactions by proximally immobilized ions. Nature **517**(7534), 347–350 (2015)
55. C. Wang et al., Nonadditive interactions mediated by water at chemically heterogeneous surfaces: nonionic polar groups and hydrophobic interactions. J. Am. Chem. Soc. **139**(51), 18536–18544 (2017)
56. T.L. Raguse et al., Toward beta-peptide tertiary structure: self-association of an amphiphilic 14-helix in aqueous solution. Org. Lett. **3**(24), 3963–3966 (2001)
57. W.C. Pomerantz et al., Distinctive circular dichroism signature for 14-helix-bundle formation by beta-peptides. Org. Lett. **10**(9), 1799–1802 (2008)
58. D.S. Daniels et al., High-resolution structure of a beta-peptide bundle. J. Am. Chem. Soc. **129**(6), 1532–1533 (2007)
59. E.J. Petersson et al., Biophysical characterization of a beta-peptide bundle: comparison to natural proteins. J. Am. Chem. Soc. **129**(17), 5344–5345 (2007)
60. W.C. Pomerantz et al., Lyotropic liquid crystals formed from ACHC-rich beta-peptides. J. Am. Chem. Soc. **133**(34), 13604–13613 (2011)
61. T.L. Raguse et al., Structure-activity studies of 14-helical antimicrobial beta-peptides: probing the relationship between conformational stability and antimicrobial potency. J. Am. Chem. Soc. **124**(43), 12774–12785 (2002)
62. A.J. Karlsson et al., Antifungal activity from 14-helical beta-peptides. J. Am. Chem. Soc. **128**(39), 12630–12631 (2006)
63. R. Akkarawongsa et al., Inhibition of herpes simplex virus type 1 infection by cationic beta-peptides. Antimicrob. Agents Chemother. **52**(6), 2120–2129 (2008)
64. B.P. Mowery et al., Mimicry of antimicrobial host-defense peptides by random copolymers. J. Am. Chem. Soc. **129**(50), 15474–15476 (2007)
65. M.W. Lee et al., Two interdependent mechanisms of antimicrobial activity allow for efficient killing in nylon-3-based polymeric mimics of innate immunity peptides. Biochim. Biophys. Acta **1838**(9), 2269–2279 (2014)

66. B.P. Mowery et al., Structure-activity relationships among random nylon-3 copolymers that mimic antibacterial host-defense peptides. J. Am. Chem. Soc. **131**(28), 9735–9745 (2009)
67. S. Chakraborty et al., Effects of cyclic vs. acyclic hydrophobic subunits on the chemical structure and biological properties of Nylon-3 co-polymers. ACS Macro Lett. **2**(8), 753–756 (2013)
68. R. Liu et al., Nylon-3 polymers with selective antifungal activity. J. Am. Chem. Soc. **135**(14), 5270–5273 (2013)
69. L.A. Rank et al., A cationic polymer that shows high antifungal activity against diverse human pathogens. Antimicrob. Agents Chemother. **61**(10), e00204–e00217 (2017)
70. L.A. Rank et al., Peptide-like Nylon-3 polymers with activity against phylogenetically diverse, intrinsically drug-resistant pathogenic fungi. mSphere **3**(3), 3845–3852 (2018)

Chapter 8
Nanomaterials and Reactive Oxygen Species (ROS)

Tao Wen, Jianbo Liu, Weiwei He, and Aiyun Yang

Abstract One fundamental mechanism widely described for nanotoxicity from nanomaterials involves oxidative damage due to generation of free radicals and other reactive oxygen species (ROSs). Indeed, the ability of nanoscale materials to facilitate the transfer of electrons, and thereby promote oxidative damage or in some instances provide antioxidant protection, may be a fundamental property of nanomaterials. Effective methods are needed to assess oxidative damage elicited by nanoscale materials. The production of ROSs induced by nanomaterials is a double-edged sword, bringing not only the benefits of efficient nanomaterials for therapeutic treatment of diseases, but also possible health and environmental risks associated with them. Therefore, it is important to give a brief review on ROSs of nanomaterials and their relation in various biomedical applications.

Keywords Nanomaterial · Reactive oxygen species (ROSs) · Oxidative stress · Antioxidant · Biomedical application

T. Wen (✉) · A. Yang
Institute of Basic Medical Sciences, Chinese Academy of Medical Sciences & Peking Union Medical College, Beijing, P.R. China
e-mail: went@ibms.pumc.edu.cn

J. Liu
College of Opto-electronic Engineering, Zaozhuang University, Zaozhuang, P.R. China

W. He
Key Laboratory of Micro-Nano Materials for Energy Storage and Conversion of Henan Province, Institute of Surface Micro and Nano Materials, College of Advanced Materials and Energy, Xuchang University, Xuchang, P.R. China

H. Xu, N. Gu (eds.), *Nanotechnology in Regenerative Medicine and Drug Delivery Therapy*, https://doi.org/10.1007/978-981-15-5386-8_8

8.1 ROS in Biology System

Reactive oxygen species (ROSs) are a group of chemical species that are continuously generated, transformed, and consumed in all living organisms, which are regarded as unavoidable by-products of aerobic metabolism [1–4]. As a family of molecules that include at least one oxygen atom in each molecule but display higher reactivities relative to molecular O_2, ROSs comprise free radicals, including singlet oxygen ($^1O_2$), hydroxyl radical ($OH^•$), and superoxide radical ($O_2^{•-}$), as well as non-radical species such as hydrogen peroxide (H_2O_2) partially reduced from atmospheric oxygen (Fig. 8.1a) [5, 6]. The appearance of ROS is hypothesized to have taken place at the same time as atmospheric oxygen molecules about 2.4–3.8 billion years ago and has been paramount to the survival of all aerobic life ever since [7].

A

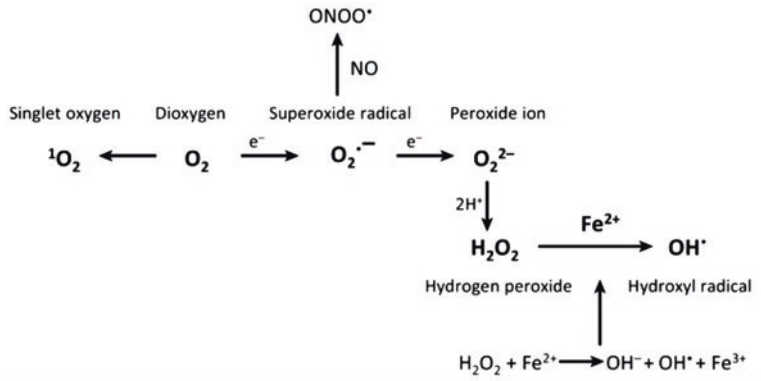

B

ROS	$t_{1/2}$	Migration distance	Mode of action	Production site	Scavenging systems
Superoxide ($O^{•-}_2$)	1–4 µs	30 nm	Reacts with Fe–S proteins Dismutates to H_2O_2	Apoplast (RBOHs), chloroplasts, mitochondria, peroxisomes, electron transfer chains	SOD, flavonoids, ascorbate...
Hydroxyl radical (OH•)	1 ns	1 nm	Extremely reactive with all biomolecules including DNA, RNA, lipids, and proteins	Iron and H_2O_2 (Fenton reaction)	Flavonoids, proline, sugars, ascorbate,...
Hydrogen peroxide (H_2O_2)	>1 ms	>1 µm	Reacts with proteins by attacking cysteine and methionine residues. Reacts with heme proteins. Reacts with DNA.	Peroxisomes, chloroplasts, mitochondria, cytosol, apoplast	APX, CAT, GPX, PER, PRX, ascorbate, glutathione,...
Singlet oxygen ($^1O_2$)	1–4 µs	30 nm	Oxidizes lipids, proteins (Trp, His, Tyr, Met, and Cys residues), and G residues of DNA	Membranes, chloroplasts, nuclei	Carotenoids and α-tocopherol

Fig. 8.1 Properties and reactivity of ROS [5]. (**a**) Formation of different ROS and reactive nitrogen species from atmospheric oxygen. (**b**) Properties ($t_{1/2}$, migration distance), reactivity (mode of action), formation (typical production systems), and scavenging (typical scavenging systems) of ROS in plant and animal cells. *APX* ascorbate peroxidase, *CAT* catalase, *GPX* glutathione peroxidase, *PER* peroxidase, *PRX* peroxiredoxin, *RBOH* respiratory burst oxidase homolog, *SOD* superoxide dismutase. (Reproduced with permission from [5])

Oxygen free radicals have inherent chemical properties that confer reactivity to different biological targets with stronger reactivity. ROSs are often associated with the principle of oxidative stress, which suggests ROSs cause oxidative damage to lipids, DNA, and proteins [8]. However, there is also the growing recognition that ROSs also serve as important physiological regulators of biological and physiological processes [9–11]. As signaling molecules, ROSs stimulate distinct cell signaling pathways and lead to diverse outcomes depending on their sites of production, levels of reactivities, and potentials to cross biological membranes (Fig. 8.1b) [6, 12]. They were most likely first used by cells as signaling molecules to monitor different metabolic reactions, or to sense unsafe levels of atmospheric oxygen, but have since evolved to regulate almost all aspects of aerobic life in animals, plants, and most eukaryotic organisms. For example, in plants, ROSs were found to regulate development, differentiation, stress signaling, redox levels, systemic responses, cell death, and interactions with other organisms [13–15]. As highly toxic by-products of oxygen metabolism, ROSs are primarily formed in mitochondria, peroxisomes, and chloroplasts, but also at any other cellular compartment that includes molecule or proteins with a sufficiently high redox potential to donate or excite an electron to molecular O_2. They are then detoxified or removed by a wide variety antioxidants and antioxidative enzymes (Fig. 8.1b) [6, 16]. This process of ROS production as harmful metabolic by-products, coupled with ROS removal by cellular antioxidative defense system, occurs constantly in cells to prevent some of the potential cellular damage of ROS that could include protein, RNA, DNA, and membrane oxidation and damage. The cellular antioxidative mechanisms of the cell therefore keep ROS at a basal nontoxic level, and the imbalance between ROS production and ROS scavenging could be used for ROS signaling reactions [17].

8.1.1 The Source of ROSs in Biology: Where the ROSs Produced?

The ROSs are generated exogenously or produced intracellularly either by the mitochondrial respiratory chain (cytochrome-oxidase complex containing NADH-dehydrogenase and ubiquinone) or by metabolism of arachidonic acid, xanthine oxidase, phospholipases, and membrane-bound oxidases [18]. This means that essentially any cell could produce ROSs, provided it contains mitochondria or enzymes involved in redox system [19]. An important consideration for ROS chemistry and biological processes is the specific cellular location where a particular metabolite is generated, because microenvironments can determine what targets these ROSs will potentially encounter in a temporal and spatial manner. The classic subcellular location with localized ROS generation includes mitochondria, endoplasmic reticulum, and the cell membranes [20].

There are two important sources of ROSs, consisting of mitochondria and a family of NADPH oxidases (NOXs). The first major source of ROS is the

mitochondria, which are within most cells and tissues. Recent studies revealed that there are eight sites in mitochondria that produce ROS. The three best characterized subcellular locations are complex I, II, and III. They are all in the mitochondrial respiratory chain, and localized to the inner mitochondrial membrane. Superoxide ($O_2^{\bullet-}$) is the proximal mitochondrial ROS generated by the one-electron reduction of O_2. Complex I, II, and III release superoxide into the matrix of mammalian mitochondria where superoxide dismutase (SOD) rapidly catalyzes dismutation of superoxide to H_2O_2. Moreover, complex III can also release superoxide into the intermembrane space. Superoxide traverses through voltage-dependent anion channels from mitochondria to cytosol and is converted into H_2O_2 by SOD1 [21]. The other key source of ROS, in the form of either $O_2^{\bullet-}$ or H_2O_2, is NOXs and their dual oxidase relatives, which are primarily localized to various plasma membranes [12]. NOX proteins are classically known as important ROS sources of most growth factor- and/or cytokine-stimulated oxidant production. The NOX catalyzes the one-electron reduction of O_2 to $O_2^{\bullet-}$, with NADPH as the electron donor [22, 23].

8.1.2 The Regulation of ROS Production in Biology

Low levels of ROS can activate signaling pathways to initiate biological processes, while high levels of ROS would incur damage to proteins, DNA, or lipids. It means that spatial and temporal regulatory mechanisms must exist to modulate ROS levels in response to oxidative stress [12, 24–28].

Generally, antioxidative enzymes can eliminate ROS. Superoxide is rapidly converted by SOD 1, 2, and 3 into H_2O_2. SODs are mainly located in the mitochondrial intermembrane space (SOD1), the matrix of mitochondria (SOD2), and the extracellular matrix (SOD3). SODs protect aerobic organisms from toxical superoxide that can damage and inactivate proteins.

As H_2O_2 is the by-product of superoxide scavenging by the SOD, there are a wide variety of enzymes that remove H_2O_2, including peroxiredoxins, glutathione peroxidases, and catalase (CAT). The function of these antioxidant enzymes is dependent on the concentration of H_2O_2, their reactivity with H_2O_2, and enzyme in vivo. The regulation of activity and expression levels of these antioxidants occurs by multiple functions and mechanisms in part to modulate ROS levels [29, 30].

Another reactive and damaging ROS is hydroxyl radical ($OH^{\bullet}$), which indiscriminately oxidizes DNA, proteins, and lipids, resulting in genomic instability or irreversible damage of cellular macromolecules. Typically, hydroxyl radicals are formed through reactions with ferrous ions (Fenton-like reaction). Therefore, cells have multiple strategies to maintain homeostasis to prevent the formation of extremely reactive hydroxyl radicals [31–33].

8.2 Biological Effects Induced by Oxidative Stress from Nanoparticles

With the spread and development of nanotechnology and nanoscience, nanomaterials have dramatically increased in biomedical and industrial applications. However, the scientific basis for the cytotoxicity and genotoxicity of most nanomaterials is not comprehensively understood. The influences on ROS are regarded as one main source of toxicity of nanomaterials. The ROSs from nanomaterials have lots of critical determinants, including size, shape, surface charges, surface-containing groups, dissolution, ions release from nanomaterials, light activation, aggregation, mode of interaction with cells, and pH of the medium. Nanomaterials can disturb the balance of ROS, leading to oxidative stress, resulting in cells failing to maintain normal physiological environment and related functions. This may lead to DNA damage, regulate cell signaling, and change in cell motility, cytotoxicity, apoptosis, and cancer initiation.

ROSs played a vital role in all living organism. The cellular signaling pathways, antioxidant defense, and oxidative stress-induced diseases are all known to be associated with the level of ROSs (Fig. 8.2). As mentioned above, there are a variety of ROS-producing pathways by nanoparticles in cells and tissues, including the NADPH oxidase, the mitochondrial, the xanthine oxidase, the cyclooxygenase, and the dioxygenase system. In most of the eukaryotic cells, mitochondria are the major sites for ROS production [16] and a synthetic site of adenosine triphosphate (ATP). During the synthesis of ATP, molecular oxygen is finally reduced to water molecules through a series of redox processes under the action of mitochondrial electron transport

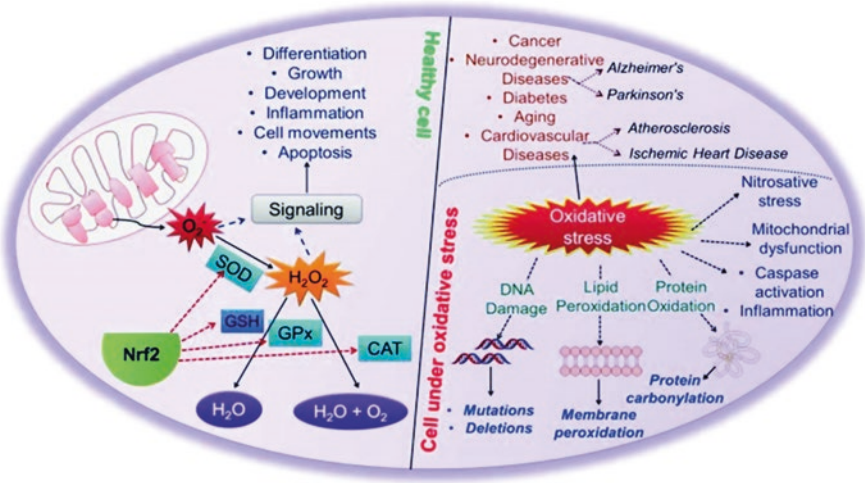

Fig. 8.2 Cellular antioxidant machinery and oxidative stress [8]. (Reproduced with permission from [8])

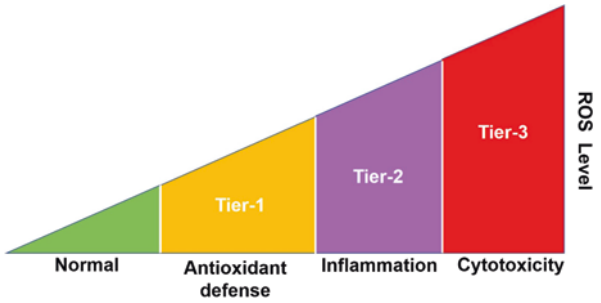

Fig. 8.3 Stratified oxidative stress model [35]. At a lower amount of oxidative stress (tier 1), antioxidant enzymes are induced via transcriptional activation of the antioxidant response element to restore cellular redox homeostasis. As ROS levels increase, this protective response is overtaken by inflammation (tier 2) and cytotoxicity (tier 3)

chain; however, a small portion of oxygen molecules is not reduced. The remaining part of the oxygen molecule is ROS, so ROS is also considered to be a by-product of cellular oxidative metabolism [34]. Generally, oxidative stress with excess ROS is viewed as a dominant mechanism of pathological changes induced by nanoparticles (NPs). Here, we talk about only the nanotoxicology caused by ROS.

Nel proposed a three-layer oxidative stress model of cellular oxidative stress in nanoparticles to explain the toxicity of nanoparticles, as shown in Fig. 8.3, that is, low levels of ROSs induce enhanced antioxidant defense of cells and higher levels of ROSs cause cellular inflammatory responses and ultimately induce cell death at very high levels of oxidative stress [35].

8.2.1 Antioxidant Defense

The production and elimination of active oxygen is maintained at a steady-state level in physiological conditions. In the body, the elimination of oxygen includes the enzymatic antioxidant defense system and the nonenzymatic antioxidant defense system, which is an effective protection mechanism for potential oxidative damage formed by nanoparticle.

In the defense systems, enzymatic antioxidants include superoxide dismutase, catalase, peroxidase, heme oxygenase, glutathione reductase, glucose-6-phosphate dehydrogenation, etc., which are mentioned in the previous chapter. Although these enzymes have different molecular weights, structures, and reaction rates, they all undergo disproportionation reactions to catalyze reactive oxygen radicals. In addition, there are nonenzymatic antioxidant defense systems. It mainly includes vitamin C, vitamin E, lipoic acid, carotenoids, uric acid, flavonoids, and coenzyme Q. These antioxidants are both synthesized in the body and absorbed from natural substances. These antioxidants react directly with free radicals by giving them electrons. The result of the reaction is that these small molecular antioxidants become

new free radical carriers, which are reduced by other substances (such as NADH) and return to a reduced state [36].

In addition, cells have evolved appropriate antioxidant signaling pathways for timely scavenging of excessive ROSs, such as Nrf2/keap1-ARE, PPAR gamma, FOXO, and SIRT [37–40]. For example, Nrf2/keap1-ARE signaling pathway is the most powerful endogenous antioxidant signaling pathway known at present. When exposed to oxidants, Nrf2 dissociates from Kelch-like ECH-related protein 1 (Keap1) and translocates to the nucleus, where it binds to promoter regions of antioxidant enzymes containing antioxidant response elements (ARE) such as Gpx2, NQO1, and GCLC. The mechanism of Nrf2-dependent effect involves the reduction of antioxidant enzyme transcription and damage-related genes, providing protection against oxidation-induced acute tissue injury [41]. Moreover, these pathways can synergistically resist oxidative stress damage and promote cell survival.

With low levels of oxidative stress, cells can start to initiate their own antioxidant reactions. The antioxidant enzymes firstly changed and then the transcription factor Nrf2 activated by the antioxidant response [42], causing a series of changes in antioxidant signaling pathways to regulate the oxidative stress response in cells. In contrast, high levels of ROS production resulting from Nrf2 deletion lead to elevated proinflammatory cytokine levels [43]. Nrf2-deficient mice exacerbate the innate immune-inflammatory response to pathogens, resulting in increased pneumonia and sepsis [11]. Antioxidants increase the survival rate of Nrf2-deficient mice in these sepsis models. Thus, while slightly elevated ROS levels may enhance immune system function, high levels of ROS may promote pathological inflammatory responses.

8.2.2 Inflammation

Inflammation is the defense response of the body to external stimuli. Nanoparticles may cause the release of a variety of inflammatory factors. As gene transcription plays an important role in regulating cells, nanoparticles are involved in the regulation of the expression of many genes, especially those related to the body's defense functions, including adhesion molecules and proinflammatory cytokines. For examples, NF-κB is often involved in cell proliferation and differentiation, as well as inflammation and immune response. Studies have shown that inhibition of NF-κB can alleviate the inflammatory response and fibrosis caused by nanomaterials [44]. There is ample evidence that ROSs are essential second messengers in innate and adaptive immune cells [45]. However, elevated levels of ROS in immune cells can lead to overactivation of the inflammatory response leading to tissue damage and pathology [41]. ROS messengers are needed to maintain the innate immune system. For example, pathogen-associated molecular patterns (PAMPs) and damage-associated molecular patterns (DAMPs) molecules are produced by pathogens, which can induce body injury activating the monitoring receptors (Toll-like receptors (TLR), RIG-I-like receptors (RLRs), and NOD-like receptors (NLRs)) and produce ROS through NADPH oxidase and mitochondria. There are lots of

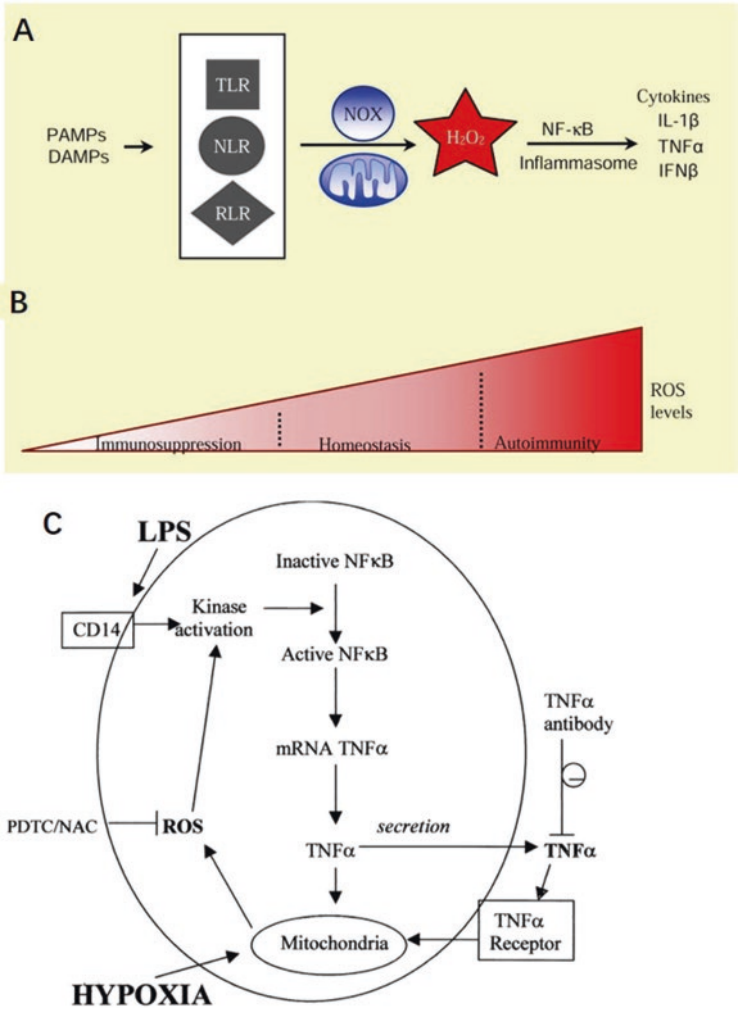

Fig. 8.4 Examples of ROS regulation of inflammation [12, 46]. (**a**) Activation of the innate immune system requires ROS signaling. (**b**) Low levels of ROS maintain a healthy immune system. (**c**) Effects of LPS and hypoxic activation of NF-κB and TNF-α mRNA. (Reproduced with permission from [12, 46])

proinflammatory cytokines, including IL-1β, TNF-α, and IFN-β, which are closely related with ROS. ROSs regulate their release and maintain the innate immune response (Fig. 8.4a). Low levels of ROSs maintain a healthy immune system. Lowering ROS level will inhibit the activation of normal immune response, leading to immune suppression. Increased ROS levels can promote autoimmunity by increasing the release of inflammatory cytokines and the proliferation of specific subsets of adaptive immune cells (Fig. 8.4b).

The earliest studies of ROS in the innate immune system were found by producing NADPH oxidase and mitochondria to produce ROS-activated cellular inflammatory factors in the presence of lipopolysaccharide (LPS). The LPS activates NF-κB and the expression of TNF-α mRNA, and TNF-α increases mitochondrial ROS through an autocrine effect of TNF-α on a cell membrane receptor. Hypoxia induces mitochondrial ROS directly, which subsequently activates NF-κB and TNF-α mRNA expression (Fig. 8.4c) [46]. Studies have found that single-walled carbon nanotubes can activate NF-κB and promote the transfer of NF-κB from cytoplasm to intracellular binding with DNA, starting transcription, resulting in the release of ROSs, oxidative damage to cells, and apoptosis pathway, and leading to cell death [47].

Existing studies have found that NP can increase the levels of some inflammatory cytokines. For example, silica NP has been shown to significantly increase the release of some proinflammatory cytokines. These increases are organ-dependent, which means that systemic administration of NP causes inflammation [48]. It has been reported that the cytotoxicity of three metal oxides (ZnO, CeO_2, TiO_2) has been compared and based on the release of zinc ions, ZnO is the most toxic in bronchial epithelial and macrophage cell lines. Furthermore, ZnO NPs not only generate hydrogen peroxide and superoxide radical, but also cause the formation of IL-8 and tumor necrosis factor-α (TNF-α) in bronchial epithelial cells and macrophages [49]. The same cytokines were also found in the bronchoalveolar lavage fluid of welders exposed to some metal oxide nanoparticles (including ZnO NPs) [50]. This exposure can cause an acute inflammatory response in the lung called metal smog [51].

8.2.3 Cytotoxicity

The toxicity of nanomaterials that damage cells is called cytotoxicity, which is one of the most important toxic effects observed in vitro. Exposure of cells to toxic amounts of nanomaterials can cause a series of changes within the cell, such as cell membrane contraction, rupture, or destruction of intracellular components, leading to apoptosis or necrosis, which can affect cell growth rates. In vitro cytotoxicity assays are commonly used to elucidate acute and chronic toxicity caused by nanomaterials. The benefits of using cultured cell lines are numerous, including reproducibility and ease of handling with test materials. Cultured cells have been shown to have significantly higher sensitivity to nanomaterials [35].

In vitro cytotoxicity assessment involves measuring the proliferation and cellular metabolism of cells exposed to nanomaterials using different assays (such as 3-(4,5-diethylthiazol-2-yl)-5-(3-carboxymethoxyphenyl)-2-(4-sulfophenyl)-2*H*-etrazolium (MTS)). The purpose of these methods is to mimic cellular responses in vitro after exposure to any toxic dose of nanomaterials. However, the in vitro simulated cytotoxicity tests are usually different from the real body; thus it is still necessary to pay attention to more detailed studies. There are publications to demonstrate how the topic of toxicity needs to be discussed [52]. In addition, they

observed that the doses used to obtain in vitro data often lacked relevance with that in vivo. In vivo effects such as dilution, surface changes, and biological interactions are particularly important [53].

The physicochemical properties of nanomaterials are key factors affecting cytotoxicity through ROS, such as the shape, size, surface charge, and chemical modification. The effects of these factors on cytotoxicity of nanomaterials have been systemically reviewed [54].

Small size is a unique property of nanomaterials, which can affect the level of ROSs in cells or tissues. Mirshafa et al. reported that oxidative stress in rat brain tissue induced by alumina nanoparticles (Al_2O_3-NPs) is much larger than that of alumina particles (Al_2O_3-MPs), and Al_2O_3-NPs can significantly induce ROS production in rat brain tissue, what is more, glutathione and potential of mitochondrial membrane decreased. Smaller-sized Al_2O_3-NPs have greater oxidative damage to the brain than Al_2O_3-MPs [55]. Neubauer et al. showed that the ability of Pd-NPs and Ni-NPs to induce ROS production in THP1 cells is significantly dependent on the particle size of nanoparticles. In the range of 4–27 nm, nanoparticles induce strong ROS production, of which 12 nm particle size-induced cells produce the highest level of ROS [56]. Conversely, a report suggested that distribution and toxicity appear to be independent of particle size within the test range [57], but surface charge rather than particle size closely regulates the pharmacokinetics of NPs [58]. This shows the toxic effects of NPs are complex.

Surface cationized nanoparticles are likely to interact with negatively charged cell membranes or nucleic acid species, thereby induce a higher oxidative stress response [59]. Platel et al. have studied the effects of negatively and positively charged polylactic acid-glycolic acid copolymer (PLGA) nanoparticles on the levels of ROSs in different cell lines. Studies have shown that the ROS levels of murine lymphoma cells (L5178Y), human lymphoblasts (TK6), and human bronchial epithelial cells (16HBE) can be significantly increased by positively charged PLGA nanoparticles. However, negatively charged PLGA nanoparticles have less effect on the ROS levels of the above three cells [60]. The result on PLGA nanoparticles is similar with gold nanoparticles, which show that positively charged gold nanoparticles are incorporated more by human umbilical vein endothelial cells (HUVECs) than negatively charged gold NPs, indicating stronger cytotoxicity and oxidation stress reaction [61]. With different surface chemical modifications, the toxicities of NPs are often different even with the same NPs. For example, to employ the polyethylene glycol (PEG) as coating material, the potential toxicity of NPs can significantly decrease by reducing intracellular ingestion and binding interactions with proteins [62]. Taking antibodies as the biomolecules on the surface of NPs, the toxicity of antibody-conjugated quantum dot is much lower than that of unconjugated quantum dot on male Wistar rats [63].

Among the studies on cytotoxicity of nanomaterials, a majority of existing researches focus on the study of endothelial cells. The vascular endothelium cell is the first tissue to contact the nanoparticles before the nanoparticles are delivered to

the target via the blood circulation. The effect of nanoparticles on blood vessels is an important issue that needs to be studied and elucidated. For example, silver (Ag) NPs were found to be taken up by vascular endothelial cells and induce intracellular ROS elevation, which is closely related to the integrity of endothelial cells. Endothelial cell leakage induced by intravenous administration of Ag NPs mediates inflammation of the liver, kidneys, and lungs [64]. Based on this, it was also found that even at noncytotoxic concentrations, an increase in intracellular ROS and CAT activity is a common effect of NPs, depending on the size distribution, composition, and surface chemistry of the NP. This action results in a gap between the endothelial cells that can be rescued by the use of antioxidant [65]. Iron oxide nanoparticles were reported to influence the phenotype and be able to induce endothelial-to-mesenchymal transition in endothelial cells at an acute noncytotoxic dose, although they were rarely taken up by endothelial cells. ROS scavengers can rescue the effect of endothelial-to-mesenchymal transition on HUVEC in vitro and in vivo [66].

With the rapid development of the production and application of nanomaterials, the evaluation of the safety and toxicity of nanomaterials-induced ROS has become a public concern; thus the detection of ROS in nanomaterials is urgently needed.

8.3 Methods of Detecting ROS in Nanomaterials

Because ROSs are easy to produce and may produce toxic effects to biological cells, it is particularly important to accurately detect ROSs. The measurement of ROSs is dependent on the analytic target along with the ROS in question. At the cellular level, specific ROS can be individually assessed from tissue culture, while at the animal level typically the effects of oxidative stress are measured from blood product (e.g., serum or plasma) or from urine samples. Methods for ROS detection can be broadly classified as either direct or indirect. Due to the short lifetimes and typically low concentrations of ROS in aquatic systems, their direct observation is only possible on the sub-millisecond timescale (Fig. 8.1b), with the relatively stable H_2O_2 being an exception. Indirect methods typically involve probes that very rapidly react with ROS to compete with antioxidants and produce stable products, which can be quantified [67–71]. By virtue of introducing additional chemical reactions, all indirect techniques risk perturbing the observed system. Some important aspects to consider when choosing an ROS analysis method include: (1) the sensitivity of the method; (2) the selectivity and specificity of the method for the analyte of interest; and (3) the ability of the method to allow measurements with sufficiently fast time resolution [72]. Additional analytical considerations are availability, robustness, portability (for field studies), the cost of the necessary instrumentation, and in some cases, the cost of the probe molecules. All these methods are mainly divided into three categories.

8.3.1 ESR Technique

Electron spin resonance and paramagnetic resonance (ESR or EPR) are unique techniques that specifically and directly "see" unpaired spins of free radicals. ESR spectroscopy is the most used method for the detection of paramagnetic species. This involves absorption of microwave energy by paramagnetic species in the presence of an external magnetic field resulting in the transition of spin states. ESR spectroscopy is a useful method for studying any materials with unpaired electrons. EPR allows researchers to detect ROS directly and it can also be used to monitor changes in the chemical forms of the oxidizable transition metal ions implicated in ROS generation. ESR spectroscopy stands out from other methods because of its unique ability to detect either short- or long-lived radicals with specificity and sensitivity [73, 74]. For short-lived ROS, the spin-trapping technique involves the reaction with the addition of the free radical to the double bond of a diamagnetic "spin trap". Spin traps are stable, diamagnetic compounds that form longer-lived radical species with transient, very reactive radicals with low half-lives of only 10^{-9} to 10^{-1} s. The paramagnetic spin adducts are stable for minutes or even hours, accumulate in the tissue, and reach a sufficient concentration for detection by ESR. The ESR spectra of the spin adducts are unique and provide a fingerprint for the presence of ROS. Two classes of spin traps are commonly used: the linear nitrones, *N-tert*-butyl-a-phenyl nitrone (PBN) and a-(4-pyridyl-1-oxide)-*N-tert*-butyl nitrone (4-PyOBN); and the pyrroline-based cyclic nitrones, 5,5,-dimethyl-pyrroline *N*-oxide (DMPO), 5-*tert*-Butoxycarbonyl-5-methyl-1-pyrroline *N*-oxide (BMPO), 5-diethoxyphosphoryl-5-methyl-1-pyrroline *N*-oxide (DEPMPO), and 5-ethoxycarbonyl-5-methyl-1-pyrroline *N*-oxide (EMPO). It is important to distinct spin traps and spin probes. Spin traps form covalent bond with the radical by addition reaction, while spin probes are stable nitroxide free radicals. Spin probes have an unpaired electron, which is able to bind to another molecule. The commonly used spin labels include 2,2,6,6-tetramethyl-1-piperidinyloxy, 2,2,6,6-tetramethylpiperidine 1-oxyl (TEMPO), 2,2,6,6,-tetramethyl-4-piperidone-1-oxyl (TEMPON), 4-hydroxy-2,2,6,6-tetramethylpiperidine 1-oxyl (TEMPOL), 4-amino-2,2,6,6-tetramethyl piperidine-1-oxyl (4-amino-TEMPO), 3-carbamoyl-2,2,5,5-tetra-methyl-3-pyrroline-1-yloxyl (CTPO), and 4-oxo-2,2,6,6-tetramethyl piperidine-d_{16}-1-^{15}N-oxyl (^{15}N-PDT). This technique is not only much more sensitive than other direct detection, but it also allows better identification of the primary radical [75, 76]. The resulting ESR spectrum often exhibits a hyperfine splitting pattern that is characteristic of the trapped radical, and therefore transient radicals that are otherwise undetectable under normal conditions can now be observed [77, 78].

Generally, $OH^{\bullet}$ and $O_2^{\bullet-}$ can react with diamagnetic nitrone spin traps and form a stable free radical (spin adduct). A commonly used spin trap for these two radicals is BMPO. The ESR spectrum of the spin adduct BMPO/$OH^{\bullet}$ shows four lines with relative intensities of 1 : 2 : 2 : 1 and hyperfine splitting parameters of $a_N = 13.56$, $a_H^{\beta} = 12.30$, and $a_H^{\gamma} = 0.66$ (Fig. 8.5a). The ESR spectral characteristics of BMPO/

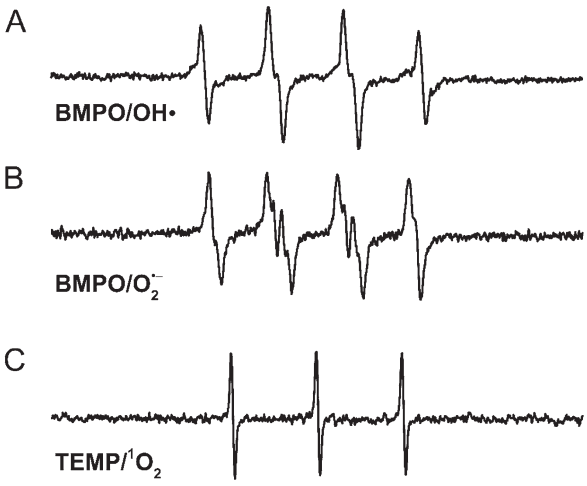

Fig. 8.5 Typical ESR spectra of adducts for (**a**) BMPO/OH$^{\bullet}$, (**b**) BMPO/$O_2^{\bullet-}$, (**c**) TEMP/$^1O_2$ (TEMPONE)

$O_2^{\bullet-}$ show four lines with relative equal intensities (1 : 1 : 1 : 1), and two hyperfine splitting parameters of a_N = 13.4 and a_H^{β} = 12.1 (Fig. 8.5b) [79]. Singlet oxygen ($^1O_2$) is another important ROS, and 2,2,6,6-tetramethyl-4-piperidine (TEMP) can be used as a spin trap to specifically capture $^1O_2$ to yield a nitroxide radical (4-oxo-2,2,6,6-tetramethylpiperidine-*N*-oxyl, TEMPONE) with a stable ESR signal. ESR spectra of TEMPONE characteristically have three lines with equal intensities, with a hyperfine splitting parameter of a_N = 16.0 (Fig. 8.5c) [79].

However, there are some limitations for ESR spin trapping during ROS determination in vivo or/and in vitro. The technique requires spin traps that reduce specificity and stability for the measurement. Another major drawback of the method is that spin adducts are only relatively persistent, and their lifetimes, especially in biological environments where they are subject to degradation by several enzymatic systems, are usually too short to allow reliable quantitative measurements. Of course, apart from these chemical limitations of the method, one of the biggest drawbacks is the cost of EPR instrumentation, which is often much greater than typical absorbance or fluorescence spectrometers [80].

8.3.2 Optical Absorption

Some ROSs (such as hydrogen peroxide, superoxide, and hydroxyl radical) absorb in the 230–350 nm region of the UV/Vis spectrum and can be quantified directly at micromolar concentrations by measuring their absorbance [67, 72]. The molar absorption coefficient of H_2O_2 is 0.01 M^{-1} cm^{-1} at 360 nm and gradually increases up to 13 M^{-1} cm^{-1} with decrease in wavelength to 260 nm. However, such a

method is not typically possible because of its limited lifetime, small absorption coefficient, and the presence of other chromophores absorbing in a similar wavelength region [67].

8.3.3 Spectroscopic Probe Technique

Because the ESR technique requires a specialized and relatively expensive ESR spectrometer, alternative methods have been developed for ROS detection with more readily available equipment. The spectroscopic probe methods make use of readily available probe molecules, do not require specialized equipment, and generally afford greater specificity, sensitivity, and lower limits of detection compared to ESR and absorbance-based methods. Spectroscopic detection strategies, including absorbance (UV/Vis), fluorescence (FL), and chemiluminescence (CL), share a common approach with several other techniques for measuring rates of ROS formation and decay in laboratory experiments. These strategies are also compatible with methods such as steady-state kinetic analyses, stopped flow methods, time-resolved laser spectroscopy, flash photolysis, and pulse radiolysis. A spectroscopic probe is a substance that changes its spectroscopic properties (light absorption or emission) upon reaction with ROS. An ideal spectroscopic probe should be highly specific for one kind of ROS form and react with it efficiently, so that it can be used at low concentration without perturbing the studied system [70, 71].

The best and simplest ROS detectors are substances with optical properties that change in reaction with ROS and show some specificity for different ROS species. However, their principal disadvantage is relatively low sensitivity compared to other probes [81, 82]. Ferricytochrome c reduction is a time-honored and accurate method for detecting large amounts of $O_2^{\bullet-}$ released by cells into the extracellular space, which is based on the reduction of ferricytochrome c by $O_2^{\bullet-}$ to ferrocytochrome *c*. This reaction can be followed by the spectrophotometric absorbance at 550 nm [70]. Nitro blue tetrazorium (NBT, 2,2′-di-*p*-nitrophenyl-5,5′-diphenyl-(3,3′-dimethoxy)-4,4′-bisphenyleneditetrazolium chloride) has also been widely used for the detection of superoxide radical. The product of univalent reduction of NBT is tetrazoinyl radical in which its dismutation generates a stable formazan. A number of colorimetric substrates such as tetramethylbenzidine (TMB) and phenol red have also been used in conjunction with horseradish peroxidase (HRP) to measure hydrogen peroxide concentrations. In general, colorimetric means are less sensitive than fluorescent detection methods, but instrumentation costs are significantly lower than those required for fluorescence-based measurements when using tube-based or microplate-based detection methodologies [81].

The fluorescence methodology, associated with the use of suitable probes, is an excellent approach to measure ROS because of its high sensitivity, high spatial resolution, and simplicity in data collection [83–85]. Fluorescence may be measured or observed with a microtiter plate reader, microscope, fluorimeter, or cytometer. Confocal microscopes offer the possibility of additionally observing cellular

topography of ROS production and can provide some degree of specificity through use of various fluorescent probes [84]. A variety of fluorescent probes have been developed recently to detect ROS in order to uncover their unique functions in biological systems. The most widely used fluorescent indicator for superoxide radical is hydroethidium (HE), a two-electron reduced form of the nucleic acid stain ethidium. HE has been employed to detect ROS production during phagocytic respiratory bursts and intracellular oxidative stress. The oxidation of 2,7-dichlorodihydrofluorescein (DCFH) originates 2,7-dichlorofluorescein (DCF), a fluorescent compound ($\lambda_{excitation}$ = 498 nm, $\lambda_{emission}$ = 522 nm) initially thought to be useful as a specific indicator for H_2O_2. However, measurements based on redox-sensitive dyes such as DCFH can be problematic because they depend on dye uptake and lack any specificity toward a particular type of ROS. The advent of protein-based redox sensors like redox-sensitive green fluorescent protein (roGFP) have improved specificity to particular ROS and can be targeted to different compartments within the cells to gather spatial resolution of ROS levels [83]. Fluorescent protein-based biosensors have been developed for the investigation of the ROS in situ in real time. This new generation of live cell fluorescent sensors produces changes in fluorescence in response to alteration in the redox state or with fluctuations in specific target analyte. These sensors are genetically encoded, based on a single fluorescent protein and do not require the addition of any other reagents or cell lysis, making them very amenable to multiplexing.

Chemiluminescent (CL) reactions have been used for their potential increase in sensitivity over absorbance-based detection methods [85–88]. Chemiluminescence (CL) is observed when the electronically excited product of an exoergic reaction relaxes to its ground state with emission of photons, and it can be defined in simplistic terms: chemical reactions that emit light (ultraviolet, visible, or infrared radiation). CL applications in analytical chemistry have obvious potential advantages, such as high sensitivity, wide linear range, simple and inexpensive instrumentation, considerable reduction of background noise, safety, controllable emission rate, and easy computer control. ROSs can generate electronically excited products, which emit the weak CL during their decay to the ground state. Although it is not easy to detect the light emission directly by CL techniques, it can be enhanced by CL substrates. Due to superoxide's brief lifetime and low steady-state concentrations, it is typically measured using highly sensitive CL probe molecules. Successful probes for decay or steady-state measurements must react at rates of at least ten times greater than that of natural superoxide disproportionation. The most widely used chemiluminescent substrate is Luminol and lucigenin. Luminol is the most widely used CL probe for chemical analysis. In the presence of a peroxidase (such as HRP), luminol-derived chemiluminescence has been used to detect cellular superoxide or H_2O_2 production under various experimental conditions. Unfortunately, because lots of species can promote the CL of luminol, this reagent is problematic for the selective analysis [87]. Among the most widely used compounds with higher specificity in their light emission with superoxide is bis-*N*-methylacridinium nitrate (i.e., lucigenin), which could be used at moderate pH [88]. Other compounds used are cypridina luciferin analogues, such as

2-methyl-6-(*p*-methoxyphenyl)-3,7-dihydroimidazo (1,2-α)pyrazin-3-one (MCLA), 2- methyl-6-phenyl-3,7-dihydroimidazo (1,2-α)-pyrazin-3-one (CLA), and 2-(4-hydroxybenzyl)-6-(4-hydroxyphenyl) 8-benzyl-3,7-dihydroximidazole [1,2-α] pyrazin-3-one (i.e., coelenterazine).

Although the use of spectroscopic probes appears to be a simple and easy means for the detection and quantification of ROS production in cellular systems, it should be noted that the techniques of fluorescence, spectrophotometry, and luminometry are less direct and less specific for the detection of free radicals versus ESR [81].

8.3.4 Nanoprobes for ROS Detection

Some drawbacks of spectroscopic probes can be overcome or ameliorated using a method of encapsulating the dye in nanoparticle delivery systems. Encapsulation of these probes by inert nanoparticles, which protect them from nonspecific interactions, provides an elegant solution for delivery into cells. Chemically inert nanoparticle delivery systems are sufficiently small (1–1000 nm) so as to be introducible into cells by standard mechanisms (microinjection, lipofection, and TAT-protein delivery). They are however large enough to encapsulate perfectly relatively large volumes of one or multiple probes, which facilitates a ratiometric measurement of the optical response [69].

Warner et al. reported the ratiometric coumarin-neutral red nanoprobe that can be utilized for detection of the hydroxyl radical. The nanoprobe was prepared by mixing poly lactide-*co*-glycolide (PLGA) nanoparticles, containing encapsulated Neutral Red, and a coumarin 3-carboxylic acid conjugated poly(sodium *N*-undecylenyl-*N*-e-lysinate) that serves as a moiety that is reactive with the hydroxyl radical. The probe was selective for hydroxyl radicals as compared to other ROS including $O_2^{\bullet-}$, H_2O_2, $^1O_2$, and OCl^{-1} [89].

Recent advances in the design and synthesis of carbon nanostructures have provided a novel route for optical biosensor development. Carbon nanotubes generally display semiconductive properties and are therefore photo-luminescent, absorbing radiation and emitting photons at specific wavelengths. One recent study highlights the potential of single-walled carbon nanotubes in the multimodal analysis of intracellular ROS by reporting detection of H_2O_2, singlet oxygen, and $OH^{\bullet}$ [90]. Wu and Zeng et al. developed the multifunctional fluorescent nanoprobe, which is prepared by covalently linking the mitochondria-targeting ligand (triphenylphosphonium, TPP) and boronated fluorescein (PF3) to carbon dots (CDs). In the presence of H_2O_2, the arylboronate moiety in PF3 is converted to a phenol, which triggers FRET from the CDs to fluorescein PF4. The results of a cell imaging study indicate that the nanoprobe can be applied for detecting endogenously produced mitochondrial H_2O_2 in RAW264.7 cells [91].

Alternatively, the detection and quantitation of ROS reaction products can also be accomplished with detector molecules using high performance liquid

chromatography (HPLC), mass spectrometry, and immunochemistry. Other methods of detecting ROS reactions include monitoring lipid peroxidation and oxidative damage to proteins as well as DNA.

8.4 Biomedical Applications of Nanomaterials by ROS Regulation

At present, ROS detection technologies have tended to be diversified. The vigorous research on ROS is not only for avoiding ROS, but also for making use of them in the treatment of human diseases.

8.4.1 Cancer Therapy

Cancer is one of the leading causes of death. From the statistical data [92], there were more than 18 million new cancer cases and 9.5 million deaths worldwide in 2018. Globally, the number of new cases is expected to rise to ~23.6 million per year by 2030. More and more people's life and health are severely threatened by this devastating disease. At present, the conventional ways commonly used in clinical treatment of cancers include chemotherapy, radiation therapy, and surgery. However, such methods bear low cure rates and adverse side effects on patients' physical and mental health. Therefore, the development of new therapeutic strategies with high efficacy and largely diminished side effects in combating cancer is urgently needed for public health. At the cutting-edge field, nanomaterials with unique physicochemical characteristics have received increasing interest for biomedical applications, especially cancer therapy [93]. ROSs have been well recognized as one of the important players, which can be beneficial to kill cancer cells [94]. Recently, many nanomaterials have been reported to generate ROS intrinsically in biologically relevant environments. Nanomedicines based on mediating ROS for cancer treatment caught enormous attention currently. As ROSs are associated with most of the stages of cancer, the therapeutic strategy based on ROS concludes two main categories: drug delivery enhancers and cell death inducers [94]. Nanomaterials triggered the production of ROS mainly through two ways: (1) the photo-irradiation excited the nanomaterials to produce ROS, and (2) the intrinsic ability of nanomaterials to facilitate electron transfer catalytically activated the generation of ROS. Such abilities have been subtly used to develop novel cancer treating modalities, such as photothermal therapy (PTT), photodynamic therapy (PDT), and catalytic reaction therapy (CRT) [95–98].

Photodynamic therapy (PDT) is a promising technique for treating various cancers. The main elements include light, photosensitizers, and oxygen. The fundamental principle of PDT is using light to activate a photosensitizer, leading to the

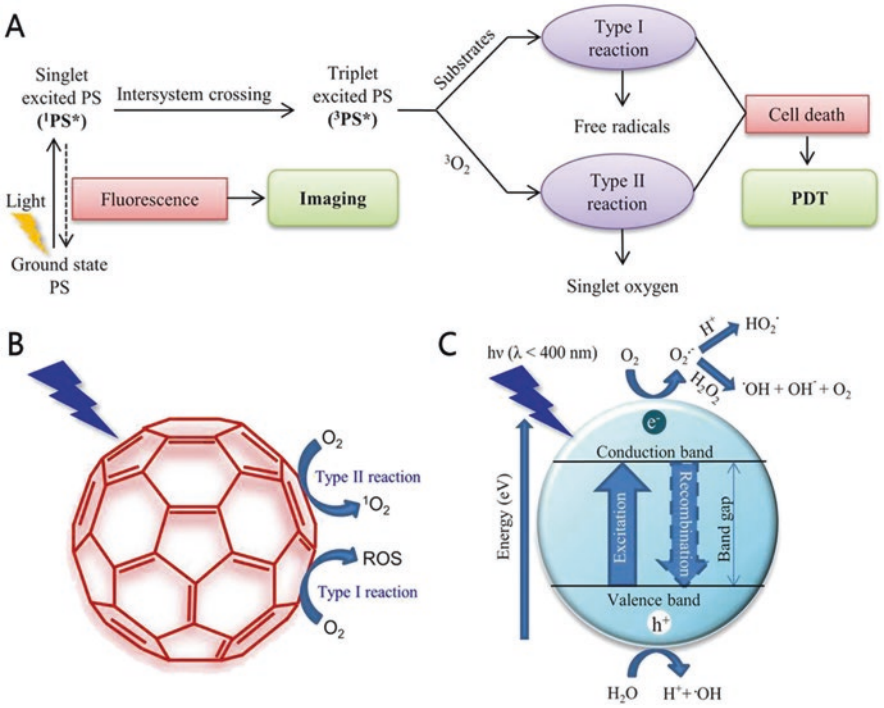

Fig. 8.6 Schematic illustration of a typical photodynamic reaction. (**a**) Two typical ways for photodynamic reaction upon light irradiation on (**b**) fullerene and (**c**) semiconductor nanoparticle [95]. (Reproduced with permission from [8])

generation and release of ROSs at the local site of cancerous body (Fig. 8.6). Though there have been developed several organic photosensitizers (e.g., porphyrins, chlorins, porphyrinoids, and biomolecule conjugates) as candidates for PDT, NPs offer several advantages over traditional treatment options, typically including low toxicity of the NPs in the absence of light irradiation, high efficacy, optimal response to light with varying wavelength, selective and specific accumulation, and deep penetration into the tumors [95]. Various nanomaterials have been prepared and employed as novel photosensitizers, including noble metal NPs, semiconductor NPs, carbon NPs and their derivate, metal organic frames, and others. Noble metal nanoparticles (Au, Ag, Pd, Ti) hold great promise as PDT agents because of their surface plasmon resonance (SPR) enhancing effect on generation of ROS [99–101]. Typically, the gold nanoparticles with tunable SPR from visible to NIR have been demonstrated as PDT agents can selectively kill cancerous cells at varying laser frequency ranges. For example, 15 nm Au nanospheres with citrate coating were reported to destroy the malignant cells upon exposure to laser light, which induced the production of ROSs [101]. The shape and structure of gold NPs can affect greatly the SPR, and consequently the PDT therapeutic efficiency [102]. Semiconductor nanostructures, such as TiO_2 and ZnO, can also produce ROS under irradiation that can be used for reducing tumor growth [103]. Another example is copper sulfide (CuS) NPs, which

is found to induce ROS production by NIR laser irradiation, showing photodynamic effects under laser irradiation and synergistically killing cells [104]. Carbon nanomaterials and their derivatives also have been revealed as PDT agents to produce ROS under irradiation in cancer therapy [105, 106]. PEG-functionalized graphene oxide was as well employed as substrate to load the photosensitizer molecule Chlorin e6, and the product is able to generate singlet oxygen under light excitation and exhibits enhanced PDT efficacy against cancer cells [107]. In addition to the single component structure, hybrid nanostructures consist of different nanocomponents, which provide an effective way to improve PDT cancer therapy [108]. For example, the nanocomposites consisting of $NaYF_4$:Yb/Er upconversion NPs embedded with methylene blue in SiO_2 and conjugated with Au nanorods, and that the integrated structure was confirmed by significantly improving ROS production under NIR irradiation and undergoing efficiency PDT both in vitro and in vivo [109]. The highly toxic ROS damaged the mitochondrial membrane, which could be induced by the cell apoptosis pathway. Note that the photothermal effect coincided with PDT when plasmonic gold NPs are irradiated. Photothermal therapy is an emerging, noninvasive, and effective treatment for cancers; the combination of PDT and PTT has been often designed for a higher efficiency of cancer therapy [110–112].

Without the assistance of light, some nanomaterials can catalyze/trigger specific chemical reactions that can generate abundant ROS in the local biological system and subsequently enable to combat cancers. Based on these findings, versatile catalytic chemical reactions (e.g., Fenton reaction) have been developed as a new strategy for cancer therapy [113]. Such therapeutic modality has higher efficacy and selectivity, as well as low side effects on normal tissues. There are reviews to summarize the very recent studies on nanostructures-triggered in situ catalytic reactions for tumor-specific therapy [96, 113]. For example, iron oxide nanoparticles have been demonstrated to mimic the peroxidase activity and activate the generation of hydroxyl radicals in the presence of hydrogen peroxide through Fenton-like reactions [114]. The highly oxidative hydroxyl radicals can be used for killing cancer cells. One case was reported by fabricated FeO_x-loaded mesoporous silica nanoparticles, which can catalyze the decomposition of H_2O_2 to generate ROS in the acidic microenvironment of lysosomes, thus causing cancer cell death [115]. In another example, by integrating Fe_3O_4 NPs and glucose oxidase into biodegradable dendritic silica nanoparticles, a concept of sequential catalytic nanomedicine for efficient tumor therapy was introduced. The authors found that highly toxic hydroxyl radicals are generated through sequential catalytic reactions to trigger the apoptosis and death of tumor cells [100]. The redox enzyme-like activity of nanomaterials could also be deployed for catalytic therapy of cancers. Nitrogen-doped porous carbon nanospheres were employed as nanozymes that catalyzed ROS generation in a tumor-specific manner, resulting in significant tumor regression in human tumor xenograft mice models [98]. A flower-like MnO_2@PtCo nanozyme was also reported to catalyze a cascade of intracellular biochemical reactions to produce ROS in both normoxic and hypoxic conditions without any external stimuli, resulting in remarkable and specific inhibition of tumor growth [116]. With the fast development of chemistry, materials, and nanotechnology, it offers great

opportunity to fabricate superstructures by assembly of different nanocomponents, which would exhibit integrational functions (e.g., PTT, PDT, CRT) for improving cancer therapy.

8.4.2 Antibacteria

When the nanostructures exposed with microbial (e.g. bacterial, fungal and biofilms), the generated ROS could induce the death of microbial. There are two prevalent mechanisms for ROS-facilitated antibacterial applications.

One is based on the enzyme-like activity, in which nanozymes accelerated the production of ROS in the presence of oxygen or hydrogen peroxides to inactivate bacterial growth. A variety of nanomaterials with peroxidase-like characteristic are listed as promising antibacterial agents. For example, a trace amount of iron oxide NPs could trigger the ROS production and completely kill *E. coli* in a low concentration of hydrogen peroxide. In contrast, the control experiment without NPs only shows a 15% antibacterial efficacy, indicating the important role of iron oxide in triggering ROS-killing strategy [117]. Pd-NPs is found to exhibit facet-dependent oxidase and peroxidase-like activities via generation of ROSs, which endow them excellent antibacterial properties against Gram-positive bacteria. The {100}-faceted Pd cubes are reported to own higher activities to kill bacteria more effectively than {111}-faceted Pd octahedrons. However, the antibacterial activity is reversed in Gram-negative bacteria [118]. Pt hollow nanostructures also exhibit high peroxidase-like activity to catalyze the decomposition of H_2O_2 to hydroxyl radicals. It is demonstrated that Pt nanostructures show excellent bactericidal activity against both Gram-negative and Gram-positive bacteria in the presence of low concentrations of H_2O_2 [119]. This antibacterial activity can be applied to treat wound infections.

Photocatalytic inactivation of bacteria is the other mechanism [120]. Upon irradiation, typically the semiconductor nanomaterials could absorb the light and be excited to create a hole or electron pairs. The separated holes in valence band and electrons in conduction band are highly oxidative and reductive, respectively, which was determined by their energy band positions. The highly active hole and electrons can in turn react with surrounding oxygen-containing molecules or ions to generate ROS, the dominant intermediates for killing bacteria. The photocatalytic properties of titanium dioxide are well known and the earliest example for use in disinfection [121]. The photoexcited TiO_2 was capable of killing a wide range of Gram-negative and Gram-positive bacteria, algae, protozoa, filamentous and unicellular fungi, mammalian viruses, and bacteriophage. The killing mechanism involves degradation of the cell wall and cytoplasmic membrane due to the production of ROSs (including hydroxyl radicals, superoxide, and singlet oxygen) caused by the irradiation of TiO_2 [122]. The antibacterial activity could be enhanced by improving the photocatalytic activity through increasing the charge carrier separation efficiency and production of ROS. It was demonstrated that the formation of ZnO/Au hybrid nanostructures could greatly enhance the photocatalytic and antibacterial activity

toward killing *S. aureus* and *E. coli* under sunlight [123]. Using ESR technique, it is found that the deposition of Au and other metal NPs resulted in a dramatic increase in light-induced generation of ROSs and production of holes and electrons. It has unraveled the important roles of metal type, particle size, and compositions on antibacterial activity of ZnO NPs [124]. Photocatalytic inactivation of bacteria has been one of hot research directions in nanomaterials because of its high antibacterial efficacy and cost-effectiveness. Since 2010, there are more than 2700 research papers found in Web of Science ("photocatalytic + antibacterial"), and more than 100 kinds of nanostructures were tested for their ability to kill bacteria in these studies. Many pathogenic pathogens develop anti-resistance nanomaterials, and the most common of which is for bacteria. The drug resistance of bacteria is a big problem that threatens human health. Owning to the different antibacterial mechanism from conventional antibiotics, the nanomaterials that kill the bacteria through triggering the production of highly toxic ROS may provide the best solution to bacterial resistance.

8.4.3 Prevention of ROS-Related Diseases

Neurodegenerative diseases, include Huntington's disease, Parkinson's disease, Alzheimer's disease, and amyotrophic lateral sclerosis, are a heterogeneous group of disorders, which can be characterized by the progressive degeneration of the structure and function of the central nervous system or peripheral nervous system. As chemically reactive molecules, ROSs have been implicated in the pathogenesis of neurodegenerative diseases. Although ROS may not be the immediate cause for neurodegenerative diseases, many evidences suggest that they are likely to exacerbate disease progression through oxidative stress-related processes [125, 126]. Therefore, the regulation of ROS levels may represent a promising treatment option to slow down neurodegeneration and alleviate associated symptoms. It was reported that Mn_3O_4 nanoparticle owns multi-enzyme-like activities, such as glutathione peroxidase, SOD, and CAT. Based on the ROS scavenging activity, Mn_3O_4 NPs exhibit an active role in protecting the cells from 1-methyl-4-phenylpyridinium (MPP+) induced cytotoxicity in a Parkinson disease-like cellular model, suggestive of a new strategy to rescue the biological structures from oxidative damage and thereby possess therapeutic potential to prevent ROS-mediated neurological disorders [127]. After this pioneered work, CuO NPs were prepared with an average size of ~65 nm and with good biocompatibility and multiple enzyme-like activities, which could inhibit neurotoxicity in a cellular model of Parkinson's disease and rescued the memory loss of mice with Parkinson's disease because of the activity of CuO NPs to eliminate ROS [128]. Recently, trimetallic nanozymes possessing multi-enzyme-mimetic activity for clearance of ROS and reactive nitrogen species (RNS) were reported, which can improve the viability of injured neural cell and significantly improve the survival rate, neuroinflammation, and reference memory of injured mice in vitro and in vivo [129]. Benefited by the intrinsic activity of scavenging

ROS, the potential application of hollow Prussian blue nanoparticles in neuroprotection against ischemic stroke primarily by scavenging ROS and RNS was demonstrated. Prussian blue NPs were also reported to not only attenuate oxidative stress, but also suppress apoptosis and counteract inflammation both in vitro and in vivo. This contributed to increased brain tolerance of ischemic injury with minimal side effects [130]. Ceria NPs have also been demonstrated to protect against ischemic stroke by scavenging ROSs and reducing apoptosis [131]. Apart from these neuro-related diseases, the nanomaterials scavenging ROS have also attempted to protect biomolecules or living body against ROS-induced protein oxidation, lipid peroxidation and DNA damages, and inflammations [8, 132, 133].

8.5 Outlook

With the low cost, easy preparation, good physiological stability, high catalytic efficiency, robust antioxidative activity, and biocompatibility, the ROS-producing and scavenging nanomaterials caught special attention, which may represent a novel class of nanomedicine for the treatment of ROS-related diseases and damages with promoting therapeutic outcomes.

References

1. K. Apel, H. Hirt, Reactive oxygen species: metabolism, oxidative stress, and signal transduction. Annu. Rev. Plant Biol. **55**, 373–399 (2004)
2. B. Halliwell, Reactive species and antioxidants. Redox biology is a fundamental theme of aerobic life. Plant Physiol. **141**(2), 312–322 (2006)
3. S.I. Liochev, Reactive oxygen species and the free radical theory of aging. Free Radic. Biol. Med. **60**, 1–4 (2013)
4. K. Brieger et al., Reactive oxygen species: from health to disease. Swiss Med. Wkly. **142**, w13659 (2012)
5. R. Mittler, ROS are good. Trends Plant Sci. **22**(1), 11–19 (2017)
6. J.G. Scandalios, The rise of ROS. Trends Biochem. Sci. **27**(9), 483–486 (2002)
7. A.D. Anbar, Elements and evolution. Science **322**(5907), 1481–1483 (2008)
8. N. Singh et al., A manganese oxide nanozyme prevents the oxidative damage of biomolecules without affecting the endogenous antioxidant system. Nanoscale **11**(9), 3855–3863 (2019)
9. L.A. Sena, N.S. Chandel, Physiological roles of mitochondrial reactive oxygen species. Mol. Cell **48**(2), 158–167 (2012)
10. M.P. Murphy et al., Unraveling the biological roles of reactive oxygen species. Cell Metab. **13**(4), 361–366 (2011)
11. T. Finkel, Signal transduction by reactive oxygen species. J. Cell Biol. **194**(1), 7–15 (2011)
12. M. Schieber, S. Navdeep, Chandel, ROS function in redox signaling and oxidative stress. Curr. Biol. **24**(10), R453–R462 (2014)
13. J. Zhang et al., ROS and ROS-mediated cellular signaling. Oxidative Med. Cell. Longev. **2016**, 4350965 (2016)
14. W. Dröge, Free radicals in the physiological control of cell function. Physiol. Rev. **82**(1), 47–95 (2002)

15. D.J. Betteridge, What is oxidative stress? Metabolism **49**(2), 3–8 (2000)
16. B.C. Dickinson, C.J. Chang, Chemistry and biology of reactive oxygen species in signaling or stress responses. Nat. Chem. Biol. **7**(8), 504–511 (2011)
17. T. Finkel, N.J. Holbrook, Oxidants, oxidative stress and the biology of ageing. Nature **408**, 239–247 (2000)
18. B. Halliwell, Reactive oxygen species in living systems: source, biochemistry, and role in human disease. Am. J. Med. **91**(3), S14–S22 (1991)
19. A. Baxter, R. Mittler, N. Suzuki, ROS as key players in plant stress signalling. J. Exp. Bot. **65**(5), 1229–1240 (2014)
20. V.J. Thannickal, B.L. Fanburg, Reactive oxygen species in cell signaling. Am. J. Physiol. Lung Cell. Mol. Physiol. **279**(6), L1005–L1028 (2000)
21. A. Glasauer, N.S. Chandel, Ros. Curr. Biol. **23**(3), R100–R102 (2013)
22. J. Foreman et al., Reactive oxygen species produced by NADPH oxidase regulate plant cell growth. Nature **422**(6930), 442–446 (2003)
23. J.D. Lambeth, NOX enzymes and the biology of reactive oxygen. Nat. Rev. Immunol. **4**(3), 181–189 (2004)
24. R. Mittler et al., ROS signaling: the new wave? Trends Plant Sci. **16**(6), 300–309 (2011)
25. B. D'Autréaux, M.B. Toledano, ROS as signalling molecules: mechanisms that generate specificity in ROS homeostasis. Nat. Rev. Mol. Cell Biol. **8**(10), 813–824 (2007)
26. E. Ginter, V. Simko, V. Panakova, Antioxidants in health and disease. Bratislava Med. J. **115**(10), 603–606 (2014)
27. E. Vranová, D. Inzé, V. Breusegem, Signal transduction during oxidative stress. J. Exp. Bot. **53**(372), 1227–1236 (2002)
28. Y.S. Bae et al., Regulation of reactive oxygen species generation in cell signaling. Mol. Cells **32**(6), 491–509 (2011)
29. L.A. Pham-Huy, H. He, C. Pham-Huy, Free radicals, antioxidants in disease and health. Int. J. Biomed. Sci. **4**(2), 89–96 (2008)
30. H. Sies, Strategies of antioxidant defense. Eur. J. Biochem. **215**(2), 213–219 (1993)
31. A.M. Pisoschi, A. Pop, The role of antioxidants in the chemistry of oxidative stress: a review. Eur. J. Med. Chem. **97**, 55–74 (2015)
32. J.M. Matés, Effects of antioxidant enzymes in the molecular control of reactive oxygen species toxicology. Toxicology **153**(1–3), 83–104 (2000)
33. M. Valko et al., Free radicals and antioxidants in normal physiological functions and human disease. Int. J. Biochem. Cell Biol. **39**(1), 44–84 (2007)
34. P.P. Fu et al., Mechanisms of nanotoxicity: generation of reactive oxygen species. J. Food Drug Anal. **22**(1), 64–75 (2014)
35. A. Nel et al., Toxic potential of materials at the nanolevel. Science **311**(5761), 622–627 (2006)
36. F. Vilhardt et al., Microglia antioxidant systems and redox signalling. Br. J. Pharmacol. **174**(12), 1719–1732 (2017)
37. S.F. Thai et al., Differential genomic effects on signaling pathways by two different CeO2 nanoparticles in HepG2 cells. J. Nanosci. Nanotechnol. **15**(12), 9925–9937 (2015)
38. M. Jarosz et al., Antioxidant and anti-inflammatory effects of zinc. Zinc-dependent NF-kappaB signaling. Inflammopharmacology **25**(1), 11–24 (2017)
39. G.S. Kumar et al., Selenium nanoparticles involve HSP-70 and SIRT1 in preventing the progression of type 1 diabetic nephropathy. Chem. Biol. Interact. **223**, 125–133 (2014)
40. C.Y. Meng et al., Resveratrol alleviate the injury of mice liver induced by cadmium sulfide nanoparticles. Kaohsiung J. Med. Sci. **35**(5), 297–302 (2019)
41. M. Mittal et al., Reactive oxygen species in inflammation and tissue injury. Antioxid. Redox Signal. **20**(7), 1126–1167 (2014)
42. X. Sun et al., NOX4- and Nrf2-mediated oxidative stress induced by silver nanoparticles in vascular endothelial cells. J. Appl. Toxicol. **37**(12), 1428–1437 (2017)
43. X. Kong et al., Enhancing Nrf2 pathway by disruption of Keap1 in myeloid leukocytes protects against sepsis. Am. J. Respir. Crit. Care Med. **184**(8), 928–938 (2011)

44. X. Chen et al., Renal interstitial fibrosis induced by high-dose mesoporous silica nanoparticles via the NF-kappaB signaling pathway. Int. J. Nanomedicine **10**, 1–22 (2015)
45. M.M. Kaminski et al., Mitochondria as oxidative signaling organelles in T-cell activation: physiological role and pathological implications. Arch. Immunol. Ther. Exp. **61**(5), 367–384 (2013)
46. N.S. Chandel et al., Role of oxidants in NF-kappa B activation and TNF-alpha gene transcription induced by hypoxia and endotoxin. J. Immunol. **165**(2), 1013–1021 (2000)
47. X. He et al., Single-walled carbon nanotubes induce fibrogenic effect by disturbing mitochondrial oxidative stress and activating NF-kappaB signaling. J. Clin. Toxicol. **S5**(5), (2012). https://doi.org/10.4172/2161-0495.S5-005
48. A. Nemmar et al., Oxidative stress, inflammation, and DNA damage in multiple organs of mice acutely exposed to amorphous silica nanoparticles. Int. J. Nanomedicine **11**, 919–928 (2016)
49. T. Xia et al., Comparison of the mechanism of toxicity of zinc oxide and cerium oxide nanoparticles based on dissolution and oxidative stress properties. ACS Nano **2**(10), 2121–2134 (2008)
50. B. Ebran et al., Radiological evidence of lung involvement in metal fume fever. Rev. Pneumol. Clin. **56**(6), 361–364 (2000)
51. H.A. Jeng, J. Swanson, Toxicity of metal oxide nanoparticles in mammalian cells. J. Environ. Sci. Health A Tox. Hazard. Subst. Environ. Eng. **41**(12), 2699–2711 (2006)
52. X. Han et al., Assessing the relevance of in vitro studies in nanotoxicology by examining correlations between in vitro and in vivo data. Toxicology **297**(1–3), 1–9 (2012)
53. S. Krol, Challenges in drug delivery to the brain: nature is against us. J. Control. Release **164**(2), 145–155 (2012)
54. P. Ganguly, A. Breen, S.C. Pillai, Toxicity of nanomaterials: exposure, pathways, assessment, and recent advances. ACS Biomater Sci. Eng. **4**(7), 2237–2275 (2018)
55. A. Mirshafa et al., Size-dependent neurotoxicity of aluminum oxide particles: a comparison between nano- and micrometer size on the basis of mitochondrial oxidative damage. Biol. Trace Elem. Res. **183**(2), 261–269 (2018)
56. N. Neubauer et al., Size-dependent ROS production by palladium and nickel nanoparticles in cellular and acellular environments—an indication for the catalytic nature of their interactions. Nanotoxicology **9**(8), 1059–1066 (2015)
57. Y.S. Kim et al., Subchronic oral toxicity of silver nanoparticles. Part. Fibre Toxicol. **7**(1), 20 (2010)
58. H.J. Paek et al., Modulation of the pharmacokinetics of zinc oxide nanoparticles and their fates in vivo. Nanoscale **5**(23), 11416–11427 (2013)
59. P.N. Navya, H.K. Daima, Rational engineering of physicochemical properties of nanomaterials for biomedical applications with nanotoxicological perspectives. Nano Converg **3**(1), 1 (2016)
60. A. Platel et al., Influence of the surface charge of PLGA nanoparticles on their in vitro genotoxicity, cytotoxicity, ROS production and endocytosis. J. Appl. Toxicol. **36**(3), 434–444 (2016)
61. D. Hühn et al., Polymer-coated nanoparticles interacting with proteins and cells: focusing on the sign of the net charge. ACS Nano **7**(4), 3253–3263 (2013)
62. C.A. Simpson et al., In vivo toxicity, biodistribution, and clearance of glutathione-coated gold nanoparticles. Nanomedicine **9**(2), 257–263 (2013)
63. L. Ma-Hock et al., Short term inhalation toxicity of a liquid aerosol of CdS/Cd(OH)(2) core shell quantum dots in male Wistar rats. Toxicol. Lett. **208**(2), 115–124 (2012)
64. H. Guo et al., Intravenous administration of silver nanoparticles causes organ toxicity through intracellular ROS-related loss of inter-endothelial junction. Part. Fibre Toxicol. **13**(1), 21 (2016)
65. T. Wen et al., Comparative study of in vitro effects of different nanoparticles at non-cytotoxic concentration on the adherens junction of human vascular endothelial cells. Int. J. Nanomedicine **14**, 4475–4489 (2019)
66. T. Wen et al., Iron oxide nanoparticles induce reversible endothelial-to-mesenchymal transition in vascular endothelial cells at acutely non-cytotoxic concentrations. Part. Fibre Toxicol. **16**(1), 30 (2019)

67. J.M. Burns et al., Methods for reactive oxygen species (ROS) detection in aqueous environments. Aquat. Sci. **74**(4), 683–734 (2012)
68. G.J. Maghzal et al., Detection of reactive oxygen species derived from the family of NOX NADPH oxidases. Free Radic. Biol. Med. **53**(10), 1903–1918 (2012)
69. J.F. Woolley, J. Stanicka, T.G. Cotter, Recent advances in reactive oxygen species measurement in biological systems. Trends Biochem. Sci. **38**(11), 556–565 (2013)
70. S.I. Dikalov, D.G. Harrison, Methods for detection of mitochondrial and cellular reactive oxygen species. Antioxid. Redox Signal. **20**(2), 372–382 (2014)
71. B.J. Marquis et al., Analytical methods to assess nanoparticle toxicity. Analyst **134**(3), 425–439 (2009)
72. Y. Nosaka, A.Y. Nosaka, Generation and detection of reactive oxygen species in photocatalysis. Chem. Rev. **117**(17), 11302–11336 (2017)
73. M. Kohno, Applications of electron spin resonance spectrometry for reactive oxygen species and reactive nitrogen species research. J. Clin. Biochem. Nutr. **47**(1), 1–11 (2010)
74. C.L. Hawkins, M.J. Davies, Detection and characterisation of radicals in biological materials using EPR methodology. Biochim. Biophys. Acta Gen. Subj. **1840**(2), 708–721 (2014)
75. N. Khan, H. Swartz, Measurements in vivo of parameters pertinent to ROS/RNS using EPR spectroscopy. Mol. Cellular Biochem. **234/235**, 341–357 (2002)
76. F.A. Villamena, J.L. Zweier, Detection of reactive oxygen and nitrogen species by EPR spin trapping. Antioxid. Redox Signal. **6**(3), 619–629 (2004)
77. A. Steffen-Heins, B. Steffens, EPR spectroscopy and its use in planta—a promising technique to disentangle the origin of specific ROS. Front. Environ. Sci. **3**(15), (2015). https://doi.org/10.3389/fenvs.2015.00015
78. S. Suzen, H. Gurer-Orhan, L. Saso, Detection of reactive oxygen and nitrogen species by electron paramagnetic resonance (EPR) technique. Molecules **22**(1) (2017)
79. W. He et al., Electron spin resonance spectroscopy for the study of nanomaterial-mediated generation of reactive oxygen species. J. Food Drug Anal. **22**(1), 49–63 (2014)
80. L. Valgimigli, G.F. Pedulli, M. Paolini, Measurement of oxidative stress by EPR radical-probe technique. Free Radic. Biol. Med. **31**(6), 708–716 (2001)
81. G. Bartosz, Use of spectroscopic probes for detection of reactive oxygen species. Clin. Chim. Acta **368**(1–2), 53–76 (2006)
82. X. Chen et al., Recent progress in the development of fluorescent, luminescent and colorimetric probes for detection of reactive oxygen and nitrogen species. Chem. Soc. Rev. **45**(10), 2976–3016 (2016)
83. A. Gomes, E. Fernandes, J.L.F.C. Lima, Fluorescence probes used for detection of reactive oxygen species. J. Biochem. Biophys. Methods **65**, 45–80 (2005)
84. B.C. Dickinson, D. Srikun, C.J. Chang, Mitochondrial-targeted fluorescent probes for reactive oxygen species. Curr. Opin. Chem. Biol. **14**(1), 50–56 (2010)
85. X. Chen et al., Fluorescent and luminescent probes for detection of reactive oxygen and nitrogen species. Chem. Soc. Rev. **40**, 4783–4804 (2011)
86. W. Adam, D.V. Kazakov, V.P. Kazakov, Singlet-oxygen chemiluminescence in peroxide reactions. Chem. Rev. **105**(9), 3371–3387 (2005)
87. C. Lu, G. Song, J.-M. Lin, Reactive oxygen species and their chemiluminescence-detection methods. TrAC Trends Anal. Chem. **25**(10), 985–995 (2006)
88. S. Yamaguchi et al., Evaluation of chemiluminescence reagents for selective detection of reactive oxygen species. Anal. Chim. Acta **665**, 74–78 (2010)
89. G.M. Ganea et al., Ratiometric coumarin-neutral red (CONER) nanoprobe for detection of hydroxyl radicals. Anal. Chem. **83**(7), 2576–2581 (2011)
90. D.A. Heller et al., Multimodal optical sensing and analyte specificity using single-walled carbon nanotubes. Nat. Nanotechnol. **4**(2), 114–120 (2009)
91. F. Du et al., A targeted and FRET-based ratiometric fluorescent nanoprobe for imaging mitochondrial hydrogen peroxide in living cells. Small **10**(5), 964–972 (2014)
92. F. Bray et al., Global cancer statistics 2018: GLOBOCAN estimates of incidence and mortality worldwide for 36 cancers in 185 countries. CA Cancer J. Clin. **68**(6), 394–424 (2018)

93. W. Fan et al., Nanotechnology for multimodal synergistic cancer therapy. Chem. Rev. **117**, 13566–13638 (2017)
94. S. Kwon et al., Nanomedicines for reactive oxygen species mediated approach: an emerging paradigm for cancer treatment. Acc. Chem. Res. **52**, 1771–1782 (2019)
95. S.S. Lucky, K.C. Soo, Y. Zhang, Nanoparticles in photodynamic therapy. Chem. Rev. **115**, 1990–2042 (2015)
96. H. Lin, Y. Chen, J. Shi, Nanoparticle-triggered in situ catalytic chemical reactions for tumour-specific therapy. Chem. Soc. Rev. **47**, 1938–1958 (2018)
97. M. Huo et al., Tumor-selective catalytic nanomedicine by nanocatalyst delivery. Nat. Commun. **8**(1), 357 (2017)
98. K. Fan et al., In vivo guiding nitrogen-doped carbon nanozyme for tumor catalytic therapy. Nat. Commun. **9**, 1440 (2018)
99. E. Boisselier, D. Astruc, Gold nanoparticles in nanomedicine: preparations, imaging, diagnostics, therapies and toxicity. Chem. Soc. Rev. **38**(6), 1759–1782 (2009)
100. Z. Xie et al., Biocompatible two-dimensional titanium nanosheets for multimodal imaging-guided cancer theranostics. ACS Appl. Mater. Interfaces **11**(25), 22129–22140 (2019)
101. J. Guo et al., Gold nanoparticles enlighten the future of cancer theranostics. Int. J. Nanomedicine **12**, 6131–6152 (2017)
102. W.-S. Kuo et al., Gold nanorods in photodynamic therapy, as hyperthermia agents, and in near-infrared optical imaging. Angew. Chem. Int. Ed. **49**(15), 2711–2715 (2010)
103. V.G. Deepagan et al., Long-circulating Au-TiO2 nanocomposite as a sonosensitizer for ROS-mediated eradication of cancer. Nano Lett. **16**(10), 6257–6264 (2016)
104. L. Li et al., CuS nanoagents for photodynamic and photothermal therapies: phenomena and possible mechanisms. Photodiagn. Photodyn. Ther. **19**, 5–14 (2017)
105. T.A. Tabish, S. Zhang, P.G. Winyard, Developing the next generation of graphene-based platforms for cancer therapeutics: the potential role of reactive oxygen species. Redox Biol. **15**, 34–40 (2018)
106. J. Ge et al., A graphene quantum dot photodynamic therapy agent with high singlet oxygen generation. Nat. Commun. **5**(1), 4596 (2014)
107. B. Tian et al., Photothermally enhanced photodynamic therapy delivered by nano-graphene oxide. ACS Nano **5**(9), 7000–7009 (2011)
108. J. Zeng et al., Porphyrin derivative conjugated with gold nanoparticles for dual-modality photodynamic and photothermal therapies in vitro. ACS Biomater. Sci. Eng. **4**(3), 963–972 (2018)
109. C.W. Chen et al., Plasmon-enhanced photodynamic cancer therapy by upconversion nanoparticles conjugated with Au nanorods. ACS Appl. Mater. Interfaces **8**(47), 32108–32119 (2016)
110. S.-H. Hu et al., Quantum-dot-tagged reduced graphene oxide nanocomposites for bright fluorescence bioimaging and photothermal therapy monitored in situ. Adv. Mater. **24**(13), 1748–1754 (2012)
111. Q. Wu et al., Reduced graphene oxide conjugated with CuInS2/ZnS nanocrystals with low toxicity for enhanced photothermal and photodynamic cancer therapies. Carbon **108**, 21–37 (2016)
112. H.T. Nguyen et al., Incorporation of chemotherapeutic agent and photosensitizer in a low temperature-sensitive liposome for effective chemo-hyperthermic anticancer activity. Expert Opin. Drug Deliv. **14**(2), 155–164 (2016)
113. H. Ranji-Burachaloo et al., Cancer treatment through nanoparticle-facilitated Fenton reaction. ACS Nano **12**(12), 11819–11837 (2018)
114. L. Gao, K. Fan, X. Yan, Iron oxide nanozyme: a multifunctional enzyme mimetic for biomedical applications. Theranostics **7**(13), 3207–3227 (2017)
115. J. Fu et al., Lysosome-controlled efficient ROS overproduction against cancer cells with a high pH-responsive catalytic nanosystem. Nanoscale **7**(16), 7275–7283 (2015)
116. Z. Wang et al., Biomimetic nanoflowers by self-assembly of nanozymes to induce intracellular oxidative damage against hypoxic tumors. Nat. Commun. **9**(1), 3334 (2018)

117. D. Zhang et al., Anti-bacterial and in vivo tumor treatment by reactive oxygen species generated by magnetic nanoparticles. J. Mater. Chem. **1**(38), 5100–5107 (2013)
118. G. Fang et al., Differential Pd-nanocrystal facets demonstrate distinct antibacterial activity against Gram-positive and Gram-negative bacteria. Nat. Commun. **9**(1), 129 (2018)
119. C. Ge et al., Synthesis of Pt hollow nanodendrites with enhanced peroxidase-like activity against bacterial infections: implication for wound healing. Adv. Funct. Mater. **28**(28), 1801484 (2018)
120. S. Rtimi et al., Advances in catalytic/photocatalytic bacterial inactivation by nano Ag and Cu coated surfaces and medical devices. Appl. Catal. B Environ. **240**, 291–318 (2019)
121. M.N. Chong et al., Recent developments in photocatalytic water treatment technology: a review. Water Res. **44**(10), 2997–3027 (2010)
122. H.A. Foster et al., Photocatalytic disinfection using titanium dioxide: spectrum and mechanism of antimicrobial activity. Appl. Microbiol. Biotechnol. **90**(6), 1847–1868 (2011)
123. W. He et al., Photogenerated charge carriers and reactive oxygen species in ZnO/Au hybrid nanostructures with enhanced photocatalytic and antibacterial activity. J. Am. Chem. Soc. **136**(2), 750–757 (2014)
124. X. Jiang et al., Light-induced assembly of metal nanoparticles on ZnO enhances the generation of charge carriers, reactive oxygen species, and antibacterial activity. J. Phys. Chem. C **122**(51), 29414–29425 (2018)
125. M.T. Lin, M.F. Beal, Mitochondrial dysfunction and oxidative stress in neurodegenerative diseases. Nature **443**, 787–795 (2006)
126. Z. Liu et al., Oxidative stress in neurodegenerative diseases: from molecular mechanisms to clinical applications. Oxidative Med. Cell. Longev. **2017**, 2525967 (2017)
127. N. Singh et al., A redox modulatory Mn3O4 nanozyme with multi-enzyme activity provides efficient cytoprotection to human cells in a Parkinson's disease model. Angew. Chem. Int. Ed. **56**(45), 14267–14271 (2017)
128. C. Hao et al., Chiral molecule-mediated porous Cu_xO nanoparticle clusters with antioxidation activity for ameliorating Parkinson's disease. J. Am. Chem. Soc. **141**(2), 1091–1099 (2019)
129. X. Mu et al., Redox trimetallic nanozyme with neutral environment preference for brain injury. ACS Nano **13**(2), 1870–1884 (2019)
130. K. Zhang et al., Hollow prussian blue nanozymes drive neuroprotection against ischemic stroke via attenuating oxidative stress, counteracting inflammation, and suppressing cell apoptosis. Nano Lett. **19**(5), 2812–2823 (2019)
131. C.K. Kim et al., Ceria nanoparticles that can protect against ischemic stroke. Angew. Chem. Int. Ed. Engl. **51**(44), 11039–11043 (2012)
132. J. Yao et al., ROS scavenging Mn_3O_4 nanozymes for in vivo anti-inflammation. Chem. Sci. **9**(11), 2927–2933 (2018)
133. H. Wu, N. Tito, J.P. Giraldo, Anionic cerium oxide nanoparticles protect plant photosynthesis from abiotic stress by scavenging reactive oxygen species. ACS Nano **11**(11), 11283–11297 (2017)

Chapter 9
Protein Corona of Nanoparticles and Its Application in Drug Delivery

Weiqi Zhang

Abstract The nanoparticles (NP) as a drug delivery system have demonstrated tremendous benefits including improved drug solubility, enhanced pharmacodynamics, targeted drug delivery, and potential of theranostics. Understanding of how NP behaves under the biological settings will provide insights to optimize the drug delivery performance. Up to now, large efforts have been focused on unveiling the NP-cell interaction, especially the NP-protein interactions. In biological fluid either *in vitro* or *in vivo*, the adsorption of proteins on NP is inevitable due to the reactive surface of NP. In fact, the NP together with its adsorbed proteins (protein corona) is what the cell really "sees" during drug delivery. For the last decade, the composition, evolution, and biological impact of protein corona on NP have attracted intensive research interests. The protein corona altered the physiochemical identity, cytotoxic profile as well as drug delivery efficiency of NP. Thus, a comprehensive understanding of protein corona will help guide the design and optimization of NP-mediated drug delivery. This chapter will introduce the current progress of protein corona researches and the challenges of modulating protein corona to improve the drug delivery of NP.

Keywords Nanoparticles · Protein corona · Drug delivery · Nanomedicine

9.1 Introduction

With the rapid expansion of nanoparticles (NP) application in drug delivery, various NPs have been fabricated and engineered to realize the controlled release, prolonged circulation, targeted delivery, and improved safety profile [1–3]. The NPs in the field of healthcare nanotechnology are routinely at the scale of several nanometers to 200 nm, or extended to sub-micrometers in some cases [2]. Due to the unique

W. Zhang (✉)
State Key Laboratory of Medical Molecular Biology, Institute of Basic Medical Sciences, Chinese Academy of Medical Sciences and Peking Union Medical College, Beijing, P. R. China
e-mail: zwq@ibms.pumc.edu.cn

H. Xu, N. Gu (eds.), *Nanotechnology in Regenerative Medicine and Drug Delivery Therapy*, https://doi.org/10.1007/978-981-15-5386-8_9

physicochemical properties of the NPs size, surface, and composition, there are multiple interactions between the interface of NP and its contacted environments, e.g., biological buffer, culture medium, and body fluid. One typical phenomenon is the adsorption of biological components such as proteins and lipids onto the NP, which may influence the NP stability, drug release, targeting efficiency, and toxicity [4–6]. In cell culture or upon administration *in vivo*, what the cell encounters is the NP plus its bioactive interface [7]. For the past decade, intensive research efforts have focused on the interactions between NPs and proteins, one of the most abundant components in biological environment [8]. This includes the efforts to probe the protein types adsorbed on the NP, the influence on proteins upon the NP-protein interaction, the toxicity profile of NP and its associated protein layers, and the effects of NP-protein interaction on drug delivery. With the understanding of NP-protein interaction evolving, tuning the NP-protein interaction to benefit drug delivery could be realized. Consequently, a thorough understanding of NP and its interaction with biological cues will be critical to optimize the drug delivery performance and further accelerate its translation towards clinic.

9.2 Overview of Protein Corona

When the NP was introduced into the biological system, there is a rapid adsorption of proteins on the NP surface [9]. Compared with the commonly used NP, the dimension of most proteins is located within several nanometers to few tens of nanometer (Fig. 9.1). Proteins contain different domains and amino acid residues that typically favor its interaction with NPs through multiple noncovalent interactions such as the electrostatic adsorption, hydrogen bonding, hydrophobic interaction, and metal coordination [10, 11]. The adsorption of protein onto the solid surface was well known since the 1962 [12, 13]. The term protein corona was firstly described by K. A. Dawson in 2007, which represents the protein layers that adsorbed on the engineered NPs [14]. Although the following studies revealed that there are other biomolecules such as lipids and cholesterol involved in NP's biological interface because of the complexity of the contacted environments [15, 16], the protein corona is still commonly used instead of "biomolecular corona." Almost all the engineered NPs have demonstrated a protein corona after its contact with the biological milieus. These include the clinically used liposomes [17–19], the hydrophobic nanomaterials [14, 20], the hydrophilic PEGylated NP [21–23], or even the protein NPs itself [24].

Compared with the pristine NP, the protein corona redefined the biological identity of the NP (Fig. 9.2), thus more or less modulating its biological fate or healthcare application both *in vitro* and *in vivo* [26]. The existence of protein corona is universal, while its compositions, dynamics, and biological outcomes varied dramatically according to the NP properties, biological fluids, environmental conditions, and so on [27–30]. The composition of protein corona is largely determined by the protein profile in buffer which the NP is in contact with. Additionally, it is also partly influenced by interaction conditions such as the temperature [31], pH [32], ionic strength [33], and exposure time [34]. There are nearly 300 kinds of

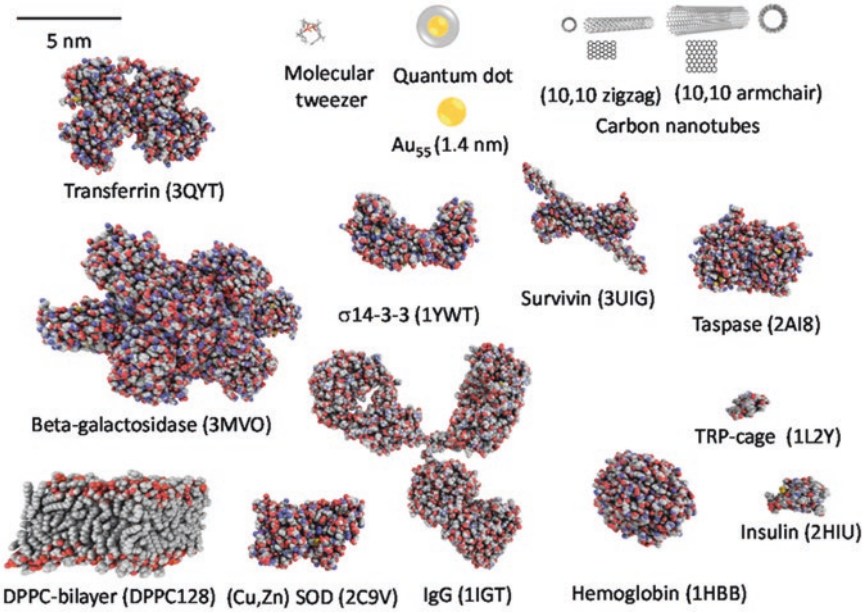

Fig. 9.1 The size of typical proteins in comparison to the phospholipid bilayer and NPs. Reprinted with permission from [25]. Copyright 2017 by American Chemical Society

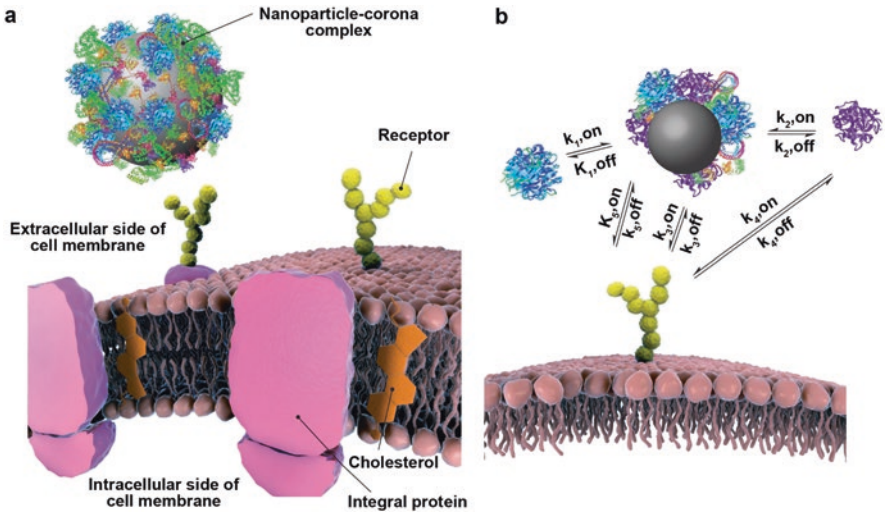

Fig. 9.2 The structure of NP plus protein corona. (**a**) What the cell really "sees" is NP together with its protein corona. (**b**) The protein corona is highly dynamic [26]

proteins present in the protein corona, which could be established in the plasma within 30 s [9]. Abundant proteins in serum or blood, such as albumin, immunoglobins, and complement proteins, are the most common components that were found in different NP's protein corona [9, 29, 35], but the total quantity of proteins and their ratio are varied case by case. The composition of the protein corona evolves following the NP's environment varied such as from extracellular medium to intracellular space *in vitro* and moving from the injection sites to organs *in vivo* [36, 37]. Thus, the fingerprint of protein corona was proposed to be able to map its trafficking in biological system [36]. However, it is still difficult to correlate the protein corona from *in vitro* to the performance *in vivo* due to the complexity of the body fluids and the dynamic property of protein corona.

The interaction of proteins with NP is highly dynamic given the dominating interactions between them are physical interactions, which are reversible [38, 39]. The adsorbed protein could be desorbed, re-adsorbed, and replaced by free proteins in a medium [40], the process of which could be largely influenced by the protein-binding affinity and concentrations. According to the binding strength, the protein corona could be clarified as "hard corona" and "soft corona," respectively [38, 41]. The hard corona corresponds to those proteins tightly bound to NP surface and is relatively stable and consistent with the exposure time elongated as well as the biological environment evolved (Fig. 9.3). The soft corona is loosely bound to NP and experiencing desorption and re-adsorption more frequently. The dynamic features and weak interaction of soft protein corona on NP make it difficult to isolate. It has been reported that the protein corona could be easily disturbed during the commonly used centrifugation [42]. Up to now the differentiation of these two corona portions is still ambiguous. However, it is generally accepted that the hard corona directly interacts with NP, while the soft corona is more likely to interact with hard corona [43]. The organized but dynamic feature of protein corona confers the biological identity to NPs, which differs in varied biological milieu, yet contributing to the NP-cell interactions including cellular uptake [44, 45], NP trafficking [46], and toxicity profile [47], all of which are highly critical in determining the drug delivery outcome.

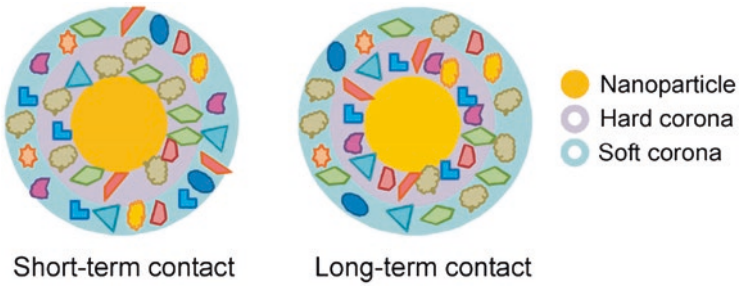

Fig. 9.3 The proposed structure of hard and soft corona. In a long-term contact, the loosely bound proteins could be replaced by proteins with stronger affinity. Reprinted with permission from [48]. Copyright 2020 by American Chemical Society

The formation of protein corona largely determines the NP's cellular uptake. In a simplified model, the protein layer could shield the NP surface including the charges and attached targeting ligand, which were highly correlated to its cellular uptake [49, 50]. In some cases the protein corona also modulate the dispersion status of the NP, which also interfere with the cellular uptake [51–53]. The PEGylation was widely used to reduce the protein absorption on NP, yet it cannot fully block the formation of protein corona [13, 19]. NP of either a charging status could have a protein corona that commonly makes the NP negatively charged [54]. For example, in serum-free medium, the positively charged NP could be easily internalized by the cell due to the electrostatic interaction, since the cell membrane was slightly negative. The adsorption of proteins reversed the NP charge status and subsequently compromised the cellular interaction and its resultant cell uptake [52]. The reduced direct interaction between NP and cell membrane also minimized the cell membrane damage, thus contributing a decreased cytotoxicity. This phenomenon was clearly observed in the case of polyplexes transfection, which has been investigated for decades [55, 56]. In addition, specific protein such as vitronectin in protein corona could mediate a selective uptake of NP by the cells with overexpression of vitronectin receptor [45]. Due to the enzymes present in cellular environment, the protein coronas could also be degraded both outside and inside cells. The protein corona is internalized together with NPs and trafficked to lysosomes in cells, while in this process the hard corona could be kept intact [57]. Several types of NPs were found to induce lysosome permeabilization (LMP), while the formation of protein corona could largely delay the LMP process [58, 59]. Thus the protein corona not only provides a physically buffering zone between NPs, but also functions as biologically capping agents for NP in cells. In the serum or blood *in vivo*, the NPs could be interacting with immune ingredients such as complement, immunoglobulin, and so on, which possibly induce complement activation and immunogenicity, thus affecting the clearance of NPs [40].

9.3 Characterization Techniques for Protein Corona

The characterization of protein corona is critical to help understand the protein corona including the NP status, protein composition, and corona thickness [60, 61]. According to the characterization strategy, the analytic techniques for protein corona could be differentiated to isolation-based methodology, *in situ* measurements, direct imaging, and other characterization routes.

9.3.1 Isolation-Based Methodology

Isolation-based methodology is straightforward and useful to gain in-depth information about protein corona, in which NP plus protein corona was firstly separated and then subjected to various protein analyses. The high-speed centrifugation,

magnetic separation, size exclusion chromatography (SEC), etc. were the mostly used tools to collect the NP and protein corona [60]. After the protein detachment, the protein corona information could be decoded using the routine protein analysis techniques including protein quantification (bicinchoninic acid (BCA) assay, *etc*.) [62], gel electrophoresis (sodium dodecyl sulfate-polyacrylamide gel electrophoresis (SDS-PAGE), two-dimensional gel electrophoresis (2-DE), *etc*.) [44], and proteomics analysis (mass spectrometry (MS), *etc*.) [41]. These strategies could provide a full map of the protein types in the NP corona in a quantitative and qualitative manner. However, the separation process takes time while the protein corona could be formed within half minute [9]. The protein corona separation provided a powerful tool to unveil the information of protein corona, yet each isolation technique may have its own limitations. For example, high-speed centrifugation may interfere with protein corona, while the magnetic separation tool can only be applied on NPs that are responsive to magnetic fields. Recently, asymmetrical flow field-flow fractionation (AF4) was utilized to isolate the NP-protein complex [42], providing a new strategy to preserve both the soft and hard corona during the separation, which may help gain a deeper understanding of the full protein corona. Features of representative characterizations for isolated proteins are listed as below.

- BCA assay: The assay is based on the reduction of Cu^{2+} to Cu^{+} by the peptide bonds in alkaline pH; then the BCA reagent reacts with Cu^{+} to generate colorimetric products with an absorption peak around 562 nm. The BCA assay is highly sensitive, so that it is routinely used to quantify proteins in biochemistry. To analyze the total protein amount, after the formation of protein corona on NP in a serum-containing environment, the protein corona ether isolated or together with its NP was subjected to the BCA assay [30, 39, 63]. This method is facile to compare the protein quantity of corona between different NPs or NP in varied incubation conditions with minimal amount of sample. It should be noted that some NPs might interfere with the BCA reagents or absorption; thus the protein corona is suggested to be isolated first before the BCA assay in this case.
- SDS-PAGE: A commonly used protein electrophoresis with capability to separate the protein based on their molecular weight. During electrophoresis, the SDS denatures the protein and the protein band in the polyacrylamide gel could be simply correlated to the protein with specific molecular weight. Due to the above features, the SDS-PAGE could provide a map of different protein mass (pattern) in a protein corona [64–66]. The protein bands from SDS-PAGE could be further transferred to membranes and subjected to western blot analysis, which is able to verify the specific protein present in protein corona [67]. In addition, the protein band of interest could be cut from gel, recovered, and analyzed further by MS [65]. Generally, other than its own role to characterize protein corona, SDS-PAGE is a flexible platform for further protein analysis.
- 2-DE: It is also named as 2D-PAGE and is designed to separate proteins based on both their isoelectric focusing (IEF) and molecular weight. Specifically, the sample was separated first in one dimension with pH gradient, and then it is separated in the second dimension similar to SDS-PAGE. 2-DE offers more

information about proteins when compared to SDS-PAGE, since it can separate up to 10,000 proteins in a single gel. Consequently, 2-DE is able to provide a 2D map of protein pattern with details in protein corona [68–70] and has been widely used to probe protein-NP interactions.

- MS: Unlike the above techniques, MS is able to confirm the protein identity and has been mostly used to identify the protein composition in the protein corona. The protein sample either desorbed from protein corona or from the gel electrophoresis is digested to fragments. Then the peptide fragments are detected and identified based on their mass-to-charge (m/z) ratio using the matrix-assisted laser desorption/ionization time-of-flight mass spectrometry (MALDI-TOF MS), tandem mass spectrometry (MS/MS), or electrospray ionization mass spectrometry (ESI-MS) [61]. The acquired mass spectra are further decoded based on the established database to obtain the protein information. Other than its role to map protein files in sample, MS also provides quantitative information; thus it is frequently used to characterize protein corona [65, 71, 72].

9.3.2 In Situ *Measurements*

In situ measurements provided a noninvasive way to probe the protein corona information, and thus was also widely used. The in situ measurements mostly relied on the physicochemical signals collected by the equipment, which were further translated to the protein information that interacted with NP. This includes dynamic light scattering (DLS), ultraviolet–visible spectroscopy (UV-Vis), thermogravimetric analysis (TGA), quartz crystal microbalance (QCM), isothermal titration calorimetry (ITC), surface plasmon resonance (SPR), circular dichroism (CD), nuclear magnetic resonance (NMR) spectroscopy, etc. [60]. The *in situ* measurements can provide intact information of protein corona including the hydrodynamic size, surface charges, protein quantification, confirmation, and so on. Additionally, the characterization process could be done in solution and even provide the dynamic information of protein corona. Features of representative in situ analysis are listed as below.

- DLS: This technique measures the hydrodynamic size of NPs based on their scattering light signals [73]. Coating of protein corona on NP alters its size or induces NP agglomeration in some cases. DLS is the most facile technique to monitor the NP size variation upon its interaction with protein [74]. For example, DLS has been used to determine the protein corona thickness [35]. However the related data need to be carefully explained; since the DLS acquires the average size from a population of NP, even a small fraction of NP agglomeration will lead to artifact of NP size increase. Another concern is the inference from the extra protein that is not adsorbed on protein, especially when the NP size is similar or smaller than the protein [61]. When DLS is used to analyze NP, it is highly recommended to combine with other characterizing (e.g., NP imaging) techniques to comprehensively understand the size effects that the protein corona exerted on NP.

- UV-Vis: The absorption spectrum could be adopted to probe the NP-protein interaction in the cases of plasmonic NPs. Because of the ease of synthesis and characterization, plasmonic NPs, e.g., gold NP, have been widely used as an NP model to study the protein corona. Due to the plasmonic features of the noble metal NP, the environmental change of NP surface greatly influences its absorption. The UV-Vis spectroscopy provides a "noninvasive" way to probe the interaction between proteins and NPs. For example, the protein coating induced a redshift of absorption peak of gold and silver NP, while the protein-induced NP aggregation led to a broadened absorption spectrum of gold nanorods [28, 75, 76].
- CD: This spectrum offers an excellent and sensitive method to probe the secondary structure of proteins in solution. In the context of NP-protein interaction, CD is mostly used to verify the conformation change of protein induced by NP adsorption [77–79]. In general, CD is a useful tool to analyze the protein conformation change even in the presence of NP, but it requires relatively more samples and cannot be used for the complex protein mixtures. Consequently, the CD was mostly used in the condition of NP interacting with a single protein type.
- TGA: This technique is typically a thermal analysis technique to determine mass variation following the temperature rising or time elongation. TGA is able to detect the overall mass of proteins adsorbed on the NP [80–82]. Unlike the BCA assay, which determines the relative amount of protein according to the protein standard curve, TGA provides a strategy to directly quantify protein corona.
- QCM: Similar to TGA, this method provides a highly sensitive analysis to determine the protein mass adsorbed on NP based on the frequency variation of a quartz crystal resonator. QCM requires the attachments of NP on the oscillating quartz surface. The adsorption of protein on NP could be reflected by the resonant frequency shift, which is correlated to the mass change. Besides its role to quantify the mass of protein corona [83–85], QCM can also be applied to monitor the real-time interaction between NP and protein.
- ITC: This methodology can characterize the thermodynamic interactions between NP and proteins, providing information of interaction affinity, stoichiometry, and enthalpy change [14, 86, 87]. Specifically, ITC measures the heat generated by the NP-protein interaction with the ambient temperature kept constant; thus it is able to monitor the interaction over time. Similar to QCM it can also provide real-time insights of NP-protein interaction; however it also requires a high concentration of sample.
- SPR: The SPR device detects the binding events of biomolecules based on the refractive index changes close to metal surface. To determine the NP-protein interaction, NP needs to be immobilized on the gold surface of the chip. When the proteins of interests in solution flow across the chip, the NP adsorbs proteins, which can be detected by SPR analysis [88–90]. Consequently, the SPR is also able to provide detail formation during the protein corona formation process.
- NMR spectroscopy: This technology has been widely used in structural biology; thus it can be adopted to probe structural information of adsorbed proteins on NP surface [61, 91]. Besides, NMR spectroscopy has also been demonstrated to reveal the increase of hydrodynamic radius of NP in a complex environment [92].

9.3.3 *Direct Imaging*

The direct imaging of protein corona involving transmission electron microscopy (TEM) (Fig. 9.4), cryo-electron microscopy (Cryo-EM), atomic force microscopy (AFM), and super-resolution microscopy is able to provide the dimensional, mechanical, and dynamic information of NP and its corona [93–97]. Dawson et al. exploited the immunogold labeled anti-transferrin antibody and TEM to image and map the active epitope of transferrin that has been adsorbed on the polystyrene NP, which successfully provided information on how proteins were organized on the NP surface [93]. Unlike the routine TEM for dense materials, the Cryo-EM is suitable for the NP composed of soft materials such as liposomes, which provide another option for decoding the ultrastructure of liposome and its protein corona [95, 98].

Similar to electron microscopy, super-resolution microscopy can image the NP down to tens of nanometers, which is within the scale range of protein. With the rapid development of super-resolution microscopy, it has been used in nanomedicine research more frequently [97, 100–102]. This is ascribed to its advantages to image NP under complex settings such as in solution and in cells, with multicolor labeling and at single particle or molecule level (Fig. 9.5). Albertazzi at al introduced the application of super-resolution microscopy to unveil the protein corona structure at the single particle level [101]. They demonstrated that protein corona adsorption is highly heterogeneous between individual NP. More recently, Caruso et al. employed the common confocal fluorescent microscopy to characterize the NP-protein corona interaction in a microfluid device, which not only mimicked the flowing environment *in vivo* but also combined the benefits of fluorescent imaging and microfluids, enabling the characterization of protein corona evolution *in situ* [96]. Unlike the other analytic methods, which mainly present the protein information from a NP population, the imaging technique could probe the NP corona at a single NP level. However, the aforementioned imaging methods of NP corona either relied on negative staining, immunogold labeling, or fluorescent dye. The AFM could be employed to measure the binding force between proteins and NP without the need of labeling. Therefore, AFM provides another option to probe the structural

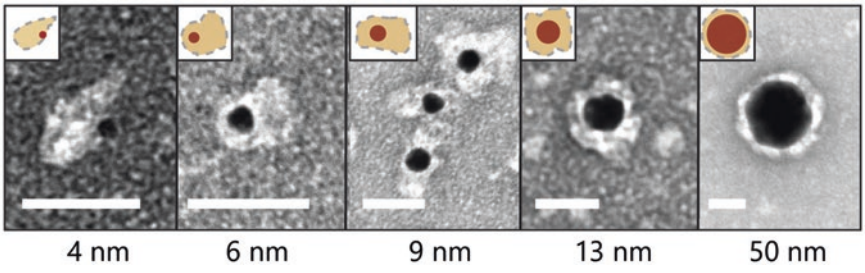

Fig. 9.4 TEM images of the protein corona on gold NPs with different diameters. The NP complexes were negatively stained and scale bars are 25 nm. Reprinted with permission from [99]. Copyright 2019 by Elsevier Ltd

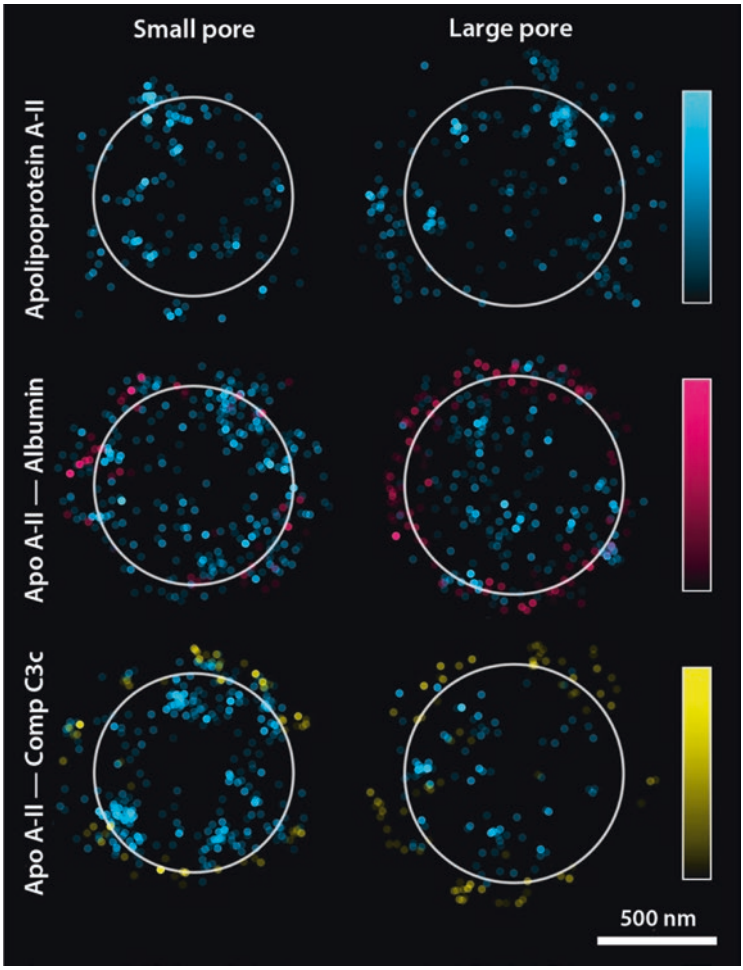

Fig. 9.5 Super-resolution microscopic image of proteins adsorbed by mesoporous silica NPs with different pore sizes. Proteins were prelabeled by different fluorescent tags. Apolipoprotein A-II (green), Albumin (magenta), Complement C3c (yellow). Reprinted with permission from [97]. Copyright 2017 by American Chemical Society

alteration of protein in protein corona [103] and mechanical change of NP after the formation of protein corona [104]. Features of representative imaging techniques are listed as below.

- TEM: As one of the mostly used techniques to characterize NPs, TEM can image NP plus its protein corona [105, 106]. In most cases, protein corona was negatively stained and thus presented with varied contrast from NP due to their different electron density. TEM provides the morphology of NP, shape, and thickness of protein corona. In TEM preparation, the sample was dropped on the grid and dried; thus the TEM image may not reflect the intact NP-protein corona

structure. In general, TEM observation is commonly used along with DLS to confirm the size effects of protein corona given that the influence of protein corona on NP dispersity could be clearly spotted by the TEM [107].

- Cryo-EM: Unlike the routine TEM, Cryo-EM is widely used for structural biology. The Cryo-EM does not need a counterstain, while the sample is imbedded in vitrified water and imaged in a cryogenic temperature. Consequently, Cryo-EM is suitable for visualizing the organic NP (e.g., liposome and micelles) and its protein corona [98, 108, 109].
- AFM: As a type of scanning probe microscopy, AFM acquires images based on scanning the cantilever over the surface of the sample to get the topography information. Simply the NPs with or without protein corona need to deposit on an ultra-flat wafer and then could be visualized using the AFM instrument. On the one hand, the AFM is able to evaluate the NP dispersity, size, and height [33]. On the other hand, it can provide the mechanical information of NP and its protein corona [104]. Unlike the electron microscopy, AFM does not need staining and offers both dimensional and mechanical information of protein corona, making itself a valuable option to characterize NP-protein interaction.
- Super-resolution microscopy: This imaging technique is able to image complex sample based on their fluorescence with a resolution down to nanometers or even at the single molecular level. Based on its principle, super-resolution microscopy could be divided into structured illumination microscopy (SIM), stimulated emission depletion (STED), single-molecule localization microscopy (SMLM), single-molecule control: stochastic optical reconstruction microscopy (STORM), photoactivated localization microscopy (PALM), point accumulation for imaging nanotopography (PAINT), etc. [100]. Both the NP and protein could be fluorescent or fluorescently tagged, which allow tracking the NP-protein interaction over time [97, 101, 110]. In addition, when the involved proteins are labeled by different fluorescence, the NP's interaction with multiple proteins could be realized using super solution microscopy.

9.3.4 Other Techniques

Other techniques include computer simulations, which provide information between NP and proteins from the atomic and molecular view by taking advantage of molecular modeling [111–113]. Using dissipative particle dynamics simulations, Ma et al. found that protein adsorption relies on the NP surface properties as well as the interaction environment, which further influence the cellular uptake [114]. It should be noted that the clues drawn from the simulation present more details of NP-protein interaction; however, experimental confirmation is still preferred to confirm those findings from the modeling. Nandi et al. applied both computer simulation and experimental studies to unveil that the surface decoration of NP is critical for NP-protein interaction. Typically a longer surface ligand is more difficult to adsorb human serum albumin [115]. Hernandez et al. combined the molecular dynamic

simulation and protein footprinting strategy to confirm the critical amino acid residues that mediate the interaction with soft corona using membrane protein cytochrome c, which potentially assists to understand the NP's cytotoxicity [116]. Currently, most computer simulations are studying the NP interacting with a single protein, while the real interaction scenario of NP with proteins in body fluid would be far more complicated.

The above analytical techniques could provide either quantitative or qualitative information of protein corona; however, each single technique is not enough to reflect the whole NP-protein interactions. The protein corona of NP is highly dynamic and complicated; thus multiple techniques were adopted to comprehensively characterize the protein corona, which would shed more light on the composition, structure, and dynamics of protein corona. For example, the SDS-PAGE is used together with MS to determine the protein composition, while the DLS and TEM are used to evaluate the NP dispersity and protein corona thickness. With the advance of new analytical techniques for protein corona and the accumulated research efforts to study NP-protein interactions, a full understanding of protein corona and its biological outcomes could be expected in future.

9.4 Influence of NP on Adsorbed Proteins

The interaction between the NP and proteins could be simply defined as two scenarios according to the dimension of proteins (Fig. 9.6). Considering the NP diameter used in nanomedicine, the protein size could be either larger or smaller than the NPs [25]. When the NP was larger than the proteins, the interaction between them was similar to the protein interacting with a bulk surface. Usually proteins adopt its conformation to favor its interaction with NP, which inevitably induce the structural

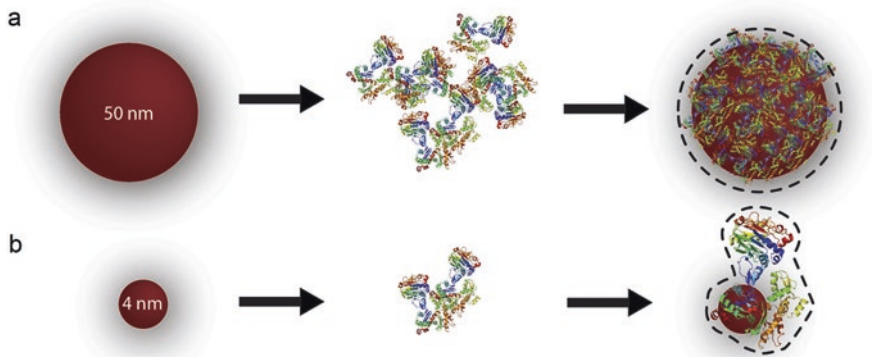

Fig. 9.6 The interaction mode between NPs and proteins. (**a**) The diameter of NP is larger than proteins. (**b**) The diameter of NP is smaller than proteins. Reprinted with permission from [99]. Copyright 2019 by Elsevier Ltd

change of the protein. The conformational change of protein in the corona could be revealed using the CD spectra, and the change could be either reversible or irreversible [117–119]. It was found that the secondary and tertiary structure of BSA underwent a conformational change during its interaction with gold NPs [118]. In the case of the interaction between transferrin and superparamagnetic iron oxide NPs, the mutual interaction induced an irreversible conformation change of the transferrin [119]. In some species of proteins such as amyloid β protein, the conformational change induced by NP further led to the protein fibrillization [120, 121]. The protein conformation change may also expose the epitopes that are originally imbedded inside the protein, which potentially induce unintended bioactivity such as immunogenicity [14, 122]. It is also noticed that the conformational change of protein was less when it is interacting with corona-coated NP compared to those protein directly exposed to pristine NP [123]. The NPs used in drug delivery could be tuned to a few nanometers to achieve a faster clearance *in vivo*. When the NP size was smaller than the proteins, the NP-protein corona scenario could be viewed as NP's adsorption on protein [25, 99]. Representative example is the NP's modulation on enzyme activity. When the NPs blocked the enzyme's active pocket, biological function of the enzyme could be largely disturbed [124]. Besides the NPs size effect on the adsorbed proteins, the NP itself could be inert or reactive in drug delivery. For example, the NPs having a reactive surface such as titanium dioxide (TiO_2) NP can generate reactive oxygen species (ROS), which further oxidizes its protein corona, causing oxidative stress [125]. Generally, the NP plus its protein corona is what the cell really encounters. The protein's change mediated by NP is highly important to determine its resultant biological outcome.

9.5 Influence of Protein Corona on NP

The as-prepared NP was once considered interacting with cells directly before the protein corona was proposed. The reality is the protein could rapidly coat the NP once it was introduced into the biofluid. The influence that the protein corona exerts on NP could be both at the physicochemical and biological levels [46, 126, 127]. Firstly, the protein corona modulates the surface charges of NP and the dispersity. The protein could influence the NP's dispersion, thus modulating NP's interaction with cells both *in vitro* and *in vivo* [128, 129]. For example, in ionic environment, the ions screen the charges of NP and subsequently destabilize the NP. The protein layer on the NPs renders the repulsive forces between NPs, reducing the chance of NP agglomeration [130, 131]. Recently, it is realized the protein concentration also determined the NP's stability [52, 75, 132]. A high concentration of serum proteins leads to a full protein wrapping of polyplexes NP, while less proteins bridge the NP together and cause aggregation (Fig. 9.7). Further, the ratio between protein and NP in the environment was found to control the agglomeration status of the NP [53, 133].

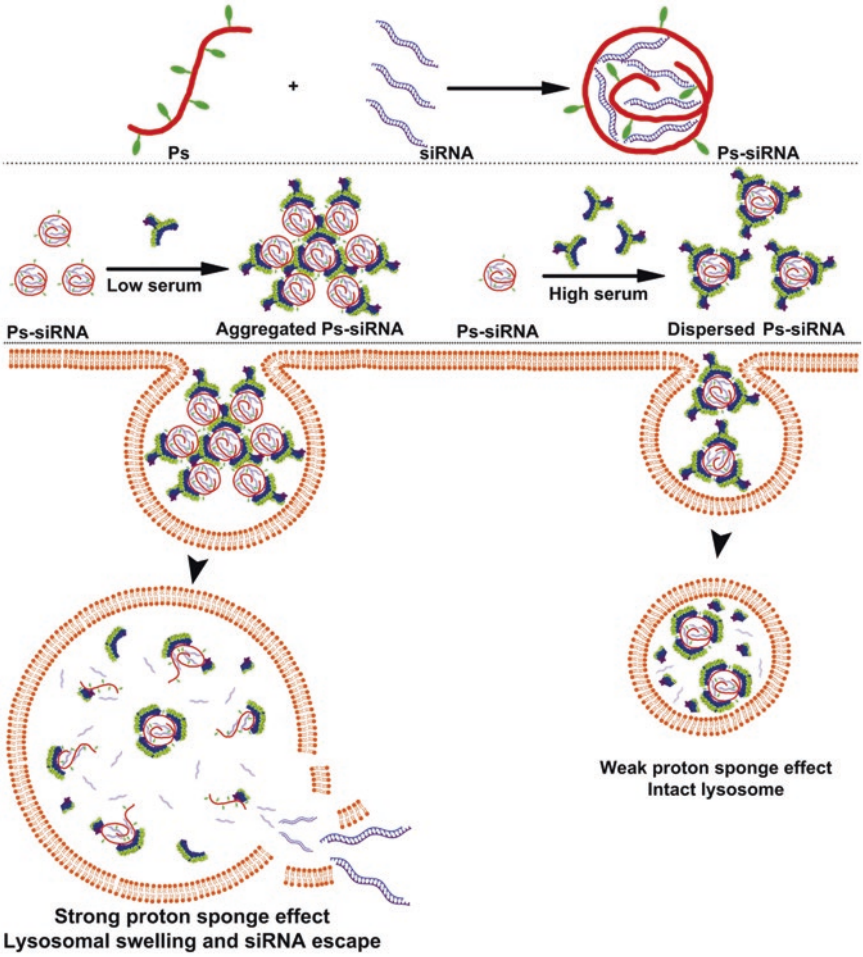

Fig. 9.7 Influence of proteins on NPs size or dispersity. The concentration of serum proteins dictates the NPs size, which led to different uptake and delivery performance (siRNA delivery). *Ps* pullulan-spermine. Readapted with permission from [52]. Copyright 2014 by Elsevier Ltd

The protein corona formation also altered the chemical and biological identity of NP. For example, the TiO_2 NP was shown to oxidize its contacted components such as lipid membranes and subsequently cause cytotoxicity. However, the protein corona adsorption could passivate the surface of TiO_2 NP, alleviating the corresponding lipid peroxidation [102]. Another extraordinary example was the loss of targeting capability of those NP installed with targeting ligands (Fig. 9.8). The coating of protein corona block the accessibility of the ligand, thus compromising the NPs targeting effect in drug delivery [50, 134].

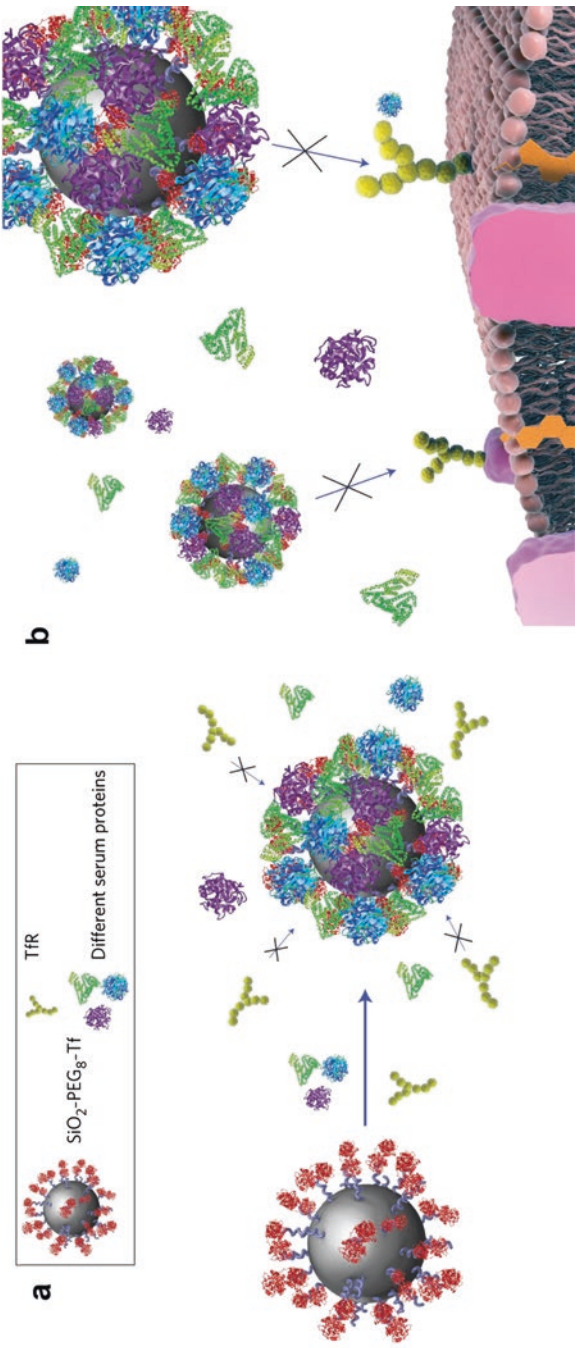

Fig. 9.8 The shielding effect of protein corona on targeted NPs. (**a**) The transferrin (Tf)-installed SiO_2 NP and its protein corona. (**b**) The protein corona blocks the recognition between Tf and its receptor (TfR), which compromises the NP's targeted delivery [50]

9.6 Influence of Protein Corona on Drug Delivery

Compared with the free drug, the NP could provide a controlled/sustained release, prolonged blood circulation, targeting delivery, etc. Before the access to its molecular targets, the drug delivered by the NP needs to overcome different barriers including avoiding the nonspecific interaction with proteins upon its injection, reducing the clearance by reticular epithelial (RES) system, accumulation at the disease site, internalization by the target cells, and avoiding the lysosome trapping [135, 136]; all of these processes could be modulated by the protein corona.

9.6.1 Influence of Protein Corona on Drug Release

As discussed above, the alteration on NP inevitably changes the NP properties, thus resulting in modulated drug delivery performance. The protein corona could also alter the drug release profile of the NP including liposomes [137], micelles [138], silica NP [139], protein NP [24], and polymeric NP [140]. The non-cross-linked micelles lose its integrity as well as drug payloads when it was interacting with lipoproteins [138]. In addition, premature release may exist when the protein replaced the drug that was loaded in the NP. Conversely, delayed drug release could happen after the formation of protein corona. Lin et al. reported that the coumarin-6 release from the poly-3-hydroxybutyrate-co-3-hydroxyhexanoate NP was significantly slowed because the BSA protein corona stabilized the NP [141]. In the case of mesoporous silica NP, it was found that the drug release from the NP was delayed due to the blockage of the NP pore by the protein corona. The increased drug release was also spotted for PEGylated NP, which was ascribed to the PEG's function to reduce the protein corona content [139, 142]. Mahmoudi et al. further revealed that the effect of protein corona on the NPs drug release behavior was largely dependent on the NP-protein interaction as well as NP type [24]. Since the dynamic property of protein corona in the biological system, the influence of protein corona on drug release from NP could also be varied following the enzyme degradation of protein corona [143].

9.6.2 Influence of Protein Corona on Targeted Delivery

The size played a pivotal role in drug delivery, especially the blood retention time and accumulation at the disease sites. For example, a large amount of NPs used in cancer drug delivery are based on the size effect, which is the perquisite for the enhanced permeation and retention (EPR) effect, namely the negative targeting strategy [144]. When the NP stability was disturbed, the NP either in the status of aggregation or broken component would lead to size variance and consequently an

altered blood retention, organ distribution, and clearance [46, 145]. Interestingly, Ferrari et al. found that serum incubation shrank the liposomes [146], suggesting another possibility that protein adsorption would influence liposome's drug delivery. As mentioned above, the layer of the protein corona may also block the targeting ligand that displayed on the NP surface, thus leading to a compromised targeting effect, which further hampers targeted drug delivery [50, 134].

9.6.3 Influence of Protein Corona on Intracellular Delivery

Accumulated evidences suggested that the NP and protein corona were concurrently internalized by the cells and trafficked to endo-lysosome [57–59, 147]. Dawson et al. reported that part of protein corona-like albumin and transferrin could be degraded in lysosomes following the lysosome trafficking of NP plus its corona [57]. This process may help the drug release process when the drug is carried in the protein corona. However, the lysosomal escape of the drug is another key factor for a successful drug delivery. The pH in lysosomes is acidic and there are more than 50 enzymes located in lysosomes, which inevitably compromise the drug efficiency especially the protein and nucleic acid drugs. In addition, trapping of NP and drug in lysosomes dramatically hampers the drug to access its therapeutic targets, since most of the drug's targets are located out of lysosomes [148–150]. One typical example of drug delivery that requires lysosomal escape is the gene (siRNA) transfection. In the case of siRNA delivery, siRNA needs to bind the RNA-induced silencing complex (RISC), which is located in the cytoplasm. Thus, an effective lysosome destabilization and siRNA escape is critical for an efficient RNAi effect mediated by NP. Recently, it was found that protein adsorption compromised or delayed the lysosome disruption of the cationic NPs [52, 59]. This may partly explain why the gene transfection efficiency of cationic NP was compromised in the presence of serum proteins. Besides above influence of protein corona on lysosomes for drug delivery, the protein corona was also reported to increase the labeling of stem cells for magnetic resonance (MR) imaging [151]. This is ascribed to increased NP's uptake and location in lysosomes with the assistance of protein corona. Undoubtedly a better understanding of the protein corona and its effect on intracellular drug delivery will help improve the design of NP for drug delivery.

9.6.4 Influence of Protein Corona on NP Toxicity

One critical parameter for a successful drug delivery of NP is its safety profile. The protein corona has been widely known for its role in modulating NP's cytotoxicity [6, 47]. In serum-free conditions, the pristine NP could interact with cell membrane directly as well as enter the cell efficiently, all of which potentially lead to enhanced cell stress and cytotoxicity [44, 152]. The formation of protein corona was reported

to reduce the nonspecific interaction between cells and NP [153]. Stauber et al. found that the bare silica NP could induce hemolytic effect, while the formation of protein corona significantly protects the red blood cell from membrane damage [9]. The layer of protein corona can also inhibit the dissolution of the NP components such as ions in the case of metal NP [154], which will reduce the toxicity inherent to the metal ions. Chen et al. reported that coating the zinc oxide NP inhibited the dissolution of zinc ion and thus contributed to reduced toxicity [155]. Last but most importantly, protein corona can relieve the ROS and cell stress that are associated with NP [102, 156], thus mitigating the NP's toxicity. For example, Vizcaya-Ruiz et al. revealed that the Fe_3O_4-PEG NP was able to induce the ROS generation and mitochondrial damage, while this side effect could be alleviated with the presence of protein corona [157]. Different from its protection role, the protein corona of NP may also mediate enhanced side effects. Xu et al. reported that the protein-induced aggregation of polyplexes NP would deposit on the cell surface, which led to severe membrane damage and associated cell death [52]. In another case, the conformational change of the protein induced by the NP may expose the originally imbedded epitopes, which may mediate unexpected immune effects such as immunogenicity and complement activation [47]. When the C1q protein was adsorbed on the hydroxyapatite NP, it could mediate the complement activation in a classical pathway, suggesting this uncontrolled complement activation may lead to immunotoxicity [158]. Generally, the altered cytotoxic profile of NP plus its protein corona could be varied case by case; thus it is critical to document the biocompatibility of NP itself when used in drug delivery.

9.7 Exploring the Protein Corona for Drug Delivery

9.7.1 Exploiting Protein Corona to Load Drugs

A full understanding of the protein corona undoubtedly will help optimize the NP-mediated drug delivery by tuning the protein corona. Actually the straightforward application is using the NP to deliver the therapeutics, e.g., proteins, DNA oligonucleotides, and drugs [159, 160]. The protein corona around the NP creates a local environment that could entrap the payloads through noncovalent interactions. Kah et al. utilized the protein corona around gold nanorods to load the hydrophobic chlorin e6 (Ce6) whose excitation matches the longitudinal surface plasmon resonance absorption of gold nanorods; thus a combination of photodynamic and photothermal therapies could be attained with one single excitation laser [161–163]. Hamad-Schifferli et al. successfully exploited the protein corona to load both negatively charged DNA and positively charged doxorubicin [164]. Further it has been suggested that tuning the ratio of serum albumin in protein corona could adjust the release behavior of the payload from the NP [165]. This work suggested that manipulating the protein corona potentially provides another option to control the drug release from NP rather than focusing on NP engineering.

9.7.2 Direct Modulation of Protein Corona to Improve Drug Delivery

Given that NP-protein corona is interacting with cells, directly modulating protein corona could be an ideal option to optimize drug delivery including drug circulation, cellular uptake, and targeting effect. The representative example is PEGylation of NP to reduce the protein adsorption and cellular uptake [23, 166]. Wurm et al. found that the stealth effect of PEGylation was actually mediated by the clusterin proteins in hard corona, which reduced the uptake by macrophages [23]. Pre-coating of the NP could be another strategy to tune the protein corona composition, thus enabling the NP for targeted delivery [159, 167]. Lin et al. revealed that a precoated albumin protein corona could reduce the adsorption of other serum proteins, increasing the blood circulation time as well as improving the biocompatibility of the polymeric NPs [168]. Furthermore, a pre-coating of liposome with plasma proteins significantly reduced the clearance by circulating leukocytes, which contributed to a prolonged circulation time [169]. Mailänder et al. revealed that the intentional pre-modification of NP with apolipoproteins ApoA4 or ApoC3 attenuated its cellular uptake, while pre-coating with ApoH enhanced the cellular uptake [170]. Similarly, installing the lipid NP with apolipoprotein E4 has been utilized to form a protein corona for brain targeting (Fig. 9.9) [171]. Pre-coating the NP with immunoglobulin-depleted plasma could reduce the internalization by the macrophages, suggesting a potential strategy to tune the NP-cell interaction by tailoring the protein corona composition [172]. More recently, Ma et al. revealed that precoating NP with ApoE inhibited the NP's uptake by macrophages, contributing to a prolonged blood circulation [113]. Conversely, the depletion of glycan from the protein corona formed on silica NP increased the NP-cell interaction and the resultant cellular uptake, which pointed out that the protein modification in the protein corona also played an important role to affect the NP-cell interaction and presumably the drug delivery [173]. Consequently, directly adjusting the composition of protein corona may also contribute to the drug's entry into cells, as most of drug-loaded NP uptake was modulated.

9.7.3 Engineering NP to Tune Protein Corona for Drug Delivery

Other than directly manipulating the protein corona, NP could be engineered to influence the protein corona [66, 113], which would also benefit the drug delivery application. Consolidating the NP will lead to a stable NP for drug delivery even with the influence exerted by the protein adsorption. Li et al. found that the non-cross-linked micelles lost their integrity and released the encapsulated drugs upon the interaction with serum proteins, while the disulfide cross-linked NP retained the original structure and thus prevented the premature release of the payloads [138].

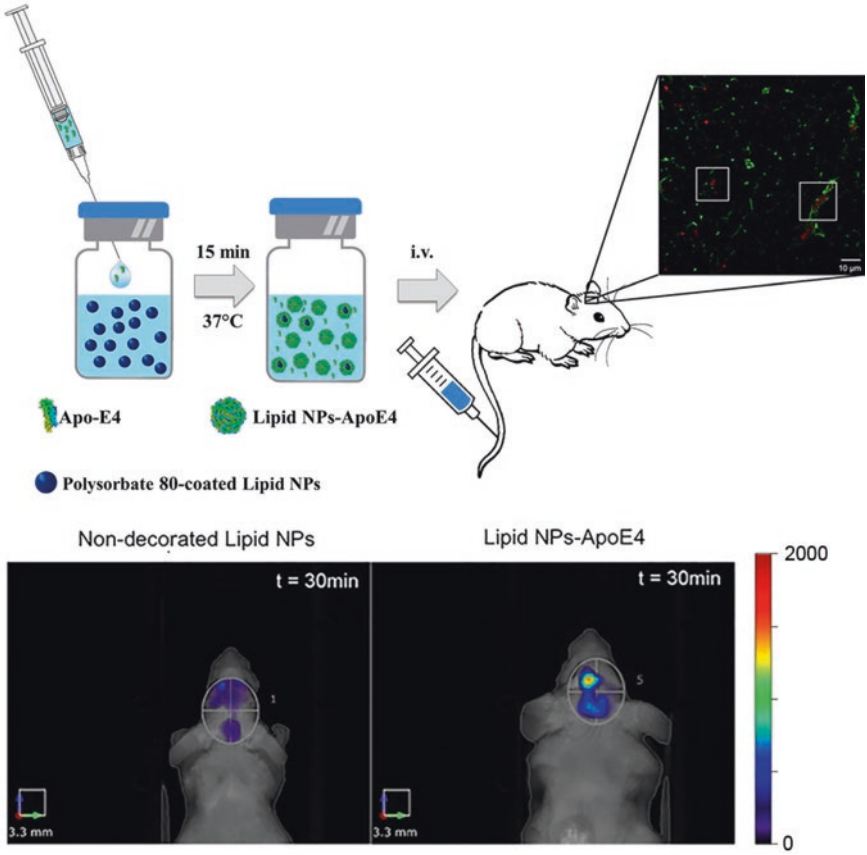

Fig. 9.9 Pre-formed protein corona improves the targeted delivery of NP. Apolipoprotein E4 (Apo-E4) adsorption on lipid NP improved the brain delivery efficiency due to the targeting effect of Apo-E4. Readapted with permission from [171]. Copyright 2018 by Elsevier Ltd

As mentioned above, surface decoration of PEG could reduce the NP's nonspecific interaction with serum component [174], thus avoiding clearance by RES system, modulating the biodistribution, and increasing the blood circulation time. Other than this application, Chan et al. found that backfilling the surface of targeted NP with PEG could significantly restored the targeting capability that was originally masked by the protein corona [22]. In addition to PEG installation, other stealth coating strategies were also proposed to modify the protein corona, thus tuning the NP's cellular uptake and its resultant drug delivery. Poly(phosphoester)-surfactant has been used to functionalize NP in a noncovalent fashion, which reduced the non-specific protein adsorption as well as the cellular uptake [66]. A combination of stealth NP and a carbohydrate targeting ligand has been proposed to overcome the blocking effect caused by protein corona [175]. Similarly the modification of both

zwitterionic and targeting ligand on the silica NP helps overcome the blocking effect from the protein corona [176]. Dong et al. labeled the polyetherimine NP with retinol, which recruited retinol binding protein 4 to NP's corona and consequently mediated a targeting delivery of antisense oligonucleotides to the hepatic stellate cells [177]. More recently, the liposome was engineered with a peptide capable of interacting with the apolipoproteins [178], which could cross the blood-brain barrier. This engineering strategy allowed the liposome to form protein corona composed of apolipoproteins *in vivo*, thus facilitating the brain targeting. The control of protein corona formation could also be realized using a NP functionalization based on host-guest interaction. Liz-Marzán et al. demonstrated a construction of gold NP with anionic dye ligand, which could be specifically recognized by a positively charged macromolecular cage through host-guest interaction [179]. The protein corona formed on NP could be disrupted by adding the macromolecular cage, while the corona could be re-formed with addition of free anionic dye, thus providing a reversible strategy to control protein corona formation as well as its associated cellular uptake. The orientation of the proteins in protein corona or the conjugated targeting protein on the NP was random, which may also compromise the targeting efficiency. Directly controlling the orientation of the targeting ligand on NP could be another strategy to improve the targeting effect of NP [4].

9.8 Challenges and Opportunities of Protein Corona in Drug Delivery

There are a huge amount of NPs that are used in drug delivery researches, while the contact of NP with proteins is unavoidable. Theoretically, the protein corona will be different when the administration route of NP was varied. The difference could be derived from the distinctive protein composition in the local environment [27]. The protein corona could be established within a few tens of seconds and meanwhile the protein quantity that the NP contacts with upon injection could be different, such as subcutaneous and intravenous injection. The NP-protein corona may also be affected due to the variation of local protein quantity. In the *in vivo* application, tremendous complexity of serum components exists and the NP is trafficked in a dynamic environment (Fig. 9.10), which are far complicated from the static culture conditions in which only single protein or part of serum is supplemented [104]. The protein corona formed under a dynamic flow that mimic the condition *in vivo* suggested a distinctive protein corona profile in comparison to those formed in static incubation [96, 166, 180, 181], and this may represent a NP-protein interaction scenario that is more realistic.

Although multiple analytic techniques could be used to characterize the protein corona both *ex situ* and *in situ*, the clear time-spatial resolution of protein corona and its interaction with cells is still lacking. In addition, most of the analytic methods mainly give average information of protein corona that is derived from a

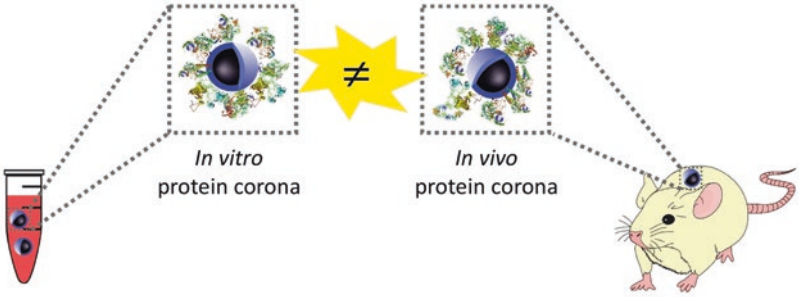

In vitro protein corona	*In vivo* protein corona
• Comprises the same amount of protein as *in vivo* corona	• Comprises a wider variety of biomolecular species
• Does not have a role in fasting, diet body tempeature, etc.	• Has a role as a fasting, diet, body temperature, etc.
• Does not have a role in personlized corona	• Has a role as a personalized corona
• Cannot mimic the dynamic and fluidic variations protein as *in vivo* corona	• Effects of dynamic and fluidic variations are considered

Fig. 9.10 Comparison of protein corona formed *in vitro* and in *vivo*, respectively. Reprinted with permission from [182]. Copyright 2017 by Elsevier Ltd

population of NP, while new reports reveal that significant heterogeneity existed in protein corona for the same NP type under a native condition [101, 183]. Super-resolution microscopy provides the opportunity to investigate the NP and protein corona dynamics as well as their trafficking in cells at the single molecular level. With the advances of the characterization techniques, new and accurate understanding of protein corona could be expected.

Up to now, most of the NP corona mechanism studies are based on the model NPs and specific proteins. The simplified interaction model largely favors the characterization process and undoubtedly provides insights into the physiology of protein corona, but it is still challenging to predict its behavior *in vivo* based on the *in vitro* data. Probing the protein corona with clinic-related NPs may provide more information about its therapeutic outcomes and thus may help develop new drug delivery NPs. Last but most importantly, since the physiochemical properties of NP, the reaction conditions including the temperature and serum conditions, all influence the protein corona [184–186], discrepancy between different researches still exists. Recently, administration methods of NP into the culture medium were found to associate with the NP-cell interaction, e.g., cellular uptake [187]. The initial formation of protein corona on NP could be influenced by how the NP immediately contacted the proteins in the medium. The standardization of NP, clear declaration of the reaction information, and careful data analysis are highly recommended in publications [188], which definitely will advance this field.

9.9 Conclusions

Since the term protein corona was introduced into the nanotechnology community over 10 years ago, there have been tremendous advances to understand the NP's protein corona as well as its biomedical applications. These include the efforts to elucidate its composition, formation dynamics, NP interaction, biological outcome, healthcare application, etc. Generally, the protein corona reflects a group of components around NP, presents a dynamic feature, and elicits distinctive biological effects that are both defined by NP and its environment. Nevertheless, protein corona is prevalent for almost all the NP in biological settings, which further influence the key processes in drug delivery such as drug loading, release behavior, targeting effect, safety profile, and therapeutic efficacy. The evolving understanding of protein corona reminds us to consider both NP and its interacting interface in drug delivery. Directly tuning the protein corona or engineering the NP to modulate the protein corona could be exploited to realize drug loading and improve drug delivery. In future, an in-depth elucidation of protein corona physiology is required to optimize NP's drug delivery and advance it towards translational applications.

References

1. G. Bao, S. Mitragotri, S. Tong, Multifunctional nanoparticles for drug delivery and molecular imaging. Annu. Rev. Biomed. Eng. **15**, 253–282 (2013)
2. P. Couvreur, Nanoparticles in drug delivery: past, present and future. Adv. Drug Deliv. Rev. **65**(1), 21–23 (2013)
3. C.M. Hartshorn et al., Nanotechnology strategies to advance outcomes in clinical cancer care. ACS Nano **12**(1), 24–43 (2017)
4. E. Mahon et al., Designing the nanoparticle–biomolecule interface for "targeting and therapeutic delivery". J. Control. Release **161**(2), 164–174 (2012)
5. J. Wolfram et al., The nano-plasma interface: Implications of the protein corona. Colloids Surf. B Biointerfaces **124**, 17–24 (2014)
6. P.P. Karmali, D. Simberg, Interactions of nanoparticles with plasma proteins: implication on clearance and toxicity of drug delivery systems. Expert Opin. Drug Deliv. **8**(3), 343–357 (2011)
7. D. Walczyk et al., What the cell "sees" in bionanoscience. J. Am. Chem. Soc. **132**(16), 5761–5768 (2010)
8. P.C. Ke et al., A decade of the protein corona. ACS Nano **11**(12), 11773–11776 (2017)
9. S. Tenzer et al., Rapid formation of plasma protein corona critically affects nanoparticle pathophysiology. Nat. Nanotechnol. **8**(10), 772 (2013)
10. L. Wang et al., Revealing the binding structure of the protein corona on gold nanorods using synchrotron radiation-based techniques: understanding the reduced damage in cell membranes. J. Am. Chem. Soc. **135**(46), 17359–17368 (2013)
11. M. Wang et al., Probing the mechanism of plasma protein adsorption on Au and Ag nanoparticles with FT-IR spectroscopy. Nanoscale **7**(37), 15191–15196 (2015)
12. L. Vroman, Effect of adsorbed proteins on the wettability of hydrophilic and hydrophobic solids. Nature **196**(4853), 476–477 (1962)
13. D. Docter et al., The nanoparticle biomolecule corona: lessons learned–challenge accepted? Chem. Soc. Rev. **44**(17), 6094–6121 (2015)

14. T. Cedervall et al., Understanding the nanoparticle–protein corona using methods to quantify exchange rates and affinities of proteins for nanoparticles. Proc. Natl. Acad. Sci. **104**(7), 2050–2055 (2007)
15. E. Hellstrand et al., Complete high-density lipoproteins in nanoparticle corona. FEBS J. **276**(12), 3372–3381 (2009)
16. S.S. Raesch et al., Proteomic and lipidomic analysis of nanoparticle corona upon contact with lung surfactant reveals differences in protein, but not lipid composition. ACS Nano **9**(12), 11872–11885 (2015)
17. G. Caracciolo, Liposome–protein corona in a physiological environment: challenges and opportunities for targeted delivery of nanomedicines. Nanomedicine **11**(3), 543–557 (2015)
18. A. Bigdeli et al., Exploring cellular interactions of liposomes using protein corona fingerprints and physicochemical properties. ACS Nano **10**(3), 3723–3737 (2016)
19. M. Papi et al., Clinically approved PEGylated nanoparticles are covered by a protein corona that boosts the uptake by cancer cells. Nanoscale **9**(29), 10327–10334 (2017)
20. K. Saha, D.F. Moyano, V.M. Rotello, Protein coronas suppress the hemolytic activity of hydrophilic and hydrophobic nanoparticles. Mater. Horiz. **1**(1), 102–105 (2014)
21. R. Gref et al., 'Stealth' corona-core nanoparticles surface modified by polyethylene glycol (PEG): influences of the corona (PEG chain length and surface density) and of the core composition on phagocytic uptake and plasma protein adsorption. Colloids Surf. B Biointerfaces **18**(3-4), 301–313 (2000)
22. Q. Dai, C. Walkey, W.C. Chan, Polyethylene glycol backfilling mitigates the negative impact of the protein corona on nanoparticle cell targeting. Angew. Chem. Int. Ed. Engl. **53**(20), 5093–5096 (2014)
23. S. Schöttler et al., Protein adsorption is required for stealth effect of poly (ethylene glycol)- and poly (phosphoester)-coated nanocarriers. Nat. Nanotechnol. **11**(4), 372 (2016)
24. S. Behzadi et al., Protein corona change the drug release profile of nanocarriers: the "overlooked" factor at the nanobio interface. Colloids Surf. B Biointerfaces **123**, 143–149 (2014)
25. M. Kopp, S. Kollenda, M. Epple, Nanoparticle–protein interactions: therapeutic approaches and supramolecular chemistry. Acc. Chem. Res. **50**(6), 1383–1390 (2017)
26. M.P. Monopoli et al., Biomolecular coronas provide the biological identity of nanosized materials. Nat. Nanotechnol. **7**(12), 779 (2012)
27. D. Docter et al., No king without a crown–impact of the nanomaterial-protein corona on nanobiomedicine. Nanomedicine **10**(3), 503–519 (2015)
28. N.V. Konduru et al., Protein corona: implications for nanoparticle interactions with pulmonary cells. Part. Fibre Toxicol. **14**(1), 42 (2017)
29. S. Tenzer et al., Nanoparticle size is a critical physicochemical determinant of the human blood plasma corona: a comprehensive quantitative proteomic analysis. ACS Nano **5**(9), 7155–7167 (2011)
30. R. García-Álvarez et al., In vivo formation of protein corona on gold nanoparticles. The effect of their size and shape. Nanoscale **10**(3), 1256–1264 (2018)
31. M. Mahmoudi et al., Temperature: the "ignored" factor at the nanobio interface. ACS Nano **7**(8), 6555–6562 (2013)
32. V. Gorshkov et al., Protein corona formed on silver nanoparticles in blood plasma is highly selective and resistant to physicochemical changes of the solution. Environ. Sci. Nano **6**(4), 1089–1098 (2019)
33. X. Liu, C. Yan, K.L. Chen, Adsorption of human serum albumin on graphene oxide: implications for protein corona formation and conformation. Environ. Sci. Technol. **53**(15), 8631–8639 (2018)
34. C. Pisani et al., The timeline of corona formation around silica nanocarriers highlights the role of the protein interactome. Nanoscale **9**(5), 1840–1851 (2017)
35. M.A. Dobrovolskaia et al., Interaction of colloidal gold nanoparticles with human blood: effects on particle size and analysis of plasma protein binding profiles. Nanomedicine **5**(2), 106–117 (2009)

36. M. Lundqvist et al., The evolution of the protein corona around nanoparticles: a test study. ACS Nano **5**(9), 7503–7509 (2011)
37. A. Cox et al., Evolution of nanoparticle protein corona across the blood–brain barrier. ACS Nano **12**(7), 7292–7300 (2018)
38. S. Milani et al., Reversible versus irreversible binding of transferrin to polystyrene nanoparticles: soft and hard corona. ACS Nano **6**(3), 2532–2541 (2012)
39. M. Hadjidemetriou, Z. Al-Ahmady, K. Kostarelos, Time-evolution of in vivo protein corona onto blood-circulating PEGylated liposomal doxorubicin (DOXIL) nanoparticles. Nanoscale **8**(13), 6948–6957 (2016)
40. F. Chen et al., Complement proteins bind to nanoparticle protein corona and undergo dynamic exchange in vivo. Nat. Nanotechnol. **12**(4), 387 (2017)
41. M. Lundqvist et al., Nanoparticle size and surface properties determine the protein corona with possible implications for biological impacts. Proc. Natl. Acad. Sci. **105**(38), 14265–14270 (2008)
42. C. Weber et al., Preservation of the soft protein corona in distinct flow allows identification of weakly bound proteins. Acta Biomater. **76**, 217–224 (2018)
43. M. Hadjidemetriou, K. Kostarelos, Nanomedicine: evolution of the nanoparticle corona. Nat. Nanotechnol. **12**(4), 288 (2017)
44. A. Lesniak et al., Effects of the presence or absence of a protein corona on silica nanoparticle uptake and impact on cells. ACS Nano **6**(7), 5845–5857 (2012)
45. G. Caracciolo et al., Selective targeting capability acquired with a protein corona adsorbed on the surface of 1, 2-dioleoyl-3-trimethylammonium propane/DNA nanoparticles. ACS Appl. Mater. Interfaces **5**(24), 13171–13179 (2013)
46. C. Gunawan et al., Nanoparticle–protein corona complexes govern the biological fates and functions of nanoparticles. J. Mater. Chem. B **2**(15), 2060–2083 (2014)
47. C. Corbo et al., The impact of nanoparticle protein corona on cytotoxicity, immunotoxicity and target drug delivery. Nanomedicine **11**(1), 81–100 (2016)
48. M.N. Gupta, I. Roy, How corona formation impacts nanomaterials as drug carriers. Mol. Pharm. **17**(3), 725–737 (2020)
49. D. Hühn et al., Polymer-coated nanoparticles interacting with proteins and cells: focusing on the sign of the net charge. ACS Nano **7**(4), 3253–3263 (2013)
50. A. Salvati et al., Transferrin-functionalized nanoparticles lose their targeting capabilities when a biomolecule corona adsorbs on the surface. Nat. Nanotechnol. **8**(2), 137 (2013)
51. M. Safi et al., The effects of aggregation and protein corona on the cellular internalization of iron oxide nanoparticles. Biomaterials **32**(35), 9353–9363 (2011)
52. W. Zhang et al., The effect of serum in culture on RNAi efficacy through modulation of polyplexes size. Biomaterials **35**(1), 567–577 (2014)
53. W. Zhang et al., Ratio of polycation and serum is a crucial index for determining the RNAi efficiency of polyplexes. ACS Appl. Mater. Interfaces **9**(50), 43529–43537 (2017)
54. N.P. Mortensen et al., Dynamic development of the protein corona on silica nanoparticles: composition and role in toxicity. Nanoscale **5**(14), 6372–6380 (2013)
55. A. Elouahabi, J.-M. Ruysschaert, Formation and intracellular trafficking of lipoplexes and polyplexes. Mol. Ther. **11**(3), 336–347 (2005)
56. H. Eliyahu et al., Novel dextran–spermine conjugates as transfecting agents: comparing water-soluble and micellar polymers. Gene Ther. **12**(6), 494 (2005)
57. F. Bertoli et al., The intracellular destiny of the protein corona: a study on its cellular internalization and evolution. ACS Nano **10**(11), 10471–10479 (2016)
58. F. Wang et al., Time resolved study of cell death mechanisms induced by amine-modified polystyrene nanoparticles. Nanoscale **5**(22), 10868–10876 (2013)
59. F. Wang et al., The biomolecular corona is retained during nanoparticle uptake and protects the cells from the damage induced by cationic nanoparticles until degraded in the lysosomes. Nanomedicine **9**(8), 1159–1168 (2013)

60. F. Pederzoli et al., Protein corona and nanoparticles: how can we investigate on? Wiley Interdiscip. Rev. Nanomed. Nanobiotechnol. **9**(6), e1467 (2017)
61. C. Carrillo-Carrion, M. Carril, W.J. Parak, Techniques for the experimental investigation of the protein corona. Curr. Opin. Biotechnol. **46**, 106–113 (2017)
62. S.K. Sohaebuddin et al., Nanomaterial cytotoxicity is composition, size, and cell type dependent. Part. Fibre Toxicol. **7**(1), 22 (2010)
63. V. Mirshafiee et al., The importance of selecting a proper biological milieu for protein corona analysis in vitro: human plasma versus human serum. Int. J. Biochem. Cell Biol. **75**, 188–195 (2016)
64. M.P. Monopoli et al., Physical– chemical aspects of protein corona: relevance to in vitro and in vivo biological impacts of nanoparticles. J. Am. Chem. Soc. **133**(8), 2525–2534 (2011)
65. C.D. Walkey et al., Protein corona fingerprinting predicts the cellular interaction of gold and silver nanoparticles. ACS Nano **8**(3), 2439–2455 (2014)
66. J. Müller et al., Coating nanoparticles with tunable surfactants facilitates control over the protein corona. Biomaterials **115**, 1–8 (2017)
67. Z. Wang et al., Specifically formed corona on silica nanoparticles enhances transforming growth factor β1 activity in triggering lung fibrosis. ACS Nano **11**(2), 1659–1672 (2017)
68. N. Ali et al., Analysis of nanoparticle–protein coronas formed in vitro between nanosized welding particles and nasal lavage proteins. Nanotoxicology **10**(2), 226–234 (2016)
69. J. Yu et al., ZnO interactions with biomatrices: effect of particle size on ZnO-protein corona. Nanomaterials **7**(11), 377 (2017)
70. T. Bewersdorff et al., Amphiphilic nanogels: influence of surface hydrophobicity on protein corona, biocompatibility and cellular uptake. Int. J. Nanomedicine **14**, 7861 (2019)
71. M. Magro et al., Analysis of hard protein corona composition on selective iron oxide nanoparticles by MALDI-TOF mass spectrometry: identification and amplification of a hidden mastitis biomarker in milk proteome. Anal. Bioanal. Chem. **410**(12), 2949–2959 (2018)
72. M. Mahmoudi et al., Variation of protein corona composition of gold nanoparticles following plasmonic heating. Nano Lett. **14**(1), 6–12 (2014)
73. S. Bhattacharjee, DLS and zeta potential–what they are and what they are not? J. Control. Release **235**, 337–351 (2016)
74. K. Fischer, M. Schmidt, Pitfalls and novel applications of particle sizing by dynamic light scattering. Biomaterials **98**, 79–91 (2016)
75. W. Zhang et al., Probing the behaviors of gold nanorods in metastatic breast cancer cells based on UV-vis-NIR absorption spectroscopy. PLoS One **7**(2), e31957 (2012)
76. A.P. Ault et al., Protein corona-induced modification of silver nanoparticle aggregation in simulated gastric fluid. Environ. Sci. Nano **3**(6), 1510–1520 (2016)
77. S. Dominguez-Medina et al., Adsorption and unfolding of a single protein triggers nanoparticle aggregation. ACS Nano **10**(2), 2103–2112 (2016)
78. D.T. Jayaram et al., Protein corona in response to flow: effect on protein concentration and structure. Biophys. J. **115**(2), 209–216 (2018)
79. S. Qu et al., In situ investigation on the protein corona formation of quantum dots by using fluorescence resonance energy transfer. Small, 1907633 (2020)
80. A.M. Clemments, P. Botella, C.C. Landry, Protein adsorption from biofluids on silica nanoparticles: corona analysis as a function of particle diameter and porosity. ACS Appl. Mater. Interfaces **7**(39), 21682–21689 (2015)
81. C. Vidaurre-Agut et al., Protein corona over mesoporous silica nanoparticles: influence of the pore diameter on competitive adsorption and application to prostate cancer diagnostics. ACS Omega **4**(5), 8852–8861 (2019)
82. A.M. Clemments et al., Effect of surface properties in protein corona development on mesoporous silica nanoparticles. RSC Adv. **4**(55), 29134–29138 (2014)
83. E.D. Kaufman et al., Probing protein adsorption onto mercaptoundecanoic acid stabilized gold nanoparticles and surfaces by quartz crystal microbalance and ζ-potential measurements. Langmuir **23**(11), 6053–6062 (2007)

84. D. Di Silvio et al., The effect of the protein corona on the interaction between nanoparticles and lipid bilayers. J. Colloid Interface Sci. **504**, 741–750 (2017)
85. S. Lindman et al., Systematic investigation of the thermodynamics of HSA adsorption to N-iso-propylacrylamide/N-tert-butylacrylamide copolymer nanoparticles. Effects of particle size and hydrophobicity. Nano Lett. **7**(4), 914–920 (2007)
86. R. Huang, B.L. Lau, Biomolecule–nanoparticle interactions: elucidation of the thermodynamics by isothermal titration calorimetry. Biochim. Biophys. Acta. Gen. Subj. **1860**(5), 945–956 (2016)
87. S. Winzen et al., Complementary analysis of the hard and soft protein corona: sample preparation critically effects corona composition. Nanoscale **7**(7), 2992–3001 (2015)
88. O.K. Kari et al., Multi-parametric surface plasmon resonance platform for studying liposome-serum interactions and protein corona formation. Drug Deliv. Transl. Res. **7**(2), 228–240 (2017)
89. A. Patra et al., Component-specific analysis of plasma protein corona formation on gold nanoparticles using multiplexed surface plasmon resonance. Small **12**(9), 1174–1182 (2016)
90. J.L. Rogowski et al., A "chemical nose" biosensor for detecting proteins in complex mixtures. Analyst **141**(19), 5627–5636 (2016)
91. M. Assfalg et al., The study of transient protein–nanoparticle interactions by solution NMR spectroscopy. Biochim. Biophys. Acta Proteins Proteomics **1864**(1), 102–114 (2016)
92. M. Carril et al., In situ detection of the protein corona in complex environments. Nat. Commun. **8**(1), 1–5 (2017)
93. P.M. Kelly et al., Mapping protein binding sites on the biomolecular corona of nanoparticles. Nat. Nanotechnol. **10**(5), 472 (2015)
94. M. Kokkinopoulou et al., Visualization of the protein corona: towards a biomolecular understanding of nanoparticle-cell-interactions. Nanoscale **9**(25), 8858–8870 (2017)
95. C. Corbo et al., Effects of the protein corona on liposome–liposome and liposome–cell interactions. Int. J. Nanomedicine **11**, 3049 (2016)
96. A.C. Weiss et al., In situ characterization of protein corona formation on silica microparticles using confocal laser scanning microscopy combined with microfluidics. ACS Appl. Mater. Interfaces **11**(2), 2459–2469 (2019)
97. A.M. Clemments, P. Botella, C.C. Landry, Spatial mapping of protein adsorption on mesoporous silica nanoparticles by stochastic optical reconstruction microscopy. J. Am. Chem. Soc. **139**(11), 3978–3981 (2017)
98. M. Hadjidemetriou et al., In vivo biomolecule corona around blood-circulating, clinically used and antibody-targeted lipid bilayer nanoscale vesicles. ACS Nano **9**(8), 8142–8156 (2015)
99. D. Glancy et al., Characterizing the protein corona of sub-10 nm nanoparticles. J. Control. Release **304**, 102–110 (2019)
100. S. Pujals, L. Albertazzi, Super-resolution microscopy for nanomedicine research. ACS Nano **13**(9), 9707–9712 (2019)
101. N. Feiner-Gracia et al., Super-resolution microscopy unveils dynamic heterogeneities in nanoparticle protein corona. Small **13**(41), 1701631 (2017)
102. S. Runa et al., TiO2 nanoparticle-induced oxidation of the plasma membrane: importance of the protein corona. J. Phys. Chem. B **121**(37), 8619–8625 (2017)
103. J. Schaefer et al., Atomic force microscopy and analytical ultracentrifugation for probing nanomaterial protein interactions. ACS Nano **6**(6), 4603–4614 (2012)
104. C. Corbo et al., Unveiling the in vivo protein corona of circulating leukocyte-like carriers. ACS Nano **11**(3), 3262–3273 (2017)
105. J. Hühn et al., Dissociation coefficients of protein adsorption to nanoparticles as quantitative metrics for description of the protein corona: a comparison of experimental techniques and methodological relevance. Int. J. Biochem. Cell Biol. **75**, 148–161 (2016)
106. T. Miclaus et al., Spatial mapping and quantification of soft and hard protein coronas at silver nanocubes. Nano Lett. **14**(4), 2086–2093 (2014)

107. M. Qin et al., Proteomic analysis of intracellular protein corona of nanoparticles elucidates nano-trafficking network and nano-bio interactions. Theranostics **10**(3), 1213 (2020)
108. O. Koshkina et al., Temperature-triggered protein adsorption on polymer-coated nanoparticles in serum. Langmuir **31**(32), 8873–8881 (2015)
109. F. Mousseau et al., Revealing the pulmonary surfactant corona on silica nanoparticles by cryo-transmission electron microscopy. Nanoscale Adv. (2020). https://doi.org/10.1039/C9NA00779B
110. N. Feiner-Gracia et al., Super-resolution imaging of structure, molecular composition, and stability of single oligonucleotide polyplexes. Nano Lett. **19**(5), 2784–2792 (2019)
111. B. Kharazian, N. Hadipour, M. Ejtehadi, Understanding the nanoparticle–protein corona complexes using computational and experimental methods. Int. J. Biochem. Cell Biol. **75**, 162–174 (2016)
112. D. Dell'Orco et al., Delivery success rate of engineered nanoparticles in the presence of the protein corona: a systems-level screening. Nanomedicine **8**(8), 1271–1281 (2012)
113. X. Lu et al., Tailoring the component of protein corona via simple chemistry. Nat. Commun. **10**(1), 1–14 (2019)
114. H.-M. Ding, Y.-Q. Ma, Computer simulation of the role of protein corona in cellular delivery of nanoparticles. Biomaterials **35**(30), 8703–8710 (2014)
115. S. Khan, A. Gupta, C.K. Nandi, Controlling the fate of protein corona by tuning surface properties of nanoparticles. J. Phys. Chem. Lett. **4**(21), 3747–3752 (2013)
116. E.J. Tollefson et al., Preferential binding of cytochrome c to anionic ligand-coated gold nanoparticles: a complementary computational and experimental approach. ACS Nano **13**(6), 6856–6866 (2019)
117. J. Wang et al., Soft interactions at nanoparticles alter protein function and conformation in a size dependent manner. Nano Lett. **11**(11), 4985–4991 (2011)
118. L. Shang et al., pH-dependent protein conformational changes in albumin: gold nanoparticle bioconjugates: a spectroscopic study. Langmuir **23**(5), 2714–2721 (2007)
119. M. Mahmoudi et al., Irreversible changes in protein conformation due to interaction with superparamagnetic iron oxide nanoparticles. Nanoscale **3**(3), 1127–1138 (2011)
120. C. Cabaleiro-Lago, O. Szczepankiewicz, S. Linse, The effect of nanoparticles on amyloid aggregation depends on the protein stability and intrinsic aggregation rate. Langmuir **28**(3), 1852–1857 (2012)
121. D. Zhang et al., Gold nanoparticles can induce the formation of protein-based aggregates at physiological pH. Nano Lett. **9**(2), 666–671 (2009)
122. A.E. Nel et al., Understanding biophysicochemical interactions at the nano–bio interface. Nat. Mater. **8**(7), 543 (2009)
123. M. Raoufi et al., Probing fibronectin conformation on a protein corona layer around nanoparticles. Nanoscale **10**(3), 1228–1233 (2018)
124. N.O. Fischer et al., Inhibition of chymotrypsin through surface binding using nanoparticle-based receptors. Proc. Natl. Acad. Sci. **99**(8), 5018–5023 (2002)
125. D.T. Jayaram et al., Nanoparticle-induced oxidation of corona proteins initiates an oxidative stress response in cells. Nanoscale **9**(22), 7595–7601 (2017)
126. H. Amiri et al., Protein corona affects the relaxivity and MRI contrast efficiency of magnetic nanoparticles. Nanoscale **5**(18), 8656–8665 (2013)
127. L. Shang et al., Effect of protein adsorption on the fluorescence of ultrasmall gold nanoclusters. Small **8**(5), 661–665 (2012)
128. M. Falahati et al., A health concern regarding the protein corona, aggregation and disaggregation. Biochim. Biophys. Acta. Gen. Subj. **1893**, 971–991 (2019)
129. W.L. Koh et al., Aggregation and protein corona formation on gold nanoparticles affect viability and liver functions of primary rat hepatocytes. Nanomedicine **11**(17), 2275–2287 (2016)
130. S. Dominguez-Medina et al., Adsorption of a protein monolayer via hydrophobic interactions prevents nanoparticle aggregation under harsh environmental conditions. ACS Sustain. Chem. Eng. **1**(7), 833–842 (2013)

131. C. Vasti et al., Effect of the protein corona on the colloidal stability and reactivity of LDH-based nanocarriers. J. Mater. Chem. B **4**(11), 2008–2016 (2016)
132. R. Cukalevski et al., IgG and fibrinogen driven nanoparticle aggregation. Nano Res. **8**(8), 2733–2743 (2015)
133. S.T. Moerz et al., Formation mechanism for stable hybrid clusters of proteins and nanoparticles. ACS Nano **9**(7), 6696–6705 (2015)
134. V. Mirshafiee et al., Protein corona significantly reduces active targeting yield. Chem. Commun. **49**(25), 2557–2559 (2013)
135. E. Blanco, H. Shen, M. Ferrari, Principles of nanoparticle design for overcoming biological barriers to drug delivery. Nat. Biotechnol. **33**(9), 941 (2015)
136. E. Polo et al., Advances toward more efficient targeted delivery of nanoparticles in vivo: understanding interactions between nanoparticles and cells. ACS Nano **11**(3), 2397–2402 (2017)
137. Z.S. Al-Ahmady et al., Formation of protein corona in vivo affects drug release from temperature-sensitive liposomes. J. Control. Release **276**, 157–167 (2018)
138. Y. Li et al., Probing of the assembly structure and dynamics within nanoparticles during interaction with blood proteins. ACS Nano **6**(11), 9485–9495 (2012)
139. A. Pourjavadi, Z.M. Tehrani, N. Mahmoudi, The effect of protein corona on doxorubicin release from the magnetic mesoporous silica nanoparticles with polyethylene glycol coating. J. Nanopart. Res. **17**(4), 197 (2015)
140. K. Obst et al., Protein corona formation on colloidal polymeric nanoparticles and polymeric nanogels: impact on cellular uptake, toxicity, immunogenicity, and drug release properties. Biomacromolecules **18**(6), 1762–1771 (2017)
141. Q. Peng et al., Enhanced biostability of nanoparticle-based drug delivery systems by albumin corona. Nanomedicine **10**(2), 205–214 (2015)
142. A.J. Paula et al., Influence of protein corona on the transport of molecules into cells by mesoporous silica nanoparticles. ACS Appl. Mater. Interfaces **5**(17), 8387–8393 (2013)
143. C. Rodriguez-Quijada et al., Protease degradation of protein coronas and its impact on cancer cells and drug payload release. ACS Appl. Mater. Interfaces **11**(16), 14588–14596 (2019)
144. H. Maeda, H. Nakamura, J. Fang, The EPR effect for macromolecular drug delivery to solid tumors: Improvement of tumor uptake, lowering of systemic toxicity, and distinct tumor imaging in vivo. Adv. Drug Deliv. Rev. **65**(1), 71–79 (2013)
145. M. Sarparanta et al., Intravenous delivery of hydrophobin-functionalized porous silicon nanoparticles: stability, plasma protein adsorption and biodistribution. Mol. Pharm. **9**(3), 654–663 (2012)
146. J. Wolfram et al., Shrinkage of pegylated and non-pegylated liposomes in serum. Colloids Surf. B Biointerfaces **114**, 294–300 (2014)
147. F. Wang, A. Salvati, P. Boya, Lysosome-dependent cell death and deregulated autophagy induced by amine-modified polystyrene nanoparticles. Open Biol. **8**(4), 170271 (2018)
148. A.K. Varkouhi et al., Endosomal escape pathways for delivery of biologicals. J. Control. Release **151**(3), 220–228 (2011)
149. W. Zhang, C.H. Tung, Real-time visualization of lysosome destruction using a photosensitive toluidine blue nanogel. Chemistry **24**(9), 2089–2093 (2018)
150. W. Zhang, C.-H. Tung, Lysosome enlargement enhanced photochemotherapy using a multifunctional nanogel. ACS Appl. Mater. Interfaces **10**(5), 4343–4348 (2018)
151. H. Nejadnik et al., The protein corona around nanoparticles facilitates stem cell labeling for clinical MR imaging. Radiology **286**(3), 938–947 (2018)
152. M. Merhi et al., Study of serum interaction with a cationic nanoparticle: implications for in vitro endocytosis, cytotoxicity and genotoxicity. Int. J. Pharm. **423**(1), 37–44 (2012)
153. C. Ge et al., Binding of blood proteins to carbon nanotubes reduces cytotoxicity. Proc. Natl. Acad. Sci. **108**(41), 16968–16973 (2011)
154. S. Kittler et al., Toxicity of silver nanoparticles increases during storage because of slow dissolution under release of silver ions. Chem. Mater. **22**(16), 4548–4554 (2010)

155. H. Yin et al., Reducing the cytotoxicity of ZnO nanoparticles by a pre-formed protein corona in a supplemented cell culture medium. RSC Adv. **5**(90), 73963–73973 (2015)
156. K. Choi, J.E. Riviere, N.A. Monteiro-Riviere, Protein corona modulation of hepatocyte uptake and molecular mechanisms of gold nanoparticle toxicity. Nanotoxicology **11**(1), 64–75 (2017)
157. V. Escamilla-Rivera et al., Protein corona acts as a protective shield against Fe3O4-PEG inflammation and ROS-induced toxicity in human macrophages. Toxicol. Lett. **240**(1), 172–184 (2016)
158. T. Ding, J. Sun, Formation of protein corona on nanoparticle affects different complement activation pathways mediated by C1q. Pharm. Res. **37**(1), 1–9 (2020)
159. A. Wang et al., Protein corona liposomes achieve efficient oral insulin delivery by overcoming mucus and epithelial barriers. Adv. Healthc. Mater. **8**(12), 1801123 (2019)
160. S. Shahabi et al., Utilizing the protein corona around silica nanoparticles for dual drug loading and release. Nanoscale **7**(39), 16251–16265 (2015)
161. E.L.L. Yeo et al., Exploiting the protein corona around gold nanorods for low-dose combined photothermal and photodynamic therapy. J. Mater. Chem. B **5**(2), 254–268 (2017)
162. E.L.L. Yeo et al., Protein corona around gold nanorods as a drug carrier for multimodal cancer therapy. ACS Biomater Sci. Eng. **3**(6), 1039–1050 (2017)
163. E.L.L. Yeo et al., Protein corona in drug delivery for multimodal cancer therapy in vivo. Nanoscale **10**(5), 2461–2472 (2018)
164. J.C.Y. Kah et al., Exploiting the protein corona around gold nanorods for loading and triggered release. ACS Nano **6**(8), 6730–6740 (2012)
165. A. Cifuentes-Rius et al., Optimizing the properties of the protein corona surrounding nanoparticles for tuning payload release. ACS Nano **7**(11), 10066–10074 (2013)
166. S. Palchetti et al., The protein corona of circulating PEGylated liposomes. Biochim. Biophys. Acta. Biomembr. **1858**(2), 189–196 (2016)
167. V. Mirshafiee et al., Impact of protein pre-coating on the protein corona composition and nanoparticle cellular uptake. Biomaterials **75**, 295–304 (2016)
168. Q. Peng et al., Preformed albumin corona, a protective coating for nanoparticles based drug delivery system. Biomaterials **34**(33), 8521–8530 (2013)
169. F. Giulimondi et al., Interplay of protein corona and immune cells controls blood residency of liposomes. Nat. Commun. **10**(1), 1–11 (2019)
170. S. Ritz et al., Protein corona of nanoparticles: distinct proteins regulate the cellular uptake. Biomacromolecules **16**(4), 1311–1321 (2015)
171. R. Dal Magro et al., Artificial apolipoprotein corona enables nanoparticle brain targeting. Nanomedicine **14**(2), 429–438 (2018)
172. J. Simon et al., Exploiting the biomolecular corona: pre-coating of nanoparticles enables controlled cellular interactions. Nanoscale **10**(22), 10731–10739 (2018)
173. S. Wan et al., The "sweet" side of the protein corona: effects of glycosylation on nanoparticle–cell interactions. ACS Nano **9**(2), 2157–2166 (2015)
174. C.D. Walkey et al., Nanoparticle size and surface chemistry determine serum protein adsorption and macrophage uptake. J. Am. Chem. Soc. **134**(4), 2139–2147 (2012)
175. B. Kang et al., Carbohydrate-based nanocarriers exhibiting specific cell targeting with minimum influence from the protein corona. Angew. Chem. Int. Ed. **54**(25), 7436–7440 (2015)
176. R. Safavi-Sohi et al., Bypassing protein corona issue on active targeting: zwitterionic coatings dictate specific interactions of targeting moieties and cell receptors. ACS Appl. Mater. Interfaces **8**(35), 22808–22818 (2016)
177. Z. Zhang et al., Corona-directed nucleic acid delivery into hepatic stellate cells for liver fibrosis therapy. ACS Nano **9**(3), 2405–2419 (2015)
178. Z. Zhang et al., Brain-targeted drug delivery by manipulating protein corona functions. Nat. Commun. **10**(1), 1–11 (2019)
179. J. Mosquera et al., Reversible control of protein corona formation on gold nanoparticles using host-guest interactions. ACS Nano (2020). https://doi.org/10.1021/acsnano.9b08752

180. D. Pozzi et al., The biomolecular corona of nanoparticles in circulating biological media. Nanoscale **7**(33), 13958–13966 (2015)
181. S. Palchetti et al., Influence of dynamic flow environment on nanoparticle-protein corona: from protein patterns to uptake in cancer cells. Colloids Surf. B Biointerfaces **153**, 263–271 (2017)
182. G. Caracciolo, O.C. Farokhzad, M. Mahmoudi, Biological identity of nanoparticles in vivo: clinical implications of the protein corona. Trends Biotechnol. **35**(3), 257–264 (2017)
183. V. Forest, J. Pourchez, The nanoparticle protein corona: the myth of average. Nano Today **11**(6), 700–703 (2016)
184. J. O'Brien, K.J. Shea, Tuning the protein corona of hydrogel nanoparticles: the synthesis of abiotic protein and peptide affinity reagents. Acc. Chem. Res. **49**(6), 1200–1210 (2016)
185. B.-J.L. Van Hong Nguyen, Protein corona: a new approach for nanomedicine design. Int. J. Nanomedicine **12**, 3137 (2017)
186. S. Galmarini et al., Beyond unpredictability: the importance of reproducibility in understanding the protein corona of nanoparticles. Bioconjug. Chem. **29**(10), 3385–3393 (2018)
187. T.L. Moore et al., Nanoparticle administration method in cell culture alters particle-cell interaction. Sci. Rep. **9**(1), 1–9 (2019)
188. H.S. Leong et al., On the issue of transparency and reproducibility in nanomedicine. Nat. Nanotechnol. **14**(7), 629 (2019)

Chapter 10
Development of Realgar Nanotherapeutics for Cancer Treatments

Tao Wang and Haiyan Xu

Abstract Realgar is a kind of mineral drug and has a long history of medical use in Chinese medicine. The active component of realgar is As_4S_4 and can be orally administrated. In past decades, several traditional Chinese prescriptions containing realgar has showed certain clinical effects in the treatment of some hematologic malignancies. However, realgar is poorly soluble in neutral or acidic aqueous solution due to its crystal structures, which not only leads to the problem of extremely low bioavailability in clinical practices but also sets up obstacles to biomedical studies to understand molecular mechanisms. Hence, there have been continuous efforts made to seek effective approaches for developing suitable processing techniques of realgar, aiming to increase the bioavailability and efficacy, and meanwhile, also to get insights into pharmaceutical mechanisms at molecular levels. This chapter briefly introduces the history of medical use of realgar in Chinese medicine prescriptions, followed by a comprehensively review of the efforts for developing realgar nanotherapeutics by using various technologies, especially a novel one-step preparation approach to fabricate nanoformulation was addressed. In the last part, therapeutic effects of realgar nanoformulations in cells and animals of acute and chronic myeloid leukemia and solid tumors are demonstrated, and molecular mechanisms are portrayed as well.

Keywords Realgar · As_4S_4 · Reactive oxygen species (ROS) · Nanoformulation · Cancer · Leukemia

T. Wang · H. Xu (✉)
Department of Biomedical Engineering, Institute of Basic Medical Sciences, Chinese Academy of Medical Sciences and Peking Union Medical College, Beijing, P. R. China
e-mail: xuhy@pumc.edu.cn

H. Xu, N. Gu (eds.), *Nanotechnology in Regenerative Medicine and Drug Delivery Therapy*, https://doi.org/10.1007/978-981-15-5386-8_10

10.1 Introduction

The therapeutic effects of arsenical compounds in some diseases have been gradually recognized over past decades especially with the poison As_2O_3 being utilized therapeutically as a potent anticancer agent. The first clinical use of As_2O_3 to treat blood cancers was carried out in China during the 1970s. Zhang and Rong prepared a prescription consisting of As_2O_3 and HgCl, which was called *Ailing* #1, and applied it to the treatment of acute myeloid leukemia (AML) through intramuscular injection [1]. Promising responses were reported especially in acute promyelocytic leukemia (APL). More clinical trials in China systematically verified the effectiveness of As_2O_3 in the treatment of APL regardless of disease stages [2, 3]. The therapeutic efficacy of As_2O_3 on APL was gradually recognized globally until its mechanism of the anticancer activity of As_2O_3 was better understood [4]. In 2000, the US Food and Drug Administration approved As_2O_3 injection, Trisenox™, as a first-line chemotherapeutic agent for newly diagnosed and refractory/relapsed APL patients. Nowadays, As_2O_3 in combination with all-*trans* retinoic acid (ATRA) is regarded as the most promising chemotherapeutic scheme for the treatment of APL. Other than APL, As_2O_3 is also applied to other malignancies such as myelodysplastic syndrome (MDS) [5, 6] and solid tumors such as liver cancer [7] and lung cancer [8]. Advanced liver cancer has been approved as an indication of As_2O_3 in 2004 by the Chinese Food and Drug Administration. The big success of As_2O_3 encouraged the interests in other arsenical compounds.

Realgar, of which the main component is tetraarsenic tetrasulfide (As_4S_4), is a mineral arsenic abundantly distributed in the earth's crust. The appearance of natural realgar is irregular block or granule with orange-red to orange-yellow color, while the concentrate powder is granular with orange color. In addition to realgar in nature, As_4S_4 can also be synthesized chemically. On an industrial scale As_4S_4 has been prepared by the reaction between sulfur and an excess of elemental arsenic or As_2O_3, and in the laboratory, As_4S_4 can be accessed by the fusion between stoichiometric quantities of arsenic metal with sulfur [9]. In contemporary medicine, the application of realgar in the treatment of APL began even earlier than that of As_2O_3. Although it has been reported to be effective in the treatment of APL and CML, realgar agents do not achieve the same success as As_2O_3. Reasons may be that the clinical effect is not so potent and pharmaceutical mechanisms are not clear enough, which are attributable to its poor solubility in pure water and acidic aqueous solutions.

This chapter briefly introduces the history of medical use of realgar in Chinese medicine prescriptions, not only in the treatment of APL but also in the treatment of solid tumors, which will be followed by a comprehensively review of the efforts for developing realgar nanotherapeutics by using various technologies, especially a novel one-step preparation approach to fabricate nanoformulation was addressed, since processing techniques are crucial for the safe and effective application of realgar. In the last part, therapeutic effects of the nanoformulation in cells and animals of acute and chronic myeloid leukemia and breast cancer are demonstrated, and the hidden molecular mechanisms are portrayed as well.

10.2 History of Use of Realgar in Medical Practices

The use of realgar has a long history. Traditionally, realgar was mainly used as a pigment and in internal medicines; other early applications include depilating and tanning hides, pyrotechnics, controlling pests, and manufacturing shot. The medical use of realgar in ancient and contemporary days is described in the following sections.

10.2.1 Realgar in Traditional Chinese Medicine

The medical use of realgar could be traced back to 2000 years ago. In ancient China, realgar (*Xiong-Huang*) was utilized in the treatment of carbuncles, boils, insect bites and snakebites, abdominal pain due to intestinal parasitosis, infantile convulsion, malaria, and psoriasis and skin diseases [10]. There are also some application records of realgar in other civilization. In traditional medicine native to India, realgar was used as a major component in Bhasma, which is a unique and representative kind of preparation used against a variety of chronic ailments. In Western medicines, Paracelsus (1493–1541) administered realgar internally to treat cancer-like tumors [11].

Enthusiasm for the use of realgar has never subsided in China, as, for example, realgar has been listed in the Chinese Pharmacopoeia since 1963 and is suggested to be made into pills or powders for use as well as for external application. The daily intake of realgar is specified to not exceed 100 mg in the latest edition of the Chinese Pharmacopoeia (i.e., the 2015 edition), with long-term administration being avoided. There are totally 37 kinds of Chinese patent medicine listed in the Chinese Pharmacopoeia (2015), and the functions are mainly focused on detoxification, disinfestation, dampness, removing phlegm, and stopping malaria. The most commonly used ones are listed in Table 10.1.

Table 10.1 Some of the realgar containing Chinese patent medicine listed in the Chinese Pharmacopoeia (2015)

Medicine	Indications
Niu Huang Jie Du pill/tablet/capsule/soft capsule	Sore throat, swollen gums, sore mouth and tongue, swollen eyes
Niu Huang Xiao Yan Wan	Swelling, pain, furuncle, carbuncle
Fu Fang Niu Huang Xiao Yan Jiao Nang	Upper respiratory tract infection, pneumonia, tracheitis
Zhu Huang Chui Hou San	Swelling, pain, and erosion of mouth and tongue
Ya Tong Yi Li Wan	Swelling and pain of gums and caries
Niu Huang Zhi Bao Wan	Functional constipation
Yi Xian Wan	Diarrhea, heatstroke
Yu Jin Yin Xie Pian	Psoriasis
Shu Zheng Pian	Heatstroke
Sha Yao	Heatstroke

10.2.2 Realgar in the Treatment of Cancer

In medical researches and clinical practices of modern medicine, anticancer activities of realgar particularly in leukemia have become the focus. Since the 1960s, realgar has been used in the clinical practice of leukemia treatment, mainly focused on myeloid leukemia, which has a history of over half century.

Realgar was first utilized for the treatment of APL. In the early 1960s, Chinese doctors found that a compound medicine named *Qinghuang* powder composed of realgar and indigo naturalis showed encouraging effects in many APL patients. Zhou et al. first reported that two newly diagnosed APL patients achieved complete remission (CR) and maintained continuous CR over 4 years using *Qinghuang* powder in 1986 [12]. Lu et al. reported long-term follow-up data in patients treated with oral realgar in 2002; the patients were administrated with a single realgar of 50 mg/kg/day, and the disease-free survival rates of 1 and 6 years were 96.7% and 87.4%, respectively [13]. All of these reports and research suggested that realgar has therapeutic effect on APL.

Because of the obvious effectiveness in the treatment of APL, one commercially available realgar agent has been developed, which is a compound medicine named realgar-indigo naturalis formula (RIF). One tablet of RIF weighted 270 mg, which contains 30 mg of realgar, 125 mg of indigo naturalis, 50 mg of radix salviae miltiorrhizae, 45 mg of radix pseudostellariae, and 20 mg of garment film [14]. RIF was first developed by Huang et al. in 1980, and the first study of RIF for APL was reported in 1988 [14]. Based on the results of systematic studies by Huang et al. and Qian et al., this drug was approved by the Chinese Food and Drug Administration in 2009 for the treatment of APL. In a randomized, multicenter, phase III noninferiority clinical trial involving 242 patients, it was confirmed that the therapeutic effect of oral RIF combined with all-*trans* retinoic acid (ATRA) on APL is no different from that of intravenous As_2O_3 combined with ATRA [15], which has been recommended as the first-line therapy for APL [16]. Another phase III clinical trial confirmed that for non-high-risk APL, the treatment scheme of fully oral RIF and ATRA has the same effect as that of intravenous As_2O_3 and ATRA [17]. A cohort study in nine pediatric patients with APL and 20 high-risk APL patients also preliminarily declared the effectiveness of the RIF combined with ATRA. More details of these clinical studies on RIF have been reviewed by Zhu et al. [14] and the effectiveness in APL has been verified.

Compared with the treatment of As_2O_3, due to the oral administration and reduction of hospitalization days, the treatment of RIF significantly reduced the median total cost, from about $24,000 in As_2O_3 group to $13,000 in RIF group, which largely eased the economic burden of patients [18]. Formula with realgar could achieve equal effectiveness to that with As_2O_3 while costs largely less, implying that realgar could be a simpler and more economical therapeutic agent.

Realgar has also been used to treat chronic myeloid leukemia (CML) in clinical practice. The application of realgar in the treatment of CML was first reported in 1981. Zhou et al. treated 25 CML patients with compound *Qinghuang* powder and

obtained 21 complete remissions and 4 partial remissions [19]. From 1985 to 1999, 86 CML patients were treated with *Qinghuang* powder, and 62 cases of complete remission 14 cases of partial remission were achieved [20]. These reports strongly implied that realgar could be a promising therapeutic and/or complementary option for CML patients.

The clinical application of realgar in cancer treatment was mostly concentrated in the category of leukemia, while there was no report about application in the treatment of solid tumors in clinical practice. Nevertheless, some *in vivo* researches reported therapeutics effects of realgar on other malignancies. Realgar could inhibit tumor growth in H-22 bearing hepatocellular carcinoma mice [21] and lung cancer mice [22], inhibit tumor growth and invasion, and induce apoptosis of xenograft MGC803 gastric cancer cells [23, 24]. These *in vivo* studies indicating realgar could be potential therapeutic options for solid tumors as well.

10.3 Traditional Processing Strategy and Challenges

Realgar is naturally a mineral and needs to be pretreated before medicinal use. Among these traditional processing techniques, grinding directly and grinding and rinsing in water were most frequently used and listed in editions before 2000 in the Chinese Pharmacopoeia. With the development of understanding of the toxicity, it was gradually realized that removal of As_2O_3 played a crucial part in the safe application of realgar. That is because the natural mineral of realgar mainly contains As_4S_4, and a small amount of As_2O_3 that is a kind of highly toxic soluble arsenic oxide, not allowed to be taken orally. Since grinding directly could not dislodge As_2O_3 effectively [25], the only recommended processing method for realgar in the Chinese Pharmacopoeia (2015) is to grind and rinse in water, so-called *Shuifei* in Chinese. The operations are as following: firstly, place the realgar in the container, add some water to grind them into paste, add more water and mix them, collect the suspension; then repeat the above steps to the residue and also collect the suspension; finally take the suspension together and, after standing, the remained sediment should be dried and ground for use. This traditional processing approach can produce realgar powder with a diameter of micrometer scale by grinding and removing As_2O_3 due to its solubility in water at the same time. Realgar particulates produced by using this processing approach are several tens of micrometers in diameter, which are used in at least 37 realgar-containing formulas of Chinese traditional medicine.

Although grinding and rinsing in water could effectively remove As_2O_3, there are still some problems to the effective application of realgar. First, due to the high lattice energy, realgar is insoluble in water and hydrochloric acid, which limits the clinical use of realgar. *Niu Huang Jie Du Pian* (translated as cow bezoar detoxifying pills) is a very common realgar-containing patented prescribed medicine used for the treatment of sore throat, swollen gums, sore mouth and tongue, and swollen eyes. Although the total arsenic present in a single pill was as high as 28 mg, only

1 mg of arsenic per pill was available for absorption into the bloodstream, implying that the bioavailability of As_4S_4 in the formula was only 4% [26]. Thus, in order to obtain effective concentration of arsenic in the blood, patients have to be orally administered As_4S_4 at high doses for up to several years in some cases. Although the therapeutic effect has been well verified especially by the application of RIF in the treatment of APL, when administered orally at 60 mg/kg/day of RIF to a patient with a body weight of ~60 kg, the daily intake of realgar would be up to 400 mg, which is three times higher than the superior limit specified in the Chinese Pharmacopoeia (2015), leading to adverse reactions and long-term exposure risks. In the 6-year follow-up data reported by Lu et al. [13] As_4S_4 caused side effects such as asymptomatic prolongation of corrected QT interval, transient elevation in liver enzyme levels, rash, and mild gastrointestinal discomfort and can cause a heavy burden in terms of medical care as well. Besides, long-term arsenic toxicity leads to multisystem disease including skin, gastrointestinal system, cardiovascular system, neurological system, genitourinary system, respiratory system, endocrine and hematological systems, and the most serious consequence is malignancy of the skin, lung, liver, kidney, and bladder [27, 28].

Second, the clinical effectiveness to a certain extent on leukemia is evident; however, it is still unclear whether the effectiveness is due to the sulfides or the oxides formed from the parent compounds [29]. To elucidate the mechanism, homogeneous suspension of realgar in aqueous solution is necessary for cellular and molecular biological experiments; however, the extremely low solubility of realgar in water makes it difficult to obtain the suspension, and this also hinders further clinical applications of realgar. So far, existing mechanistic studies had realgar dissolved in concentrate alkaline solution, usually sodium hydroxide. The realgar dissolved in sodium hydroxide is used for *in vitro* and *in vivo* study by intraperitoneal injection [21] and intravenous injection [30]. However, it should be noted that when dissolved in alkaline solution, realgar reacts with alkali solution to form a new arsenic compounds as presented in the following chemical equation, which means that the arsenic components in the cellular or animal experiments are not realgar (As_4S_4) anymore [31].

$$3As_4S_4 + 36NaOH + 3O_2 = 8Na_3AsO_3 + 4Na_3AsS_3 + 18H_2O$$

There is an example to describe the difference between the realgar dissolved in sodium hydroxide and the realgar in nanoparticulate As_4S_4 that forms intuitively. The two formulas of realgar were applied to K562 cell [32–34], which is one of the human CML cell lines and expresses the fusion protein BCR-ABL as the characteristic molecule. Both formulas induced apoptosis of K562 cells and decreased the BCR-ABL. A molecular mechanism study revealed that realgar dissolved in sodium hydroxide binds to the ring finger domain of c-CBL to inhibit its own ubiquitination and degradation, so as to ubiquitously degrade BCR-ABL protein [35]. However, our recent investigation showed that realgar in the form of nanoparticulate As_4S_4 degraded BCR-ABL through autophagy-associated pathways without affecting the expression of c-CBL [34]. To sum up, increasing the solubility without changing the

chemical composition of realgar is of great significance to both clinical and mechanism studies.

10.4 Development of Realgar Nanotherapeutics

Currently, there are limited numbers of formulation approaches available for compounds that are poorly water-soluble. The most direct approach to enhance the solubility of a compound is to generate a salt. However, the poor water solubility of realgar is due to its high lattice energy, which leads to difficulty in breaking apart molecules in the solid state [36]. Since realgar is non-ionizable, other approaches have to be developed to improve its solubility.

Nanotechnology could be a potential approach to improve the solubility and bioavailability of realgar. The size effect of realgar nanoparticles was described by Deng et al. [37]; four different suspensions of realgar nanoparticles with diameters in the range of 100–500 nm prepared by regulating the milling time, which contained equivalent doses of As_4S_4, were investigated to determine their effects on the viability of cells. Remarkable cytotoxic effects were achieved by exposure of cells to realgar particles of 100 and 150 nm in diameter after incubation for 2 h at a dose of 0.2 μM, whereas the treatment of cells with particles of a diameter of 200 and 500 nm for the same duration and at the same dose had only slight effects on cell viability, which strongly suggested that the reduction of particle size may contribute to the enhancement of therapeutic efficacy. As listed in Table 10.2 and detailed in the following text, researchers have developed different methods to generate nanoparticles of realgar over recent years, which are mainly divided into two categories: bottom-up and top-down.

Table 10.2 Methods and the principles to generate nanoparticles of realgar: a brief overlook

Categories	Methods	Principles	References
Top-down	Milling	Mechanical force between highly kinetic colliding balls can trap powder particles	[33, 37–52]
	Microfluidizer	Jet stream can lead to particle collision to form particles of nanoscale	[53]
Bottom-up	Chemical precipitation	Realgar can react with Na_2S, and addition of hydrochloric acid allows realgar nanoparticles to grow from the solution	[54, 55]
	Solvent relay	Realgar can be dissolved in the mixture of CS_2, 1,2-propanediol, and acetone, and the nano-realgar suspension dispersed in 1,2-propanediol can be obtained by evaporating CS_2 and acetone	[56]
	Quantum dots	Realgar can be dissolved in ethylenediamine and ethanolamine, and the cluster can be transformed to quantum dots assisted by consumption of ethylenediamine and ethanolamine by heating	[57, 58]

10.4.1 Top-Down Approaches

Top-down techniques are high energy processes, which are used to break down the particle size of drugs to nanoscale by mechanical force. The two main top-down approaches for preparing realgar nanoparticles are media milling and high-pressure homogenization.

10.4.1.1 Milling

Recently, mechanical milling has been proved to be an effective and simple technique without involving high temperature treatment for the production of nanocrystalline powders, with the possibility of obtaining large quantities of materials with modified properties. In this technique, starting powder particles are trapped between highly kinetic colliding balls and the inner surface of the vial, which causes repeated deformation, rewelding, and fragmentation of premixed powders resulting in the formation of fine, dispersed particles in the grain-refined matrix.

Mechanical milling was the most widely utilized method for preparing realgar nanoparticles [33, 37–52]. Water was selected as milling media at the earliest stage [37]. The particle size of realgar decreased to nanoscale under the effect of high kinetic energy colliding ball, and the size could be customized by adjusting the milling time [37]. However, this processing could only decrease the size of the realgar particles to nanoscale, but could not increase the solubility of the particles effectively, therefore showing some weakness. At the same time, when the particle size is dropped down dramatically, the specific surface area would increase largely, which is more likely to lead to quick oxidation when exposed in air to form As_2O_3 and cause toxicity. In an in *vivo* study, after oral administration of realgar nanoparticles, a total of five mice died during the experiment, and the authors pointed out that the death of the mice might be attributable to the toxicity of high concentration of As_2O_3 in realgar nanoparticles prepared by milling [41]. In addition, nanoparticles prepared by milling are easy to agglomerate. All these shortcomings would bring difficulties for its clinical application.

To prevent from oxidation and aggregation, the technique of cryo-milling [36] has been applied for the preparation of realgar nanoparticles as well as the introduction of polymer such as polyvinylpyrrolidone (PVP) [36, 38, 40], Poloxamer 407 [59], and sodium dodecyl sulfate (SDS) [36, 52] as milling media. In a scheme of cryo-milling, in the presence of PVP and/or SDS, all of the obtained mixtures were vague colloidal solutions and slightly yellowish in color, while the raw realgar powder and milling realgar nanoparticles without additive(s) were clear solutions after 48 h standing at room temperature. After a single oral administration of the cryo-milling realgar particle suspension, a remarkable increase in urinary recovery of arsenic was observed in rats, ranging from 58.5 to 69.6% of the administered dose of arsenic recovered in urine in the first 48 h from the realgar nanoparticle suspension; while the raw realgar powder gave a urinary recovery of only 24.9% [36]. The introduction of a polymer could partly reduce As_2O_3 production compared to

directly milling in water. However, even under the protection of a polymer, the As_2O_3 content in the resulting nanoparticles is 9.75 mg/g, which is still higher than that in the raw realgar that is 2.82 mg/g [52]. Several post-milling procedures were also used for further application and further processing of the nanoformulation. In order to avoid oxidation and increase the stability at the same time, realgar nanoparticles prepared by milling was mixed with polymeric materials by melting methods [60]. The carrier material F68 and PEG6000 were put into the evaporating dish heated to melting; then the realgar nanoparticles powder was added into the melting carrier and mixed with high shear to obtain the mixture after cooling and drying. The realgar nanoparticles resulting from milling was also encapsulated in (−)-Epigallocatechin-3-gallate (EGCG) chemical coprecipitation method, in which mixed solution of the nano-realgar and EGCG was lyophilized using a vacuum freeze dryer [39]. Realgar nanoparticle-based microcapsules were also prepared by solvent evaporation techniques [41]. The realgar nanoparticles were also mixed and emulsified with a cream including seven ingredients for transdermal drug delivery in a mice model of melanoma [51].

10.4.1.2 Microfluidizer

The microfluidizer technique is one of the high-pressure homogenization technique, which is also known as the IDD-P technique, i.e., insoluble drug delivery particle technology [61]. This technology is based on the jet stream that can lead to particle collision, shear forces, and cavitation forces, and generate particulates by a frontal collision of two fluid streams in a Y-type or Z-type chamber under pressures up to 1700 bar [62]. Zhan et al. obtained realgar nanoparticles by using microfluidizer technique [53]. The realgar was put in water before subjected to the microfluidizer, obtaining nanoparticles with average diameter of 280 nm. However, the nanoparticles were easy to regroup into larger particles. The dispersibility and stability of particles was further improved by adding dispersant such as carboxymethylcellulose (CMC) and PVP.

The top-down strategies could obtain realgar in nanoscale through mechanical force, and the milling technique is the most used approach for the preparation of realgar nanoparticles since its first application. However, the nanoparticle obtained from these two top-down approaches were dispersed in solution and brought inconvenience to long-term preservation and further pharmaceutical preparations. The milling process also introduced impurities into the product inevitably.

10.4.2 Bottom-Up Approaches

Bottom-up techniques are also referred to as precipitation techniques as nanosized drug particles are formed by precipitation, which can be in a crystalline or amorphous form. In this method, drug is precipitated from supersaturated drug solution, or by evaporation of a solvent, or by mixing the drug with a non-solvent. Some bottom-up techniques are used for preparing realgar nanoparticles.

10.4.2.1 Chemical Precipitation

Guo et al. developed a method of chemical precipitation [54, 55]. Realgar was processing by acid to remove the impurity, and then added to Na_2S solution and magnetic stirred to make full reaction. Afterwards, hydrochloric acid was added slowly to the solution and continuously stirred. At the same time, solutions of CMC, PVP, and bovine serum protein (BSA) were added to the reactive system. The polymers were assumed to act as a soft template in the preparation of realgar nanoparticles, which allowed realgar nanoparticles to grow orderly.

10.4.2.2 Solvent Relay

Ning et al. prepared nano-realgar suspension by using the solvent relay method [56]. Carbon disulfide (CS_2), 1, 2-propanediol, and acetone were mixed in a specific proportion, and then refluxed continuously in Soxhlet extractor to dissolve realgar. Afterwards, the carbon disulfide and acetone in the crude product were evaporated and concentrated under reduced pressure to obtain the nano-realgar suspension dispersed in 1, 2-propanediol with an average particle size of 159.0 nm.

10.4.2.3 Quantum Dots

Wang et al. fabricated quantum dots of As_4S_4 by a wet process from the raw realgar through cluster-mediated transformation [57]. The As_4S_4 can be easily dissolved in ethylenediamine to form a solution-like cluster (As_4S_4−$NH_2C_2H_4NH_2$). The cluster can be transformed to quantum dots assisted by consumption of ethylenediamine in protic polar solvents with mild thermal treatment. The resulting quantum dots show size-dependent fluorescence ranging from UV to blue and two-photon fluorescence. Ethanolamine also acts as a solvent of As_4S_4 to fabricate quantum dots [58].

Taken in all, according to the characterizations provided in the literatures, realgar nanoparticles were successfully prepared by these methods, even though only a few research groups made efforts to adopt the bottom-up strategy. The core step of bottom-up mentality is to dissolve realgar in solvent; researchers took advantage of Na_2S and organic solvents such as CS_2, 1, 2-propanediol, ethylenediamine, and ethanolamine. However, the realgar did not just simply dissolve in these chosen agents; it may react with Na_2S to form new arsenic compounds. For example, it was found that there was an unexpectable increase of sulfur portion in the prepared nanoparticles, which implied the realgar was transformed to other arsenical compounds [54]. Besides, the reactions between As_4S_4 with solvents may introduce more uncertainty and risk in the application, together with more complexity of mechanistic studies. In the aspect of organic solvents, impurities are brought into the obtained-realgar nanoparticles, which count against further medical applications. In addition, by using those technologies, the resulting realgar nanoparticles were mostly prepared and stored in solutions. Herein it should be addressed that for

experimental studies *in vitro*, the nanoparticles can be used in their as-received forms such as aqueous dispersions or solutions with organic solvents; however, when they are intended to be clinical medicines and applied to patients, in most situation especially the orally administrated medicines they are not in the form of solution for convenience. There was a hidden issue that the realgar nanoparticles in solution were not friendly to the pharmaceutical preparation process, because they need to be further solidified to make pills or tablets.

10.5 Development of One-Step Preparation of Solid Dispersion

Solid dispersion is considered one of the most successful strategies to improve the dissolution profile of poorly soluble drugs. It refers to the technology of preparing drugs into a dispersion system, which is uniformly dispersed in a certain carrier material such as sugars, wax-based systems, and polymers in the state of molecule, colloid, amorphous, and microcrystalline to enhance oral bioavailability [63]. Due to the advantages of solid dispersion technology in improving the solubility and bioavailability of insoluble drugs, the technology has received more attention from scientific research institutions and pharmaceutical enterprises, and new preparation technologies have been reported constantly. Solid dispersions of realgar have also been prepared through hot melt extrusion (HME).

HME is one of the fast developing solid dispersion technologies, which can continuously prepare solid dispersion with less processing steps. HME was originally developed by the plastics industry and was mainly used in plastics, rubber, and food manufacturing in the early stage. Since the 1990s, HME has been widely employed in the field of pharmaceutical preparations and has become an innovative technology in the application of pharmaceutical preparations [64]. HME is a continuous melt manufacturing process consisting of the elementary steps of solids conveying, melting, mixing, devolatilization, pumping, and pressurization for shaping. In a typical twin-screw extruder, the active pharmaceutical ingredients and the polymer carrier and other excipients are fed to the extruder through the hopper and then conveyed by one or more screws down the length of the extruder barrel, followed by melting of the polymer carrier. The lattice energy of the drugs was overcome by heating and the shear force generated by the screws; consequently the crystal drugs may change into amorphous state and evenly disperse into the polymer carrier through the mixing effect of the screws. Finally, pressure is generated, and the molten blend is forced through the die with the desired shape. After the material exits the die, the process stream is then cooled and subjected to secondary processing steps [65].

The product of HME can be directly molded and processed, so it is very economical, easy to scale, high output, and has a wide range of expansion and application. Moreover, it does not use organic solvents, avoiding the residual problem of organic solvents in the preparation. Some of the applications of pharmaceutical

HME include products designed to promote oral absorption, sustained release (either for oral delivery or implants), targeted release, and prevention of substance abuse. Statistics show that since the 1980s, the number of patent authorizations of preparation process involving hot melt extrusion has exceeded 200 worldwide, and several drugs such as Pfizer's ruirulin Rezulin® for diabetes and Abbott's klika kaletra® for antiviral therapy (HIV) have been on the market.

HME was used to increase the bioavailability of realgar in our laboratory. Ma et al. reported a one-step method to prepare realgar solid dispersion by HME [66]. The raw realgar powder mixed with an amphiphilic polymer, namely polyvinyl caprolactam-polyvinyl acetate-polyethylene glycol (PVCL-PVAc-PEG, commercial name: Soluplus), was subjected to the HME. Under the shear force generated by the screw's rotation, realgar powders were crushed to nanoparticles and simultaneously wrapped with Soluplus molecules on the surface of realgar particles. The resulting realgar nanoformulation (named as e-As_4S_4) could disintegrate in water and acid solution, therefore forming a uniform yellow colloidal solution by dispersing realgar particles in Soluplus micelles (Fig. 10.1). The average hydrated size of realgar particles in solution was 400–700 nm, significantly smaller than that of the raw realgar. Powder-XRD patterns indicated the presence of amorphous As_4S_4, possibly because some part of the crystal structure was destroyed during the extrusion process. The e-As_4S_4 had a much higher dissolution rate increasing over time, reaching its highest value of 24.55% after 60 min of immersion, while the highest dissolution rate of the raw realgar was only 0.12%. Consequently, the bioavailability of e-As_4S_4 was 12.6 times that of r-As_4S_4 when orally administrated to rats. Due to the

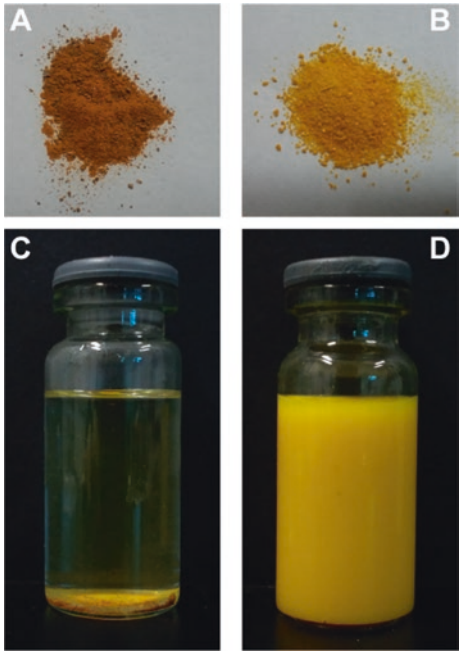

Fig. 10.1 Comparisons of the e-As_4S_4 and raw realgar. (**a**) Powder of the raw As_4S_4. (**b**) Powder of the e-As_4S_4. (**c**) The raw realgar dispersed in aqueous solution. (**d**) The e-As_4S_4 dispersed in aqueous solution

higher bioavailability, the e-As_4S_4 showed stronger inhibitory effects on the cell viability of several cancer cell lines including AML cell line of HL-60 [66], CML cell line of K562 [34], murine breast cancer cell line of 4T1 [67], and better therapeutic efficiency in mice model of AML [66] and breast cancer [67] comparing to the raw realgar. Another advantage of the nanoformulation prepared by HME is that it is solid and do not need further solidification, making it more convenient for preservation and pharmaceutical preparations. This new preparation strategy is expected to provide a more economical and efficient solution for the difficulties in the medical and pharmaceutical applications for realgar.

10.6 Therapeutic Effects of Realgar Nanoformulations in Cancer

The *in vivo* and *in vitro* therapeutic effects of realgar nanoformulations have been investigated in several models of malignant diseases including myeloid leukemia and solid tumor and are described in the following section.

10.6.1 Therapeutics Effects of Realgar Nanoformulations in AML

As mentioned before, realgar has been clinically used as one main component of Chinese traditional compound medicine in the treatment of AML, especially APL, in China. APL is listed in the WHO classification of myeloid malignancies within the category of AML with recurrent genetic abnormalities. Most APL patients have a reciprocal cytogenetic translocation, t(15;17)(q24.1;q21.2), associated with rearrangement of the PML and RARA genes and formation of a novel fusion gene (PML-RARA) [68]. The combination of ATRA and As_2O_3 has become the first-line therapeutic option for APL worldwide, and RIF, of which the main functional component was realgar, has also been approved by Chinese Food and Drug Administration as the first-line therapy for APL in China.

There have been literatures reporting that realgar nanoformulations were able to induce apoptosis of APL cells of HL-60. Ye et al. reported a realgar nanoformulation prepared by milling-induced cytotoxicity in HL-60 cells [49]. Exposure to the realgar nanoformulation caused a time-dependent growth inhibition in HL-60 cells through the induction of apoptosis. When HL-60 cells were treated with this realgar nanoformulation for 36 h, the cells exhibited typical apoptotic morphological changes such as cell membrane blebbing, chromatin condensation, and formation of apoptotic bodies. Further confirmation for the induction effects of apoptosis was provided by the DNA ladders and flow cytometric analysis with large increase of sub-G1 cell population. The induction of apoptosis was attributed to acute toxicity

to cell membrane, by potentiating lipid peroxidation, increasing lactate dehydrogenase release, and reducing membrane fluidity [49]. Wang et al. also reported growth inhibition induction by realgar nanoformulation prepared by milling [43].

The realgar nanoparticles prepared by milling can be further encapsulated by EGCG to form a new nanoformulation named EGCG-RNPs [39]. The formulation also inhibited HL-60 cell growth. Other than the anti-leukemic effect *in vitro*, the EGCG-RNPs also showed antitumor effects *in vivo*. The animal model used in this investigation is that HL-60 cells were xenografted into NOD/SCID mice subcutaneously to establish a solid tumor. Researchers observed that intratumoral injections of EGCG-RNPs reduced the tumor volume, indicating the inhibitory effect of the nanoformulation on the tumor growth [39].

The nanoformulation of realgar prepared by HME (named as e-As_4S_4) in our group also showed cytotoxicity to HL-60 cells in a time- and dose-dependent manner, while Soluplus was not toxic to cells within 72 h [66]. The e-As_4S_4 could be dissolved in water or saline quickly to form colloid solution, in which the As_4S_4 particulates showed the average hydrodynamic diameter of 680 nm. With the same As_4S_4 content, e-As_4S_4 exhibited much higher cytotoxicity than the raw realgar at each time point. The 50% inhibiting concentration (IC_{50}) on HL-60 cells of e-As_4S_4 after incubation for 48 h was 22.8 mg/L, while that of the raw realgar was 99.4 mg/L. The underlying mechanism of the inhibitory effect was apoptosis induction. When HL-60 cells incubated with e-As_4S_4 were stained with Hoechst 33342 and subjected to fluorescence microscopy, strong blue fluorescence was observed in the cells (Fig. 10.2a). Quantification of apoptosis was also performed using annexin V/PI staining and flow cytometry. When treated with e-As_4S_4 at 40 mg/L, the HL-60 cells underwent apoptosis in the first 6 h of incubation and after 48 h incubation the apoptosis rate could reach up to ~90% (Fig. 10.2b).

To be more encouraging, the e-As_4S_4 showed remarkable effects on a xenograft leukemia mice model. The leukemia mice model was established by intravenous injection of HL-60 cells (1×10^6) into sublethally irradiated (250 cGy) NOD/SCID mice. At about 20 days after transplantation, the mice showed signs of leukemia, including paresis in the rear limbs, ruffled fur, and a markedly hunched posture compared with healthy control mice. On day 20 after HL-60 cell transplantation, the e-As_4S_4 or raw realgar was intragastrically administrated to the mice twice every day, each time with 1.8 mg As_4S_4 suspended in 200 μL saline. Oral administration of e-As_4S_4 prolonged the survival of the mice significantly; the median survival of e-As_4S_4 group was 49.5 days while that of raw realgar group was 44.5 days and that of the saline group was 40.5 days (Fig. 10.3a). Moreover, after 3-weeks treatment, the body weight of mice in the e-As_4S_4 group did not exhibit significant loss, indicating that e-As_4S_4 was both safe and effective. Splenomegaly is a typical symptom resulting from leukemia cell infiltration. This condition was relieved by the administration of e-As_4S_4, evidenced by the reduced spleen weight, which was similar to that of the healthy mice (Fig. 10.3b). Moreover, the e-As_4S_4 treatment also decreased the percentage of HL-60 cells ($CD33^+$) significantly, from 13 to 3% in peripheral blood and from 65 to 30% in bone marrow (Fig. 10.3c). Furthermore, extramedullary infiltration in the spleen and liver was largely reduced by e-As_4S_4. As shown in

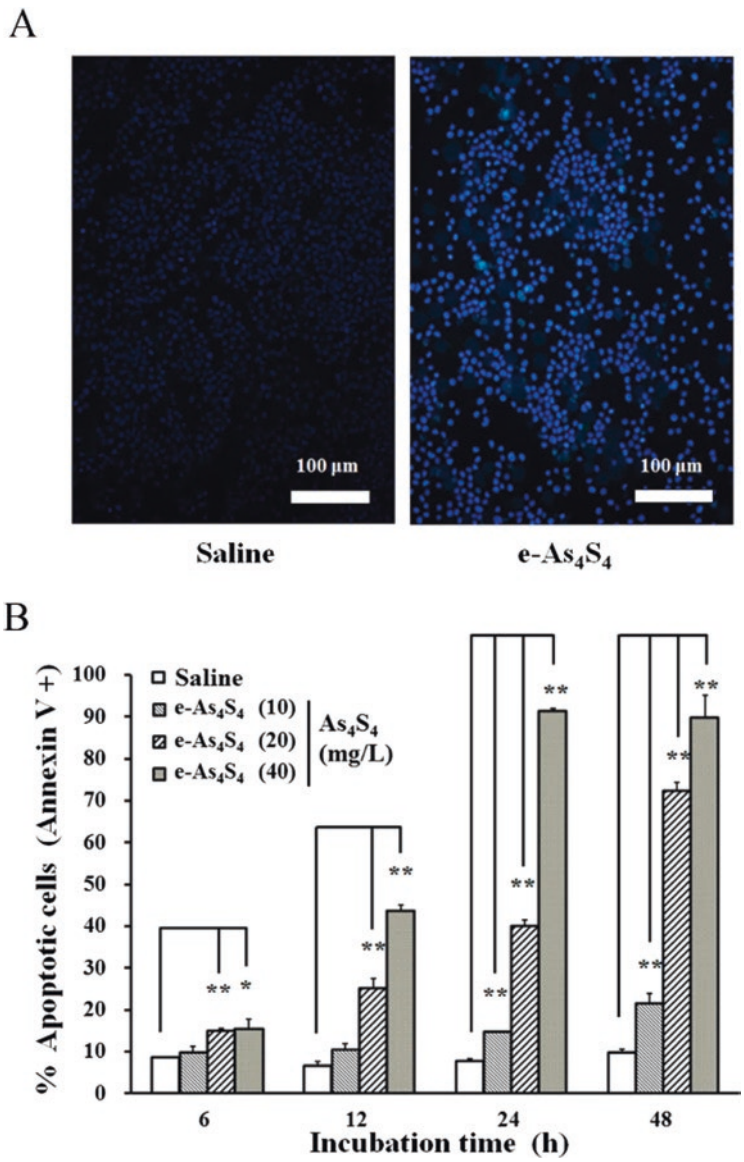

Fig. 10.2 The e-As_4S_4 induced apoptosis in HL-60 cells. (**a**) Apoptosis of HL-60 cells incubated with e-As_4S_4 for 48 h detected by staining with Hoechst 33342. The scale bar in all images indicates 100 μm. (**b**) The e-As_4S_4 induced apoptosis in HL-60 cells in a dose- and time-dependent manner assessed by flow cytometry after annexin V staining. $**P < 0.01$, $*P < 0.05$ [66]

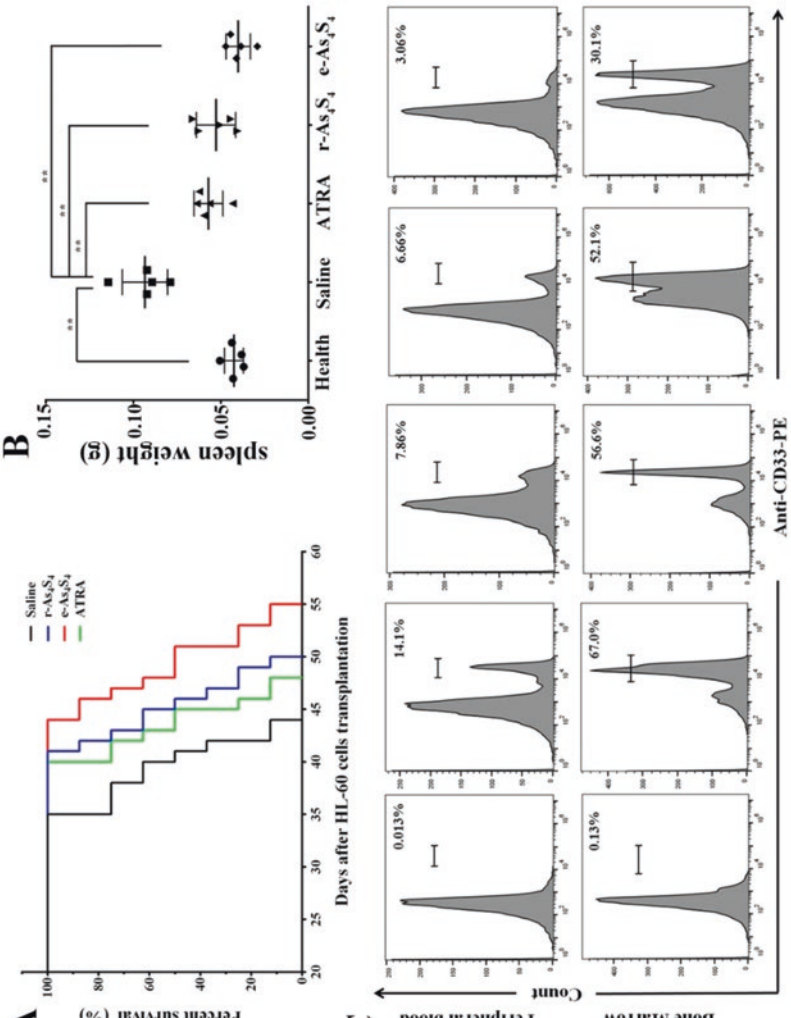

Fig. 10.3 Therapeutic effects of the e-As_4S_4 on AML mice. (**a**) The e-As_4S_4 prolonged the survival of AML mice. (**b**) The e-As_4S_4 reduced spleen weight of mice after 3-weeks treatment. $^{**}P < 0.01$. (**c**) The e-As_4S_4 reduced AML cells in peripheral blood and bone marrow after 3-weeks treatment [66]

H&E staining and anti-CD33 antibody staining, in the spleen and liver of the control group, there were obvious diffuse infiltration of HL-60 cells, while the HL-60 cells staining weakened a lot in the e-As_4S_4 group after 3-weeks treatment (Fig. 10.4) [66]. Taken together, oral administration of e-As_4S_4 largely eliminated the APL cells in peripheral blood and bone marrow due to the apoptosis-inducing effect, which prolonged the survival of the mice and showed reduced extramedullary infiltration in spleens and livers.

Differentiation therapy is a potentially less toxic approach than apoptosis induction and provides an alternative treatment of cancer. The differentiation induction effect may also constitute the cellular basis of the clinical action of realgar. Other than the induction of apoptosis, Wang et al. reported realgar nanoformulation pared by milling-induced myeloid differentiation in HL-60 cells [43]. Cell morphology examined by staining with Hoechst 33258 showed difference in the control group and the realgar nanoformulation-treated cells. The realgar nanoformulation-treated cells were shrunken, with relatively small and deformed nuclei, which was

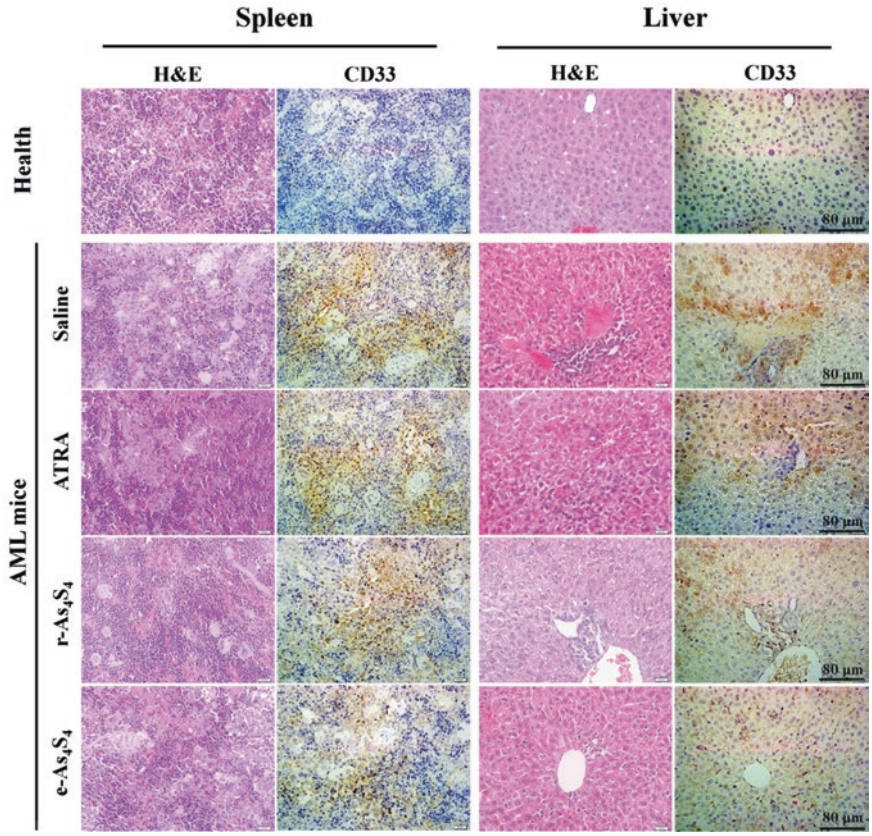

Fig. 10.4 The e-As_4S_4 reduced extramedullary infiltration in spleens and livers after 3-weeks treatment. The scale bar indicates 80 μm [66]

characteristic of mature neutrophils. In contrast, the untreated cells had relatively large and round nuclei. The realgar nanoformulation also increased the nitro-blue tetrazolium (NBT) positive portion and CD11b expression in HL-60 cells.

These *in vitro* and *in vivo* studies suggested that realgar nanoformulations showed more patent therapeutic efficacy than the raw realgar, which provided a promising strategy to decrease the total intake of As_4S_4 for patients. The mechanism of realgar nanoformulations was involved in the induction of apoptosis and differentiation.

10.6.2 Therapeutics Effects of Realgar Nanoformulations in CML

Chronic myeloid leukemia (CML) is a myeloproliferative neoplasm caused by the fusion of the human homologue of the murine Abelson (ABL) gene on chromosome 9 with the breakpoint cluster region (BCR) gene on chromosome 22, which results in the expression of oncoprotein termed BCR-ABL. The BCR-ABL is a constitutively active tyrosine kinase that promotes growth and replication through downstream pathways such as RAS, RAF, JNK, MYC, and STAT [69]. Considering the anti-apoptosis and differentiation retardation effect of the fusion protein, small molecule tyrosine kinase inhibitors (TKIs) were developed and have shown to potently interfere with the interaction between the BCR-ABL protein and adenosine triphosphate (ATP), blocking cellular proliferation of the malignant clone, which changed the landscape dramatically [70]. Nevertheless, TKIs resistance or intolerance happened sometimes, and TKIs caused side effects after a long time such as neutropenia, thrombocytopenia, and anemia [71, 72]; hence it is of significance to develop alternative or supplementary therapeutic options for CML therapy. As described in Sect. 7.2.2, realgar in Chinese traditional compound medicine has showed effectiveness in the treatment of CML. Hence, the nanoformulations of realgar have been investigated in CML for seeking novel therapeutic effects.

In many studies, human CML cell lines were taken as models to investigate the effects of realgar nanoformulation on CML. Shi et al. reported that a realgar nanoformulation prepared by milling decreased relative survival rate of K562 cells in a dose- and time-dependent manner, which could be attributed to the induction of apoptosis and autophagy [33]. Cytometry analysis showed that the realgar nanoformulation increased the portion of annexin V^+ cells and increased cleaved caspase-3 significantly, which is a molecular marker of apoptosis, whereas Bcl2/Bax, which indicates anti-apoptosis intensity, was significantly decreased, all of which indicated apoptosis was induced. Besides, this realgar nanoformulation could also induce autophagy in K562 cells after 24 h incubation possibly by inhibiting PI3K/Akt/mTOR pathway [33]. It was also reported that the realgar nanoformulation reduced the level of BCR-ABL in K562 cells as well as the phosphorylation level of CrkL, a known downstream effector of BCR-ABL after incubation for 24 h.

In this study, the authors have also showed morphologic changes in K562 cells incubated with the milling-prepared realgar nanoformulation by Wright-Giemsa staining: the cytoplasm became more abundant, the nuclei to cytoplasm ratio decreased, and the nucleus became semilunar, implying a differentiation tendency for K562 cells. Wang et al. [34] and Jia et al. [73] unveiled the capacity and underlying mechanisms of hydrophilic realgar nanoparticles in the solid dispersion prepared by HME and further modification (ee-As_4S_4) to induce erythroid and megakaryocytic differentiation, which will be introduced and demonstrated in detail below.

The average hydrodynamic diameter of ee-As_4S_4 was about 470 nm that was significantly reduced comparing to 680 nm of ee-As_4S_4 showed much more potent cytotoxicity than that of the raw realgar, with the IC_{50} of ee-As_4S_4 being 2.4 mg/L in K562 cells after 72 h incubation, while that of the raw realgar being 428.1 mg/L. When incubated with K562 cells, the ee-As_4S_4 could be taken up and reached the highest accumulation in the cells after 12 h incubation, while the raw realgar could hardly be taken up (Fig. 10.5a). Apoptosis has also occurred upon the ee-As_4S_4 incubation. Besides, the ee-As_4S_4 also arrested cell cycle at G2/M phase, which was proved to be associated with the phosphorylation of ERK1/2, since the inhibition of phosphorylation of ERK1/2 inhibited the cell cycle arrest. The apoptosis induction and the arrest of cell cycle together caused cytotoxicity of the e-As_4S_4 towards K562 cells.

Other than the cytotoxicity effect, we also found out that the ee-As_4S_4 also showed the ability to induce erythroid differentiation at non-acute cytotoxic concentrations [34]. When K562 cells were incubated with ee-As_4S_4 72 h followed by benzidine staining, the number of blue-colored cells increased remarkably in the population compared to the untreated group, indicating the occurrence of erythroid differentiation in the cells under ee-As_4S_4 treatment (Fig. 10.5b). Flow cytometric analysis of CD235a, which is a typical surface marker of erythroid differentiation, also agreed with the result of benzidine staining (Fig. 10.5c), indicating that ee-As_4S_4 induced erythroid differentiation in K562 cells. Note that the optimal ee-As_4S_4 dose for erythroid differentiation induction was 2.0 mg/L, which was lower than the IC_{50} at 72 h, implying that the ee-As_4S_4 could induce erythroid differentiation at a relatively less cytotoxic dose.

Importantly, the ee-As_4S_4-induced erythroid differentiation was also detected in bone marrow mononuclear cells isolated from CML patients (Fig. 10.5d). The 1# CML patient was newly diagnosed and had not received any treatment; the proportion of erythroid cells was only about 0.43%, while that of granulocyte cells was 97.5% under the optical microscope, which meant the situation was extremely severe. In this worse status, the treatment with 0.5, 1.0, and 2.0 mg/L of ee-As_4S_4 for 7 days could raise the proportion of CD235a to 1.07%, 1.86%, and 2.36%, respectively, which was equivalent to 2.49-folds, 4.33-folds, and 5.49-folds, respectively. This is a significant improvement for Patient 1#. The 2# CML patient was post-treated with Imatinib for 6 months; the proportion of granulocyte cells was 37.5% and that of erythroid cells was 31.5%. The ee-As_4S_4 was also capable of further increasing the proportion of $CD235a^+$ cells. These results provided valuable clinical evidence that ee-As_4S_4 could induce effective erythroid differentiation.

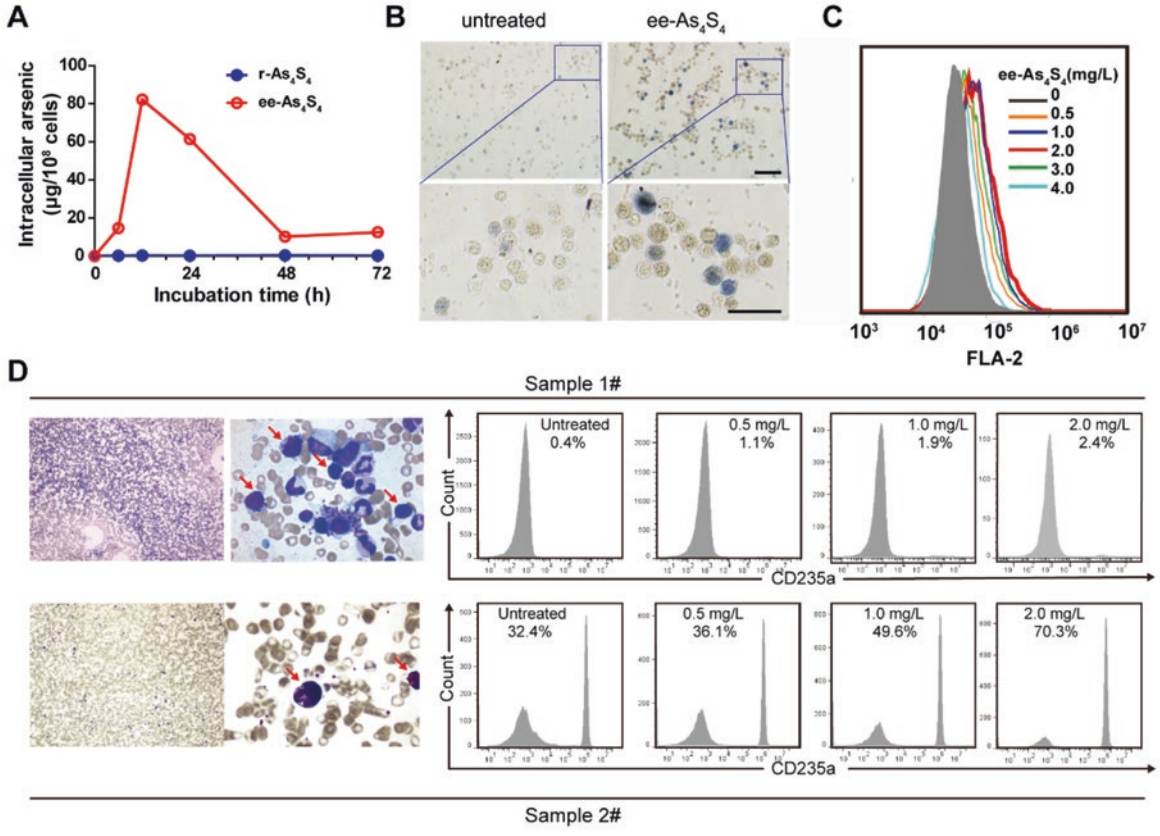

Fig. 10.5 The ee-As_4S_4 induced erythroid differentiation in CML cells. (**a**) Cellular uptake of As_4S_4 in K562 cells incubated with 4.0 mg/L ee-As_4S_4 or r-As_4S_4. (**b**) Representative benzidine staining images of K562 cells incubated with or without ee-As_4S_4; the scale bar indicates 100 μm. (**c**) Overlap distribution of CD235a in K562 cells after incubation with ee-As_4S_4 for 72 h. (**d**) Bone marrow examination images of two CML patients and the percentage of $CD235a^+$ cells in the bone marrow mononuclear cells derived from the two CML patients and incubated with or without ee-As_4S_4 [34]

CML cell differentiation is largely involved with BCR-ABL blockade [74]. It was shown that the ee-As_4S_4 incubation led to a significant reduction of the total amount of BCR-ABL protein that stayed unchanged after the incubation of Imatinib (Fig. 10.6a), suggesting that ee-As_4S_4 interacted with BCR-ABL in a different mechanism from Imatinib. The mRNA of *BCR-ABL* was not changed after the same incubation (Fig. 10.6b), indicating that the ee-As_4S_4-induced BCR-ABL elimination did not take place at the transcriptional level but at post-translational modification. The BCR-ABL fusion protein could be degraded in the autophagy-dependent pathway [75]; the expression of LC3B-II began to increase only after 1 h of ee-As_4S_4 incubation, while BCR-ABL remained unchanged at that time point (Fig. 10.6c), indicating ee-As_4S_4 triggered the autophagy prior to the BCR-ABL elimination, suggesting the BCR-ABL degradation was associated with the induction of autophagy. The autophagosomes accumulation was observed in the cells incubated with ee-As_4S_4 under transmission electron microscope, providing more direct evidence for the induction of autophagy (Fig. 10.6d). Taken together, the ee-As_4S_4 was able to induce erythroid differentiation of both K562 cells and bone marrow mononuclear cells due to the autophagic degradation of BCR-ABL.

Jia et al. showed that the ee-As_4S_4 was also able to induce megakaryocytic differentiation in K562 cells [73]. After incubation with ee-As_4S_4 for 72 h, results obtained from DAPI and Wright-Giemsa staining showed typical morphological change in K562 cells, i.e., the appearance of multiple nuclei (yellow arrow) and giant nuclear structure (red arrow) of megakaryocytes (Fig. 10.7a), clearly indicating the ability of ee-As_4S_4 to induce megakaryocytic differentiation. The megakaryocytic differentiation was confirmed by flow cytometric analysis of CD41a, which is one of the surface markers of megakaryocytes (Fig. 10.7b).

RUNX1 was one of the most important transcription factors involved in megakaryocytic differentiation [76]. It was showed that the mRNA expression level of *RUNX1* was largely improved by ee-As_4S_4 incubation (Fig. 10.7c), and knockdown of *RUNX1* by siRNA reversed the ee-As_4S_4-induced megakaryocytic differentiation (Fig. 10.7d), and strongly confirmed that the ee-As_4S_4 induced megakaryocytic differentiation in K562 cells through transcriptional activation of *RUNX1*. *RUNX1* expression was regulated by HDAC activity. *RUNX1* was repressed by H3 deacetylation and can be reversed by HDAC inhibitors [75]. Chromatin immunoprecipitation (ChIP) assay showed that the ee-As_4S_4 treatment significantly increased the acetylation of histone H3 at *RUNX1* promoter (Fig. 10.7e), indicating that ee-As_4S_4 activated *RUNX1* transcription through acetylation of H3. Furthermore, it was proved that the HDAC activity was downregulated after incubating with ee-As_4S_4 (Fig. 10.7f), therefore drawing the complete picture of the mechanism for megakaryocytic differentiation induction by ee-As_4S_4. The ee-As_4S_4 was able to inhibit HDAC activity and activate *RUNX1* expression, thereby inducing significant megakaryocytic differentiation in CML cells. The erythroid and megakaryocytic differentiation induction effects and mechanisms were illustrated in Fig. 10.8.

Although both realgar nanoformulations (prepared by milling and by HEM) led to the reduction of BCR-ABL, we have noted that the effects of realgar nanoformulations and TKIs on BCR-ABL were largely different in mechanisms. It is well

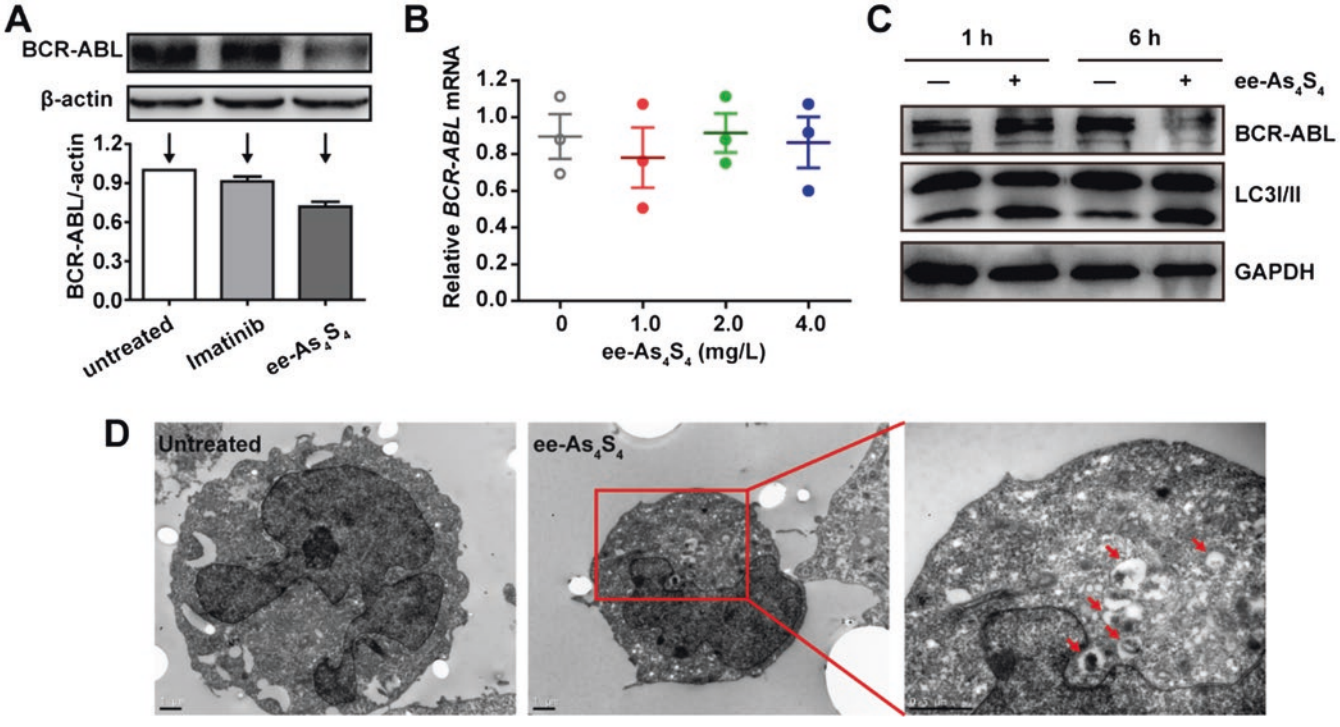

Fig. 10.6 The erythroid differentiation was induced by autophagic degradation of BCR-ABL fusion protein. (**a**) The expression of BCR-ABL in K562 cells incubated with Imatinib and ee-As_4S_4 for 6 h. β-actin served as loading control. (**b**) Expression level of BCR-ABL mRNA in K562 cells incubated with ee-As_4S_4. (**c**) The expression of LC3B and BCR-ABL in K562 cells incubated with ee-As_4S_4 for 1 or 6 h. (**d**) TEM images of K562 cells incubated with ee-As_4S_4. The autophagosomes were pointed by red arrows. The scale bar indicates 1 μm [34]

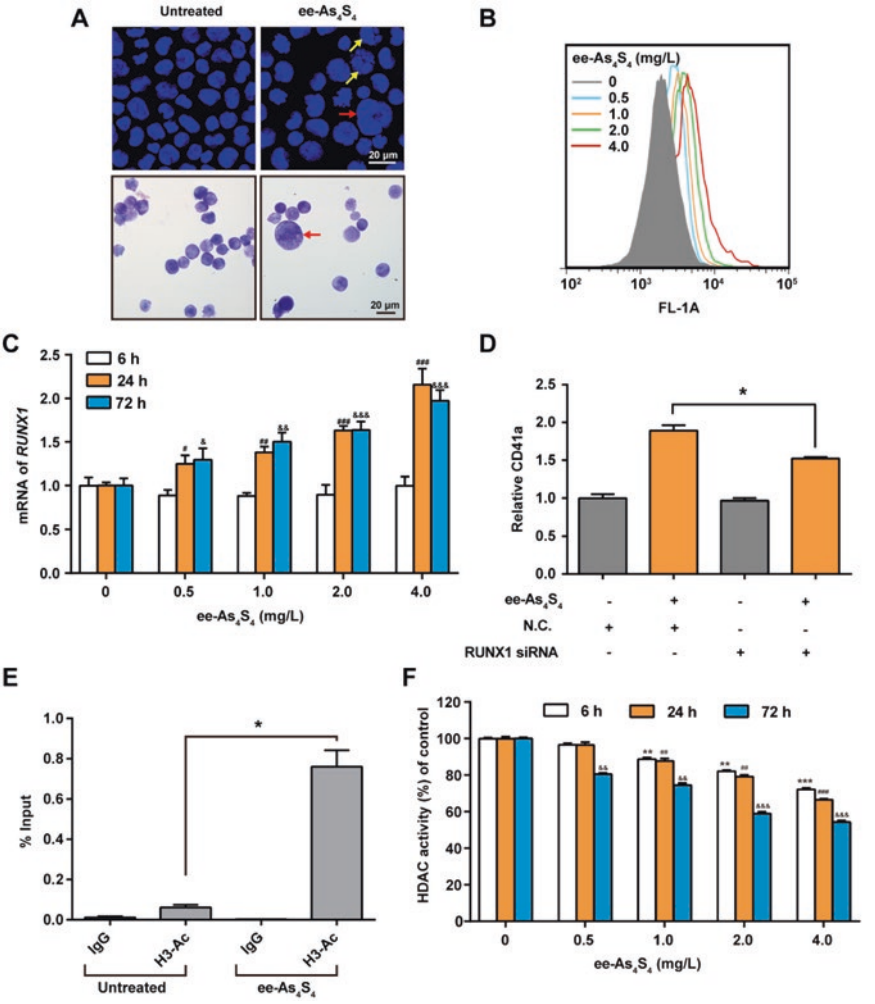

Fig. 10.7 The ee-As_4S_4 induced megakaryocytic differentiation in K562 cells through inhibition of HDAC and the subsequent transcriptional activation of *RUNX1*. (**a**) Morphological changes of K562 cells after incubation with ee-As_4S_4 for 72 h determined by DAPI staining and Wright-Giemsa staining, multiple nuclei was pointed by yellow arrows, and giant nuclear structure was pointed by red arrows. (**b**) Overlap distribution of CD41a in K562 cells after incubation with ee-As_4S_4 for 72 h. (**c**) The ee-As_4S_4 decreased gene expression of *RUNX1* in K562 cells. # $P < 0.05$, ## $P < 0.01$, ### $P < 0.001$ compared to untreated group of 24 h incubation. & $P < 0.05$, && $P < 0.01$, &&& $P < 0.001$ compared to untreated group of 72 h incubation. (**d**) Knockdown of *RUNX1* by siRNA decreased CD41a induced by ee-As_4S_4 in K562 cells. ∗ $P < 0.05$. (**e**) Representative ChIP analysis of *RUNX1* promoter in K562 cells after incubation with ee-As_4S_4 using acetylated H3-specific antibody or control IgG. ∗ $P < 0.05$. (**f**) The ee-As_4S_4 inhibited HDAC activity in K562 cells. ∗∗ $P < 0.01$, ∗∗∗ $P < 0.001$ compared to untreated group of 6 h incubation. # $P < 0.05$, ## $P < 0.01$, ### $P < 0.001$ compared to untreated group of 24 h incubation. & $P < 0.05$, && $P < 0.01$, &&& $P < 0.001$ compared to untreated group of 72 h incubation [73]

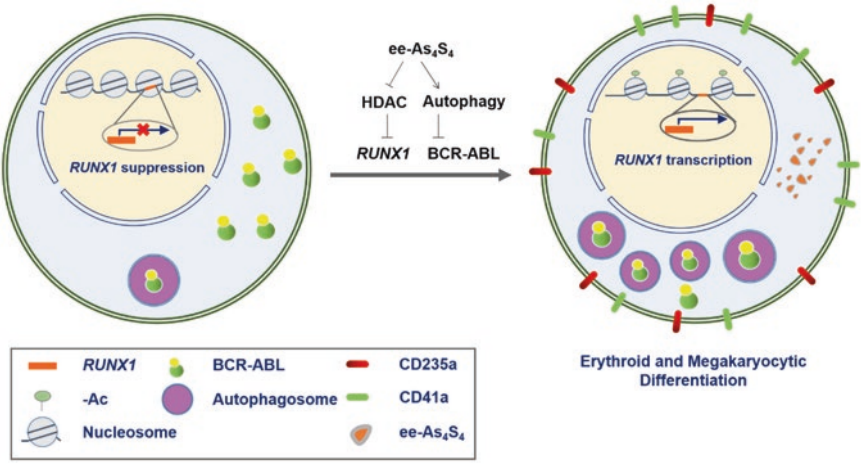

Fig. 10.8 Effects and mechanisms of the e-As_4S_4 on CML cells. The e-As_4S_4 could induce erythroid differentiation through autophagic degradation of BCR-ABL and induce megakaryocytic differentiation through inhibition of HDAC activity and following transcriptional activation of *RUNX1*. (Modified from ref [73])

known that TKIs inhibit the activity of BCR-ABL, therefore inhibiting the phosphorylation of the downstream molecules, while ee-As_4S_4 degraded BCR-ABL directly. The difference provided a chance for synergic administration of the realgar nanoformulations and Imatinib to obtain more effective regime for CML patients. It should be also noted that the induced differentiation on K562 cells and bone marrow cells of CML patients was only reported in ee-As_4S_4 but not As_4S_4 dissolved in sodium hydroxide, which indicated the important role of the compound As_4S_4 in its original chemical structure and in nanoscale size distribution and with hydrophilicity.

Differentiation therapy emerged from the fact that cancer cells may undergo differentiation *ex vivo* when triggered by hormones or cytokines, resulting in irreversibly changing the phenotype of cancer cells [77]. It has gained hallmark success in the treatment of APL by ATRA and As_2O_3. Differentiation therapy is a potentially less toxic approach than apoptosis induction and offers benefit for the improvement of hematopoietic function for leukemia patients, therefore providing an alternative treatment option for CML. Since retarded erythroid differentiation, myeloid differentiation, and megakaryocytic differentiation were largely involved in the occurrence of anemia, neutropenia, and thrombocytopenia, respectively, the ability of differentiation induction for ee-As_4S_4 would be beneficial for the improvement of hematopoietic function of leukemia patients, and dropped a hint that the realgar nanoformulation may also be effective to other diseases related to hematopoietic differentiation, such as MDS.

10.6.3 Therapeutics Effects of Realgar Nanoformulations in Solid Tumor

Other than leukemia, realgar nanoformulations also showed promising *in vivo* therapeutic effects on several solid tumors including breast cancer, melanoma, and hepatoma.

Worldwide, breast cancer is an important cause of suffering for women and premature mortality and accounts for more cancer deaths in women than any site other than lung cancer. In particular, triple-negative breast cancer (TNBC), which is characterized by the absence of estrogen receptors (ER), progesterone receptors (PR), and HER2 receptors, is one of the most aggressive types of breast cancers, marked by high rates of relapse, visceral metastases, and early death [78, 79]. Due to lack of the receptors, TNBC is associated with poor prognosis and limited treatment options [80]. Therefore, there is still an unmet need in the treatment of breast cancer, especially TNBC.

Encouraged by the effectiveness of e-As_4S_4 on mice model of AML, Wang et al. also investigated its therapeutic effects on TNBC [67]. Mouse model of TNBC was established by orthotopically injecting mouse TNBC cells 4T1 close to the nipples, in the mammary fat pad of the naive female BALB/c mice in the right flank. The dosage regime was the same as that in mice of APL [66]. As a result, the e-As_4S_4 prolonged the survival of TNBC mice; specifically, the median survival was 50 days for mice treated with e-As_4S_4, while that was about 30 days for the saline group and 38 days for the raw realgar group. The prolonged survival was attributable to the inhibition of metastasis. The 3-weeks treatment of e-As_4S_4 led to the significant decrease in the number of metastatic foci observed on the lung surface. The histological staining by H&E showed that large metastasis nodules were observed in the lung of saline and Soluplus group while no obvious metastasis nodules were observed in the lung of the e-As_4S_4 group. In addition, there were metastasis nodules distributing in the liver cortex and close to the portal vein of mice in the saline group, while the e-As_4S_4 group showed less and smaller metastasis nodules (Fig. 10.9).

The hypoxic condition in the central area of the solid tumor because of the rapid growth of tumor cells may enhance abnormal angiogenesis, invasion, and metastasis of tumors. Hypoxia-inducible factors (HIF) are activated upon hypoxia. The e-As_4S_4 effectively accumulated in the tumor tissues and showed remarkable effects. After 21 days administration, the tumor mass was collected, followed by digestion and analysis by atomic fluorescence spectroscopy. It was found out that a considerable increase of arsenic was detected in the tumor mass, about 80 ng/g in the e-As_4S_4 group and 20 ng/g in the r-As_4S_4 group, reaching a more than fourfold increase. Immunohistochemical (IHC) and Western blot analysis of HIF-1α showed that the HIF-1α expression in tumor tissues of the TNBC mice was largely decreased in the e-As_4S_4 group (Fig. 10.10a, b). Consequently, the gene expression of *VEGF*, one of the downstream of HIF-1α, was also decreased, which caused the downregulation of angiogenesis, evidenced by decreased positive area in IHC staining of CD31,

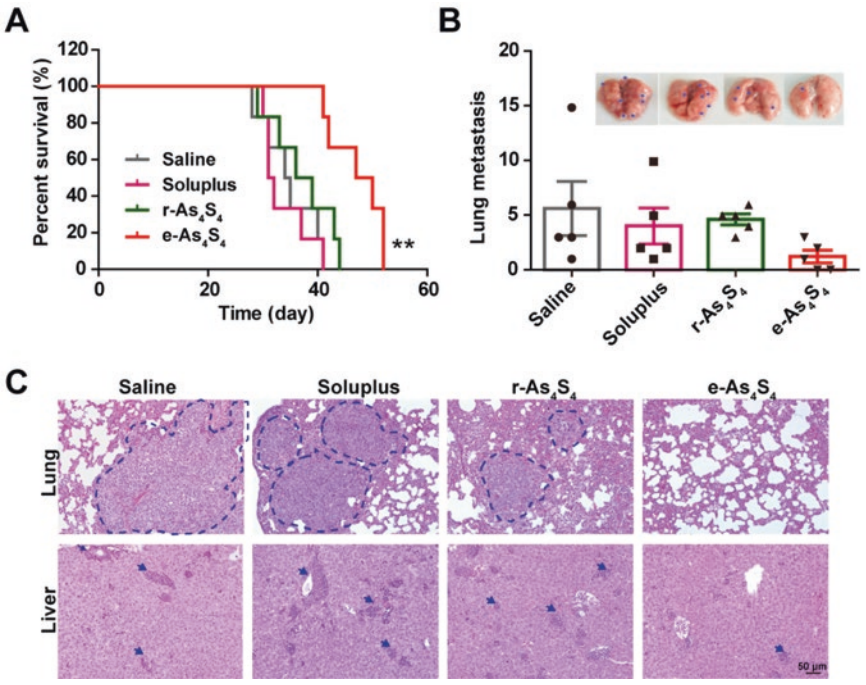

Fig. 10.9 Therapeutic effects of the e-As_4S_4 on breast cancer mice. (**a**) Survival curve of tumor-bearing mice of saline, Soluplus, r-As_4S_4, and e-As_4S_4. $**P < 0.01$. (**b**) Lung metastasis nodules of the four groups after 21-day treatment. The insets were representative gross observation of lung metastasis. (**c**) Representative H&E staining of lung and liver tissues for saline, Soluplus, r-As_4S_4, and e-As_4S_4 [67]

weakened expression level in Western blot analysis, and less pericyte positive endothelial structures in combined staining of CD31 and α-SMA (Fig. 10.10c, d). It has been well established that inflammation is involved in the metastasis of solid tumor [81–83]. In the TNBC mice, oral administration of e-As_4S_4 significantly inhibited the expression of NLRP3 that is constitutively activated and leads to sustained local and systemic inflammation mediated by IL-1β in the tumor (Fig. 10.10e).

Taken together, e-As_4S_4 inhibited liver and lung metastasis and prolonged the survival through regulating the hypoxic microenvironment, angiogenesis, and inflammation. In another investigation, realgar nanoformulation prepared by milling could effectively suppress the abilities of tumor growth, as well as metastasis and angiogenesis in the murine breast cancer metastasis model in a time- and dose-dependent manner through the inhibition of the expression of MMP-2 and MMP-9 [84]. Note that the e-As_4S_4 did not show a significant change in the tumor size and weight, while the milling-prepared nanoformulation suppressed tumor growth, suggesting that nanoformulations of realgar prepared by different approaches may address different effects.

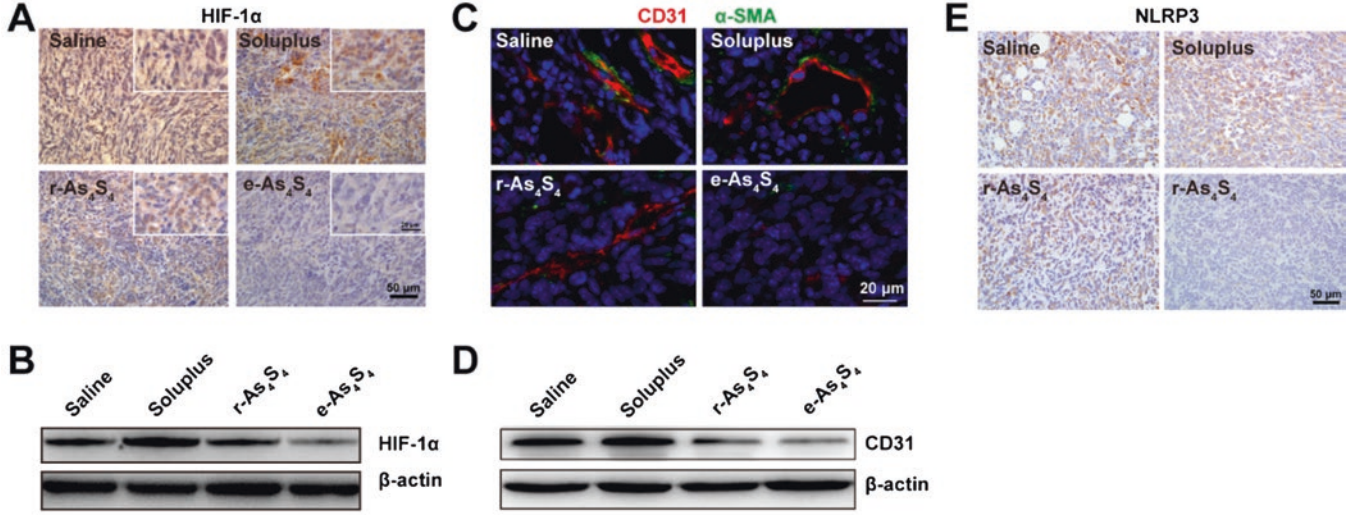

Fig. 10.10 The e-As_4S_4 regulated the hypoxic microenvironment, angiogenesis, and inflammation. The e-As_4S_4 downregulated HIF-1α in tumor tissue detected by IHC (**a**) and Western blot (**b**). (**c**) The e-As_4S_4 decreased CD31 (red) and α-SMA (green) in tumor tissue. (**d**) The e-As_4S_4 decreased CD31 expression in tumor tissue detected by Western blot. (**e**) The e-As_4S_4 decreased NLRP3 expression in tumor tissue detected by IHC [67]

Zhao et al. prepared realgar nanoparticles by milling and then mixed and emulsified with cream for further transdermal drug delivery in a mice model of melanoma that was generated by intradermal injections of mouse melanoma cell line B16 on the dorsal sides of the mice [51]. Transdermal drug delivery of the realgar/cream formulation reduced the tumor volume and therefore improved the survival time of tumor-bearing mice through inhibition of angiogenesis evidenced by a drop in the level of VEGF protein and tumor microvessel densities. Realgar has been used in the treatment of skin diseases in the past. This study suggests that the nanoformulation of realgar can be used as transdermal administration, which broadened the application scope of realgar nanoformulation. The nanoformulations of realgar nanoparticles prepared by milling and the subsequent microcapsules were applied in a mice model of hepatoma by subcutaneously inoculating mouse hepatoma cells H22 into the right axilla. Intragastric administration of the two nanoformulations inhibited the tumor growth and showed 53.14% and 48.55% reduction in tumor volume, respectively [41].

10.6.4 Therapeutic Mechanisms of Realgar in Different Forms

ROS is upregulated in tumor cells and plays a vital part in the survival, proliferation, invasion, and metastasis [85–87]. We have shown that e-As_4S_4 or ee-As_4S_4 could induce myeloid differentiation that has not been observed in the investigations with raw realgar. Existing experimental evidence has indicated the link of the novel effects with the ROS scavenging capacity of nanosized realgar, and the capacity relies on the intrinsic reducibility of As_4S_4. It is known that the arsenic element in realgar is As(II), which is in the lower valence state and can be oxidized to the higher valence state, i.e., As(III) or As(V), meaning realgar has intrinsic reducibility. Different from the raw realgar that has crystal size of several tens of micrometer and not able to be taken up by cells, ee-As_4S_4 could be internalized by cells due to the nanoscaled particle size. When As_4S_4 entered the cells, they could interact with superoxide anion and hydroxyl radicals, and they could also enter the tumor tissues to scavenge reactive oxygen species (ROS) (Fig. 10.11a). Moreover, the effect of suppressing histone deacetylase (HDAC) activity resulted in the inhibition of mitochondrial respiration that is the major source of intracellular ROS, leading to further decrease of ROS (Fig. 10.11b). Taken together, the elimination of ROS by nanosized As_4S_4 was a temporal regulation process; once taken by cells, the As_4S_4 nanoparticles acted as an antioxidant nanoparticles, reacting with intracellular ROS and being oxidized themselves, and the follow-up inhibition of respiration kept ROS downregulating over time. As a result, after incubation with e-As_4S_4 or ee-As_4S_4, ROS in K562 cells decreased over the incubation time (Fig. 10.11c). And for the breast tumor-bearing mice, the oral administration of e-As_4S_4 accumulated in the tumor tissue mass and decreased the ROS in the environment (Fig. 10.11d).

Autophagy has been demonstrated to be associated with the intracellular ROS [88–90]; for example, an antioxidant resveratrol was reported to induce autophagy

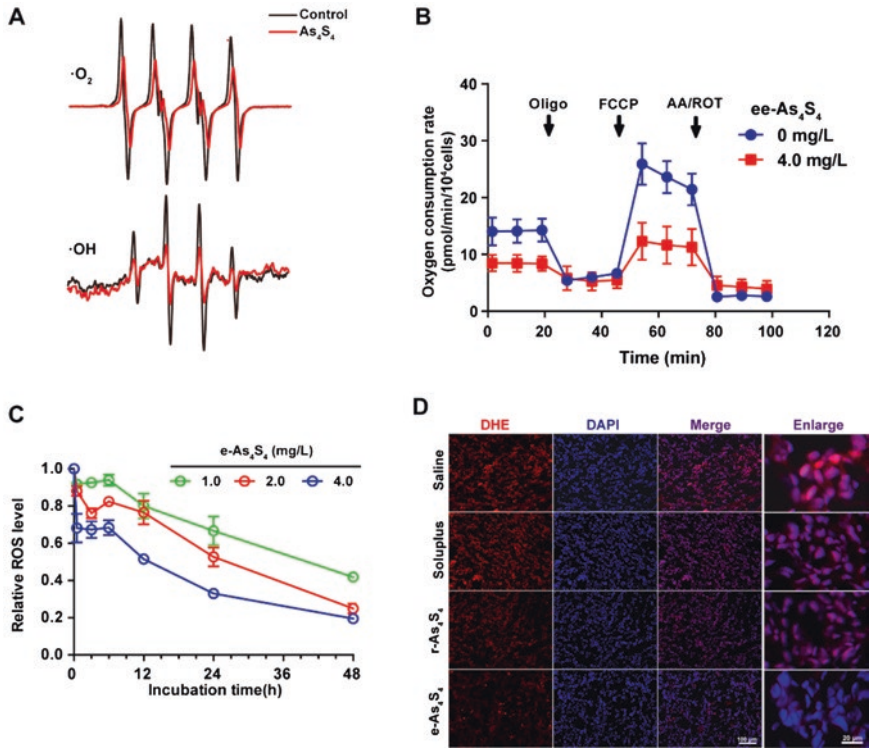

Fig. 10.11 Temporal regulation of ROS by the e-As_4S_4. (**a**) The e-As_4S_4 scavenge superoxide anion and hydroxyl radicals measured by ESR [67]. (**b**) The oxygen consumption rate was weakened after incubation with ee-As_4S_4 for 24 h [73]. (**c**) The ee-As_4S_4 diminished intracellular ROS in K562 cells along with incubation time [34]. (**d**) The e-As_4S_4 downregulated ROS in the tumor tissues of breast mice [67]

by scavenging intracellular ROS [88]. The variation of intracellular ROS was also closely related with the activity of HDAC [45, 91–93]; for example, it was reported that scavenging ROS by quercetin prevented Ni^2+-induced histone hypoacetylation [91]. In our opinion, the reduction of ROS triggered by ee-As_4S_4 in CML cells could be the cause of autophagy and the following degradation of BCR-ABL fusion protein and inhibition of HDAC activity, which induced the erythroid differentiation and megakaryocytic differentiation, respectively [34, 73]. It is well documented that ROS can regulate HIF-1a through both transcriptional and post-translation level [94, 95]; therefore we inferred that the resulting downregulation of HIF-1α by e-As_4S_4 was at least partly regulated by the reduced ROS. Oxidative stress was also closely associated with the formation and activation of NLPR3 inflammasomes [96], so the eliminated NLRP3 could also be triggered by the ROS reduction caused by e-As_4S_4 exposure. Therefore, the ROS scavenging ability may take a crucial part as the common cause for the therapeutic effects on both leukemia and solid tumor.

Except for e-As_4S_4 or ee-As_4S_4, the ROS scavenging ability of realgar has not been reported in any other formulations. Realgar in other different formulations has reported upregulatory effect of intracellular ROS. As examples, Realgar dissolved in sodium hydroxide, in which the arsenic was a compound of As(III) as mentioned before, increased ROS in HL-60 cells [97] and human osteosarcoma cells [98]. Besides, bioleaching preparation of realgar by *Acidithiobacillus ferrooxidans* [99], of which the product was a mixture of As(III) and As(V) compound [100], could also increase ROS in *Caenorhabditis elegans* [101] and hepatoma cell line HepG2 [102]. All these studies implied that realgar was capable of scavenging ROS only when it is in the form of As_4S_4.

Taken together, arsenic in realgar nanoformulation is in the form of As_4S_4, which is totally different from that in any other existing formulations of realgar, thereby exhibiting therapeutic effects unseen before. The mechanisms may explain the existence of some confused issues for a quite long time about the role of arsenic component in cancer treatment and make it possible to unveil the mystery of realgar.

10.7 Summary and Perspectives

The antitumor effect of realgar, especially in APL, has been fully confirmed by *in vitro*, *in vivo*, and clinical studies. Realgar nanotherapeutics have been developed to improve the bioavailability and thereby promote the wider, safer, and more economical application of realgar. These nanotherapeutics especially the hydrophilic arsenic sulfide nanoparticles (e-As_4S_4 or ee-As_4S_4) prepared by HME not only showed much stronger cytotoxic effect than the raw realgar, but also exhibited the capacity of inducing differentiation at non-acute cytotoxic concentrations, therefore describing broad prospects of application due to the unmasking of novel effects and mechanisms.

References

1. T. Zhang, F. Rong, Treatment of acute myeloid leukemia with the injection. Med. Heilongjiang **04**, 7–11 (1979)
2. G.Q. Chen et al., Use of arsenic trioxide (As2O3) in the treatment of acute promyelocytic leukemia (APL).1. As2O3 exerts dose-dependent dual effects on APL cells. Blood **89**(9), 3345–3353 (1997)
3. Z.X. Shen et al., Use of arsenic trioxide (As2O3) in the treatment of acute promyelocytic leukemia (APE).2. Clinical efficacy and pharmacokinetics in relapsed patients. Blood **89**(9), 3354–3360 (1997)
4. G.Q. Chen et al., In vitro studies on cellular and molecular mechanisms of arsenic trioxide (As2O3) in the treatment of acute promyelocytic leukemia: As2O3 induces NB4 cell apoptosis with downregulation of bcl-2 expression and modulation of PML-RAR alpha/PML proteins. Blood **88**(3), 1052–1061 (1996)

5. G.J. Schiller et al., Phase II multicenter study of arsenic trioxide in patients with myelodysplastic syndromes. J. Clin. Oncol. **24**(16), 2456–2464 (2006)
6. N. Vey et al., Arsenic trioxide in patients with myelodysplastic syndromes: a phase II multicenter study. J. Clin. Oncol. **24**(16), 2465–2471 (2006)
7. F.L. Qu et al., Multicenter phase II clinical trial of arsenic trioxide injection in the treatment of primary hepatocarcinoma. Chin. J. Oncol. **33**(9), 697 (2011)
8. X.M. Tan, Q.Y. Xiu, L.I. Bing, Intracavitary administration of Arsenic Trioxide in treatment of lung cancer complicated with pleural effusion. Acad. J. Second Mil. Med. Uni. **29**(7), 866–868 (2009)
9. M.Á. Muñoz-Hernández, Arsenic: inorganic chemistry based in part on the article arsenic: inorganic chemistry, in *Encyclopedia of Inorganic Chemistry*, ed. by R. A. Zingaro, 1st edn., (American Cancer Society, New York, 2011)
10. G.F. Bennett, Environmental chemistry of arsenic. J. Hazard. Mater. **92**(2), 213–215 (2002)
11. J. Wu et al., The medicinal use of realgar (As(4)S(4)) and its recent development as an anticancer agent. J. Ethnopharmacol. **135**(3), 595–602 (2011)
12. A. Zhou et al., Experience in the treatment of acute non lymphocytic leukemia. Shanghai J. Tradit. Chin. Med. **02**, 15–16 (1986)
13. D.P. Lu et al., Tetra-arsenic tetra-sulfide for the treatment of acute promyelocytic leukemia: a pilot report. Blood **99**(9), 3136–3143 (2002)
14. H.H. Zhu et al., The simpler, the better: oral arsenic for acute promyelocytic leukemia. Blood **134**(7), 597–605 (2019)
15. H.H. Zhu et al., Oral tetra-arsenic tetra-sulfide formula versus intravenous arsenic trioxide as first-line treatment of acute promyelocytic leukemia: a multicenter randomized controlled trial. J. Clin. Oncol. **31**(33), 4215 (2013)
16. M.A. Sanz et al., Management of acute promyelocytic leukemia: recommendations from an expert panel on behalf of the European LeukemiaNet. Blood **113**(9), 1875–1891 (2009)
17. H.H. Zhu et al., Oral arsenic plus retinoic acid versus intravenous arsenic plus retinoic acid for non-high-risk acute promyelocytic leukaemia: a non-inferiority, randomised phase 3 trial. Lancet Oncol. **19**(7), 871–879 (2018)
18. H. Jiang et al., Reduced medical costs and hospital days when using oral arsenic plus ATRA as the first-line treatment of acute promyelocytic leukemia. Leuk. Res. **39**(12), 1319–1324 (2015)
19. A. Zhou, B. Yao, J. Zheng, The short-term effect of Qinghuang powder on 25 cases of chronic myeloid leukemia. Chin. J. Integr. Med. **1**, 16–18 (1981)
20. A. Zhou et al., Clinical observation on 86 cases of chronic myeloid leukemia treated with Qinghuang powder. World Congress of Integrated Medicine (1997)
21. S.D. Wang et al., Anti-liver cancer effect and the mechanism of arsenic sulfide in vitro and in vivo. Cancer Chemother. Pharmacol. **83**(3), 519–530 (2019)
22. W.P. Ding et al., Arsenic sulfide as a potential anti-cancer drug. Mol. Med. Rep. **11**(2), 968–974 (2015)
23. L. Zhang et al., Arsenic sulfide inhibits cell migration and invasion of gastric cancer in vitro and in vivo. Drug Des. Devel. Ther. **9**, 5579–5590 (2015)
24. L. Zhang et al., Arsenic sulfide, the main component of realgar, a traditional Chinese medicine, induces apoptosis of gastric cancer cells in vitro and in vivo. Drug Des. Devel. Ther. **9**, 79–92 (2015)
25. X. Liu, The processing method of Realgar in Chinese Pharmacopoeia and the content of As2O3 in Chinese patent medicine. Beijing Journal of Traditional Chinese Medicine. **1**, 42–43 (2000)
26. I. Koch et al., Bioaccessibility and excretion of arsenic in Niu Huang Jie Du Pian pills. Toxicol. Appl. Pharmacol. **222**(3), 357–364 (2007)
27. R.N. Ratnaike, Acute and chronic arsenic toxicity. Postgrad. Med. J. **79**(933), 391–396 (2003)
28. T. Tisler, J. Zagorc-Koncan, Acute and chronic toxicity of arsenic to some aquatic organisms. Bull. Environ. Contam. Toxicol. **69**(3), 421–429 (2002)

29. J.Z. Wu, P.C. Ho, Speciation of inorganic and methylated arsenic compounds by capillary zone electrophoresis with indirect UV detection. Application to the analysis of alkali extracts of As2S2 (realgar) and As2S3 (orpiment). J. Chromatogr. A **1026**(1-2), 261–270 (2004)
30. T. Yin et al., Combined effects of As4S4 and imatinib on chronic myeloid leukemia cells and BCR-ABL oncoprotein. Blood **104**(11), 246b–247b (2004)
31. F. Kosek et al., New analytic method for investigation of the distribution of bonds in as-S system. J. Non Cryst. Solids **90**(1–3), 401–404 (1987)
32. J.E. Li et al., Apoptotic effect of As2S2 on K562 cells and its mechanism. Acta Pharmacol. Sin. **23**(11), 991–996 (2002)
33. D. Shi et al., Caveolin-1 contributes to realgar nanoparticle therapy in human chronic myelogenous leukemia K562 cells. Int. J. Nanomedicine **11**, 5823–5835 (2016)
34. T. Wang et al., Arsenic sulfide nanoformulation induces erythroid differentiation in chronic myeloid leukemia cells through degradation of BCR-ABL. Int. J. Nanomedicine **14**, 5581–5594 (2019)
35. J.H. Mao et al., As4S4 targets RING-type E3 ligase c-CBL to induce degradation of BCR-ABL in chronic myelogenous leukemia. Proc. Natl. Acad. Sci. U. S. A. **107**(50), 21683–21688 (2010)
36. J.Z. Wu, P.C. Ho, Evaluation of the in vitro activity and in vivo bioavailability of realgar nanoparticles prepared by cryo-grinding. Eur. J. Pharm. Sci. **29**(1), 35–44 (2006)
37. Y. Deng et al., Size effects of realgar particles on apoptosis in a human umbilical vein endothelial cell line: ECV-304. Pharmacol. Res. **44**(6), 513–518 (2001)
38. D. Cholujova et al., Realgar nanoparticles versus ATO arsenic compounds induce in vitro and in vivo activity against multiple myeloma. Br. J. Haematol. **179**(5), 756–771 (2017)
39. W. Fang et al., (-)-Epigallocatechin-3-gallate encapsulated realgar nanoparticles exhibit enhanced anticancer therapeutic efficacy against acute promyelocytic leukemia. Drug Deliv. **26**(1), 1058–1067 (2019)
40. M. Pastorek et al., Realgar (As4S4) nanoparticles and arsenic trioxide (As2O3) induced autophagy and apoptosis in human melanoma cells in vitro. Neoplasma **61**(6), 700–709 (2014)
41. F. Shi, N. Feng, E. Omari-Siaw, Realgar nanoparticle-based microcapsules: preparation and in-vitro/in-vivo characterizations. J. Pharm. Pharmacol. **67**(1), 35–42 (2015)
42. Y. Tian et al., Enhanced antitumor activity of realgar mediated by milling it to nanosize. Int. J. Nanomedicine **9**, 745–757 (2014)
43. N. Wang et al., Realgar-induced differentiation is associated with MAPK pathways in HL-60 cells. Cell Biol. Int. **32**(12), 1497–1505 (2008)
44. X.B. Wang et al., Nanoparticle realgar powders induce apoptosis in U937 cells through caspase MAPK and mitochondrial pathways. Arch. Pharm. Res. **30**(5), 653–658 (2007)
45. C.C. Wu et al., Upregulation of Znf179 acetylation by SAHA protects cells against oxidative stress. Redox Biol. **19**, 74–80 (2018)
46. R.G. Xi et al., Roles of PI3-K/Akt pathways in nanoparticle realgar powders-induced apoptosis in U937 cells. Acta Pharmacol. Sin. **29**(3), 355–363 (2008)
47. W. Xu et al., Reno-protective effect of realgar nanoparticles on lupus nephritis of MRL/Lpr mice through STAT1. Iran. J. Immunol. **16**(2), 170–181 (2019)
48. H. Ye et al., Realgar nanoparticles induced cytotoxicity in promyelocytic leukemia HL-60 cells. Conf. Proc. IEEE Eng. Med. Biol. Soc. **2005**, 7714–7717 (2005)
49. H.Q. Ye et al., Membrane toxicity accounts for apoptosis induced by realgar nanoparticles in promyelocytic leukemia HL-60 cells. Biol. Trace Elem. Res. **103**(2), 117–132 (2005)
50. M.H. Zhang et al., Combination of LC/MS and GC/MS based metabolomics to study the hepatotoxic effect of realgar nanoparticles in rats. Chin. J. Nat. Med. **15**(9), 684–694 (2017)
51. Q.H. Zhao et al., Anticancer effect of realgar nanoparticles on mouse melanoma skin cancer in vivo via transdermal drug delivery. Med. Oncol. **27**(2), 203–212 (2010)
52. W. Zhao et al., Effect of size and processing method on the cytotoxicity of realgar nanoparticles in cancer cell lines. Int. J. Nanomedicine **6**, 1569–1577 (2011)

53. X.Q. Zhan et al., A study on preparation and diameter determination of realgar granule of micron or nanometer dimension. J. Nanjing Univ. Tradit. Chin. Med. (2003)
54. Y. Guo, *Preparation of Chinese Medicine-Realgar Nanoparticles by Templates and the Studies of Its Biological Effects* (Guangxi Normal University, Guilin, 2005)
55. Y.L. An et al., Preparation and characterization of realgar nanoparticles and their inhibitory effect on rat glioma cells. Int. J. Nanomedicine **6**, 3187–3194 (2011)
56. N. Ning et al., Realgar nano-particles induce apoptosis and necrosis in leukemia cell lines K562 and HL-60. China J. Chin. Mater. Med. **30**(2), 136–140 (2005)
57. J. Wang et al., Arsenic(II) sulfide quantum dots prepared by a wet process from its bulk. J. Am. Chem. Soc. **130**(35), 11596–11597 (2008)
58. H. Wang et al., Apoptosis and necrosis induced by novel realgar quantum dots in human endometrial cancer cells via endoplasmic reticulum stress signaling pathway. Int. J. Nanomedicine **10**, 5505–5512 (2015)
59. Z. Bujnakova et al., Preparation, properties and anticancer effects of mixed As4S4/ZnS nanoparticles capped by Poloxamer 407. Korean J. Couns. Psychother. **71**, 541–551 (2017)
60. T. Guo et al., Effect of stability and dissolution of realgar nano-particles using solid dispersion technology. China J. Chin. Mater. Med. **38**(17), 2782–2787 (2013)
61. J.P. Moschwitzer, Drug nanocrystals in the commercial pharmaceutical development process. Int. J. Pharm. **453**(1), 142–156 (2013)
62. R. Shegokar, R.H. Muller, Nanocrystals: industrially feasible multifunctional formulation technology for poorly soluble actives. Int. J. Pharm. **399**(1-2), 129–139 (2010)
63. P. Tran et al., Overview of the manufacturing methods of solid dispersion technology for improving the solubility of poorly water-soluble drugs and application to anticancer drugs. Pharmaceutics **11**(3), 132 (2019)
64. M.F. Simoes, R.M.A. Pinto, S. Simoes, Hot-melt extrusion in the pharmaceutical industry: toward filing a new drug application. Drug Discov. Today **24**(9), 1749–1768 (2019)
65. C. Brown et al., *Hot-Melt Extrusion for Solid Dispersions: Composition and Design Considerations* (Springer, New York, 2014)
66. Q. Ma et al., Fabrication of water-soluble polymer-encapsulated As4S4 to increase oral bioavailability and chemotherapeutic efficacy in AML mice. Sci. Rep. **6**, 29348 (2016)
67. T. Wang et al., Inhibition of murine breast cancer metastases by hydrophilic As4S4 nanoparticles is associated with decreased ROS and HIF-1alpha downregulation. Front. Oncol. **9**, 333 (2019)
68. H.J. Iland, Curative strategies in APL. Semin. Hematol. **56**(2), 131–138 (2019)
69. E. Jabbour, H. Kantarjian, Chronic myeloid leukemia: 2014 update on diagnosis, monitoring, and management. Am. J. Hematol. **89**(5), 547–556 (2014)
70. J.M. Goldman, Chronic myeloid leukemia: a historical perspective. Semin. Hematol. **47**(4), 302–311 (2010)
71. A. Hochhaus et al., Long-term outcomes of imatinib treatment for chronic myeloid leukemia. N. Engl. J. Med. **376**(10), 917–927 (2017)
72. T. O'Hare et al., Pushing the limits of targeted therapy in chronic myeloid leukaemia. Nat. Rev. Cancer **12**(8), 513–526 (2012)
73. M. Jia et al., Arsenic Sulfide Nanoformulation Induces Megakaryocytic Differentiation through Histone Deacetylase Inhibition. Advanced Therapeutics **3**(5), 1900151 (2020)
74. A. Pierce et al., BCR-ABL alters the proliferation and differentiation response of multipotent hematopoietic cells to stem cell factor. Oncogene **21**(19), 3068–3075 (2002)
75. B.A. Vishwakarma et al., Runx1 repression by histone deacetylation is critical for Setbp1-induced mouse myeloid leukemia development. Leukemia **30**(1), 200–208 (2016)
76. N. Pencovich et al., Dynamic combinatorial interactions of RUNX1 and cooperating partners regulates megakaryocytic differentiation in cell line models. Blood **117**(1), e1–e14 (2011)
77. H. de The, Differentiation therapy revisited. Nat. Rev. Cancer **18**(2), 117–127 (2018)
78. A.D. Elias, Triple-negative breast cancer a short review. Am. J. Clin. Oncol. **33**(6), 637–645 (2010)

79. M. Montagner et al., SHARP1 suppresses breast cancer metastasis by promoting degradation of hypoxia-inducible factors. Nature **487**(7407), 380–384 (2012)
80. F. Tomao et al., Triple-negative breast cancer: new perspectives for targeted therapies. Oncotargets Ther. **8**, 177–193 (2015)
81. L.M. Coussens, Z. Werb, Inflammation and cancer. Nature **420**(6917), 860–867 (2002)
82. B.Z. Qian, Inflammation fires up cancer metastasis. Semin. Cancer Biol. **47**, 170–176 (2017)
83. C.T. Vincent, J. Fuxe, EMT, inflammation and metastasis. Semin. Cancer Biol. **47**, 168–169 (2017)
84. X. Xi, et al. Realgar Nanoparticles Inhibit Migration, Invasion and Metastasis in a Mouse Model of Breast Cancer by Suppressing Matrix Metalloproteinases and Angiogenesis. Curr Drug Deliv. **17**(2), 148–158 (2020)
85. J.G. Gill, E. Piskounova, S.J. Morrison, Cancer, oxidative stress, and metastasis. Cold Spring Harb. Symp. Quant. Biol. **81**, 163–175 (2016)
86. J.N. Moloney, T.G. Cotter, ROS signalling in the biology of cancer. Semin. Cell Dev. Biol. **80**, 50–64 (2018)
87. V. Sosa et al., Oxidative stress and cancer: an overview. Ageing Res. Rev. **12**(1), 376–390 (2013)
88. Y. Cao et al., ROS functions as an upstream trigger for autophagy to drive hematopoietic stem cell differentiation. Hematology **21**(10), 613–618 (2016)
89. Q. Liang, X.P. Wang, T.S. Chen, Resveratrol protects rabbit articular chondrocyte against sodium nitroprusside-induced apoptosis via scavenging ROS. Apoptosis **19**(9), 1354–1363 (2014)
90. M.A. Moosavi et al., Photodynamic N-TiO2 nanoparticle treatment induces controlled ROS-mediated autophagy and terminal differentiation of leukemia cells. Sci. Rep. **6** (2016)
91. F. Chen et al., Inhibition of histone deacetylase reduces transcription of NADPH oxidases and ROS production and ameliorates pulmonary arterial hypertension. Free Radic. Biol. Med. **99**, 167–178 (2016)
92. J. Chen, J. Han, J. Wang, Prevention of cytotoxicity of nickel by quercetin: the role of reactive oxygen species and histone acetylation. Toxicol. Ind. Health **29**(4), 360–366 (2013)
93. Z. Zhang et al., Role of histone acetylation in activation of nuclear factor erythroid 2-related factor 2/heme oxygenase 1 pathway by manganese chloride. Toxicol. Appl. Pharmacol. **336**, 94–100 (2017)
94. L. Iommarini et al., Non-canonical mechanisms regulating hypoxia-inducible factor 1 alpha in cancer. Front. Oncol. **7**, 286 (2017)
95. S. Movafagh, S. Crook, K. Vo, Regulation of hypoxia-inducible factor-1a by reactive oxygen species: new developments in an old debate. J. Cell. Biochem. **116**(5), 696–703 (2015)
96. K. Schroder, J. Tschopp, The inflammasomes. Cell **140**(6), 821–832 (2010)
97. X.M. Hu et al., Involvement of oxidative stress associated with glutathione depletion and p38 mitogen-activated protein kinase activation in arsenic disulfide-induced differentiation in HL-60 cells. Leuk. Lymphoma **55**(2), 392–404 (2014)
98. G. Wang et al., Arsenic sulfide induces apoptosis and autophagy through the activation of ROS/JNK and suppression of Akt/mTOR signaling pathways in osteosarcoma. Free Radic. Biol. Med. **106**, 24–37 (2017)
99. X. Zhang et al., Biological extraction of realgar by *Acidithiobacillus ferrooxidans* and its in vitro and in vivo antitumor activities. Pharm. Biol. **48**(1), 40–47 (2010)
100. P. Chen et al., Properties of realgar bioleaching using an extremely acidophilic bacterium and its antitumor mechanism as an anticancer agent. Biol. Res. **50** (2017)
101. J. Zhi de et al., Realgar bioleaching solution suppress ras excessive activation by increasing ROS in *Caenorhabditis elegans*. Arch. Pharm. Res. **37**(3), 390–398 (2014)
102. P. Song et al., Realgar transforming solution displays anticancer potential against human hepatocellular carcinoma HepG2 cells by inducing ROS. Int. J. Oncol. **50**(2), 660–670 (2017)

Chapter 11
Fabrication and Applications of Magnetic Nanoparticles-Based Drug Delivery System: Challenges and Perspectives

Fei Xiong and Yuxiang Sun

Abstract Engineered magnetic nanoparticles (MNPs) have aroused great interest due to their excellent physicochemical properties such as optic, electronic, and especially magnetics, which could be in combination with the nano-size effect favorable for biomedical applications. Recently, MNPs as multifunctional nanoplatforms have opened a new avenue for simultaneous therapeutic systems and magnetic resonance imaging (MRI) monitoring systems. In particular, the use of the external magnetic field could enhance the penetration into the hypoxic tumor regions overcoming the inefficiency of conventional cancer therapeutic methods. Among the versatile MNPs-based nanocarriers, iron oxides mainly consisted of superparamagnetic maghemite (γ-Fe_2O_3) and magnetite (Fe_3O_4) nanoparticles with a size of 10–100 nm have been widely utilized owing to the good biocompatibility and feasible surface modification by organic and/or inorganic agents for drug loading. In this chapter, we discuss the role of size, surface, and shape (3S) in influencing the in vitro cellular uptake and in vivo biodistribution behaviors and focus on the current challenges regarding the translational of MNPs in clinics aiming at optimizing the system for effective drug transportation. New perspectives are also put forward to outline the future development tendency of MNPs-based drug delivery system.

Keywords Magnetic nanoparticles · Drug delivery system · Iron oxides · Theranostics

F. Xiong (✉) · Y. Sun
State Key Laboratory of Bioelectronics, Jiangsu Key Laboratory for Biomaterials and Devices, School of Biological Science and Medical Engineering & Collaborative Innovation Center of Suzhou Nano-Science and Technology, Suzhou Key Laboratory of Biomaterials and Technologies, Southeast University, Nanjing, P.R. China
e-mail: xiongfei@seu.edu.cn

H. Xu, N. Gu (eds.), *Nanotechnology in Regenerative Medicine and Drug Delivery Therapy*, https://doi.org/10.1007/978-981-15-5386-8_11

11.1 Composition of MNPs Drug Carriers

The composition of MNPs drug carriers not only needs the MNPs at the core, but also needs proper drugs to be loaded. In general, the MNPs drug carriers have a core-shell structure, the MNPs act as the core and the surface modifiers and drugs show as the shell layer. Various kinds of MNPs have been applied to the delivery of drugs, including Fe_3O_4 NPs, γ-Fe_2O_3 NPs, and ferroferric oxide doped with other elements such as Mn, Co, and Zn [1]. For the multicomponent MNPs, the magnetic properties of MNPs can be controlled by changing the composition. This can be seen in MFe_2O_4 (M = Fe, Co, Ni, and Mn), a magnetic ferrite with a reverse spinel structure [2]. In the Fe_3O_4 structure, oxygen ions form a close-packed structure, and Fe ions are located in octahedral (O) and tetrahedral (T) gaps. Fe_3O_4 can be written as $[Fe^{3+}]_T[Fe^{2+}Fe^{3+}]_OO_4$. In this structure, Fe–O–Fe bond of Fe^{3+} in T and O position leads to the elimination of antiferromagnetic coupling and Fe^{3+} magnetic moment. Therefore, the total magnetic moment of Fe_3O_4 structure comes from the net magnetic moment of Fe^{2+}. By doping Mn^{2+} (d 5), Co^{2+} (d 7), or Ni^{2+} (d 8) instead of Fe^{2+} (d 6), the net magnetization of MFe_2O_4 can be adjusted from 4 to 5, 3, and 2 μB, respectively (μB, Bohr magneton, natural unit of electronic magnetic moment). In fact, the same trend has been verified in a series of monodisperse MFe_2O_4 MNPs with the same size at 12 nm [2]. The saturation magnetic moments of $MnFe_2O_4$, Fe_3O_4, $CoFe_2O_4$, and $NiFe_2O_4$ MNPs are 110, 101, 99, and 85 EMU g^{-1} metal, respectively. Doping Zn^{2+} in the structure can further improve the magnetization of MFe_2O_4 MNPs [3]. This modulation of MNPs is very important for further development of sensitive magnetic probes for biomedical applications.

In addition, alloy NPs (e.g., Fe@Pt and Fe@Au [4, 5]) and multifunctional MNPs with core/shell, dumbbell, or multicomponent hybrid structures were attractive and have also been developed to deliver drugs (Fig. 11.1) [6]. Although the noble metal-modified MNPs un-succeeded to improve the magnetic properties, it increased the photothermal conversion efficiency of the nanoparticles, thereby increasing the sensitivity of the tumor to chemotherapy drugs and promoting tumor killing. Therefore, the fabrication of MMPs core is crucial for the application for drug delivery.

There are many kinds of surface modifiers, including small molecular compounds, polymeric materials, and natural materials. And the surface modifier is usually necessary. The surface modification of MNPs can affect the cytotoxicity in vitro and the distribution and excretion of particles in vivo. When testing the cytotoxicity of Fe_3O_4 nanoparticles in vitro, the untreated Fe_3O_4 nanoparticles are easier to adsorb OH^{-1} and CL^{-1} on the surface, which will be negatively charged. The electric field generated by the charge will attract the counterions, so it is easy to combine with the protein and is easily removed by the endothelial system. When the exposed MNPs act on living organisms, the particles are easily combined with plasma proteins and quickly swallowed by macrophages. When there are inclusions on the particle surface, the functional groups carried by the inclusions are ionized in the solution to make the particles charged. For example, when the functional group is a

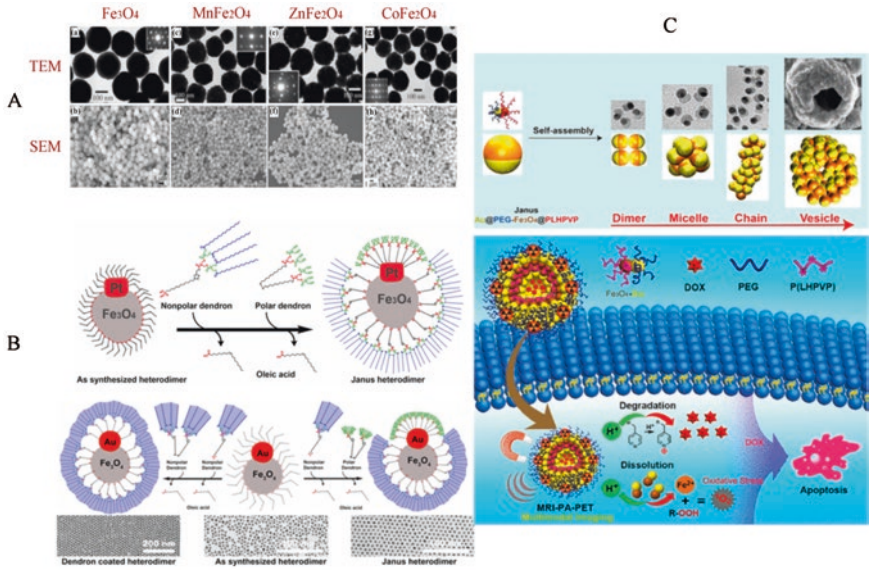

Fig. 11.1 Ferroferric oxide doped with other elements such as Mn, Co, and Zn (**a**) [1]. Alloy NPs Fe@Pt and Fe@Au and their behavior of drug loading (**b**, **c**) [4, 5]

carboxyl group, the particles will be negatively charged. When the functional group is an amine group, the particles will be positively charged. A particle surface charge and the charge type both will affect the distribution of the particle in the body. Because the cell membrane carries a negative point charge, when the particles are positively charged, nonspecific binding occurs with the cells. When the particles are negatively charged, nonspecific binding occurs with the tissue. When the particles are not charged, it is not easy to bind to plasma proteins, but self-agglomeration is prone to reduce the blood circulation time of the particles. Regardless of whether the particles are positively or negatively charged, increasing the charge will make the particles easier to be swallowed and reduce the blood circulation time of the particles. Different encapsulation materials have different toxicity to cells. Some studies have shown that the surface containing carboxyl groups is more toxic than the iron oxide nanoparticles containing amine groups, which may be related to the type of charges on the particle surface.

Of course, a variety of different surface modifiers can be modified on the same MNPs surface to give full play to their own characteristics, but balance the adverse effects of different materials. Mn–Zn ferrite NPs rendered more excellent magnetic properties; Xie et al. [7] prepared the Mn–Zn ferrite NPs coated with a biocompatible PEG-phospholipid (DSPE-PEG2000) and further modified by a cyclic tripeptide of arginine-glycine-aspartic acid (RGD). The PEG-based MNPs passive targeting can successfully accumulate to the tumor due to the enhanced permeability and retention (EPR) effects, in which the phospholipid layer of DSPE can increase the affinity between the MNPs surface and the cell membrane, meanwhile,

PEG endows the nanoparticles with long-term blood circulation, and RGD peptides provide the properties to actively targeting to the tumor, because most tumors overexpress integrin receptors, which can actively bind to RGD peptides. However, the composition of MNPs drug carriers is the key to determine its drug loading characteristics. In this process, not only the feasibility of particle preparation, but also the feasibility of combination of carrier and drugs should be considered. This will be described in detail in the following section.

11.2 Applications of MNPs

11.2.1 Drugs Carriers

Chemotherapy drugs generally lack specificity, and they can cause damage to the normal cells. The application of drug carriers theoretically provides sustained release of drugs and reduces the side effects of chemotherapy drugs. Nanocarriers have advantages in drugs targeted delivery and accumulation of synergetic agents into the lesions, in reducing drug dosage and adverse effects to the normal cells, and in controlling drug release and the prolonged blood circulating time to avoid quick biodegradation, as well as in overcoming drug resistance [8, 9].

In 1979, Widder et al. [10] reported the application of MNPs to treat tumors. Their research confirmed that SPIONs coupled with adriamycin are effective for tumors by intravenous injection. The application of MNPs as a drug carrier significantly shortened the course of treatment; meanwhile, injection drug-containing SPIONs into the tumor site through the arteries showed a 200-fold increase in targeting compared to intravenous injections. Doxorubicin (DOX) is a widely used antitumor drug in clinic, but its toxic and side effects limit its use. Zou et al. [11] reported a general approach to create polyethylenimine (PEI)-based hybrid nanogels (NGs) incorporated with ultrasmall Fe_3O_4 MNPs and DOX for T1-weighted MR imaging-guided chemotherapy of tumors. The formed hybrid NGs possess good water dispersibility and colloidal stability, excellent DOX loading efficiency (51.4%), and pH-dependent release profile of DOX with an accelerated release rate under acidic pH; in contrast to the drug-free NGs that possess good cytocompatibility, the DOX-loaded hybrid NGs display appreciable therapeutic activity and can be taken up by cancer cells in vitro.

DOX is the most widely investigated chemotherapeutic drug assembled with MNPs; in fact, various chemotherapeutic drugs have also been reportedly assembled such as paclitaxel, methotrexate, platinum (Pt)-based drugs, and mitoxantrone. These loaded drugs enhanced the therapeutic effect to a certain extent by MNPs delivery. Yang et al. [12] coupled paclitaxel and Fe_3O_4 MNPs to form a complex, which acted on the pathological site of mice injected with human myeloma stem cells. The results showed that paclitaxel nanocomposites significantly inhibited the secretion of IL-6, increased the expression of apoptotic protease-8, apoptotic protease-9, and apoptotic protease-3, and induced the apoptosis of tumor cells. Li et al. [13] synthesized

multifunctional MNPs drug carriers containing mitoxantrone; in vitro experiments showed that the inhibition rate of the drug carrier on 4T1 cells was 2.5 times that of mitoxantrone alone, and in vivo experiments also showed that the inhibition rate of the drug carrier on tumor tissue was as high as 83.14%, but the toxicity is significantly reduced.

In addition, based on the excellent magnetic performance, MNPs also show great pre-application in magnetically targeted drug delivery, as well as in magnetic hyperthermia, magnetic resonance imaging (MRI), and tumor theranostics.

11.2.2 Targeted Drugs Carriers

However, the drugs released in the body will still circulate in the blood; the loading system of nontargeted drug delivery still faces the problems of systemic toxicity and low utilization. MNPs have the potential of multiple targeting; on the one hand, they can be passively targeted to the specific human tissue according to the size, surface, and shape of nanoparticles (this is described in detail below), and on the other hand, drugs-loaded MNPs can achieve magnetic-guided targeting under the effect of external magnetic field. The targeted delivery of MNPs after drug binding mainly depends on the strength of external magnetic field and the size of IONPs. Passive target delivery is mainly due to the size of IONPs that can reach the required parts [14]. In tumor microenvironment, small particles can penetrate tumor tissue because of the imperfection of tumor vasculature and the absence of the lymphatic system. This is the so-called enhanced penetration and retention effect, which is also considered to be an important standard for the development of antitumor drugs [15]. The intensity of external magnetic field can not only maintain the position of particles reaching the target but also maintain a certain gradient by adjusting the intensity, which is conducive to the release of drugs reaching the target.

Nigam et al. [16] evaluated the magnetically guided delivery of DOX-loaded dendritic-Fe_3O_4 nanoparticles and their tumor regression efficacy in subcutaneous melanoma in C57BL/6 mice. They found that the NPs localized in lungs, liver, and spleen suggesting nonspecific uptake; however, in tumor-bearing mice, substantially higher localization in magnetically targeted tumor was observed when compared to passive localization in nontargeted tumor. The animals of treated group also showed significantly higher iron levels (161 μg of Fe/mg dry organ weight) in the tumor than that of the control (<25 μg of Fe/mg dry organ weight). This magnetically targeted localization led to high concentrations of DOX in the tumor which not only induced significant tumor regression but also arrested further growth. Interestingly, it has also been proved in vitro that magnetic guidance can promote tumor cells to englobe more drugs-loaded MNPs. Platinum (Pt)-based drugs are popular in clinics as chemotherapeutic agents to treat solid tumors, in spite of severe side effects such as nephrotoxicity and neurotoxicity. Quarta et al. [17] synthesized the complex by covalently binding Pt(ii) complexes to IONPs; the intracellular uptake and cell distribution studies of Pt-tethered MNPs on breast and ovarian

cancer cell line models indicate that Pt@MNPs facilitate cellular internalization, and the magnetic nanoparticles (MNPs) enhance the uptake of MNP-Pt conjugates if a magnet is placed beneath the culture dish of tumor cells.

IONPs MNPs can not only load drug molecules and targeted delivery but also protect drug molecules to a certain extent, so that they can reach the lesion site smoothly. Sato et al. [18] loaded paclitaxel onto Fe_3O_4 MNPs to act on human prostate cancer cells. The results showed that Fe_3O_4 MNPs enhanced the killing effect of paclitaxel on human prostate cancer cells, and proved that Fe_3O_4-paclitaxel complex could inhibit the expression of NF-κB in human prostate cancer cell line, but not in Fe_3O_4 MNPs and paclitaxel alone.

11.2.3 Magnetic Hyperthermia

Magnetic hyperthermia is a kind of therapy that can make thermogenic materials gather at the tumor site by direct injection, intravenous injection, or intervention, and generate magnetic thermogenic effect under the action of alternating magnetic field to heat tumor tissue and kill cancer cells. In general, cancer cells are more sensitive to temperature rise than normal cells. By regulating the alternating magnetic field in the tumor tissue area, the heating area and temperature can be precisely controlled. In addition, the ability of alternating magnetic field to penetrate is strong, and it is almost unaffected by the biological tissue, so it can focus on the tumor inside the human body. Magnetic hyperthermia needs the help of materials with magnetocaloricity. Fe_2O_3 and Fe_3O_4 MNPs are the most widely studied magnetocaloric materials. Horst et al. [19] measured the superparamagnetic Fe_3O_4 NPs synthesized by Arabic gum by the magnetic method to study the potential of magnetic thermotherapy under radiofrequency magnetic fields. Magnetocalorimetric measurements were performed in a wide range of field amplitude and frequency. Specific absorption rate of 218 W/g Fe was determined at a field frequency of 260 kHz and amplitude of 52 kA/m. These results demonstrate their viability to be applied in tumor ablation treatments. Using the linear response theory and restricting field parameters to the accepted biomedical window, maximum useful value of 74 w/g Fe is predicted at 417 kHz and 12 kA/m. Fabio et al. [20] also evaluated the feasibility of folate-modified MNPs for intracellular hyperthermia of solid tumors. It was observed that the uptake ability of ferrite NPs modified by folate and peg by oral epithelial cancer cells (with high expression of folate receptor) increased by 6.8 times, compared with HeLa cells with low expression of folate receptor and MCF7 cells had significant differences. And in three kinds of tumor cells, the uptake of folate-modified MNPs was significantly correlated with the expression of folate receptor. In order to determine whether the amount of nanoparticles absorbed by the cells is enough to achieve an effective and rapid temperature rise, the concentration of nanoparticles in the cell structure was estimated. The results showed that the concentration of iron in the endocytolytic enzyme reached 3 mg/mL, and the high amount of iron particles in the cells could heat the local cells to 43 °C, causing selective cell injury and death.

However, it is a challenge to improve the efficacy at 42 °C therapeutic temperatures without resistance to induced thermal stress. Zhang et al. [21] designed a magnetic hydrogel MNPs utilizing inclusion complexation between PEGylated Fe_3O_4 NPs and α-cyclodextrin, which can enhance tumor oxidative stress levels by generating reactive oxygen species through nanozyme-catalyzed reactions based on tumor magnetic hyperthermia. MNPs can be injected and diffused into the tumor tissue due to shear thinning as well as magnetocaloric phase transition properties, and magnetic heat generated by the Fe_3O_4 NPs first gives 42 °C of hyperthermia to the tumor. The nanozyme effect of Fe_3O_4 NPs exerts peroxidase-like properties in the acidic environment of tumor to generate hydroxyl radicals (•OH) by the Fenton reaction. The hyperthermia promotes the enzymatic activity of Fe_3O_4 nanozyme to produce more •OH. Simultaneously, •OH further damages the protective heat shock protein 70, which is highly expressed in hyperthermia to enhance the therapeutic effect of hyperthermia. This single magnetic nanoparticle exerts dual functions of hyperthermia and catalytic therapy to synergistically treat tumors, overcoming the resistance of tumor cells to induced thermal stress without causing severe side effects to normal tissues at 42 °C hyperthermia.

In addition to increasing the target temperature of the body to kill tumor cells, magnetic hyperthermia can also initiate the mechanism of adjuvant therapy. The heat generated above the mammalian euthermic temperature of 37 °C induces apoptotic cell death and/or enhances the susceptibility of the target tissue to other therapies such as radiation and chemotherapy. While most hyperthermia techniques currently in development are targeted towards cancer treatment, hyperthermia is also used to treat restenosis, to remove plaques, to ablate nerves, and to alleviate pain by increasing regional blood flow [22]. Moreover, it has been shown that magnetic hyperthermia can cause the increase of reactive oxygen species (ROS) and abnormal protein expression, such as the increase of HSP70 expression. In addition, magnetic hyperthermia may also activate the immune system of the body and improve the recognition and killing ability of immune cells to tumor cells. At present, the damage mechanism of magnetic hyperthermia is believed to be associated with the change of cell membrane function, the collapse of cytoskeleton, the escape of lysosomal contents, the apoptotic pathway of mitochondria, the direct or indirect damage of DNA, and so on. For details, please refer to the relevant research, which will not be introduced here.

11.2.4 MRI Contrast Agents

MRI, also known as spin imaging, is a diagnostic technique that uses the nuclear magnetic resonance phenomenon of a certain nucleus in human tissue to reconstruct the image of a certain level of human body through electronic computer processing. This diagnostic technique has become one of the clinical conventional imaging diagnosis methods for solid tumors. According to an uncompleted statistic, nearly 50% of MRI examinations have involved the use of MRI contrast agents, so as to

improve the imaging contrast [23]. MR contrast agents can be divided into two types according to the principle of their functions, i.e., longitudinal relaxation (T1) and transverse relaxation (T2). Gadolinium compounds are the main research object of T1 contrast agent, while iron and ferromagnetic materials are the core of T2 contrast agent. T1 contrast agent shortens the transverse relaxation time of tissue and increases the signal intensity of tissue on T1-weighted image, so it is also called positive enhancement contrast agent. On the contrary, T2 contrast agent reduces the signal intensity of tissue substance on T2-weighted image by shortening the longitudinal relaxation time of liver tissue, so it is also called negative enhancement or "negativity" contrast agent.

IONPs, especially the superparamagnetic IONPs, are the most widely investigated MRI T2-weighted image contrast agents for their excellent paramagnetic and biocompatibility. In fact, Feridex and Ferumoxytol whose main ingredient is the IONPs have been approved as magnetic resonance imaging (MRI) contrast agents (Feridex) or iron supplement for treating iron deficiency (Ferumoxytol) by the US FDA [24]. However, it has to be considered that the traditional MRI contrast agents do not have the ability of targeting, and they tend to gather to the tissues of rich reticuloendothelial system, such as liver, spleen, lymph nodes, bone marrow, and other parts, which enables this kind of contrast agents to obtain better contrast effect in these tissues. In 1996, Lubbe et al. [25] first used the magnetic drug microspheres containing epirubicin in the first phase of clinical targeted drug treatment. The results show that the method is less toxic and can target the lesion; however, further MRI tests showed that more than 50% of the microspheres were entrapped by the liver. Some research teams also attempted to combine targeted molecules with MNPs to achieve enhanced imaging of specific tissues. Chen et al. [26] developed a MNPs MRI contrast agent based on the 22 nm Fe_3O_4 nanoparticles and a novel dual-specific nanoprobe to target integrin and death receptor (DR4/DR5) on tumor cells simultaneously. The probe showed good magnetic properties, specific binding ability with target cells, and anti-nonspecific phagocytosis in vitro. As a result of these advantages, further MRI results of tumor in vivo showed that the mice injected with the dual-targeting probes obtained a more sensitive and effective contrast effect compared with the passive target probe group.

11.2.5 Tumor Theranostics

The diagnosis and treatment of tumor (Tumor theranostics) can be conducted by taking advantage of MNPs-based functions of MRI contrast and drug-targeted delivery. That is, enhanced MRI observation was performed simultaneously when drug-targeted delivery therapy was applied to the tumor. Zhang et al. [27] designed a novel targeted theranostic nanoplatform LDH-Fe_3O_4-HA/DOX for enhanced T1-weighted magnetic resonance (MR) imaging-guided chemotherapy by constructing layered double hydroxide (LDH)-stabilized ultrasmall iron oxide (Fe_3O_4) nanoparticles with hyaluronic acid (HA) modified as targeting agents and

anticancer drug doxorubicin (DOX) loaded with a high loading efficiency. In vitro experiments demonstrate that the theranostic nanoplatform is able to specifically target to B16 cells overexpressing CD44 receptors and effectively release DOX to nucleus, and in vivo results show that the designed nanoplatforms have a better tumor penetration for significantly enhanced MR imaging of tumors and tumor chemotherapy with low side effects. Sun et al. [28] also prepared paclitaxel-loaded Mn–Zn ferrite MNPs coupled with RGD targeting peptide for cancer theranostic nanoagents. They demonstrated that the worm-like theranostic nanoagents exhibited increased delivery of paclitaxel in the integrin-enriched cells than that of the monodisperse sphere and the cluster, and the content of PTX was far more than that of the wild-type Taxol control group. In vivo results demonstrated that the worm-like theranostic nanoagents not only gained good MRI imaging in the tumor but also achieved longer blood circulation time and more PTX-targeted delivery to the tumor, as well as more efficiency in killing tumor cells, conducting the simultaneous diagnosis and treatment of tumors.

11.2.6 Nanozyme

In 2007, the research group of Professor Yan [29] found that IONPs can simulate horseradish peroxidase (HRP) activity and catalyze hydrogen peroxide (H_2O_2) to oxidize substrates (3,3,5,5-tetramethylbenzidine (TMB), diaminobenzidine (DAB), *o*-phenylenediamine (OPD)) to produce color changes. Its catalytic activity is similar to that of HRP and depends on H_2O_2 concentration, pH, and reaction temperature, and the catalytic process accords with Michaelis kinetics. The catalytic activity of IONPs is similar to that of peroxidase (POD), so scientists tend to name this kind of nanomaterials with simulated biological enzyme activity as nanozyme. IONPs are one of the most widely studied nanozymes, which were reported to exhibit the activity of POD and catalase (CAT) [30]. In general, they show peroxidase-like activity in pH < 7.0 and catalase-like activity in pH > 7.0 [30]. It is not difficult to find that the nanozyme activity of IONPs is more suitable for the regulation of ROS, which has been widely demonstrated as the key regulator for the survival of cancer cells and some bacteria. Therefore, some research teams combined the nanozyme effect and drug loading function of IONPs to build a nanoplatform for multiple therapeutic effects.

Huang et al. [31] reported that pH-responsive SPION-micelles can synergize with β-lapachone for improved cancer therapy. These SPION-micelles selectively release iron ions inside cancer cells and interact with H_2O_2 through Fenton reactions, escalating the ROS stress in β-lapachone-exposed cancer cells. The nanoplatform thereby greatly enhanced the therapeutic index of β-lapachone. More specifically, a tenfold increase in ROS stress was detected in β-lapachone-exposed cells pretreated with SPION-micelles over those treated with β-lapachone alone, which also correlates with significantly increased cell death. In addition, ROS mediated a key role in therapeutic effects of platinum drugs. Ma et al. [32] demonstrated tumor site-specific conversion

of ROS generation induced by released cisplatin and Fe^{2+}/Fe^{3+} from IONPs nanocarriers with cisplatin(IV) prodrugs for enhanced anticancer activity but minimized systemic toxicity. On the one hand, cisplatin can produce adducts with DNA and induce apoptosis, and on the other hand, cisplatin can activate NOx enzyme, which transforms NADPH into $NADP^+$, releases electrons, and combines with oxygen molecules to produce superoxide radicals, then hydrogen peroxide is produced under the action of SOD, and finally hydroxyl radicals are produced under the effect of iron oxide pod, playing a synergistic role in enhancing the efficacy.

11.2.7 Summary

Magnetic nanoparticles (MNPs) own promising features in drugs targeted delivery [33], coordination therapy [34], and cancer diagnosis and treatment based on its excellent magnetic performance [35, 36] (Fig. 11.2). MNPs, composed of metal, alloy metal, and ferrites doped with magnetic elements (MFe2O4, M = Fe, Co, Ni, Mn), have also been widely studied as drug carriers. The reactive functional groups on the surface and magnetic responsiveness also make MNPs more suitable as nanocarriers because the surface modifiability facilitates the drug loading and magnetic responsiveness encourages it to target to the diseased tissues under magnetic field

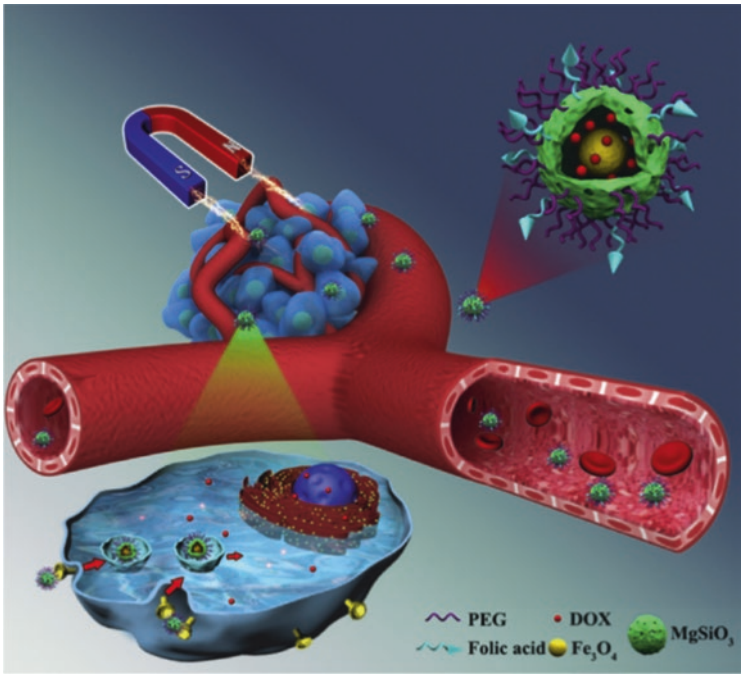

Fig. 11.2 The applications of magnetic nanoparticles [36]

guidance. Therefore, the functionalization of MNPs on the surface is very significant. In addition, the unique magnetic properties of MNPs enable MRI, and with magnetic targeted drug delivery, MNPs is an ideal theranostic nanoagent for cancer synchronous diagnosis and treatment, that is, MRI observation was performed simultaneously when drug-targeted delivery therapy was applied to tumors.

The potential toxicity and drug delivery of nanocarriers depend on the nanoparticle composition, coating materials, size, shape, and surface charge (which we call as the 3S effects of NPs); for example, Guo et al. indicated that small MNPs exhibited greater cellular internalization and deeper penetration into multicellular spheroids, and larger MNPs showed greater accumulation in tumors, thereby inducing more efficient tumor growth inhibition. And our reports also revealed that anisotropic drug carriers exhibited prolonged blood circulation time, indicating the significance of the shape effect in controlling and comparison of biological behaviors and properties of drug-loaded MNPs.

That is, in addition to the magnetism, the size effect also played a key role in affecting the application of MNPs drug carriers. Moreover, many scientists have attempted to ameliorate the drug loading of MNPs through controlling the shape and the modifications on the surface of MNPs. Multi-shaped MNPs including monodisperse sphere [37], cube [38], nanocluster [39], and worm-like nano-chain [40] were reportedly developed for drug loading, where the modifications on the surface of MNPs played the significant role. Polymers with amino and carboxyl groups are the most common materials to be utilized [41]. As a matter of fact, amphiphilic polymers-modified nanoparticles not only reformed the drug loading of MNPs but also effectively ameliorated the blood circulation time of MNPs, avoiding captured by cells of reticuloendothelial systems (RES). Additionally, lipids and inorganic materials have been developed and serve as drug carriers to control the release behavior of payloads [41]. In a word, the effect of size, shape, and surface (3S effects) is still an important factor that should be considered when the MNPs are used as drug carriers. We will introduce it in detail in Sect. 11.3.

11.3 Magnetic Drug Loading System

Magnetic drug loading system (MDLS) is mainly composed of magnetic targeted drug carriers, drug loading methods, and candidate drugs. Because many types of drug candidates are involved, these will not be introduce here.

11.3.1 Magnetic Targeted Drug Carriers

Many MNPs have been reportedly developed; regretfully, not all MNPs are suitable for loading drugs. MNPs used in drug carriers should meet the following requirements. (1) The MNPs carriers should have a suitable size, so that the magnetic field

can generate a strong enough attraction to the MNPs, to target the carriers to the lesion and its surrounding tissue. (2) The skeleton material on the surface of the MNPs carriers can be metabolized in the body and the metabolites are nontoxic. And it can be metabolized or excreted after a certain period of time and will not cause side effects after being metabolized by human tissues. (3) The iron content from the MNPs drug carrier should be appropriate, generally speaking, not exceeding the total amount of iron supplemented for anemia. Thus, Fe_3O_4 and γ-Fe_2O_3 nanoparticles with good biocompatibility were generally chosen, and they are easy to be metabolized and eliminated from the human body through the liver, spleen, and bone marrow. Comparatively, Ni or Co alloy MNPs are with good magnetic targeting ability, but their toxic effects will lead to damage to normal cells and tissues [42]. Another important reason is that the FDA of United States has approved intravenous Ferumoxytol as a safe and effective treatment for anemia, and Ferumoxytol is a superparamagnetic iron oxide nanocolloid coated by the carbohydrate and the size is about 6 nm [43, 44]. Therefore, IONPs are widely used in the study of pharmaceutical carriers.

11.3.1.1 Fabrication of Monodisperse IONPs

According to the classical explosion nucleation and growth model proposed by Lamar and Dinegar, the synthesis of monodisperse MNPs involves several successive stages. That is, the precursor, surfactant, and solvent are mixed at room temperature, and then the mixture is heated to the required temperature to initiate the nucleation process and control the growth of MNPs. This method is suitable for the synthesis of more complex MNPs, such as core-shell and dumbbell MNPs, because the formation of this composite structure usually requires heterogeneous nucleation and second component growth on pre-planted monodisperse MNPs. This is the most common method to fabricate the monodisperse MNPs such as γ-Fe_2O_3 NPs and Fe_3O_4 NPs (Fig. 11.3). In 1999, Rockenberger et al. first employed the injection method of precursor *N*-nitrosohydroxyaniline iron to prepare the 4–10 nm γ-Fe_2O_3 NPs with narrow particle size distribution, high crystallinity and dispersible in organic solvents [45]. Hyeon and Euliss both synthesized the monodisperse γ-Fe_2O_3 NPs with the size less than 20 nm [46, 47]. Based on the same method, Sun, Yu, and Li fabricated the monodisperse Fe_3O_4 NPs with the particle size distribution from 6 to 30 nm [48–50]. This method triggers very successful preparation of monodisperse MNPs, but the MNPs prepared are dispersible in organic solvents. Therefore, surface modification of MNPs can significantly increase the solubility in water, which is conducive to drug loading and escaping the RES. As it should be, other methods like coprecipitation method and physical method are able to prepare MNPs, but MNPs produced by these methods are very easily aggregated and hard in small size.

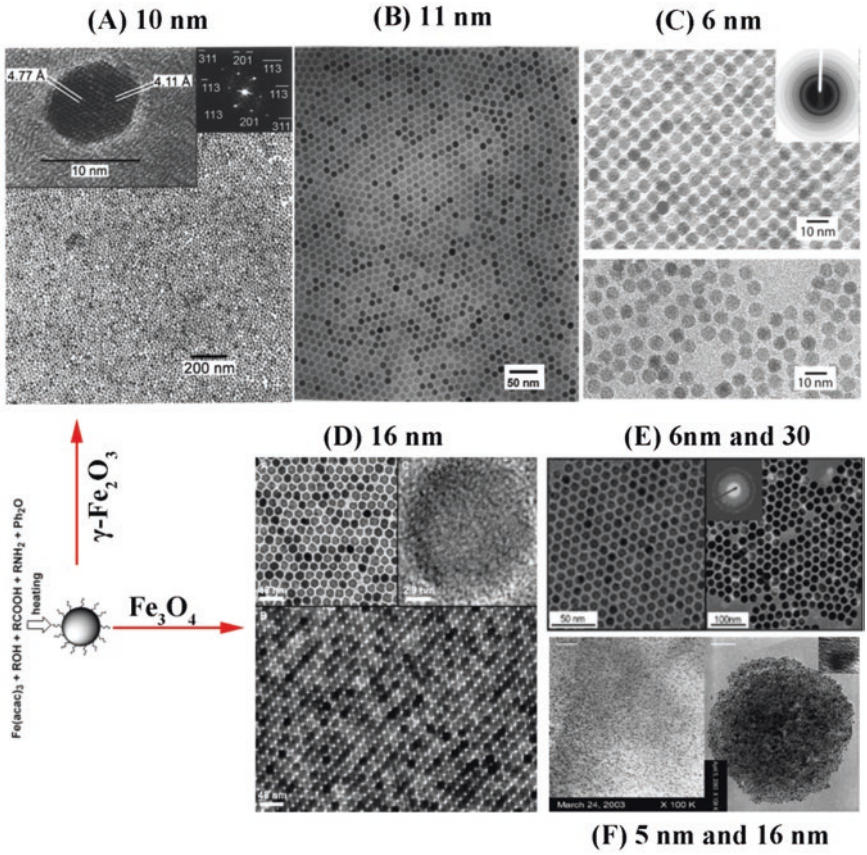

Fig. 11.3 TEM of γ-Fe_2O_3 NPs in the size of (**a**) 10 nm [45], (**b**) 11 nm [46], (**c**) 6 nm [47] and Fe_3O_4 NPs in the size of (**d**) 16 nm [48], (**e**) 6 nm and 30 nm [49], (**f**) 5 nm and 16 nm [50], which were prepared through thermal decomposition of precursors

11.3.1.2 Fabrication of Elements-Doping IONPs

In addition to pursuing MNPs of small size to get better magnetism according to the surface effect and small-size effect of nanoparticles, elements doping also endows MNPs with better magnetism. Reportedly, Mn, Zn, and Co were successfully doped into the IONPs, which exhibited better magnetism and superparamagnetism [51, 52]. Many other methods are able to be used to synthesize Mn–Zn ferrite MNPs including chemical coprecipitation method, hydrothermal method, sol-gel method, micro-emulsion method, and so on. However, the toxic effects of Mn and Co increased potential risks of MNPs in the organism, and drug carriers based on Mn and Co doped MNPs reported relatively less.

11.3.1.3 Fabrication of Core/Shell IONPs

A composite material of a core-shell structure is a type of particle with a two-layer or multilayer structure, generally composed of a central core and a shell that coats the outside. Because of the type of material that changes the core and the thickness of the shell layer, the ideal composite MNPs with excellent properties can be obtained. Therefore, combination with the MNPs and the alloy or nonmetal nanoparticles through the core/shell structure is able to obtain a composite nanoparticle with both magnetic nanoparticle and other nanoparticles' surface characteristic. Fe_3O_4 is one of the most studied MNPs. The shell layer of core/shell magnetic composite nanoparticles is composed of noble metal gold nano-shells and non-metallic silica nano-shells, representatively (Fig. 11.4). There are various techniques to fabricate

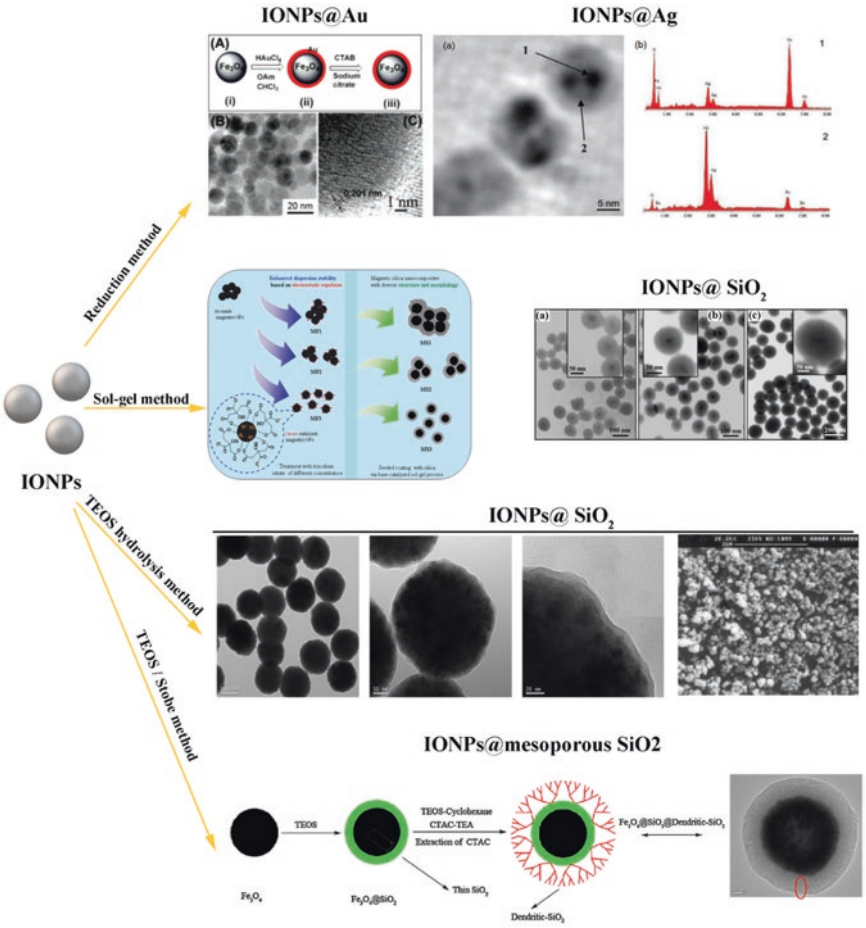

Fig. 11.4 Fabrication methods of core/shell IONPs including reduction method to prepare core/shell IONPs@ noble metal [53, 54], sol-gel and TEOS hydrolysis method to prepare core/shell IONPs@ SiO_2 [55, 56], and TEOS-Stober method to prepare core/shell IONPs@ mesoporous SiO_2 [59]

the core/shell MNPs. Sun et al. synthetized the core/shell Fe_3O_4 MNPs surrounded by the Au NPs shell through the $HAuCl_4$ reduction method [53]. Chudasama et al. selected the silver nitrate reduction method to directly attach the Ag NPs on the surface of Fe_3O_4 NPs [54]. Yang et al. prepared IONPs/SiO_2 core/shell composite nanoparticles by the sol-gel method [55]. In non-metallic silica-coated IONPs, ethyl orthosilicate (TEOS) hydrolysis method provided a good selection. Ian J. Bruce et al. and Gye Seok An et al. wrapped SiO_2 multiple times on the surface of Fe_3O_4 NPs by hydrolyzing a solution of ethyl silicate [56]. And N_2 adsorption-desorption data indicated that the composite nanoparticles prepared by TEOS method had a larger specific surface area. Of course, as the potential drug carrier, MNPs coated by mesoporous SiO_2 also exhibited excellent potential in loading drugs [57, 58], where the combination of TEOS method and Stober method was widely applied to synthetize the mesoporous SiO_2 coated MNPs [59].

11.3.2 Drug Loading Methods

The combination of MNPs and drugs is an important technology. In general, non-covalent self-assembly and chemical bonding are the common drug loading methods presently. Because of the side effects of chemotherapy drugs, the application of magnetic targeted drug carriers can reduce the damage to normal cells. Frequently used chemotherapy drugs include biological agents, doxorubicin, epirubicin, daunorubicin, methotrexate, paclitaxel, mitoxantrone, and cisplatin. These drugs have different chemical structures and physical properties, thus the different connection modes are required when they are coupled with magnetic targeted carriers.

11.3.2.1 Non-covalent Self-Assembly

Physical package, electrostatic, dipole–dipole interactions (hydrogen bonding), van der Waals forces (hydrophobic), coordination, and encapsulation chemistries play major roles in promoting the non-covalent self-assembly between drugs and MNPs carriers (Fig. 11.5).

Doxorubicin (DOX) and its related anthracycline family are the most widely used chemotherapeutic anticancer drugs, while free DOX may potentiate the risk of myocardial damage and congestive heart failure [60]. Gautier et al. prepared DOX-loaded PEGylated SPIONs through non-covalent self-assembly, and the toxicity of the treatment was reduced substantially [61]. Yang et al. prepared magnetic IONPs conjugated with the amino-terminal fragment (ATF) peptide of uPA (urokinase plasminogen activator) and DOX through adsorption self-assembly. The DOX-ATF-IONPs functionalized NPs not only exhibited multiple targeting but also strongly inhibited the growth of 4T1 tumor cells [62].

The majority of protein molecular, plasmid DNA, and biological agent tend to be with charge, which are suitable for self-assembling with MNPs carriers through

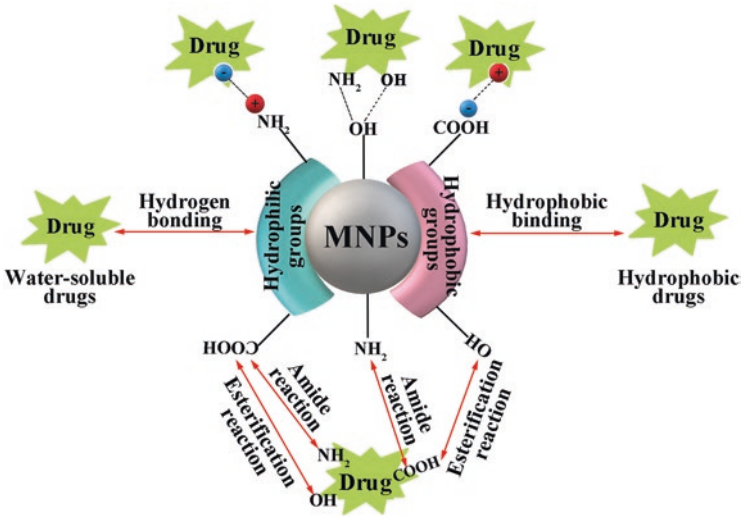

Fig. 11.5 Common drug loading methods of magnetic nanocarriers

electrostatic interactions. Polyethyleneimine (PEI) modified IONPs is with positive charge; Steitz [63], Chorny [64], Park [65], and Kim et al. [66] transferred the negatively charged plasmid DNA through a PEI-modified IONPs transfection vector, with the help of electrostatic self-assembly.

Dipole–dipole interactions are frequently used for the self-assembly between drugs and MNPs. Hydrophobic/hydrophilic interactions is a typical example. Hydrophobic drugs are easy to be adsorbed to the MNPs engineered with hydrophobic layers, and then gradually release the coated drugs during the layer degrading. Singh et al. prepared and characterized MNPs embedded in polylactide-*co*-glycolide matrixes (PLGA-MNPs) as a dual drug delivery and imaging system capable of encapsulating both hydrophilic and hydrophobic drugs in a 2:1 ratio [67]. Hydrogen bonding between hydroxyl and amino groups can also be used to assemble drugs on the surface of MNPs. Shufang Yu et al. successfully loaded the DOX into the MNPs via combined actions of hydrophobic interaction and hydrogen bonding [68].

Non-covalent self-assembly can trigger rapid bonding, high efficiency, and simple process, but meanwhile, which also make the interaction between drugs and carriers lack enough stability during the travelling.

11.3.2.2 Chemical Bonding

Chemical bonding depends on the functional groups on the surface of the drugs and the MNPs. Most chemotherapeutic drugs or protein molecules have one or more of the functional groups of amino, carboxyl, hydroxyl, etc. [41]. Thus, amide reaction and esterification reaction are the two common bonding methods in chemical bonding. In fact, nanoscale MNPs is extremely easy to absorb the hydroxyl, which facilitates the ester bonding between MNPs and carboxylic drugs such as polypeptide (Fig. 11.5). Sousa et al. previously succeed to synthetize a carboxylic acid ester through a carboxyl group (–COOH) in an amino acid molecule and a hydroxyl group (–OH) on the surface of γ-Fe_2O_3 NPs, and increased the biocompatibility of γ-Fe_2O_3 NPs [69]. Meanwhile, many chemotherapeutic drugs and biological agents possess the amino group and carboxyl group, which are conducive to amide group bonding after the MNPs modified by –COOH or –NH_2. Zhang et al. modified the surface of Fe_3O_4 NPs with PEG and folic acid, which not only improved their water solubility and biocompatibility, but also increased the targeting of cancer cells and the ability to enter cancer cells [70].

In addition to amide linkages and esterification linkages, Si–O covalent bond is also conducive to the combination between drugs and MNPs carriers. Kohler et al. fabricated the monodisperse Fe_3O_4 NPs bonded with a –NH_2 functional group via a Si–O covalent bond, and then bonded the methotrexate molecule via the –NH_2 functional group [37]. This drug loading nano-system can be applied to enhance MRI and magnetic targeting to cancer cells.

11.4 3S Effects of MNPs

MNPs carriers as one of the key factors in magnetism-targeted drug delivery systems, their parameters of size, surface, and shape (3S) are decisive in drugs loading and targeted delivery. Regrettably, there is no consistent conclusion to guide the researcher to choose the suitable magnetic carrier.

11.4.1 Size Effects

The magnetic properties of MNPs are one of the most important physical properties, which can be used in MRI and magnetism-guided drug delivery after they are assembled with drugs. As the size of the magnetic materials decreases to a certain degree, it will exhibit a single-domain structure. When the size of the magnetic materials is less than the critical size (generally 20 nm), the magnetic spins of magnetic nanomaterials will be arranged disorderly, showing superparamagnetism, manifested by the fact that they will be rapidly magnetized under the action of an

alternating magnetic field, and can be oriented to move with the magnetic field. Once the magnetic field is removed, its magnetization decreases to zero, that is, it does not show magnetism without an external magnetic field. Therefore, superparamagnetic MNPs have the potential advantages to deliver therapeutics onto specific sites in the body with the assistance of external magnetic field [71]. This requires a proper size of MNPs drug carriers, which means that the MNPs with smaller size will be more suitable for drug loading. Meanwhile, MNPs with smaller nanoscale have a larger specific surface area, so more drugs can be loaded per unit mass.

However, the distribution and metabolism of MNPs in the body also need an appropriate size. The drug-loaded nanoparticles have a natural passive targeting. About 60–90% are retained by a large number of reticuloendothelial cells (Kupffer cells) in the liver after the nanoparticles entered the circulatory system. Researches revealed that this passive targeting is mainly determined by the size of the particles. Less than 20 nm NPs tend to be excreted renally [72], 30–150 nm NPs tend to accumulate in the bone marrow [73], heart, kidney, and stomach [47], and more than 200 nm NPs were mainly targeted to the liver and spleen [74]. At the same time, the nanoparticles with <100 nm were easy to escape the phagocytosis of Kupffer cells, but to be trapped by bone marrow cells [48, 75]. Additionally, nanoparticles ranging from approximately 10 to 100 nm preferentially accumulate in the tumors as opposed to normal tissues [76, 77]. Injumpa et al. found that when the particle size was 20–100 nm, only a small amount of inflammatory factors were produced by macrophages, while when the particle size was more than 200 nm, a large number of inflammatory factors were produced [78]. Therefore, we think MNPs with large diameter or magnetic microsphere carriers are suitable for the drugs targeted delivery to the liver and spleen, while MNPs carriers with small size are more suitable for non-hepatic spleen targeted drug delivery (Fig. 11.6). Because of the lack of systematic research, there is no stronger evidence to support our views. According to reports available, MNPs of less than 100 nm seem to be more popular, and there is a tendency to pursue smaller sizes.

In addition to consideration of the passive targeting of MNPs, external magnetic field-mediated active targeting should be taken into consideration. The force of the magnetic field on the MNPs can be expressed by the following formula [79]:

$$F_{\mathrm{m}} = -V\chi BB' / \mu_0$$

where F_{m} is the magnetic force, V is the volume of the magnetic particles, χ is the volume magnetic susceptibility of the magnetic particles, and μ_0 is the magnetic permeability of the vacuum. B and B' are the magnetic field and the magnetic field gradient of the magnet, respectively. It is not hard to find that the magnetic force is also controlled by the size (V) of the MNPs, that is, the larger the MNPs are, the easier the MNPs are affected. Accordingly, pursuing the smaller size blindly may not meet the requirements of drug loading of MNPs.

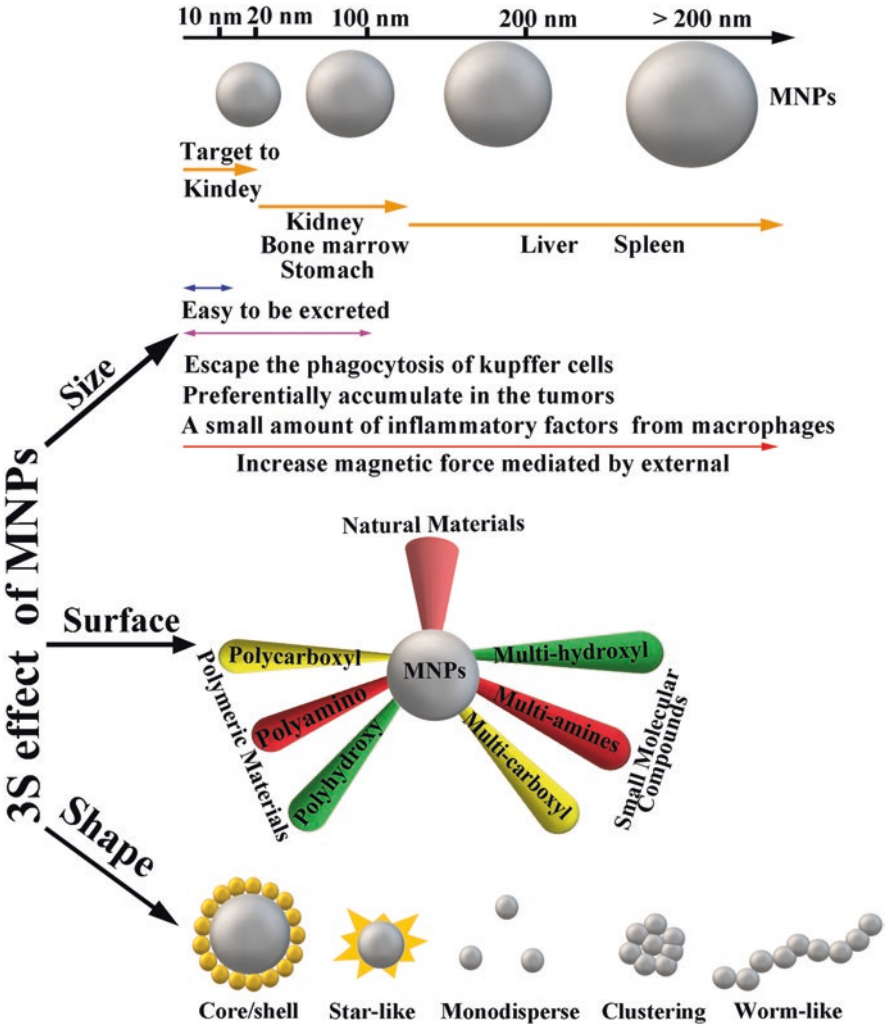

Fig. 11.6 Schematic diagram of 3S effect of magnetic nanoparticles

11.4.2 Surface Effects

The charge and distribution on the surface of MNPs drug carriers play a decisive role in maintaining colloidal stability. The surface charge of MNPs also determines their reaction in cells, especially when they are endocytosis and phagocytosis. As a drug carrier, MNPs must be coated. The surface coating not only enables MNPs to

better combine with drugs or target cells, increases the histocompatibility between them, enhances the reaction efficiency of each other, but also avoids the aggregation of particles and resists oxidation reaction. Surface modification is the most critical factor in controlling the combination of drugs and MNPs, the release of drugs from MDLS in vivo, the degradation of MDLS in vivo and the cytotoxicity, etc. In general, small molecular compounds, polymers, and natural materials are selected widely, although various modified materials reportedly exhibited their respective superiority (Fig. 11.6).

11.4.2.1 Small Molecular Compounds

Multi-amines, multi-carboxyl, and multi-hydroxyl groups can endow MNPs with active groups, which not only increase the water solubility and biocompatibility of MNPs but also make it easier for chemotherapeutic drugs to be loaded. Wang et al. converted the oil-soluble MNPs into water-soluble MNPs through the interaction between oleic acid and α-cyclodextrin and skillfully utilized multiple –OH groups on the surface of the cyclodextrin [80]. Folic acid (FA), which contains dicarboxylic and amino groups, can not only provide active groups, but also target to folate receptors highly expressed in various tumor cells. Bonvin et al. synthetized FA-modified IONPs as a platform with high potential for simultaneous targeting, MRI detection, and hyperthermia treatment of lymph node metastases of prostate cancer [81]. Gupta et al. prepared a pH-responsive FA-DOX-Fe_3O_4 NPs used for targeted chemo-thermal therapy and MRI diagnosis [82]. FA-conjugated MNPs showed good colloidal stability and achieved ~95% loading efficiency of doxorubicin (DOX), which could be due to strong electrostatic interaction of highly negatively charged FA-MNPs and the positively charged DOX. Other small molecular compounds such as dimercaptosuccinic acid (DMSA) [83], citric acid [84], and amino acid [85] have been reported for the surface modification of MNPs.

11.4.2.2 Polymer

Polyhydroxy polymers, polyamino polymers, and polycarboxyl polymers have been widely used in the surface modification of MNPs. Polyethylene glycol (PEG) and functionalized PEG are one kind of polymers used mostly. Excellent water solubility and biocompatibility as well as low immunogenicity and antigenicity make it functionally avoid the RES system. Zhou et al. constructed PEG-β-Glu-MNPs by a bonding between methoxy PEG succinimidyl carboxy-methylester

(SC-NHS-PEG) and β-glucosidase immobilized magnetic iron oxide-nanoparticles (β-Glu-MNP) [86]. Results showed that β-Glu-MNPs were cleared by 80% in vivo after 1 h of administration, while PEG-β-Glu-MNPs still retained 20% after 2 h of administration, indicating a longer blood circulation time of PEG-modified MNPs [86]. Many PEG-coated MNPs were applied to load the chemotherapeutic drugs including DOX [87] and Paclitaxel [88].

Polyethylenimine (PEI) with proton sponge mechanism can endow MNPs with multiple amino and positive charge, which is conducive to drugs loading of MNPs. Ninet Avedian prepared pH-sensitive biocompatible mesoporous MNPs through amide covalent conjugation by the $–NH_2$ from PEI and the –COOH from FA [89]. Jingchao Li fabricated the Fe_3O_4@Au core/shell nanostars, where PEI and hyaluronic acid affords endue the nanostars MNPs with excellent colloidal stability and good biocompatibility [90].

Co-modification of multiple polymers functionalized the MNPs. For example, PEG-poly(ε-caprolactone)-assembled PEG–PCCL-MNPs showed good biocompatibility and little in vitro or in vivo cytotoxicity, as well as effective, tumor-specific cell targeting for paclitaxel delivery when an external magnetic field was applied [88]. Chen et al. developed triphenylamine-poly(lactide-*co*-glycolide)-poly (ethyleneglycol)-poly(lactide-*co*-glycolide) and folate-poly(2-ethyl-2oxazoline)-poly (D,L-lactide) where IONPs and PTX were co-encapsulated [91].

The polymer materials involved in the construction of numerous drug carriers include synthetic polymers and natural polymers, but the synthesis of co-polymers is a great challenge. Although some simple polymers have been commercialized, the fancy price also pushes up the input prices of the fabrication of MNPs carriers.

11.4.2.3 Natural Materials

Fortunately, natural materials including natural polymers provide with a good choice. Chitosan is a representative natural high molecular polymer, which is biodegradable and can be easily degraded into nontoxic glucosamine by the action of various enzymes in the living body and then absorbed by the organism. Kostevsek et al. modified dumbbell-shaped Au/Fe_3O_4 nanoparticles by a simple and novel method using natural chitosan as matrix [92]. Yang et al. developed a chitosan-PEI-uric acid micelle that exhibited dual pH/redox sensitivity and targeting effects through chitosan material [93]. Furthermore, a large number of hydroxyl groups and amino groups present in the molecular chain make it easy to be chemically modified and thus are often used as an outer shell of MNPs in the field of enzyme immobilization.

Due to the poly-hydroxyl structure, the dextran/Fe_3O_4 NPs were prepared by coprecipitation method. Results demonstrated that the dextran not only isolated the interior Fe_3O_4 NPs from oxygen and water to enhance the photothermal stability but also enhanced the biocompatibility of Fe_3O_4 NPs [94–96]. Weihong Chen et al. connected dextran to Fe_3O_4 MNPs to prepare dextran-coated Fe_3O_4 NPs and graphene oxide (Fe_3O_4-GO) complex NPs. Aminodextran-coated Fe_3O_4-GO possess good physiological stability and low cytotoxicity [97].

Overall, the surface modification can impart more functional groups to the magnetic nano carrier, provide the necessary surface charge, increase the water solubility and biocompatibility, of course the active targeting included, etc.

11.4.3 Shape Effects

According to the research reports currently available, monodisperse MNPs are more popular. Generally, the shape of NPs has prominent impacts on the cell phagocytosis, blood circulation time, tissue biodistribution, metabolism, and organic toxicity [98, 99]. Compared with the spherical particles, the torsion force of the oblate particles will cause the particles to flip and rotate, and then drift to the inner wall of the blood vessel. The shape of the particles also affects the contact between the particles and the cell surface, and the shape of the particles dominates the clearance of the reticuloendothelial system. Compared with spherical particles, oblate particles are less likely to be engulfed by macrophages and have longer blood circulation time. Nanoparticles entering into normal or cancer cells are also controlled by the shape of particles. For particles with long aspect ratio, the internalization speed of long axis parallel cell membrane is lower than that of short axis parallel cell membrane. Compared with the cubic Fe_3O_4 nanoparticles, the cubic particles have higher crystallinity, larger single crystal, higher saturation magnetization, and T2 relaxation. Compared with spherical Fe_3O_4 nanoparticles, rod-shaped nanoparticles have stronger toxicity to mouse macrophages. Yong Hu et al. developed multifunctional Fe_3O_4 @ Au core/shell nanostars, which showed excellent colloidal stability, good cytocompatibility in a given concentration range, and specific recognition to cancer cells overexpressing FA receptors [97].

Compared to the wide research of monodisperse sphere MNPs and clustering shape MNPs, worm-like MNPs reported less. In our study, superparamagnetic anisotropic nano-assemblies (SANs) were fabricated and loaded with vincristine (VCR) to form VCR-SANs. SANs were found to be more promising than isotropic nano-assemblies via our in vivo and in vitro examinations [40]. Moreover, anisotropic MNPs exhibit less mononuclear phagocytic system (MPS) uptake and longer blood circulating time in comparison with the spherical ones [40, 100–103]. Namely, worm-like MNPs probably are advantageous in enhancing MRI, delivery efficiency, and therapeutic effects in cancer theranostic [28].

11.5 Perspectives and Future Challenges

With the development of nano-manufacturing technology, the preparation of MNPs with various requirements can be realized. The development of small-sized, monodisperse, narrow distribution, high-saturation magnetization, superparamagnetic, and functionalized MNPs provides the basis for the application of MNPs drug

carriers. Small-sized MNPs have a similar size comparable to that of viruses (20–450 nm), proteins (5–50 nm), DNA, or genes (2 nm wide and 10–100 nm long). Thus when the MNPs are used as drug carriers, they not only can move to the target site of the diseased organ or tissue, but also can enter the interior of the tumor cell.

However, it is undeniable that there is currently no definite mechanism and method to make the preparation and functionalization of MNPs simple and inexpensive. In terms of the functionalization of MNPs, the properties of the MNPs imparted by self-assembly are not stable in tissues or cells due to the diversity of the in vivo environment. Since MNPs covalently bonded with drugs is subject to high cost and cumbersome methods of preparation, there is an urgent need to find a simple, stable, and cheap preparation method to establish a drug loading system of MNPs.

Additionally, there is no systematic study currently to determine the effects of surface modification, size, and shape of magnetic nanoparticles on drug loading, drug delivery, and the effects of these factors on the biological safety and biocompatibility of drug loading systems. At least for now, we cannot track the specific biological effects of MNPs in organisms yet. Especially, the nano-enzymatic effect of IONPs reported in recent years brought more difficulties and uncertainties to the application of magnetic nano-drug carriers [29, 30], because the mimic-enzyme functionalization of IONPs originally has a significant effect on the cells survival [31].

Nevertheless, scientists around the world have well solved the problem of preparing magnetic nanoparticles and developed many synthetic technologies in the field of drug assembly. With the in-depth research, we believe that magnetic nano-drug carriers will have great application in the fields of chemotherapeutic drug delivery, MRI, and photothermal coordinated therapy.

References

1. J. Guo, W. Yang, C. Wang, Magnetic colloidal supraparticles: design, fabrication and biomedical applications. Adv. Mater. **25**(37), 5196–5214 (2013)
2. J.H. Lee et al., Artificially engineered magnetic nanoparticles for ultra-sensitive molecular imaging. Nat. Med. **13**(1), 95–99 (2007)
3. J.T. Jang et al., Critical enhancements of MRI contrast and hyperthermic effects by dopant-controlled magnetic nanoparticles. Angew. Chem. Int. Ed. Engl. **48**(7), 1234–1238 (2009)
4. J. Song et al., Self-assembled responsive bilayered vesicles with adjustable oxidative stress for enhanced cancer imaging and therapy. J. Am. Chem. Soc. **141**(20), 8158–8170 (2019)
5. D. Jishkariani et al., Preparation and self-assembly of dendronized janus Fe3O4-Pt and Fe3O4-Au heterodimers. ACS Nano **11**(8), 7958–7966 (2017)
6. K.C. Leung et al., Gold and iron oxide hybrid nanocomposite materials. Chem. Soc. Rev. **41**(5), 1911–1928 (2012)
7. J. Xie et al., Multi-modal Mn-Zn ferrite nanocrystals for magnetically-induced cancer targeted hyperthermia: a comparison of passive and active targeting effects. Nanoscale **8**(38), 16902–16915 (2016)
8. C. von Roemeling et al., Breaking down the barriers to precision cancer nanomedicine. Trends Biotechnol. **35**(2), 159–171 (2017)

9. D. Peer et al., Nanocarriers as an emerging platform for cancer therapy. Nat. Nanotechnol. **2**(12), 751–760 (2007)
10. K.J. Widder, A.E. Senyei, D.F. Ranney, Magnetically responsive microspheres and other carriers for the biophysical targeting of antitumor agents. Adv. Pharmacol. Chemother. **16**, 213–271 (1979)
11. Y. Zou et al., Polyethylenimine nanogels incorporated with ultrasmall iron oxide nanoparticles and doxorubicin for MR imaging-guided chemotherapy of tumors. Bioconjug. Chem. **31**(3), 907–915 (2020)
12. C. Yang et al., Paclitaxel-Fe3O4 nanoparticles inhibit growth of CD138(−) CD34(−) tumor stem-like cells in multiple myeloma-bearing mice. Int. J. Nanomedicine **8**, 1439–1449 (2013)
13. Z. Li et al., Preparation and evaluation of multifunctional autofluorescent magnetic nanoparticle-based drug delivery systems against mammary cancer. J. Pharm. Sci. **107**(10), 2694–2701 (2018)
14. F. Danhier, O. Feron, V. Preat, To exploit the tumor microenvironment: passive and active tumor targeting of nanocarriers for anti-cancer drug delivery. J. Control. Release **148**(2), 135–146 (2010)
15. S. Acharya, S.K. Sahoo, PLGA nanoparticles containing various anticancer agents and tumour delivery by EPR effect. Adv. Drug Deliv. Rev. **63**(3), 170–183 (2011)
16. S. Nigam, D. Bahadur, Doxorubicin-loaded dendritic-Fe3O4 supramolecular nanoparticles for magnetic drug targeting and tumor regression in spheroid murine melanoma model. Nanomedicine **14**(3), 759–768 (2018)
17. A. Quarta et al., Novel synthesis of platinum complexes and their intracellular delivery to tumor cells by means of magnetic nanoparticles. Nanoscale **11**(48), 23482–23497 (2019)
18. A. Sato et al., Magnetic nanoparticles of Fe3O4 enhance docetaxel-induced prostate cancer cell death. Int. J. Nanomedicine **8**, 3151–3160 (2013)
19. M.F. Horst et al., Hybrid nanomaterials based on gum Arabic and magnetite for hyperthermia treatments. Mater. Sci. Eng. C Mater. Biol. Appl. **74**, 443–450 (2017)
20. F. Sonvico et al., Folate-conjugated iron oxide nanoparticles for solid tumor targeting as potential specific magnetic hyperthermia mediators: synthesis, physicochemical characterization, and in vitro experiments. Bioconjug. Chem. **16**(5), 1181–1188 (2005)
21. H. Wu et al., Enhanced tumor synergistic therapy by injectable magnetic hydrogel mediated generation of hyperthermia and highly toxic reactive oxygen species. ACS Nano **13**(12), 14013–14023 (2019)
22. P. Chandrasekharan et al., Using magnetic particle imaging systems to localize and guide magnetic hyperthermia treatment: tracers, hardware, and future medical applications. Theranostics **10**(7), 2965–2981 (2020)
23. K. Shiraishi et al., Polyion complex micelle MRI contrast agents from poly(ethylene glycol)-b-poly(l-lysine) block copolymers having Gd-DOTA; preparations and their control of T(1)-relaxivities and blood circulation characteristics. J. Control. Release **148**(2), 160–167 (2010)
24. K.C. Briley-Saebo et al., Fractionated feridex and positive contrast: in vivo MR imaging of atherosclerosis. Magn. Reson. Med. **59**(4), 721–730 (2008)
25. A.S. Lubbe et al., Clinical experiences with magnetic drug targeting: a phase I study with 4′-epidoxorubicin in 14 patients with advanced solid tumors. Cancer Res. **56**(20), 4686–4693 (1996)
26. L. Chen et al., Improving sensitivity of magnetic resonance imaging by using a dual-targeted magnetic iron oxide nanoprobe. Colloids Surf. B Biointerfaces **161**, 339–346 (2018)
27. N. Zhang et al., LDH-stabilized ultrasmall iron oxide nanoparticles as a platform for hyaluronidase-promoted MR imaging and chemotherapy of tumors. Theranostics **10**(6), 2791–2802 (2020)
28. Y. Sun et al., High-performance worm-like Mn-Zn ferrite theranostic nanoagents and the application on tumor theranostics. ACS Appl. Mater. Interfaces **11**(33), 29536–29548 (2019)
29. L.Z. Gao et al., Intrinsic peroxidase-like activity of ferromagnetic nanoparticles. Nat. Nanotechnol. **2**(9), 577–583 (2007)

30. Z.W. Chen et al., Dual enzyme-like activities of iron oxide nanoparticles and their implication for diminishing cytotoxicity. ACS Nano **6**(5), 4001–4012 (2012)
31. G. Huang et al., Superparamagnetic iron oxide nanoparticles: amplifying ROS stress to improve anticancer drug efficacy. Theranostics **3**(2), 116–126 (2013)
32. P. Ma et al., Enhanced cisplatin chemotherapy by iron oxide nanocarrier-mediated generation of highly toxic reactive oxygen species. Nano Lett. **17**(2), 928–937 (2017)
33. J. Huang et al., Magnetic nanoparticle facilitated drug delivery for cancer therapy with targeted and image-guided approaches. Adv. Funct. Mater. **26**(22), 3818–3836 (2016)
34. D. Hu et al., Indocyanine green-loaded polydopamine-iron ions coordination nanoparticles for photoacoustic/magnetic resonance dual-modal imaging-guided cancer photothermal therapy. Nanoscale **8**(39), 17150–17158 (2016)
35. T. Kang et al., Surface design of magnetic nanoparticles for stimuli-responsive cancer imaging and therapy. Biomaterials **136**, 98–114 (2017)
36. Y. Wang et al., In vivo dual-targeted chemotherapy of drug resistant cancer by rationally designed nanocarrier. Biomaterials **75**, 71–81 (2016)
37. N. Kohler et al., Methotrexate-modified superparamagnetic nanoparticles and their intracellular uptake into human cancer cells. Langmuir **21**(19), 8858–8864 (2005)
38. D. De, M.M. Goswami, Shape induced acid responsive heat triggered highly facilitated drug release by cube shaped magnetite nanoparticles. Biomicrofluidics **10**(6), 064112 (2016)
39. L.L. Chen et al., Designed fabrication of unique eccentric mesoporous silica nanocluster-based core-shell nanostructures for pH-responsive drug delivery. ACS Appl. Mater. Interfaces **5**(15), 7282–7290 (2013)
40. F. Xiong et al., Superparamagnetic anisotropic nano-assemblies with longer blood circulation in vivo: a highly efficient drug delivery carrier for leukemia therapy. Nanoscale **8**(39), 17085–17089 (2016)
41. K. El-Boubbou, Magnetic iron oxide nanoparticles as drug carriers: preparation, conjugation and delivery. Nanomedicine **13**(8), 929–952 (2018)
42. D.R. Lima et al., Employing calcination as a facile strategy to reduce the cytotoxicity in CoFe2O4 and NiFe2O4 nanoparticles. ACS Appl. Mater. Interfaces **9**(45), 39830–39838 (2017)
43. S. Zanganeh et al., Iron oxide nanoparticles inhibit tumour growth by inducing pro-inflammatory macrophage polarization in tumour tissues. Nat. Nanotechnol. **11**(11), 986–994 (2016)
44. V. Trujillo-Alonso et al., FDA-approved ferumoxytol displays anti-leukaemia efficacy against cells with low ferroportin levels. Nat. Nanotechnol. **14**(6), 616–622 (2019)
45. J. Rockenberger, E.C. Scher, A.P. Alivisatos, A new nonhydrolytic single-precursor approach to surfactant-capped nanocrystals of transition metal oxides. J. Am. Chem. Soc. **121**(49), 11595–11596 (1999)
46. T. Hyeon et al., Synthesis of highly crystalline and monodisperse maghemite nanocrystallites without a size-selection process. J. Am. Chem. Soc. **123**(51), 12798–12801 (2001)
47. L.E. Euliss et al., Cooperative assembly of magnetic nanoparticles and block copolypeptides in aqueous media. Nano Lett. **3**(11), 1489–1493 (2003)
48. S.H. Sun, H. Zeng, Size-controlled synthesis of magnetite nanoparticles. J. Am. Chem. Soc. **124**(28), 8204–8205 (2002)
49. W.W. Yu et al., Synthesis of monodisperse iron oxide nanocrystals by thermal decomposition of iron carboxylate salts. Chem. Commun. **20**, 2306–2307 (2004)
50. Z. Li et al., One-pot reaction to synthesize water-soluble magnetite nanocrystals. Chem. Mater. **16**(8), 1391–1393 (2004)
51. W. Montha et al., Synthesis of doxorubicin-PLGA loaded chitosan stabilized (Mn, Zn)Fe2O4 nanoparticles: biological activity and pH-responsive drug release. Mater. Sci. Eng. C Mater. Biol. Appl. **59**, 235–240 (2016)
52. M.U. Witt et al., Distribution of CoFe2O4 nanoparticles inside PNIPAM-based microgels of different cross-linker distributions. J. Phys. Chem. B **123**(10), 2405–2413 (2019)

53. Z. Xu, Y. Hou, S. Sun, Magnetic core/shell Fe3O4/Au and Fe3O4/Au/Ag nanoparticles with tunable plasmonic properties. J. Am. Chem. Soc. **129**(28), 8698–8699 (2007)
54. B. Chudasama et al., Enhanced antibacterial activity of bifunctional Fe3O4-Ag core-shell nanostructures. Nano Res. **2**(12), 955–965 (2009)
55. D. Yang, J.H. Hu, S.K. Fu, Controlled synthesis of magnetite-silica nanocomposites via a seeded sol-gel approach. J. Phys. Chem. C **113**(18), 7646–7651 (2009)
56. I.J. Bruce et al., Synthesis, characterisation and application of silica-magnetite nanocomposites. J. Magn. Magn. Mater. **284**, 145–160 (2004)
57. G.L. Zhang et al., Iron oxide nanoparticles immobilized to mesoporous NH2-SiO2 spheres by sulfonic acid functionalization as highly efficient catalysts. Nanoscale **7**(3), 1102–1109 (2015)
58. H.R. Zheng et al., Organosilane and polyethylene glycol functionalized magnetic mesoporous silica nanoparticles as carriers for CpG immunotherapy in vitro and in vivo. PLoS One **10**(10), e0140265 (2015)
59. Z.B. Sun et al., Multifunctional magnetic core-shell dendritic mesoporous silica nano spheres decorated with tiny Ag nanoparticles as a highly active heterogeneous catalyst. Appl. Surf. Sci. **360**, 252–262 (2016)
60. Y. Barenholz, Doxil (R)—the first FDA-approved nano-drug: lessons learned. J. Control. Release **160**(2), 117–134 (2012)
61. J. Gautier et al., Efficacy and hemotoxicity of stealth doxorubicin-loaded magnetic nanovectors on breast cancer xenografts. J. Biomed. Nanotechnol. **11**(1), 177–189 (2015)
62. L. Yang et al., Development of receptor targeted magnetic iron oxide nanoparticles for efficient drug delivery and tumor imaging. J. Biomed. Nanotechnol. **4**(4), 439–449 (2008)
63. B. Steitz et al., Characterization of PEI-coated superparamagnetic iron oxide nanoparticles for transfection: size distribution, colloidal properties and DNA interaction. J. Magn. Magn. Mater. **311**(1), 300–305 (2007)
64. M. Chorny et al., Magnetically driven plasmid DNA delivery with biodegradable polymeric nanoparticles. FASEB J. **21**(10), 2510–2519 (2007)
65. I.K. Park et al., Determination of nanoparticle vehicle unpackaging by MR imaging of a T-2 magnetic relaxation switch. Biomaterials **29**(6), 724–732 (2008)
66. Y.S. Kim et al., SPION nanoparticles as an efficient probe and carrier of DNA to umbilical cord blood-derived mesenchymal stem cells. J. Nanosci. Nanotechnol. **11**(2), 1507–1510 (2011)
67. A. Singh et al., Composite polymeric magnetic nanoparticles for co-delivery of hydrophobic and hydrophilic anticancer drugs and MRI imaging for cancer therapy. ACS Appl. Mater. Interfaces **3**(3), 842–856 (2011)
68. S.F. Yu et al., Magnetic and pH-sensitive nanoparticles for antitumor drug delivery. Colloids Surf. B Biointerfaces **103**, 15–22 (2013)
69. M.H. Sousa et al., Biocompatible magnetic fluid precursors based on aspartic and glutamic acid modified maghemite nanostructures. J. Magn. Magn. Mater. **225**(1–2), 67–72 (2001)
70. Y. Zhang, N. Kohler, M.Q. Zhang, Surface modification of superparamagnetic magnetite nanoparticles and their intracellular uptake. Biomaterials **23**(7), 1553–1561 (2002)
71. M. Zhao et al., Magnetic paclitaxel nanoparticles inhibit glioma growth and improve the survival of rats bearing glioma xenografts. Anticancer Res. **30**(6), 2217–23 (2010)
72. Choi, H.S., et al., Renal clearance of quantum dots. Nat. Biotechnol. **25**(10), 1165–1170 (2007)
73. S.M. Moghimi, Exploiting bone-marrow microvascular structure for drug-delivery and future therapies. Adv. Drug Deliv. Rev. **17**(1), 61–73 (1995)
74. S.M. Moghimi, Mechanisms of splenic clearance of blood-cells and particles—towards development of new splenotropic agents. Adv. Drug Deliv. Rev. **17**(1), 103–115 (1995)
75. J. Panyam et al., Rapid endo-lysosomal escape of poly(DL-lactide-co-glycolide) nanoparticles: implications for drug and gene delivery. FASEB J. **16**(10), 1217–1226 (2002)
76. O. Veiseh, J.W. Gunn, M.Q. Zhang, Design and fabrication of magnetic nanoparticles for targeted drug delivery and imaging. Adv. Drug Deliv. Rev. **62**(3), 284–304 (2010)
77. M.S. Muthu, S. Singh, Targeted nanomedicines: effective treatment modalities for cancer, AIDS and brain disorders. Nanomedicine **4**(1), 105–118 (2009)

78. W. Injumpa, P. Ritprajak, N. Insin, Size-dependent cytotoxicity and inflammatory responses of PEGylated silica-iron oxide nanocomposite size series. J. Magn. Magn. Mater. **427**, 60–66 (2017)
79. D.C. Yin, Protein crystallization in a magnetic field. Prog. Cryst. Growth Charact. Mater. **61**(1), 1–26 (2015)
80. Y. Wang et al., "Pulling" nanoparticles into water: phase transfer of oleic acid stabilized monodisperse nanoparticles into aqueous solutions of alpha-cyclodextrin. Nano Lett. **3**(11), 1555–1559 (2003)
81. D. Bonvin et al., Folic acid on iron oxide nanoparticles: platform with high potential for simultaneous targeting, MRI detection and hyperthermia treatment of lymph node metastases of prostate cancer. Dalton Trans. **46**(37), 12692–12704 (2017)
82. J. Gupta et al., A pH-responsive folate conjugated magnetic nanoparticle for targeted chemo-thermal therapy and MRI diagnosis. Dalton Trans. **45**(6), 2454–2461 (2016)
83. Y. Xiang et al., Lead adsorption, anticoagulation and in vivo toxicity studies on the new magnetic nanomaterial Fe3O4@ SiO2@DMSA as a hemoperfusion adsorbent. Nanomed. Nanotechnol. Biol. Med. **13**(4), 1341–1351 (2017)
84. B. Antic et al., Complementary approaches for the evaluation of biocompatibility of Y-90-labeled superparamagnetic citric acid (Fe,Er)(3)O-4 coated nanoparticles. Mater. Sci. Eng. C Mater. Biol. Appl. **75**, 157–164 (2017)
85. A. Antosova et al., Amino acid functionalized superparamagnetic nanoparticles inhibit lysozyme amyloid fibrillization. Chemistry **25**(31), 7501–7514 (2019)
86. J. Zhou, J. Zhang, W.X. Gao, Enhanced and selective delivery of enzyme therapy to 9L-glioma tumor via magnetic targeting of PEG-modified, beta-glucosidase-conjugated iron oxide nanoparticles. Int. J. Nanomedicine **9**, 2905–2917 (2014)
87. L.J. Zhu et al., Multifunctional pH-sensitive superparamagnetic iron-oxide nanocomposites for targeted drug delivery and MR imaging. J. Control. Release **169**(3), 228–238 (2013)
88. X.Y. Li et al., Enhanced tumor targeting effects of a novel paclitaxel-loaded polymer: PEG-PCCL-modified magnetic iron oxide nanoparticles. Drug Deliv. **24**(1), 1284–1294 (2017)
89. N. Avedian et al., pH-sensitive biocompatible mesoporous magnetic nanoparticles labeled with folic acid as an efficient carrier for controlled anticancer drug delivery. J. Drug Deliv. Sci. Technol. **44**, 323–332 (2018)
90. J.C. Li et al., Hyaluronic acid-modified Fe3O4@Au core/shell nanostars for multimodal imaging and photothermal therapy of tumors. Biomaterials **38**, 10–21 (2015)
91. Y.C. Chen et al., Paclitaxel and iron oxide loaded multifunctional nanoparticles for chemotherapy, fluorescence properties, and magnetic resonance imaging. J. Biomed. Mater. Res. A **100A**(5), 1279–1292 (2012)
92. N. Kostevsek et al., The one-step synthesis and surface functionalization of dumbbell-like gold-iron oxide nanoparticles: a chitosan-based nanotheranostic system. Chem. Commun. **52**(2), 378–381 (2016)
93. S.D. Yang et al., Nucleolin-targeting AS1411-aptamer-modified graft polymeric micelle with dual pH/redox sensitivity designed to enhance tumor therapy through the codelivery of doxorubicin/TLR4 siRNA and suppression of invasion. Mol. Pharm. **15**(1), 314–325 (2018)
94. C. Tassa, S.Y. Shaw, R. Weissleder, Dextran-coated iron oxide nanoparticles: a versatile platform for targeted molecular imaging, molecular diagnostics, and therapy. Acc. Chem. Res. **44**(10), 842–852 (2011)
95. M.J. Jeon et al., The intratumoral administration of ferucarbotran conjugated with doxorubicin improved therapeutic effect by magnetic hyperthermia combined with pharmacotherapy in a hepatocellular carcinoma model. J. Exp. Clin. Cancer Res. **33**(1), 57 (2014)
96. M.L. Peng et al., Dextran-coated superparamagnetic nanoparticles as potential cancer drug carriers in vivo. Nanoscale **7**(25), 11155–11162 (2015)
97. W.H. Chen et al., Composites of aminodextran-coated Fe3O4 nanoparticles and graphene oxide for cellular magnetic resonance imaging. ACS Appl. Mater. Interfaces **3**(10), 4085–4091 (2011)

98. J.H. Park et al., Magnetic iron oxide nanoworms for tumor targeting and imaging. Adv. Mater. **20**(9), 1630–1635 (2008)
99. J.A. Champion, S. Mitragotri, Role of target geometry in phagocytosis. Proc. Natl. Acad. Sci. U. S. A. **103**(13), 4930–4934 (2006)
100. D. Li et al., A bio-inspired rod-shaped nanoplatform for strongly infecting tumor cells and enhancing the delivery efficiency of anticancer drugs. Adv. Funct. Mater. **26**(1), 66–79 (2016)
101. J.A. Champion, S. Mitragotri, Shape induced inhibition of phagocytosis of polymer particles. Pharm. Res. **26**(1), 244–249 (2009)
102. Z. Liu et al., In vivo biodistribution and highly efficient tumour targeting of carbon nanotubes in mice. Nat. Nanotechnol. **2**(1), 47–52 (2007)
103. M.J. Ernsting et al., Factors controlling the pharmacokinetics, biodistribution and intratumoral penetration of nanoparticles. J. Control. Release **172**(3), 782–794 (2013)